

---

---

# **Nuclear Physics in a finite volume: Investigation of two-particle and $\alpha$ -cluster systems**

---

---

DISSERTATION  
ZUR  
ERLANGUNG DES DOKTORGRADES (DR. RER. NAT.)  
DER  
MATHEMATISCH-NATURWISSENSCHAFTLICHEN FAKULTÄT  
DER  
RHEINISCHEN FRIEDRICH-WILHELMS-UNIVERSITÄT BONN

VORGELEGT VON

**GIANLUCA STELLIN**

AUS  
PADUA, ITALIEN



Bonn, 2020

Angefertigt mit Genehmigung der Mathematisch-Naturwissenschaftlichen Fakultät der  
Rheinischen Friedrich-Wilhelms-Universität Bonn

1. Gutachter:	Prof. Dr. Dr. h.c. Ulf-G. Meißner
2. Gutachter:	Prof. Thomas Luu, Ph.D.
Tag der Promotion:	17.12.2020
Erscheinungsjahr:	2021

<b>Metadata</b>	<b>v</b>
<b>Acknowledgements</b>	<b>vii</b>
<b>Preface</b>	<b>ix</b>
 <b>I Two-particle bound and scattering states in a finite volume including Quantum Electrodynamics</b>	 <b>1</b>
<b>1 Effective Field Theory for non-relativistic fermions</b>	<b>3</b>
1.1 Preamble . . . . .	3
1.2 Infinite-volume formalism . . . . .	6
1.2.1 The inclusion of QED . . . . .	8
1.3 Finite volume formalism . . . . .	13
<b>2 S-Wave short-range interactions</b>	<b>17</b>
2.1 Two-body scattering in infinite volume . . . . .	18
2.1.1 Coulomb corrections . . . . .	20
2.1.2 Repulsive channel . . . . .	22
2.1.3 Attractive channel . . . . .	25
2.2 The finite-volume environment . . . . .	27
2.2.1 Quantization Condition . . . . .	27
2.2.2 Finite Volume Effective Range Expansion . . . . .	32
2.2.3 Approximate Energy Eigenvalues . . . . .	33
a) The Unbound Ground State . . . . .	34
b) The Bound Ground State . . . . .	37
<b>3 P-Wave short-range interactions</b>	<b>41</b>
3.1 Two-body scattering in infinite volume . . . . .	42
3.1.1 Coulomb corrections . . . . .	44
3.1.2 Repulsive channel . . . . .	47
3.1.3 Attractive channel . . . . .	54
3.2 The finite-volume environment . . . . .	59

3.2.1	Quantization Condition	60
3.2.2	Finite Volume Effective Range Expansion	66
3.2.3	Approximate Energy Eigenvalues	67
a)	The Lowest Unbound State	67
b)	The Lowest Bound State	75
3.3	Outlook	78

## II Breaking and restoration of rotational symmetry in the low energy spectrum of light $\alpha$ -conjugate nuclei on the lattice 81

<b>4</b>	<b>Formalism and numerical techniques</b>	<b>83</b>
4.1	Preamble	83
4.2	Theoretical framework	85
4.2.1	The Hamiltonian	85
4.3	Operators on the lattice	86
4.3.1	Kinetic energy	87
4.3.2	Potentials	90
4.3.3	Angular momentum	90
4.4	Symmetries	93
4.5	Physical Observables	95
4.5.1	Space coordinates	96
4.5.2	Binding energy	97
4.5.3	Multiplet averaging	97
4.6	Boundary conditions	97
4.7	Deterministic approaches	98
4.7.1	The Lanczos algorithm	98
a)	Parallel implementation	100
4.7.2	The Adiabatic Projection Method	101
4.8	Stochastic approaches	103
4.8.1	The Worldline Monte Carlo algorithm	104
a)	The extension to excited states	110
<b>5</b>	<b>The <math>^8\text{Be}</math> nucleus</b>	<b>115</b>
5.1	The spectrum	115
5.2	The $0_1^+$ and $2_1^+$ energy levels	117
5.3	The $4_2^+$ and $6_1^+$ energy levels	123
<b>6</b>	<b>The <math>^{12}\text{C}</math> nucleus</b>	<b>131</b>
6.1	The spectrum	131
6.2	The $0_1^+$ , $2_1^+$ and $3_1^-$ energy levels	133
<b>7</b>	<b>The <math>^{16}\text{O}</math> nucleus</b>	<b>141</b>
7.1	The spectrum	141
7.2	The $0_1^+$ and $2_1^+$ energy levels	144
7.3	The $2_1^-$ and $3_1^+$ energy levels	148
7.4	The $3_1^-$ and $4_1^-$ energy levels	151

---

<b>8 Variational calculation of the strength parameter of the three-body potential in the <math>\alpha</math>-cluster model for <math>^{16}\text{O}</math></b>	<b>155</b>
8.1 Preamble . . . . .	155
8.2 The Hamiltonian . . . . .	157
8.3 The model space . . . . .	158
8.4 The matrix elements . . . . .	160
8.5 Estimation of the parameters . . . . .	166
8.5.1 Optimized approach . . . . .	166
8.5.2 Non-optimized approach . . . . .	168
<b>Summary</b>	<b>173</b>
<b>Appendices</b>	<b>177</b>
A.1 Feynman rules . . . . .	179
A.2 Integrals in Dimensional Regularization . . . . .	179
A.3 Three dimensional integrations . . . . .	184
A.4 Dirac Delta function . . . . .	187
B.1 Three-dimensional Riemann sums . . . . .	189
B.1.1 Single sums . . . . .	189
B.1.2 Double Sums . . . . .	193
B.2 Lüscher functions . . . . .	197
B.2.1 The $S_2$ sum . . . . .	198
B.2.2 The $S_3$ sum . . . . .	204
C.1 Discretization of derivatives . . . . .	209
C.2 Vandermonde Matrices . . . . .	213
C.3 The cubic group . . . . .	215
<b>List of publications</b>	<b>223</b>
<b>Bibliography</b>	<b>225</b>

---



**Title:** Nuclear Physics in a finite volume: Investigation of two-particle and  $\alpha$ -cluster systems

**Abstract:** In this dissertation we investigate both analytically and numerically some artifacts introduced by the lattice environment in two-body charged fermion and antifermion systems and in  $\alpha$ -conjugate nuclei. The finite (hyper)cubic lattice as a surrogate of the continuum and infinite-volume configuration space represents the context in which the properties of compounds of quarks or nucleons are computationally investigated in nuclear and subnuclear physics. The modified topology of the space in which many-body wave functions and fields find their support produces sizable changes in the average values of physical observables and namely energy eigenvalues, that can be controlled by reducing the lattice spacing and increasing the number of mesh points.

The first problem that we address in this thesis concerns the finite-volume energy corrections for two-fermion bound and scattering states in a cubic finite volume in presence of strong and electromagnetic interactions. After reviewing the formalism of pionless Effective Field Theory and non-relativistic Quantum Electrodynamics, we derive the amplitude and the leading order scattering parameters for the two-body elastic scattering process in the presence of a strong interaction that couples the fermion fields to zero angular momentum. Then, the latter is replaced by a P-wave strong interaction, and new scattering amplitudes are obtained, accounting again for the Coulomb photon exchanges to all orders in the fine-structure constant. Motivated by the research on particle-antiparticle bound states, we extend the results to fermions of identical mass and opposite charge. Second, we transpose the system onto a cubic box with periodic boundary conditions and we calculate the finite volume corrections to the energy of the lowest bound and unbound  $T_1$  eigenstates, which are the finite-volume counterpart of the states transforming as the  $\ell = 1$  irreducible representation (irrep) of the rotation group. The procedure for the derivation of the mass shifts for the lowest  $A_1$  states, *i.e.* transforming as the  $\ell = 0$  irrep of  $SO(3)$ , is also reviewed. In particular, power law corrections proportional to the fine structure constant and resembling the recent results for S-wave states are found. Higher order contributions in  $\alpha$  are neglected, since the gapped nature of the momentum operator in the finite-volume environment allows for a perturbative treatment of the QED interactions.

The second main thread of this thesis covers the breaking of rotational symmetry in the low-energy spectrum of the three lightest  $A = 4N$  self-conjugate nuclei on the lattice. In this part, that may be regarded as the numerical continuation of the previous one, a macroscopic  $\alpha$ -cluster model is used for investigating the general problems associated with the representation of the nuclear many-body problem on a cubic lattice. In the context of a descent from the three-dimensional rotation group to the cubic group symmetry, the role of the squared total

angular momentum operator in the classification of the lattice eigenstates in terms of  $SO(3)$  irreps is discussed. In particular, the behaviour of the average values of the latter operator, the Hamiltonian and the inter-particle distance as a function of lattice spacing and size is studied by considering the  $0_1^+$ ,  $2_1^+$ ,  $4_1^+$  and  $6_1^+$  states of  $^8\text{Be}$ , the  $0_1^+$ ,  $2_1^+$  and  $3_1^-$  states of  $^{12}\text{C}$  and the  $0_1^+$ ,  $2_1^\pm$ ,  $3_1^\pm$  and  $4_1^-$  states of  $^{16}\text{O}$ . Among these, special attention is reserved to the ground states, from which the binding energies,  $BE(N, Z)$ , of the three nuclei depend. It is found that  $BE(6, 6)$  is faithfully reproduced in the infinite volume limit by construction, whereas  $BE(4, 4)$  and  $B(8, 8)$  display shifts of 1.2 and 10.9 MeV, respectively.

As a consequence, the concluding part of the work is dedicated to the fitting of the strength parameter,  $V_3$ , of the three-body potential of the adopted  $\alpha$ -cluster model to the  $4\alpha$  and the  $\alpha + ^{12}\text{C}$  thresholds of  $^{16}\text{O}$ . For the purpose, the variational calculation developed on three body relative harmonic oscillator states is adopted and the relevant matrix elements are expressed in terms of standard Moshinsky brackets. The extracted values of  $V_3$  at increasing dimensions of the truncated basis are exploited for the extraction of the estimation of the expectation value of the parameter.

**Keywords:** Electromagnetic Processes and Properties, Two-Nucleon System, Lattice Gauge Theory, Few-Body Systems, Rotational Symmetry, Nuclear Structure Models and Methods, Cluster Models, Point Groups, Variational Calculation, Moshinsky Brackets



## ACKNOWLEDGEMENTS

The results presented in this thesis are essentially fruit of my work, carried out under the supervision of Prof. Dr. Ulf-G. Meißner, that I thank for the constance (and the patience) with which he followed the progress of my projects. Especially in the first two years, I have benefitted from the close collaboration with Dr. Serdar Elhatisari, whose assistance in the early phase of my project turned out to be essential for addressing a computational problem apparently out of reach on the path towards its solution. Despite the distance, our collaboration in the past two years permitted to develop also the necessary stochastic algorithms for the extraction of the energy eigenvalues of  $^{16}\text{O}$  in a regime in which the storage itself of numerical eigenvectors becomes prohibitive for any available computational resource. Even our apparently fruitless experience with the implementation of Auxiliary Field Monte Carlo algorithm provided me a precious insight on how the nuclear few-body problem is solved in the framework of lattice Effective Field Theory for pions and nucleons. Rather more oriented in overcoming the obstacles imposed by the hardware limitations than in the formal aspects, he measured up to share part of his vast computational knowledge, whose scope extend far beyond my reasearch project. Additionally, I can not but express my gratitude to Dr. Bing Nan Lu and Dr. Sebastian König for introducing me to lattice calculations, derivative discretization schemes and finite-volume corrections.

Then, I wish to express some words of thanks to whom I consider the bridge between the two main projects of my doctorate, Prof. Dr. Dean Lee, who enriched the analysis of the low-energy spectrum of  $\alpha$ -conjugate nuclei with suggestions and inspired the analytical part of my researches at HISKP. Secondly, I acknowledge the collaboration of PD Dr. Akaki Ruetsky and Dr. Andria Agadjanov, which provided assistance and advice during the delicate stages of the carrying out of the analytical part of this dissertation. Even if their influence in the development of my research project was minor, I wish to thank Ferenc Pittler and Maxim Mai, former members of the theory division of the HISKP and Wael Elkamhawy from TU Darmstadt. Besides his field-theoretical expertise, Andria Agadjanov in the recent years has been - together with his brother Dimitri - also a friendly and supportive colleague, beyond scientific matters.

I also owe a lot to my colleagues Dr. Naeem Muhammad Anwar, Dr. Meng Lin Du, Chaitra Kalmahalli Guruswamy, Bai Long Hoid, Dr. Nico Klein, Dr. Mikhail Mikhasenko, Fabian Müller, Dr. Stefan Ropertz, Nikolas Schlage, Martin Ueding, Dr. Guang Juan Wang and Falk Zimmermann for the discussions and some free time spent together. The lively and rich academic environment of the university of Bonn gave me the opportunity to compare myself with doctoral students of other disciplines, among these Sahar Brahim, Catia Domingos, Dr. Francesca Lopez, Vittoria Lopez and Dr. Javier Muro. Additionally I express gratitude

to Amitayus Banik, Bardia Najjari Farizhendi, Inka Hammer, Christopher Nega, Dr. Urmi Ninad, Johann Ostmeyer and Benoit Scholtes, with which I have had the occasion to collaborate during the preparation of the exercise lessons for the courses of *Group Theory* and *General Relativity and Cosmology* during the winter and summer terms in the academic years 2017/2018 and 2018/2019 at the University of Bonn. Next, I express words of thanks to Dieter An Mey, Paul Kapinos, Dr. Timo A. Lähde, Prof. Dr. Tom C. Luu, Dr. Andreas Nogga and Alexandre Strube for making it possible for me to exploit the computational resources of the Forschungszentrum Jülich (PAJ 1830 test project) and the Rheinisch-Westfälische Technische Hochschule Aachen (JARA 0015 project), with their supercomputing machines *Jureca* and *Claix*, respectively. The technical assistance they offered proved to be essential for the proper exploitation of the resources and the development of the numerical calculations.

Then I cannot but acknowledge the financial support from the Deutsche Forschungsgemeinschaft (Sino-German CRC 110, grant No. TRR 110) and the VolkswagenStiftung (grant No. 93562), that has been indispensable for this crucial part of my educational path. Thanks to my thesis advisor, Prof. Dr. Ulf-G. Meißner, and the secretaries of the HISKP, I have also had the unique opportunity to take part in scientific conferences and workshops abroad. Among these, I mention the General Meeting of the CRC 110 collaboration held at the Institute of Physics in Peking (Haidian District), the 57th International Winter Meeting on Nuclear Physics in Bormio and the 7th RDP School and Workshop in Tbilisi. In the latter two meetings, a significant part of the results reported in this thesis has been presented, arousing the interest, in particular, of Prof. Dr. Pierre Capel and Dr. Maral Salajegheh.

I seize also the occasion to thank my B.Sc and M.Sc. thesis supervisor, Prof. Dr. Lorenzo Fortunato, together with Prof. Dr. Andrea Vitturi for my participation to the 8th and 9th editions of the Quantum Phase Transitions in Nuclei and Many-Body Systems workshop held in Prague and Padova, respectively. In the two events, the material of my first two scientific publications has been presented to the audience and I acknowledge some discussions with the professors Amiram Leviatan, Curro Perez-Bernal, Roelof Bijker, Jerzy Dudek, Francesco Iachello and the researcher Kosuke Nomura.

This thesis would have not come into being without the moral and material support of my parents, Paolo and Flavia, and my sister Tatiana, her boyfriend Emanuele and my aunt Laura, that helped me during the relocation from Padova to Bonn. The distance did not succeed in interrupting the relations with the other relatives and friends, such as Gianluca Greggio and Irene Cazzaro. A special mention goes to my twin brother Filippo, that followed a nearly-overlapping academical path at the University of Padova, eventually specializing in condensed matter physics. After his Master's degree, he carried out his Ph.D. at the Université Paris Diderot, where he defended the thesis on *Anderson Localization* of interacting quantum particles few months ago. Afterwards, he joined the École Normale Supérieure Paris Saclay as a postdoctoral researcher. These facts permitted me to benefit of a person capable of delivering appropriate advice and contributing ideas as a forge almost all the time, despite being away. At the same time, I have had the chance to keep sporadically the contact with another academic environment, the Laboratoire Matériaux et Phénomènes Quantiques, of which I remember Dr. Jared Lolli, Prof. Dr. Giuliano Orso, Cassia Naudet Beaulieu, Dr. Manpreet Singh, Dr. Mario Spagnuolo and Dr. Florent Storme.

*Gianluca Stellin*

The present dissertation focuses on two main issues, *two-particle bound and scattering states in a finite volume including Quantum Electrodynamics* and *breaking and restoration of rotational symmetry in the low energy spectrum of light  $\alpha$ -conjugate nuclei on the lattice*. Hence we have considered it appropriate to organize the material into two distinct threads, *Part I* and *Part II*. Each of the two begins with an explanatory chapter, with a preamble that contextualizes the investigation and recapitulates the major advances on the topic achieved in the past. The introduction is followed by an extended summary of the formalism which provides the theoretical framework to the results presented in the subsequent chapters. The concepts, formulas, algorithms and notation contained in this introductory chapter are often borrowed from existing literature, therefore the already experienced reader is encouraged to skip (at least) part of this material. Conversely, the chapters that follow hold predominantly the fruits of the new investigation and are opened by a short summary of their content. The only exception is represented by chap. 2, which can be considered as a summary of the work in ref. [1], albeit enriched with the details of the calculations and endowed by a partly new notation.

Concerning *Part I*, its main goal is the analytical understanding of the distortions induced by a finite cubic configuration space on the energy eigenvalues and eigenfunctions of two fermions subject to both strong and electromagnetic interactions. After a review of the main results in ref. [2] and [1] for S-wave strong interaction in chap. 2, low energy fermion-fermion and fermion-antifermion scattering under the action of a P-wave short-range potential and non relativistic QED is analysed in both the finite and the infinite volume environment. The treatment, then, culminates with the presentation of the finite volume energy corrections for the lowest bound and scattering states transforming as a  $T_1$  irreducible representation (irrep) of the cubic group, the counterpart of the  $\ell = 1$  irrep of  $SO(3)$  in the cubic finite volume. The material in app. 8.5.2 and 8.5.2 provides support for analytical derivation of the latter formulas and reserves special attention to the numerical evaluation of three-dimensional Riemann sums, appearing in the power series expansions of the Lüscher functions in chap. 3. Since the cubic lattice is a common playground for numerical simulations in nuclear and subnuclear physics, the obtained closed expressions may find an immediate application in systems of hadrons in the low-energy regime.

The second part, instead, is devoted to the numerical analysis of the artifacts introduced by the lattice environment - namely finite volume and discretization effects - to eigenvalues and average values of physical observables for the three lightest  $\alpha$ -conjugate nuclei,  $^8\text{Be}$ ,  $^{12}\text{C}$  and  $^{16}\text{O}$ . The framework for the investigation is provided by the macroscopic  $\alpha$ -cluster model in ref. [3], according to which strong interactions are modeled by a superposition of an Ali-

Bodmer potential [4] and a  $3\alpha$  Gaussian potential [5]. Attached to the introductory chapter, in which the latter model is reviewed, is app. B.2.2, where the discretization scheme for the differential operators is presented in detail and the cubic group is recalled, paying attention to the connection between the latter and the rotation group in the three-dimensional space. In chap. 5-7, the behaviour of the energy eigenvalue and the average values of the squared angular momentum and the  $\alpha$ - $\alpha$  separation as a function of lattice spacing and size are studied in the  $0_1^+$ ,  $2_1^+$ ,  $4_2^+$  and  $6_1^+$  (artificial) bound states of  $^8\text{Be}$ , in the  $0_1^+$ ,  $2_1^+$  and  $3_1^-$  multiplets of  $^{12}\text{C}$  and in the  $0_1^+$ ,  $2_1^\pm$ ,  $3_1^\pm$  and  $4_1^-$  of  $^{16}\text{O}$ . Subsequently, the results of a variational calculation for the fitting of the strength parameter of the three-body potential to the  $\alpha+^{12}\text{C}$  and  $4\alpha$  decay thresholds of  $^{16}\text{O}$  are presented. As hinted in chap. 7, in fact, the parameters of the  $3\alpha$  Gaussian interaction in the model in ref. [3] underbind the  $^{16}\text{O}$  nucleus by  $\approx 11$  MeV. Although the results of chap. 8 have not been employed for the analysis in chap. 7, they may find immediate application in the reconstruction of the low-energy spectrum and the basic properties of the nucleus, to be benchmarked with other  $\alpha$ -cluster models such as the ones in refs. [6] and [7,8]. The ordering of the chapters in *Part II* finds, thus, its justification. After chap. 8, the summary of the work in the body of the dissertation is presented together with the conclusions and some hints for an extension of the analysis in chaps. 5-7, whereas the perspectives of the investigations in chaps. 3 and 7 are outlined in the last sections of the respective chapters.

## **Part I**

# **Two-particle bound and scattering states in a finite volume including Quantum Electrodynamics**



# CHAPTER 1

## EFFECTIVE FIELD THEORY FOR NON-RELATIVISTIC FERMIONS

### 1.1 Preamble

Effective Field Theories [9–16] nowadays play a fundamental role in the description of many-body systems in nuclear and subnuclear physics, employing the quantum fields which can be excited in a given regime of energy. Once the breakdown scale  $\Lambda$  of the EFT is set, the scattering amplitudes are usually expressed in power series of  $p/\Lambda$ , where  $p$  represents the characteristic momentum of the processes under consideration. The Lagrangian density is typically written in terms of local operators of increasing dimensions obeying pertinent symmetry constraints.

Moreover, power counting rules establish a hierarchy among the interaction terms to include in the Lagrangian, thus permitting to filter out the contributions that become relevant only at higher energy scales [15].

In the case of systems of stable baryons at energies lower than the pion mass, the Lagrangian density contains only the nucleon fields and their Hermitian conjugates, often combined together with differential operators. The corresponding theory, the so-called pionless EFT [10, 17–20] counts a number of successes in the description of nucleon-nucleon scattering and structure properties of few-nucleon systems. Despite the original difficulties in the reproduction of S-wave scattering lengths, that were solved via the introduction of the Power Divergence Subtraction (PDS) as a regularization scheme [18, 21, 22], the theory has permitted so far to reproduce the  $^1S_0$   $np$  phase shift [23, 24], structure properties of the triton as a  $dn$  S-wave compound [20, 25, 26] and the scattering length [27, 28] and the phase shift [29–31] of the elastic  $dn$  scattering process.

In the first applications of QED in pionless EFT, the electromagnetic interactions were treated perturbatively, as in the case of the electromagnetic form factor [32] and electromagnetic polarizability [33] for the deuteron or the inelastic process of radiative neutron capture on protons [34]. Afterwards, a non-perturbative treatment of electromagnetic (Coulomb) interactions on top of the same EFT was set up, in the context of proton-proton S-wave elastic [2] and inelastic [35, 36] scattering. The formalism of ref. [2] and part of its results are reviewed in the first part of next chapter.

Inspired by the P-wave interactions presented in refs. [37–39], we generalize in secs. 3.1 and 3.1.1–3.1.3 of chap. 3 the analysis in ref. [2] to fermion-fermion low-energy elastic scattering

ruled by the interplay between the Coulomb and the strong forces transforming as the  $\ell = 1$  representation of the rotation group (cf. ref. [40] for the empirical S- and P-wave phase shifts in the  $pp$  case). As in ref. [2], we treat the Coulomb photon exchanges both in a perturbative and in a non-perturbative fashion. During the derivation of the T-matrix elements, we observe that at sufficiently low energy, the repulsion effects from the Coulomb ladders become comparable to the ones of the strong forces, leading to the breakdown of the perturbative regime of non-relativistic QED. In the determination of the closed expressions for the scattering parameters in terms of the coupling constants, we take advantage of the separation of the Coulomb interaction from the strong forces, proposed first in refs. [41, 42] and eventually generalized to strong couplings of arbitrary angular momentum  $\ell$  in ref. [43]. The importance of particle-antiparticle systems led us to the application of the formalism to fermion-antifermion scattering, where the attractive Coulomb force gives rise to bound states. This case provides a laboratory for the study of  $p\bar{p}$  bound [44] and unbound states [45], also referenced as *protonium*.

Of fundamental importance for the study of few- and many-particle systems with QED are Lattice Effective Field Theories and Lattice Quantum Chromodynamics (LQCD). The latter has matured to the point where basic properties of light mesons and baryons are being calculated at or close to the physical pion mass [46, 47]. In particular, in the case of the lowest-lying mesons, their properties are attaining a level of accuracy where it is necessary to embed the strong interactions within the full standard model [48–53]. Despite the open computational challenges represented by the inclusion of the full QED in LQCD simulations, in the last decade quenched QED [54] together with flavour-symmetry violating terms have been included in the Lagrangian, with the aim of reproducing some features of the observed hadron spectrum [55–63].

Conversely, the perspective to add QED interactions in LQCD simulations for systems with more than three nucleons appears still futuristic, due to the limitations in the computational resources. Nevertheless, the interplay between QCD and QED has been very recently explored also in the ground state energy of bound systems up to three nucleons like deuteron,  ${}^3\text{H}$  and  ${}^3\text{He}$  in ref. [64]. Additionally, in two-body processes like  $\pi^\pm\pi^\pm$  [64–66],  $\bar{K}^0\bar{K}^0$  [64] and nucleon-meson scattering [64], time is ripe for the introduction of electromagnetic interactions in the present LQCD calculations.

It is exactly in this context that, in the second part of chap. 2 and 3, we immerse our fermion-fermion EFT into a cubic box with periodic boundary conditions (PBC). The finite-volume environment has a number of consequences, the most glaring of them are the breaking of rotational symmetry [3, 67–69] and the discretization of the spectrum of the operators representing physical observables [70–72]. Concerning the Hamiltonian, its spectrum consists of levels that in the infinite-volume limit become part of the continuum (scattering states) and in others that are continuously transformed into the bound states. For two- and three-body systems governed by strong interactions, the shifts of the bound energy levels with respect to the counterparts at infinite volume depend on the spatial extent of the cubic volume  $L$  through negative exponentials, often multiplied by nontrivial polynomials in  $L$ . Apart from the pioneering work on two-bosons subject to hard-sphere potentials in ref. [73], these effects for two-body systems have been extensively analyzed by Lüscher in refs. [74, 75] ([76]), where the energy of the lowest unbound (bound) states has been expressed in terms of the scattering parameters and the box size.

In the last three decades, Lüscher formulas for the energy shifts have been extended in



several directions including non-zero angular momenta [71, 77–79] moving frames [79–85], generalized boundary conditions [86–91] and particles with intrinsic spin [92, 93]. Moreover, considerable efforts have been made in the derivation of analogous formulas for the energy corrections of bound states of three-body [72, 94, 95] and N-body systems [96, 97]. See also the review [98].

However, the presence of the long-range interactions induced by QED leads to significant modifications in the form of the corrections associated to the finite volume energy levels. Irrespective on whether a state is bound or unbound, in fact, the energy shifts take the form of polynomials in the reciprocal of the box size [46] and the exponential damping factors disappear. Moreover, the gapped nature of the momentum of the particles in the box allows for a perturbative treatment of the QED contributions, even at low energies [1, 46, 47, 54, 99]. In this regime, composite particles receive corrections of the same kind both in their mass [46] and in the energies of the two-body states that they can form [1].

As shown in ref. [1] and in sec. 2.2.3 b) of chap. 2, the leading-order energy shift for the lowest S-wave bound state is proportional to the fine-structure constant and has the same sign of the counterpart in absence of QED, presented in refs. [71, 77]. In sec. 3.2.3 b) of chap. 3, we demonstrate that the same relation holds for the lowest bound P-wave state, whose finite volume correction is negative as the one for the counterpart without electromagnetic interactions. Additionally, we prove that the QED energy-shifts for S- and P-wave eigenstates have the same magnitude if order  $1/L^3$  terms are neglected, a fact that remains valid in the absence of interactions of electromagnetic nature. At least for the  $\ell = 0$  and 1 two-body bound eigenstates, in fact, the sign of the correction depends directly on the parity of the wavefunction associated to the energy state, whose tails are truncated at the boundaries of the cubic box, as observed in ref. [71].

Although bound states between two hadrons of the same charge have not been observed in nature, at unphysical values of the quark masses in Lattice QCD these states do appear [100–103]. It is possible that such two-body bound states manifest themselves also when QED is included in the Lagrangian. Moreover, two-boson bound states originated by strong forces are expected to explain certain features of heavy quark compounds. In particular, the interpretation of observed lines  $\Upsilon(4626)$ ,  $\Upsilon(4630)$  and  $\Upsilon(4660)$  of the hadron spectrum in terms of P-wave  $[cs][\bar{c}\bar{s}]$  tetraquark states with  $1^{--}$  seems promising [104].

Pairwise interesting are recent studies on proton-proton collisions, which revealed the presence of intermediate P-wave  $\Delta N$  states with spin 0 and 2 at 2.197(8) and 2.201(5) GeV respectively, see ref [105]. Although these states are not classified as *dibaryons* [106] because of their large decay width ( $\Gamma \gtrsim 100$  MeV) [105, 107], an attractive force appears to lower the expected energy of the  $\Delta - N$  system by  $\approx 30$  MeV.

Additionally, loosely bound binary compounds of hadrons appearing in the vicinity of a P-wave strong decay threshold are not forbidden by the theory of hadronic molecules [108]. Possible candidates of such two-body systems are represented by the hidden charm pentaquark states  $P_c^+(4380)$  and  $P_c^+(4450)$ , located slightly below the  $\bar{D}\Sigma_c^*$  and  $\bar{D}^*\Sigma_c$  energy thresholds at 4385.3 MeV and 4462.2 MeV, respectively. Although a wide variety of different studies on the two states have been conducted [109–111], a very recent one advances the molecular hypothesis [112] with orbital angular momentum equal to one in the framework of heavy quark spin symmetry (HQSS).

Concerning scattering states, the energy shift formula for the lowest P-wave state that we

derive in sec. 3.2.3 a) of chap. 3 has close similarities with the one in ref. [1] and reviewed in sec. 3.2.3 a) of chap. 2, despite an overall  $\xi/M \equiv 4\pi^2/ML^2$  factor, owing to the fact that the energy of the lowest unbound state with analogous transformation properties under discrete rotations ( $T_1$  irrep<sup>1</sup> of the cubic group) is different from zero. Additionally, further scattering parameters appear in the expression for the  $\ell = 1$  finite volume energy correction, even as coefficients of the smallest powers of  $1/L$ .

## 1.2 Infinite-volume formalism

Our analysis of two-particle scattering and bound states in the infinite- and finite-volume context is based on pionless Effective Field Theory [17, 18, 21, 22, 113–116]. The theory, developed more than two decades ago [17], describes the strong interactions between nucleons at energy scales smaller than the pion mass,  $M_\pi$  [2, 15, 113]. In this regime the matter fields are non-relativistic and the nature of the problem allows for the introduction of a small expansion parameter  $|\mathbf{p}|/M$ , where  $\mathbf{p}$  is a typical three-momentum in the system (soft scale) and  $M$  is a mass of a non-relativistic particle (hard scale) [117]. The non-relativistic action is constructed by including all the possible potential terms made of nucleon fields and their derivatives, fulfilling the symmetry requirements of the strong interactions at low energies, that is parity, time reversal and Galilean invariance [117]. The importance of the various interaction terms decreases with their canonical dimension while approaching the zero-energy limit. Besides, even the dominant contribution at low energies for local contact interactions between four-nucleon fields is of dimension six, thus making the theory non-renormalizable [2] in the classical sense.

Analogously to ref. [1], we begin by extending pionless EFT to spinless fermions of mass  $M$  and charge  $e$ , and we assume that the theory is valid below an upper energy  $\Lambda_E$  in the center-of-mass frame (CoM). More specifically, if the fermions represent hadrons, the latter energy cutoff can be chosen to coincide with the pion mass. In this reference frame, each fermion propagates according to the Feynman rule in app. A.1 (cf. the solid line in fig. A.3) and the two-body retarded (+) and advanced (−) unperturbed Green's function operator reads,

$$\hat{G}_0^{(\pm)}(E) = \frac{1}{E - \hat{H}_0 \pm i\epsilon} , \quad (1.1)$$

where  $\hat{H}_0$  is the two-body free Hamiltonian in relative coordinates,  $\hat{H}_0 = \hat{\mathbf{p}}^2/M$ , and  $M/2$  is the reduced mass of a system of identical fermions. Inserting a complete set of plane wave eigenstates  $|\mathbf{q}\rangle$  in the numerator, the latter expression becomes

$$\hat{G}_0^{(\pm)}(E) = M \int_{\mathbb{R}^3} \frac{d^3q}{(2\pi)^3} \frac{|\mathbf{q}, -\mathbf{q}\rangle \langle \mathbf{q}, -\mathbf{q}|}{\mathbf{p}^2 - \mathbf{q}^2 \pm i\epsilon} , \quad (1.2)$$

where  $\pm \mathbf{p}$  ( $\pm \mathbf{q}$ ) are the three-momenta of two incoming (outcoming) particles in the CoM frame, such that  $|\mathbf{p}| = |\mathbf{q}|$  and  $E = \mathbf{p}^2/M$  is the energy eigenvalue at which the retarded (+) and advanced (−) Green's functions are evaluated. In configuration space the latter take the form

$$\langle \mathbf{q}, -\mathbf{q} | \hat{G}_0^{(\pm)}(E) | \mathbf{p}, -\mathbf{p} \rangle = \frac{(2\pi)^3 \delta(\mathbf{p} - \mathbf{q})}{E - \mathbf{p}^2/M \pm i\epsilon} , \quad (1.3)$$

---

<sup>1</sup>Throughout, we use the abbreviation “irrep” for an irreducible representation.

that is diagrammatically depicted by two propagation lines.

Second, we construct the interactions in terms of four-fermion operators, selecting the ones that transform explicitly as the  $2\ell + 1$ -dimensional irreducible representation of  $\text{SO}(3)$ ,

$$V^{(\ell)}(\mathbf{p}, \mathbf{q}) \equiv \langle \mathbf{q}, -\mathbf{q} | \hat{\mathcal{V}}^{(\ell)} | \mathbf{p}, -\mathbf{p} \rangle = \left( c_0^{(\ell)} + c_2^{(\ell)} \mathbf{p}^2 + c_4^{(\ell)} \mathbf{p}^4 + \dots \right) \mathcal{P}_\ell(\mathbf{p} \cdot \mathbf{q}) \quad (1.4)$$

where  $\mathcal{P}_\ell$  is a Legendre polynomial,  $\hat{\mathcal{V}}^{(\ell)}$  is the potential in terms of second quantized operators and the  $c_{2j}^{(\ell)}$  are low-energy (LECs) constants, whose importance at low-energy scales diminishes for increasing values of  $j$ . In particular, for the three lowest angular momentum couplings ( $\ell \leq 2$ ), the interaction potentials take the form

$$V^{(0)}(\mathbf{p}, \mathbf{q}) = C_0 + C_2 \mathbf{p}^2 + C_4 \mathbf{p}^4 + \dots, \quad (1.5)$$

$$V^{(1)}(\mathbf{p}, \mathbf{q}) = \left( D_0 + D_2 \mathbf{p}^2 + D_4 \mathbf{p}^4 + \dots \right) \mathbf{p} \cdot \mathbf{q}, \quad (1.6)$$

and

$$V^{(2)}(\mathbf{p}, \mathbf{q}) = \left( F_0 + F_2 \mathbf{p}^2 + F_4 \mathbf{p}^4 + \dots \right) \left[ 3(\mathbf{p} \cdot \mathbf{q})^2 - 1 \right]. \quad (1.7)$$

As shown in sec. II of ref. [1], the terms within the round brackets in eq. (1.5) (eqs. (1.6) and (1.7)), that represent polynomials with even powers of the momentum (a gradient expansion in configuration space), can be encoded by a single interaction with energy-dependent coefficient  $C(E^*)$  ( $D(E^*)$  and  $F(E^*)$ ) for S-waves (P- and D-waves), where  $E^*$  represents the CoM energy of the colliding particles, equal to  $2M + \mathbf{p}^2/M$ . In particular, the case of fermions coupled to zero angular momentum via a single contact interaction proportional to  $C(E^*)$  is the starting-point of the analysis in ref. [1], that is subject of a detailed review in chap. 2.

On the other hand, the P-wave interaction in eq. (1.6) with energy-dependent coefficient  $D(E^*)$  becomes the key tool of our recent study in ref. [118] and presented in chap. 3. Although interactions of the same form had been already adopted in pionless EFT for nucleons (cf. eq. (4) in ref. [37]) and in EFT with dimeron fields (cf. eq. (2) in ref. [119]), the P-wave counterpart of Kong and Ravndal's analysis on fermion-fermion scattering in ref. [2] was not available in literature prior to our investigation [118]. For completeness, the potentials newly introduced permit to define the two-body retarded (+) and advanced (+) strong Green's function operator with  $\hat{V}_S \equiv \hat{\mathcal{V}}^{(\ell)}$ ,

$$\hat{G}_S^{(\pm)}(E) = \frac{1}{E - \hat{H}_0 - \hat{V}_S \pm i\epsilon}. \quad (1.8)$$

Combining the last equation with the definition of the free Green's function operators in eq. (1.1) a self-consistent identity between  $\hat{G}_S^{(\pm)}(E)$  and  $\hat{G}_0^{(\pm)}(E)$  can be obtained,

$$\hat{G}_S^{(\pm)} = \hat{G}_0^{(\pm)} + \hat{G}_0^{(\pm)} \hat{V}_S \hat{G}_S^{(\pm)}, \quad (1.9)$$

an operator that is intimately related to the two-body scattering T-matrix.

A quantity that is natural to calculate in a field theory, in fact, is the sum of Feynman graphs pertinent to a few-body process, which originates the T-matrix element [18]. In the case of two-body scattering ruled by central short range forces the latter quantity, that we denote as

$T_S$ , is independent on the azimuthal angle  $\phi$ <sup>2</sup> and can be expanded in partial waves,

$$T_S(\mathbf{p}', \mathbf{p}) = -\frac{4\pi}{M} \sum_{\ell=0}^{+\infty} (2\ell+1) \left[ \frac{e^{2i\delta_\ell} - 1}{2i|\mathbf{p}|} \right] \mathcal{P}_\ell(\cos \theta) , \quad (1.10)$$

where  $\theta$  is the elevation angle and  $\delta_\ell$  is the phase shift, which is real under the constraint of unitarity for the S-matrix. While the T-matrix is singular in the zero momentum limit and displays a branch cut in the  $p^2$  axis, the quantity  $\mathbf{p}^{2\ell} \cot \delta_\ell$  admits an expansion in power series of  $\mathbf{p}^2$ , the *effective range expansion* (cf. eq. (5.20) in ref. [120]),

$$|\mathbf{p}|^{2\ell} \cot \delta_\ell = -\frac{1}{a^{(\ell)}} + \frac{1}{2} r_0^{(\ell)} \mathbf{p}^2 + r_1^{(\ell)} \mathbf{p}^4 + r_2^{(\ell)} \mathbf{p}^6 + \dots , \quad (1.11)$$

where  $a^{(\ell)}$ ,  $r_0^{(\ell)}$  and  $r_1^{(\ell)}$  are the scattering length, the effective range and the shape parameter respectively. Eq. (1.11) is consistent with the one presented in eq. (2.6) of ref. [18], provided suitable negative powers of the breakdown scale,  $\Lambda \equiv \Lambda_E$ , for the EFT are reabsorbed in the definition of the scattering parameters. Since the importance of each of the  $r_n^{(\ell)}$  parameters with  $n = 0, 1, 2, \dots$  decreases as  $\Lambda_E^{2n-1}$ , the convergence of the expansion is ensured by a non-zero value of the scattering length.

Irrespectively on the angular momentum content of the strong interactions, the Feynman diagrams contributing to  $T_S$ , for the two-body fermion-fermion or fermion-antifermion scattering processes assume the form of chains of bubbles, whose ultraviolet divergence is enhanced by the positive powers of the momentum operator appearing in  $\hat{\mathcal{V}}^{(\ell)}$ . These diagrams will be shown and discussed explicitly in secs. 2.1 and 2.1.2 (secs. 3.1 and 3.1.2) for S-wave (P-wave) interactions.

### 1.2.1 The inclusion of QED

Our implementation of the electromagnetic interactions is based on the non Lorentz-covariant approach in refs. [121] and [122]. The formalism of non-relativistic quantum electrodynamics (NRQED), introduced in ref. [122], is designed to reproduce the low-momentum behaviour of QED to any desired accuracy. In particular, contributions from relativistic and non-relativistic scales are isolated and undergo a separate treatment. Besides, only non-relativistic momenta are allowed in the loops and in the external legs of the diagrams. The terms arising from relativistic momenta in the QED loops, in fact, are absorbed as renormalizations of the coupling constants of the local interactions in the non-relativistic counterpart of QED [122]. The Lagrangian is determined by the particle content and by the symmetries of the theory, such as gauge invariance, locality, hermiticity, parity conservation, time reversal symmetry and Galilean invariance. The particles are fermionic, characterized by mass  $M$  and unit charge  $e$ , and are represented by two-component non-relativistic Pauli spinor fields  $\Psi$ . In compliance to these prescriptions, the NRQED Lagrangian density in ref. [122] assumes the form,

---

<sup>2</sup>i.e. displays cylindrical symmetry

$$\begin{aligned} \mathcal{L}^{\text{NRQED}} = & -\frac{1}{2} (\mathbf{E}^2 - \mathbf{B}^2) + \Psi^\dagger \left( i\partial_t - e\phi + \frac{\mathbf{D}^2}{2M} \right) \Psi + \Psi^\dagger \left[ c_1 \frac{\mathbf{D}^4}{8M^3} + c_2 \frac{e}{2M} \boldsymbol{\sigma} \cdot \mathbf{B} \right. \\ & \left. + c_3 \frac{e}{8M^2} \nabla \cdot \mathbf{E} + c_4 \frac{e}{8M^2} i\mathbf{D} \times \boldsymbol{\sigma} \right] \Psi + \Psi^\dagger \left[ d_1 \frac{e}{8M^3} \{ \mathbf{D}^2, \boldsymbol{\sigma} \cdot \mathbf{B} \} \right] \Psi + \dots, \end{aligned} \quad (1.12)$$

where  $\mathbf{D} = \nabla + ie\mathbf{A}$  is the covariant derivative, while  $\mathbf{E} = -\nabla\phi - \partial_t\mathbf{A}$  and  $\mathbf{B} = \nabla \times \mathbf{A}$  denote the electric and magnetic fields, respectively. The terms in the first row encode the leading ones of  $\mathcal{L}^{\text{NRQED}}$ , containing the minimal coupling of the fermionic fields with the vector potential  $\mathbf{A}$  and the scalar potential,  $\phi$ . The interactions proportional to the constants  $c_1$ - $c_4$  and  $d_1$  in eq. (1.36) are next-to-leading-order terms, corresponding to corrections of order  $v^4/c^4$  and  $v^6/c^6$ , respectively [121], whereas the ellipses represent contributions containing higher order covariant derivatives,  $\mathcal{O}(v^8/c^8)$ .

Since the Coulomb force dominates at very low energies and transverse photons couple proportionally to the fermion momenta, in the present treatment we choose to retain in the Lagrangian only the scalar field and its lowest order coupling to the fermionic fields as in ref. [2]. Moreover, we reduce the latter to spinless fields  $\psi$ , consistently with sec. 2.1 and with ref. [1]. In this guise, the full Lagrangian density of the system becomes the superposition of the one presented in the opening of sec. 2.1 (sec. 3.1) for S-waves (P-waves) with the one involving the electrostatic potential and its leading-order coupling to the spinless fermions, namely

$$\mathcal{L}^{\text{NRQED corr}} = -\frac{1}{2} \nabla\phi \cdot \nabla\phi - e\phi \psi^\dagger \psi. \quad (1.13)$$

Alternatively, on top of the S-wave (P-wave) interaction in eq. (1.5) (eq. (1.6)) the Coulomb force, that in momentum space is regulated by an IR cutoff  $\lambda$ , reads

$$V_C(\mathbf{p}, \mathbf{q}) \equiv \langle \mathbf{q}, -\mathbf{q} | \hat{V}_C | \mathbf{p}, -\mathbf{p} \rangle = \frac{e^2}{(\mathbf{p} - \mathbf{q})^2 + \lambda^2}, \quad (1.14)$$

has been added. The introduction of the electrostatic potential generates the additional Feynman rules listed in app. A.1. Consequently, the T-matrix is enriched by new classes of diagrams (cf. secs. 2.1.1 and 3.1.1), in which the Coulomb photon insertions either between the external legs and within the loops begin to emerge. Unlike transverse photons, the scalar ones in fact do not propagate between different bubbles and lead only to the appearance of photon *ladders* within the bubbles or between the external legs in the diagrams for two-body processes.

In the next two chapters, most of our attention will be devoted to the low-momentum,  $\mathbf{p}$ , sector of two-particle elastic scattering. This regime is characterized by large values of the parameter  $\eta \equiv \alpha M/2|\mathbf{p}|$ , that regulates the viability of a perturbative treatment for the Coulomb interaction. As it will be shown in sec. 2.2.1 (sec. 3.2.1) for S-wave (P-wave) interactions, values of  $\eta$  near or exceeding unity prevent the application of the latter treatment, thus Coulomb photon exchanges in the T-matrix of the two-body scattering process have to be incorporated to all orders in the fine structure constant,  $\alpha \equiv \alpha_{\text{QED}} = \frac{e^2}{4\pi}$ .

For scalar photons, this amounts to replacing the free-fermion propagators in the bubble diagrams presented in sec. 2.1 (sec. 3.1) for S-waves (P-waves) with the Coulomb propagators in fig. 1.1. To this aim, we follow the procedure outlined in ref. [2] and introduce the Coulomb Green's functions. The inclusion of the Coulomb potential (cf. eq. (1.14)) in the Hamiltonian

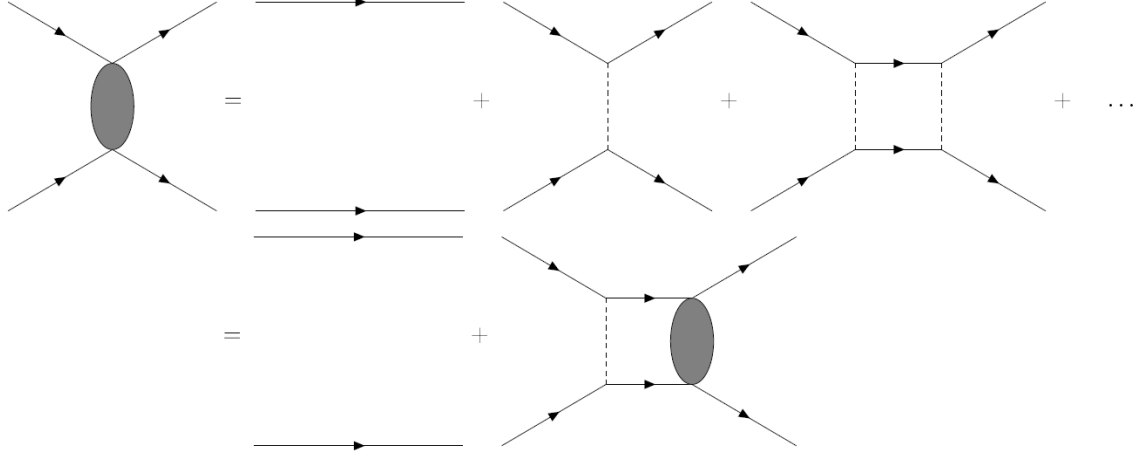


FIGURE 1.1 – The Coulomb propagator  $G_C$  as an infinite superposition of ladder diagrams (upper row), which can be compactly incorporated in a self-consistent identity (lower row).

yields the Coulomb Green's function operator,

$$\hat{G}_C^{(\pm)}(E) = \frac{1}{E - \hat{H}_0 - \hat{V}_C \pm i\epsilon} , \quad (1.15)$$

an expression that, together with eq. (1.1), admits a self-consistent rewriting *à la* Dyson [123],

$$\hat{G}_C^{(\pm)} = \hat{G}_0^{(\pm)} + \hat{G}_0^{(\pm)} \hat{V}_C \hat{G}_C^{(\pm)} , \quad (1.16)$$

that can be diagrammatically represented as in fig. 1.1. Moreover, the solutions of Schrödinger equation with a repulsive Coulomb potential,  $(\hat{H}_0 + V_C - E)|\Psi_{\mathbf{p}}^{(\pm)}\rangle$ , can be formally expressed in terms of the free ones as

$$|\psi_{\mathbf{p}}^{(\pm)}\rangle = \hat{G}_C^{(\pm)} \hat{G}_0^{-1} |\mathbf{p}\rangle = \left[ 1 + \hat{G}_C^{(\pm)} \hat{V}_C \right] |\mathbf{p}\rangle , \quad (1.17)$$

see eq. (18) in ref. [2]. The above eigenstates share with the plane waves the generalized normalization property, i.e.  $\langle \psi_{\mathbf{p}}^{(\pm)} | \psi_{\mathbf{q}}^{(\pm)} \rangle = (2\pi)^3 \delta(\mathbf{q} - \mathbf{p})$ . If the potential is repulsive, the solution with outgoing spherical waves in the distant future is given by

$$\psi_{\mathbf{p}}^{(+)}(\mathbf{r}) = e^{-\frac{1}{2}\pi\eta} \Gamma(1 + i\eta) M(-i\eta, 1; i\mathbf{p}\mathbf{r} - i\mathbf{p} \cdot \mathbf{r}) e^{i\mathbf{p} \cdot \mathbf{r}} , \quad (1.18)$$

while the state with incoming spherical waves in the distant past coincides with

$$\psi_{\mathbf{p}}^{(-)}(\mathbf{r}) = e^{-\frac{1}{2}\pi\eta} \Gamma(1 - i\eta) M(i\eta, 1; -i\mathbf{p}\mathbf{r} - i\mathbf{p} \cdot \mathbf{r}) e^{i\mathbf{p} \cdot \mathbf{r}} , \quad (1.19)$$

where  $M(a, b; c)$  is a Kummer function. In particular, the squared modulus of the two given spherical waves evaluated in the origin, i.e. the probability of finding the two fermions at zero separation, is equal to

$$C_\eta^2 \equiv |\psi_{\mathbf{p}}^{(\pm)}(0)|^2 = e^{-\pi\eta} \Gamma(1 + i\eta) \Gamma(1 - i\eta) = \frac{2\pi\eta}{e^{2\pi\eta} - 1} , \quad (1.20)$$

known as the *Sommerfeld factor* [124, 125]. Since the scattering eigenfunctions of the repulsive Coulomb Hamiltonian form a complete set of wavefunctions, they can be employed in an



operatorial definition of the Coulomb Green's functions analogous to eq. (1.15),

$$\hat{G}_C^{(\pm)} = M \int_{\mathbb{R}^3} \frac{d^3 \mathbf{q}}{(2\pi)^3} \frac{|\psi_{\mathbf{q}}^{(\pm)}\rangle \langle \psi_{\mathbf{q}}^{(\pm)}|}{\mathbf{p}^2 - \mathbf{q}^2 \pm i\varepsilon} . \quad (1.21)$$

In a guise analogous to the one with which we have defined the Coulomb Green's function operators in eq. (1.17), we introduce the full Green's function operator, including both the strong and the electrostatic interactions. Therefore, we add the operator  $\hat{V}_S = \hat{\mathcal{V}}^{(\ell)}$  to the kinetic and Coulomb potential in eq. (1.15), so that

$$\hat{G}_{SC}^{(\pm)}(E) = \frac{1}{E - \hat{H}_0 - \hat{V}_C - \hat{V}_S \pm i\varepsilon} . \quad (1.22)$$

Then, we define the incoming and outgoing wavefunctions as in ref. [2],

$$|\chi_{\mathbf{p}}^{(\pm)}\rangle = \left[ 1 + \hat{G}_{SC}^{(\pm)} (\hat{V}_S + \hat{V}_C) \right] |\mathbf{p}\rangle , \quad (1.23)$$

similar to the eq. (1.17). Exploiting the operator relation  $A^{-1} - B^{-1} = B^{-1}(B - A)A^{-1}$  with  $A = \hat{G}_{SC}^{(\pm)}(E)$  and  $B = \hat{G}_C^{(\pm)}(E)$  we find the self-consistent Dyson-like identity

$$\hat{G}_{SC}^{(\pm)} - \hat{G}_C^{(\pm)} = \hat{G}_C^{(\pm)} \hat{V}_S \hat{G}_{SC}^{(\pm)} , \quad (1.24)$$

that permits to rewrite the eigenstates of the full Hamiltonian in terms of the Coulomb states,

$$|\chi_{\mathbf{p}}^{(\pm)}\rangle = \left[ 1 + \sum_{n=1}^{+\infty} (\hat{G}_C^{(\pm)} \hat{V}_S)^n \right] |\psi_{\mathbf{p}}^{(\pm)}\rangle . \quad (1.25)$$

Subsequently, the scattering amplitude can be computed via the S-matrix element, given by the overlap between an incoming state with momentum  $\mathbf{p}$  and an outgoing state  $\mathbf{p}'$ ,

$$S(\mathbf{p}', \mathbf{p}) = \langle \chi_{\mathbf{p}'}^{(-)} | \chi_{\mathbf{p}}^{(+)} \rangle = (2\pi)^3 \delta(\mathbf{p}' - \mathbf{p}) - 2\pi i \delta(E' - E) T(\mathbf{p}', \mathbf{p}) \quad (1.26)$$

where  $T(\mathbf{p}', \mathbf{p}) = T_C(\mathbf{p}', \mathbf{p}) + T_{SC}(\mathbf{p}', \mathbf{p})$  as in eq. (4) in ref. [126] (for the complete derivation of eq. (1.26) we refer to chap. 5 of ref. [127]). In particular  $T_C(\mathbf{p}', \mathbf{p}) = \langle \mathbf{p}' | \hat{V}_C | \psi_{\mathbf{p}}^{(+)} \rangle$  is the *purely electrostatic* scattering amplitude and  $T_{SC}(\mathbf{p}', \mathbf{p}) = \langle \psi_{\mathbf{p}'}^{(-)} | \hat{V}_S | \chi_{\mathbf{p}}^{(+)} \rangle$  coincides with the *strong* scattering amplitude modified by *Coulomb corrections*. Since the eigenstates  $\psi_{\mathbf{p}}$  of the former are known, the scattering amplitude due to the Coulomb interaction alone can be computed in closed form and admits the following partial wave expansion [2],

$$T_C(\mathbf{p}', \mathbf{p}) = -\frac{4\pi}{M} \sum_{\ell=0}^{+\infty} (2\ell + 1) \left[ \frac{e^{2i\sigma_\ell} - 1}{2i|\mathbf{p}|} \right] \mathcal{P}_\ell(\cos \theta) , \quad (1.27)$$

where  $\theta$  is the angle between  $\mathbf{p}$  and  $\mathbf{p}'$  and  $\sigma_\ell = \arg \Gamma(1 + \ell + i\eta)$  is the Coulomb phase shift. In particular, the strong scattering amplitude  $T_{SC}(\mathbf{p}, \mathbf{p}')$  possesses a phase shift  $\sigma_\ell + \delta_\ell$ . Furthermore, the Coulomb corrected version of  $T_S$  can be expanded in terms of the Legendre polynomials  $\mathcal{P}_\ell$  as

$$T_{SC}(\mathbf{p}', \mathbf{p}) = -\frac{4\pi}{M} \sum_{\ell=0}^{+\infty} (2\ell + 1) e^{2i\sigma_\ell} \left[ \frac{e^{2i\delta_\ell} - 1}{2i|\mathbf{p}|} \right] \mathcal{P}_\ell(\cos \theta) \quad (1.28)$$

where  $\delta_\ell$  is the strong contribution to the total phase shift. If the strong interaction couples the fermions to  $\ell$  units of angular momentum and Coulomb forces are central, the only nonzero component of  $T_{\text{SC}}$  of the expansion in eq. (1.28) is the one proportional to the Legendre polynomial  $\mathcal{P}_\ell(\cos \theta)$ ,

$$|\mathbf{p}|^{2\ell+1}(\cot \delta_\ell - i) = -(2\ell + 1)\mathbf{p}^{2\ell} \frac{4\pi}{M} \frac{e^{2i\sigma_\ell} \mathcal{P}_\ell(\cos \theta)}{T_{\text{SC}}(\mathbf{p}', \mathbf{p})} . \quad (1.29)$$

The r.h.s. of the last equation can be replaced with the  $\ell$ -version (cf. ref. [43]) of the generalized effective-range expansion formulated in ref. [42] for the T-matrix (cf. fig. 1.2) in presence of the repulsive Coulomb interaction,

$$\mathbf{p}^{2\ell} Q_\ell(\eta) \left[ C_\eta^2 |\mathbf{p}|(\cot \delta_\ell - i) + \alpha M H(\eta) \right] = -\frac{1}{a_C^{(\ell)}} + \frac{1}{2} r_0^{(\ell)} \mathbf{p}^2 + r_1^{(\ell)} \mathbf{p}^4 + \dots , \quad (1.30)$$

where  $a_C^{(\ell)}$ ,  $r_0^{(\ell)}$  and  $r_1^{(\ell)}$  are the generalized scattering length, the effective range and the shape parameter respectively. Besides,  $Q_\ell(\eta)$  on the l.h.s. of the eq. (1.30), is a polynomial containing all even powers of  $\eta$  from zero to  $2\ell$ ,

$$Q_\ell(\eta) = \left[ \frac{\eta^\ell}{\ell!} \right]^2 \sum_{l=0}^{\ell} c_l(\ell) \eta^{-2l} , \quad (1.31)$$

where the coefficients  $c_l(\ell)$  are rational numbers, presented in eq. (7.18) of ref. [125] and in the appendix of ref. [43],

$$\begin{aligned} c_0(\ell) &= 1 , \quad c_1(\ell) = \frac{1}{6} \ell(\ell+1)(2\ell+1) , \quad c_\ell(\ell) = (\ell!)^2 , \\ c_2(\ell) &= \frac{1}{360} (2\ell-1)(\ell-1)\ell(\ell+1)(2\ell+1)(5\ell+6) , \\ c_3(\ell) &= \frac{1}{45360} (2\ell-3)(2\ell-1)(\ell-2)(\ell-1)\ell(\ell+1)(2\ell+1)(35\ell^2 + 91\ell + 60) . \end{aligned} \quad (1.32)$$

Finally, the function  $H(\eta)$ , that represents the effects of Coulomb force on the strong interactions at short distances, is given by

$$H(\eta) = \psi(i\eta) + \frac{1}{2i\eta} - \log(i\eta) , \quad (1.33)$$

where  $\psi(z) = \Gamma'(z)/\Gamma(z)$  is the Digamma function. Despite the appearance, the generalized ERE is real, since the imaginary parts arising from  $H(\eta)$  cancel exactly with the imaginary part in the l.h.s. of eq. (1.30). Due to the following identity on the logarithmic derivative of the Gamma function,

$$\Im \psi(i\eta) = \frac{1}{2\eta} + \frac{\pi}{2} \coth \pi \eta , \quad (1.34)$$

in fact, the imaginary part of  $H(\eta)$  proves to coincide with  $C_\eta^2/2\eta$ . For the sake of completeness, in the case of fermion-antifermion scattering the Coulomb potential is attractive and  $H(\eta)$  in the effective range expansion (cf. eq. (1.30)) has to be replaced by

$$\bar{H}(\eta) = \psi(i\eta) + \frac{1}{2i\eta} - \log(-i\eta) , \quad (1.35)$$



where  $\eta = -\alpha M/2p$  is defined as a negative real parameter.

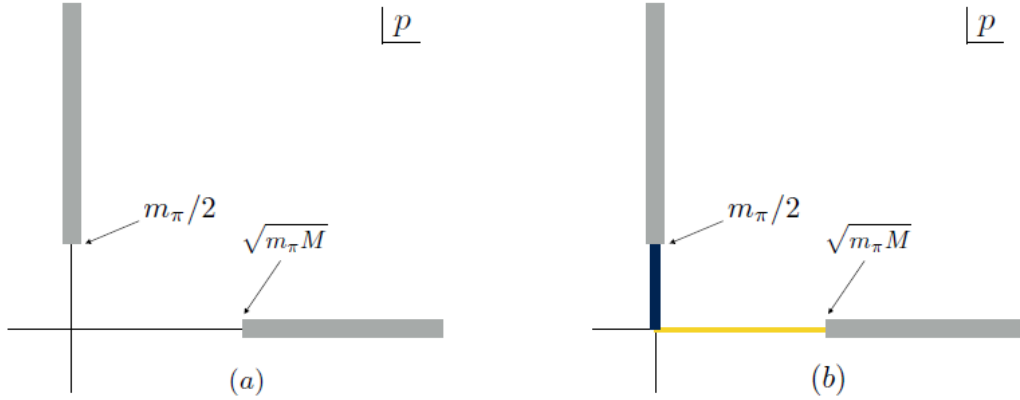


FIGURE 1.2 – Analytic structure of the hadron-hadron elastic scattering amplitude  $T_S$  (a) and  $T_{SC}$  (b) in the complex  $|p|$  plane, in absence and in presence of Coulomb interactions respectively (see ref. [1]). If we let the fermion field  $\psi$  represent a hadron, the scattering amplitude  $T_S$  displays a QCD t-channel cut with threshold  $m_\pi/2$  along  $\Im|p|$ . The real momentum axis is marked by a branch cut at threshold  $\sqrt{m_\pi M}$  corresponding to the onset of inelastic pion production. In presence of QED both the branch cuts start at the origin. However, if the ERE in eq. (1.10) is replaced by its generalized version in eq. (1.30), the threshold of the branch cut along  $\Im|p|$  is restored to its original value (black segment). Although the position of the cut along  $\Re|p|$  remains fixed at the origin, the inelastic  $\pi$ -production is suppressed by a power of  $\alpha$  as compared to the t-channel reactions.

### 1.3 Finite volume formalism

Aware of the role of numerical simulations for quantum field theories in finite regions of the configuration space, we consider the transposition of the physical system outlined in secs. 1.2 and 1.2.1 onto a cubic finite volume with side  $L$ . In this environment, it is customary to continue analytically the fields and the wavefunctions outside the cubic box by means of periodic boundary conditions (PBCs). It follows that a free particle subject to PBCs carries a momentum  $\mathbf{p} = 2\pi\mathbf{n}/L$ , where  $L \equiv Na$  and  $\mathbf{n}$  is a dimensionless three-dimensional vector of integers. Unlike QCD fields, the photon field in QED is truncated and modified by the boundary of the volume. In particular, when PBCs are implemented, the validity of Ampère's and Gauss's law is compromised. The problem is circumvented by introducing a uniform background charge density, a procedure that proves to be equivalent to the removal of the zero modes of the photon [1, 64]. Once the latter are canceled, the Coulomb potential between two identical charges  $e$  becomes (cf. fig. 1.3)

$$V_C^L(\mathbf{r}) = \frac{\alpha}{\pi L} \sum_{\mathbf{n} \neq 0} \frac{1}{|\mathbf{n}|^2} e^{i\frac{2\pi}{L}\mathbf{n} \cdot \mathbf{r}}, \quad (1.36)$$

where the  $\mathbf{n} \in \mathbb{Z}^3$  encodes the dimensionless finite-volume momenta. Discarding the zero modes, the latter are restricted to  $|\mathbf{p}| \geq 2\pi/L$ , whereas the validity of a perturbation treatment of QED is again controlled by the parameter  $\eta = \alpha M/2|\mathbf{p}|$ , which scales as the inverse of the momentum of the interacting particles. Combining the above constraint with the definition of  $\eta$ , it follows that  $\eta \sim \alpha ML$  and the photon field insertions can be treated perturbatively if  $ML \ll 1/\alpha$ . As  $\eta$  grows linearly with the spatial volume, for any value of  $M$  exists a critical

value of  $L$  that regulates the applicability of perturbation theory. On top of the condition  $\eta \ll 1$ , we assume henceforth the limit  $M \gg 1/L$ , since for the current Lattice QCD calculations large volumes are employed [1].

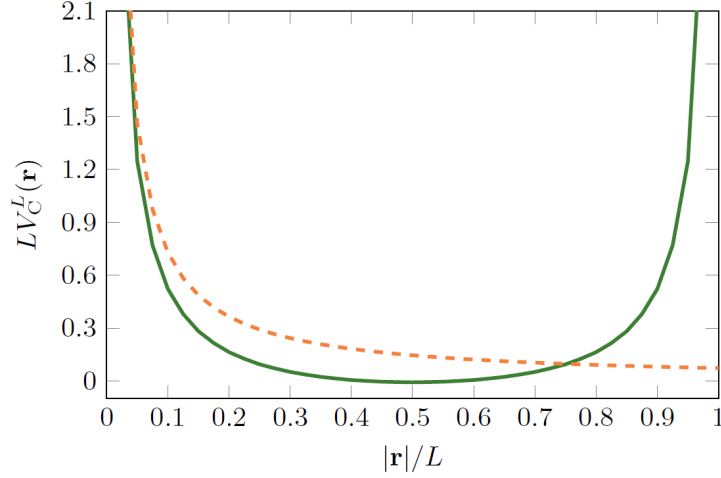


FIGURE 1.3 – Behaviour of the finite-volume Coulomb potential energy between unit charges along an axis parallel to an edge of the cube (solid curve) obtained from  $V_C^L(\mathbf{r})$  in eq. (1.36) and the infinite-volume Coulomb potential  $V_C(\mathbf{r})$  (dashed curve) [1, 46], whose Fourier transform with IR regulator is presented in eq. (1.14).

Furthermore, the finite volume QED effects are such that the energy eigenvalues of two charged fermions (e.g. hadrons) are modified in the same way by their self-interactions and by their interactions with each other, and the shifts take the form of power laws in  $L$  [46]. As a consequence, in presence of Coulomb photons the kinematics of two-body processes receives power law modifications in the finite volume context [46, 54]. In particular, if the infinite-volume effective range expansion in eq. (1.30) is rewritten in terms of the center of mass energy,

$$\mathbf{p}^{2\ell} Q_\ell(\eta) [C_\eta^2 |\mathbf{p}| (\cot \delta_\ell - i) + \alpha M H(\eta)] = -\frac{1}{a_C^{(\ell)}} + \frac{1}{2} r_0^{(\ell)} M (E^* - 2M) + r_1^{(\ell)} M^2 (E^* - 2M)^2 + \dots, \quad (1.37)$$

then  $E^* = 2M + T$  in the above expression is replaced by its finite volume counterpart<sup>3</sup>. Eq. (1.37) thus becomes

$$\mathbf{p}^{2\ell} Q_\ell(\eta) [C_\eta^2 |\mathbf{p}| (\cot \delta_\ell - i) + \alpha M H(\eta)] = -\frac{1}{a_C^{(\ell)}} + \frac{1}{2} r_0^{(\ell)} M (E^{*L} - 2M) + r_1^{(\ell)} M^2 (E^{*L} - 2M)^2 + \dots. \quad (1.38)$$

The original dependence of the r.h.s. of the last equation on the powers of the finite volume kinetic energy  $T^L = E^{*L} - 2M^L$  can be restored by exploiting the expression of the finite-volume shift for the masses of spinless particles with unit charge in eqs. (6) and (19) of ref. [46],

$$\Delta M \equiv M^L - M = \frac{\alpha}{2\pi L} \left[ \sum_{\mathbf{n} \neq 0}^{\Lambda_n} \frac{1}{|\mathbf{n}|^2} - 4\pi \Lambda_n \right] + \mathcal{O}\left(\alpha^2; \frac{\alpha}{L^2}\right), \quad (1.39)$$

<sup>3</sup>Finite volume physical quantities will be denoted henceforth with an  $L$  in the superscript.

where the sum of the three-dimensional Riemann series regulated by the spherical cutoff  $\Lambda_n$  is denoted with  $\mathcal{G}^{(0)} \approx -8.913632$  (cf. app. B.1.1). To this purpose, primed scattering parameters are introduced

$$\frac{1}{a_C'^{(\ell)}} = \frac{1}{a_C^{(\ell)}} - \frac{\alpha r_0^{(\ell)} M}{2\pi L} \mathcal{G}^{(0)} + \mathcal{O}\left(\alpha^2; \frac{\alpha}{L^2}\right) , \quad (1.40)$$

$$r_0'^{(\ell)} = r_0^{(\ell)} + \frac{4\alpha r_1^{(\ell)} M}{\pi L} \mathcal{G}^{(0)} + \mathcal{O}\left(\alpha^2; \frac{\alpha}{L^2}\right) , \quad (1.41)$$

$$r_1'^{(\ell)} = r_1^{(\ell)} + \frac{3\alpha r_2^{(\ell)} M}{\pi L} \mathcal{G}^{(0)} + \mathcal{O}\left(\alpha^2; \frac{\alpha}{L^2}\right) , \quad (1.42)$$

$$r_2'^{(\ell)} = r_2^{(\ell)} + \frac{4\alpha r_3^{(\ell)} M}{\pi L} \mathcal{G}^{(0)} + \mathcal{O}\left(\alpha^2; \frac{\alpha}{L^2}\right) , \quad (1.43)$$

and

$$r_3'^{(\ell)} = r_3^{(\ell)} + \frac{5\alpha r_4^{(\ell)} M}{\pi L} \mathcal{G}^{(0)} + \mathcal{O}\left(\alpha^2; \frac{\alpha}{L^2}\right) , \quad \dots , \quad (1.44)$$

differing from the original ones by corrections of order  $\alpha$  and scaling as the inverse of the box size. Explicitly, the infinite volume effective-range expansion in eq. (1.38) rewritten in terms of the translated parameters in eqs. (1.40)-(1.44) for unbound states with  $T^L = \mathbf{p}^2/M^L$  assumes the form

$$\mathbf{p}^{2\ell} Q_\ell(\eta) [C_\eta^2 |\mathbf{p}| (\cot \delta_\ell - i) + \alpha M H(\eta)] = -\frac{1}{a_C'^{(\ell)}} + \frac{1}{2} r_0'^{(\ell)} \mathbf{p}^2 + r_1'^{(\ell)} \mathbf{p}^4 + \dots , \quad (1.45)$$

where the changes in the total energy have been incorporated in the primed scattering parameters. Finally, also the validity region of the last expansion is modified by the finite-volume environment, due to the changes in the analytic structure of the scattering amplitude in the complex  $|\mathbf{p}|$  plane. The absence of the zero mode in the Coulomb potential in eq. (1.36), in fact, yields a shift in the branch cut of the imaginary  $|\mathbf{p}|$  axis from the origin to  $\sqrt{2\pi M/L} + \mathcal{O}(1/M)$ , which fixes the inelastic threshold for the two-hadron state (cf. fig. (1.3) [1] in the next chapter).

The last version of the ERE, combined with the quantization conditions in sec. 2.2.1 (sec. 3.2.1), will turn out to be the key ingredient for the derivation of the finite volume energy corrections for scattering and bound states with zero (one) unit of angular momentum.



## CHAPTER 2

### S-WAVE SHORT-RANGE INTERACTIONS

This chapter is structured into two parts and its content can be summarized as follows. After this preamble, the theoretical framework that provides the basis for both the infinite and the finite volume treatment is introduced, by starting from the Lagrangian with the strong S-wave interactions alone. Next, in the end of sec. 2.1, the T-matrix for two-body fermion-fermion scattering to all orders in the strength parameter of the potential is computed. Subsequently, in sec. 2.1.1, Coulomb photon exchanges from non-relativistic QED in refs. [121, 122] are allowed to appear in the two-particle scattering diagrams. After displaying the amplitudes corresponding to tree-level and one-loop diagrams with one Coulomb photon exchange, the  $\ell = 0$  effective range expansion is presented. In the subsequent section, the non-perturbative treatment of the Coulomb interaction recapitulated in sec. 1.3 is implemented in the case of fermion-fermion scattering. Thanks to the Dyson-like identities that hold among the free, the Coulomb and the full two-body Green's functions, in fact, the T-matrix matrix element accounting for both Coulomb and strong interactions is derived to all orders in  $\alpha$ . As in ref. [2], section 2.1.2 closes with the expressions of the scattering length and the effective range in terms of the physical constants of our EFT Lagrangian, that are obtained from the effective-range expansion. The first part of the analysis is concluded in sec. 2.1.3 with the calculation of the same amplitude for the fermion-antifermion scattering case.

Afterwards, the two fermion-system is transposed onto a cubic box of side  $L$  and the distortions induced by the new environment in the laws of electrodynamics [46, 128] and in the masses of possibly composite particles [46] are briefly summarized in sec. 2.2. Next, the quantization conditions, that give access to the energy spectrum in finite volume through the expression of the T-matrix elements [1], are reviewed (cf. sec. 2.2.1) in the perturbative regime of QED. Then, the finite volume counterpart of the  $\ell = 0$  effective range expansion is displayed, together with the expressions of the Lüscher functions obtained in ref. [1]. Subsequently, the energy eigenvalues of the lowest bound and scattering states in ref. [1] are shown along with the details of the whole derivation, which can be skipped by an experienced reader. The appendices provide supplemental material to the reader interested in the three-dimensional Riemann sums arising from the approximations of the Lüscher functions in secs. 2.2.1, 2.2.2 and 2.2.3.

## 2.1 Two-body scattering in infinite volume

We begin our analysis by considering spinless fermions interacting locally via two-body forces that carry zero units of angular momentum. The Lagrangian density of the system is constructed from the leading order S-wave interaction presented in eq. 1.5,

$$\mathcal{L}^{(0)} = \psi^\dagger \left( i\hbar\partial_t + \frac{\hbar^2\nabla^2}{2M} \right) \psi - \frac{C(E^*)}{2} (\psi\psi)^\dagger (\psi\psi) , \quad (2.1)$$

where the constant coefficient  $C_0$  is replaced by CoM-energy dependent one,  $C(E^*)$ , in order to account for the higher-order  $\ell = 0$  interactions [1]. Equivalently,  $\mathcal{L}^{(0)}$  can be obtained from  $\mathcal{L}_0$  in eq. (1) of [2], by replacing the nucleon field operators  $N$  ( $N^\dagger$ ) with  $\psi$  ( $\psi^\dagger$ ) and the  $\mathbf{\Pi}$  vector by the one for spin-singlet interactions,  $\sigma_2\tau_2\vec{\tau}/\sqrt{8}$ . The Lagrangian is also consistent with the one appearing in eq. (3.1) in ref. [17], provided  $C(E^*)$  is identified with  $C = (C_S - 3C_T)$ . Upon replacing in the latter equation the vector of Pauli matrices  $\vec{\sigma}$  with the ones acting on the individual spinor fields,  $\vec{\sigma}_1$  and  $\vec{\sigma}_2$ , the scalar product between the latter can be evaluated,

$$2\frac{1}{2}(N^\dagger\vec{\sigma}_1N) \cdot \frac{1}{2}(N^\dagger\vec{\sigma}_2N) = (N^\dagger N)^2[S(S+1) - s_1(s_1+1) - s_2(s_2+1)] , \quad (2.2)$$

where  $S$  is the eigenvalue of the coupled system while  $s_1$  and  $s_2$  are the eigenvalues of the individual particles. In case of a spin-singlet coupled state made of spin 1/2 fermions, the r.h.s. of eq. 2.2 yields  $-3/2$  and the Lagrangian in eq. (3.1) in ref. [17] reduces to the one in eq. (2.1). The scalar product of the two pairs of creation and annihilation operators in the aforementioned eq. (3.1) can be, in fact, interpreted as the product of the field operators referring to the evolution of particle 1 (resp. 2) with spin  $\vec{\sigma}_1/2$  (resp.  $\vec{\sigma}_2/2$ ).

Considering the Feynman rules listed in app. A.1, that assign a factor of  $-iC(E^*)$  to each four-fermion vertex, the diagrams contributing to the T-matrix of a fermion-fermion scattering process are represented by chains of bubbles (cf. fig. 2.1). Recalling the tree-level diagrams, the two-body strong potential in momentum space assumes the form

$$V^{(0)}(\mathbf{p}, \mathbf{q}) \equiv \langle \mathbf{q}, -\mathbf{q} | \hat{\mathcal{V}}^{(0)} | \mathbf{p}, -\mathbf{p} \rangle = C(E^*) , \quad (2.3)$$

where the average value in the middle coincides with the relevant amplitude multiplied by the imaginary unit.

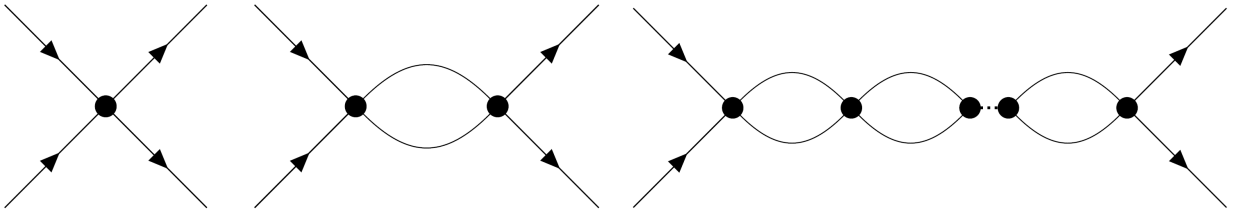


FIGURE 2.1 – Tree-level (upper line, left), 1-loop (upper line, right) and n-loops diagrams (lower line) representing fermion-fermion elastic scattering with the strong S-wave potential in eq. (2.3).

With reference to the bubble diagrams in momentum space with amputated legs and the conventions for the plane-wave eigenstates in sec. 1.2, the full scattering amplitude in absence of QED becomes

$$iT_S(\mathbf{p}, \mathbf{q}) = i\langle \mathbf{q}, -\mathbf{q} | \hat{\mathcal{V}}^{(0)} (1 + \hat{G}_0^E \hat{\mathcal{V}}^{(0)} + \hat{G}_0^E \hat{\mathcal{V}}^{(0)} \hat{G}_0^E \hat{\mathcal{V}}^{(0)} + \dots) | \mathbf{p}, -\mathbf{p} \rangle , \quad (2.4)$$

where  $\hat{G}_0^E \equiv \hat{G}_0^{(+)}$  represents the unperturbed two-body retarded Green's function operator in eq. (1.2). The explicit computation of the three lowest order contributions to the sum in eq. (2.4) leads to

$$i\langle \mathbf{q}, -\mathbf{q} | \hat{\psi}^{(0)} | \mathbf{p}, -\mathbf{p} \rangle = iC(E^*), \quad (2.5)$$

$$i\langle \mathbf{q}, -\mathbf{q} | \hat{\psi}^{(0)} \hat{G}_0^E \hat{\psi}^{(0)} | \mathbf{p}, -\mathbf{p} \rangle = i[C(E^*)]^2 \int_{\mathbb{R}^3} \frac{d^3 \mathbf{p}'}{(2\pi)^3} \int_{\mathbb{R}^3} \frac{d^3 \mathbf{p}''}{(2\pi)^3} \langle \mathbf{p}', -\mathbf{p}' | \hat{G}_0^E | \mathbf{p}'', -\mathbf{p}'' \rangle = i[C(E^*)]^2 J_0, \quad (2.6)$$

and

$$\begin{aligned} i\langle \mathbf{q}, -\mathbf{q} | \hat{\psi}^{(0)} \hat{G}_0^E \hat{\psi}^{(0)} \hat{G}_0^E \hat{\psi}^{(0)} | \mathbf{p}, -\mathbf{p} \rangle &= i[C(E^*)]^3 \int_{\mathbb{R}^3} \frac{d^3 \mathbf{p}'}{(2\pi)^3} \int_{\mathbb{R}^3} \frac{d^3 \mathbf{p}''}{(2\pi)^3} \langle \mathbf{p}', -\mathbf{p}' | \hat{G}_0^E | \mathbf{p}'', -\mathbf{p}'' \rangle \\ &\cdot \int_{\mathbb{R}^3} \frac{d^3 \mathbf{p}'''}{(2\pi)^3} \int_{\mathbb{R}^3} \frac{d^3 \mathbf{p}'''}{(2\pi)^3} \langle \mathbf{p}''', -\mathbf{p}''' | \hat{G}_0^E | \mathbf{p}''', -\mathbf{p}''' \rangle = i[C(E^*)]^3 J_0^2, \end{aligned} \quad (2.7)$$

where  $J_0 \equiv G_0^E(\mathbf{0}, \mathbf{0})$  is the Fourier transform of the two-body unperturbed Green's function in eq. (1.3) to configuration space, evaluated at the origin of the coordinate axes. Exploiting eqs. (2.5)-(2.7), the infinite sum of the amplitudes of chains of bubbles in eq. (2.4) can be recast into a geometric series with ratio equal to  $C(E^*)G_0^E(\mathbf{0}, \mathbf{0})$ . Consequently, the sought scattering amplitude can be determined analytically to all the orders in perturbation theory, giving

$$T_S(\mathbf{p}, \mathbf{q}) = \frac{C(E^*)}{1 - C(E^*)J_0}. \quad (2.8)$$

The calculation can be likewise performed in configuration space, by Fourier transforming the two-body potential in eq. (2.2),

$$V^{(0)}(\mathbf{r}, \mathbf{r}') \equiv \langle \mathbf{r}', -\mathbf{r}' | \hat{\psi}^{(0)} | \mathbf{r}, -\mathbf{r} \rangle = C(E^*)\delta(\mathbf{r})\delta(\mathbf{r}'), \quad (2.9)$$

and observing again that

$$\langle \mathbf{r}', -\mathbf{r}' | \hat{\psi}^{(0)} \underbrace{\hat{G}_0^E \hat{\psi}^{(0)} \dots \hat{G}_0^E \hat{\psi}^{(0)}}_{n \text{ times}} | \mathbf{r}, -\mathbf{r} \rangle = \delta(\mathbf{r})\delta(\mathbf{r}') [C(E^*)]^{n+1} G_0^E(\mathbf{0}, \mathbf{0})^n. \quad (2.10)$$

Therefore, the scattering amplitude to all orders in the bubble insertions in the space of coordinates becomes

$$T_S(\mathbf{r}, \mathbf{r}') = \frac{C(E^*)\delta(\mathbf{r})\delta(\mathbf{r}')}{1 - C(E^*)J_0}, \quad (2.11)$$

a formula that still depends on the free two-body Green's function evaluated at  $\mathbf{r} = \mathbf{r}' = 0$ , an object that diverges in  $d$ -dimensional space, but turns out to converge for  $d = 3$ . As shown in ref. [17], the computation can be carried out in dimensional regularization, giving

$$J_0(d) = \int_{\mathbb{R}^3} \frac{d^d \mathbf{q}}{(2\pi)^d} \frac{1}{(E - \mathbf{q}^2/M + i\epsilon)} = -\frac{\Gamma(1 - \frac{d}{2})}{(4\pi)^{d/2}} M(-ME - i\epsilon)^{(d-2)/2}, \quad (2.12)$$

that is, in three dimensions,

$$\lim_{d \rightarrow 3} J_0(d) = G_0^E(\mathbf{0}, \mathbf{0}) = \frac{M\sqrt{-ME - i\epsilon}}{4\pi} = -\frac{iM|\mathbf{p}|}{4\pi}. \quad (2.13)$$

where  $|\mathbf{p}| = |\mathbf{q}|$  is an on-shell three-momentum corresponding to the total energy of  $E = \mathbf{p}^2/M$

in the CoM frame. In the Power Divergence Subtraction (PDS) renormalization scheme [22], the last expression of the Green's function becomes (cf. eq. (4) in [2])

$$J_0(\mu) \Big|_{\text{PDS}} = -\frac{M}{4\pi} (i|\mathbf{p}| + \mu) \quad (2.14)$$

where  $\mu$  is a renormalization parameter with the same dimensions of a momentum. Now, recalling the expression of the  $\ell = 0$  partial wave amplitude (cf. eq. (1.10) and eq. (5) in ref. [2]),

$$T_S(\mathbf{p}, \mathbf{q}) = -\frac{4\pi}{M} \frac{1}{|\mathbf{p}| \cot \delta_0 - i|\mathbf{p}|} , \quad (2.15)$$

and the effective-range expansion (ERE) for elastic two-body scattering coupled to zero angular momentum in eq. 1.11,

$$|\mathbf{p}| \cot \delta_0 = -\frac{1}{a^{(0)}} + \frac{1}{2} r_0^{(0)} \mathbf{p}^2 + r_1^{(0)} \mathbf{p}^4 + r_2^{(0)} \mathbf{p}^6 + \dots , \quad (2.16)$$

one finds by comparison between eq. (2.8) and eqs. (2.15)-(2.17) that the coupling constant of the contact interaction is proportional to the scattering length  $a$ ,

$$C(E^*) = \frac{4\pi a^{(0)}}{M} , \quad (2.17)$$

an expression that in the power divergence subtraction (PDS) scheme [22] for renormalization becomes (cf. eq. (7) in ref. [2]) depends on the dimensionful parameter  $\mu$

$$C(E^*, \mu) = \frac{4\pi}{M} \frac{1}{1/a^{(0)} - \mu} . \quad (2.18)$$

Conversely, the effective range parameter  $r_0$  turns out to be equal to zero [17], since the two-body potential in configuration space is a contact interaction (cf. eq. (2.9)).

### 2.1.1 Coulomb corrections

At this stage, we add the Lagrangian density in eq. (1.13) on top of the one in eq. (2.1). Consequently, Coulomb photon exchanges begin to appear within the bubbles and the external legs of the scattering diagrams. These interactions prevail at very low energy scales in proton-proton scattering [129]. As energy increases, the Coulomb potential will still dominate in the forward and backward directions, but is overwhelmed by strong interactions in the intermediate directions.

Like in the previous section, we consider the T-matrix for two-body elastic scattering processes. The lowest order correction to the elastic scattering amplitude  $T_S$  in eq. (2.8) due to Coulomb interaction is given by the tree-level diagram with a four-fermion vertex and a one-photon exchange between two external legs. The application of Feynman rules in momentum space (cf. A.1) yields

$$-i T_{\text{SC}}^{\text{tree}}(\mathbf{p}, \mathbf{p}') = -i C(E^*) \int_{\mathbb{R}^4} \frac{d^4 l}{(2\pi)^4} \frac{-ie^2}{\mathbf{l}^2 + \lambda^2} \frac{i}{\frac{E}{2} + l_0 - \frac{(-\mathbf{p}+\mathbf{l})^2}{2M} + i\epsilon} \frac{i}{\frac{E}{2} - l_0 - \frac{(\mathbf{p}-\mathbf{l})^2}{2M} + i\epsilon} . \quad (2.19)$$



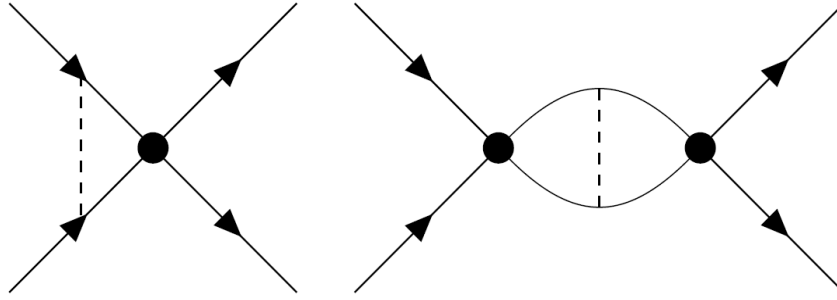


FIGURE 2.2 – The tree-level (left) and one-loop (right) fermion-fermion scattering diagram for strong  $\ell = 0$  interactions with one Coulomb photon insertion (dashed lines).

Carrying out the integration over the free energy  $l_0$ , the latter equation becomes

$$-iT_{\text{SC}}^{\text{tree}}(\mathbf{p}, \mathbf{p}') = C(E^*) \int_{\mathbb{R}^3} \frac{d^3 l}{(2\pi)^3} \frac{-ie^2}{l^2 + \lambda^2} \frac{M}{\mathbf{p}^2 - (\mathbf{p} - \mathbf{l})^2 + i\epsilon} , \quad (2.20)$$

an expression that can be evaluated in dimensional regularization as in the appendix of ref. [2],

$$T_{\text{SC}}^{\text{tree}}(\mathbf{p}, \mathbf{p}') = -C(E^*) \frac{\alpha M}{2|\mathbf{p}|} \left( \frac{\pi}{2} + i \log \frac{2|\mathbf{p}|}{\lambda} \right) + \mathcal{O}(\lambda) , \quad (2.21)$$

where the second term on the r.h.s. is divergent for zero photon mass. Nevertheless, since the latter is imaginary and the cross section to order  $\alpha$  is proportional to  $|T_S + T_{\text{SC}}^{\text{tree}}|^2 = C(E^*)[C(E^*) + 2 \Re T_{\text{SC}}^{\text{tree}}]$ , the logarithmic term will not contribute. The cross section to that order turns out to be infrared finite and proportional to  $1 - \pi\eta$  where  $\eta$ , for fermions with arbitrary charge, is equal to  $Z_1 Z_2 \frac{M\alpha}{2p}$  with  $Z_1, Z_2 \in \mathbb{Z}$ . As observed in ref. [2], the inclusion of  $n$ -Coulomb photon exchanges, results into contributions in the amplitude and in the cross section that are proportional to  $\eta^n$ . Therefore, the feasibility of a perturbative treatment for the Coulomb force is regulated by the smallness of the parameter  $\eta$ , i.e. by a constraint on the momenta of the incoming particles,  $p \gg \alpha M/2$ . As a consequence, if the momentum scale of the incoming particles is too soft, Coulomb force is expected to have a strong influence on the cross-section of the elastic process and a non-perturbative approach becomes necessary. Analogously to the tree-level diagrams, the Coulomb interaction affects also the  $n$ -loop bubble diagrams in fig. 2.1. In particular, considering the 1-loop diagram with 1-Coulomb photon exchange within the bubble, the corresponding amplitude computed via the aforementioned Feynman rules in momentum space gives

$$-iT_{\text{SC}}^{1\text{-loop}}(\mathbf{p}, \mathbf{p}') = [-iC(E^*)]^2 \int_{\mathbb{R}^4} \frac{d^4 l}{(2\pi)^4} \int_{\mathbb{R}^4} \frac{d^4 k}{(2\pi)^4} \frac{i}{\frac{E}{2} + l_0 - \frac{l^2}{2M} + i\epsilon} \frac{i}{\frac{E}{2} - l_0 - \frac{l^2}{2M} + i\epsilon} \frac{-ie^2}{(\mathbf{l} - \mathbf{k})^2 + \lambda^2} \frac{i}{\frac{E}{2} + k_0 - \frac{k^2}{2M} + i\epsilon} \frac{i}{\frac{E}{2} - k_0 - \frac{k^2}{2M} + i\epsilon} . \quad (2.22)$$

The subsequent integration on the energies  $l_0$  and  $k_0$  yields

$$T_{\text{SC}}^{1\text{-loop}}(\mathbf{p}, \mathbf{p}') = [C(E^*)]^2 \int_{\mathbb{R}^3} \frac{d^3 l}{(2\pi)^3} \int_{\mathbb{R}^3} \frac{d^3 k}{(2\pi)^3} \frac{M}{\mathbf{p}^2 - \mathbf{l}^2 + i\epsilon} \frac{e^2}{(\mathbf{l} - \mathbf{k})^2 + \lambda^2} \frac{M}{\mathbf{p}^2 - \mathbf{k}^2 + i\epsilon} . \quad (2.23)$$

Even if the amplitude proves to be infrared finite, the explicit computation of  $T_{\text{SC}}^{1\text{-loop}}$  carried out in the appendix of ref. [2] in dimensional regularization requires the introduction of an ultraviolet cutoff for the momenta, represented by the renormalization mass  $\mu$  in the PDS scheme. In particular, the calculation leads to

$$T_{\text{SC}}^{1\text{-loop}}(\mathbf{p}, \mathbf{p}') = \alpha \frac{[C(E^*)]^2 M^2}{8\pi} \left( \frac{1}{\epsilon} + 2 \log \frac{\mu \sqrt{\pi}}{2p} + 1 - \gamma_E + i\pi \right) \quad (2.24)$$

where  $\epsilon \equiv d - 3$  is zero in the present three dimensional case and  $\gamma_E \approx 0.5772$  is the Euler-Mascheroni constant. The ultraviolet divergent terms can be reabsorbed into a redefinition of the strength parameter  $C(E^*)$ , via the renormalization process. Besides, the logarithmic divergence for vanishing momenta highlights the infeasibility of a perturbative approach when the momenta of the colliding fermions is small. In such cases, the Coulomb corrections have to be resummed to all the orders in  $\alpha$ .

Since we are mainly interested also in the low-momentum sector of fermion-fermion elastic scattering, we incorporate the Coulomb insertions in the amplitude of the process non-perturbatively as shown in sec. 1.2.1. Exploiting the Coulomb Green's functions, the T-matrix element  $T_{\text{SC}}$  for S-wave strong interactions (cf. fig. 1.3) can be analytically computed and the phase shift  $\delta_0$  can be extracted from the relevant T-matrix as in eq. (1.29),

$$|\mathbf{p}|(\cot \delta_0 - i) = -\frac{4\pi}{M} \frac{e^{2i\sigma_0}}{T_{\text{SC}}(\mathbf{p}', \mathbf{p})} . \quad (2.25)$$

Finally, due to the non-perturbative nature of the Coulomb interactions for small momenta  $\mathbf{p}$ , the ERE cf. eq. (2.17) does not apply [42] and has to be replaced by the generalized expansion in eq. (1.30),

$$C_\eta^2 |\mathbf{p}|(\cot \delta_0 - i) + \alpha M H(\eta) = -\frac{1}{a_C^{(0)}} + \frac{1}{2} r_0^{(0)} \mathbf{p}^2 + r_1^{(0)} \mathbf{p}^4 + \dots , \quad (2.26)$$

where  $a_C^{(0)}$  is the S-wave strong scattering length,  $r_0^{(0)}$  the effective range and  $r_1^{(0)}$  is the shape parameter, both of the latter modified by the Coulomb interaction.

### 2.1.2 Repulsive channel

Recalling the expression of the full eigenstates in terms of the Coulomb ones in eq. (1.25), the strong scattering amplitude with electrostatic corrections can be rewritten as

$$T_{\text{SC}}(\mathbf{p}', \mathbf{p}) = \sum_{n=0}^{+\infty} \langle \psi_{\mathbf{p}'}^{(-)} | \hat{V}_S \left( \hat{G}_C^{(+)} \hat{V}_S \right)^n | \psi_{\mathbf{p}}^{(+)} \rangle , \quad (2.27)$$

where  $\hat{V}_S \equiv \hat{V}^{(0)}$  is the lowest order strong  $\ell = 0$  potential. The first order contribution to the Coulomb-corrected strong scattering amplitude,  $n = 1$ , can be represented by a single strong vertex with infinitely many Coulomb-photon insertions in the incoming or outgoing legs. As in the QED-free case, the corresponding amplitude can be evaluated analytically, giving

$$\begin{aligned} T_{\text{SC}}^{\text{tree}}(\mathbf{p}', \mathbf{p}) &= \int_{\mathbb{R}^3} \frac{d^3 q}{(2\pi)^3} \int_{\mathbb{R}^3} \frac{d^3 q'}{(2\pi)^3} \langle \psi_{\mathbf{p}'}^{(-)} | \mathbf{q}' \rangle \langle \mathbf{q}' | \hat{V}_S | \mathbf{q} \rangle \langle \mathbf{q} | \psi_{\mathbf{p}}^{(+)} \rangle \\ &= C(E^*) \psi_{\mathbf{p}'}^{(-)*}(0) \psi_{\mathbf{p}}^{(+)}(0) = C(E^*) C_\eta^2 e^{2i\sigma_0} . \end{aligned} \quad (2.28)$$

To the one-loop order, the scattering amplitude can be depicted as single bubble diagram with infinitely many Coulomb-photon insertions inside the loop and yields

$$T_{\text{SC}}^{1\text{-loop}}(\mathbf{p}', \mathbf{p}) = [C(E^*)]^2 C_\eta^2 e^{2i\sigma_0} G_C^{(+)}(E, \mathbf{0}, \mathbf{0}) , \quad (2.29)$$

where

$$G_C^{(+)}(E, \mathbf{0}, \mathbf{0}) = \int_{\mathbb{R}^3} \frac{d^3q}{(2\pi)^3} \int_{\mathbb{R}^3} \frac{d^3q'}{(2\pi)^3} \langle \mathbf{q}' | \hat{G}_C^{(+)}(E) | \mathbf{q} \rangle = M \int_{\mathbb{R}^3} \frac{d^3k}{(2\pi)^3} \frac{\psi_{\mathbf{k}}^{(+)}(0) \psi_{\mathbf{k}}^{(+)*}(0)}{\mathbf{p}^2 - \mathbf{k}^2 + i\epsilon} \quad (2.30)$$

represents the propagation of the two fermions from zero to zero relative separation. Proceeding order by order, it turns out that the summation of all the contributions, i.e. the ladder corrections (cf. fig. 1.1) to the zero angular momentum bubbles, can be interpreted again as a geometric series, whose sum is given by

$$T_{\text{SC}}(\mathbf{p}', \mathbf{p}) = \frac{C_\eta^2 C(E^*) e^{2i\sigma_0}}{1 - C(E^*) G_C^{(+)}(E, \mathbf{0}, \mathbf{0})} , \quad (2.31)$$

a formula that bears some resemblance with eq. (2.8). Now, we switch to the evaluation of the Green's function  $G_C^{(+)}(E, \mathbf{0}, \mathbf{0}) \equiv J_C(\mathbf{p})$ . Firstly, the integrand appearing in the propagator in eq. (2.30) can be split into two parts by means of the trick  $(\mathbf{p}^2 - \mathbf{q}^2)^{-1} = -\mathbf{q}^{-2} + \mathbf{p}^2 \mathbf{q}^{-2} (\mathbf{p}^2 - \mathbf{q}^2)^{-1}$  and secondly the Feynman convention can be restored in the term depending on  $\mathbf{p}$  and  $\mathbf{q}$ ,

$$\begin{aligned} J_C(\mathbf{p}) &= M \int_{\mathbb{R}^3} \frac{d^3q}{(2\pi)^3} \frac{2\pi\eta(\mathbf{q})}{e^{2\pi\eta(\mathbf{q})} - 1} \frac{1}{\mathbf{p}^2 - \mathbf{q}^2 + i\epsilon} \\ &= M \int_{\mathbb{R}^3} \frac{d^3q}{(2\pi)^3} \frac{2\pi\eta(\mathbf{q})}{e^{2\pi\eta(\mathbf{q})} - 1} \frac{1}{\mathbf{q}^2} \frac{\mathbf{p}^2}{\mathbf{p}^2 - \mathbf{q}^2 + i\epsilon} - M \int_{\mathbb{R}^3} \frac{d^3q}{(2\pi)^3} \frac{2\pi\eta(\mathbf{q})}{e^{2\pi\eta(\mathbf{q})} - 1} \frac{1}{\mathbf{q}^2} , \end{aligned} \quad (2.32)$$

where the latter integral proves to be ultraviolet divergent, hence we denote it by  $J_C^{\text{div}}$ . Concerning the convergent part,  $J_C^{\text{fin}}$ , its integration can be carried out via the change of variables  $q \mapsto x \equiv 2\pi\eta(q) = \pi\alpha M/q$  where  $q = |\mathbf{q}|$  and exploiting the following integral identity

$$\int_0^{+\infty} dx \frac{x}{(e^x - 1)(x^2 + a^2)} = \frac{1}{2} \left[ \log\left(\frac{a}{2\pi}\right) - \frac{\pi}{a} - \psi\left(\frac{a}{2\pi}\right) \right] \quad (2.33)$$

with  $a = 2\pi i\eta(p)$ . Recalling the definition of  $H(\eta)$  in eq. (1.33), the finite part of the propagator of interest turns out to be proportional to the former,

$$J_C^{\text{fin}}(\mathbf{p}) = -\frac{\alpha M^2}{4\pi} H(\eta) . \quad (2.34)$$

It follows by substitution of the latter equation into the one of the generalized ERE (cf. eq. (2.25)), that all the parts depending on  $H(\eta)$  cancel out and that the scattering length is contained in the divergent part of the Green's function,

$$\frac{1}{a_C^{(0)}} = \frac{4\pi}{M} \left[ \frac{1}{C(E^*)} - J_C^{\text{div}}(\mathbf{p}) \right] . \quad (2.35)$$

On the other hand, the absorption of quadratic and higher order terms in the momentum (cf. eq. (1.5)) within the energy-dependent coefficient  $C(E^*)$ , keeps the effective range  $r_0^{(0)}$  equal to

zero, as observed in the case with strong contact interaction alone (cf. sec. 3.1 of ref. [17]). Now, setting  $\epsilon \equiv d - 3$  we evaluate the divergent part of the Green's function in dimensional regularization [2]

$$J_C^{\text{div}}(d; \mathbf{p}) = -M \left(\frac{\mu}{2}\right)^\epsilon \frac{\Omega_d}{(2\pi)^d} \int_0^{+\infty} dq q^{-\epsilon} \frac{2\pi\eta(q)}{e^{2\pi\eta(q)} - 1}, \quad (2.36)$$

where  $\Omega_d = 2\pi^{d/2}/\Gamma(\frac{d}{2})$  is the surface area of the  $d$ -dimensional unit sphere. Performing again the variable change  $x = 2\pi\eta(q)$ , the integration can be carried out,

$$J_C^{\text{div}}(d; \mathbf{p}) = -M \left(\frac{\mu}{2}\right)^\epsilon \frac{2\pi^{d/2}}{\Gamma(\frac{d}{2})(2\pi)^d} (\alpha\pi M)^{d-2} \int_0^{+\infty} dx \frac{x^{\epsilon-1}}{e^x - 1} = -\frac{\alpha M^2}{4\sqrt{\pi}} \left(\frac{\mu}{2}\right)^\epsilon \frac{\Gamma(\epsilon)\zeta(\epsilon)}{\Gamma(\frac{3-\epsilon}{2})} \quad (2.37)$$

where  $\mu$  is a renormalization scale introduced by the minimal subtraction (MS) scheme (cf. sec. 3.6 of [130]). In the  $d \rightarrow 3$  limit, the divergent part is given by the Euler's Gamma function  $\Gamma(\epsilon)$  where  $\epsilon \equiv 3 - d$ , that has to be expanded in Laurent series for small arguments. Besides, even if the Riemann Zeta function is finite for zero arguments, its series expansion around zero,

$$\zeta(\epsilon) = \zeta(0) + \zeta'(0)\epsilon + \mathcal{O}(\epsilon^2) \approx -\frac{1}{2}[1 + \epsilon \log(2\pi)] + \mathcal{O}(\epsilon^2), \quad (2.38)$$

yields a nonzero contribution to the expression of the Coulomb Green's function  $J_C^{\text{div}}$  when the second term on the r.h.s. of eq. (2.38) multiplies the pole  $1/\epsilon$  from the expanded Gamma function. A similar argument holds for the Gamma function at the denominator of eq. (2.37), where  $\Gamma(\frac{3-\epsilon}{2})$  should be expanded around  $\frac{3}{2}$ ,

$$\Gamma\left(\frac{3-\epsilon}{2}\right) = \Gamma\left(\frac{3}{2}\right) - \frac{\epsilon}{2}\Gamma'\left(\frac{3}{2}\right) + \mathcal{O}\left(\frac{\epsilon^2}{4}\right) \approx \frac{\sqrt{\pi}}{2} \left[1 - \epsilon \left(1 - \log 2 - \frac{\gamma_E}{2}\right)\right], \quad (2.39)$$

where the particular value  $\psi(\frac{3}{2}) = \Gamma'(\frac{3}{2})/\Gamma(\frac{3}{2}) = 2 - 2\log 2 - \gamma_E$  for the derivative of the Gamma function has been exploited. Additionally, the poles in the 2-dimensional limit of  $J_C^{\text{div}}(d; \mathbf{p})$ , should be subtracted to  $J_C^{\text{div}}(d; \mathbf{p})$ , in accordance with the PDS regularization scheme. Since the Zeta function is divergent  $\zeta(\epsilon) \equiv \zeta(1 + 2 - d) = 1/(2 - d) + \gamma_E$ , in the latter limit we have

$$\lim_{d \rightarrow 2} J_C^{\text{div}}(d, \mathbf{p}) = \frac{\mu M}{4\pi} \frac{1}{d - 2}. \quad (2.40)$$

All these premises considered, the divergent part of the Green's function  $J_C(\mathbf{p})$  in the PDS scheme becomes

$$J_C^{\text{div}}(\mathbf{p}) = \frac{\alpha M^2}{4\pi} \left[ \frac{1}{\epsilon} + \log \frac{\mu\sqrt{\pi}}{\alpha M} + 1 - \frac{3}{2}\gamma_E \right] - \frac{\mu M}{4\pi}. \quad (2.41)$$

Replacing the last result in eq. (2.35), the desired expression for the Coulomb scattering length can be obtained,

$$\frac{1}{a_C^{(0)}} = \frac{4\pi}{MC(E^*)} + \mu - \alpha M \left[ \frac{1}{\epsilon} + \log \frac{\mu\sqrt{\pi}}{\alpha M} + 1 - \frac{3}{2}\gamma_E \right]. \quad (2.42)$$

After renormalization, the divergent pole is reabsorbed from the definition of the strong coupling constant  $C(E^*)$  and the scattering length,

$$\frac{1}{\alpha_C^{(0)}(\mu)} = \frac{4\pi}{MC(E^*, \mu)} + \mu. \quad (2.43)$$

Furthermore, excluding the divergent pole, that is expected to be canceled by counterterms describing short-distance electromagnetic and other isospin-breaking interactions due to quark mass differences in case the fermions are hadrons [2], the renormalized scattering length takes the form

$$\frac{1}{\alpha_C^{(0)}(\mu)} = \frac{1}{\alpha_C^{(0)}} + \alpha M \left[ \log \frac{\mu\sqrt{\pi}}{\alpha M} + 1 - \frac{3}{2}\gamma_E \right]. \quad (2.44)$$

From the latter expression, we observe that the Coulomb-modified scattering length is non-perturbative in the fine structure constant, since  $\alpha$  appears in the combination  $\alpha \log \alpha$ . The Coulomb interaction, indeed, can overcome in magnitude the strong force for small values of the renormalization mass  $\mu$  and determine the magnitude of the scattering length [2].

### 2.1.3 Attractive channel

We shall consider the scattering between two non-relativistic fermions with opposite charges, such as fermion-antifermion scattering. Even if the strong-Coulomb T-matrix is again given by eq. (2.27), the Coulomb propagator  $\bar{G}_C^{(+)}(E; \mathbf{0}, \mathbf{0})$  involves now both bound and scattering states. Nevertheless, the scattering amplitude preserves its form [2],

$$\bar{T}_{\text{SC}}(\mathbf{p}', \mathbf{p}) = \frac{C_\eta^2 \bar{C}(E^*) e^{2i\sigma_0}}{1 - \bar{C}_0 \bar{G}_C^{(+)}(E, \mathbf{0}, \mathbf{0})}, \quad (2.45)$$

where  $\bar{C}(E^*)$  is the coupling constant of the strong contact pseudopotential in this channel and  $\eta = -\alpha M/2|\mathbf{p}|$  is the Coulomb parameter. Differently from the previous case,  $\bar{G}_C(E; \mathbf{0}, \mathbf{0}) \equiv \bar{J}_C(\mathbf{p})$  can be decomposed as a sum of a bound states  $\bar{J}_C^b(\mathbf{p})$  and a scattering states Green's function  $\bar{J}_C^s(\mathbf{p})$ . In particular, the former part of the Coulomb propagator can be written as

$$\bar{J}_C^b(\mathbf{p}) = \sum_{n\ell} \frac{|\psi_{n\ell}(0)|^2}{E - E_{n\ell}}, \quad (2.46)$$

where  $\psi_{n\ell}$  are bound eigenstates with angular momentum  $\ell$  and energy given by Bohr's formula,  $E_{n\ell} = -\alpha^2 M/4n^2$ . Recalling that the probability to find particles at the origin of a bound state is non-zero only for zero angular momentum states,  $|\psi_{n\ell}(0)|^2 = (\alpha M)^3/(8\pi n^3) \delta_{\ell 0}$ , the last equation can be rewritten in closed form as

$$\bar{J}_C^b(\mathbf{p}) = \frac{\alpha M^2}{4\pi} \sum_{n=1}^{+\infty} \frac{2\eta^2}{n(n^2 + \eta^2)} = \frac{\alpha M^2}{4\pi} [\psi(i\eta) + \psi(-i\eta) + 2\zeta(1)], \quad (2.47)$$

where the Euler's Digamma function has been rewritten in terms of a telescoping series. In particular,  $\zeta(1)$  is the sum of the harmonic series, whose Cauchy principal value is finite and given by  $\gamma_E$ . Then, we consider the scattering part of the Green's function, where the states in the expansion have eigenvalue  $E = \mathbf{p}^2/M$ , as before. Since the  $\eta$  is negative, we can recast

the denominator with the Sommerfeld factor in the integrand as

$$\frac{1}{e^{2\pi\eta(q)} - 1} = \frac{1}{1 - e^{-2\pi\eta(q)}} - 1, \quad (2.48)$$

thus allowing for a separation of the original Green's function into three parts,  $\bar{J}_C^s = \bar{J}_C^{\text{div}} + \bar{J}_C^{\text{fin}} + \bar{J}_C^{\text{new}}$ , where the finite part gives

$$\bar{J}_C^{\text{fin}}(\mathbf{p}) = M \int_{\mathbb{R}^3} \frac{d^3q}{(2\pi)^3} \frac{-2\pi\eta(\mathbf{q})}{e^{-2\pi\eta(\mathbf{q})} - 1} \frac{1}{\mathbf{q}^2} \frac{\mathbf{p}^2}{\mathbf{p}^2 - \mathbf{q}^2 + i\epsilon} = \frac{\alpha M^2}{4\pi} \left[ \frac{1}{i\eta} - \bar{H}(\eta) - \psi(-i\eta) + \psi(i\eta) \right]. \quad (2.49)$$

The computation of the divergent part of the Green's function in dimensional regularization is now straightforward, since the integrand coincides with the one of eqs. (2.34) and (2.36),

$$\bar{J}_C^{\text{div}}(\mathbf{p}) = -M \int_{\mathbb{R}^3} \frac{d^3q}{(2\pi)^3} \frac{-2\pi\eta(\mathbf{q})}{e^{-2\pi\eta(\mathbf{q})} - 1} \frac{1}{\mathbf{q}^2} = \frac{\alpha M^2}{4\pi} \left[ \frac{1}{\epsilon} + \log \frac{\mu\sqrt{\pi}}{\alpha M} + 1 - \frac{3}{2}\gamma_E \right] - \frac{\mu M}{4\pi}, \quad (2.50)$$

taking into account that  $\eta$  has now an opposite sign. The new contribution,  $\bar{J}_C^{\text{new}}(\mathbf{p})$ , assumes the form

$$\bar{J}_C^{\text{new}}(\mathbf{p}) = M \int_{\mathbb{R}^3} \frac{d^3q}{(2\pi)^3} \frac{-2\pi\eta(q)}{\mathbf{p}^2 - \mathbf{q}^2 + i\epsilon}, \quad (2.51)$$

and can be evaluated in dimensional regularization in a similar way to the one of the unperturbed Green's function in eq. (2.37),

$$\bar{J}_C^{\text{new}}(\mathbf{p}) = -\frac{\alpha M^2}{2\pi} \left[ \frac{1}{\epsilon} + \log \frac{\mu\sqrt{\pi}}{\alpha M} + \log(-i\eta) + 1 - \frac{1}{2}\gamma_E \right]. \quad (2.52)$$

Putting the three contributions together, we obtain the expression of the scattering part of the Green's function

$$\bar{J}_C^s(\mathbf{p}) = -\frac{\mu M}{4\pi} - \frac{\alpha M^2}{4\pi} \left[ \frac{1}{\epsilon} + \log \frac{\mu\sqrt{\pi}}{\alpha M} + \log(-i\eta) - \frac{1}{2i\eta} + \psi(-i\eta) + 1 + \frac{1}{2}\gamma_E \right]. \quad (2.53)$$

Reabsorbing the  $1/\epsilon$  divergence via an unknown counter-term and replacing  $\zeta(1)$  with its Cauchy principal value, the total Coulomb Green's function  $\bar{G}_C^{(+)}(E; \mathbf{0}, \mathbf{0}) = \bar{J}_C^b(\mathbf{p}) + \bar{J}_C^s(\mathbf{p})$  takes the form

$$\bar{J}_C(\mathbf{p}) = -\frac{\mu M}{4\pi} - \frac{\alpha M^2}{4\pi} \left[ \log \frac{\mu\sqrt{\pi}}{\alpha M} + 1 - \frac{3}{2}\gamma_E - \bar{H}(\eta) \right], \quad (2.54)$$

that, combined with eq. (2.45) and the effective range expansion in eq. (2.26) with  $H(\eta)$  replaced by  $\bar{H}(\eta)$ , permits to obtain the scattering length. The renormalized scattering length  $\bar{a}_C^{(0)}(\mu)$  can be obtained from the measured one  $\bar{a}_C^{(0)}$  via the relation

$$\frac{1}{\bar{a}_C^{(0)}(\mu)} = \frac{1}{\bar{a}_C^{(0)}} - \alpha M \left[ \log \frac{\mu\sqrt{\pi}}{\alpha M} + 1 - \frac{3}{2}\gamma_E \right]. \quad (2.55)$$

By comparison with eq. (2.44), it can be observed that the result of the repulsive channel coincides with the one in eq. (2.55), except for a sign inversion of  $\alpha$  in front of the square bracket. Eventually, we relate the renormalized scattering length with the renormalized coupling con-

stant of the strong interaction through the formula

$$\frac{1}{\bar{a}_C^{(0)}} = \frac{4\pi}{M\bar{C}(E^*, \mu)} + \mu, \quad (2.56)$$

in all analogous to eq. (2.43).

## 2.2 The finite-volume environment

Still concentrating on two-body processes, we embed the physical system of non-relativistic spinless fermions interacting via Coulomb photons in a cubic spatial volume with edges of length  $L$ . Due to the imposition of periodic boundary conditions on the matter fields and the wavefunctions, a free particle subject to PBCs carries a momentum  $\mathbf{p} = 2\pi\mathbf{n}/L$  where  $\mathbf{n}$  is a dimensionless three-vector of integers and  $L \equiv Na$ . In numerical simulations, the finite-volume configuration space is even discretized, so that for each direction only  $N$  points separated by a spacing  $a$  are considered and the cubic box reduces to a cubic lattice.

As shown in sec. 1.3, it is exactly this gapped nature of the momentum that allows for a perturbative treatment of QED, provided  $L$  is large enough to satisfy the constraint  $L \gg 1/M$ . Assuming this limit throughout the rest of the chapter and taking the LO modification on the particle's masses into account (cf. eq. (1.39)), the infinite-volume ERE in the repulsive case (cf. eq. (1.45)) is recast in terms of the primed scattering parameters in eqs. (1.40)-(1.44) with  $\ell = 0$ ,

$$C_\eta^2|\mathbf{p}|(\cot\delta_0 - i) + \alpha MH(\eta) = -\frac{1}{a_C'^{(0)}} + \frac{1}{2}r_0'^{(0)}\mathbf{p}^2 + r_1'^{(0)}\mathbf{p}^4 + \dots, \quad (2.57)$$

and, finally, rewritten in terms of finite-volume quantities, denoted by the  $L$  superscript. The last version of the ERE in sec. 2.2.2, combined with the quantization conditions discussed in the next section, will pave the way for the derivation of the finite volume energy corrections for scattering and bound states with zero angular momentum.

### 2.2.1 Quantization Condition

After introducing the finite and discretized configuration space, we derive the conditions that determine the counterpart of the  $\ell = 0$  energy eigenvalues in the cubic finite volume. These states transform as the trivial irreducible representation  $A_1$  (in Schönflies's notation [131]) of the cubic group [3, 68, 69], the finite group of the 24 rotations of the cube that replaces the original  $SO(3)$  symmetry in the continuum and infinite volume context [67].

As it can be inferred from eq. (1.22), the eigenvalues of the full Hamiltonian of the system  $\hat{H}_0 + \hat{V}_C + \hat{V}_S$  can be identified with the singularities of the two-point correlation function  $G_{SC}(\mathbf{r}, \mathbf{r}')$  and are known in literature [1, 74–76] as *quantization conditions*. Rewriting eq. (1.22) in terms of a geometric series of ratio  $\hat{G}_C \hat{V}_S$ ,

$$\hat{G}_{SC}^{(\pm)} = \frac{1}{1 - \hat{G}_C^{(\pm)} \hat{V}_S} \hat{G}_C \quad (2.58)$$

the two-point Green's function operator can be rewritten in powers of  $\hat{G}_C$ , which, in turn, can be expanded in terms of the fine structure constant  $\alpha$ . Thus, the full two-body correlation



function can be rewritten perturbatively as

$$\langle \mathbf{r} | \hat{G}_{SC}^{(\pm)} | \mathbf{r}' \rangle = \langle \mathbf{r} | \hat{G}_C^{(\pm)} | \mathbf{r}' \rangle + \langle \mathbf{r} | \hat{G}_C^{(\pm)} \hat{V}_S \hat{G}_C^{(\pm)} | \mathbf{r}' \rangle + \langle \mathbf{r} | \hat{G}_C^{(\pm)} \hat{V}_S \hat{G}_C^{(\pm)} \hat{V}_S \hat{G}_C^{(\pm)} | \mathbf{r}' \rangle + \dots \quad (2.59)$$

In particular, the computation of the three lowest order contributions in  $C(E^*)$  yields respectively (cf. eq. (2.9))

$$\langle \mathbf{r}' | \hat{G}_C^{(\pm)} | \mathbf{r} \rangle = G_C^{(\pm)}(\mathbf{r}', \mathbf{r}) , \quad (2.60)$$

$$\langle \mathbf{r}' | \hat{G}_C^{(\pm)} \hat{V}_S \hat{G}_C^{(\pm)} | \mathbf{r} \rangle = C(E^*) G_C(\mathbf{r}', \mathbf{0})^{(\pm)} G_C^{(\pm)}(\mathbf{0}, \mathbf{r}) , \quad (2.61)$$

and

$$\langle \mathbf{r}' | \hat{G}_C^{(\pm)} \hat{V}_S \hat{G}_C^{(\pm)} \hat{V}_S \hat{G}_C^{(\pm)} | \mathbf{r} \rangle = [C(E^*)]^2 G_C^{(\pm)}(\mathbf{r}, \mathbf{0}) G_C^{(\pm)}(\mathbf{0}, \mathbf{0}) G_C^{(\pm)}(\mathbf{0}, \mathbf{r}) . \quad (2.62)$$

From the latter equations, the expression of  $(N+1)^{\text{th}}$  order contribution to the full two-point correlation function can be inferred,

$$\langle \mathbf{r}' | \hat{G}_C^{(\pm)} \underbrace{\hat{V}_S \hat{G}_C^{(\pm)} \dots \hat{V}_S \hat{G}_C^{(\pm)}}_{N \text{ times}} | \mathbf{r} \rangle = G_C^{(\pm)}(\mathbf{r}', \mathbf{0}) \underbrace{C(E^*) G_C^{(\pm)}(\mathbf{0}, \mathbf{0}) \dots C(E^*) G_C^{(\pm)}(\mathbf{0}, \mathbf{r})}_{N \text{ times}} , \quad (2.63)$$

thus allowing for the rewriting of the original Green's function in terms of a geometric series of ratio  $C(E^*) G_C^{(\pm)}(\mathbf{0}, \mathbf{0})$ , in the same fashion of the original operator identity (cf. eq. (2.58)),

$$G_{SC}^{(\pm)}(\mathbf{r}', \mathbf{r}) = \langle \mathbf{r}' | \hat{G}_{SC}^{(\pm)} | \mathbf{r} \rangle = G_C^{(\pm)}(\mathbf{r}', \mathbf{r}) + G_C^{(\pm)}(\mathbf{r}', \mathbf{0}) \frac{C_0(E^*)}{1 - C(E^*) G_C^{(\pm)}(\mathbf{0}, \mathbf{0})} G_C^{(\pm)}(\mathbf{0}, \mathbf{r}) , \quad (2.64)$$

where  $\sqrt{C(E^*)} G_C^{(\pm)}(\mathbf{r}', \mathbf{0})$  and  $\sqrt{C(E^*)} G_C^{(\pm)}(\mathbf{0}, \mathbf{r})$  can be interpreted as a *source* and a *sink* coupling the fermions to an S-wave state respectively. Furthermore, the inhomogeneous term,  $G_C^{(\pm)}(\mathbf{r}', \mathbf{r})$ , is absent when  $\mathbf{r}'$  and  $\mathbf{r}$  coincide with the origin. From the last equation, the infinite volume quantization conditions can be inferred and identified with the pole of the correlation function  $G_{SC}^{(\pm)}(\mathbf{r}', \mathbf{r})$  and can be written as

$$\frac{1}{C(E^*)} = G_C^{(\pm)}(\mathbf{0}, \mathbf{0}) , \quad (2.65)$$

where the CoM energy dependent coupling constant is equal to the inverse of the Coulomb's two-point Green Function evaluated at the origin. Moreover, we observe that the embedding of the system in a finite volume does not affect the form of the complete two-point Green's function  $G_{SC}^{(\pm)}$  given in eq. (2.64). Considering only the retarded correlation function and adopting the simplified notation in sec. 3.1.2 for the Coulomb two-point function evaluated at the origin,  $G_C^{(\pm)}(\mathbf{0}, \mathbf{0})$ , eq. (2.64) in finite volume becomes

$$G_{SC}^{(+),L}(\mathbf{r}', \mathbf{r}) = G_C^{(+),L}(\mathbf{r}', \mathbf{r}) + G_C^{(+),L}(\mathbf{r}', \mathbf{0}) \frac{C^L(E^*)}{1 - C^L(E^*) J_C^L(\mathbf{p})} G_C^{(+),L}(\mathbf{0}, \mathbf{r}) . \quad (2.66)$$

yielding the sought finite volume quantization condition,

$$\frac{1}{C^L(E^*)} = J_C^L(\mathbf{p}) , \quad (2.67)$$

which determines the  $A_1$  eigenvalues. In order to exploit the latter relation perturbatively, it is necessary to approximate  $J_C^L(\mathbf{p})$  in eq. (2.63) to order  $\alpha$ . Since the two-point Coulomb



Green's function is evaluated at the origin, the external legs in the ladders appearing in the expansion of  $G_C^{(\pm)}(\mathbf{r}, \mathbf{r}')$  in fig. 1.1 converge pairwise, generating bubbles with Coulomb photon insertions. Therefore, the contributions to  $J_C(\mathbf{p})$  correspond to loop integrals closed at the two extrema on S-wave vertexes, and can be derived analytically via repeated application of the Dyson identity between  $\hat{G}_C^{(\pm)}$  and  $\hat{G}_0^{(\pm)}$  in eq. (1.16). In particular, the first two ladder diagrams in the expansion of fig. 1.1 become bubble diagrams, respectively with and without a Coulomb photon insertion inside. In infinite volume, their contribution reads

$$\begin{aligned} J_C(\mathbf{p}) &= G_C^{(+)}(\mathbf{0}, \mathbf{0}) = \langle \mathbf{r}' | \hat{G}_0^{(\pm)} | \mathbf{r} \rangle \Big|_{\mathbf{r}'=\mathbf{0}}^{\mathbf{r}=\mathbf{0}} + \langle \mathbf{r}' | \hat{G}_0^{(\pm)} \hat{V}_C \hat{G}_0^{(\pm)} | \mathbf{r} \rangle \Big|_{\mathbf{r}'=\mathbf{0}}^{\mathbf{r}=\mathbf{0}} + \dots \\ &= -M \int_{\mathbb{R}^3} \frac{d^3 q}{(2\pi)^3} \frac{1}{\mathbf{q}^2 - \mathbf{p}^2} + 4\pi\alpha M^2 \int_{\mathbb{R}^3} \frac{d^3 q}{(2\pi)^3} \int_{\mathbb{R}^3} \frac{d^3 k}{(2\pi)^3} \frac{1}{\mathbf{q}^2 - \mathbf{p}^2} \frac{1}{\mathbf{k}^2 - \mathbf{p}^2} \frac{1}{|\mathbf{q} - \mathbf{k}|^2} + \dots, \end{aligned} \quad (2.68)$$

Replacing the integrals over continuous momenta by sums over three-vectors of integers  $\mathbf{n}, \mathbf{m} \in \mathbb{Z}^3$ ,

$$\int_{\mathbb{R}^3} \frac{d^3 q}{(2\pi)^3} \leftrightarrow \frac{1}{L^3} \sum_{\mathbf{n}}, \quad (2.69)$$

and removing the zero-modes from the Coulomb photon propagator, the finite volume counterpart of eq. (2.37) is obtained

$$J_C^L(\mathbf{p}) = -\frac{M^L}{4\pi^2 L} \sum_{\mathbf{n}} \frac{1}{|\mathbf{n}|^2 - \tilde{p}^2} + \frac{\alpha(M^L)^2}{16\pi^5} \sum_{\mathbf{n}} \sum_{\mathbf{m} \neq \mathbf{n}}^{\Lambda_n} \frac{1}{|\mathbf{n}|^2 - \tilde{p}^2} \frac{1}{|\mathbf{m}|^2 - \tilde{p}^2} \frac{1}{|\mathbf{n} - \mathbf{m}|^2} + \dots, \quad (2.70)$$

where adimensional finite-volume momentum  $\tilde{p} \equiv L|\mathbf{p}|/2\pi$  and a spherical cutoff  $\Lambda_n \equiv L\Lambda/2\pi$  have been introduced, in order to regulate the divergent sums. Additionally, the infinite volume mass has been replaced by its finite volume counterpart, even if in sec. 2.2.2 we will notice that these corrections [1, 46] carry only  $\mathcal{O}(\alpha^2)$  contributions, which can be neglected in our perturbative treatment of QED.

Since discretization does not alter the ultraviolet behaviour of the infinite volume integrals, the renormalization of divergences in finite and in infinite volume produce the same results. With the aim of regulating the sums in eq. (2.70) for numerical evaluation while maintaining the mass-independent renormalization scheme (cf. sec. II B of ref. [1]), we rewrite the finite volume quantization conditions as

$$\frac{1}{C^L(E^*)} - \Re J_C^{\{\text{DR}\}}(\mathbf{p}) = J_C^L(\mathbf{p}) - \Re J_C^{\{\Lambda\}}(\mathbf{p}), \quad (2.71)$$

where  $J_C^{\{\Lambda\}}(\mathbf{p})$  and  $J_C^{\{\text{DR}\}}(\mathbf{p})$  represent the  $\mathcal{O}(\alpha)$  approximations of  $J_C$  evaluated in the cutoff- and dimensional regularization methods, without implementing the PDS scheme [22]. We begin with the computation of  $J_C(\mathbf{p})$  in the former regularization technique and consider its expression given in eq. (2.68),

$$J_C^{\{\Lambda\}}(\mathbf{p}) = -M \int_{S_\Lambda^2} \frac{d^3 q}{(2\pi)^3} \frac{1}{\mathbf{q}^2 - \mathbf{p}^2} + 4\pi\alpha M^2 \int_{S_\Lambda^2} \frac{d^3 q}{(2\pi)^3} \int_{\mathbb{R}^3} \frac{d^3 k}{(2\pi)^3} \frac{1}{\mathbf{q}^2 - \mathbf{p}^2} \frac{1}{\mathbf{k}^2 - \mathbf{p}^2} \frac{1}{|\mathbf{q} - \mathbf{k}|^2} + \dots, \quad (2.72)$$

where  $S_\Lambda^2$  denotes the three-dimensional sphere with arbitrarily large radius  $\Lambda$ . Considering the  $\mathcal{O}(\alpha^0)$  contribution, we obtain

$$\begin{aligned} -M \int_{S_\Lambda^2} \frac{d^3\mathbf{q}}{(2\pi)^3} \frac{1}{\mathbf{q}^2 - \mathbf{p}^2} &= -\frac{M}{2\pi^2} \int_0^\Lambda d\mathbf{q} - \frac{M\mathbf{p}^2}{2\pi^2} \int_0^\Lambda d\mathbf{q} \frac{1}{\mathbf{q}^2 - \mathbf{p}^2} \\ &= -\frac{M\Lambda}{2\pi^2} + \frac{M}{4\pi^2} \log \left( \frac{1 + \frac{|\mathbf{p}|}{\Lambda}}{-1 + \frac{|\mathbf{p}|}{\Lambda}} \right) = -\frac{M\Lambda}{2\pi^2} + \mathcal{O}(\Lambda^0) \approx -\frac{M\Lambda}{2\pi^2}, \end{aligned} \quad (2.73)$$

where the constant terms, independent on the spherical cutoff, have been discarded. Second, the  $\mathcal{O}(\alpha)$  dependent contribution to  $J_C^{\{\Lambda\}}(\mathbf{p})$  can be recast as follows

$$\begin{aligned} \mathfrak{J} &\equiv 4\pi\alpha M^2 \int_{S_\Lambda^2} \frac{d^3\mathbf{q}}{(2\pi)^3} \int_{\mathbb{R}^3} \frac{d^3\mathbf{k}}{(2\pi)^3} \frac{1}{\mathbf{q}^2 - \mathbf{p}^2} \frac{1}{\mathbf{k}^2 - \mathbf{p}^2} \frac{1}{|\mathbf{q} - \mathbf{k}|^2} \\ &= 4\pi\alpha M^2 \int_0^1 d\omega \int_{S_\Lambda^2} \frac{d^3\mathbf{q}}{(2\pi)^3} \frac{1}{\mathbf{q}^2 - \mathbf{p}^2} \int_{\mathbb{R}^3} \frac{d^3\mathbf{k}}{(2\pi)^3} \frac{1}{[\mathbf{k}^2 - 2(1-\omega)\mathbf{k} \cdot \mathbf{q} + \Xi_1]^2}, \end{aligned} \quad (2.74)$$

where  $\Xi_1 \equiv (1-\omega)\mathbf{q}^2 - \omega\mathbf{p}^2$  and Feynman parametrization for the denominators has been applied. Making use of the integration formula in eq. (B16) of ref. [132], the integral over  $\mathbf{k}$  can be carried out, yielding

$$\begin{aligned} \mathfrak{J} &= 4\pi\alpha M^2 \frac{\Gamma(\frac{1}{2})}{(4\pi)^{\frac{3}{2}}} \int_0^1 d\omega \int_{S_\Lambda^2} \frac{d^3\mathbf{q}}{(2\pi)^3} \frac{1}{\mathbf{q}^2 - \mathbf{p}^2} \frac{1}{[\omega(1-\omega)\mathbf{q}^2 - \mathbf{p}^2\omega]^{\frac{1}{2}}} \\ &= 4\pi\alpha M^2 \frac{\Gamma(\frac{1}{2})}{(4\pi)^{\frac{3}{2}}} \int_0^1 d\omega \int_{S_\Lambda^2} \frac{d^3\mathbf{q}}{(2\pi)^3} \frac{1}{\mathbf{q}^2 - \mathbf{p}^2} \frac{1}{[\omega(1-\omega)\mathbf{q}^2 - \mathbf{p}^2\omega]^{\frac{1}{2}}}. \end{aligned} \quad (2.75)$$

At this stage, integration over the angular variables in eq. (2.75) can be performed immediately and the outcoming integrand can be conveniently split into two terms,  $\mathfrak{J} \equiv \mathfrak{J}_1 + \mathfrak{J}_2$ , where

$$\mathfrak{J}_1 = M^2 4\pi\alpha \frac{\Gamma(\frac{1}{2})}{(4\pi)^{\frac{3}{2}}} \int_0^1 \frac{d\omega}{2\pi^2} \frac{1}{\sqrt{\omega(1-\omega)}} \int_0^\Lambda d\mathbf{q} \frac{1}{[\mathbf{q}^2 - \frac{\mathbf{p}^2}{1-\omega}]^{\frac{1}{2}}}, \quad (2.76)$$

and

$$\mathfrak{J}_2 = M^2 4\pi\alpha \frac{\Gamma(\frac{1}{2})}{(4\pi)^{\frac{3}{2}}} \int_0^1 \frac{d\omega}{2\pi^2} \frac{1}{\sqrt{\omega(1-\omega)}} \int_0^\Lambda d\mathbf{q} \frac{\mathbf{p}^2}{\mathbf{q}^2 - \mathbf{p}^2} \frac{1}{[\mathbf{q}^2 - \frac{\mathbf{p}^2}{1-\omega}]^{\frac{1}{2}}}, \quad (2.77)$$

that is expected to generate the subleading contributions in  $\Lambda$ . Starting from  $\mathfrak{J}_1$ , the integration over the momentum  $\mathbf{q}$  gives

$$\mathfrak{J}_1 = M^2 4\pi\alpha \frac{\Gamma(\frac{1}{2})}{(4\pi)^{\frac{3}{2}}} \int_0^1 \frac{d\omega}{2\pi^2} \frac{1}{\sqrt{\omega(1-\omega)}} \left[ \operatorname{arccoth} \left( \frac{1}{\sqrt{1 - \frac{\mathbf{p}^2}{\Lambda^2(1-\omega)}}} \right) - \frac{i\pi}{2} \right]. \quad (2.78)$$

Since the spherical cutoff is arbitrarily large,  $|\mathbf{p}|/\Lambda \ll 1$ , the integrand in eq. (2.78) can be further simplified and the integration over the Feynman variable  $\omega$  can be performed by means of the relations

$$\int_0^1 d\omega \frac{1}{\sqrt{\omega(1-\omega)}} = \pi, \quad \int_0^1 d\omega \frac{\log \sqrt{1-\omega}}{\sqrt{\omega(1-\omega)}} = -\pi \log 2. \quad (2.79)$$

Neglecting the cutoff-independent term, after these operations the desired expression for  $\mathfrak{J}_1$  is obtained,

$$\mathfrak{J}_1 = \frac{\alpha M^2}{4\pi} \log \left( \frac{\Lambda}{|\mathbf{p}|} \right) + \mathcal{O}(\Lambda^0) . \quad (2.80)$$

Concerning  $\mathfrak{J}_1$ , integration over the angular variables together with few manipulations in the constants leads to

$$\mathfrak{J}_2 = \frac{\alpha M^2}{4\pi^2} \int_0^1 d\omega \frac{1}{\sqrt{\omega(1-\omega)}} \int_0^\Lambda dq \frac{\mathbf{p}^2}{\mathbf{q}^2 + \Xi_2} \frac{1}{\left[ \mathbf{q}^2 - \frac{\mathbf{p}^2}{1-\omega} \right]^{\frac{1}{2}}} , \quad (2.81)$$

where  $\Xi_2 \equiv -\mathbf{p}^2$  and  $\Xi_3 \equiv -\mathbf{p}^2/(1-\omega)$ . Subsequently, the integration over the radial component of the momentum  $|\mathbf{q}|$  yields

$$\mathfrak{J}_2 = \frac{\alpha M^2}{4\pi^2} \int_0^1 d\omega \frac{\mathbf{p}^2}{\sqrt{\omega(1-\omega)}} \left[ \frac{\log \left( 1 + \Lambda \sqrt{\frac{\Xi_2 - \Xi_3}{\Xi_2(\Xi_3 + \Lambda^2)}} \right)}{2\sqrt{\Xi_2(\Xi_2 - \Xi_3)}} - \frac{\log \left( 1 + \frac{\Lambda}{\Xi_2} \sqrt{\frac{\Xi_2(\Xi_2 - \Xi_3)}{\Xi_2 + \Lambda^2}} \right)}{2\sqrt{\Xi_2(\Xi_2 - \Xi_3)}} \right] . \quad (2.82)$$

Considering again the large spherical cutoff limit,  $|\mathbf{p}|/\Lambda \ll 1$ , the last expression turns out to be independent on  $\Lambda$  and can be recast as

$$\mathfrak{J}_2 = \frac{\alpha M^2}{4\pi^2} \int_0^1 d\omega \operatorname{arccot} \left( \sqrt{\frac{\omega}{1-\omega}} \right) . \quad (2.83)$$

Even if the remaining integral over  $\omega$  is not finite, it is independent on  $\Lambda$ , therefore it can be left aside together with the other  $\mathcal{O}(\Lambda^0)$  terms. Moreover, the latter divergence can be removed by means of a translation in the momenta such as  $\mathbf{k} \mapsto \mathbf{k} - \mathbf{q}$  in the original expression of the  $\mathcal{O}(\alpha)$  part of  $J_C^{\{\Lambda\}}(\mathbf{p})$  in eq. (2.74). Juxtaposing the contributions from eq. (2.73) and (2.83), and taking the real part of the whole expression we find

$$\Re J_C^{\{\Lambda\}}(\mathbf{p}) = -\frac{M\Lambda}{2\pi^2} - \frac{\alpha M^2}{4\pi} \log \left( \frac{|\mathbf{p}|}{\Lambda} \right) , \quad (2.84)$$

where the term depending linearly on the cutoff regulates the  $\mathcal{O}(\alpha^0)$  part of eq. (2.72), whereas the logarithmic term is paired with the second sum in  $J_C^L(\mathbf{p})$ . Furthermore, starting from the exact expression of  $J_C(\mathbf{p})$  in arbitrary  $d$  dimension given in eq. (2.32),

$$\begin{aligned} J_C^{\{\text{DR}\}}(\mathbf{p}) &= M \int_{\mathbb{R}^d} \frac{d^d q}{(2\pi)^d} \frac{2\pi\eta(\mathbf{q})}{e^{2\pi\eta(\mathbf{q})} - 1} \frac{1}{\mathbf{p}^2 - \mathbf{q}^2 + i\epsilon} \\ &\approx M \int_{\mathbb{R}^d} \frac{d^d q}{(2\pi)^d} \frac{1}{\mathbf{p}^2 - \mathbf{q}^2 + i\epsilon} - \alpha M^2 \int_{\mathbb{R}^d} \frac{d^d q}{(2\pi)^d} \frac{\pi}{2|\mathbf{q}|} \frac{1}{\mathbf{p}^2 - \mathbf{q}^2 + i\epsilon} , \end{aligned} \quad (2.85)$$

we derive  $\Re J_C^{\{\text{DR}\}}(\mathbf{p})$  to the first order in the fine structure constant. First, we observe that the  $\alpha$  independent part coincides with the free two-point correlation function,

$$-M \int_{\mathbb{R}^3} \frac{d^3 q}{(2\pi)^3} \frac{1}{\mathbf{q}^2 - \mathbf{p}^2 - i\epsilon} = G_0^{(+)}(\mathbf{0}, \mathbf{0}) . \quad (2.86)$$

From eq. (2.13) follows that its contribution in dimensional regularization is finite, therefore we switch to the  $d$ -dimensional version of the second integral in the second row of eq. (2.74).

Applying Feynman parametrization for denominators and introducing the ancillary variables  $\gamma = -i|\mathbf{p}|$  and  $\Omega^2 \equiv \gamma^2(1 - \omega)$ , the  $\mathcal{O}(\alpha)$  contribution to  $J_C(\mathbf{p})$  in dimension  $d$  becomes

$$\begin{aligned} \alpha M^2 \int_{\mathbb{R}^d} \frac{d^d q}{(2\pi)^d} \frac{\pi}{2|\mathbf{q}|} \frac{1}{\mathbf{q}^2 - \mathbf{p}^2} &= \frac{\alpha M^2 \pi \Gamma(\frac{3}{2})}{2\Gamma(\frac{1}{2})} \int_0^1 \frac{d\omega}{\sqrt{\omega}} \int_{\mathbb{R}^d} \frac{d^d q}{(2\pi)^d} \frac{1}{[\omega \mathbf{q}^2 + (\mathbf{q}^2 - \mathbf{p}^2)(1 - \omega)]^{3/2}} \\ &= \frac{\alpha M^2 \pi \Gamma(\frac{3}{2})}{2\Gamma(\frac{1}{2})} \int_0^1 \frac{d\omega}{\sqrt{\omega}} \int_{\mathbb{R}^d} \frac{d^d q}{(2\pi)^d} \frac{1}{[\mathbf{q}^2 + \Omega^2]^{3/2}}. \end{aligned} \quad (2.87)$$

Then, integrating over the loop momenta via the dimensional regularization identity (B.12) in ref. [132], we obtain

$$\frac{\alpha M^2 \pi}{2\Gamma(\frac{1}{2})} \int_0^1 \frac{d\omega}{\sqrt{\omega}} \frac{\Gamma(\frac{3}{2} - \frac{d}{2}) (\Omega^2)^{d/2-3/2}}{(4\pi)^{d/2}} = \frac{\alpha M^2 \pi}{2(4\pi)^{3/2}} \frac{\Gamma(\frac{3-d}{2})}{\Gamma(\frac{1}{2})} \left( \frac{\pi \mu^2}{\gamma^2} \right)^{\frac{3-d}{2}} \int_0^1 d\omega \omega^{-1/2} (1 - \omega)^{-(3-d)/2} \quad (2.88)$$

where the divergence is limited to Euler's Gamma, displaying a simple pole in  $\epsilon = 3 - d$ . In fact, the integral over  $\omega$  is finite and admits an expansion in powers of  $\epsilon$ ,

$$\int_0^1 d\omega \omega^{-1/2} (1 - \omega)^{-(3-d)/2} \approx \int_0^1 d\omega \frac{1 - \epsilon \log \sqrt{1 - \omega}}{\sqrt{\omega}} = 2(1 + \epsilon - \epsilon \log 2). \quad (2.89)$$

Expanding also the term proportional to the renormalization mass  $\mu$ , eq. (2.78) becomes

$$\frac{\alpha M^2 \pi}{\sqrt{\pi}} \frac{\Gamma(\frac{\epsilon}{2})}{(4\pi)^{3/2}} \left[ 1 + \frac{\epsilon}{2} \log \left( \frac{\mu^2 \pi}{\gamma^2} \right) \right] [1 - \epsilon - \epsilon \log 2]. \quad (2.90)$$

As the last expression is finite in the  $d \rightarrow 2$  limit, no PDS pole is present and the three-dimensional limit can be taken, obtaining the sought expression for  $J_C^{\{\text{DR}\}}(\mathbf{p})$ ,

$$J_C^{\{\text{DR}\}}(\mathbf{p}) = -\frac{\alpha M^2}{4\pi} \left[ -\frac{1}{\epsilon} + \log \left( \frac{2|\mathbf{p}|}{\mu} \right) - 1 + \frac{\gamma_E}{2} - \log \sqrt{\pi} - \frac{i\pi}{2} \right]. \quad (2.91)$$

Retaining the real part of the last expression and collecting the result from cutoff regularization in eq. (2.84) with the fermion mass replaced by its finite-volume counterpart, the original finite-volume quantization condition can be finally rewritten as

$$\begin{aligned} \frac{1}{C^L(E^*)} &= -\frac{\alpha(M^L)^2}{4\pi} \left[ -\frac{1}{\epsilon} + \log \left( \frac{4\pi}{\mu} \right) - 1 + \frac{\gamma_E}{2} - \log \sqrt{\pi} \right] - \frac{M^L}{4\pi^2 L} \left[ \sum_{\mathbf{n}}^{\Lambda_n} \frac{1}{|\mathbf{n}|^2 - \tilde{p}^2} - 4\pi \Lambda_n \right] \\ &+ \frac{\alpha(M^L)^2}{16\pi^5} \left[ \sum_{\mathbf{n}}^{\Lambda_n} \sum_{\mathbf{m} \neq \mathbf{n}}^{\infty} \frac{1}{|\mathbf{n}|^2 - \tilde{p}^2} \frac{1}{|\mathbf{m}|^2 - \tilde{p}^2} \frac{1}{|\mathbf{n} - \mathbf{m}|^2} - 4\pi^4 \log \Lambda_n \right] + \dots, \end{aligned} \quad (2.92)$$

an expression that will be exploited for the rewriting of the effective range expansion.

## 2.2.2 Finite Volume Effective Range Expansion

Let us start by writing the infinite volume expression of the effective range expansion. By plugging the expression of  $T_{\text{SC}}$  given in eq. (2.31) into eq. (2.25) and exploiting the closed form

of  $J_C(\mathbf{p})$  in dimensional regularization to all orders in  $\alpha$  given in eqs. (2.34) and (2.41), we find

$$C_\eta^2 |\mathbf{p}| \cot \delta_0 + \alpha M H(\eta) = -\frac{4\pi}{MC(E^*)} + \alpha M \left[ \frac{1}{\epsilon} + \log \left( \frac{\mu\sqrt{\pi}}{\alpha M} \right) + 1 - \frac{3}{2}\gamma_E \right]. \quad (2.93)$$

Since the asymptotic behaviour of the momentum integrals in the ultraviolet region remains unaffected by discretization, the latter expression can be immediately applied to the cubic finite volume case, provided the infinite volume parameters are replaced by finite volume ones,

$$C_\eta^2 |\mathbf{p}| \cot \delta_0 + \alpha M^L H(\eta) = -\frac{4\pi}{M^L C^L(E^*)} + \alpha M^L \left[ \frac{1}{\epsilon} + \log \left( \frac{\mu\sqrt{\pi}}{\alpha M^L} \right) + 1 - \frac{3}{2}\gamma_E \right], \quad (2.94)$$

where  $M$  has been replaced by the finite volume one,  $M^L$ , thus obtaining an expression valid also in the non-perturbative treatment of the Coulomb photons. At this point, we substitute the inverse of the strong coupling constant with its expression in eq. (2.92),

$$\begin{aligned} C_\eta^2 |\mathbf{p}| \cot \delta_0 + \alpha M^L H(\eta) = & \alpha M^L \left[ \log \left( \frac{4\pi}{\alpha M^L L} \right) - \gamma_E \right] + \frac{1}{\pi L} \left[ \sum_{\mathbf{n}}^{\Lambda_n} \frac{1}{\mathbf{n}^2 - \tilde{\mathbf{p}}^2} - 4\pi \Lambda_n \right] \\ & - \frac{\alpha M^L}{4\pi^4} \left[ \sum_{\mathbf{n}}^{\Lambda_n} \sum_{\mathbf{m} \neq \mathbf{n}}^{\infty} \frac{1}{\mathbf{n}^2 - \tilde{\mathbf{p}}^2} \frac{1}{\mathbf{m}^2 - \tilde{\mathbf{p}}^2} \frac{1}{|\mathbf{n} - \mathbf{m}|^2} - 4\pi^4 \log \Lambda_n \right] + \dots \end{aligned} \quad (2.95)$$

As it can be observed, in the last equation the mass of the fermions is multiplied by a power of  $\alpha$  in all the occurrences. As the leading order finite volume corrections to  $M^L$  scale as  $\alpha/L$ , these shifts should be consistently ignored in the  $\mathcal{O}(\alpha)$  approximation of the Coulomb Green's function. Therefore, in eq. (2.95) we are allowed to replace  $M^L$  by its infinite volume counterpart,  $M$ , and exploit the expansion with shifted scattering parameters presented in eq. (2.95), obtaining

$$-\frac{1}{\alpha'_C{}^{(0)}} + \frac{1}{2} r_0'^{(0)} \mathbf{p}^2 + r_1'^{(0)} \mathbf{p}^4 + \dots = \frac{1}{\pi L} S_1(\tilde{\mathbf{p}}) - \frac{\alpha M}{4\pi^4} S_2(\tilde{\mathbf{p}}) + \dots + \alpha M \left[ \log \left( \frac{4\pi}{\alpha M L} \right) - \gamma_E \right], \quad (2.96)$$

that corresponds to the desired finite volume effective range expansion, in which the cutoff-regulated series have been denoted as

$$S_1(\tilde{\mathbf{p}}) = \sum_{\mathbf{n}}^{\Lambda_n} \frac{1}{\mathbf{n}^2 - \tilde{\mathbf{p}}^2} - 4\pi \Lambda_n \quad (2.97)$$

and

$$S_2(\tilde{\mathbf{p}}) = \sum_{\mathbf{n}}^{\Lambda_n} \sum_{\mathbf{m} \neq \mathbf{n}}^{\infty} \frac{1}{\mathbf{n}^2 - \tilde{\mathbf{p}}^2} \frac{1}{\mathbf{m}^2 - \tilde{\mathbf{p}}^2} \frac{1}{|\mathbf{n} - \mathbf{m}|^2} - 4\pi^4 \log \Lambda_n, \quad (2.98)$$

that are collectively known in literature as *Lüscher's functions*.

### 2.2.3 Approximate Energy Eigenvalues

Since the Sommerfeld factor is not a rational function of the momentum of the colliding particles in the CoM frame, a non-perturbative counterpart in  $\alpha$  of the eq. (2.96) in the low momentum limit would admit only numerical solutions for  $\mathbf{p}^2$ . Nevertheless, assuming that the expansions are perturbative in  $1/L$  times the length scale which characterizes the strength

of the interaction, embodied by the scattering parameters, and assuming that  $ML \ll 1/\alpha$ , the Coulomb photon insertions in the bubble diagrams can be treated perturbatively. Under these conditions, the approximated expression of the ERE presented in eq. (2.96) can be exploited for an analytical derivation of the finite volume corrections to the energy eigenvalues.

### a) The Unbound Ground State

The perturbative expansion of the finite volume ERE around the zero momentum ground state, corresponding to a total energy  $E^* = 2M$  yields zero  $\mathcal{O}(\alpha)$  contributions when strong interactions are absent. This is a consequence of the removal of the photon zero mode, when the uniform background charge density in the free state cancels exactly the particle charge density [1].

However, in presence of strong interactions, the assertion ceases to be true and  $\mathcal{O}(\alpha)$  corrections begin to appear. Since  $E^* = 2M$  implies zero finite-volume momentum, the discrete sums appearing in the ERE in eq. (2.95) have to be expanded in Taylor series about  $\tilde{p}^2 \equiv \tilde{\mathbf{p}}^2 = 0$  and only small or negative powers of the latter have to be retained. Concerning the Lüscher function  $S_1(\tilde{p})$ , the approximation yields

$$S_1(\tilde{p}) = -\frac{1}{\tilde{p}^2} + \sum_{\mathbf{n} \neq 0}^{\Lambda_n} \frac{1}{|\mathbf{n}|^2} - 4\pi\Lambda_n + \tilde{p}^2 \sum_{\mathbf{n} \neq 0}^{\infty} \frac{1}{|\mathbf{n}|^4} + \tilde{p}^4 \sum_{\mathbf{n} \neq 0}^{\infty} \frac{1}{|\mathbf{n}|^6} + \tilde{p}^6 \sum_{\mathbf{n} \neq 0}^{\infty} \frac{1}{|\mathbf{n}|^8} + \tilde{p}^8 \sum_{\mathbf{n} \neq 0}^{\infty} \frac{1}{|\mathbf{n}|^{10}} + \dots, \quad (2.99)$$

where the dots denote terms of order  $|\mathbf{n}|^{-12}$  and the limit  $\Lambda_n \rightarrow \infty$  for the convergent power series has been taken. Adopting the notation in the appendix of ref. [1], where the sums of the leading three dimensional Riemann sums are presented, eq. (2.99) becomes

$$S_1(\tilde{p}) = -\frac{1}{\tilde{p}^2} + \mathcal{G}^{(0)} + \tilde{p}^2 \mathcal{J}^{(0)} + \tilde{p}^4 \mathcal{K}^{(0)} + \tilde{p}^6 \mathcal{L}^{(0)} + \tilde{p}^8 \mathcal{O}^{(0)} + \dots \quad (2.100)$$

Second, the expansion of the double sum  $S_2(\tilde{p})$  in powers of  $\tilde{p}^2$  gives

$$S_2(\tilde{p}) = -\frac{2}{\tilde{p}^2} \sum_{\mathbf{m} \neq 0}^{\infty} \frac{1}{\mathbf{m}^4} \frac{1}{1 - \frac{\tilde{p}^2}{\mathbf{m}^2}} + \sum_{\mathbf{n} \neq 0}^{\Lambda_n} \sum_{\mathbf{m} \neq 0, \mathbf{n}}^{\infty} \frac{1}{\mathbf{n}^2 - \tilde{p}^2} \frac{1}{\mathbf{m}^2 - \tilde{p}^2} \frac{1}{|\mathbf{n} - \mathbf{m}|^2} - 4\pi^4 \log \Lambda_n \equiv S_2^{(1)}(\tilde{p}) + S_2^{(2)}(\tilde{p}), \quad (2.101)$$

where the spherical cutoff for the convergent series has been suppressed convergent and a grouping among the three-dimensional series is introduced. As for  $S_1(\tilde{p})$ , only one of the implied summations turns out to require the intervention of a cutoff, due to a logarithmic UV divergence. Still pursuing with the notation of ref. [1], the term  $S_2^{(1)}(\tilde{p})$  containing only single sums can be succinctly rewritten as

$$S_2^{(1)}(\tilde{p}) = -\frac{2}{\tilde{p}^2} \mathcal{J}^{(0)} - 2\mathcal{K}^{(0)} - 2\tilde{p}^2 \mathcal{L}^{(0)} - 2\tilde{p}^4 \mathcal{O}^{(0)} + \dots, \quad (2.102)$$

where the dots indicate series proportional to  $|\mathbf{n}|^{-12}$ . Then, we define the fundamental double sum, regulated by the logarithm of the spherical cutoff (cf. app. B.1.2),

$$\mathcal{R}^{(0)} = \sum_{\mathbf{n} \neq 0}^{\Lambda_n} \sum_{\mathbf{m} \neq 0, \mathbf{n}}^{\infty} \frac{1}{|\mathbf{n}|^2} \frac{1}{|\mathbf{m}|^2} \frac{1}{|\mathbf{n} - \mathbf{m}|^2} - 4\pi^4 \log \Lambda_n, \quad (2.103)$$

and the higher-order sums,

$$\mathcal{R}_{ij} = \sum_{\mathbf{n} \neq 0}^{\Lambda_n} \sum_{\mathbf{m} \neq 0, \mathbf{n}}^{\infty} \frac{1}{|\mathbf{n}|^i} \frac{1}{|\mathbf{m}|^j} \frac{1}{|\mathbf{n} - \mathbf{m}|^2} . \quad (2.104)$$

which converge without cutoff dependent subtraction provided  $(s, t) \geq (2, 4)$  or  $(4, 2)$  and are symmetric under index exchange,  $\mathcal{R}_{ij}^{(0)} = \mathcal{R}_{ji}^{(0)}$ . In terms of  $\mathcal{R}$  and  $\mathcal{R}_{st}^{(0)}$ , the addend  $\mathcal{S}_2^{(1)}(\tilde{p})$  in eq. (2.101) becomes

$$\mathcal{S}_2^{(2)}(\tilde{p}) = \mathcal{R}^{(0)} + 2\tilde{p}^2 \mathcal{R}_{24}^{(0)} + \tilde{p}^4 \mathcal{R}_{44}^{(0)} + 2\tilde{p}^4 \mathcal{R}_{26}^{(0)} + \dots , \quad (2.105)$$

where the ellipsis refers to  $\mathcal{O}(\tilde{p}^6)$ , proportional to double sums with  $s + t \geq 10$ . After defining

$$\tilde{\mathcal{R}}^{(0)} = \mathcal{R}^{(0)} - 4\pi^4 \left[ \log \left( \frac{4\pi}{\alpha ML} \right) - \gamma_E \right] , \quad (2.106)$$

we insert the approximated  $\mathcal{S}_1(\tilde{p})$  and  $\mathcal{S}_2(\tilde{p})$  sums into the original ERE in eq. (2.95) and find

$$\begin{aligned} & -\frac{1}{\alpha'_C{}^{(0)}} + \frac{1}{2} \frac{4\pi^2 r_0'^{(0)}}{L^2} \tilde{p}^2 + \frac{16\pi^4 r_1'^{(0)}}{L^4} \tilde{p}^4 + \dots = \frac{1}{\pi L} \left[ -\frac{1}{\tilde{p}^2} + \mathcal{G}^{(0)} + \tilde{p}^2 \mathcal{J}^{(0)} + \tilde{p}^4 \mathcal{K}^{(0)} + \dots \right] \\ & -\frac{\alpha M}{4\pi^4} \left[ -\frac{2}{\tilde{p}^2} \mathcal{J}^{(0)} - 2\mathcal{K}^{(0)} - 2\mathcal{L}^{(0)} \tilde{p}^2 - 2\mathcal{O}^{(0)} \tilde{p}^4 + \dots + \tilde{\mathcal{R}}^{(0)} + 2\tilde{p}^2 \mathcal{R}_{24}^{(0)} + \tilde{p}^4 \mathcal{R}_{44}^{(0)} + 2\tilde{p}^4 \mathcal{R}_{26}^{(0)} + \dots \right] + \dots . \end{aligned} \quad (2.107)$$

Once the finite volume ERE is rewritten in the small momentum limit and the series are expanded around  $\tilde{p}^2 = 0$ , the finite volume energy corrections can be derived by following an iteration procedure. To this aim, we introduce the following *small* auxiliary constants

$$c_0 = \frac{\alpha'_C{}^{(0)}}{\pi L} , \quad c_1 = \frac{\alpha M}{4\pi^4} \alpha'_C{}^{(0)} , \quad c_2 = \frac{4\pi^2}{L^2} \alpha'_C{}^{(0)} r_0'^{(0)} , \quad c_3 = \frac{16\pi^4}{L^4} \alpha'_C{}^{(0)} r_1'^{(0)} , \quad (2.108)$$

and collect the terms appearing in eq. (2.107) into groups bearing the same power of the squared finite-volume momentum,

$$\begin{aligned} & \frac{1}{\tilde{p}^2} \left( -c_0 + 2c_1 \mathcal{J}^{(0)} \right) + 1 + c_0 \mathcal{G}^{(0)} - c_1 \tilde{\mathcal{R}}^{(0)} + 2\mathcal{K}^{(0)} c_1 \\ & + \tilde{p}^2 \left[ c_0 \mathcal{J}^{(0)} + c_1 (2\mathcal{L}^{(0)} - 2\mathcal{R}_{24}^{(0)}) - \frac{c_2}{2} \right] + \tilde{p}^4 \left[ c_0 \mathcal{K}^{(0)} + c_1 (2\mathcal{O}^{(0)} - \mathcal{R}_{44}^{(0)} + 2\mathcal{R}_{26}^{(0)}) - c_3 \right] + \dots = 0 . \end{aligned} \quad (2.109)$$

Due to the smallness of  $\tilde{p}$ , contributions multiplied by higher positive powers of the finite-volume momentum are increasingly suppressed. It follows that the dominant finite volume corrections are expected to be found by solving the truncated version of eq. (2.109) to order  $\mathcal{O}(\tilde{p}^0)$ ,

$$\frac{1}{\tilde{p}^2} \left( -c_0 + 2c_1 \mathcal{J}^{(0)} \right) + 1 + c_0 \mathcal{G}^{(0)} - c_1 \tilde{\mathcal{R}}^{(0)} + 2\mathcal{K}^{(0)} c_1 = 0 . \quad (2.110)$$



Solving the latter for  $\tilde{p}^2$  and performing an expansion of the denominator in powers of the small constants  $c_0$ ,  $c_1$  and  $c_2$ , we obtain

$$\begin{aligned} \tilde{p}^2 = & c_0 - c_0^2 \mathcal{G}^{(0)} + c_0^3 \mathcal{G}^{(0)2} - 2c_1 \mathcal{G}^{(0)} + c_0 c_1 \tilde{\mathcal{R}}^{(0)} + 2c_0 c_1 \mathcal{G}^{(0)} \\ & - 2c_0^2 c_1 \tilde{\mathcal{R}}^{(0)} \mathcal{G}^{(0)} - 2c_0^2 c_1 \mathcal{G}^{(0)} \mathcal{G}^{(0)2} - 2c_0 c_1 \mathcal{K}^{(0)} + 4c_0^2 c_1 \mathcal{G}^{(0)} \mathcal{K}^{(0)} + \dots, \end{aligned} \quad (2.111)$$

where the dots indicate  $\mathcal{O}(c_0^3)$ ,  $\mathcal{O}(c_1 c_0^3)$ ,  $\mathcal{O}(c_0^2 c_2)$ ,  $\mathcal{O}(c_1^2)$  and  $\mathcal{O}(c_1 c_2)$  terms, which have been discarded for simplicity. Even if the multiplication of  $\tilde{p}^2$  by the dimensionful factor  $4\pi^2/ML^2$  would have delivered the leading finite volume energy corrections to the lowest unbound state, we mark the solution of eq. (2.110) in eq. (2.111) as  $\tilde{p}_0^2$  and proceed with the next to leading order approximation. Considering the  $\mathcal{O}(\tilde{p}^2)$  approximation of eq. (2.109) and plugging  $\tilde{p}_0^2$  into the quadratic term in the finite-volume momentum, we find

$$\frac{1}{\tilde{p}^2} \left( -c_0 + 2c_1 \mathcal{G}^{(0)} \right) + 1 + c_0 \mathcal{G}^{(0)} - c_1 \tilde{\mathcal{R}}^{(0)} + 2\mathcal{K}^{(0)} c_1 + \tilde{p}_0^2 \left[ c_0 \mathcal{G}^{(0)} + c_1 (2\mathcal{L}^{(0)} - 2\mathcal{R}_{24}^{(0)}) - \frac{c_2}{2} \right] = 0. \quad (2.112)$$

The substitution is justified by the smallness of  $\tilde{p}^2$  with respect to the  $\tilde{p}^{-2}$ , which is dominant in eq. (2.111) and plays a pivotal role. Solving the latter equation for  $\tilde{p}^2$ , an improved expression for the squared finite-volume momentum follows,

$$\begin{aligned} \tilde{p}_2^2 = & c_0 - c_0^2 \mathcal{G}^{(0)} - c_0^3 \mathcal{G}^{(0)} + c_0^3 \mathcal{G}^{(0)2} - 2c_1 \mathcal{G}^{(0)} + c_0 c_1 \mathcal{R}^{(0)} + 2c_0 c_1 \mathcal{G}^{(0)} \mathcal{G}^{(0)} - 2c_0 c_1 \mathcal{K}^{(0)} \\ & + 4c_0^2 c_1 \mathcal{G}^{(0)2} - 2c_0^2 c_1 \mathcal{R}^{(0)} \mathcal{G}^{(0)} - 2c_0^2 c_1 \mathcal{G}^{(0)} \mathcal{G}^{(0)2} + 4c_0^2 c_1 \mathcal{G}^{(0)} \mathcal{K}^{(0)} - 2c_0^2 c_1 \mathcal{L}^{(0)} + 2c_0^2 c_1 \mathcal{R}_{24}^{(0)} + \frac{c_0^2 c_2}{2}. \end{aligned} \quad (2.113)$$

Equipped with the last result, the energy of the lowest  $A_1$  bound state is obtained by restoring the dimensionful quantities and by exploiting the energy-momentum relation for free states,

$$\begin{aligned} E_S^{(0,A_1)} = & 0 + \Delta E_S^{(0,A_1)} = \frac{4\pi^2 \tilde{p}_2^2}{ML^2} = \frac{4\pi a_C'^{(0)}}{ML^3} \left\{ 1 - \left( \frac{a_C'^{(0)}}{\pi L} \right) \mathcal{G}^{(0)} + \left( \frac{a_C'^{(0)}}{\pi L} \right)^2 [\mathcal{G}^{(0)2} - \mathcal{G}^{(0)}] \right. \\ & + \dots \left. \right\} - \frac{2\alpha a_C'^{(0)}}{L^2 \pi^2} \left\{ \mathcal{G}^{(0)} + \left( \frac{a_C'^{(0)}}{\pi L} \right) [\mathcal{K}^{(0)} - \mathcal{G}^{(0)} \mathcal{G}^{(0)} - \tilde{\mathcal{R}}^{(0)}/2] + \frac{2a_C'^{(0)} r_0'^{(0)} \pi^2}{L^2} \mathcal{G}^{(0)} \right. \\ & + \left. \left( \frac{a_C'^{(0)}}{\pi L} \right)^2 [\tilde{\mathcal{R}}^{(0)} \mathcal{G}^{(0)} + \mathcal{G}^{(0)} \mathcal{G}^{(0)} - 2\mathcal{G}^{(0)2} - 2\mathcal{G}^{(0)} \mathcal{K}^{(0)} + \mathcal{L}^{(0)} - \mathcal{R}_{24}^{(0)}] + \dots \right\}, \end{aligned} \quad (2.114)$$

where the ellipses denote again  $\mathcal{O}(c_0^3)$ ,  $\mathcal{O}(c_1 c_0^3)$ ,  $\mathcal{O}(c_0^2 c_2)$ ,  $\mathcal{O}(c_1^2)$  and  $\mathcal{O}(c_1 c_2)$  terms. Moreover, since the energy of the corresponding free state is zero, the terms on the r.h.s. of the last equation can be interpreted as the modifications that a free state on a finite cubic configuration space with PBC receives from the strong and electromagnetic interactions. In particular, the first term within the curly braces can be interpreted as the energy shift due to strong interactions (descending from QCD), whereas all the terms enclosed within the second bracket correspond to the interplay between QCD and QED interactions. Interestingly, the expression of the FVECs in eq. (2.114) remains almost unaffected if the original physical scattering



parameters are restored (cf. eqs. (1.40)-(1.44)),

$$\begin{aligned} \Delta E_S^{(0,A_1)} &= \frac{4\pi^2 \tilde{p}_2^2}{ML^2} = \frac{4\pi a_C^{(0)}}{ML^3} \left\{ 1 - \left( \frac{a_C^{(0)}}{\pi L} \right) \mathcal{G}^{(0)} + \left( \frac{a_C^{(0)}}{\pi L} \right)^2 [\mathcal{G}^{(0)2} - \mathcal{G}^{(0)}] + \dots \right\} \\ &\quad - \frac{2\alpha a_C^{(0)}}{L^2 \pi^2} \left\{ \mathcal{G}^{(0)} + \left( \frac{a_C^{(0)}}{\pi L} \right) [\mathcal{K}^{(0)} - \mathcal{G}^{(0)} \mathcal{G}^{(0)} - \tilde{\mathcal{R}}^{(0)}/2] + \frac{a_C'^{(0)} r_0'^{(0)} \pi^2}{L^2} \mathcal{G}^{(0)} \right. \\ &\quad \left. + \left( \frac{a_C^{(0)}}{\pi L} \right)^2 [\tilde{\mathcal{R}}^{(0)} \mathcal{G}^{(0)} + \mathcal{G}^{(0)} \mathcal{G}^{(0)} - 2\mathcal{G}^{(0)2} - 2\mathcal{G}^{(0)} \mathcal{K}^{(0)} + \mathcal{L}^{(0)} - \mathcal{R}_{24}^{(0)}] + \dots \right\}. \end{aligned} \quad (2.115)$$

### b) The Bound Ground State

Although doubly charged bound states made of two hadrons have not been observed in nature so far, such systems do appear at unphysical values of the quark masses in Lattice QCD calculations [100] [101] [102] [103]. Therefore, it is instructive to evaluate the finite volume ERE in eq. (2.96) in the purely imaginary momentum sector,  $\mathbf{p} = i\boldsymbol{\kappa}$ . If the limit of large finite-volume binding momentum,  $\tilde{\kappa} = |\tilde{\boldsymbol{\kappa}}| \gg 1$ , is considered, an approximation procedure for the Lüscher functions should be repeated. In this regime, the Lüscher function  $\mathcal{S}_1(i\tilde{\boldsymbol{\kappa}})$ ,

$$\mathcal{S}_1(i\tilde{\boldsymbol{\kappa}}) = \sum_{\mathbf{n}}^{\Lambda_n} \frac{1}{|\mathbf{n}|^2 + \tilde{\kappa}^2} - 4\pi\Lambda_n \quad (2.116)$$

can be immediately computed by replacing the sum with the integral sign,

$$\int_{S_{\Lambda_n}^2} d^3n \frac{1}{|\mathbf{n}|^2 + \tilde{\kappa}^2} = 4\pi \int_0^{\Lambda_n} dn - 4\pi \int_0^{\Lambda_n} \frac{\tilde{k}^2 dn}{n^2 + \tilde{\kappa}^2} = 4\pi\Lambda_n - 4\pi\tilde{k} \arctan\left(\frac{\Lambda_n}{\tilde{\kappa}}\right). \quad (2.117)$$

since the series is a smooth enough function of the binding momentum. Therefore, taking the limit  $\Lambda_n \rightarrow +\infty$ , the original expression of  $\mathcal{S}_1(i\tilde{\boldsymbol{\kappa}})$  becomes

$$\mathcal{S}_1(i\tilde{\boldsymbol{\kappa}}) \approx 4\pi\Lambda_n - 2\pi^2\tilde{\kappa} - 4\pi\Lambda_n = -2\pi^2\tilde{\kappa}, \quad (2.118)$$

see eq. (43) in ref. [1]. Concerning the approximation of the Lüscher function  $\mathcal{S}_2(i\tilde{\boldsymbol{\kappa}})$ , the procedure is more involved (cf. B.2.1 and eq. (44) in ref. [1]) and yields

$$\begin{aligned} \mathcal{S}_2(i\tilde{\boldsymbol{\kappa}}) &= \sum_{\mathbf{n}}^{\Lambda_n} \sum_{\mathbf{m} \neq \mathbf{n}} \frac{1}{|\mathbf{n}|^2 + \tilde{\kappa}^2} \frac{1}{|\mathbf{m}|^2 + \tilde{\kappa}^2} \frac{1}{|\mathbf{n} - \mathbf{m}|^2} - 4\pi^4 \log \Lambda_n \\ &\approx 4\pi^4 [\log \Lambda_n - \log(2\tilde{\kappa})] + \frac{\pi^2}{\tilde{\kappa}} \mathcal{G}^{(0)} - 4\pi^4 \log \Lambda_n = -4\pi^4 \log(2\tilde{\kappa}) + \frac{\pi^2}{\tilde{\kappa}} \mathcal{G}^{(0)}. \end{aligned} \quad (2.119)$$

Inserting the expressions of the approximated Lüscher sums (cf. eqs. (2.118) and (2.119)) into the ERE in eq. (2.119) with imaginary momentum, we obtain

$$-\frac{1}{a_C'^{(0)}} - \frac{1}{2} r_0'^{(0)} \boldsymbol{\kappa}^2 + r_1'^{(0)} \boldsymbol{\kappa}^4 + \dots = -|\boldsymbol{\kappa}| - \frac{\alpha M \mathcal{G}^{(0)}}{2\pi L |\boldsymbol{\kappa}|} + \alpha M \left[ \log\left(\frac{4|\boldsymbol{\kappa}|}{\alpha M}\right) - \gamma_E \right] + \dots \quad (2.120)$$

where the dimensionful binding momentum  $\kappa = |\boldsymbol{\kappa}| = 2\pi\tilde{\kappa}/L$  has been restored. By reintroducing the infinite volume scattering parameters and discarding any dependence from the the

shape parameter  $r_1^{(0)}$ , the last equation can be recast as

$$-\frac{1}{a_C^{(0)}} - \frac{1}{2}r_0^{(0)}\kappa^2 + \dots = -\kappa - \frac{\alpha M}{2\pi L} \frac{\mathcal{G}^{(0)}}{\kappa} (1 + r_0^{(0)}\kappa) - \alpha M \left[ \log \left( \frac{\alpha M}{4\kappa} \right) + \gamma_E \right]. \quad (2.121)$$

At this point, we highlight the dependence on the fine structure constant by rewriting the binding momentum in power series,

$$\kappa = \kappa_0 + \kappa_1 + \kappa_2 + \kappa_3 + \dots, \quad (2.122)$$

where  $\kappa_0$  results from strong interactions alone and the subscript corresponds to the power of  $\alpha$  on which each term in the expansion depends. Plugging the latter into eq. (2.121), we first observe that the identity

$$-\frac{1}{a_C^{(0)}} - \frac{1}{2}r_0^{(0)}\kappa_0^2 = -\kappa_0 \quad (2.123)$$

holds, since the three quantities do not depend on nonzero powers of  $\alpha$ . Neglecting consistently the  $\mathcal{O}(\alpha^2)$  terms in the approximated ERE in eq. (2.121) and exploiting the relation in eq. (2.123), an expression for  $\kappa_1$  in terms of the lowest order scattering parameter and the unperturbed binding momentum is found,

$$\kappa_1 = -\frac{\alpha M}{1 - r_0^{(0)}\kappa_0} \left[ \log \left( \frac{\alpha M}{4\kappa_0} \right) + \gamma_E \right] - \frac{\alpha M}{2\pi L} \frac{\mathcal{G}^{(0)}}{\kappa_0} \frac{1 + r_0^{(0)}\kappa_0}{1 - r_0^{(0)}\kappa_0} + \dots, \quad (2.124)$$

where the ellipsis represents  $\mathcal{O}(\alpha)$  non-relativistic corrections coming from higher order scattering parameters and contributions from transverse photons. Now, considering the binding energy of the fundamental bound state in the linear approximation in  $\alpha$ ,

$$E_B^{(0,A_1)} = \frac{\kappa^2}{M} = \frac{\kappa_0^2}{M} + 2\frac{\kappa_0\kappa_1}{M} + \dots, \quad (2.125)$$

and exploiting eq. (2.124), we find the desired expression in terms of the infinite volume scattering parameters,

$$E_B^{(0,A_1)} = \frac{\kappa_0^2}{M} - \frac{2\kappa_0\alpha}{1 - r_0^{(0)}\kappa_0} \left[ \log \left( \frac{\alpha M}{4\kappa_0} \right) + \gamma_E \right] - \frac{\alpha \mathcal{G}^{(0)}}{\pi L} \frac{1 + r_0^{(0)}\kappa_0}{1 - r_0^{(0)}\kappa_0} \dots, \quad (2.126)$$

where the second term represents the QED modification to the binding energy due to strong interactions and the third term represents the sought leading order finite volume correction. Since  $r_0^{(0)}$  scales as  $\Lambda_E^{-1}$  [22], if the binding momentum is much smaller than the breakdown scale of the EFT,  $\kappa_0/\Lambda_E \ll 1$ , the inequality  $r_0^{(0)}\kappa_0 \ll 1$  is verified and the mass shift with respect to the finite-volume energy eigenvalue assumes the simplified form presented in eq. (46) of ref. [1],

$$\Delta E_B^{(0,A_1)} \equiv E_B^{(0,A_1)}(\infty) - E_B^{(0,A_1)}(L) = \frac{\alpha \mathcal{G}^{(0)}}{\pi L} \frac{1 + r_0^{(0)}\kappa_0}{1 - r_0^{(0)}\kappa_0} \approx \frac{\alpha \mathcal{G}^{(0)}}{\pi L}, \quad (2.127)$$

which corresponds to the leading term in the expansion in powers of  $r_0^{(0)}2\pi\kappa_0/L$  of the third term on the r.h.s. of eq. (2.126). Additionally, recalling the expression of mass shifts for  $\ell = 0$  states of two-Body systems with strong interactions alone in ref. [71], we can conclude that the

QED corrections presented in eq. (2.127) are pairwise negative, since  $\mathcal{G}^{(0)} < 0$ .



## CHAPTER 3

### P-WAVE SHORT-RANGE INTERACTIONS

The present chapter naturally inherits its structure from the preceeding one. In the opening, the Lagrangian with the strong P-wave interactions alone is presented. Focusing on two-body fermion-fermion scattering, the T-matrix element is computed to all orders in the strength parameter of the strong potential. In sec. 3.1.1, the Lagrangian is enriched by the scalar photon kinetic term and by the Coulomb interaction term with matter fields in the framework of non-relativistic QED in refs. [121, 122]. Then, the amplitudes corresponding to tree-level and one-loop diagrams with one Coulomb photon exchange are computed in dimensional regularization, implementing again the PDS renormalization scheme. By virtue of the Dyson-like identities that hold among the free, the Coulomb and the full two-body Green's functions presented in sec. 1.2.1 of chap. 1, the T-matrix element of the fermion-fermion scattering process with Coulomb interaction is obtained non-perturbatively in closed form.

From the latter amplitude and the P-wave generalized ERE, the expressions of the scattering length and the effective range are derived in terms of the physical constants of our EFT Lagrangian. The first part of the analysis is concluded in sec. 3.1.3 with the calculation of the same amplitude for the case of fermion-antifermion scattering.

Then, the two fermion-system is transposed into a cubic box of side  $L$  and periodic boundary conditions are imposed on the matter fields and on the wavefunctions of particles. The discrete nature of the finite-volume momentum operator allows for a perturbative treatment of QED, provided  $L$  is sufficiently large. As a consequence, the quantization conditions are derived (sec. 3.2.1) in the perturbative regime of QED. Next, the finite volume counterpart of the  $\ell = 1$  effective range expansion is presented, together with the expressions of the new Lüscher functions, shown in the end of sec. 3.2.2. Subsequently, the energy eigenvalues of the lowest bound and scattering states are displayed alongwith the details of the whole derivation. The pivotal results of the calculation are indeed given by the concluding formulas of secs. 3.2.3 a) and b). In the concluding section some hints are given concerning possible future extensions of our work. In particular, the inclusion of transverse photon interactions within the EFT Lagrangian and the introduction of strong forces coupled to two units of angular momentum are discussed.

The appendices A and B provide supplemental material regarding the derivation of the scattering amplitudes in sec. 3.1.1 and 3.1.2 and the three-dimensional Riemann sums arising from the approximations of the Lüscher functions in secs. 3.2.2, 3.2.3 a) and b).

### 3.1 Two-body scattering in infinite volume

We extend the analysis in the previous chapter to the case of spinless fermions coupled to one unit of angular momentum. Adopting the conventions in ref. [37] for the coupling constants, the Lagrangian density (cf. eq. (1.6)) now assumes the form

$$\mathcal{L} = \psi^\dagger \left[ i\hbar\partial_t + \frac{\hbar^2\nabla^2}{2M} \right] \psi + \frac{D(E^*)}{8} (\psi \overleftrightarrow{\nabla}_i \psi)^\dagger (\psi \overleftrightarrow{\nabla}_i \psi) , \quad (3.1)$$

where  $\overleftrightarrow{\nabla} = \overleftarrow{\nabla} - \overrightarrow{\nabla}$  denotes the Galilean invariant derivative for fermions. Recalling the Feynman rules in app. A.1, two-body elastic scattering processes without QED are represented by chains of bubbles, analogous to the ones in fig. 2.1. In particular, the tree-level diagram, consisting of a single four-fermion vertex, leads to an amplitude equal to  $-iD(E^*)\mathbf{p} \cdot \mathbf{p}'$  (cf. ref. [39]) where  $\pm\mathbf{p}$  and  $\pm\mathbf{p}'$  are, respectively, the momenta of the incoming and outgoing particles in the CoM frame. As a consequence, the two-body  $\ell = 1$  (pseudo)potential in momentum space takes the form

$$V^{(1)}(\mathbf{p}, \mathbf{q}) \equiv \langle \mathbf{q}, -\mathbf{q} | \hat{\mathcal{V}}^{(1)} | \mathbf{p}, -\mathbf{p} \rangle = D(E^*) \mathbf{p} \cdot \mathbf{q} , \quad (3.2)$$

which coincides with the tree-level diagram multiplied by the imaginary unit.

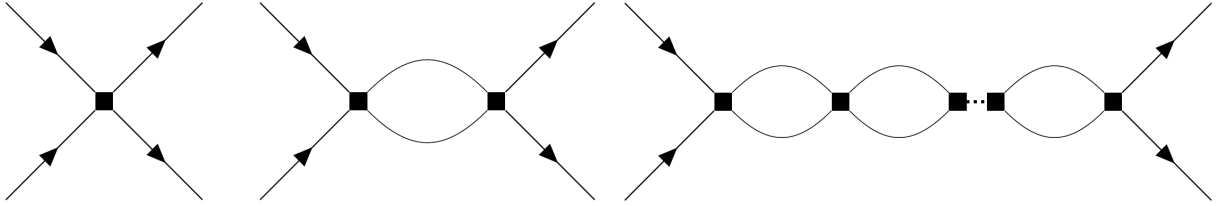


FIGURE 3.4 – Tree-level (upper line, left), 1-loop (upper line, right) and n-loops diagrams (lower line) representing fermion-fermion elastic scattering with the strong P-wave potential in eq. (3.1).

Considering also the other possible diagrams in momentum space with amputated legs in fig. 3.1, the expression for the full scattering amplitude due to strong interactions can be written as,

$$iT_S(\mathbf{p}, \mathbf{q}) = i\langle \mathbf{q}, -\mathbf{q} | \left[ \hat{\mathcal{V}}^{(1)} + \hat{\mathcal{V}}^{(1)} \hat{G}_0^E \hat{\mathcal{V}}^{(1)} + \hat{\mathcal{V}}^{(1)} \hat{G}_0^E \hat{\mathcal{V}}^{(1)} \hat{G}_0^E \hat{\mathcal{V}}^{(1)} + \dots \right] | \mathbf{p}, -\mathbf{p} \rangle . \quad (3.3)$$

where  $\hat{G}_0^E \equiv \hat{G}_0^{(+)}(E)$  is the two-body unperturbed retarded (+) Green's function operator in eq. (1.1). The explicit computation of the three lowest order contributions to the sum in eq. (3.3) yields

$$i\langle \mathbf{q}, -\mathbf{q} | \hat{\mathcal{V}}^{(1)} | \mathbf{p}, -\mathbf{p} \rangle = iD(E^*) \mathbf{p} \cdot \mathbf{q} , \quad (3.4)$$

$$i\langle \mathbf{q}, -\mathbf{q} | \hat{\mathcal{V}}^{(1)} \hat{G}_0^E \hat{\mathcal{V}}^{(1)} | \mathbf{p}, -\mathbf{p} \rangle = iD(E^*)^2 p_i q_j \partial_i \partial_j G_0^E(\mathbf{r}, \mathbf{r}') \Big|_{\substack{\mathbf{r}=0 \\ \mathbf{r}'=0}} \equiv iD(E^*)^2 \mathbf{q} \cdot \mathbb{J}_0 \mathbf{p} , \quad (3.5)$$

and

$$i\langle \mathbf{q}, -\mathbf{q} | \hat{\mathcal{V}}^{(1)} \hat{G}_0^E \hat{\mathcal{V}}^{(1)} \hat{G}_0^E \hat{\mathcal{V}}^{(1)} | \mathbf{p}, -\mathbf{p} \rangle = iD(E^*)^3 q_i p_k \partial_i \partial_j G_0^E(\mathbf{r}, \mathbf{r}') \Big|_{\substack{\mathbf{r}=0 \\ \mathbf{r}'=0}} \cdot \partial_j \partial_k' G_0^E(\mathbf{r}', \mathbf{r}'') \Big|_{\substack{\mathbf{r}'=0 \\ \mathbf{r}''=0}} = iD(E^*)^3 \mathbf{q} \cdot \mathbb{J}_0^2 \mathbf{p} , \quad (3.6)$$

where  $\partial_i \equiv \partial/\partial r_i$ ,  $\partial'_i \equiv \partial/\partial r'_i$  and  $\partial''_i \equiv \partial/\partial r''_i$ , while  $\mathbb{J}_0$  is a symmetric matrix whose elements are given by

$$(\mathbb{J}_0)_{ij} = \partial_i \partial'_j G_0^E(\mathbf{r}, \mathbf{r}') \Big|_{\substack{\mathbf{r}=0 \\ \mathbf{r}'=0}}, \quad (3.7)$$

and Einstein's index convention is henceforth understood. Extending the computation to higher orders, it is evident that the infinite superposition of chains of bubbles translates into a geometric series in the total scattering amplitude, as in the  $\ell = 0$  case, and a formula analogous to eq. (2) in ref. [2] is obtained,

$$iT_S(\mathbf{p}, \mathbf{q}) = iD(E^*) \mathbf{q} \cdot \left( \mathbb{1} + D(E^*)\mathbb{J}_0 + D(E^*)^2\mathbb{J}_0^2 + D(E^*)^3\mathbb{J}_0^3 + \dots \right) \mathbf{p} = \mathbf{q} \cdot \frac{D(E^*)}{\mathbb{1} - D(E^*)\mathbb{J}_0} \mathbf{p}. \quad (3.8)$$

Furthermore, performing the Fourier transform of the potential in eq. (3.2) into configuration space,

$$V^{(1)}(\mathbf{r}, \mathbf{r}') \equiv \langle \mathbf{r}' | \hat{\mathcal{V}}^{(1)} | \mathbf{r} \rangle = D(E^*) \nabla \delta(\mathbf{r}) \cdot \nabla' \delta(\mathbf{r}'), \quad (3.9)$$

the full scattering amplitude can be recovered independently in position space by means of partial integrations and cancellations of surface integrals at infinity,

$$T_S(\mathbf{r}, \mathbf{r}') = \nabla \delta(\mathbf{r}) \cdot \frac{D(E^*)}{\mathbb{1} - D(E^*)\mathbb{J}_0} \nabla' \delta(\mathbf{r}'). \quad (3.10)$$

The matrix elements of  $\mathbb{J}_0$  can be evaluated by dimensional regularization. Applying the formula in eq. (B18) of ref. [132] for  $d$ -dimensional integration, eq. (3.7) in arbitrary  $d$ -dimensions becomes

$$\begin{aligned} (\mathbb{J}_0)_{ij}(d) &= \partial_i \partial'_j G_0^E(d; \mathbf{r}, \mathbf{r}') \Big|_{\substack{\mathbf{r}=0 \\ \mathbf{r}'=0}} = \left( \frac{\mu}{2} \right)^{3-d} \int_{\mathbb{R}^d} \frac{d^d \mathbf{k}}{(2\pi)^d} \frac{k_i k_j}{E - \mathbf{k}^2/M + i\epsilon} \\ &= -\delta_{ij} \frac{M^2(E + i\epsilon)}{d(4\pi)^{d/2}} \left( \frac{\mu}{2} \right)^{3-d} [-M(E + i\epsilon)]^{d/2-1} \Gamma\left(\frac{2-d}{2}\right) \end{aligned} \quad (3.11)$$

where  $\mu$  is the renormalization scale introduced by the minimal subtraction (MS) scheme. Like the S-wave counterpart, the integral proves to be finite in three dimensions and, within this limit, is given by

$$\lim_{d \rightarrow 3} \partial_i \partial'_j G_0^E(\mathbf{r}, \mathbf{r}'; d) \Big|_{\substack{\mathbf{r}, \mathbf{r}'=0}} = \partial_i \partial'_j G_0^E(\mathbf{r}, \mathbf{r}') \Big|_{\substack{\mathbf{r}, \mathbf{r}'=0}} = -\delta_{ij} \frac{M}{4\pi} \frac{i|\mathbf{p}|^3}{3}, \quad (3.12)$$

where the energy  $E$  in the CoM frame has been eventually expressed as  $\mathbf{p}^2/M$ . For the sake of completeness, we derive the contribution to  $(\mathbb{J}_0)_{ij}$  from the power divergence subtraction (PDS) regularization scheme, in which the power counting of the EFT is manifest [18,22]. With this aim, the eventual poles of the regularized integral for  $d \rightarrow 2$  should be taken into account. In this limit, it turns out from eq. (3.11) that the Euler's Gamma has a pole singularity of the kind  $2/(2-d)$ . As a consequence, the original dimensional regularization result in eq. (3.11) acquires a finite PDS contribution, transforming into

$$(\mathbb{J}_0)_{ij}^{\text{PDS}} = \partial_i \partial'_j G_0^E(3; \mathbf{r}, \mathbf{r}') \Big|_{\substack{\mathbf{r}=0 \\ \mathbf{r}'=0}}^{\text{PDS}} = -\delta_{ij} \frac{M}{4\pi} \left( \frac{i|\mathbf{p}|^3}{3} + \mu \frac{\mathbf{p}^2}{2} \right). \quad (3.13)$$

This can be compared with the one in eq. (4) in ref. [2] for the S-wave interactions. Since the  $\mathbb{J}_0$  matrix is diagonal (eq. (3.13)), few efforts are needed for the computation of the fermion-fermion scattering amplitude,

$$T_S(\mathbf{p}, \mathbf{q}) = \frac{12\pi}{M} \frac{D(E^*) \mathbf{p} \cdot \mathbf{q}}{\frac{12\pi}{M} + iD(E^*)|\mathbf{p}|^3} . \quad (3.14)$$

With reference to scattering theory [120], the  $T_S$  matrix for P-wave elastic scattering with phase shift  $\delta_1$  can be written as

$$T_S(\mathbf{p}, \mathbf{q}) = -\frac{4\pi}{M} \frac{e^{i2\delta_1} - 1}{2i|\mathbf{p}|} 3 \cos \theta = -\frac{12\pi}{M} \frac{\mathbf{p} \cdot \mathbf{q}}{|\mathbf{p}|^3 \cot \delta_1 - i|\mathbf{p}|^3} , \quad (3.15)$$

where  $\theta$  is the angle between the incoming and outgoing direction of particles in the CoM frame. Recalling the effective-range expansion (ERE) [120] for  $\ell = 1$  scattering in eq. (1.11),

$$|\mathbf{p}|^3 \cot \delta_1 = -\frac{1}{a} + \frac{1}{2} r_0 \mathbf{p}^2 + r_1 \mathbf{p}^4 + r_2 \mathbf{p}^6 + \dots , \quad (3.16)$$

an expression for the scattering parameters in terms of the momenta of the particles, the coupling constant and the mass  $M$  can be drawn. In particular, a formula for the scattering length analogous to eq. (2.16) of ref. [22] can be recovered,

$$a = \frac{M}{4\pi} \frac{D(E^*)}{3} . \quad (3.17)$$

Furthermore, the effective range parameter  $r_0$  vanishes, as in the zero angular momentum case. Plugging the PDS-regularized expression of  $\mathbb{J}_0$  in eq. (3.13) into eq. (3.8) and exploiting the ERE again, finally, the renormalized form of the coupling constant  $D(E^*)$  is obtained,

$$D(E^*, \mu) = 3a \left( \frac{4\pi}{M} + \mu \frac{\mathbf{p}^2}{2} \right) . \quad (3.18)$$

Unlike in the  $\ell = 0$  case, we note that the  $\mu$ -dependent version of  $D(E^*) = 12\pi a/M$  is quadratic in the momentum of the incoming fermions.

### 3.1.1 Coulomb corrections

As in sec. 2.1.1, we now examine in detail the amplitudes associated to two-body scattering diagrams with one scalar photon insertion. For the purpose, we add the Lagrangian density in eq. (1.13) on top of the one in eq. (3.1). Analogously to the S-wave case, Coulomb photon exchanges occur within the bubbles and the external legs of the scattering diagrams.

In the same fashion as in sec. 2.1.1, we treat the order  $\alpha$  diagrams as corrections to the two-body elastic scattering amplitude  $T_S$  in eq. (3.8) and we begin with the tree-level diagram with a four-fermion vertex and a one-photon exchange between two external legs. From the Feynman rules in app. A.1, the amplitude of such diagram (cf. the left part of fig. 3.2) proves to be

$$-iT_{SC}^{\text{tree}}(\mathbf{p}, \mathbf{p}') = -D(E^*) \int_{\mathbb{R}^4} \frac{d^4 l}{(2\pi)^4} \frac{i e}{\frac{E}{2} + l_0 - \frac{(\mathbf{p}-\mathbf{l})^2}{2M} + i\epsilon} \frac{(\mathbf{p}-\mathbf{l}) \cdot \mathbf{p}'}{\mathbf{l}^2 + \lambda^2} \frac{i e}{\frac{E}{2} - l_0 - \frac{(\mathbf{l}-\mathbf{p})^2}{2M} + i\epsilon} . \quad (3.19)$$



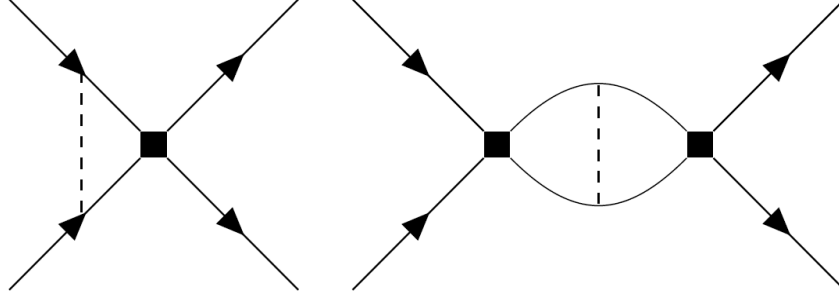


FIGURE 3.2 – The tree-level (left) and one-loop (right) fermion-fermion scattering diagram for strong  $\ell = 1$  interactions with one Coulomb photon insertion (dashed lines).

After integrating over the free energy  $l_0$ , the tree-level amplitude in eq. (3.19) can be decomposed as follows

$$-iT_{\text{SC}}^{\text{tree}}(\mathbf{p}, \mathbf{p}') = \int_{\mathbb{R}^3} \frac{d^3\mathbf{l}}{(2\pi)^3} \frac{-ie^2}{\mathbf{l}^2 + \lambda^2} \frac{MD(E^*)}{\mathbf{p}^2 - (\mathbf{p} - \mathbf{l})^2 + i\epsilon} \frac{\mathbf{p} \cdot \mathbf{p}'}{\mathbf{l}^2 - 2\mathbf{p} \cdot \mathbf{l} - i\epsilon} - i \int_{\mathbb{R}^3} \frac{d^3\mathbf{l}}{(2\pi)^3} \frac{e^2}{\mathbf{l}^2 + \lambda^2} \frac{D(E^*)M}{\mathbf{l}^2 - 2\mathbf{p} \cdot \mathbf{l} - i\epsilon} \frac{\mathbf{l} \cdot \mathbf{p}'}{\mathbf{l}^2 - 2\mathbf{p} \cdot \mathbf{l} - i\epsilon}. \quad (3.20)$$

In particular, in the last rewriting the first integral on the r.h.s. turns out to be identical to the one in eq. (2.20) except for the factor  $\mathbf{p} \cdot \mathbf{p}' = \mathbf{p}^2 \cos \theta$ , therefore it can be immediately integrated. Conversely, the last integral in eq. (3.20) represents a new contribution, whose evaluation in dimensional regularization is carried out in app. A.2. Adding the two contributions together, the tree level amplitude with Coulomb photon insertion in eq. (3.20) becomes

$$T_{\text{SC}}^{\text{tree}}(\mathbf{p}, \mathbf{p}') = \cos \theta D(E^*) \frac{\alpha M}{2} \cdot \left[ |\mathbf{p}| \left( i - \frac{\pi}{2} \right) - i |\mathbf{p}| \log \frac{2|\mathbf{p}|}{\lambda} \right] + \mathcal{O}(\lambda), \quad (3.21)$$

where the limit  $\lambda \rightarrow 0$  for the  $\mathcal{O}(\lambda)$  terms is understood. From the last equation we infer that, due to the linear dependence in the momenta of the incoming particles  $\mathbf{p}$  in the CoM frame, P-wave fermion-fermion scattering is suppressed with respect to the S-wave one in the low- $\mathbf{p}$  limit. However, both the  $\ell = 0$  and  $\ell = 1$  tree level amplitudes with one Coulomb photon insertion are divergent in the  $\lambda \rightarrow 0$  limit.

Nevertheless, due to the fact that the latter logarithmic contribution is imaginary, the infinite term does not contribute to the  $\mathcal{O}(\alpha)$  corrections of the strong cross section, which is proportional to  $D(E^*)[D(E^*) + 2\Re T_{\text{SC}}^{\text{tree}}]$ , as observed in sec. 2.1.1. The corrected cross section to that order turns out to be again IR finite and proportional to  $1 - \pi\eta$ . Analogously, the inclusion of  $n$  Coulomb photon exchanges leads to corrections proportional to  $\eta^n$  in the cross section. As a result, the feasibility of a perturbative treatment for the Coulomb force is again regulated by the smallness of the parameter  $\eta$ , inversely proportional to the CoM momentum of the incoming particles. In the very small momentum regime, the Coulomb force exerts a strong influence on the cross-section of the elastic process and a non-perturbative treatment of QED becomes necessary.

Furthermore, the Feynman rules for the one-loop diagram with one photon insertion on

the right part of fig. 3.2 yield

$$-iT_{\text{SC}}^{1-\text{loop}}(\mathbf{p}, \mathbf{p}') = \int_{\mathbb{R}^4} \frac{d^4 l}{(2\pi)^4} \int_{\mathbb{R}^4} \frac{d^4 k}{(2\pi)^4} \frac{-ie^2}{(\mathbf{l} - \mathbf{k})^2 + \lambda^2} \cdot \frac{D(E^*)}{\frac{E}{2} + l_0 - \frac{l^2}{2M} + i\epsilon} \cdot \frac{\mathbf{ip} \cdot \mathbf{l}}{\frac{E}{2} - l_0 - \frac{l^2}{2M} + i\epsilon} \frac{\mathbf{ik} \cdot \mathbf{p}'}{\frac{E}{2} + k_0 - \frac{k^2}{2M} + i\epsilon} \frac{D(E^*)}{\frac{E}{2} - k_0 - \frac{k^2}{2M} + i\epsilon}. \quad (3.22)$$

Besides, the contour integration with respect to the free energies  $k_0$  and  $l_0$ , followed by the momentum translation  $\mathbf{l} \mapsto \mathbf{q} \equiv \mathbf{l} - \mathbf{k}$ , leads to

$$-iT_{\text{SC}}^{1-\text{loop}}(\mathbf{p}, \mathbf{p}') = -M^2 \int_{\mathbb{R}^3} \frac{d^3 \mathbf{k}}{(2\pi)^3} \int_{\mathbb{R}^3} \frac{d^3 \mathbf{q}}{(2\pi)^3} \frac{-ie^2 [D(E^*)]^2}{\mathbf{q}^2 + \lambda^2} \frac{\mathbf{ik} \cdot \mathbf{p}'}{\mathbf{p}^2 - (\mathbf{q} + \mathbf{k})^2 + i\epsilon} \frac{\mathbf{ip} \cdot (\mathbf{q} + \mathbf{k})}{\mathbf{p}^2 - \mathbf{k}^2 + i\epsilon}. \quad (3.23)$$

The remaining momentum integrations are performed in dimensional regularization (cf. app. A.2) and give

$$T_{\text{SC}}^{1-\text{loop}}(\mathbf{p}, \mathbf{p}') = \cos \theta [D(E^*)]^2 \frac{\alpha M^2}{4\pi} \frac{\mathbf{p}^4}{6} \left[ \frac{1}{\epsilon} - \gamma_E + \frac{7}{3} + i\pi - \log \left( \frac{2\mathbf{p}^2}{\pi\mu} \right) \right], \quad (3.24)$$

where  $\epsilon \equiv 3 - d$ . The amplitude in eq. (3.24) displays a pole at  $d = 3$  as the one in eq. (2.24), an ultraviolet divergence that can be reabsorbed through a redefinition of the strength parameter  $D(E^*)$  via the renormalization process. However,  $T_{\text{SC}}^{1-\text{loop}}$  is devoid of the logarithmic divergence in the zero-momentum limit, due to the multiplication by a factor  $\mathbf{p}^2$ . Consequently, in comparison with the zero angular momentum counterpart, the  $\ell = 1$  one-loop scattering amplitude with one-photon insertion is suppressed in the limit of zero momentum  $\mathbf{p}$  of the incoming particles in the CoM frame. Since  $T_{\text{SC}}^{1-\text{loop}}$  possesses also a pole in the  $d \rightarrow 2$  limit, the implementation of the PDS scheme results into an additional term proportional to the renormalization scale (or mass),

$$T_{\text{SC}}^{1-\text{loop}}(\mathbf{p}, \mathbf{p}') \Big|_{\text{PDS}} = \cos \theta [D(E^*)]^2 \frac{\alpha M^2}{4\pi} \frac{\mathbf{p}^2}{2} \left[ \frac{\mathbf{p}^2}{3} \left( \frac{1}{\epsilon} - \gamma_E + \frac{7}{3} - \log \frac{2\mathbf{p}^2}{\pi\mu} + i\pi \right) + \frac{\mu}{2} \right]. \quad (3.25)$$

Differently from the  $\ell = 0$  counterpart in eq. (2.24), the logarithmic term in the CoM momentum of the colliding fermions does not give rise to a divergence in the zero momentum limit, due to the  $\mathbf{p}^4$  prefactor. Nevertheless, the dressing of the one-bubble diagram with two or more Coulomb photon insertions results in the multiplication of  $T_{\text{SC}}^{1-\text{loop}}$  by one or more powers of  $\eta = \alpha M/2|\mathbf{p}|^2$ , so that, at order higher than four in  $\alpha$ , the amplitude becomes singular in the limit  $|\mathbf{p}| \rightarrow 0$ . As previously noticed, at sufficiently low momenta the perturbative approach breaks down and the effects of Coulomb repulsion need to be treated to all orders in  $\alpha$ . With reference to sec. 1.2.1, the scattering T-matrix can be written in closed form even when the Coulomb ladders are incorporated to all orders in the fine structure constant. From comparison between the self-consistent formulas in eqs. (1.9) and (1.24), this amounts to replacing the free-fermion propagators in the bubble diagrams of fig. 3.1 with the Coulomb propagators in fig. 1.1.

Once the eigenstates of the full Hamiltonian are expressed in terms of the Coulomb eigenstates (cf. eq. (1.25)), the relevant T-matrix element to be calculated,  $T_{\text{SC}}$ , assumes the form given in eq. (1.28). Since the strong interaction couples the fermions to one unit of angular momentum and Coulomb forces are central, the only nonzero component of  $T_{\text{SC}}$  of the ex-

pansion in eq. (1.28) is the one with  $\ell = 1$ . Analogously to eq. (31) in ref. [2], we can, thus, write

$$|\mathbf{p}|^3(\cot \delta_1 - i) = -\cos \theta \frac{12\pi \mathbf{p}^2}{M} \frac{e^{2i\sigma_1}}{T_{\text{SC}}(\mathbf{p}', \mathbf{p})} , \quad (3.26)$$

and we replace the ERE of the l.h.s. of the last equation with the  $\ell = 1$  version in eq. (1.30),

$$\mathbf{p}^2 \left(1 + \eta^2\right) \left[ C_\eta^2 |\mathbf{p}| (\cot \delta_1 - i) + \alpha M H(\eta) \right] = -\frac{1}{a_C^{(1)}} + \frac{1}{2} r_0^{(1)} \mathbf{p}^2 + r_1^{(1)} \mathbf{p}^4 + \dots , \quad (3.27)$$

where  $a_C^{(1)}$ ,  $r_0^{(1)}$  and  $r_1^{(1)}$  are the scattering length, the effective range and the shape parameter, respectively. By comparison with the S-wave counterpart in eq. (2.26), we can observe that, apart from the different power of the momentum of the incoming particles in front of the  $\cot \delta_1 - i$  term, the most significant difference is provided by the polynomial on the l.h.s. of the eq. (3.27), containing all even powers of  $\eta$  from zero to  $2\ell$ , as shown in eq. (1.31).

### 3.1.2 Repulsive channel

Considering the results of the previous section, all the elements for the derivation of the Coulomb-corrected strong scattering amplitude,  $T_{\text{SC}}(\mathbf{p}, \mathbf{p}')$ , are available. Recalling the definition and eq. (1.25), the amplitude can be computed by evaluating each of the terms in the expansion, whose insertions are given by retarded Coulomb propagators  $\hat{G}_C^{(+)}$  followed by  $\ell = 1$  four-point vertices,  $\hat{V}_S = \hat{\mathcal{V}}^{(1)}$ . In particular, the lowest order contribution to the T-matrix reads

$$\begin{aligned} \langle \psi_{\mathbf{p}'}^{(-)} | \hat{\mathcal{V}}^{(1)} | \psi_{\mathbf{p}}^{(+)} \rangle &= \int_{\mathbb{R}^3} d^3 r' \int_{\mathbb{R}^3} d^3 r \langle \psi_{\mathbf{p}'}^{(-)} | \mathbf{r}' \rangle \langle \mathbf{r}' | \hat{\mathcal{V}}^{(1)} | \mathbf{r} \rangle \\ &\quad \cdot \langle \mathbf{r} | \psi_{\mathbf{p}}^{(+)} \rangle = D(E^*) \nabla' \psi_{\mathbf{p}'}^{(-)*}(\mathbf{r}') \Big|_{\mathbf{r}'=0} \cdot \nabla \psi_{\mathbf{p}}^{(+)}(\mathbf{r}) \Big|_{\mathbf{r}=0} , \end{aligned} \quad (3.28)$$

where eqs. (1.18)-(1.19) and (3.9) have been exploited, partial integration for the two variables has been performed and the vanishing surface terms dropped. The explicit computation of the two integrals over the Coulomb wavefunctions (cf. eqs. (1.18)-(1.19)) in the last row is carried out in app. A.3, and yields

$$D(E^*) \nabla' \psi_{\mathbf{p}'}^{(-)*}(\mathbf{r}') \Big|_{\mathbf{r}'=0} \cdot \nabla \psi_{\mathbf{p}}^{(+)}(\mathbf{r}) \Big|_{\mathbf{r}=0} = D(E^*) (1 + \eta^2) C_\eta^2 e^{i2\sigma_1} \mathbf{p}' \cdot \mathbf{p} , \quad (3.29)$$

where  $C_\eta^2$  is the Sommerfeld factor, a function of  $\eta = \alpha M/2|\mathbf{p}|$ . As it can be observed, the polynomial  $1 + \eta^2$  in the l.h.s. of the generalized effective range expansion appears, see eq. (3.27). As shown in app. A.3, the P-wave strong vertex *projects out* of the integral all the components of the Coulomb wavefunctions  $\psi_p^{(\pm)}$  with  $\ell \neq 1$  appearing in the angular momentum expansion

$$\psi_{\mathbf{p}}^{(+)}(\mathbf{r}) = \frac{4\pi}{|\mathbf{p}|r} \sum_{\ell=0}^{+\infty} \sum_{m=-\ell}^{\ell} i^\ell e^{i\sigma_\ell} Y_\ell^{m*}(\hat{\mathbf{p}}) Y_\ell^m(\hat{\mathbf{r}}) F_\ell(\eta, |\mathbf{p}|r) , \quad (3.30)$$

where  $\hat{\mathbf{p}}$  and  $\hat{\mathbf{r}}$  are unit vectors parallel to  $\mathbf{p}$  and  $\mathbf{r} \equiv r \hat{\mathbf{r}}$  respectively and  $F_\ell(\eta, |\mathbf{p}|r)$  is the *regular* Coulomb wavefunction for unbound states. The latter functions, derived by Yost, Wheeler and Breit in ref. [133], display a regular behaviour in the vicinity of the origin, in

contrast with the  $G_\ell(\eta, |\mathbf{p}|r)$ , linearly independent solutions of the Whittaker equation for a repulsive Coulomb potential which are *irregular* for  $r \rightarrow 0$ . Explicitly,  $F_\ell(\eta, |\mathbf{p}|r)$  has the form given in ref. [125],

$$F_\ell(\eta, |\mathbf{p}|r) = \frac{2^\ell e^{-\pi\eta/2} |\Gamma(1 + \ell + i\eta)|}{(2\ell + 1)!} (|\mathbf{p}|r)^{\ell+1} e^{i|\mathbf{p}|r} M(1 + \ell + i\eta, 2\ell + 2, -2i|\mathbf{p}|r) . \quad (3.31)$$

The expansion for the incoming waves is obtained via the complex-conjugation property  $\psi_{\mathbf{p}}^{(-)}(\mathbf{r}) = \psi_{-\mathbf{p}}^{(+)*}(\mathbf{r})$ . Next, we proceed with derivation of the next-to-leading order contribution to the scattering amplitude,

$$\begin{aligned} \langle \psi_{\mathbf{p}'}^{(-)} | \hat{\psi}_1 \hat{G}_C^{(+)} \hat{\psi}_1 | \psi_{\mathbf{p}}^{(+)} \rangle &= M[D(E^*)]^2 \int_{\mathbb{R}^3} d^3\mathbf{r}' \delta(\mathbf{r}') \int_{\mathbb{R}^3} d^3\mathbf{r}'' \delta(\mathbf{r}'') \int_{\mathbb{R}^3} d^3\mathbf{r}''' \delta(\mathbf{r}''') \\ &\cdot \int_{\mathbb{R}^3} d^3\mathbf{r}'''' \delta(\mathbf{r}''') \partial_i \psi_{\mathbf{p}}^{(-)*}(\mathbf{r}') \partial_i' \partial_j'' G_C^{(+)}(\mathbf{r}'', \mathbf{r}''') \partial_j''' \psi_{\mathbf{p}}^{(+)}(\mathbf{r}''') , \end{aligned} \quad (3.32)$$

where partial integration has been exploited and Einstein summation convention over repeated indices is understood. More succinctly, the last equation can be recast as

$$\begin{aligned} \langle \psi_{\mathbf{p}'}^{(-)} | \hat{\psi}_1 \hat{G}_C^{(+)} \hat{\psi}_1 | \psi_{\mathbf{p}}^{(+)} \rangle &= M[D(E^*)]^2 \left. \partial_i \psi_{\mathbf{p}'}^{(-)*}(\mathbf{r}') \right|_{\mathbf{r}'=0} \left. \partial_i' \partial_j'' G_C^{(+)}(\mathbf{r}'', \mathbf{r}''') \right|_{\mathbf{r}'', \mathbf{r}'''=0} \\ &\cdot \left. \partial_j''' \psi_{\mathbf{p}}^{(+)}(\mathbf{r}''') \right|_{\mathbf{r}''''=0} \equiv [D(E^*)]^2 \left. \nabla' \psi_{\mathbf{p}'}^{(-)*}(\mathbf{r}') \right|_{\mathbf{r}'=0} \cdot \mathbb{J}_C \nabla \psi_{\mathbf{p}}^{(+)}(\mathbf{r}) \Big|_{\mathbf{r}=0} . \end{aligned} \quad (3.33)$$

where in the second row, the Coulomb-corrected counterpart of the  $\mathbb{J}_0$  matrix defined in eq. (3.7) has been introduced,

$$(\mathbb{J}_C)_{ij} = \partial_i \partial_j' G_C^{(+)}(\mathbf{r}, \mathbf{r}') \Big|_{\mathbf{r}, \mathbf{r}'=0} . \quad (3.34)$$

Analogously to the  $\ell = 0$  case, the higher order contributions to the T-matrix possess the same structure of eqs. (3.29) and (3.33) differ from the latter only in the powers of  $\mathbb{J}_C$  and the coupling constant  $D(E^*)$ . Therefore we can again write

$$iT_{\text{SC}}(\mathbf{p}', \mathbf{p}) = iD(E^*) \left. \nabla' \psi_{\mathbf{p}'}^{(-)*}(\mathbf{r}') \right|_{\mathbf{r}'=0} \left[ \mathbb{1} + D(E^*) \mathbb{J}_C + D(E^*)^2 \mathbb{J}_C^2 + D(E^*)^3 \mathbb{J}_C^3 + \dots \right] \left. \nabla \psi_{\mathbf{p}}^{(+)}(\mathbf{r}) \right|_{\mathbf{r}=0} , \quad (3.35)$$

and we can treat the terms enclosed by the round brackets as a geometric series,

$$T_{\text{SC}}(\mathbf{p}', \mathbf{p}) = \left. \nabla' \psi_{\mathbf{p}'}^{(-)*}(\mathbf{r}') \right|_{\mathbf{r}'=0} \cdot \frac{D(E^*)}{\mathbb{1} - D(E^*) \mathbb{J}_C} \left. \nabla \psi_{\mathbf{p}}^{(+)}(\mathbf{r}) \right|_{\mathbf{r}=0} . \quad (3.36)$$

Denoting the outer product between vectors with  $\otimes$  and recalling the definition of the Coulomb Green's function operators in eq. (1.21), it is convenient to rewrite the  $\mathbb{J}_C$  matrix as

$$\mathbb{J}_C = M \int_{\mathbb{R}^3} d^3\mathbf{r} \delta(\mathbf{r}) \int_{\mathbb{R}^3} d^3\mathbf{r}' \delta(\mathbf{r}') \int_{\mathbb{R}^3} \frac{d^3\mathbf{s}}{(2\pi)^3} \frac{\nabla \psi_{\mathbf{s}}^{(+)}(\mathbf{r}) \otimes \nabla' \psi_{\mathbf{s}}^{(+)*}(\mathbf{r}')}{\mathbf{p}^2 - \mathbf{s}^2 + i\epsilon} , \quad (3.37)$$

and we observe that the numerator can be considerably simplified by means of the results of app. A.3. In particular, eq. (A.100) can be applied twice, yielding

$$\int_{\mathbb{R}^3} d^3\mathbf{r} \delta(\mathbf{r}) \int_{\mathbb{R}^3} d^3\mathbf{r}' \delta(\mathbf{r}') \nabla \psi_s^{(+)}(\mathbf{r}) \otimes \nabla' \psi_s^{(+)*}(\mathbf{r}') = C_\eta^2 (1 + \eta^2) \mathbf{s} \otimes \mathbf{s} . \quad (3.38)$$

Equipped with the last result together with eq. (1.20), we recast the components of the  $\mathbb{J}_C$  matrix as

$$(\mathbb{J}_C)_{ij} = M \int_{\mathbb{R}^3} \frac{d^3\mathbf{s}}{(2\pi)^3} \frac{2\pi\eta(\mathbf{s})}{e^{2\pi\eta(\mathbf{s})} - 1} \frac{s_i s_j}{\mathbf{p}^2 - \mathbf{s}^2 + i\epsilon} \frac{1 + \eta(\mathbf{s})^2}{\mathbf{p}^2 - \mathbf{s}^2 + i\epsilon} , \quad (3.39)$$

where the dependence of  $\eta$  on the integrated momentum  $\mathbf{s}$  has been made explicit. As the  $\ell = 0$  counterpart in eq. (43) of ref. [2], the integral is ultraviolet divergent. Additionally, all the off-diagonal matrix elements of  $\mathbb{J}_C$  vanish, as the integrand is manifestly rotationally symmetric in three dimensions except for the components  $s_i s_j$ , that are integrated over a symmetric interval around zero, see eq. (4.3.4) in ref. [130]. In dimensional regularization, eq. (3.39) can be rewritten as

$$(\mathbb{J}_C)_{ij}(d) = M \frac{\delta_{ij}}{d} \int_{\mathbb{R}^d} \frac{d^d s}{(2\pi)^d} \frac{2\pi\eta(s)}{e^{2\pi\eta(s)} - 1} \frac{s^2}{\mathbf{p}^2 - \mathbf{s}^2 + i\epsilon} \frac{1 + \eta(s)^2}{\mathbf{p}^2 - \mathbf{s}^2 + i\epsilon} \equiv \mathbb{J}_C(d) \delta_{ij} , \quad (3.40)$$

an expression that in three dimensions, combined with the results in app. A.3, allows to simplify the Coulomb-corrected strong scattering amplitude as

$$T_{\text{SC}}(\mathbf{p}', \mathbf{p}) = (1 + \eta^2) C_\eta^2 \frac{D(E^*)}{1 - D(E^*)} \frac{e^{2i\sigma_1} \mathbf{p} \cdot \mathbf{p}'}{\mathbb{J}_C} , \quad (3.41)$$

in momentum space. Returning to eq. (3.36) and ignoring the Feynman prescription in the denominator, we first exploit the trick for eq. (2.32) and split the integral into three parts,

$$\begin{aligned} \mathbb{J}_C(d) &= \frac{M}{d} \int_{\mathbb{R}^d} \frac{d^d s}{(2\pi)^d} \frac{2\pi\eta}{e^{2\pi\eta} - 1} \frac{\mathbf{p}^2}{\mathbf{s}^2} \frac{\mathbf{p}^2}{\mathbf{p}^2 - \mathbf{s}^2} (1 + \eta^2) \\ &\quad - \frac{M}{d} \int_{\mathbb{R}^d} \frac{d^d s}{(2\pi)^d} \frac{2\pi\eta}{e^{2\pi\eta} - 1} \frac{\mathbf{p}^2}{\mathbf{s}^2} (1 + \eta^2) \\ &\quad - \frac{M}{d} \int_{\mathbb{R}^d} \frac{d^d s}{(2\pi)^d} \frac{2\pi\eta}{e^{2\pi\eta} - 1} (1 + \eta^2) \\ &\equiv \mathbb{J}_C^{\text{fin}}(d; \mathbf{p}) + \mathbb{J}_C^{\text{div},1}(d; \mathbf{p}) + \mathbb{J}_C^{\text{div},2}(d; \mathbf{p}) . \end{aligned} \quad (3.42)$$

While the first one proves to be finite, the other two display a pole for  $d \rightarrow 3$  and the PDS regularization scheme has to be implemented. We begin with the integral in the first row of eq. (3.42),  $\mathbb{J}_C^{\text{fin}}$ . The numerator of the latter can be split into two parts, according to the terms of the polynomial in  $\eta$  inside the round brackets. Taking the limit  $d \rightarrow 3$ , we observe that one of the two parts coincides with  $J_C^{\text{fin}}$  in eq. (2.34), up to a proportionality constant equal to  $\mathbf{p}^2/3$ . In comparison with the latter, the other part of  $\mathbb{J}_C^{\text{fin}}$  in eq. (3.42) is suppressed by two further powers of  $\eta$ , therefore it is pairwise UV-finite and the three-dimensional limit finds a justification. After these manipulations,  $\mathbb{J}_C^{\text{fin}}$  becomes

$$\mathbb{J}_C^{\text{fin}}(\mathbf{p}) \equiv \lim_{d \rightarrow 3} \mathbb{J}_C^{\text{fin}}(d; \mathbf{p}) = -H(\eta) \frac{\alpha M^2}{4\pi} \frac{\mathbf{p}^2}{3} + \frac{M}{d} \int_{\mathbb{R}^d} \frac{d^d s}{(2\pi)^{d-1}} \frac{\eta^3}{e^{2\pi\eta} - 1} \frac{\mathbf{p}^2}{\mathbf{s}^2} \frac{\mathbf{p}^2}{\mathbf{p}^2 - \mathbf{s}^2} . \quad (3.43)$$

Due to spherical symmetry, the integration over the angular variables in the last term can be immediately performed. By means of the substitution  $s \mapsto 2\pi\eta = \pi\alpha M/s$ , the integral in the second row of eq. (3.43) can be simplified as

$$\frac{M}{3} \int_{\mathbb{R}^3} \frac{d^3s}{(2\pi)^2} \frac{\eta^3}{e^{2\pi\eta} - 1} \frac{\mathbf{p}^4}{\mathbf{s}^2} \frac{1}{\mathbf{p}^2 - \mathbf{s}^2} = -\frac{\mathbf{p}^2}{3} \frac{\alpha M^2}{(2\pi)^3} \left[ \int_0^{+\infty} \frac{dx}{x} \frac{x^2}{e^x - 1} - \int_0^{+\infty} dx \frac{xa^2}{(e^x - 1)(x^2 + a^2)} \right] . \quad (3.44)$$

where  $a \equiv i\pi\alpha M/|\mathbf{p}|$ . The first of the two integrals in the last row can be evaluated by means of the following identity

$$\zeta(\omega)\Gamma(\omega) = \int_0^{+\infty} \frac{dt}{t} \frac{t^\omega}{e^t - 1} , \quad (3.45)$$

connecting Euler's Gamma function with Riemann's Zeta function, while the second one in eq. (3.43) is analogous to the integral in eq. (46) of ref. [2], modulo a constant factor. Considering the last two identities, eq. (3.44) can be recast into

$$\frac{\mathbf{p}^2}{3} \frac{\alpha M^2}{(2\pi)^3} \left\{ \zeta(2)\Gamma(2) - \frac{a^2}{2} \left[ \log\left(\frac{a}{2\pi}\right) - \frac{\pi}{a} - \psi\left(\frac{a}{2\pi}\right) \right] \right\} = \frac{\mathbf{p}^2}{3} \frac{\alpha M^2}{(2\pi)^3} \left[ \frac{\pi^2}{6} - \frac{\pi^2 \alpha^2 M^2}{2\mathbf{p}^2} H(\eta) \right] , \quad (3.46)$$

where the definition of  $H(\eta)$  in eq. (1.33) and the fact that  $\zeta(2) = \pi^2/6$  have been exploited. The subsequent addition of the last result to the already calculated contribution to eq. (3.43) yields the sought closed expression for  $\mathbb{J}_C^{\text{fin}}(\mathbf{p})$ ,

$$\mathbb{J}_C^{\text{fin}}(\mathbf{p}) = \frac{M}{3} \int_{\mathbb{R}^3} \frac{d^3s}{(2\pi)^3} \frac{2\pi\eta}{e^{2\pi\eta} - 1} \frac{\mathbf{p}^2}{\mathbf{s}^2} \frac{\mathbf{p}^2}{\mathbf{p}^2 - \mathbf{s}^2} (1 + \eta^2) = \frac{\alpha M^2}{48\pi} \frac{\mathbf{p}^2}{3} - \frac{\alpha M^2}{4\pi} \frac{\mathbf{p}^2}{3} (1 + \eta^2) H(\eta) . \quad (3.47)$$

Now we focus on the term in the second row of eq. (3.42). By comparison with the integrand of eq. (2.36), we expect the integral of interest to display an UV singularity. Splitting the polynomial within the round brackets on the numerator of the integrand, we recognize, in fact, the already available  $J_C^{\text{div}}$  in eq. (2.42) (cf. eq. (53) in ref. [2]),

$$\mathbb{J}_C^{\text{div},1}(d; \mathbf{p}) \equiv -\frac{M}{d} \int_{\mathbb{R}^d} \frac{d^d s}{(2\pi)^d} \frac{2\pi\eta}{e^{2\pi\eta} - 1} \frac{\mathbf{p}^2}{\mathbf{s}^2} (1 + \eta^2) = \frac{\mathbf{p}^2}{d} J_0^{\text{div}}(d; \mathbf{p}) - \frac{M}{d} \int_{\mathbb{R}^d} \frac{d^d s}{(2\pi)^{d-1}} \frac{\eta^3}{e^{2\pi\eta} - 1} \frac{\mathbf{p}^2}{\mathbf{s}^2} . \quad (3.48)$$

Again, spherical symmetry permits to integrate over the angular variables of the last integral on the r.h.s. of eq. (3.48) and the substitution  $s \mapsto 2\pi\eta = \pi\alpha M/s$  allows for the exploitation of the integral relation between the Gamma- and the Riemann Zeta function in eq. (3.45), obtaining

$$\begin{aligned} -\frac{M}{d} \int_{\mathbb{R}^d} \frac{d^d s}{(2\pi)^d} \frac{2\pi\eta^3}{e^{2\pi\eta} - 1} \frac{\mathbf{p}^2}{\mathbf{s}^2} &= -\left(\frac{\mu}{2}\right)^{3-d} \frac{\alpha^{d-2} M^{d-1} \pi^{d/2-4}}{2^{d+1} \Gamma\left(\frac{d}{2}\right)} \frac{\mathbf{p}^2}{d} \int_0^{+\infty} \frac{dx}{x} \frac{x^{5-d}}{e^x - 1} \\ &= -\left(\frac{\mu}{2}\right)^{3-d} \frac{\alpha^{d-2} M^{d-1} \pi^{d/2-4}}{2^{d+1} \Gamma\left(\frac{d}{2}\right)} \frac{\mathbf{p}^2}{d} \zeta(5-d) \Gamma(5-d) . \end{aligned} \quad (3.49)$$

Unlike the first term on the r.h.s. of eq. (3.48), the present integral proves to be convergent in three dimensions, since  $\zeta(2) = \pi^2/6$  is finite and the arguments of the Gamma functions are positive integers or half-integers. Additionally, no PDS poles are found in the same expression.



Therefore, the limit  $d \rightarrow 3$  can be safely taken, yielding

$$\lim_{d \rightarrow 3} -\frac{M}{d} \int_{\mathbb{R}^d} \frac{d^d s}{(2\pi)^d} \frac{2\pi\eta^3}{e^{2\pi\eta} - 1} \frac{\mathbf{p}^2}{s^2} = -\frac{\alpha M^2}{16\pi} \frac{\mathbf{p}^2}{9}. \quad (3.50)$$

Plugging the available result in eq. (2.42), we can finally write a closed expression for  $\mathbb{J}_{\text{SC}}^{\text{div},1}(\mathbf{p})$  in the PDS regularization scheme,

$$\mathbb{J}_{\text{C}}^{\text{div},1}(\mathbf{p}) = \frac{\alpha M^2}{4\pi} \frac{\mathbf{p}^2}{3} \left[ \frac{1}{3-d} + \log \frac{\mu\sqrt{\pi}}{\alpha M} + \frac{4}{3} - \frac{3}{2}\gamma_E \right] - \frac{\mu M}{8\pi} \mathbf{p}^2 - \frac{\alpha M^2}{16\pi} \frac{\mathbf{p}^2}{9}. \quad (3.51)$$

Finally, we concentrate our attention on the term in the third row of eq. (3.42). From that equation, we infer that the only difference with respect to integrand of  $\mathbb{J}_{\text{C}}^{\text{div},1}$  consists in the absence of the factor  $1/s^2$ , which enhances the divergent behaviour of the integral in the  $s \rightarrow +\infty$  limit. Therefore, we expect also this third contribution to  $\mathbb{J}_{\text{C}}$  to be UV divergent. After splitting the integral as in eq. (3.48), we obtain

$$\mathbb{J}_{\text{SC}}^{\text{div},2}(d; \mathbf{p}) = -\frac{M}{d} \int_{\mathbb{R}^d} \frac{d^d s}{(2\pi)^d} \frac{2\pi\eta}{e^{2\pi\eta} - 1} (1 + \eta^2) = -\frac{M}{d} \int_{\mathbb{R}^d} \frac{d^d s}{(2\pi)^d} \frac{2\pi\eta}{e^{2\pi\eta} - 1} - \frac{M}{d} \int_{\mathbb{R}^d} \frac{d^d s}{(2\pi)^d} \frac{2\pi\eta^3}{e^{2\pi\eta} - 1}. \quad (3.52)$$

Now we focus on the first term on the r.h.s. of the last equation. Rotational invariance allows again for the integration over the angular variables in  $d$  dimensions. Then, change of variables  $s \mapsto x \equiv 2\pi\eta$  permits to exploit again the multiplication identity between the Riemann Zeta and the Euler's Gamma functions (cf. eq. (3.44)). Additionally, thanks to the fundamental properties of the Gamma function and the definition of  $\epsilon \equiv 3 - d$  we obtain

$$\begin{aligned} & -\left(\frac{\mu}{2}\right)^{3-d} \frac{M}{d} \frac{2\pi^{d/2}}{\Gamma(\frac{d}{2})} \int_0^{+\infty} \frac{ds}{(2\pi)^d} \frac{s^{d-1}}{e^{2\pi\eta} - 1} \frac{2\pi\eta}{e^{2\pi\eta} - 1} = -\left(\frac{\mu}{2}\right)^{3-d} \frac{M}{d} \frac{2\pi^{d/2}}{\Gamma(\frac{d}{2})} \frac{(\alpha M\pi)^d}{(2\pi)^d} \int_0^{+\infty} \frac{dx}{x} \frac{x^{1-d}}{e^x - 1} \\ & = -\left(\frac{\mu}{2}\right)^{3-d} \frac{\alpha^d M^{1+d} \pi^{d/2}}{2^{d-1} \Gamma(\frac{d}{2}) d} \zeta(1-d) \Gamma(1-d) = -\frac{\alpha^3 M^4 \pi^{3/2} (1 - \frac{\epsilon}{3})^{-1}}{24(1 - \frac{\epsilon}{2})(1 - \epsilon)} \left(\frac{\mu}{\alpha M \sqrt{\pi}}\right)^\epsilon \frac{\zeta(\epsilon - 2) \Gamma(\epsilon)}{\Gamma(\frac{3-\epsilon}{2})}, \end{aligned} \quad (3.53)$$

where, in the last step, the Gamma functions and the physical constants have been rewritten in order to highlight the dependence on the small quantity  $\epsilon$ . From the last row of eq. (3.53), we can infer that, while the Gamma function has a simple pole for  $d \rightarrow 3$ , the Riemann Zeta function analytically continued to the whole complex plane is zero in that limit, since it is evaluated at a negative even integer, i.e.  $\zeta(-2n) = 0$   $n \in \mathbb{N}^+$ . Therefore, the fourth expression in eq. (3.53) cannot be immediately evaluated in the three-dimensional limit. Performing a Taylor expansion of the Zeta function about  $-2$ , we obtain

$$\zeta(1-d) \equiv \zeta(\epsilon - 2) = \zeta(-2) + \zeta'(-2)\epsilon + \mathcal{O}(\epsilon^2) \approx 0 - \frac{\zeta(3)}{4\pi^2} \epsilon, \quad (3.54)$$

where  $\zeta(3) \approx 1.20205$  is an irrational number, known as the Apéry constant. Furthermore, also the expansion of  $\Gamma(\frac{3-\epsilon}{2})$  about  $3/2$  up to first order in  $\epsilon$  has to be taken into account. Combining eq. (3.54) with the Taylor expansion of the physical constants with exponent  $\epsilon$  in the round bracket and the Laurent expansion of the Gamma function, eq. (3.53) transforms

into

$$-\lim_{d \rightarrow 3} \frac{M}{d} \int_{\mathbb{R}^d} \frac{d^d s}{(2\pi)^d} \frac{2\pi\eta}{e^{2\pi\eta} - 1} = \frac{\alpha^3 M^4}{16\pi} \frac{\zeta(3)}{3} \lim_{\epsilon \rightarrow 0} \frac{\epsilon \left( \frac{1}{\epsilon} - \gamma_E \right) \left[ 1 + \frac{\epsilon}{2} (2 - 2 \log 2 - \gamma_E) \right]}{(1 - \epsilon) \left( 1 - \frac{\epsilon}{2} \right) \left( 1 - \frac{\epsilon}{3} \right)} = \frac{\alpha^3 M^4}{16\pi} \frac{\zeta(3)}{3}, \quad (3.55)$$

where negligible terms in  $\epsilon$  have been omitted in the intermediate step. As it can be inferred from eq. (3.55), the result of the integration becomes finite in the framework of dimensional regularization, even if the corresponding integral in the first row of eq. (3.53) is divergent for  $d = 3$  due to the singularity at  $x = 0$ . Since the original expression in third row of eq. (3.53) contains a pole at  $d = 2$  while  $\Gamma(1) = 1$  and  $\zeta(-1) = -\frac{1}{12}$  in the two-dimensional limit, the PDS correction should be taken into account. Therefore, the complete application of the PDS scheme into eq. (3.55) gives

$$-\lim_{d \rightarrow 3} \frac{M}{d} \int_{\mathbb{R}^d} \frac{d^d s}{(2\pi)^d} \frac{2\pi\eta}{e^{2\pi\eta} - 1} \Big|_{\text{PDS}} = \frac{\alpha^3 M^4}{16\pi} \frac{\zeta(3)}{3} - \frac{\alpha^2 M^3 \pi \mu}{32} \frac{\mu}{3}. \quad (3.56)$$

Next, we switch to the evaluation of the last term on the r.h.s. of eq. (3.52). Proceeding exactly as in eq. (3.53), we find

$$\begin{aligned} -\left(\frac{\mu}{2}\right)^{3-d} \frac{M}{d} \frac{2\pi^{d/2}}{\Gamma\left(\frac{d}{2}\right)} \int_0^{+\infty} \frac{ds}{(2\pi)^d} \frac{s^{d-1}}{e^{2\pi\eta} - 1} \frac{2\pi\eta^3}{e^{2\pi\eta} - 1} &= -\left(\frac{\mu}{2}\right)^{3-d} \frac{M}{d} \frac{2\pi^{d/2}}{\Gamma\left(\frac{d}{2}\right)} \frac{(\alpha M \pi)^d}{(2\pi)^{d+2}} \int_0^{+\infty} \frac{dx}{x} \frac{x^{3-d}}{e^x - 1} \\ &= -\left(\frac{\mu}{2}\right)^{3-d} \frac{M}{d} \frac{2\pi^{d/2}}{\Gamma\left(\frac{d}{2}\right)} \frac{(\alpha M \pi)^d}{(2\pi)^{d+2}} \zeta(3-d) \Gamma(3-d) = -\frac{\alpha^3 M^4}{3} \frac{\zeta(\epsilon)}{2^4 \sqrt{\pi} \left(1 - \frac{\epsilon}{3}\right)} \left(\frac{\mu}{\alpha M \sqrt{\pi}}\right)^\epsilon \frac{\Gamma(\epsilon)}{\Gamma\left(\frac{3-\epsilon}{2}\right)}. \end{aligned} \quad (3.57)$$

Differently from the previous case, the Riemann Zeta function is nonzero in the three-dimensional limit and the only singularity for  $\epsilon = 0$  belongs to the Gamma function in the numerator of the second row of eq. (3.57). Considering the expansions of all the  $\epsilon$ -dependent functions about zero, the asymptotic expression for eq. (3.57) is recovered

$$\lim_{d \rightarrow 3} -\frac{M}{d} \int_{\mathbb{R}^d} \frac{d^d s}{(2\pi)^d} \frac{2\pi\eta^3}{e^{2\pi\eta} - 1} = \frac{\alpha^3 M^4}{16\pi} \frac{1}{3} \left[ \frac{1}{3-d} - \frac{3}{2} \gamma_E + \frac{4}{3} + \log \frac{\mu \sqrt{\pi}}{\alpha M} \right]. \quad (3.58)$$

As it can be inferred from eq. (3.57), also a PDS singularity at  $d \rightarrow 2$  is present, since the Riemann Zeta function displays a simple pole at unit arguments. In particular, the Laurent expansion of the Zeta function around 1 yields

$$\zeta(3-d) = \zeta(1+2-d) = \frac{1}{2-d} + \gamma_E + \mathcal{O}(2-d). \quad (3.59)$$

Applying the PDS regularization scheme and subtracting the correction corresponding to the  $d = 2$  pole, the expression in eq. (3.58) becomes

$$-\lim_{d \rightarrow 3} \frac{M}{d} \int_{\mathbb{R}^d} \frac{d^d s}{(2\pi)^d} \frac{2\pi\eta^3}{e^{2\pi\eta} - 1} \Big|_{\text{PDS}} = \frac{\alpha^3 M^4}{16\pi} \frac{1}{3} \left[ \frac{1}{3-d} - \frac{3}{2} \gamma_E + \frac{4}{3} + \log \frac{\mu \sqrt{\pi}}{\alpha M} \right] - \frac{\alpha^2 M^3 \mu}{16\pi} \frac{\mu}{2}. \quad (3.60)$$

Thanks to the last expression and eq. (3.60), a closed form for the third contribution to the diagonal elements of the  $\mathbb{J}_{\mathbb{C}}$  matrix is found,

$$\mathbb{J}_{\mathbb{C}}^{\text{div},2}(\mathbf{p}) = \frac{\alpha^3 M^4}{16\pi} \frac{\zeta(3)}{3} - \frac{\alpha^2 M^3 \pi \mu}{32} \frac{\mu}{3} + \frac{\alpha^3 M^4}{16\pi} \frac{1}{3} \left[ \frac{1}{3-d} - \frac{3}{2} \gamma_E + \frac{4}{3} + \log \frac{\mu \sqrt{\pi}}{\alpha M} \right] - \frac{\alpha^2 M^3 \mu}{16\pi} \frac{\mu}{2}. \quad (3.61)$$



Finally, collecting the three results in eqs. (3.47), (3.51) and (3.61), the latter matrix elements are obtained

$$\begin{aligned} \mathbb{j}_C(\mathbf{p}) = \mathbb{j}_C^{\text{fin}}(\mathbf{p}) + \mathbb{j}_C^{\text{div},1}(\mathbf{p}) + \mathbb{j}_C^{\text{div},2}(\mathbf{p}) = & \frac{\alpha^3 M^4}{48\pi} \left[ \frac{1}{3-d} + \zeta(3) - \frac{3}{2}\gamma_E + \frac{4}{3} + \log \frac{\mu\sqrt{\pi}}{\alpha M} \right] \\ & + \frac{\alpha M^2}{4\pi} \frac{\mathbf{p}^2}{3} \left[ \frac{1}{3-d} + \frac{4}{3} - \frac{3}{2}\gamma_E + \log \frac{\mu\sqrt{\pi}}{\alpha M} \right] - \frac{\alpha^2 M^3}{32\pi} \frac{\mu}{3} (\pi^2 - 3) - \frac{\mu M}{4\pi} \frac{\mathbf{p}^2}{2} - \frac{\alpha M^2}{4\pi} \frac{\mathbf{p}^2}{3} H(\eta)(1 + \eta^2). \end{aligned} \quad (3.62)$$

A direct comparison with the  $\ell = 0$  counterpart of the last expression, eqs. (2.34) and (2.41), shows that the QED contributions to  $\mathbb{j}_C$  include terms of higher order in the fine-structure constant  $\alpha$ . Moreover, owing to the elements  $\mathbb{j}_C^{\text{fin}}$  and  $\mathbb{j}_C^{\text{div},1}$ , an explicit dependence on the momenta of the incoming fermions  $\pm \mathbf{p}$  outside  $H(\eta)$  appears. Since  $\mathbb{j}_C$  contains quadratic terms in  $\mathbf{p}$ , eq. (3.62) gives rise to a non-zero value for the effective range parameter  $r_0^{(1)}$  in the ERE formula in eq. (3.27). Combining the  $\ell = 1$  component of the T-matrix expansion in terms of Legendre polynomials in eq. (1.28) with eq. (3.42), an expression for  $|\mathbf{p}|^3(\cot \delta_1 - i)$  can be found,

$$|\mathbf{p}|^3(\cot \delta_1 - i) = -\frac{12\pi}{M} \frac{1 - D(E^*)}{D(E^*)} \frac{\mathbb{j}_C(\mathbf{p})}{C_\eta^2(1 + \eta^2)}. \quad (3.63)$$

Plugging the last expression into the  $\ell = 1$  generalized ERE formula, the term of eq. (3.62) proportional to  $H(\eta)$  cancels out with its counterpart in eq. (1.33), and all the momentum-independent contributions can be collected, yielding the expression for the Coulomb-corrected  $\ell = 1$  scattering length,

$$\frac{1}{a_C^{(1)}} = \frac{12\pi}{MD(E^*)} + \frac{\alpha^2 M^2 \mu}{8} (\pi^2 - 3) - \frac{\alpha^3 M^3}{4} \left[ \frac{1}{3-d} + \zeta(3) - \frac{3}{2}\gamma_E + \frac{4}{3} + \log \frac{\mu\sqrt{\pi}}{\alpha M} \right]. \quad (3.64)$$

which represents the measured P-wave fermion-fermion scattering length. As in the  $\ell = 0$  case, the ultraviolet pole is expected to be removed by counterterms which describe short-distance electromagnetic and other isospin-breaking interactions due to the differences between the quark masses [134]. The subsidiary terms transform the coupling constant  $D(E^*)$  into a renormalization mass dependent coefficient,  $D(E^*, \mu)$ , which allows for a redefinition of the scattering length as in eq. (2.43),

$$\frac{1}{a_C^{(1)}(\mu)} = \frac{12\pi}{MD(E^*, \mu)} + \frac{\alpha^2 M^2 \mu}{8} (\pi^2 - 3). \quad (3.65)$$

The latter quantity is non-measurable and depends on the renormalization point  $\mu$ , related to the physical scattering length through the relation

$$\frac{1}{a_C^{(1)}(\mu)} = \frac{1}{a_C^{(1)}} + \frac{\alpha^3 M^3}{4} \left[ \zeta(3) - \frac{3}{2}\gamma_E + \frac{4}{3} + \log \frac{\mu\sqrt{\pi}}{\alpha M} \right], \quad (3.66)$$

which is the  $\ell = 1$  counterpart of eq. (2.44). Besides, grouping the quadratic terms in the momentum of the fermions arising in the l.h.s. of eq. (3.27), an expression for the effective range is recovered,

$$r_0^{(1)} = \alpha M \left[ \frac{2}{3-d} + \frac{8}{3} - 3\gamma_E + 2 \log \frac{\mu\sqrt{\pi}}{\alpha M} \right] - 3\mu, \quad (3.67)$$

As in the case of the inverse of the scattering length in eq. (3.66),  $r_0^{(1)}$  possesses a simple pole at  $d = 3$ . If the energy-dependent coefficient of our P-wave interaction  $D(E^*)$  is replaced by  $D_0$ , the singularity can be removed by means of counterterms coming from the  $\mathbf{p}^2$ -dependent  $\ell = 0$  interactions, proportional to  $(\psi \overleftrightarrow{\nabla}^2 \psi)^\dagger \psi \overleftrightarrow{\nabla}^2 \psi$  in momentum space. These interactions correspond to the term with coefficient  $C_2$  of the potential in eq. (1.5) in momentum space and yield the leading contribution to the effective range in the low-momentum regime when only zero-angular-momentum interactions are present.

Despite the difference in the  $\text{SO}(3)$  transformation properties induced by the interaction, both the Lagrangian density with  $\ell = 0$  (cf. eq. (1.5)) interactions and the one with  $\ell = 1$  (cf. eq. (1.6)) potentials give rise to a scattering amplitude  $T_S(\mathbf{p}, \mathbf{p}')$  whose  $|\mathbf{p}|^{2\ell+1} \cdot (\cot \delta_\ell - i)$  factor leads to a vanishing effective range. As soon as the Coulomb interaction is included in the Lagrangian, when the potential couples the fermions to one unit of angular momentum, a purely electrostatic non-zero effective range emerges, in contrast with the  $\ell = 0$  case, see sec. 2.1.2. Therefore, we shall expect that, for higher angular momentum interactions further coefficients in the generalized expansion of  $|\mathbf{p}|^{2\ell+1} \cot \delta_\ell$  in even powers of the momentum of the fermions in the CoM frame become non-zero when the colliding particles are allowed to exchange Coulomb photons.

### 3.1.3 Attractive channel

We consider the scattering of two non-relativistic fermions with opposite charges, such as fermion-antifermion pairs. Concerning elastic scattering, the continuum eigenstates are again represented by the spherical wave solutions in eqs. (1.18)-(1.19), with  $\eta$  now given by  $-\alpha M/2|\mathbf{p}|$ . Besides, the phenomenology of the scattering process is now enriched by the presence of bound states. In addition, annihilation is possible, but this will not be considered here. The Coulomb Green's function, in fact, is enriched by discrete states,  $\phi_{n,\ell,m}(\mathbf{r})$ , corresponding to bound states with principal quantum number  $n \geq 1$  and rotation group labels given by  $(\ell, m)$ ,

$$\langle \mathbf{r}' | \hat{G}_C^{(\pm)} | \mathbf{r} \rangle = \sum_{n=1}^{+\infty} \sum_{\ell=0}^{+\infty} \sum_{m=-\ell}^{\ell} \frac{\phi_{n,\ell,m}(\mathbf{r}') \phi_{n,\ell,m}^*(\mathbf{r})}{E - E_n} + \int_{\mathbb{R}^3} \frac{d^3 \mathbf{s}}{(2\pi)^3} \frac{\psi_{\mathbf{s}}^{(\pm)}(\mathbf{r}') \psi_{\mathbf{s}}^{(\pm)*}(\mathbf{r})}{E - E_s \pm i\epsilon}, \quad (3.68)$$

where  $E_s$  is equal to  $\alpha^2 M/4\eta^2$  and the bound state eigenvalues,  $E_n$ , are given by Bohr's formula for a system with reduced mass equal to  $M/2$ ,

$$E_n = -\frac{\alpha^2 M}{4n^2}, \quad (3.69)$$

in natural units. As in the previous case, the Coulomb-corrected strong scattering amplitude of the elastic scattering process in configuration space takes the form

$$\bar{T}_{\text{SC}}(\mathbf{p}', \mathbf{p}) = \nabla' \psi_{\mathbf{p}'}^{(-)*}(\mathbf{r}') \Big|_{\mathbf{r}'=0} \cdot \frac{\bar{D}(E^*)}{\mathbb{1} - \bar{D}(E^*) \bar{\mathbb{J}}_C} \nabla \psi_{\mathbf{p}}^{(+)}(\mathbf{r}) \Big|_{\mathbf{r}=0}, \quad (3.70)$$

where  $\bar{D}(E^*)$  is the strong P-wave coupling constant in presence of attractive electrostatic interaction and the matrix  $\bar{\mathbb{J}}_C$  is, now, given by

$$\bar{\mathbb{J}}_C = \bar{\mathbb{J}}_C^d + \bar{\mathbb{J}}_C^c, \quad (3.71)$$

which corresponds to the addition of the contributions from discrete and continuum states,

$$\mathbb{J}_C^d = \sum_{n=1}^{+\infty} \sum_{\ell=0}^{+\infty} \sum_{m=-\ell}^{+\ell} \int_{\mathbb{R}^3} d^3 r' \delta(\mathbf{r}') \int_{\mathbb{R}^3} d^3 r \delta(\mathbf{r}) \frac{\nabla' \phi_{n,\ell,m}(\mathbf{r}') \otimes \nabla \phi_{n,\ell,m}^*(\mathbf{r})}{E - E_n + i\epsilon}, \quad (3.72)$$

and

$$\mathbb{J}_C^c = \int_{\mathbb{R}^3} d^3 r' \delta(\mathbf{r}') \int_{\mathbb{R}^3} d^3 r \delta(\mathbf{r}) \int_{\mathbb{R}^3} \frac{d^3 s}{(2\pi)^3} \frac{\nabla' \psi_s^{(+)}(\mathbf{r}') \otimes \nabla \psi_s^{(+)*}(\mathbf{r})}{E - E_s + i\epsilon}, \quad (3.73)$$

respectively. Let us start by evaluating the term  $\mathbb{J}_C^d$ . With reference to the expression of the eigenfunctions belonging to the discrete spectrum,

$$\phi_{n,\ell,m}(\mathbf{r}) = \sqrt{\left(\frac{\alpha M}{n}\right)^3 \frac{n - \ell - 1!}{n + \ell!} \frac{1!}{2n}} e^{-\frac{\alpha M}{2n} r} \left(\frac{\alpha M r}{n}\right)^\ell L_{n-\ell-1}^{2\ell+1}\left(\frac{\alpha M}{n} r\right) Y_\ell^m(\theta, \varphi), \quad (3.74)$$

where  $L_k^n(x)$  are the associated Laguerre polynomials, we first evaluate the integrals containing the gradient of the latter in the expression for  $\mathbb{J}_C^d$  in eq. (3.72), that can be performed separately for each of the wavefunctions, since the denominator does not depend on the coordinates. The application of the gradient on the bound state wavefunctions,  $\nabla \phi_{n,\ell,m}(\mathbf{r})|_{\mathbf{r}=0}$ , yields

$$\begin{aligned} -\left(\frac{\alpha M}{n}\right)^{\frac{3}{2}} \sqrt{\frac{n - \ell - 1!}{n + \ell!} \frac{1!}{2n}} \int_0^{+\infty} dr \frac{\delta(r)}{4\pi} \left\{ \nabla \left[ e^{-\frac{\alpha M}{2n} r} \left(\frac{\alpha M r}{n}\right)^\ell L_{n-\ell-1}^{2\ell+1}\left(\frac{\alpha M}{n} r\right) \right] \int_{\partial S^2} d\Omega Y_\ell^m(\Omega) \right. \\ \left. + \frac{e^{-\frac{\alpha M}{2n} r}}{r} \left(\frac{\alpha M}{n} r\right)^\ell L_{n-\ell-1}^{2\ell+1}\left(\frac{\alpha M}{n} r\right) \int_{\partial S^2} d\Omega \nabla Y_\ell^m(\Omega) \right\}, \end{aligned} \quad (3.75)$$

where the spherical symmetry of the Dirac delta has been exploited. Of the latter equation, we consider now the first term on the right hand side. Firstly, expressing the radius vector componentwise as a spherical tensor of rank 1 (cf. eq. (5.24) and sec. 5.1 in ref. [135]), the aforementioned part of eq. (3.75) becomes

$$\begin{aligned} -\frac{1}{\sqrt{4\pi}} \left(\frac{\alpha M}{n}\right)^{\frac{3}{2}} \sqrt{\frac{n - \ell - 1!}{n + \ell!} \frac{1!}{2n}} \sum_{\mu=-1}^1 \int_0^{+\infty} dr \delta(r) \frac{e^{-\frac{\alpha M}{2n} r}}{r} \left(\frac{\alpha M}{n} r\right)^\ell \left\{ \left[ \ell - \frac{\alpha M}{2n} r \right] L_{n-\ell-1}^{2\ell+1}\left(\frac{\alpha M}{n} r\right) \right. \\ \left. - \frac{\alpha M}{n} r L_{n-\ell-2}^{2\ell+2}\left(\frac{\alpha M}{n} r\right) \right\} \int_0^{2\pi} d\varphi \int_0^\pi d\theta \sin \theta (110|\mu - \mu 0) Y_1^\mu(\theta, \varphi) Y_\ell^m(\theta, \varphi) \mathbf{e}_{-\mu}. \end{aligned} \quad (3.76)$$

Now, recalling the expression of the constant term of the associated Laguerre polynomials,

$$L_m^k(0) = \frac{m + k!}{m! k!}, \quad (3.77)$$

eq. (3.76) can be concisely recast into

$$-\frac{1}{\sqrt{4\pi}} \frac{\alpha M}{n} \left(\frac{\alpha M}{n}\right)^{\frac{3}{2}} \sqrt{\frac{n - \ell - 1!}{n + \ell!} \frac{1!}{2n}} \frac{n + 1!}{n - 2! 3!} (110| - m m 0) (-1)^m \delta_{\ell 1} \mathbf{e}_m, \quad (3.78)$$

where the integration over the angular variables  $\Omega$  has been performed. After replacing the Clebsch-Gordan coefficient  $(110| - m m 0)$  with  $(-1)^{m+1}/\sqrt{3}$ , and performing few manipulations,

the sought expression is recovered,

$$\frac{1}{12} \left( \frac{\alpha^5 M^5}{6\pi n^5} \right)^{\frac{1}{2}} \sqrt{(n+1)(n-1)} \delta_{\ell 1} \mathbf{e}_m . \quad (3.79)$$

Concerning the second term on the r.h.s. of eq. (3.75), the rewriting of the gradient of a spherical harmonic into linear combination of spherical tensors (cf. eqs. (5.24) and (5.27) in ref. [135]) gives

$$\begin{aligned} & \frac{1}{\sqrt{4\pi}} \left( \frac{\alpha M}{n} \right)^{3/2} \sqrt{\frac{n-\ell-1!}{n+\ell!} \frac{1}{2n}} \int_0^{+\infty} dr \delta(r) \frac{e^{-\frac{\alpha M}{2n} r}}{r} \left( \frac{\alpha M}{n} r \right)^\ell L_{n-\ell-1}^{2\ell+1} \left( \frac{\alpha M}{n} r \right) \\ & \cdot \sum_{\mu, \mu'} \int_0^{2\pi} d\varphi \int_0^\pi d\theta \sin \theta \left[ \sqrt{\frac{\ell(\ell+1)^2}{2\ell+1}} (\ell-1 \ 1 \ \ell | \mu \ \mu' \ m) Y_{\ell-1}^\mu(\theta, \varphi) Y_0^{0*}(\theta, \varphi) \mathbf{e}_{\mu'} \right. \\ & \left. + \sqrt{\frac{\ell^2(\ell+1)}{2\ell+1}} (\ell+1 \ 1 \ \ell | \mu \ \mu' \ m) Y_{\ell+1}^\mu(\theta, \varphi) Y_0^{0*}(\theta, \varphi) \mathbf{e}_{\mu'} \right] , \end{aligned} \quad (3.80)$$

thus, allowing again for an immediate integration over the angular variables,

$$\frac{1}{\sqrt{4\pi}} \left( \frac{\alpha M}{n} \right)^{3/2} \sqrt{\frac{n-\ell-1!}{n+\ell!} \frac{n+1!}{2n} \frac{1}{n-2!}} \cdot \frac{\alpha M}{6n} \frac{2}{\sqrt{3}} \sum_{\mu} (011|0\mu m) \delta_{\ell 1} \mathbf{e}_{\mu} , \quad (3.81)$$

where the eq. (3.77) for the evaluation of the Laguerre polynomials at the origin has been exploited. Subsequently, the replacement  $(011|0mm) = 1$  gives the desired expression for the second term of eq. (3.75),

$$\frac{1}{6} \left( \frac{\alpha^5 M^5}{6\pi n^5} \right)^{\frac{1}{2}} \sqrt{(n+1)(n-1)} \delta_{\ell 1} \mathbf{e}_m . \quad (3.82)$$

Equipped with the results in eqs. (3.79) and (3.82), the original integral can be immediately evaluated,

$$\int_{\mathbb{R}^3} d^3r \delta(\mathbf{r}) \nabla \phi_{n,\ell,m}(\mathbf{r}) = \frac{1}{4} \left( \frac{\alpha^5 M^5}{6\pi n^5} \right)^{\frac{1}{2}} \sqrt{(n+1)(n-1)} \delta_{\ell 1} \mathbf{e}_m . \quad (3.83)$$

Now, taking the tensor product of the latter expression with its complex-conjugate version, as required by eq. (3.72),  $\bar{\mathbb{J}}_C^d$  reduces to

$$\bar{\mathbb{J}}_C^d = \sum_{n=1}^{+\infty} \sum_{m=-1}^1 \frac{\alpha^5 M^5}{16} \frac{(n+1)(n-1)}{6\pi n^5} \frac{\mathbf{e}_m \otimes \mathbf{e}_m^*}{E - E_n} = \frac{\alpha^3 M^4}{24\pi} \sum_{n=1}^{+\infty} \frac{\eta^2 (n+1)(n-1)}{n^3 (n^2 + \eta^2)} \sum_{m=-1}^1 \mathbf{e}_m \otimes \mathbf{e}_m^* . \quad (3.84)$$

Since the diagonal form of the matrix in the spherical complex basis (cf. eq. (2.141) in ref. [135]) is preserved in the Cartesian basis and the sum over the principal quantum number can be decomposed and evaluated in terms of the Digamma function  $\psi(z)$ ,

$$\sum_{n=1}^{+\infty} \frac{\eta^2}{n(n^2 + \eta^2)} = \zeta(1) + \frac{1}{2} \psi(i\eta) + \frac{1}{2} \psi(-i\eta) , \quad (3.85)$$

and

$$\sum_{n=1}^{+\infty} \frac{\eta^2}{n^3(n^2 + \eta^2)} = -\frac{\zeta(1)}{\eta^2} + \zeta(3) - \frac{1}{2\eta^2}\psi(-i\eta) - \frac{1}{2\eta^2}\psi(i\eta), \quad (3.86)$$

the contribution to the scattering matrix due to the discrete states,

$$\bar{\mathbb{J}}_{\mathbb{C}}^{\text{d}} \equiv \bar{\mathbb{J}}_{\mathbb{C}}^{\text{d}}(\mathbf{p}) \mathbb{1}, \quad (3.87)$$

can be ultimately rewritten as

$$\bar{\mathbb{J}}_{\mathbb{C}}^{\text{d}}(\mathbf{p}) = (1 + \eta^2) \frac{\alpha M^2 \mathbf{p}^2}{3\pi} \frac{1}{2} \left[ \zeta(1) + \frac{1}{2}\psi(-i\eta) + \frac{1}{2}\psi(i\eta) \right] - \frac{\alpha^3 M^4}{24\pi} \zeta(3). \quad (3.88)$$

As observed in sec. 2.1.3, the divergent sum of the harmonic series,  $\zeta(1)$ , appears in the last formula. Its presence is only due to the numerable infinity of states in the discrete spectrum, whose energy depends on the inverse square of  $n$ , while the modulus square of the gradient of the eigenfunctions evaluated at the origin yields a factor  $\propto n^2$ . The replacement of  $\zeta(1)$  in eq. (3.88) by its Cauchy principal value, equal to  $\gamma_E$ , allows to assign a finite value to  $\bar{\mathbb{J}}_{\mathbb{C}}^{\text{d}}$  and, thus, circumvent the divergence.

At this stage, we switch to the continuous contribution to the auxiliary scattering matrix,  $\bar{\mathbb{J}}_{\mathbb{C}}^{\text{c}}$ . As for the repulsive counterpart in sec. 3.1.2, the possible divergences in the three-dimensional limit require the rewriting of the relevant integrals in arbitrary complex dimension  $d$ . Therefore, the dimensionally regularized version of the second term on the r.h.s. of eq. (3.71) gives

$$\bar{\mathbb{J}}_{\mathbb{C}}^{\text{c}}(d) = \mathbb{1} \frac{M}{d} \int_{\mathbb{R}^d} \frac{d^d s}{(2\pi)^d} \frac{-2\pi\eta}{e^{-2\pi\eta} - 1} \frac{1 + \eta^2}{\mathbf{p}^2 - \mathbf{s}^2 + i\epsilon} \mathbf{s}^2 + \mathbb{1} \frac{M}{d} \int_{\mathbb{R}^d} \frac{d^d s}{(2\pi)^d} \frac{-2\pi\eta}{\mathbf{s}^{-2}} \frac{1 + \eta^2}{\mathbf{p}^2 - \mathbf{s}^2 + i\epsilon}, \quad (3.89)$$

where the initial integral has been split into two parts, making use of the trick in eq. (3.42). Due to the sign change in  $\eta$ , the first term on the r.h.s. of eq. (3.89),

$$\bar{\mathbb{J}}_{\mathbb{C}}^{\text{old}}(d; \mathbf{p}) = \frac{M}{d} \int_{\mathbb{R}^d} \frac{d^d s}{(2\pi)^d} \frac{-2\pi\eta}{e^{-2\pi\eta} - 1} \frac{1 + \eta^2}{\mathbf{p}^2 - \mathbf{s}^2 + i\epsilon} \mathbf{s}^2, \quad (3.90)$$

can be immediately evaluated, since it coincides with eq. (3.39). Therefore the result in eq. (3.62) can be directly exported, rewriting eq. (3.90) as

$$\begin{aligned} \bar{\mathbb{J}}_{\mathbb{C}}^{\text{old}}(\mathbf{p}) = & \frac{\alpha^3 M^4}{48\pi} \left[ \frac{1}{3-d} + \zeta(3) - \frac{3}{2}\gamma_E + \frac{4}{3} + \log \frac{\mu\sqrt{\pi}}{\alpha M} \right] - (1 + \eta^2) \frac{\alpha M^2}{4\pi} \frac{\mathbf{p}^2}{3} \left[ \psi(-i\eta) - \frac{1}{2i\eta} \right. \\ & \left. - \log(-i\eta) \right] + \frac{\alpha M^2}{4\pi} \frac{\mathbf{p}^2}{3} \left[ \frac{1}{3-d} + \frac{4}{3} - \frac{3}{2}\gamma_E + \log \frac{\mu\sqrt{\pi}}{\alpha M} \right] - \frac{\alpha^2 M^3}{32\pi} \frac{\mu}{3} (\pi^2 - 3) - \frac{\mu M}{4\pi} \frac{\mathbf{p}^2}{2}, \end{aligned} \quad (3.91)$$

where the  $H(-\eta)$  function has been replaced by its definition in terms of the Digamma function in eq. (1.33), in sight of the next developments. Subsequently, we evaluate the second term on the r.h.s. of eq. (3.89), the new part of the continuum states contribution. In order to bring  $\mathbf{s}^2$  to the denominator, we apply again the trick introduced in eq. (3.42) and split the integral into

three parts,

$$\begin{aligned} \mathbb{J}_C^{\text{new}}(d; \mathbf{p}) &= \frac{M}{d} \int_{\mathbb{R}^d} \frac{d^d s}{(2\pi)^d} \frac{-2\pi\eta}{\mathbf{s}^{-2}} \frac{1 + \eta^2}{\mathbf{p}^2 - \mathbf{s}^2 + i\epsilon} = -\frac{M}{d} \int_{\mathbb{R}^d} \frac{d^d s}{(2\pi)^d} (-2\pi\eta) \\ &\quad + \frac{M}{d} \int_{\mathbb{R}^d} \frac{d^d s}{(2\pi)^d} \frac{-2\pi\eta\mathbf{p}^2}{\mathbf{p}^2 - \mathbf{s}^2} + \frac{\alpha^2 M^3}{4d} \int_{\mathbb{R}^d} \frac{d^d s}{(2\pi)^d} \frac{-2\pi\eta}{\mathbf{p}^2 - \mathbf{s}^2}. \end{aligned} \quad (3.92)$$

Concerning the first term on the r.h.s. of the latter equation, it vanishes in dimensional regularization, see eq. (4.3.1a) in ref. [130]. Therefore, we can switch to the subsequent term of eq. (3.92) and apply Feynman's trick for denominators, finding

$$\frac{M}{d} \int_{\mathbb{R}^d} \frac{d^d s}{(2\pi)^d} \frac{-2\pi\eta\mathbf{p}^2}{\mathbf{p}^2 - \mathbf{s}^2} = -\frac{\alpha M^2}{d} \frac{\Gamma(\frac{3}{2})}{\Gamma(1)\Gamma(\frac{1}{2})} \int_0^1 d\omega \omega^{-1/2} \int_{\mathbb{R}^d} \frac{d^d \mathbf{s}}{(2\pi)^d} \frac{\pi\mathbf{p}^2}{[\mathbf{s}^2 - (1-\omega)\mathbf{p}^2]^{3/2}}, \quad (3.93)$$

Defining again the auxiliary variable  $\gamma = -i|\mathbf{p}|$ , we perform the momentum integration in eq. (3.93),

$$-\frac{\alpha M^2}{d} \frac{\mathbf{p}^2 \pi}{\gamma^{3-d}(4\pi)^{d/2}} \frac{\Gamma(\frac{3}{2} - \frac{d}{2})}{\Gamma(\frac{1}{2})} \int_0^1 d\omega \frac{(1-\omega)^{\frac{d}{2} - \frac{3}{2}}}{\sqrt{\omega}}. \quad (3.94)$$

Then, since the remaining integration over  $\omega$  turns out to be finite in two dimensions and the rest of the expression does not display any PDS singularity, we can directly reintroduce  $\epsilon \equiv 3 - d$  and consider the three-dimensional limit. In particular, the integral over  $\omega$  in eq. (3.94) can be evaluated in first-order approximation in  $\epsilon$ , obtaining

$$\int_0^1 d\omega \frac{(1-\omega)^{-\frac{\epsilon}{2}}}{\sqrt{\omega}} \approx 2 + 2\epsilon - 2\epsilon \log 2. \quad (3.95)$$

Second, the terms depending on  $\epsilon$  in the exponent can be grouped and expanded to first order in  $\epsilon$  as in eq. (3.55), whereas the Gamma function can be expressed in Laurent series up to order  $\epsilon^0$ . Performing few manipulations and taking the  $\epsilon \rightarrow 0$  limit, the original expression in eq. (3.93) becomes

$$\begin{aligned} \lim_{d \rightarrow 3} \frac{M}{d} \int_{\mathbb{R}^d} \frac{d^d s}{(2\pi)^d} \frac{-2\pi\eta\mathbf{p}^2}{\mathbf{p}^2 - \mathbf{s}^2} &= -\frac{\alpha M^2}{3\pi} \frac{\mathbf{p}^2}{4} \lim_{\epsilon \rightarrow 0} \frac{(1 + \epsilon - \epsilon \log 2) (\frac{2}{\epsilon} - \gamma_E)}{(1 - \frac{\epsilon}{3}) (1 - \frac{\epsilon}{2} \log \frac{\pi\mu^2}{\gamma^2})} \\ &= -\frac{\alpha M^2 \mathbf{p}^2}{6\pi} \left[ \frac{1}{3-d} + \frac{4}{3} - \frac{\gamma}{2} + \log \frac{\mu\sqrt{\pi}}{\alpha M} + \log(-i\eta) \right]. \end{aligned} \quad (3.96)$$

Subsequently, we compute the last term on the r.h.s. of eq. (3.92). As it can be inferred, the integral coincides with the one in of eq. (3.96), except for an overall factor of  $\alpha^2 M^2/4\mathbf{p}^2 = \eta^2$ . Therefore, its evaluation is straightforward and gives

$$\lim_{d \rightarrow 3} \frac{\alpha^2 M^3}{4d} \int_{\mathbb{R}^d} \frac{d^d s}{(2\pi)^d} \frac{-2\pi\eta}{\mathbf{p}^2 - \mathbf{s}^2} = -\frac{\alpha M^2}{6\pi} \frac{\alpha^2 M^2}{4} \left[ \frac{1}{3-d} + \frac{4}{3} - \frac{\gamma_E}{2} + \log \frac{\mu\sqrt{\pi}}{\alpha M} + \log(-i\eta) \right]. \quad (3.97)$$

Collecting both the results in eqs. (3.96) and (3.97), we obtain the sought expression for  $\mathbb{J}_C^{\text{new}}(d; \mathbf{p})$  in the three-dimensional limit,

$$\mathbb{J}_C^{\text{new}}(\mathbf{p}) = -(1 + \eta^2) \frac{\alpha M^2 \mathbf{p}^2}{6\pi} \left[ \frac{1}{3-d} + \frac{4}{3} - \frac{\gamma_E}{2} + \log(-i\eta) + \log \frac{\mu\sqrt{\pi}}{\alpha M} \right]. \quad (3.98)$$

We now collect all the contributions in eqs. (3.88), (3.92) and (3.98) and write a closed form for the diagonal matrix elements of  $\mathbb{J}_C$ ,

$$\begin{aligned} \bar{\mathbb{J}}_C^d(\mathbf{p}) + \bar{\mathbb{J}}_C^{\text{old}}(\mathbf{p}) + \bar{\mathbb{J}}_C^{\text{new}}(\mathbf{p}) = & -\frac{\alpha M^2 \mathbf{p}^2}{4\pi} \left[ \frac{1}{3-d} + \frac{4}{3} - \frac{3}{2}\gamma_E + \log \frac{\mu\sqrt{\pi}}{\alpha M} \right] - \frac{\mu M \mathbf{p}^2}{4\pi} \frac{1}{2} \\ & - \frac{\alpha^3 M^4}{48\pi} \left[ \frac{1}{3-d} + \zeta(3) - \frac{3}{2}\gamma_E + \frac{4}{3} + \log \frac{\mu\sqrt{\pi}}{\alpha M} \right] + \frac{\alpha M^2 \mathbf{p}^2}{12\pi} \bar{H}(\eta)(1 + \eta^2) - \frac{\alpha^2 M^3 \mu}{32\pi} \frac{1}{3} (\pi^2 - 3), \end{aligned} \quad (3.99)$$

where the definition of  $\bar{H}(\eta)$  in eq. (1.35) has been exploited and the Cauchy principal value of  $\zeta(1)$  has been taken. A direct comparison with the repulsive counterpart of the last formula in eq. (3.62) shows that the map between the two expression is provided by the sign reversal in front of all the terms containing odd powers of the fine-structure constant and the replacement of  $H(\eta)$  by  $\bar{H}(\eta)$ . This fact is consistent with the conclusions drawn from eq. (2.54), where all the PDS-corrective terms remained unaffected by the sign change in the charge of one of the interacting fermions. We conclude this section with the derivation of an expression for the scattering length and the effective range, by making use of the attractive counterpart of the generalized effective-range expansion in eq. (3.27), obtained by replacing again  $H(\eta)$  by  $\bar{H}(\eta)$  with  $\eta < 0$ . As a consequence of the attraction of the electrostatic interaction, the Coulomb corrections in the strong scattering parameters change sign, consistent with eq. (3.99). Concerning the scattering length, we have

$$\frac{1}{\bar{a}_C^{(1)}} = \frac{12\pi}{M\bar{D}(E^*)} + \frac{\alpha^3 M^3}{4} \left[ \frac{1}{3-d} + \zeta(3) - \frac{3}{2}\gamma_E + \frac{4}{3} + \log \frac{\mu\sqrt{\pi}}{\alpha M} \right] + \frac{\alpha^2 M^2 \mu}{8} (\pi^2 - 3), \quad (3.100)$$

where the divergence can be reabsorbed by the P-wave strong coupling constant. Analogously to eq. (2.55), the renormalized version of the scattering length,  $\bar{a}_C^{(1)}(\mu)$ , can be defined in terms of the physical one,  $\bar{a}_C^{(1)}$ ,

$$\frac{1}{\bar{a}_C^{(1)}(\mu)} = \frac{1}{\bar{a}_C^{(1)}} - \frac{\alpha^3 M^3}{4} \left[ \zeta(3) - \frac{3}{2}\gamma_E + \frac{4}{3} + \log \frac{\mu\sqrt{\pi}}{\alpha M} \right]. \quad (3.101)$$

Finally, the terms proportional to the square of the momentum of the fermions  $\mathbf{p}$  give rise to a nonzero value for the effective range, as in eq. (3.67),

$$\bar{r}_0^{(1)} = -\alpha M \left[ \frac{2}{3-d} + \frac{8}{3} - 3\gamma_E + 2 \log \frac{\mu\sqrt{\pi}}{\alpha M} \right] - 3\mu, \quad (3.102)$$

whose divergent part, in case the energy-dependent coefficient of the  $\ell = 1$  interaction  $D(E^*)$  is replaced by  $D_0$ , can be again reabsorbed by counterterms coming from  $\mathbf{p}^2$ -dependent  $\ell = 0$  interactions.

## 3.2 The finite-volume environment

As in the S-wave case, we transpose the physical system of non-relativistic spinless fermions interacting via scalar photons onto a cubic finite volume with edges of length  $L$ . Discarding the zero modes, the finite-volume momenta obey the constraint  $|\mathbf{p}| \geq 2\pi/L$  that, together with the assumption  $L \gg 1/M$ , ensure the viability of a perturbative treatment for the QED interactions [1].



Considering the leading modification on the masses of the spinless fermions (cf. eq. (1.39)), the infinite volume ERE in eq. (1.39) rewritten in terms of the translated parameters in eqs. (1.40)-(1.44) for unbound states with  $T^L = \mathbf{p}^2/M$  and  $\ell = 1$  assumes the form

$$\mathbf{p}^2(1 + \eta^2)[C_\eta^2|\mathbf{p}|(\cot \delta_1 - i) + \alpha MH(\eta)] = -\frac{1}{a'_C{}^{(1)}} + \frac{1}{2}r'_0{}^{(1)}\mathbf{p}^2 + r'_1{}^{(1)}\mathbf{p}^4 + \dots, \quad (3.103)$$

where the changes in the total energy have been absorbed in the primed scattering parameters.

The rewriting of eq. (3.103) in terms of finite-volume quantities, combined with the quantization conditions discussed below, will provide the key ingredient for the derivation of the finite volume energy corrections for scattering and bound states with one unit of angular momentum.

### 3.2.1 Quantization Condition

After introducing the finite and discretized configuration space, we derive the conditions that determine the counterpart of the  $\ell = 1$  energy eigenvalues in the cubic finite-volume. Their associated eigenstates transform as the three-dimensional irreducible representation  $T_1$  (in Schönflies notation [131]) of the cubic group.

As it can be inferred from eq. (1.22), the eigenvalues of the full Hamiltonian of the system  $\hat{H}_0 + \hat{V}_C + \hat{V}_S$  can be identified with the singularities of the two-point correlation function  $G_{SC}(\mathbf{r}, \mathbf{r}')$ . The Green's functions  $G_{SC}(\mathbf{r}', \mathbf{r})$ , in turn, can be computed from the terms in the expansion over the P-wave interaction insertions stemming from eq. (1.24), with  $\hat{V}_S$  in momentum space given in eq. (1.2). In particular, the three lowest order contributions in  $D(E^*)$  yield, respectively,

$$\langle \mathbf{r}' | \hat{G}_C^{(\pm)} | \mathbf{r} \rangle = G_C^{(\pm)}(\mathbf{r}', \mathbf{r}), \quad (3.104)$$

$$\langle \mathbf{r}' | \hat{G}_C^{(\pm)} \hat{V}_S \hat{G}_C^{(\pm)} | \mathbf{r} \rangle = D(E^*) \nabla_{\mathbf{r}_1} G_C^{(\pm)}(\mathbf{r}', \mathbf{r}_1) \Big|_{\mathbf{r}_1=0} \cdot \nabla_{\mathbf{r}_2} G_C^{(\pm)}(\mathbf{r}_2, \mathbf{r}) \Big|_{\mathbf{r}_2=0}, \quad (3.105)$$

and

$$\begin{aligned} \langle \mathbf{r}' | \hat{G}_C^{(\pm)} \hat{V}_S \hat{G}_C^{(\pm)} \hat{V}_S \hat{G}_C^{(\pm)} | \mathbf{r} \rangle &= [D(E^*)]^2 \nabla_{\mathbf{r}_1} G_C^{(\pm)}(\mathbf{r}, \mathbf{r}_1) \Big|_{\mathbf{r}_1=0} \\ &\quad \cdot \nabla_{\mathbf{r}_2} \otimes \nabla_{\mathbf{r}_3} G_C^{(\pm)}(\mathbf{r}_2, \mathbf{r}_3) \Big|_{\mathbf{r}_2=0, \mathbf{r}_3=0} \nabla_{\mathbf{r}_4} G_C^{(\pm)}(\mathbf{r}_4, \mathbf{r}) \Big|_{\mathbf{r}_4=0}. \end{aligned} \quad (3.106)$$

Extending the calculation to higher orders, the expression of  $(N+1)^{\text{th}}$  order contribution to the full two-point correlation function can be derived,

$$\begin{aligned} \langle \mathbf{r}' | \hat{G}_C^{(\pm)} \underbrace{\hat{V}_S \hat{G}_C^{(\pm)} \dots \hat{V}_S \hat{G}_C^{(\pm)}}_{N \text{ times}} | \mathbf{r} \rangle &= D(E^*) \nabla_{\mathbf{r}_1} G_C^{(\pm)}(\mathbf{r}', \mathbf{r}_1) \Big|_{\mathbf{r}_1=0} \\ &\quad \cdot \prod_{i=2}^N \left[ D(E^*) \nabla_{\mathbf{r}_i} \otimes \nabla_{\mathbf{r}_{i+1}} G_C^{(\pm)}(\mathbf{r}_i, \mathbf{r}_{i+1}) \Big|_{\substack{\mathbf{r}_i=0 \\ \mathbf{r}_{i+1}=0}} \right] \nabla_{\mathbf{r}_{N+2}} G_C^{(\pm)}(\mathbf{r}_{N+2}, \mathbf{r}) \Big|_{\mathbf{r}_{N+2}=0}, \end{aligned} \quad (3.107)$$

thus allowing to rewrite the original Green's function in terms of a geometric series of ratio

$$D(E^*) \nabla_{\mathbf{r}_i} \otimes \nabla_{\mathbf{r}_{i+1}} G_C^{(\pm)}(\mathbf{r}_i, \mathbf{r}_{i+1}) \Big|_{\substack{\mathbf{r}_i=0 \\ \mathbf{r}_{i+1}=0}},$$



that we identify as  $\mathbb{J}_C$  (cf. eq. (3.37)),

$$G_{SC}^{(\pm)}(\mathbf{r}', \mathbf{r}) = \langle \mathbf{r}' | \hat{G}_{SC}^{(\pm)} | \mathbf{r} \rangle = G_C^{(\pm)}(\mathbf{r}', \mathbf{r}) + \nabla_{\mathbf{r}_1} G_C^{(\pm)}(\mathbf{r}', \mathbf{r}_1) \Big|_{\mathbf{r}_1=0} \cdot \frac{D(E^*)}{1 - D(E^*)\mathbb{J}_C} \nabla_{\mathbf{r}_2} G_C^{(\pm)}(\mathbf{r}_2, \mathbf{r}) \Big|_{\mathbf{r}_2=0}, \quad (3.108)$$

where

$$\sqrt{D(E^*)} \nabla_{\mathbf{r}_1} G_C^{(\pm)}(\mathbf{r}', \mathbf{0}) \Big|_{\mathbf{r}_1=0} \quad \text{and} \quad \sqrt{D(E^*)} \nabla_{\mathbf{r}_2} G_C^{(\pm)}(\mathbf{r}_2, \mathbf{r}) \Big|_{\mathbf{r}_2=0},$$

can be interpreted as a source and a sink coupling the fermions to a P-wave state, respectively. As in the  $\ell = 0$  case, the pole in the second term of eq. (3.108) permits to express the infinite-volume quantization conditions,

$$\frac{\mathbb{1}}{D(E^*)} = \nabla_{\mathbf{r}_i} \otimes \nabla_{\mathbf{r}_{i+1}} G_C^{(\pm)}(\mathbf{r}_i, \mathbf{r}_{i+1}) \Big|_{\substack{\mathbf{r}_i=0 \\ \mathbf{r}_{i+1}=0}}, \quad (3.109)$$

where the identity matrix multiplied by the CoM energy dependent coupling constant is equal to the inverse of the matrix of the double derivatives of the Coulomb two-point Green's function evaluated at the origin,  $\mathbb{J}_C$ . Concentrating again on the retarded two-point correlation function and adopting the notation of ref. [1], the finite-volume counterpart of eq. (3.108) becomes

$$G_{SC}^{(+),L}(\mathbf{r}', \mathbf{r}) = G_C^{(+),L}(\mathbf{r}', \mathbf{r}) + \nabla_{\mathbf{r}_1} G_C^{(+),L}(\mathbf{r}', \mathbf{r}_1) \Big|_{\mathbf{r}_1=0} \cdot \frac{D^L(E^*)}{1 - D(E^*)\mathbb{J}_C^L} \nabla_{\mathbf{r}_2} G_C^{(+),L}(\mathbf{r}_2, \mathbf{r}) \Big|_{\mathbf{r}_2=0}. \quad (3.110)$$

Similarly, the pole in the second term on the r.h.s. of eq. (3.110) yields the finite-volume quantization condition,

$$\frac{\mathbb{1}}{D^L(E^*)} = \nabla_{\mathbf{r}_i} \otimes \nabla_{\mathbf{r}_{i+1}} G_C^{(+),L}(\mathbf{r}_i, \mathbf{r}_{i+1}) \Big|_{\substack{\mathbf{r}_i=0 \\ \mathbf{r}_{i+1}=0}}, \quad (3.111)$$

that determines the  $T_1$  eigenvalues. As in the  $\ell = 0$  case, we proceed by expanding  $G_C^{(+),L}(\mathbf{r}_i, \mathbf{r}_{i+1})$  in powers of the fine-structure constant and truncate the series to order  $\alpha$ . Moreover, we notice that the directional derivatives of the two-point Coulomb Green's function evaluated at the origin correspond to the pairwise closure of the external legs of the Coulomb ladders in the expansion of  $G_C^{(+)}$  in fig. 1.1 to two-fermion vertices, evaluated at the origin in configuration space. As a consequence, the matrix elements of  $\mathbb{J}_C^L$  can be interpreted as bubble diagrams with multiple Coulomb-photon insertions inside. Analytically, the two lowest order contributions to  $\mathbb{J}_C$ , that correspond to loop diagrams, respectively with and without a Coulomb-photon insertions, read

$$\begin{aligned} \mathbb{J}_C(\mathbf{p}) &= \nabla_{\mathbf{r}'} \otimes \nabla_{\mathbf{r}} G_C^{(\pm)}(\mathbf{r}', \mathbf{r}) \Big|_{\substack{\mathbf{r}'=0 \\ \mathbf{r}=0}} = \nabla_{\mathbf{r}'} \otimes \nabla_{\mathbf{r}} \langle \mathbf{r}' | \hat{G}_0^{(\pm)} | \mathbf{r} \rangle \Big|_{\substack{\mathbf{r}'=0 \\ \mathbf{r}=0}} + \nabla_{\mathbf{r}'} \otimes \nabla_{\mathbf{r}} \langle \mathbf{r}' | \hat{G}_0^{(\pm)} \hat{V}_C \hat{G}_0^{(\pm)} | \mathbf{r} \rangle \Big|_{\substack{\mathbf{r}'=0 \\ \mathbf{r}=0}} \\ &+ \dots = -M \int_{\mathbb{R}^3} \frac{d^3 q}{(2\pi)^3} \frac{\mathbf{q} \otimes \mathbf{q}}{\mathbf{q}^2 - \mathbf{p}^2} + 4\pi\alpha M^2 \int_{\mathbb{R}^3} \frac{d^3 q}{(2\pi)^3} \int_{\mathbb{R}^3} \frac{d^3 k}{(2\pi)^3} \frac{1}{\mathbf{q}^2 - \mathbf{p}^2} \frac{1}{\mathbf{k}^2 - \mathbf{p}^2} \frac{\mathbf{q} \otimes \mathbf{k}}{|\mathbf{q} - \mathbf{k}|^2} + \dots, \end{aligned} \quad (3.112)$$

where the Dyson identity between  $\hat{G}_C^{(\pm)}$  and  $\hat{G}_0^{(\pm)}$  (cf. eq. (1.16)) has been exploited and  $\varepsilon$  has been set to zero. Replacing again the integrals over the momenta by sums over the

dimensionless momenta  $\mathbf{n}, \mathbf{m} \in \mathbb{Z}^3$ , the finite-volume counterpart of eq. (3.112) is obtained,

$$\mathbb{J}_C^L(\mathbf{p}) = -\frac{M^L}{L^3} \sum_{\mathbf{n}}^{\Lambda_n} \frac{\mathbf{n} \otimes \mathbf{n}}{|\mathbf{n}|^2 - \tilde{p}^2} + \frac{\alpha(M^L)^2}{4\pi^3 L^2} \sum_{\mathbf{n}}^{\Lambda_n} \sum_{\mathbf{m} \neq \mathbf{n}}^{\infty} \frac{1}{|\mathbf{n}|^2 - \tilde{p}^2} \frac{1}{|\mathbf{m}|^2 - \tilde{p}^2} \frac{\mathbf{n} \otimes \mathbf{m}}{|\mathbf{n} - \mathbf{m}|^2} + \dots, \quad (3.113)$$

where the finite-volume mass  $M^L$ , the spherical cutoff  $\Lambda_n$  and the dimensionless CoM momentum of the incoming particles  $\tilde{p}$  have been reintroduced. With the aim of regulating the sums in eq. (3.113) for numerical evaluation as in sec. 2.2.1, we recast the finite volume quantization conditions as

$$\frac{\mathbb{1}}{D^L(E^*)} - \Re \mathbb{J}_C^{\{\text{DR}\}}(\mathbf{p}) = \mathbb{J}_C^L(\mathbf{p}) - \Re \mathbb{J}_C^{\{\Lambda\}}(\mathbf{p}), \quad (3.114)$$

where  $\mathbb{J}_C^{\{\Lambda\}}(\mathbf{p})$  and  $\mathbb{J}_C^{\{\text{DR}\}}(\mathbf{p})$  denote the  $\mathcal{O}(\alpha)$  approximations of  $\mathbb{J}_C$  computed in the cutoff- and dimensional regularization schemes. Starting again from eq. (3.112), we insert the spherical cutoffs as in its discrete counterpart (cf. eq. (3.113)), in sight of the evaluation of  $\mathbb{J}_C^{\{\Lambda\}}$ ,

$$\mathbb{J}_C^{\{\Lambda\}}(\mathbf{p}) = -M \int_{S_\Lambda^2} \frac{d^3 \mathbf{q}}{(2\pi)^3} \frac{\mathbf{q} \otimes \mathbf{q}}{\mathbf{q}^2 - \mathbf{p}^2} + 4\pi\alpha M^2 \int_{S_\Lambda^2} \frac{d^3 \mathbf{q}}{(2\pi)^3} \int_{\mathbb{R}^3} \frac{d^3 \mathbf{k}}{(2\pi)^3} \frac{1}{\mathbf{q}^2 - \mathbf{p}^2} \frac{1}{\mathbf{k}^2 - \mathbf{p}^2} \frac{\mathbf{q} \otimes \mathbf{k}}{|\mathbf{q} - \mathbf{k}|^2} + \dots, \quad (3.115)$$

where  $S_\Lambda^2$  denotes the three-dimensional sphere with radius  $\Lambda$ . Isolating the  $\mathcal{O}(\alpha)$  contribution, we obtain

$$\begin{aligned} M \int_{S_\Lambda^2} \frac{d^3 \mathbf{q}}{(2\pi)^3} \frac{\mathbf{q} \otimes \mathbf{q}}{\mathbf{p}^2 - \mathbf{q}^2} &= -\frac{\mathbb{1}}{3} \frac{M}{2\pi^2} \int_0^\Lambda d\mathbf{q} \mathbf{q}^2 \\ -\frac{\mathbb{1}}{3} \frac{M}{2\pi^2} \int_0^\Lambda d\mathbf{q} \mathbf{p}^2 + \frac{\mathbb{1}}{3} \frac{M}{2\pi^2} \int_0^\Lambda d\mathbf{q} \frac{\mathbf{p}^4}{\mathbf{p}^2 - \mathbf{q}^2} &= -\frac{M\Lambda}{6\pi^2} \left( \frac{\Lambda^2}{3} + \mathbf{p}^2 \right) \mathbb{1} + \mathcal{O}(\Lambda^0), \end{aligned} \quad (3.116)$$

where the isotropy of the cutoff has been exploited in the second step and  $\mathcal{O}(\Lambda^0)$  denotes constant or vanishing terms in the  $\Lambda \rightarrow +\infty$  limit. Concerning the  $\mathcal{O}(\alpha)$  term, the integral can be simplified as follows

$$4\pi\alpha M^2 \int_0^1 d\omega \int_{S_\Lambda^2} \frac{d^3 \mathbf{q}}{(2\pi)^3} \frac{1}{\mathbf{q}^2 - \mathbf{p}^2} \int_{\mathbb{R}^3} \frac{d^3 \mathbf{k}}{(2\pi)^3} \frac{\mathbf{q} \otimes \mathbf{k}}{[\mathbf{k}^2 - 2(1-\omega)\mathbf{k} \cdot \mathbf{q} + \Xi_1]^2}, \quad (3.117)$$

where  $\Xi_1 \equiv (1-\omega)\mathbf{q}^2 - \omega\mathbf{p}^2$  and Feynman parametrization for the denominators has been applied. The subsequent integration over the momentum  $\mathbf{k}$  through eq. (B17) in ref. [132] and the exploitation of rotational symmetry in the outgoing integrand (cf. eq. (4.3.1a) in ref. [130]) gives

$$\frac{\Gamma(\frac{1}{2})}{(4\pi)^{\frac{3}{2}}} \frac{\mathbb{1}}{3} \int_0^1 d\omega \int_{S_\Lambda^2} \frac{d^3 \mathbf{q}}{(2\pi)^3} \frac{4\pi\alpha M^2}{\mathbf{q}^2 - \mathbf{p}^2} \frac{(1-\omega)\mathbf{q}^2}{[\omega(1-\omega)\mathbf{q}^2 - \mathbf{p}^2\omega]^{\frac{1}{2}}}. \quad (3.118)$$

Then, it is convenient to split the integrand of eq. (3.118) into two parts and to simplify the numerator,

$$\begin{aligned} \frac{\Gamma(\frac{1}{2})}{(4\pi)^{\frac{3}{2}}} \frac{\mathbb{1}}{3} \int_0^1 d\omega \int_{S_\Lambda^2} \frac{d^3 \mathbf{q}}{(2\pi)^3} \frac{4\pi\alpha M^2(1-\omega)}{[\omega(1-\omega)\mathbf{q}^2 - \mathbf{p}^2\omega]^{\frac{1}{2}}} \\ + \frac{\Gamma(\frac{1}{2})}{(4\pi)^{\frac{3}{2}}} \frac{\mathbb{1}}{3} \int_0^1 d\omega \int_{S_\Lambda^2} \frac{d^3 \mathbf{q}}{(2\pi)^3} \frac{\mathbf{p}^2}{\mathbf{q}^2 - \mathbf{p}^2} \frac{4\pi\alpha M^2(1-\omega)}{[\omega(1-\omega)\mathbf{q}^2 - \mathbf{p}^2\omega]^{\frac{1}{2}}} \equiv \mathfrak{J}_1 + \mathfrak{J}_2, \end{aligned} \quad (3.119)$$

where  $\mathfrak{J}_1$  ( $\mathfrak{J}_2$ ) corresponds to the first (second) integral on the l.h.s. of the last equation and it will generate the leading contributions in  $\Lambda$ . Beginning with the latter term, integration over the momentum  $\mathbf{l}$  yields

$$\mathfrak{J}_1 = \frac{\alpha M^2}{16\pi^2} \frac{1}{3} \int_0^1 d\omega \left[ \frac{2\mathbf{p}^2}{1-\omega} \operatorname{arccoth} \left( \frac{1}{\Xi_2} \right) + 2\Lambda^2 \Xi_2 - \frac{i\pi \mathbf{p}^2}{1-\omega} \right]. \quad (3.120)$$

where  $\Xi_2$  is an ancillary variable,

$$\Xi_2 \equiv \sqrt{1 - \frac{\mathbf{p}^2}{\Lambda^2(1-\omega)}}.$$

Exploiting the fact that  $\mathbf{p}/\Lambda \ll 1$ , the integrand in the latter expression can be considerably simplified. Equipped with the results

$$\int_0^1 d\omega \frac{1}{\sqrt{\omega(1-\omega)}} = 2 \int_0^1 d\omega \sqrt{\frac{1-\omega}{\omega}} = \pi \quad (3.121)$$

and

$$\int_0^1 d\omega \frac{\log \sqrt{1-\omega}}{\sqrt{\omega(1-\omega)}} = -\pi \log 2, \quad (3.122)$$

the remaining integration can be performed, obtaining the desired expression for  $\mathfrak{J}_1$

$$\mathfrak{J}_1 = \frac{\alpha M^2}{16\pi} \frac{1}{3} \left[ \Lambda^2 - \frac{2i}{\pi} |\mathbf{p}| \Lambda + 2\mathbf{p}^2 \log \left( \frac{\Lambda}{|\mathbf{p}|} \right) \right] + \mathcal{O}(\Lambda^0). \quad (3.123)$$

Concerning the  $\mathfrak{J}_2$  term, its rotational symmetry and integration over the angular variables permits to split it in turn into two terms,

$$\begin{aligned} \mathfrak{J}_2 = & M^2 4\pi \alpha \frac{\Gamma(\frac{1}{2})}{(4\pi)^{\frac{3}{2}}} \frac{1}{3} \frac{\mathbf{p}^2}{2\pi^2} \int_0^1 d\omega \int_0^\Lambda dq \frac{1}{\left[ \mathbf{q}^2 - \frac{\mathbf{p}^2}{1-\omega} \right]^{\frac{1}{2}}} \\ & + M^2 4\pi \alpha \frac{\Gamma(\frac{1}{2})}{(4\pi)^{\frac{3}{2}}} \frac{1}{3} \frac{\mathbf{p}^2}{2\pi^2} \int_0^1 d\omega \int_0^\Lambda dq \frac{\mathbf{p}^2}{\mathbf{q}^2 - \mathbf{p}^2} \frac{1}{\left[ \mathbf{q}^2 - \frac{\mathbf{p}^2}{1-\omega} \right]^{\frac{1}{2}}}. \end{aligned} \quad (3.124)$$

Considering the first term on the r.h.s. of eq. (3.124), integration over the radial momentum yields again an  $\operatorname{arccoth}(x)$  function, which is eventually responsible of a further logarithmic divergence in the UV region,

$$\frac{\alpha M^2 \mathbf{p}^2}{4\pi^2} \frac{1}{3} \int_0^1 d\omega \int_0^\Lambda dq \frac{1}{\left[ \mathbf{q}^2 - \frac{\mathbf{p}^2}{1-\omega} \right]^{\frac{1}{2}}} = \frac{\alpha M^2 \mathbf{p}^2}{4\pi^2} \frac{1}{3} \int_0^1 d\omega \left[ -\frac{i\pi}{2} + \operatorname{arccoth} \left( \frac{1}{\Xi_2} \right) \right]. \quad (3.125)$$

Approximating the expression again under the assumption  $\mathbf{p}/\Lambda \ll 1$  and performing the integration over  $\omega$  (cf. eq. (3.121)), the expression on the r.h.s. of eq. (3.125) becomes

$$\frac{\alpha M^2 \mathbf{p}^2}{4\pi^2} \frac{1}{3} \int_0^1 d\omega \sqrt{\frac{1-\omega}{\omega}} \left[ -\frac{i\pi}{2} + \log \left( \frac{2\Lambda}{|\mathbf{p}|} \right) + \log \sqrt{1-\omega} \right] = \frac{\alpha M^2}{8\pi} \frac{1}{3} \mathbf{p}^2 \log \left( \frac{\Lambda}{|\mathbf{p}|} \right) + \mathcal{O}(\Lambda^0), \quad (3.126)$$

i.e. it carries the second logarithmic contribution to  $\mathbb{J}_C^{\{\Lambda\}}$  to order  $\alpha$  in the perturbative ex-

pansion. Finally, we consider the second term on the r.h.s. of eq. (3.124) and introduce the auxiliary variables  $\gamma^2 \equiv -\mathbf{p}^2$  and  $\Xi_3 \equiv \gamma^2/(1-\omega)$ . The integration over the radial momentum  $|\mathbf{q}|$  yields

$$\frac{\alpha M^2 \mathbb{1}}{4\pi^2} \frac{1}{3} \int_0^1 d\omega \sqrt{\frac{1-\omega}{\omega}} \left[ \frac{\log \left( 1 + \Lambda \sqrt{\frac{\gamma^2 - \Xi_3}{\gamma^2(\Xi_3 + \Lambda^2)}} \right)}{2\sqrt{\gamma^2(\gamma^2 - \Xi_3)}} - \frac{\log \left( 1 + \frac{\Lambda}{\gamma^2} \sqrt{\frac{\gamma^2(\gamma^2 - \Xi_3)}{\gamma^2 + \Lambda^2}} \right)}{2\sqrt{\gamma^2(\gamma^2 - \Xi_3)}} \right], \quad (3.127)$$

an expression that can be simplified in the large cutoff limit,  $\mathbf{p}/\Lambda \ll 1$ , obtaining

$$\frac{\alpha M^2 \mathbb{1}}{4\pi^2} \frac{1}{3} \mathbf{p}^2 \int_0^1 d\omega \frac{1-\omega}{\omega} \operatorname{arccot} \left( \sqrt{\frac{\omega}{1-\omega}} \right) + \mathcal{O}(\Lambda^0). \quad (3.128)$$

Although the remaining integral is unbound, the overall expression is independent of the cutoff  $\Lambda$ , therefore it can be neglected as the whole  $\mathcal{O}(\Lambda^0)$  contributions. This divergence is analogous to the one found in the  $\ell = 0$  case, and turns out to disappear if a translation in the momenta such as  $\mathbf{k} \mapsto \mathbf{k} - \mathbf{q}$  in the original expression of the  $\mathcal{O}(\alpha)$  term of  $\mathbb{J}_C^{(\Lambda)}$  in eq. (3.115) is performed. Now, collecting the results in eqs. (3.116) and (3.123), the cutoff-regularized version of  $\mathbb{J}_C$  is obtained to the desired order in the fine-structure constant,

$$\mathbb{J}_C^{(\Lambda)}(\mathbf{p}) = -\frac{M\Lambda}{2\pi^2} \frac{1}{3} \left( \frac{\Lambda^2}{3} + \mathbf{p}^2 \right) + \frac{\alpha M^2 \mathbb{1}}{16\pi} \frac{1}{3} \left[ \Lambda^2 - \frac{2i}{\pi} |\mathbf{p}| \Lambda + 4\mathbf{p}^2 \log \frac{\Lambda}{|\mathbf{p}|} \right] + \mathcal{O}(\alpha^2), \quad (3.129)$$

where the  $\mathcal{O}(\Lambda^0)$  contributions have been discarded. Now we proceed with the calculation in dimensional regularization of  $\mathbb{J}_C$ . To this purpose, it is convenient to start from the exact expression of  $\mathbb{J}_C$  to all orders in  $\alpha$  in arbitrary  $d$  dimensions (cf. eq. (3.40)),

$$\begin{aligned} \mathbb{J}_C^{\{\text{DR}\}}(\mathbf{p}) &= \int_{\mathbb{R}^d} \frac{d^d \mathbf{q}}{(2\pi)^d} \frac{2\pi M \eta(\mathbf{q})}{e^{2\pi \eta(\mathbf{q})} - 1} \frac{1 + \eta^2(\mathbf{q})}{\mathbf{p}^2 - \mathbf{q}^2 + i\epsilon} \mathbf{q} \otimes \mathbf{q} \\ &= M \int_{\mathbb{R}^d} \frac{d^d \mathbf{q}}{(2\pi)^d} \frac{\mathbf{q} \otimes \mathbf{q}}{\mathbf{p}^2 - \mathbf{q}^2 + i\epsilon} - \alpha M^2 \int_{\mathbb{R}^d} \frac{d^d \mathbf{q}}{(2\pi)^d} \frac{\pi}{2|\mathbf{q}|} \frac{\mathbf{q} \otimes \mathbf{q}}{\mathbf{p}^2 - \mathbf{q}^2 + i\epsilon} + \mathcal{O}(\alpha^2), \end{aligned} \quad (3.130)$$

where the integrand has been expanded up to the first order in  $\alpha$ . In particular, the  $\alpha$ -independent contribution in eq. (3.130) gives

$$M \int_{\mathbb{R}^d} \frac{d^d \mathbf{q}}{(2\pi)^d} \frac{\mathbf{q} \otimes \mathbf{q}}{\mathbf{p}^2 - \mathbf{q}^2} = -M \frac{1}{d} \int_{\mathbb{R}^d} \frac{d^d q}{(2\pi)^d} - M \frac{1}{d} \int_{\mathbb{R}^d} \frac{d^d q}{(2\pi)^d} \frac{\mathbf{p}^2}{\mathbf{p}^2 - \mathbf{q}^2}, \quad (3.131)$$

where the rotational invariance of the integrand has been exploited and  $\epsilon$  has been set to zero. Since the integrand is a polynomial in the momentum, the first contribution in the second row of the last equation vanishes in dimensional regularization, whereas the remaining term turns out to coincide with the purely strong counterpart of  $\mathbb{J}_C(d; \mathbf{p})$  in eq. (3.11),

$$\mathbb{J}_0(d; \mathbf{p}) = -M \frac{1}{d} \int_{\mathbb{R}^d} \frac{d^d q}{(2\pi)^d} \frac{\mathbf{p}^2}{\mathbf{p}^2 - \mathbf{q}^2} = M \mathbf{p}^2 \frac{1}{3} \frac{(-\mathbf{p}^2)^{\frac{d}{2}-1}}{(4\pi)^{\frac{d}{2}}} \Gamma\left(1 - \frac{d}{2}\right), \quad (3.132)$$

thus is finite and the limit  $d \rightarrow 3$  can be safely taken, obtaining

$$\mathbb{T}_S^{\{\text{DR}\}}(\mathbf{p}) = \frac{1}{3} \frac{iM|\mathbf{p}|^3}{4\pi}. \quad (3.133)$$

Due to the presence of the imaginary unit in the r.h.s. of the last equation, it turns out that the  $\alpha$ -independent component of  $\mathbb{J}_C^{\{\text{DR}\}}$  does not contribute in eq. (3.114), since only real parts are retained. Regarding the  $\mathcal{O}(\alpha)$  term of  $\mathbb{J}_C$  in arbitrary dimension, the integral can be recast as

$$\begin{aligned} M \int_{\mathbb{R}^d} \frac{d^d \mathbf{q}}{(2\pi)^d} \frac{\pi \eta(\mathbf{q}) \mathbf{q} \otimes \mathbf{q}}{\mathbf{q}^2 - \mathbf{p}^2} &= M \frac{1}{d} \int_{\mathbb{R}^d} \frac{d^d \mathbf{q}}{(2\pi)^d} \frac{\pi \eta(\mathbf{q}) \mathbf{q}^2}{\mathbf{q}^2 - \mathbf{p}^2} \\ &= \frac{\alpha M^2 \pi}{2} \frac{1}{d} \int_{\mathbb{R}^d} \frac{d^d \mathbf{q}}{(2\pi)^d} \frac{1}{|\mathbf{q}|} + \frac{\alpha M^2 \pi}{2} \frac{1}{d} \frac{\Gamma(\frac{3}{2})}{\Gamma(\frac{1}{2})} \int_0^1 \frac{d\omega}{\sqrt{\omega}} \int_{\mathbb{R}^d} \frac{d^d \mathbf{q}}{(2\pi)^d} \frac{\mathbf{p}^2}{[\mathbf{q}^2 + \gamma^2(1-\omega)]^{\frac{3}{2}}}, \end{aligned} \quad (3.134)$$

where  $\gamma \equiv -i|\mathbf{p}|$  and the Feynman parametrization for the denominators has been adopted. The subsequent momentum integration in the latter yields

$$\frac{1}{d} \frac{\alpha M^2 \pi}{2(4\pi)^{d/2}} \frac{\mathbf{p}^2 \Gamma(\frac{3}{2} - \frac{d}{2})}{\Gamma(\frac{1}{2})} \left(\frac{\mu}{2}\right)^{3-d} \int_0^1 \frac{d\omega}{\sqrt{\omega}} [\gamma^2(1-\omega)]^{\frac{d}{2} - \frac{3}{2}}, \quad (3.135)$$

where the renormalization scale  $\mu$  has been introduced. Conversely, the first term in the second row of eq. (3.134) vanishes like the first integral on the r.h.s. of eq. (3.131). Introducing the small quantity  $\epsilon = 3 - d$ , the integral over  $\omega$  can be computed to first order in  $\epsilon$ , obtaining

$$\int_0^1 \frac{d\omega}{\sqrt{\omega}} (1-\omega)^{-\frac{\epsilon}{2}} = 2 + 2\epsilon - \epsilon \log 2 + \mathcal{O}(\epsilon^2). \quad (3.136)$$

Exploiting the result in the last formula, eq. (3.134) partially expanded to order  $\epsilon$  becomes

$$\frac{1}{3} \frac{\alpha M^2 \mathbf{p}^2}{8\pi} \left(\frac{\mu\sqrt{\pi}}{\gamma}\right)^\epsilon \Gamma\left(\frac{\epsilon}{2}\right) \frac{1+\epsilon-\epsilon \log 2 + \mathcal{O}(\epsilon^2)}{1-\frac{\epsilon}{3} + \mathcal{O}(\epsilon^2)}. \quad (3.137)$$

Expanding in turn the Gamma function and the power term  $\mu\sqrt{\pi}/\gamma$  in Laurent and Taylor series, respectively, and truncating the expansion to order  $\epsilon^0$ , the desired expression for  $\mathbb{T}_{\text{SC}}(\mathbf{p})$  in dimensional regularization is recovered

$$\mathbb{J}_C^{\{\text{DR}\}}(\mathbf{p}) = \frac{1}{4\pi} \frac{\mathbf{p}^2}{3} \left[ \frac{1}{\epsilon} - \frac{\gamma_E}{2} + \frac{4}{3} + i\pi + \log\left(\frac{\mu\sqrt{\pi}}{2|\mathbf{p}|}\right) \right]. \quad (3.138)$$

Then, we bring further simplification to the finite volume quantization condition by taking the trace of eq. (3.114),

$$\frac{3}{D^L(E^*)} - \text{tr} \left[ \Re \mathbb{J}_C^{\{\text{DR}\}}(\mathbf{p}) \right] = \text{tr} \left[ \mathbb{J}_C^L(\mathbf{p}) \right] - \text{tr} \left[ \Re \mathbb{J}_C^{\{\Lambda\}}(\mathbf{p}) \right], \quad (3.139)$$

thus transforming a matrix identity into a scalar one as the one for S-waves. Finally, we take the real part of the expressions in eqs. (3.129) and (3.137) and replace the fermion mass by its finite-volume counterpart, obtaining the regulated version of the finite volume quantization

condition (cf. eq. (3.111)) in explicit form,

$$\begin{aligned} \frac{1}{D^L(E^*)} = & -\frac{M^L}{3L^3} \left[ \sum_{\mathbf{n}}^{\Lambda_n} 1 - \frac{4\pi}{3} \Lambda_n^3 \right] - \frac{M^L}{4\pi^2 L} \frac{\mathbf{p}^2}{3} \left[ \sum_{\mathbf{n}}^{\Lambda_n} \frac{1}{\mathbf{n}^2 - \tilde{\mathbf{p}}^2} - 4\pi \Lambda_n \right] + \frac{\alpha(M^L)^2}{4\pi} \frac{\mathbf{p}^2}{3} \left[ \frac{1}{\epsilon} - \frac{\gamma_E}{2} + \right. \\ & \left. \frac{4}{3} + \log \left( \frac{\mu L}{4\sqrt{\pi}} \right) \right] + \frac{\alpha(M^L)^2}{4\pi^3 L^2} \frac{1}{3} \left[ \sum_{\mathbf{n}}^{\Lambda_n} \sum_{\mathbf{m} \neq \mathbf{n}}^{\infty} \frac{1}{\mathbf{n}^2 - \tilde{\mathbf{p}}^2} \frac{1}{\mathbf{m}^2 - \tilde{\mathbf{p}}^2} \frac{\mathbf{m} \cdot \mathbf{n}}{|\mathbf{n} - \mathbf{m}|^2} - 4\pi^4 \tilde{\mathbf{p}}^2 \log \Lambda_n - \pi^4 \Lambda_n^2 \right]. \end{aligned} \quad (3.140)$$

Thanks to the last identity, the finite-volume version of the effective range expansion in eq. (3.103) can be rewritten in an explicit form. Besides, we drop in the next developments of the derivation the pole  $1/\epsilon$  arising from dimensional regularization, since it does not deliver information on the energy eigenvalues of our two-body system.

### 3.2.2 Finite Volume Effective Range Expansion

First of all, we concentrate on the infinite volume version of the effective range expansion. By inserting the expression of  $T_{\text{SC}}$  given in eq. (3.27) into eq. (3.36) and exploiting the closed form of  $j_{\text{C}}$  in dimensional regularization given in eq. (3.62) we obtain a relation between the P-wave phase shift and the strong coupling constant  $D(E^*)$  in the presence of Coulomb photon exchanges,

$$\mathbf{p}^2(1 + \eta^2)[C_\eta^2|\mathbf{p}|(\cot \delta_1 - i) + \alpha M H(\eta)] = -\frac{12\pi}{MD(E^*)} + \alpha M \mathbf{p}^2 \left[ \frac{4}{3} - \frac{3}{2} \gamma_E + \log \left( \frac{\mu \sqrt{\pi}}{\alpha M} \right) \right], \quad (3.141)$$

where on the r.h.s of the last equation the PDS terms have been discarded, together with ones multiplied by three powers of  $\alpha$ . Since the asymptotic behaviour of the momentum integrals in the ultraviolet region is left invariant by discretization, eq. (3.141) can be straightforwardly adapted to the cubic finite-volume case, provided the infinite volume parameters are replaced by finite volume ones,

$$\mathbf{p}^2(1 + \eta^2)[C_\eta^2|\mathbf{p}|(\cot \delta_1^L - i) + \alpha M^L H(\eta)] = -\frac{12\pi}{M^L D^L(E^*)} + \alpha M^L \mathbf{p}^2 \left[ \frac{4}{3} - \frac{3}{2} \gamma_E + \log \left( \frac{\mu \sqrt{\pi}}{\alpha M^L} \right) \right], \quad (3.142)$$

which is valid to all orders in the fine-structure constant. Now, the quantization conditions derived in the previous section can be exploited by replacing the inverse of the finite-volume strong-coupling constant with the expression in eq. (3.140). Thus, the following equation is obtained,

$$\begin{aligned} \mathbf{p}^2(1 + \eta^2)[C_\eta^2|\mathbf{p}|(\cot \delta_1^L - i) + \alpha M^L H(\eta)] = & \frac{4\pi}{L^3} \left[ \sum_{\mathbf{n}}^{\Lambda_n} 1 - \frac{4\pi}{3} \Lambda_n^3 \right] + \frac{\mathbf{p}^2}{\pi L} \left[ \sum_{\mathbf{n}}^{\Lambda_n} \frac{1}{\mathbf{n}^2 - \tilde{\mathbf{p}}^2} - 4\pi \Lambda_n \right] \\ & - \frac{\alpha M^L}{\pi^2 L^2} \left[ \sum_{\mathbf{n}}^{\Lambda_n} \sum_{\mathbf{m} \neq \mathbf{n}}^{\infty} \frac{1}{\mathbf{n}^2 - \tilde{\mathbf{p}}^2} \frac{1}{\mathbf{m}^2 - \tilde{\mathbf{p}}^2} \frac{\mathbf{m} \cdot \mathbf{n}}{|\mathbf{n} - \mathbf{m}|^2} - \pi^4 \Lambda_n^2 - 4\pi^4 \tilde{\mathbf{p}}^2 \log \Lambda_n \right] \\ & + \alpha M^L \mathbf{p}^2 \left[ \log \left( \frac{4\pi}{\alpha M^L L} \right) - \gamma_E \right]. \end{aligned} \quad (3.143)$$

Similarly to the  $\ell = 0$  case, we notice that the finite-volume mass of the fermions is multiplied by the fine-structure constant in all the occurrences. It follows that, in the  $\mathcal{O}(\alpha)$  approximation

of the Coulomb Green's functions and their derivatives, we can consistently ignore the leading-order corrections to  $M^L$  and replace the latter with  $M$ , at least in eq. (3.143). Nevertheless, we account for the QED power law modifications of the masses [46] in the finite-volume version of the effective-range expansion in eq. (3.27) by means of the shifted scattering parameters (cf. eqs. (1.40)-(1.44)),

$$\mathbf{p}^2(1 + \eta^2)[C_\eta^2|\mathbf{p}|(\cot \delta_1^L - i) + \alpha MH(\eta)] = -\frac{1}{\alpha'_C(1)} + \frac{1}{2}r_0'^{(1)}\mathbf{p}^2 + r_1'^{(1)}\mathbf{p}^4 + \dots, \quad (3.144)$$

where the ellipsis stands for higher-order scattering parameters. Combining the latter expression with eq. (3.103) and isolating the regulated sums, we obtain the desired explicit version of the effective-range expansion to order  $\alpha$ ,

$$\begin{aligned} & -\frac{1}{\alpha'_C(1)} + \frac{1}{2}r_0'^{(1)}\mathbf{p}^2 + r_1'^{(1)}\mathbf{p}^4 + r_2'^{(1)}\mathbf{p}^6 + r_3'^{(1)}\mathbf{p}^8 + \dots \\ & = \frac{4\pi}{L^3}S_0(\tilde{\mathbf{p}}) + \frac{\mathbf{p}^2}{\pi L}S_1(\tilde{\mathbf{p}}) - \frac{\alpha M\mathbf{p}^2}{4\pi^4}S_2(\tilde{\mathbf{p}}) - \frac{\alpha M}{\pi^2 L^2}S_3(\tilde{\mathbf{p}}) + \dots + \alpha M\mathbf{p}^2 \left[ \log \left( \frac{4\pi}{\alpha ML} \right) - \gamma_E \right], \end{aligned} \quad (3.145)$$

in terms of the *Lüscher functions*,

$$S_0(\tilde{\mathbf{p}}) = \sum_{\mathbf{n}}^{\Lambda_n} 1 - \frac{4\pi}{3}\Lambda_n^3, \quad S_1(\tilde{\mathbf{p}}) = \sum_{\mathbf{n}}^{\Lambda_n} \frac{1}{\mathbf{n}^2 - \tilde{\mathbf{p}}^2} - 4\pi\Lambda_n, \quad (3.146)$$

$$S_2(\tilde{\mathbf{p}}) = \sum_{\mathbf{n}}^{\Lambda_n} \sum_{\mathbf{m} \neq \mathbf{n}}^{\infty} \frac{1}{\mathbf{n}^2 - \tilde{\mathbf{p}}^2} \frac{1}{\mathbf{m}^2 - \tilde{\mathbf{p}}^2} \frac{1}{|\mathbf{n} - \mathbf{m}|^2} - 4\pi^4 \log \Lambda_n, \quad (3.147)$$

and

$$S_3(\tilde{\mathbf{p}}) = \sum_{\mathbf{n}}^{\Lambda_n} \sum_{\mathbf{m} \neq \mathbf{n}}^{\infty} \frac{1}{\mathbf{n}^2 - \tilde{\mathbf{p}}^2} \frac{1}{\mathbf{m}^2 - \tilde{\mathbf{p}}^2} \frac{\mathbf{m} \cdot \mathbf{n} - \tilde{\mathbf{p}}^2}{|\mathbf{n} - \mathbf{m}|^2} - \pi^4 \Lambda_n^2. \quad (3.148)$$

As shown in app. B.1.1, the  $\tilde{\mathbf{p}}$ -independent Lüscher sum in eq. (3.146) vanishes, whereas  $S_3(\tilde{\mathbf{p}})$  generates the new series of double sums to be computed in the low- $\mathbf{p}$  limit.

### 3.2.3 Approximate Energy Eigenvalues

Since the Sommerfeld factor is not a rational function of the momentum of the colliding particles in the CoM frame, a non-perturbative counterpart in  $\alpha$  of the eq. (3.145) in the low-momentum limit would allow only numerical solutions for  $\mathbf{p}^2$ , which lie beyond our purpose. Nevertheless, under the hypothesis that the expansions are perturbative in  $1/L$  times the length scale characterizing the strength of the interaction, governed by the scattering parameters, and assuming that  $ML \ll 1/\alpha$ , the Coulomb photon insertions in the diagrams can be treated perturbatively. Under these conditions, the approximate expression of the ERE presented in eq. (3.103) can be exploited for an analytical derivation of the finite volume corrections to the energy eigenvalues.

#### a) The Lowest Unbound State

Differently from the S-wave case in sec. 2.2.3 a), the perturbative expansion of the arguments of the summations in the Lüscher functions around zero finite-volume momentum  $\tilde{\mathbf{p}}$ , cor-



responding to a total energy equal to  $2M$  now loses significance, due to symmetry reasons. Given that  $\ell = 1$  states in the continuum and infinite volume are mapped to  $T_1$  states in a finite cubic finite-volume, the latter are expected to be three-fold degenerate. While the multiplicity of the zero energy scattering state is one, its nearest neighbour with  $|\tilde{\mathbf{p}}| = 1$  is six-fold degenerate with total energy equal to  $2M + 4\pi^2/ML^2$ , thus making it a suitable candidate for both  $T_1$  and  $T_2$  eigenstates. Moreover, if the box size is large enough, the momentum  $|\mathbf{p}| = 2\pi/L$  is small, thus the effective-range expansion in the l.h.s. of eq. (3.145) remains valid and can be truncated at any power of  $\mathbf{p}^2$ . Otherwise, the non-perturbative approach in sec. 2.5 of ref. [74] needs to be considered, and the energy eigenvalues would be expressed in terms of the phase shift  $\delta_1$ . Following the small-momentum approach, we expand the Lüscher functions in eqs. (3.146)-(3.148) in Taylor series about  $\tilde{p}^2 = 1$  and retain only small or negative powers of the quantity  $\delta\tilde{p}^2 \equiv \tilde{p}^2 - 1$ . Concerning the Lüscher function  $S_1(\tilde{p})$ , the approximation yields

$$\begin{aligned} S_1(\tilde{\mathbf{p}}) = & -\frac{6}{\delta\tilde{p}^2} + \sum_{|\mathbf{n}|\neq 1}^{\Lambda_n} \frac{1}{|\mathbf{n}|^2 - 1} - 4\pi\Lambda_n + \delta\tilde{p}^2 \sum_{|\mathbf{n}|\neq 1}^{\infty} \frac{1}{(|\mathbf{n}|^2 - 1)^2} \\ & + (\delta\tilde{p}^2)^2 \sum_{|\mathbf{n}|\neq 1}^{\infty} \frac{1}{(|\mathbf{n}|^2 - 1)^3} + (\delta\tilde{p}^2)^3 \sum_{|\mathbf{n}|\neq 1}^{\infty} \frac{1}{(|\mathbf{n}|^2 - 1)^4} + (\delta\tilde{p}^2)^4 \sum_{|\mathbf{n}|\neq 1}^{\infty} \frac{1}{(|\mathbf{n}|^2 - 1)^5} + \dots, \end{aligned} \quad (3.149)$$

where the dots denote terms of order  $(\delta\tilde{p}^2)^6$  and the large  $\Lambda_n$  limit is understood. In the notation of app. B.1.1 and ref. [1], eq. (3.149) is concisely recast into

$$S_1(\tilde{\mathbf{p}}) = -\frac{6}{\delta\tilde{p}^2} + \mathcal{G}^{(1)} + \delta\tilde{p}^2 \mathcal{G}^{(1)} + (\delta\tilde{p}^2)^2 \mathcal{K}^{(1)} + (\delta\tilde{p}^2)^3 \mathcal{L}^{(1)} + (\delta\tilde{p}^2)^4 \mathcal{O}^{(1)} + \dots, \quad (3.150)$$

where the sums of the implied three-dimensional Riemann series are reported in app. B.1.1. Regarding the function  $S_2(\tilde{p})$ , we proceed by isolating and expanding the double sums with  $|\mathbf{n}|$  or  $|\mathbf{m}|$  equal to one,

$$\sum_{|\mathbf{n}|=1}^{\infty} \sum_{|\mathbf{m}|\neq 1}^{\infty} \frac{1}{1 - \tilde{p}^2} \frac{1}{\mathbf{m}^2 - \tilde{p}^2} \frac{1}{|\mathbf{n} - \mathbf{m}|^2} + \sum_{|\mathbf{m}|=1}^{\infty} \sum_{|\mathbf{n}|\neq 1}^{\Lambda_n} \frac{1}{1 - \tilde{p}^2} \frac{1}{\mathbf{n}^2 - \tilde{p}^2} \frac{1}{|\mathbf{n} - \mathbf{m}|^2}. \quad (3.151)$$

The subsequent expansion of the argument of the two series in the same fashion of eq. (3.149) shows that all the resulting sums converge in the infinite- $\Lambda_n$  limit. Therefore, we are allowed to remove the spherical cutoff and the two double sums in eq. (3.151) merge, yielding

$$2 \sum_{|\mathbf{n}|=1}^{\infty} \sum_{|\mathbf{m}|\neq 1}^{\infty} \frac{1}{1 - \tilde{p}^2} \frac{1}{\mathbf{m}^2 - \tilde{p}^2} \frac{1}{|\mathbf{n} - \mathbf{m}|^2} = -\frac{2}{\delta\tilde{p}^2} \chi_1 - 2\chi_2 - 2\delta\tilde{p}^2 \chi_3 - 2(\delta\tilde{p}^2)^2 \chi_4 + \dots. \quad (3.152)$$

where, differently from the ones in the appendix of ref. [1], the series  $\chi_i$  with  $i \geq 1$  include  $\mathbf{n} = \mathbf{0}$  and are defined as

$$\chi_i = \sum_{|\mathbf{n}|=1}^{\infty} \sum_{|\mathbf{m}|\neq 1}^{\infty} \frac{1}{(|\mathbf{m}|^2 - 1)^i} \frac{1}{|\mathbf{n} - \mathbf{m}|^2}. \quad (3.153)$$



Furthermore, the expansion of the remaining term of the Lüscher function  $S_2$  leads to results in analogous to the ones of the S-wave case,

$$\begin{aligned} \sum_{|\mathbf{n}| \neq 1}^{\Lambda_n} \sum_{\substack{|\mathbf{m}| \neq 1 \\ \mathbf{m} \neq \mathbf{n}}}^{\infty} \frac{1}{|\mathbf{n}|^2 - \tilde{p}^2} \frac{1}{|\mathbf{m}|^2 - \tilde{p}^2} \frac{1}{|\mathbf{n} - \mathbf{m}|^2} - 4\pi \log \Lambda_n \\ = \mathcal{R}^{(1)} + \delta \tilde{p}^2 \left( \mathcal{R}_{24}^{(1)} + \mathcal{R}_{42}^{(1)} \right) + (\delta \tilde{p}^2)^2 \left( \mathcal{R}_{44}^{(1)} + \mathcal{R}_{26}^{(1)} + \mathcal{R}_{62}^{(1)} \right) + \dots, \end{aligned} \quad (3.154)$$

where the ellipsis stands for terms of order  $(\delta \tilde{p}^2)^3$ . The  $\mathcal{R}^{(1)}$  and  $\mathcal{R}_{ij}^{(1)}$  sums in the last equation coincide with the P-wave counterparts of the sums in eqs. (A6) and (A9) in ref. [1], namely

$$\mathcal{R}^{(1)} \equiv \sum_{|\mathbf{n}| \neq 1}^{\Lambda_n} \sum_{\substack{|\mathbf{m}| \neq 1 \\ \mathbf{m} \neq \mathbf{n}}}^{\infty} \frac{1}{|\mathbf{n}|^2 - 1} \frac{1}{|\mathbf{m}|^2 - 1} \frac{1}{|\mathbf{n} - \mathbf{m}|^2} - 2\pi^4 \log \Lambda_n, \quad (3.155)$$

and

$$\mathcal{R}_{2i \ 2j}^{(1)} \equiv \sum_{|\mathbf{n}| \neq 1}^{\infty} \sum_{\substack{|\mathbf{m}| \neq 1 \\ \mathbf{m} \neq \mathbf{n}}}^{\infty} \frac{1}{(|\mathbf{n}|^2 - 1)^i} \frac{1}{(|\mathbf{m}|^2 - 1)^j} \frac{1}{|\mathbf{n} - \mathbf{m}|^2}, \quad (3.156)$$

with  $i, j \geq 2$  and  $i + j \geq 6$ , which are invariant under permutation of the lower indices,  $\mathcal{R}_{ij}^{(1)} = \mathcal{R}_{ji}^{(1)}$ , and convergent for  $i, j \geq 1$  and  $i + j > 2$ . Exploiting the symmetry property under index exchange and combining the results in eqs. (3.155) and (3.156), we find the desired result

$$S_2(\tilde{p}) = -\frac{2}{\delta \tilde{p}^2} \chi_1 + \mathcal{R}^{(1)} - 2\chi_2 + 2\delta \tilde{p}^2 \left( \mathcal{R}_{24}^{(1)} - \chi_3 \right) + (\delta \tilde{p}^2)^2 \left( \mathcal{R}_{44}^{(1)} + 2\mathcal{R}_{26}^{(1)} - 2\chi_4 \right) + \dots. \quad (3.157)$$

Subsequently, we treat the genuinely new Lüscher function,  $S_3(\tilde{p})$ . With this purpose, we decompose the initial double series into three pieces,

$$\begin{aligned} S_3(\tilde{p}) = \lim_{\Lambda_m \rightarrow +\infty} \left\{ \frac{1}{2} \sum_{\mathbf{n}}^{\Lambda_n} \sum_{\substack{\mathbf{m} \neq \mathbf{n} \\ \mathbf{m} \neq \mathbf{0}}}^{\Lambda_m} \frac{1}{|\mathbf{m}|^2 - \tilde{p}^2} \frac{1}{|\mathbf{n} - \mathbf{m}|^2} + \frac{1}{2} \sum_{\mathbf{n}}^{\Lambda_n} \sum_{\substack{\mathbf{m} \neq \mathbf{n} \\ \mathbf{m} \neq \mathbf{0}}}^{\Lambda_m} \frac{1}{|\mathbf{n}|^2 - \tilde{p}^2} \frac{1}{|\mathbf{n} - \mathbf{m}|^2} \right. \\ \left. - \frac{1}{2} \sum_{\mathbf{n}}^{\Lambda_n} \sum_{\substack{\mathbf{m} \neq \mathbf{n} \\ \mathbf{m} \neq \mathbf{0}}}^{\Lambda_m} \frac{1}{|\mathbf{m}|^2 - \tilde{p}^2} \frac{1}{|\mathbf{n}|^2 - \tilde{p}^2} \right\} - \pi^4 \Lambda_n^2, \end{aligned} \quad (3.158)$$

where a subsidiary spherical cutoff  $\Lambda_m$  has been introduced in order to highlight the divergent nature of the three terms. In particular, the first and the second contribution to  $S_3(\tilde{p})$  on the r.h.s. of the last equation, can be recast as

$$\begin{aligned} -\frac{1}{\delta \tilde{p}^2} \mathcal{P}^{(1)} + \chi_1 + \frac{1}{2} \left( \mathcal{P}_{022}^{(1)} + \mathcal{P}_{202}^{(1)} \right) + \frac{\delta \tilde{p}^2}{2} \left( \mathcal{P}_{042}^{(1)} + \mathcal{P}_{402}^{(1)} + 2\chi_2 \right) \\ + \frac{(\delta \tilde{p}^2)^2}{2} \left( \mathcal{P}_{062}^{(1)} + \mathcal{P}_{602}^{(1)} + 2\chi_3 \right) + \dots, \end{aligned} \quad (3.159)$$

where the dots denote terms of order  $(\delta\tilde{p}^2)^3$ , while the non-symmetric and divergent generalizations of  $\chi_0$  in eq. (B.131) and of  $\mathcal{R}_{ij}^{(1)}$  in eq. (3.156) have been introduced,

$$\mathcal{G}^{(1)} = \sum_{|\mathbf{m}|=1} \sum_{|\mathbf{n}| \neq 1}^{\Lambda_n} \frac{1}{|\mathbf{m} - \mathbf{n}|^2}, \quad (3.160)$$

and

$$\mathcal{G}_{2i \ 2j \ 2k}^{(1)} = \sum_{|\mathbf{n}| \neq 1}^{\Lambda_n} \sum_{\substack{|\mathbf{m}| \neq 1 \\ \mathbf{m} \neq \mathbf{n}}}^{\Lambda_m} \frac{1}{(|\mathbf{n}|^2 - 1)^i} \frac{1}{(|\mathbf{m}|^2 - 1)^j} \frac{1}{|\mathbf{n} - \mathbf{m}|^{2k}}, \quad (3.161)$$

respectively. Quite similarly, the third contribution to  $\mathcal{S}_3(\tilde{\mathbf{p}})$  in eq. (3.158) can be subdivided and expanded as follows

$$-\frac{1}{2} \sum_{|\mathbf{n}| \neq 1}^{\Lambda_n} \sum_{\substack{|\mathbf{m}| \neq 1 \\ \mathbf{n} \neq \mathbf{m}}}^{\Lambda_m} \frac{1}{|\mathbf{m}|^2 - \tilde{p}^2} \frac{1}{|\mathbf{n}|^2 - \tilde{p}^2} + \frac{3}{\delta\tilde{p}^2} \sum_{|\mathbf{n}| \neq 1}^{\Lambda_n} \frac{1}{|\mathbf{n}|^2 - \tilde{p}^2} + \frac{3}{\delta\tilde{p}^2} \sum_{|\mathbf{m}| \neq 1}^{\Lambda_m} \frac{1}{|\mathbf{m}|^2 - \tilde{p}^2}, \quad (3.162)$$

where the two terms involving single sums can be, in turn, expanded in pairs, obtaining

$$\frac{3}{\delta\tilde{p}^2} \left( \mathcal{G}_{\Lambda_n}^{(1)} + \mathcal{G}_{\Lambda_m}^{(1)} \right) + 6\mathcal{G}^{(1)} + 6\delta\tilde{p}^2 \mathcal{K}^{(1)} + 6(\delta\tilde{p}^2)^2 \mathcal{L}^{(1)} + \dots, \quad (3.163)$$

where the neglected terms are again of order  $(\delta\tilde{p}^2)^3$  and for the resulting convergent series the limit  $\Lambda_n, \Lambda_m \rightarrow +\infty$  is understood. On the other hand, this limit can not be taken for the non-regularized counterpart of  $\mathcal{G}^{(1)}$ ,

$$\mathcal{G}_{\Lambda_s}^{(1)} = \sum_{\mathbf{s} \neq 0}^{\Lambda_s} \frac{1}{|\mathbf{s}|^2}, \quad (3.164)$$

whose divergence will cancel with the one from  $\mathcal{P}^{(1)}$  in eq. (3.160). Secondly, the expansion of the double sum in eq. (3.162) yields the appearance of further  $\mathcal{P}_{2i \ 2j \ 2k}^{(1)}$  terms,

$$-\frac{1}{2} \mathcal{P}_{220}^{(1)} - \frac{1}{2} \delta\tilde{p}^2 \left( \mathcal{P}_{240}^{(1)} + \mathcal{P}_{420}^{(1)} \right) - \frac{1}{2} (\delta\tilde{p}^2)^2 \left( \mathcal{P}_{440}^{(1)} + \mathcal{P}_{260}^{(1)} + \mathcal{P}_{620}^{(1)} \right). \quad (3.165)$$

Collecting the expansions of the three contributions in eqs. (3.163) and (3.165) we can finally write

$$\begin{aligned} -\frac{1}{2} \sum_{\mathbf{n}}^{\Lambda_n} \sum_{\mathbf{m} \neq \mathbf{n}}^{\infty} \frac{1}{|\mathbf{m}|^2 - \tilde{p}^2} \frac{1}{|\mathbf{n}|^2 - \tilde{p}^2} &= \frac{3}{\delta\tilde{p}^2} \left( \mathcal{G}_{\Lambda_n}^{(1)} + \mathcal{G}_{\Lambda_m}^{(1)} \right) + 6\mathcal{G}^{(1)} - \frac{1}{2} \mathcal{P}_{220}^{(1)} \\ &+ \delta\tilde{p}^2 \left[ 6\mathcal{K}^{(1)} - \frac{1}{2} \left( \mathcal{P}_{240}^{(1)} + \mathcal{P}_{420}^{(1)} \right) \right] + (\delta\tilde{p}^2)^2 \left[ 6\mathcal{L}^{(1)} - \frac{1}{2} \left( \mathcal{P}_{440}^{(1)} + \mathcal{P}_{260}^{(1)} + \mathcal{P}_{620}^{(1)} \right) \right] + \dots. \end{aligned} \quad (3.166)$$

Now, the two partial results in eqs. (3.159) and (3.166) can be summed together, obtaining the sought expression of  $\mathcal{S}_3(\tilde{\mathbf{p}})$  as a power series in  $\delta\tilde{p}^2$ . In particular, we notice that the sum of all the series appearing at each order in  $\delta\tilde{p}^2$  has to be finite in the limit  $\Lambda_n, \Lambda_m \rightarrow +\infty$ , irrespective of the convergent or divergent behaviour of each individual sum. In particular, we observe

that the latter limit can be directly taken to all orders in the small quantity, with the only exception of the sums in the  $\delta\tilde{p}^2$ -independent contribution, that are regularized quadratically in the cutoff  $\Lambda_n$ . As a consequence, we can simplify our  $\delta\tilde{p}^2$ -expansion for  $S_3(\tilde{p})$  by grouping the divergent sums order by order and defining the finite coefficients

$$\mathfrak{Q}_0 \equiv \lim_{\substack{\Lambda_n \rightarrow +\infty \\ \Lambda_m \rightarrow +\infty}} -\frac{1}{2} \left( 3\mathcal{G}_{\Lambda_n}^{(1)} + 3\mathcal{G}_{\Lambda_m}^{(1)} - \mathcal{P}^{(1)} \right) = \sum_{|\mathbf{n}|=1} \sum_{|\mathbf{m}| \neq 1}^{\infty} \frac{\mathbf{m} \cdot \mathbf{n} - 1}{(|\mathbf{m}|^2 - 1)|\mathbf{m} - \mathbf{n}|^2} , \quad (3.167)$$

$$\mathfrak{Q}_1 \equiv \lim_{\substack{\Lambda_n \rightarrow +\infty \\ \Lambda_m \rightarrow +\infty}} \frac{1}{2} \left( \mathcal{P}_{022}^{(1)} + \mathcal{P}_{202}^{(1)} - \mathcal{P}_{220}^{(1)} \right) - \pi^4 \Lambda_n^2 = \sum_{|\mathbf{n}| \neq 1}^{\Lambda_n} \sum_{\substack{\mathbf{m} \neq \mathbf{n} \\ |\mathbf{m}| \neq 1}}^{\infty} \frac{1}{|\mathbf{n}|^2 - 1} \frac{1}{|\mathbf{m}|^2 - 1} \frac{\mathbf{n} \cdot \mathbf{m} - 1}{|\mathbf{n} - \mathbf{m}|^2} - \pi^4 \Lambda_n^2 , \quad (3.168)$$

$$\mathfrak{Q}_2 \equiv \lim_{\substack{\Lambda_n \rightarrow +\infty \\ \Lambda_m \rightarrow +\infty}} \frac{1}{2} \left( \mathcal{P}_{042}^{(1)} + \mathcal{P}_{402}^{(1)} - \mathcal{P}_{240}^{(1)} - \mathcal{P}_{420}^{(1)} \right) = \sum_{|\mathbf{n}| \neq 1}^{\infty} \sum_{\substack{\mathbf{m} \neq \mathbf{n} \\ |\mathbf{m}| \neq 1}}^{\infty} \frac{1 - 2\mathbf{m} \cdot \mathbf{n} - |\mathbf{m}|^2 |\mathbf{n}|^2 + \mathbf{n} \cdot \mathbf{m} (|\mathbf{m}|^2 + |\mathbf{n}|^2)}{(|\mathbf{m}|^2 - 1)^2 (|\mathbf{n}|^2 - 1)^2 |\mathbf{m} - \mathbf{n}|^2} , \quad (3.169)$$

and

$$\mathfrak{Q}_3 \equiv \lim_{\substack{\Lambda_n \rightarrow +\infty \\ \Lambda_m \rightarrow +\infty}} \frac{1}{2} \left( \mathcal{P}_{062}^{(1)} + \mathcal{P}_{602}^{(1)} - \mathcal{P}_{440}^{(1)} - \mathcal{P}_{620}^{(1)} - \mathcal{P}_{602}^{(1)} \right) = \sum_{|\mathbf{n}| \neq 1}^{\infty} \sum_{\substack{\mathbf{m} \neq \mathbf{n} \\ |\mathbf{m}| \neq 1}}^{\infty} \frac{q_S(\mathbf{n}, \mathbf{m}) + \mathbf{m} \cdot \mathbf{n} q_X(\mathbf{n}, \mathbf{m})}{(|\mathbf{m}|^2 - 1)^3 (|\mathbf{n}|^2 - 1)^3 |\mathbf{m} - \mathbf{n}|^2} , \quad (3.170)$$

where the polynomials  $q_S(\mathbf{n}, \mathbf{m})$  and  $q_X(\mathbf{n}, \mathbf{m})$  are defined as

$$q_S(\mathbf{n}, \mathbf{m}) = -1 + 3|\mathbf{n}|^2 |\mathbf{m}|^2 - |\mathbf{m}|^2 |\mathbf{n}|^2 (|\mathbf{n}|^2 + |\mathbf{m}|^2) \quad (3.171)$$

and

$$q_X(\mathbf{n}, \mathbf{m}) = 3 - 3(|\mathbf{n}|^2 + |\mathbf{m}|^2) + |\mathbf{m}|^2 |\mathbf{n}|^2 + |\mathbf{m}|^4 + |\mathbf{n}|^4 . \quad (3.172)$$

Equipped with the definitions in eqs. (3.167)-(3.170), we can write compactly the final expression for the expansion of  $S_3(\tilde{p})$  in terms of convergent sums up to the quadratic order in  $\delta\tilde{p}^2$ ,

$$S_3(\tilde{p}) = -\frac{2}{\delta\tilde{p}^2} \mathfrak{Q}_0 + \chi_1 + 6\mathcal{J}^{(1)} + \mathfrak{Q}_1 + \delta\tilde{p}^2 \left[ \chi_2 + 6\mathcal{K}^{(1)} + \mathfrak{Q}_2 \right] + (\delta\tilde{p}^2)^2 \left[ \chi_3 + 6\mathcal{L}^{(1)} + \mathfrak{Q}_3 \right] + \dots . \quad (3.173)$$

After redefining the regularized sum in eq. (3.157) through the addition of the last term on the r.h.s. of eq. (3.145),

$$\tilde{\mathcal{R}}^{(1)} \equiv \mathcal{R}^{(1)} - 4\pi^4 \left[ \log \left( \frac{4\pi}{\alpha ML} \right) - \gamma_E \right] , \quad (3.174)$$

we plug the expressions in eqs. (3.150), (3.159), (3.160) and (3.173) in the finite volume effective range expansion and obtain

$$\begin{aligned}
& -\frac{1}{a'_C{}^{(1)}} + \frac{1}{2} \frac{4\pi^2 r_0'^{(1)}}{L^2} \tilde{p}^2 + \frac{16\pi^4 r_1'^{(1)}}{L^4} \tilde{p}^4 + \frac{64\pi^6 r_2'^{(1)}}{L^6} \tilde{p}^6 + \frac{256\pi^8 r_3'^{(1)}}{L^8} \tilde{p}^8 + \dots \\
& = -\frac{\alpha M}{\pi^2 L^2} \left\{ -\frac{2}{\delta \tilde{p}^2} \mathfrak{Q}_0 + \chi_1 + 6\mathcal{G}^{(1)} + \mathfrak{Q}_1 + \delta \tilde{p}^2 \left[ \chi_2 + 6\mathcal{K}^{(1)} + \mathfrak{Q}_2 \right] + (\delta \tilde{p}^2)^2 \left[ \chi_3 + 6\mathcal{L}^{(1)} + \mathfrak{Q}_3 \right] + \dots \right\} \\
& -\frac{\alpha M \mathbf{p}^2}{4\pi^4} \left[ -\frac{2}{\delta \tilde{p}^2} \chi_1 + \mathcal{R}^{(1)} - 2\chi_2 + 2\delta \tilde{p}^2 \left( \mathcal{R}_{24}^{(1)} - \chi_3 \right) + (\delta \tilde{p}^2)^2 \left( \mathcal{R}_{44}^{(1)} + 2\mathcal{R}_{26}^{(1)} - 2\chi_4 \right) + \dots \right] \\
& + \frac{\mathbf{p}^2}{\pi L} \left[ -\frac{6}{\delta \tilde{p}^2} + \mathcal{G}^{(1)} + \delta \tilde{p}^2 \mathcal{G}^{(1)} + (\delta \tilde{p}^2)^2 \mathcal{K}^{(1)} + \dots \right] + \dots .
\end{aligned} \tag{3.175}$$

where the shifted higher-order scattering parameters  $r_2'^{(1)}$  and  $r_3'^{(1)}$  on the l.h.s. of the last equation have been included, see eqs. (1.40) and (1.44). The subsequent multiplication of the last equation by the scattering length permits to introduce coefficients identical to the ones in eqs. (2.114) and (2.115),

$$\begin{aligned}
d_0 &= \xi \frac{a'_C{}^{(1)}}{\pi L} , \quad d_1 = \xi \frac{\alpha M}{4\pi^4} a'_C{}^{(1)} , \quad d_2 = \xi^2 a'_C{}^{(1)} r_0'^{(1)} , \\
d_3 &= \xi^3 a'_C{}^{(1)} r_1'^{(1)} , \quad d_4 = \xi^4 a'_C{}^{(1)} r_2'^{(1)} , \quad d_5 = \xi^5 a'_C{}^{(1)} r_3'^{(1)} ,
\end{aligned} \tag{3.176}$$

modulo an overall damping factor  $\xi \equiv 4\pi^2/L^2$ . If the scattering parameters are small and of the same magnitude of  $1/L$  as in the S-wave case, the importance of the auxiliary parameters just introduced can be quantitatively assessed. In particular, by assigning one unit of 'weight' for each scattering parameter in the effective-range expansion and one unit for  $1/L$ , we find that, neglecting the fine-structure constant, the largest parameter is  $d_1$  (order three), followed by  $d_0$  and  $d_2$  (order four), whereas the constants  $d_3$ ,  $d_4$  and  $d_5$  are of order six, eight and ten respectively. With the aim of finding a perturbative formula exact to third order in  $d_0$ , we observe that in the final expression for the squared momentum shift  $\delta \tilde{p}^2$ , only terms of order smaller or equal to twelve in  $1/L$  and in the scattering parameters should be retained. This fact justifies the inclusion of the above higher order scattering parameters in the effective range expansion in eq. (3.175). Furthermore, rewriting  $\tilde{p}^2$  in the latter equation as  $\delta \tilde{p}^2 + 1$ , the approximated effective range expansion can be rewritten as a power series of the squared momentum shift,

$$\begin{aligned}
0 &= \frac{2}{\delta \tilde{p}^2} (\chi_1 d_1 + \mathfrak{Q}_0 d_1 - 3d_0) + 1 + d_0 (\mathcal{G}^{(1)} - 6) + d_1 (\chi_1 + 2\chi_2 - 6\mathcal{G}^{(1)} - \mathfrak{Q}_1 - \tilde{\mathcal{R}}^{(1)}) \\
& -\frac{d_2}{2} - d_3 - d_4 - d_5 + \delta \tilde{p}^2 \left[ d_0 (\mathcal{G}^{(1)} + \mathcal{G}^{(1)}) + d_1 \left( \chi_2 + 2\chi_3 - 6\mathcal{K}^{(1)} - \mathfrak{Q}_2 - 2\mathcal{R}_{24}^{(1)} - \tilde{\mathcal{R}}^{(1)} \right) \right. \\
& \quad \left. -\frac{d_2}{2} - 2d_3 - 3d_4 - 4d_5 \right] + (\delta \tilde{p}^2)^2 \left[ d_0 (\mathcal{K}^{(1)} + \mathcal{G}^{(1)}) - d_3 - 3d_4 - 6d_5 \right. \\
& \quad \left. + d_1 \left( \chi_3 + 2\chi_4 - 6\mathcal{L}^{(1)} - \mathfrak{Q}_3 - \mathcal{R}_{44}^{(1)} - 2\mathcal{R}_{26}^{(1)} - 2\mathcal{R}_{24}^{(1)} \right) \right] .
\end{aligned} \tag{3.177}$$

Due to the smallness of  $\delta \tilde{p}^2$ , contributions multiplied by higher positive powers of the finite-volume momentum are increasingly suppressed. It follows that the dominant finite volume corrections are expected to be found by solving the truncated version of eq. (3.177) to order

zero in  $\delta\tilde{p}^2$ ,

$$\begin{aligned} & \frac{2}{\delta\tilde{p}^2}(\chi_1 d_1 + \varrho_0 d_1 - 3d_0) + 1 + d_0(\mathcal{G}^{(1)} - 6) - \frac{d_2}{2} - d_3 \\ & + d_1 \left( \chi_1 + 2\chi_2 - 6\mathcal{G}^{(1)} - \varrho_1 - \tilde{\mathcal{R}}^{(1)} \right) - d_4 - d_5 = 0. \end{aligned} \quad (3.178)$$

Solving the last equation for  $\delta\tilde{p}^2$  and expanding the denominator up to order twelve in the small constants, we find

$$\begin{aligned} \delta\tilde{p}^2 = d_1 \Big\{ & -2(\chi_1 + \varrho_0) \left[ 1 + \frac{d_2}{2} + \frac{d_2^2}{4} + d_3 + d_4 \right] + d_0(1 + d_2) \left[ 2(\mathcal{G}^{(1)} - 6)(\varrho_0 + \chi_1) \right. \\ & + 6(\varrho_1 - \chi_1 - 2\chi_2 + \tilde{\mathcal{R}}^{(1)} + 6\mathcal{G}^{(1)}) \Big] + d_0^2(\mathcal{G}^{(1)} - 6) \left[ 12(\varrho_1 - \chi_1 - 2\chi_2 \right. \\ & + \tilde{\mathcal{R}} + 6\mathcal{G}^{(1)}) + (\mathcal{G}^{(1)} - 6)(\varrho_0 + 2\chi_1) \Big] \Big\} + 6d_0 \left[ 1 + \frac{d_2}{2} - d_0(1 + d_2)(\mathcal{G}^{(1)} - 6) \right. \\ & \left. + d_0^2(\mathcal{G}^{(1)} - 6)^2 + \frac{d_2^2}{4} + d_3 + d_4 \right]. \end{aligned} \quad (3.179)$$

Denoting the outcome of the first iteration as  $\delta\tilde{p}_0^2$ , we proceed with an improvement of the last result by plugging the latter into the term proportional to  $\delta\tilde{p}^2$  of the expansion in eq. (3.177) truncated to the terms quadratic in the squared momentum shift,

$$\begin{aligned} & \frac{1}{\delta\tilde{p}^2} (2\chi_1 d_1 + 2\varrho_0 d_1 - 6d_0) + 1 + d_0(\mathcal{G}^{(1)} - 6) - d_3 - d_4 + d_1(\chi_1 + 2\chi_2 - 6\mathcal{G}^{(1)} - \varrho_1 - \tilde{\mathcal{R}}^{(1)}) \\ & - \frac{d_2}{2} - d_5 + \delta\tilde{p}_0^2 \left[ d_0(\mathcal{G}^{(1)} + \mathcal{G}^{(1)}) - \frac{d_2}{2} - 2d_3 - 3d_4 - 4d_5 \right. \\ & \left. + d_1 \left( \chi_2 + 2\chi_3 - 6\mathcal{K}^{(1)} - \varrho_2 - 2\mathcal{R}_{24}^{(1)} - \tilde{\mathcal{R}}^{(1)} \right) \right] = 0. \end{aligned} \quad (3.180)$$

Solving the last equation and retaining only terms up to order twelve in  $1/L$  and the scattering parameters, we obtain a refined version of the momentum shift,

$$\begin{aligned} \delta\tilde{p}_2^2 \equiv \delta\tilde{p}^2 = d_1 \Big\{ & -2(\chi_1 + \varrho_0) \left[ 1 + d_2 + d_2^2 + d_3 + d_4 \right] + d_0(1 + 2d_2) \left[ 2(\mathcal{G}^{(1)} - 6)(\varrho_0 + \chi_2) \right. \\ & + 6(\varrho_1 - \chi_1 - 2\chi_2 + \tilde{\mathcal{R}}^{(1)} + 6\mathcal{G}^{(1)}) \Big] + 12d_0 d_2 (\varrho_0 + \chi_1) - d_0^2(\mathcal{G}^{(1)} - 6) [12(\varrho_1 - \chi_1 - 2\chi_2 \\ & + \tilde{\mathcal{R}}^{(1)} + 6\mathcal{G}^{(1)}) + 2(\mathcal{G}^{(1)} - 6)(\varrho_0 + \chi_1)] + 12d_0^2 \left[ 3(\varrho_2 + \tilde{\mathcal{R}}^{(1)} + 6\mathcal{K}^{(1)} + 2\mathcal{R}_{24}) \right. \\ & \left. - 3(\chi_2 + 2\chi_3) + 2(\mathcal{G}^{(1)} + \mathcal{G}^{(1)})(\varrho_0 + \chi_1) \right] \Big\} + 6d_0 \left[ 1 + d_2 + d_2^2 + d_3 + d_4 \right. \\ & \left. - d_0(1 + 2d_2)(\mathcal{G}^{(1)} - 6) + 3d_0 d_2 + d_0^2(\mathcal{G}^{(1)} - 6)^2 - 6d_0^2(\mathcal{G}^{(1)} + \mathcal{G}^{(1)}) \right], \end{aligned} \quad (3.181)$$

in which the new contributions appearing at each order in the auxiliary constants (cf. eq. (3.179)) have been isolated. Restoring the dimensional constants in the momenta, the energy of the

lowest  $T_1$  scattering state can be now obtained in few steps,

$$\begin{aligned}
E_S^{(1,T_1)} &= \frac{4\pi^2}{ML^2} + \frac{4\pi^2\delta\tilde{p}_2^2}{ML^2} = \frac{4\pi^2}{ML^2} + 6\xi \frac{4\pi\alpha'_C{}^{(1)}}{ML^3} \left[ 1 + \xi^2\alpha'_C{}^{(1)}r_0'^{(1)} + \xi^3\alpha'_C{}^{(1)}r_1'^{(1)} \right. \\
&\quad \left. + \xi^4\alpha'_C{}^{(1)}\left(\alpha'_C{}^{(1)}(r_0'^{(1)})^2 + r_2'^{(1)}\right) - \xi\left(\frac{\alpha'_C{}^{(1)}}{\pi L}\right)\left(1 + 2\xi^2\alpha'_C{}^{(1)}r_0'^{(1)}\right)(\mathcal{G}^{(1)} - 6) \right. \\
&\quad \left. + 3\xi^3\left(\frac{\alpha'_C{}^{(1)}}{\pi L}\right)\alpha'_C{}^{(1)}r_0'^{(1)} + \xi^2\left(\frac{\alpha'_C{}^{(1)}}{\pi L}\right)^2(\mathcal{G}^{(1)} - 6)^2 - 6\xi^2\left(\frac{\alpha'_C{}^{(1)}}{\pi L}\right)^2(\mathcal{G}^{(1)} + \mathcal{G}^{(1)}) + \dots \right] \\
&+ \xi \frac{\alpha}{L^2\pi^2} \left\{ - (2\chi_1 + 2\Omega_0) \left[ 1 + \xi^2\alpha'_C{}^{(1)}r_0'^{(1)} + \xi^3\alpha'_C{}^{(1)}r_1'^{(1)} + \xi^4\alpha'_C{}^{(1)}\left(\alpha'_C{}^{(1)}(r_0'^{(1)})^2 + r_2'^{(1)}\right) \right] \right. \\
&\quad \left. + \xi\left(\frac{\alpha'_C{}^{(1)}}{\pi L}\right)\left(1 + 2\xi^2\alpha'_C{}^{(1)}r_0'^{(1)}\right) \left[ (\mathcal{G}^{(1)} - 6)(2\Omega_0 + 2\chi_1) + 6(\Omega_1 - \chi_1 - 2\chi_2 + \tilde{\mathcal{R}}^{(1)} + 6\mathcal{G}^{(1)}) \right] \right. \\
&\quad \left. - \xi^2\left(\frac{\alpha'_C{}^{(1)}}{\pi L}\right)^2(\mathcal{G}^{(1)} - 6) \left[ 12(\Omega_1 - \chi_1 - 2\chi_2 + \tilde{\mathcal{R}} + 6\mathcal{G}^{(1)}) + (\mathcal{G}^{(1)} - 6)(2\Omega_0 + 2\chi_1) \right] \right. \\
&\quad \left. + 12\xi^2\left(\frac{\alpha'_C{}^{(1)}}{\pi L}\right)^2 \left[ 3(\Omega_2 + \tilde{\mathcal{R}}^{(1)} + 6\mathcal{K}^{(1)} + 2\mathcal{R}_{24}) - 3(\chi_2 + 2\chi_3) + (\mathcal{G}^{(1)} + \mathcal{G}^{(1)})(2\Omega_0 + 2\chi_1) \right] \right. \\
&\quad \left. + 6\xi^3\left(\frac{\alpha'_C{}^{(1)}}{\pi L}\right)\alpha'_C{}^{(1)}r_0'^{(1)}(2\Omega_0 + 2\chi_1) + \dots \right\} + \dots,
\end{aligned} \tag{3.182}$$

where the ellipsis stands for terms of higher order in the scattering and  $1/L$  parameters and in the fine-structure constant. Besides, all the terms on the r.h.s of the last equation with the only exception of the first represent the modifications of a free  $T_1$  finite-volume state with energy  $\xi/M$  induced by the strong and the electromagnetic interactions. Analogously to the  $\ell = 0$  case, only the interplay between strong and electromagnetic forces generates the linear corrections in  $\alpha$ , and the leading QED corrections are of the same order of the modifications due to the QCD forces alone. By comparison with the S-wave counterpart of eq. (3.182) (cf. eq. (2.114)), we observe that contributions from higher order scattering parameters such as  $r_2'^{(1)}$  and  $r_2'^{(1)}$  begin to appear, whereas all the terms arising from  $r_3'^{(1)}$ , included in the original version of the ERE, vanish in the order twelve expansion in the scattering parameters. Furthermore, by explicit computation it can be proven that the subsequent iteration step for the improvement of the squared momentum shift,  $\delta\tilde{p}_4^2$ , does not lead to the appearance of further addend on the r.h.s. of eq. (3.182) in the chosen approximation scheme. Finally, we conclude the treatment by isolating the corrections in the last equation and restoring the infinite volume scattering parameters,

$$\begin{aligned}
\Delta E_S^{(1, T_1)} = & 6\xi \frac{4\pi a_C^{(1)}}{ML^3} \left\{ 1 + \xi^2 a_C^{(1)} r_0^{(1)} + \xi^3 a_C^{(1)} r_1^{(1)} + \xi^4 a_C^{(1)} \left( a_C^{(1)} r_0^{(1)2} + r_2^{(1)} \right) \right. \\
& + \xi \left( \frac{a_C^{(1)}}{\pi L} \right) \left[ 3\xi^2 a_C^{(1)} r_0^{(1)} - \left( 1 + 2\xi^2 a_C^{(1)} r_0^{(1)} \right) (\mathcal{G}^{(1)} - 6) \right] + \xi^2 \left( \frac{a_C^{(1)}}{\pi L} \right)^2 \left[ (\mathcal{G}^{(1)} - 6)^2 - 6(\mathcal{G}^{(1)} + \mathcal{G}^{(1)}) \right] \\
& + \dots \left. \right\} + \xi \frac{\alpha a_C^{(1)}}{L^2 \pi^2} \left\{ 3a_C^{(1)} \mathcal{G}^{(0)} \left( r_0^{(1)} + 8\xi^2 r_1^{(1)} + 6\xi^4 r_2^{(1)} \right) + 3\xi a_C^{(1)2} r_0^{(1)} \mathcal{G}^{(0)} (1 + \xi) \left( r_0^{(1)} + \xi^2 r_1^{(1)} \right) \right. \\
& - (2\chi_1 + 2\mathcal{Q}_0) \left[ 1 + \xi^2 a_C^{(1)} r_0^{(1)} + \xi^3 a_C^{(1)} r_1^{(1)} + \xi^4 a_C^{(1)} \left( a_C^{(1)} r_0^{(1)2} + r_2^{(1)} \right) \right] + 6\xi^3 \left( \frac{a_C^{(1)}}{\pi L} \right) a_C^{(1)} r_0^{(1)} (2\mathcal{Q}_0 + 2\chi_1) \\
& + \xi \left( \frac{a_C^{(1)}}{\pi L} \right) \left( 1 + 2\xi^2 a_C^{(1)} r_0^{(1)} \right) \left[ (\mathcal{G}^{(1)} - 6)(2\mathcal{Q}_0 + 2\chi_1) + 6(\mathcal{Q}_1 - \chi_1 - 2\chi_2 + \tilde{\mathcal{R}}^{(1)} + 6\mathcal{G}^{(1)}) \right] \\
& - \xi^2 \left( \frac{a_C^{(1)}}{\pi L} \right)^2 (\mathcal{G}^{(1)} - 6) \left[ 12(\mathcal{Q}_1 - \chi_1 - 2\chi_2 + \tilde{\mathcal{R}} + 6\mathcal{G}^{(1)}) + (\mathcal{G}^{(1)} - 6)(2\mathcal{Q}_0 + 2\chi_1) \right] \\
& + 12\xi^2 \left( \frac{a_C^{(1)}}{\pi L} \right)^2 \left[ 3(\mathcal{Q}_2 + \tilde{\mathcal{R}}^{(1)} + 6\mathcal{K}^{(1)} + 2\mathcal{R}_{24}) - 3(\chi_2 + 2\chi_3) + (\mathcal{G}^{(1)} + \mathcal{G}^{(1)})(2\mathcal{Q}_0 + 2\chi_1) \right] \\
& \left. - 3\xi \left( \frac{a_C^{(1)}}{\pi L} \right) a_C^{(1)} r_0^{(1)} (1 + \xi) \mathcal{G}^{(0)} (\mathcal{G}^{(1)} - 6) + \dots \right\} + \dots,
\end{aligned} \tag{3.183}$$

where the differences with respect to eq. (3.182) involve only the linear term in the fine-structure constant and are proportional to  $\mathcal{G}^{(0)}$ .

### b) The Lowest Bound State

As hinted in the opening of chap. 1, some observed lines in the hadron spectrum such as the  $Y(4626)$ ,  $Y(4630)$  and  $Y(4660)$  [104] or the  $P_c^+(4380)$  and  $P_c^+(4450)$  [109, 112] are susceptible to the interpretation as two-body bound states between lighter colorless quark compounds with one unit of orbital angular momentum.

Therefore, it remains instructive to study the lowest two-fermion  $T_1$  bound state, by switching to imaginary momenta  $\mathbf{p} = i\boldsymbol{\kappa}$ , where  $\kappa = |\boldsymbol{\kappa}|$  represents the imaginary part of the momentum. To this purpose, we rewrite the FV effective range expansion in eq. (3.145), truncated on the l.h.s. to the sextic term in the binding momentum,

$$\begin{aligned}
-\frac{1}{a_C^{(1)}} - \frac{1}{2} r_0'^{(1)} \kappa^2 + r_1'^{(1)} \kappa^4 - r_2'^{(1)} \kappa^6 = & \frac{4\pi}{L^3} S_0(i\tilde{\kappa}) + \frac{\tilde{\kappa}^2}{\pi L} S_1(i\tilde{\kappa}) \\
& - \frac{\alpha M \tilde{\kappa}^2}{4\pi^4} S_2(i\tilde{\kappa}) - \frac{\alpha M}{\pi^2 L^2} S_3(i\tilde{\kappa}) + \alpha M \tilde{\kappa}^2 \left[ \log \left( \frac{4\pi}{\alpha M L} \right) - \gamma_E \right].
\end{aligned} \tag{3.184}$$

First, we consider the limit of large lattice binding momentum,  $\tilde{\kappa} = |\tilde{\kappa}| \gg 1$ , which corresponds to a tightly-bound state. Thus, an approximation for the Lüscher functions in this regime becomes necessary. In particular, we observe that the asymptotic behaviour of  $S_1(i\tilde{\kappa})$  and

$S_2(i\tilde{\kappa})$  is already available in literature and gives,

$$S_1(i\tilde{\kappa}) = \sum_{\mathbf{n}}^{\Lambda_n} \frac{1}{|\mathbf{n}|^2 + \tilde{\kappa}^2} - 4\pi\Lambda_n \rightarrow -2\pi^2\tilde{\kappa} \quad (3.185)$$

(cf. eq. (43) in ref. [1]) and

$$S_2(i\tilde{\kappa}) = \sum_{\mathbf{n}}^{\Lambda_n} \sum_{\mathbf{m} \neq \mathbf{n}}^{\infty} \frac{1}{|\mathbf{n}|^2 + \tilde{\kappa}^2} \frac{1}{|\mathbf{m}|^2 + \tilde{\kappa}^2} \frac{1}{|\mathbf{n} - \mathbf{m}|^2} - 4\pi^4 \log \Lambda_n \rightarrow -4\pi^4 \log(2\tilde{\kappa}) + \frac{\pi^2}{\tilde{\kappa}} \mathcal{G}^{(0)}, \quad (3.186)$$

see app. (B.2.1) and eq. (44) in ref. [1]. On the other hand, the large binding energy limit of  $S_3(i\tilde{\kappa})$  requires a new derivation, presented in detail in app. (B.2.2),

$$S_3(i\tilde{\kappa}) = \sum_{\mathbf{n}}^{\Lambda_n} \sum_{\mathbf{m} \neq \mathbf{n}}^{\infty} \frac{1}{|\mathbf{n}|^2 + \tilde{\kappa}^2} \frac{1}{|\mathbf{m}|^2 + \tilde{\kappa}^2} \frac{\mathbf{n} \cdot \mathbf{m} + \tilde{\kappa}^2}{|\mathbf{n} - \mathbf{m}|^2} - \pi^4 \Lambda_n^2 \rightarrow \frac{\pi^2}{2\tilde{\kappa}} - 2\pi^2\tilde{\kappa} \mathcal{G}^{(0)} - 2\pi^4\tilde{\kappa}^2. \quad (3.187)$$

Recalling the fact that  $S_0(\tilde{\kappa}) = \Upsilon = 0$  (cf. eq. (B.107)) and collecting the results in eqs. (3.185)-(3.187), the above finite volume effective range expansion becomes,

$$-\frac{1}{a'_C} - \frac{1}{2} r_0'^{(1)} \kappa^2 + r_1'^{(1)} \kappa^4 - r_2'^{(1)} \kappa^6 = \kappa^3 + \frac{\alpha M}{2} \kappa^2 + \frac{3}{2} \frac{\alpha M}{\pi L} \mathcal{G}^{(0)} \kappa - \frac{\alpha M \pi}{L^3 \kappa} - \alpha M \kappa^2 \left[ \log \left( \frac{4\kappa}{\alpha M} \right) - \gamma_E \right]. \quad (3.188)$$

Second, we highlight the dependence on the fine-structure constant in the last equation by rewriting the binding momentum in a power series,

$$\kappa = \kappa_0 + \kappa_1 + \kappa_2 + \kappa_3 + \dots, \quad (3.189)$$

where  $\kappa_0$  results from strong interactions alone and the subscript corresponds to the power of  $\alpha$  on which each term in the expansion depends. Replacing in eq. (3.188) the shifted scattering parameters with the infinite volume ones in eqs. (1.40)-(1.44) and discarding all the terms of order  $\alpha^2$  or higher in the expansions, eq. (3.188) transforms into

$$\begin{aligned} & -\frac{1}{a'_C} + \frac{\alpha M \mathcal{G}^{(0)}}{2\pi L} r_0^{(1)} - \frac{1}{2} r_0^{(1)} \kappa_0^2 - r_0^{(1)} \kappa_0 \kappa_1 + r_1^{(1)} \kappa_0^4 - \frac{2\alpha M \mathcal{G}^{(0)}}{\pi L} r_1^{(1)} \kappa_0^2 + 4r_1^{(1)} \kappa_0^3 \kappa_1 \\ & + \frac{3\alpha M \mathcal{G}^{(0)}}{\pi L} r_2^{(1)} \kappa_0^4 - r_2^{(1)} \kappa_0^6 - 6r_2^{(1)} \kappa_0^5 \kappa_1 - \frac{4\alpha M \mathcal{G}^{(0)}}{\pi L} r_3^{(1)} \kappa_0^6 = \kappa_0^3 + \frac{3}{2} \frac{\alpha M}{2\pi L} \mathcal{G}^{(0)} \kappa_0 \\ & - 3\kappa_0^2 \kappa_1 - \frac{\alpha M \pi}{L^3 \kappa_0} + \frac{\alpha M}{2} \kappa_0^2 + \alpha M \kappa_0^2 \left[ \log \left( \frac{4\kappa_0}{\alpha M} \right) - \gamma_E \right]. \end{aligned} \quad (3.190)$$

Grouping all the terms independent on  $\alpha$ , we observe that the following equality

$$-\frac{1}{a'_C} - \frac{1}{2} r_0^{(1)} \kappa_0^2 + r_1^{(1)} \kappa_0^4 - r_2^{(1)} \kappa_0^6 = \kappa_0^3, \quad (3.191)$$



holds, since the remaining terms in eq. (3.190) depend linearly on  $\alpha$ . Therefore, an expression for  $\kappa_1$  can be drawn from the original eq. (3.190) by dropping the terms listed in eq. (3.191),

$$\begin{aligned} \kappa_1 \left( 3\kappa_0^2 - r_0^{(1)}\kappa_0 + 4r_1^{(1)}\kappa_0^3 - 6\kappa_0^5 r_2^{(1)} \right) &= \frac{\alpha M \mathcal{G}^{(0)}}{2\pi L} \left( 3\kappa_0 - r_0^{(1)} + 2r_1^{(1)}\kappa_0^2 \right. \\ &\quad \left. - 6r_2^{(1)}\kappa_0^4 + 8r_3^{(1)}\kappa_0^6 \right) - \frac{\alpha M \pi}{L^3 k_0} + \alpha M \kappa_0^2 \left[ \log \left( \frac{4\kappa_0}{\alpha M} \right) - \gamma_E + \frac{1}{2} \right]. \end{aligned} \quad (3.192)$$

In particular, retaining only the terms depending on the two lowest order scattering parameters as in the zero angular momentum case (cf. eqs. (45)-(46) in ref. [1]), a more approximated expression for  $\kappa_1$  in terms of  $\kappa_0$ ,  $\alpha_C^{(1)}$  and  $r_0^{(1)}$  can be obtained,

$$\kappa_1 \approx \frac{\alpha M \mathcal{G}^{(0)}}{2\pi L \kappa_0} - \frac{\alpha M}{\pi^3 L^3} \frac{\pi^4}{3\kappa_0^3 - r_0^{(1)}\kappa_0^2} + \frac{\alpha M \kappa_0^2}{3\kappa_0^2 - r_0^{(1)}\kappa_0} \left[ \log \left( \frac{4\kappa_0}{\alpha M} \right) - \gamma_E + \frac{1}{2} \right]. \quad (3.193)$$

From the latter equation the first two terms generate finite-volume corrections, whereas the third one introduces QED modifications to the unperturbed binding momentum  $\kappa_0$  which do not vanish in the infinite volume limit. Now, considering the binding energy of the lowest  $T_1$  state in the linear approximation in  $\alpha$ ,

$$E_B^{(1,T_1)} = \frac{\kappa^2}{M} = \frac{\kappa_0^2}{M} + 2\frac{\kappa_0\kappa_1}{M} + \dots, \quad (3.194)$$

and substituting the simplified expression of  $\kappa_1$  in eq. (3.193), we find an approximate expression for the energy of the lowest  $T_1$  bound state,

$$E_B^{(1,T_1)}(L) = \frac{\kappa_0^2}{M} + \frac{2\alpha\kappa_0^3}{3\kappa_0^2 - r_0^{(1)}\kappa_0} \left[ \log \left( \frac{4\kappa_0}{\alpha M} \right) - \gamma_E + \frac{1}{2} \right] + \frac{\alpha \mathcal{G}^{(0)}}{\pi L} - \frac{\alpha}{\pi^3 L^3} \frac{2\pi^4}{\kappa_0^2} \frac{1}{3\kappa_0 - r_0^{(1)}}. \quad (3.195)$$

where the first two terms represent the infinite volume binding energy up to  $\mathcal{O}(\alpha)$ , while the third contribution vanishes for  $L \rightarrow +\infty$  together with the fourth one. Furthermore, if  $r_0^{(0)}$  is small enough, the denominator in the second and in the fourth term of the last equation can be expanded in powers of  $r_0^{(0)}/\kappa_0 \ll 1$  and the leading order mass shift for tightly-bound  $T_1$  two-body states eventually becomes,

$$\Delta E_B^{(1,T_1)} \equiv E_B^{(1,T_1)}(\infty) - E_B^{(1,T_1)}(L) = -\frac{\alpha \mathcal{G}^{(0)}}{\pi L} + \frac{\alpha}{\pi^3 L^3} \frac{2\pi^4}{3\kappa_0^3 - r_0^{(1)}\kappa_0^2} \approx -\frac{\alpha \mathcal{G}^{(0)}}{\pi L} + \frac{\alpha}{\pi^3 L^3} \frac{2\pi^4}{3\kappa_0^3}. \quad (3.196)$$

From the r.h.s. of the last expression we can infer that the leading QED corrections to  $E_B^{(1,T_1)}(L)$  presented in eq. (3.196) are positive ( $\mathcal{G}^{(0)} < 0$ , see eq. (B.119)), analogously to the LO mass shifts for  $\ell = 1$  states of two-body systems with strong interactions alone in eq. (53) of refs. [71, 77]. Also noteworthy is the fact that, when compared to the S-wave case in eq. (2.127) (cf. eq. (46) in ref. [1]), the sign of the P-wave shift is reversed while the magnitude remains unchanged. As discussed in refs. [71, 77], the significance of this behaviour can be traced back to the spatial profile of the  $\ell = 0$  and  $\ell = 1$  two-body wavefunctions associated to the considered bound eigenstates. Qualitatively, the relationship found between the two finite volume energy corrections means that zero angular momentum states are more deeply bound when embedded in a finite volume, while the counterpart with one unit of angular momentum are less bound. In conclusion, together with the derivation of  $\Delta E_B^{(1,T_1)}$ , we have simultaneously

proven that the addition of a long-range force on top of strong forces in two-fermion systems within a cubic finite-volume produces changes of the same magnitude on S- and P-wave bound energy eigenvalues.

### 3.3 Outlook

Now, we qualitatively outline the possible improvements to the analysis presented in the last two chapters. There are two main directions for the generalization of the present study. These consist in the inclusion of transverse photons in the Lagrangian density of the system and in the treatment of strong interactions with higher angular momentum couplings.

Let us start from the former. Thanks to their vector nature, transverse photons can couple to the fermionic fields in several different ways, see eq. (1.12). Among these, here we retain only the Dipole vertex (cf. app. A.1), which is expected to yield the leading-order contributions to the T-matrix and the full Green's function. As we previously hinted, these photons, denoted by wavy lines, can propagate also between different bubbles. Consequently, at each order in  $D(E^*)$  a numerable infinity of new diagrams with different topologies and transverse-photon exchanges inside and outside the bubbles appears. Unfortunately, part of the amplitudes associated to these diagrams can not be written as powers of the loop (bubble) integrals, since the transverse photons propagating outside the fermion loops introduce a correlation between the bubbles (cf. fig. (4) in ref. [1] and fig. 3.3). It follows that an expression for the T-matrix element of the two-body scattering process,  $T_{\text{SCT}}$ , written in terms of a geometric series of ratio proportional to the interaction strength,  $D(E^*)$ , can not be found. More formally, a self-consistent rewriting of the full Green's function operator  $\hat{G}_{\text{SCT}}$  in the form of a self-consistent equation *à la Dyson* separating the QED Green's function operator,  $\hat{G}_{\text{CT}}$ , from the strong interaction operator  $\mathcal{V}^{(1)}$  (cf. eq. (3.2)) does not exist. These facts prevent the exact determination of  $T_{\text{SCT}}$  to all orders in the fine-structure constant.

Nevertheless, the gapped nature of the momentum in the finite-volume environment allows for a perturbative treatment of the whole non-relativistic QED. Therefore, approximate expressions for  $T_{\text{SCT}}$  that incorporate the effects of the transverse photons up to the desired order in  $\alpha$  can be derived.

One of these approaches consists in writing the infinite-volume T-matrix element  $T_{\text{SCT}}$  exactly as  $T_{\text{SC}}$  in eq. (3.36) with  $D(E^*)$  at the denominator replaced by a *dressed* strong P-wave coupling constant  $D_{\text{T}}(E^*)$ , that includes the effects of transverse photons up to first order in the fine-structure constant. Analytically, this energy-dependent constant can be derived by evaluating the contributions of all the possible bubble diagrams with one transverse-photon exchange in fig. 3.3. Moreover, considering the fact that diagrams with one transverse photon across  $n$ -bubbles are suppressed by a factor  $(\sqrt{|\mathbf{p}|})^n$ , the numerable infinity of contributions on the r.h.s. of fig. 3.3 can be reduced to a finite set. The amplitudes corresponding to these diagrams can be evaluated via dimensional regularization as the ones containing radiation pions in refs. [22, 32, 136] or via the cutoff approach and, in finite volume, they can be constructed by replacing the relevant integrals with three-dimensional sums, eventually regularized by a spherical cutoff.

Furthermore, the finite-volume quantization conditions can be derived as in sec. 3.2.1, keeping track of the transverse-photon contributions via the aforementioned redefinition of the strong coupling constant. In the end of the process, an expression for  $1/D(E^*)$  analogous

to eq. (3.109) is found, provided the powers of the original strong coupling constant in the QED contributions to  $D_T(E^*)$  in fig. 3.3 are replaced by scattering parameters (cf. sec. III B of ref. [1]) using the expression of  $D(E^*)$  in eq. (3.18).

In the present first-order approximation in the fine-structure constant, the latter operation is, in fact, justified. Dressing the S-wave strong interaction through the diagrams with one transverse-photon exchange between the legs of the strong vertex and the interaction-to-bubble exchange in fig. 4 (c) of ref. [1], the low-energy constant  $C(E^*)$  picks up the  $\mathcal{O}(\alpha)$  corrections shown in eq. (25), which lead to the appearance of a term proportional to the square of the Lüscher function  $S_1(\vec{p}) \equiv S(\vec{p})$  (cf. eq. (28) of ref. [1]) in the expression of the finite-volume ERE in eq. (26) of ref. [1]. By means of a procedure analogous to the one outlined in sec. 2.2.3 b), it can be demonstrated that transverse-photon contributions materialise in the last term within the second curly brackets on the r.h.s. of eqs. (36), (37) and (39) of ref. [1]. Albeit pertinent, this contribution constitutes a subleading order correction to the term proportional to  $\mathcal{G}^{(0)} \equiv \mathcal{G}$  within the same parentheses of the latter equations and is comparable in magnitude with the terms proportional to  $(a_C^{(0)}/\pi L)^2$  in eq. (2.115) (cf. eq. (39) of ref. [1]).

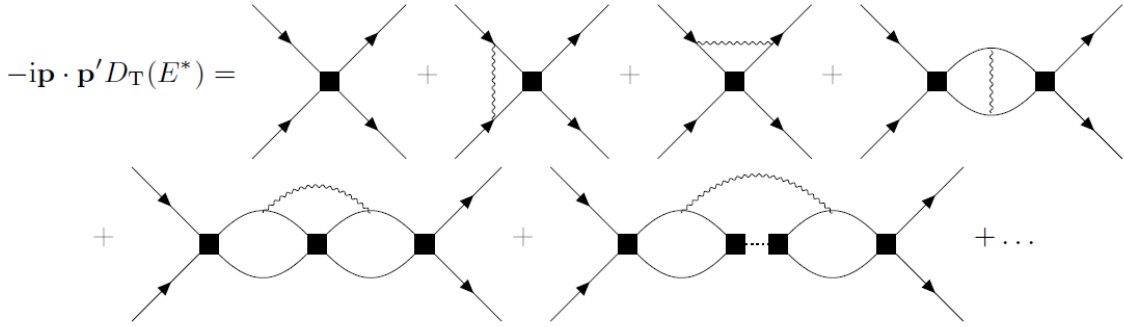


FIGURE 3.3 – The *dressed* strong vertex coupling to one unit of angular momentum as a superposition of the original fermion-fermion interaction vertex plus a numerable infinity of tree-level and bubble diagrams containing one transverse-photon exchange. The ellipses represent other diagrams featuring one or more strong vertices and single transverse-photon insertions.

As we previously noted, the second main generalization of our work consists of the adoption of strong interactions coupled to more units of angular momentum. The most significant of these extensions is represented by the D-wave case, where the strong part of the EFT Lagrangian density becomes

$$\mathcal{L} = \psi^\dagger \left[ i\hbar\partial_t - \frac{\hbar^2\nabla^2}{2M} \right] \psi + \frac{F(E^*)}{6} (\psi\psi)^\dagger (\psi\psi) - \frac{F(E^*)}{32} (\psi \overleftrightarrow{\partial}_i \overleftrightarrow{\partial}_j \psi)^\dagger (\psi \overleftrightarrow{\partial}_i \overleftrightarrow{\partial}_j \psi), \quad (3.197)$$

where  $F(E^*)$  is a new suitable energy-dependent coupling constant (cf. sec. 1.2 and fig. A.3). Due to the presence of higher-order differential operators acting on the fermionic fields, the computation of the strong scattering amplitude,  $T_S$ , via a geometric series on the loop integrals, as in eq. (3.15), involves a rank-four tensor as a ratio. The elements of the D-wave counterpart of  $\mathbb{J}_0$  correspond to double mixed derivatives of the free Green's function, except for the diagonal terms, in which an additional contribution proportional to  $G_0(\mathbf{0}, \mathbf{0})$  is expected to be present. Also the full Green's function  $G_{SC}(\mathbf{0}, \mathbf{0})$  is likely to undergo similar changes, which lead to the onset of more rapidly UV-divergent integrals in the D-wave counterpart of  $\mathbb{J}_{SC}$ . Besides, some novelties are expected to arise from the quantization condition stemming from the full two-point correlation function  $G_{SC}$ . The D-wave counterpart of  $\mathbb{J}_C$  in finite volume gener-

ates the constraints on  $1/F^L(E^*)$  for energy states transforming as two distinct representations of the cubic group,  $\mathcal{O}$ . The  $\ell = 2$  irreducible representation of  $\text{SO}(3)$ , in fact, decomposes into the  $E \oplus T_2$  irreps [67, 137] of  $\mathcal{O}$ . As a consequence, the one-to-one correspondence between the transformation properties of the selected multiplet of states under the operations of  $\text{SO}(3)$  and  $\mathcal{O}$  is no longer valid. It is, thus, possible that a derivation of the finite-volume corrections that makes use of the effective range expansion for D-waves in ref. [43],

$$\left(\eta^4 + 5\eta^2 + 4\right) \frac{\mathbf{p}^4}{4} \left[ C_\eta^2 |\mathbf{p}| (\cot \delta_2 - i) + \alpha M H(\eta) \right] = -\frac{1}{a_{\text{C}}^{(2)}} + \frac{1}{2} r_0^{(2)} \mathbf{p}^2 + r_1^{(2)} \mathbf{p}^4 + \dots, \quad (3.198)$$

has to follow two separate paths for the  $E$  and the  $T_2$  states. New challenges arise also in the evaluation of the cutoff-regularized double sums stemming from the  $\delta \tilde{\mathbf{p}}^2$  expansions (cf. sec. 3.2.3 a)) of the Lüscher functions. Nevertheless, the reference finite-volume state for the lowest unbound energy level is expected to correspond again to the one with  $|\tilde{\mathbf{p}}| = 1$  and energy  $4\pi^2/L^2 M$ . Therefore, the final formulae for the finite-volume energy corrections to the lowest  $E$  and  $T_2$  scattering states are likely to conserve some resemblance with the one presented in eq. (3.183). Concerning the lowest bound state, it would be certainly of interest to compare the magnitude of the outcoming corrections with the existing ones for the energy of the most bound S- and P-wave states.

## **Part II**

# **Breaking and restoration of rotational symmetry in the low energy spectrum of light $\alpha$ -conjugate nuclei on the lattice**



## 4.1 Preamble

The wealth of available literature on lattice calculations is, perhaps, self-explanatory on the role that the latter play in the investigation of relativistic field theories and quantum few-body and many-body systems. After the first study of nuclear matter on the lattice in ref. [138] in the framework of quantum hadrodynamics [139], lattice simulations have begun to be employed for several other systems involving nuclear matter, fostered by the development of effective field theories [12, 140] such as Chiral Effective Field Theories (ChEFT) [12, 13, 15, 141].

In the lattice framework, the continuous space-time is discretized and compactified on a hypercubic box so that differential operators become matrices and the relevant path-integrals are evaluated numerically. When periodic boundary conditions are imposed in all the space directions, the whole configuration space is reduced to a three-dimensional torus and translational invariance is preserved. Nevertheless, the average values of physical observables on the lattice eigenstates will, in general, depend on the features of the box employed for the description of the physical system rather than obey to their continuum and infinite-volume counterparts.

Starting from Lüscher's early works [74–76], in the last three decades much effort has been devoted to investigate the finite-volume dependence of physical observables on the lattice, with a special attention for the energy of bound states.

The original formula connecting the leading-order finite-volume correction for the energy eigenvalues to the asymptotic properties of the two-particle bound wavefunctions in the infinite volume in ref. [74] has been extended in several directions including non-zero angular momenta [71, 77–79], moving frames [79–85], generalized boundary conditions [86–91], particles with intrinsic spin [92, 93] and perturbative Coulomb shifts [1, 118] (cf. *Part I*). In addition, considerable advances have been made in the derivation of analogous formulas for the energy corrections of bound states of three-body [94, 95] and N-body systems [96, 97].

While closed expressions for leading-order finite-volume corrections to certain physical observables already exist, artifacts due to the finite lattice spacing remain more difficult to keep under control.

Nevertheless, systematic schemes for the improvement of discretized expressions of quantities of physical interest have been developed. In these approaches, correction terms are identified

using continuum language and are added with suitable coefficients, so that corrections up to the desired order in the lattice spacing vanish.

In the context of field theories, namely Yang-Mills theories, discretization effects can be reduced via the Symanzik improvement program [142–146]. The latter is based on the systematic inclusion of higher-dimensional operators into the lattice action, whose coefficients are determined through a perturbative or nonperturbative matching procedure [146]. A similar approach, reviewed in apps. C.1 and C.2, can be implemented for differential operators applied to wavefunctions, in which the derivation of the coefficients in front of the corrective terms stems only from algebraic considerations [146], differently from the previous case.

Another consequence of transposing a physical system into a cubic lattice is given by the reduction of the rotational symmetry group to the finite group of the rotations of a cube. If the former is ruled by central forces, the rotation group on three dimensions,  $SO(3)$ , shrinks into the rotation subgroup,  $\mathcal{O}$ , of the octahedral group  $\mathcal{O}_h$ . Therefore, lattice eigenstates of a few-body Hamiltonian cannot be unambiguously classified in terms of irreducible representations of  $SO(3)$  or  $SU(2)$  [67]. In the transition between infinitesimal and finite spacing, the  $2\ell + 1$ -fold degeneracy in the energies of the members of a multiplet of states transforming according to the same irreducible representation  $\ell$  of  $SO(3)$  reduces to 1-, 2- or 3-fold degeneracy, depending on the cubic-group irreps that appear in the decomposition of the original representation of the rotation group (cf. sec. 4.4). In particular, the energy separation between the ensuing  $\mathcal{O}$  multiplets grows smoothly with increasing lattice spacings.

This descent in symmetry has been recapitulated in ref. [67], where the problem of the identification of the cubic lattice eigenstates in terms of  $SO(3)$  irreps has been first outlined. The increasing importance of the discretization of the Euclidean spacetime in the context of gauge theories [147–149] led soon to an extension of the work in ref. [67] to the case of an hypercubic lattice [150].

In the meantime, investigations explicitly devoted to rotational symmetry breaking appeared in the context of scalar  $\lambda\phi^4$  [151] and gauge field theories [152, 153] on the lattice. More recently, quantitative estimations of rotational symmetry breaking have been performed in both the frameworks in ref [154] and in Lattice QCD for exotic mesons in ref. [155], via the construction of operators with sharply defined angular momentum.

Nevertheless, the restoration of the full rotational invariance on the lattice can be achieved by projecting the lattice wavefunctions onto angular momentum quantum numbers via the construction of projectors on  $SO(3)$  irreps. The use of such a technique has been firstly reported in ref. [156], in the context of cranked Hartree-Fock self-consistent calculations for  $^{24}\text{Mg}$ .

However, in chaps. 5, 6 and 7 we aim at investigating rotational symmetry breaking in bound states of  $^8\text{Be}$ ,  $^{12}\text{C}$  and  $^{16}\text{O}$  nuclei on the lattice rather than at removing these effects. At the same time, the analysis of the low-energy spectra of the three light  $\alpha$ -conjugate nuclei provides us an occasion to highlight the general issues associated to finite volume and discretization in energies, angular momenta and average interparticle distances.

Since the framework allows for a robust analysis over a wide range of lattice spacings and cubic box sizes, for the purpose we adopt a simplified description in terms of  $\alpha$  particles instead of individual nucleons, following on the recent literature on the same subject, cf. refs. [3, 68]. The propensity of nucleons to congregate in clusters is known from the inception of nuclear physics [157] and its influence in literature continues to the present day [158–160]. Even if they can explain only a part of the spectra of  $4N$  self-conjugate nuclei,  $\alpha$ -cluster models



succeeded in describing certain ground-state properties of this class of nuclei [161–163] or lifetimes [164, 165] and energies [8, 166–171] of excited states as well as the occurrence of  $\alpha$ -decay thresholds (cf. the *Ikeda diagram* [172, 173]). Reaction properties have been also investigated in these models, such as  $p$ - $^{12}\text{C}$  and  $\pi$ - $^{12}\text{C}$  scattering [174–178]. For a recent review on  $\alpha$  clustering in light nuclei, see ref. [179].

The interaction between  $\alpha$  particles can be realistically described by microscopically based potentials within the method of generator coordinates [180], the resonating group model [181, 182], the orthogonality condition model [163], the WKB model of ref. [183], the energy-density or the folding model [184]. Alternatively, phenomenological potentials constructed from  $\alpha - \alpha$  scattering data, like the Woods-Saxon ones of ref. [185] and ref. [186], or the Gaussian ones of ref. [4], can be considered. Our two-body interaction, presented in sec. 4.2.1, builds on the work of ref. [3] and consists of an isotropic Ali-Bodmer type potential, i.e. a superposition of a positive and a negative-amplitude Gaussian.

The sought extension of the finite-volume and discretization analysis in secs. III. A and B of ref. [3] to higher angular momentum multiplets has been here achieved through the introduction of an additional tool, the discretized version of the squared total angular momentum operator. If the lattice spacing is sufficiently small (e.g.  $a \lesssim 1.5$  fm and  $a \lesssim 0.65$  fm in the two  $^8\text{Be}$  configurations considered in chap. 5) and the lattice volume is large enough (e.g.  $L \equiv Na \gtrsim 18$  fm and  $Na \gtrsim 12$  fm respectively), the average values of the squared total angular momentum operator on the states turn out to provide precise information on the  $\text{SO}(3)$  multiplets to which the eigenstates belong in the continuum and infinite-volume limit. The capability of the latter operator of drawing this information also from the lowest energy bound states of  $^{12}\text{C}$  and  $^{16}\text{O}$  is tested and discussed in chaps. 6 and 7, respectively.

## 4.2 Theoretical framework

We recapitulate the  $\alpha$ -cluster model introduced in ref. [3] and adopted also in the more recent analysis in ref. [68]. To the realization of the kinetic part of the Hamiltonian operator in the lattice environment we dedicate in sec. 4.3.1.

### 4.2.1 The Hamiltonian

In the phenomenological picture considered here, individual nucleons are grouped into  $^4\text{He}$  clusters, that are treated as spinless spherically-charged particles of mass  $m \equiv m_{^4\text{He}}$  subject to both two-body  $V^{\text{II}}$  and three-body potentials  $V^{\text{III}}$ . Therefore, the Hamiltonian of the system reads

$$H = -\frac{\hbar^2}{2m} \sum_{i=1}^M \nabla_i^2 + \sum_{i<j} V^{\text{II}}(\mathbf{r}_i, \mathbf{r}_j) + \sum_{i<j<k} V^{\text{III}}(\mathbf{r}_i, \mathbf{r}_j, \mathbf{r}_k) . \quad (4.1)$$

The global effects of the strong force between two  $\alpha$  particles at a distance  $\mathbf{r}$  are described by an isotropic version [187] of the phenomenological Ali-Bodmer potential (cf. fig. 4.1),

$$V_{AB}(\mathbf{r}) = V_0 e^{-\eta_0^2 r^2} + V_1 e^{-\eta_1^2 r^2} , \quad (4.2)$$

consisting of a superposition of a long range attractive Gaussian and a short range repulsive one with the parameters

$$\begin{aligned}\eta_0^{-1} &= 2.29 \text{ fm} , & V_0 &= -216.3 \text{ MeV} , \\ \eta_1^{-1} &= 1.89 \text{ fm} , & V_1 &= -353.5 \text{ MeV} .\end{aligned}$$

Moreover, the range parameter of the attractive part of this isotropic Ali-Bodmer potential agrees with the ones fitting the  $\alpha - \alpha$  scattering lengths with  $\ell = 0, 2$  and  $4$  to their experimental values [4], whereas the compatibility of  $V_0$  with the best fits of the latter (cf.  $d'_0$ ,  $d_2$  and  $d_4$  in ref. [4]) is poorer ( $\approx 30\%$ ). As the repulsive part of this potential is strongly angular momentum dependent, its parameters reproduce within 10% likelihood only the ones for  $D$ -wave scattering lengths,  $d_2$  [4]. Assuming that the charge distribution of the  $\alpha$ -particles is spherical and obeys a Gaussian law with an rms radius  $R_\alpha = 1.44 \text{ fm}$  [4], the Coulomb interaction between the  $^4\text{He}$  nuclei takes the form

$$V_C(\mathbf{r}) = \frac{4e^2}{4\pi\epsilon_0} \frac{1}{r} \text{erf}\left(\frac{\sqrt{3}r}{2R_\alpha}\right) . \quad (4.3)$$

in terms of the error function,  $\text{erf}(x) = (1/\sqrt{\pi}) \int_x^\infty e^{-t^2} dt$ . The three-body term of the Hamiltonian,  $V^{\text{III}}$ , consists of a Gaussian attractive potential,

$$V_T(\mathbf{r}_{ij}, \mathbf{r}_{jk}, \mathbf{r}_{ik}) = V_3 e^{-\lambda(r_{ij}^2 + r_{jk}^2 + r_{ik}^2)} , \quad (4.4)$$

whose range  $\lambda = 0.005 \text{ fm}^{-2}$  and amplitude parameters  $V_3 = -4.41 \text{ MeV}$  were originally fitted to reproduce, respectively, the binding energy of the  $^{12}\text{C}$  and the spacing between the Hoyle state, *i.e.* the  $0_2^+$  at  $7.65 \text{ MeV}$  and  $2_1^+$  one at  $4.44 \text{ MeV}$  [5] of the same nuclide in the case the original angular momentum dependent Ali-Bodmer potential, *i.e.* a superposition of three pairs of Gaussians of the form (4.2) with parameters  $d'_0$ ,  $d_2$  and  $d_4$  [4], was adopted. However, in the present case, the three pairs of quadratic exponentials, corresponding to the best fitting potentials for the  $S$ ,  $D$  and  $G$ -wave  $\alpha - \alpha$  scattering amplitudes [4], have been resummed into a single pair of Gaussians that adjusts the zero of the energy on the Hoyle state rather than on the  $3\alpha$  decay threshold. Since the spacing between the latter two is experimentally well-established, the possibility of reproducing the binding energy of the nucleus still remains.

### 4.3 Operators on the lattice

We construct the operators of physical interest acting on a discretized and finite configuration space, *i.e.* a lattice with  $N$  points per dimension and spacing  $a$ . For the details on the adopted discretization scheme for the differential operators, we address the reader to apps. C.1 and C.2.

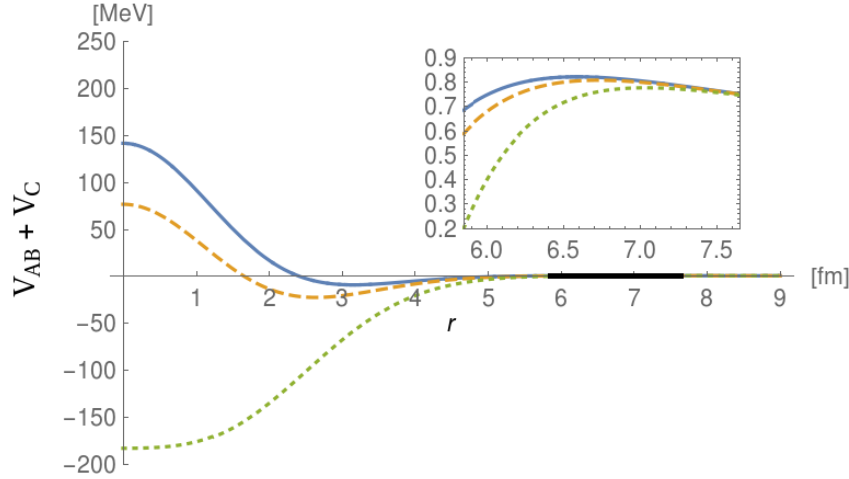


FIGURE 4.1 – Behaviour of the two-body potentials for a system of two particles in presence of Coulomb (cf. eq. 4.3) and Ali-Bodmer (cf. eq. 4.2) interactions with  $V_0$  equal to 100% (solid line), 130% (dashed line) and 250% (dotted line) of its value presented in eq. 4.3. The latter two potentials with artificially enhanced strength parameter have been introduced in order to generate a set of low-lying bound states with different angular momenta, at the root of the analysis presented in chap 5. The increase of  $V_0$  leads to the disappearance of the absolute maximum at zero interaction distance simulating the short-range Pauli repulsion between the  $\alpha$ -particles. In particular, the shape of the dotted curve resembles the one of a Woods-Saxon potential except for the remaining shallow maximum at 7.0 fm, highlighted in the magnification.

### 4.3.1 Kinetic energy

We choose to concentrate first on the many-body kinetic energy operator in the absolute reference frame, presented together with the two and three-body potentials in eq. (4.1),

$$K = -\frac{\hbar^2}{2m} \sum_{i=1}^M \nabla_i^2. \quad (4.5)$$

Applying the operator in eq. (4.5) on a general  $M$ -body wavefunction in configuration space

$$\Psi(\mathbf{r}_1, \mathbf{r}_2, \dots, \mathbf{r}_M) = \langle \Psi | \mathbf{r}_1, \mathbf{r}_2, \dots, \mathbf{r}_M \rangle \quad (4.6)$$

and replacing the exact derivatives with their discretized version in eq. (C.219), the explicit form of lattice counterpart of  $K$  can be derived. For the purpose, it is customary to introduce ladder operators,  $a_i^\dagger(\mathbf{r}_i)$  and  $a_i(\mathbf{r}_i)$ , acting on the discretized version of the kets of eq. (4.6), whose meaning is respectively the creation and the destruction of the particle  $i$  at the position  $\mathbf{r}_i$ . Therefore, applying the discretization scheme outlined in app. C.1 [146] with improvement index  $K$ , the kinetic energy operator on the cubic lattice  $\mathcal{N}$  becomes

$$\mathcal{K} = -\frac{\hbar^2}{2m} \sum_{\substack{\alpha \in \\ x,y,z}} \sum_{i=1}^M \sum_{\mathbf{r}_i \in \mathcal{N}} \sum_{k=1}^K C_k^{(2D,K)} \left[ -2a_i^\dagger(\mathbf{r}_i)a_i(\mathbf{r}_i) + a_i^\dagger(\mathbf{r}_i)a_i(\mathbf{r}_i + k\mathbf{a}_\alpha) + a_i^\dagger(\mathbf{r}_i)a_i(\mathbf{r}_i - k\mathbf{a}_\alpha) \right], \quad (4.7)$$

where  $\mathbf{e}_\alpha$  are unit-vectors parallel to the axes of the lattice. The latter equation can be more succinctly rewritten as

$$\hat{\mathcal{K}} = -\frac{\hbar^2}{2m} \sum_{\substack{\alpha \in \\ x,y,z}} \sum_{i=1}^M \sum_{\mathbf{r}_i \in \mathcal{N}} \sum_{l=-K}^K C_{|l|}^{(2P,K)} a_i^\dagger(\mathbf{r}_i) a_i(\mathbf{r}_i + l\mathbf{e}_\alpha) . \quad (4.8)$$

After defining dimensionless lattice momenta as

$$\mathbf{p}_i = \frac{2\pi\mathbf{n}_i}{N} \quad \mathbf{n}_i \in \mathcal{N} \subset \mathbb{Z}^3 , \quad (4.9)$$

by imposing periodic boundary conditions (cf. sec. 4.6), we can switch to the momentum space via the discrete Fourier transform of the lattice ladder operators,

$$\hat{\mathcal{K}} = \sum_{i=1}^M \sum_{\mathbf{p}_i \in \mathcal{N}} a_i^\dagger(\mathbf{p}_i) \mathcal{K}_{\mathbf{p}_i} a_i(\mathbf{p}_i) . \quad (4.10)$$

Therefore, we can extract the analytical expression of the eigenvalues of a system of free particles from the original expression of  $\hat{\mathcal{K}}$  in configuration space in eq. (4.8),

$$\mathcal{K}_{\mathbf{p}_i} = \frac{\hbar^2}{2m} \sum_{\substack{\alpha \in \\ x,y,z}} \sum_{k=1}^K C_k^{(2P,K)} [2 - \cosh(k p_{i,\alpha})] \quad (4.11)$$

(cf. fig. 4.2). From the final form of lattice dispersion relation in eq. (4.11), we can conclude that Galilean invariance is broken on the lattice, since the dependence of the former on the  $\mathbf{p}_i$ 's is not quadratic [70].

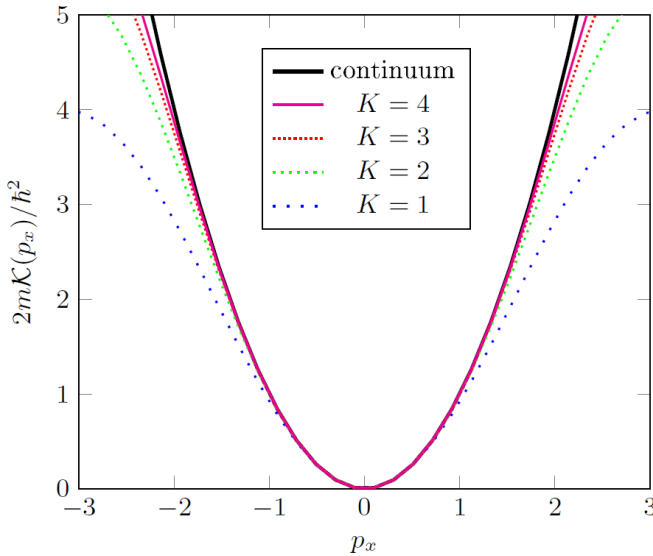


FIGURE 4.2 – Behaviour of the eigenvalues of a free particle in one dimension,  $x$ , as function of the lattice momentum  $p_x$  for four different values of the second derivative improvement index and unit spacing. For increasing values of  $K$  the eigenvalues of  $\mathcal{K}(p_x)$  approach the continuum ones with increasing likelihood.

In the absolute reference frame, the elements of the kinetic energy matrix are given by

$$\mathcal{K}_{\mathbf{r},\mathbf{r}'}^{(a)} \equiv \langle \mathbf{r}_1, \mathbf{r}_2, \dots, \mathbf{r}_M | \hat{\mathcal{K}} | \mathbf{r}'_1, \mathbf{r}'_2, \dots, \mathbf{r}'_M \rangle \quad (4.12)$$

where  $\mathbf{n}_i$  denote dimensionless position vectors, such that  $\mathbf{r}_i = a\mathbf{n}_i$ , and

$$|\mathbf{n}_1, \mathbf{n}_2, \dots, \mathbf{n}_M\rangle = \prod_{i=1}^M \left[ \sum_{\mathbf{p}_i \in \mathcal{N}} e^{-i\mathbf{n}_i \cdot \mathbf{p}_i} \right] |\mathbf{p}_1, \mathbf{p}_2, \dots, \mathbf{p}_M\rangle, \quad (4.13)$$

are the relevant Fock states in the absolute basis. The extent of the configuration space and the dimension of  $\mathcal{K}_{\mathbf{r}, \mathbf{r}'}^{(a)}$  can be reduced from  $N^{3M}$  to  $N^{3M-3}$  by singling out the center of mass motion of the  $M$  alpha particles. Accordingly, we introduce the following non-orthogonal transformation into relative coordinates

$$\mathbf{r}_{jM} \equiv \mathbf{r}_j - \mathbf{r}_M \quad \mathbf{r}_{CM} = \sum_{i=1}^M \frac{\mathbf{r}_i}{M} \quad j = 1, 2, \dots, M-1 \quad (4.14)$$

together with the associated basis of Fock states,

$$|\mathbf{n}_{1M}, \mathbf{n}_{2M}, \dots, \mathbf{n}_{M-1M}, \mathbf{n}_{CM}\rangle = \prod_{i=1}^{M-1} \left[ \sum_{\mathbf{p}_{iM} \in \mathcal{N}} e^{-i\mathbf{n}_{iM} \cdot \mathbf{p}_{iM}} \right] e^{-i\mathbf{n}_{CM} \cdot \mathbf{p}_{CM}} |\mathbf{p}_{1M}, \mathbf{p}_{2M}, \dots, \mathbf{p}_{M-1M}, \mathbf{p}_{CM}\rangle. \quad (4.15)$$

Consequently, the matrix elements of the kinetic energy operator in the relative basis just introduced become

$$\begin{aligned} \langle \mathbf{n}_{1M}, \mathbf{n}_{2M}, \dots, \mathbf{n}_{CM} | \hat{\mathcal{K}} | \mathbf{n}'_{1M}, \mathbf{n}'_{2M}, \dots, \mathbf{n}'_{CM} \rangle &\equiv \mathcal{K}_{\mathbf{n}, \mathbf{n}'}^{(r)} = -\frac{\hbar^2}{2ma^2} \sum_{\alpha} \sum_{\substack{l=-K \\ l \neq 0}}^K C_{|l|}^{(2P, K)} \\ &\cdot \left[ -\langle \mathbf{n}_{1M}, \mathbf{n}_{2M}, \dots, \mathbf{n}_{CM} | \mathbf{n}'_{1M}, \mathbf{n}'_{2M}, \dots, \mathbf{n}'_{CM} \rangle + \langle \mathbf{n}_{1M}, \dots, \mathbf{n}_{CM} | \mathbf{n}'_{1M} + \mathbf{l}\mathbf{e}_{\alpha}, \mathbf{n}'_{2M}, \dots, \mathbf{n}'_{CM} + \mathbf{l}\mathbf{e}_{\alpha}/M \rangle \right. \\ &+ \langle \mathbf{n}_{1M}, \dots, \mathbf{n}_{CM} | \mathbf{n}'_{1M}, \mathbf{n}'_{2M} + \mathbf{l}\mathbf{e}_{\alpha}, \dots, \mathbf{n}'_{CM} + \mathbf{l}\mathbf{e}_{\alpha}/M \rangle + \dots \\ &\left. + \langle \mathbf{n}_{1M}, \dots, \mathbf{n}_{CM} | \mathbf{n}'_{1M} + \mathbf{l}\mathbf{e}_{\alpha}, \mathbf{n}'_{2M} + \mathbf{l}\mathbf{e}_{\alpha}, \dots, \mathbf{n}'_{CM} - \mathbf{l}\mathbf{e}_{\alpha}(M-1)/M \rangle \right]. \end{aligned} \quad (4.16)$$

Replacing the brakets with the pertinent Kronecker deltas, we finally obtain

$$\begin{aligned} \mathcal{K}_{\mathbf{n}, \mathbf{n}'}^{(r)} &= -\frac{\hbar^2}{2ma^2} \sum_{\alpha} \sum_{\substack{l=-K \\ l \neq 0}}^K C_{|l|}^{(2P, K)} \left[ \delta_{\mathbf{n}_{CM}, \mathbf{n}'_{CM} - \mathbf{l}\mathbf{e}_{\alpha} \frac{M-1}{M}} \prod_{i=1}^{M-1} \delta_{\mathbf{n}_{iM}, \mathbf{n}'_{iM} + \mathbf{l}\mathbf{e}_{\alpha}} \right. \\ &\left. - \delta_{\mathbf{n}_{CM}, \mathbf{n}'_{CM}} \prod_{i=1}^{M-1} \delta_{\mathbf{n}_{iM}, \mathbf{n}'_{iM}} + \delta_{\mathbf{n}_{CM}, \mathbf{n}'_{CM} + \mathbf{l}\mathbf{e}_{\alpha} \frac{1}{M}} \sum_{i=1}^{M-1} \delta_{\mathbf{n}_{iM}, \mathbf{n}'_{iM} + \mathbf{l}\mathbf{e}_{\alpha}} \prod_{\substack{j=1 \\ j \neq i}}^{M-2} \delta_{\mathbf{n}_{jM}, \mathbf{n}'_{jM}} \right]. \end{aligned} \quad (4.17)$$

Choosing a reference frame in which the center of mass is at rest (i.e.  $\mathbf{p}_{CM} = 0$ ), the matrix elements of  $\hat{\mathcal{K}}$  become independent on the position of the center of the nucleus and the relevant deltas can be dropped from the last formula, thus

$$\mathcal{K}_{\mathbf{n}, \mathbf{n}'}^{(r, 0)} \equiv \langle \mathbf{n}_{1M}, \mathbf{n}_{2M}, \dots, \mathbf{n}_{CM} | \hat{\mathcal{T}} | \mathbf{n}'_{1M}, \mathbf{n}'_{2M}, \dots, \mathbf{n}'_{CM} \rangle_{\mathbf{p}_{CM}=0} = -\frac{\hbar^2}{2ma^2} \sum_{\alpha} \sum_{\substack{l=-K \\ l \neq 0}}^K C_{|l|}^{(2P, K)} \Delta_{(l, \alpha)} \quad (4.18)$$

where

$$\Delta_{(l,\alpha)} \equiv \prod_{i=1}^{M-1} \delta_{\mathbf{n}_{iM}, \mathbf{n}'_{iM} + l\mathbf{e}_\alpha} - \prod_{i=1}^{M-1} \delta_{\mathbf{n}_{iM}, \mathbf{n}'_{iM}} + \sum_{i=1}^{M-1} \delta_{\mathbf{n}_{iM}, \mathbf{n}'_{iM} + l\mathbf{e}_\alpha} \prod_{\substack{j=1 \\ j \neq i}}^{M-2} \delta_{\mathbf{n}_{jM}, \mathbf{n}'_{jM}} \quad (4.19)$$

reproduces the Laplace operator. After the reduction of the system to  $N^{3M-3}$  degrees of freedom, one may wonder whether the matrix elements of  $\mathcal{K}^{(r)}$  are invariant when the coordinate change in eq. (4.14) is performed *before* the discretization of  $K$  (cf. eq. (4.7)). The answer to this point is negative and the reason can be traced back to the non-orthogonality of the transformation into relative coordinates (cf. eq. (4.14)). Denoting the latter as  $\mathbf{r}'_i \equiv \mathbf{r}_{iM}$  for  $i < M$  and  $\mathbf{r}'_M \equiv \mathbf{r}_{CM}$  and computing the Jacobian matrix of the transformation,  $\mathbb{J}$ ,

$$\mathbb{J} \equiv \begin{pmatrix} 1 & 0 & \dots & \dots & 0 & -1 \\ 0 & 1 & 0 & \dots & 0 & -1 \\ \vdots & \ddots & \ddots & \ddots & \vdots & \vdots \\ 0 & \dots & 0 & 1 & 0 & -1 \\ 0 & \dots & \dots & 0 & 1 & -1 \\ 1/M & 1/M & \dots & \dots & \dots & 1/M \end{pmatrix}, \quad (4.20)$$

the resulting kinetic energy operator, in fact, is non-diagonal in the particle space,

$$K = -\frac{\hbar^2}{2m} \sum_{i,j,k=1}^M \mathbb{J}_{ji}^{-1} \mathbb{J}_{ki}^{-1} \nabla'_j \cdot \nabla'_k. \quad (4.21)$$

It is exactly the presence of different kinds of differential operators, namely pure and mixed second derivatives, that prevents the final rewriting of the matrix elements of eq. (4.20), after the cancellation of the center of mass momentum, to be consistent with eq. (4.18). Nevertheless, the equivalence between the latter two can be approached in the large volume and small lattice spacing limit ( $L \equiv Na \gtrsim 18$  fm).

Eventually, if Jacobi coordinates instead of the relative ones in eq. (4.14) were adopted, the coordinate transformation should have been effected *before* the discretization of  $K$  in eq. (4.7). The application of  $\mathcal{K}$  in absolute coordinates on the transformed basis of states, in fact, would have generated fractional displacements on both the CM coordinates and in all the other relative ones, thus implying the existence of nonzero matrix elements between non-existing lattice sites.

### 4.3.2 Potentials

Unlike the kinetic term, the definition of the lattice counterpart of the potentials (4.3) and (4.3) is straightforward, due to their locality and independence on spatial derivatives.

### 4.3.3 Angular momentum

A crucial role in the analysis in the next three chapters is played by the square of the collective angular momentum operator,  $L_{\text{tot}}^2$ , whose importance resides in the identification of the multiplets of eigenstates of the lattice Hamiltonian that share the same orbital quantum number and the same energy in the continuum limit. Differently from the previous case, the

functional form of this operator is left invariant by linear transformations of the coordinates  $\mathbb{J}$ ,

$$\begin{aligned} L_{\text{tot},\alpha} &= \sum_{i=1}^M L_{i,\alpha} = -i\hbar\epsilon_{\alpha\beta\gamma} \sum_{i=1}^M \beta_i \frac{\partial}{\partial \gamma_i} = -i\hbar\epsilon_{\alpha\beta\gamma} \sum_{i,j,k=1}^M \mathbb{J}_{ij}^{-1} \mathbb{J}_{ki} \beta'_j \frac{\partial}{\partial \gamma'_i} \\ &= -i\hbar\epsilon_{\alpha\beta\gamma} \sum_{j,k=1}^M \delta_{kj} \beta'_j \frac{\partial}{\partial \gamma'_i} = \sum_{i=1}^M L'_{i,\alpha} , \end{aligned} \quad (4.22)$$

where  $\alpha, \beta, \gamma \in x, y, z$ ,  $\epsilon_{\alpha\beta\gamma}$  is the Levi-Civita tensor with  $\epsilon_{xyz} = 1$  and summations over repeated greek indices are understood. Accordingly, the square of the collective angular momentum operator can be written irrespectively of the coordinate system as

$$\begin{aligned} L_{\text{tot}}^2 &= 2 \sum_{i < j} \mathbf{L}_i \cdot \mathbf{L}_j + \sum_i L_i^2 = -\hbar^2 \sum_{\beta, \gamma} \sum_{i < j} \left( 2\beta_i \beta_j \frac{\partial^2}{\partial \gamma_i \partial \gamma_j} - 2\beta_i \gamma_j \frac{\partial^2}{\partial \beta_j \partial \gamma_i} \right) \\ &\quad - \hbar^2 \sum_{\beta, \gamma} \sum_i \left( \beta_i^2 \frac{\partial^2}{\partial \gamma_i^2} - \gamma_i \frac{2}{3} \frac{\partial}{\partial \gamma_i} - \gamma_i \beta_i \frac{\partial^2}{\partial \beta_i \partial \gamma_i} \right) . \end{aligned} \quad (4.23)$$

Since all the contributions from the second-derivative terms with  $\beta = \gamma$  on the right hand side of eq. (4.23) vanish, each of the first three terms on the same side of the formula is Hermitian. The latter property is not fulfilled by the remaining two terms unless they are summed together.

Applying the improvement scheme outlined in C.1 with index  $K$ , the subsequent discretization of the  $\gamma_i \partial / \partial \gamma_i$  term of one-body part of eq. (4.23) gives

$$\mathcal{L}_i^2 \Big|_1 \equiv 2a\hbar^2 \sum_{\mathbf{n}_i \in \mathcal{N}} \sum_{\gamma} \sum_{k=1}^K C_k^{(1,K)}(\mathbf{n}_i)_{\gamma} \left[ a_i^{\dagger}(\mathbf{n}_i + k\mathbf{e}_{\gamma}) a_i(\mathbf{n}_i) - a_i^{\dagger}(\mathbf{n}_i - k\mathbf{e}_{\gamma}) a_i(\mathbf{n}_i) \right] , \quad (4.24)$$

whereas the one of the remaining one-body part of the same operator,  $\beta_i^2 \partial^2 / \partial \gamma_i^2$ , yields

$$\begin{aligned} \mathcal{L}_i^2 \Big|_2 &\equiv -\hbar^2 \sum_{\mathbf{n}_i \in \mathcal{N}} \sum_{\beta \neq \gamma} \sum_{k=1}^K C_k^{(2,K)} \left\{ 4(\mathbf{n}_i)_{\beta}^2 \left[ -2a_i^{\dagger}(\mathbf{n}_i) a_i(\mathbf{n}_i) + a_i^{\dagger}(\mathbf{n}_i + k\mathbf{e}_{\gamma}) a_i(\mathbf{n}_i) + a_i^{\dagger}(\mathbf{n}_i - k\mathbf{e}_{\gamma}) a_i(\mathbf{n}_i) \right] - (\mathbf{n}_i)_{\beta} (\mathbf{n}_i)_{\gamma} \right. \\ &\quad \cdot \left. \left[ a_i^{\dagger}(\mathbf{n}_i + k\mathbf{e}_{\beta} + k\mathbf{e}_{\gamma}) a_i(\mathbf{n}_i) + a_i^{\dagger}(\mathbf{n}_i - k\mathbf{e}_{\beta} - k\mathbf{e}_{\gamma}) a_i(\mathbf{n}_i) - a_i^{\dagger}(\mathbf{n}_i + k\mathbf{e}_{\beta} - k\mathbf{e}_{\gamma}) a_i(\mathbf{n}_i) - a_i^{\dagger}(\mathbf{n}_i - k\mathbf{e}_{\beta} + k\mathbf{e}_{\gamma}) a_i(\mathbf{n}_i) \right] \right\} . \end{aligned} \quad (4.25)$$

where  $C_k^{(2,K)} \equiv a^2 C_k^{(2P,K)}$ . Before introducing the ladder operators, all the diagonal terms in the greek indices of this part of  $L_{\text{tot}}^2$  have been ruled out. The presence of two different kinds of differential operators prevents, in fact, the cancellation of one half of the hopping terms coming from the second pure and mixed derivatives. Concerning the two-body part of eq. (4.23), the discretization process gives

$$\begin{aligned} \mathcal{L}_i \cdot \mathcal{L}_j \Big|_1 &= -a^2 \hbar^2 \sum_{\mathbf{n}_i, \mathbf{n}_j \in \mathcal{N}} \sum_{\beta, \gamma} \sum_{k=1}^K C_k^{(2M,K)}(\mathbf{n}_i)_{\beta} (\mathbf{n}_j)_{\beta} \\ &\quad \cdot \left[ a_i^{\dagger}(\mathbf{n}_i + k\mathbf{e}_{\gamma}) a_j^{\dagger}(\mathbf{n}_j + k\mathbf{e}_{\gamma}) a_j(\mathbf{n}_j) a_i(\mathbf{n}_i) + a_i^{\dagger}(\mathbf{n}_i - k\mathbf{e}_{\gamma}) a_j^{\dagger}(\mathbf{n}_j - k\mathbf{e}_{\gamma}) a_j(\mathbf{n}_j) a_i(\mathbf{n}_i) \right. \\ &\quad \left. - a_i^{\dagger}(\mathbf{n}_i + k\mathbf{e}_{\gamma}) a_j^{\dagger}(\mathbf{n}_j - k\mathbf{e}_{\gamma}) a_j(\mathbf{n}_j) a_i(\mathbf{n}_i) - a_i^{\dagger}(\mathbf{n}_i - k\mathbf{e}_{\gamma}) a_j^{\dagger}(\mathbf{n}_j + k\mathbf{e}_{\gamma}) a_j(\mathbf{n}_j) a_i(\mathbf{n}_i) \right] \end{aligned} \quad (4.26)$$

and

$$\begin{aligned} \mathcal{L}_i \cdot \mathcal{L}_j \Big|_2 &= a^2 \hbar^2 \sum_{\mathbf{n}_i, \mathbf{n}_j \in \mathcal{N}} \sum_{\beta, \gamma} \sum_{k=1}^K C_k^{(2M, K)}(\mathbf{n}_i)_\beta (\mathbf{n}_j)_\gamma \\ &\cdot \left[ a_i^\dagger(\mathbf{n}_i + \mathbf{k} \mathbf{e}_\gamma) a_j^\dagger(\mathbf{n}_j + \mathbf{k} \mathbf{e}_\beta) a_j(\mathbf{n}_j) a_i(\mathbf{n}_i) + a_i^\dagger(\mathbf{n}_i - \mathbf{k} \mathbf{e}_\gamma) a_j^\dagger(\mathbf{n}_j - \mathbf{k} \mathbf{e}_\beta) a_j(\mathbf{n}_j) a_i(\mathbf{n}_i) \right. \\ &\left. - a_i^\dagger(\mathbf{n}_i + \mathbf{k} \mathbf{e}_\gamma) a_j^\dagger(\mathbf{n}_j - \mathbf{k} \mathbf{e}_\beta) a_j(\mathbf{n}_j) a_i(\mathbf{n}_i) - a_i^\dagger(\mathbf{n}_i - \mathbf{k} \mathbf{e}_\gamma) a_j^\dagger(\mathbf{n}_j + \mathbf{k} \mathbf{e}_\beta) a_j(\mathbf{n}_j) a_i(\mathbf{n}_i) \right] . \end{aligned} \quad (4.27)$$

Due to the invariance of  $L_{\text{tot}}^2$ , we are allowed to apply the square of the collective angular momentum operator in relative coordinates to the relative basis of states (cf. eq. (4.14)), exploiting the results presented in eqs. (4.24)-(4.26). The subsequent cancellation of center of mass momentum,  $\mathbf{p}_{CM} = 0$ , yields finally the expression of the matrix element of the operator in the  $N^{3M-3} \times N^{3M-3}$  lattice,

$$\begin{aligned} \mathcal{L}_{\mathbf{n}, \mathbf{n}'}^{(r, 0)} &= \sum_i \langle \mathbf{n}_{1M} \dots \mathbf{n}_{CM} | \mathcal{L}_i'^2 | \mathbf{n}'_{1M} \dots \mathbf{n}'_{CM} \rangle_{\mathbf{p}_{CM}=0} \\ &\quad + 2 \sum_{i < j} \langle \mathbf{n}_{1M} \dots \mathbf{n}_{CM} | \mathcal{L}_i' \cdot \mathcal{L}_j' | \mathbf{n}'_{1M} \dots \mathbf{n}'_{CM} \rangle_{\mathbf{p}_{CM}=0} , \end{aligned} \quad (4.28)$$

where the one-body contribution is given by

$$\begin{aligned} \langle \mathbf{n}_{1M} \mathbf{n}_{2M} \dots \mathbf{n}_{CM} | \mathcal{L}_i'^2 | \mathbf{n}'_{1M} \mathbf{n}'_{2M} \dots \mathbf{n}'_{CM} \rangle_{\mathbf{p}_{CM}=0} &= -a^2 \hbar^2 \sum_{\beta \neq \gamma} \sum_{k=1}^K C_k^{(2P, K)} \left[ \prod_{\substack{l=1 \\ l \neq i}}^{M-1} \delta_{\mathbf{n}'_{lM}, \mathbf{n}_{lM}} \right] \left[ (\mathbf{n}_{iM})_\beta^2 \right. \\ &\cdot 4 \left( \delta_{\mathbf{n}_{iM}, \mathbf{n}'_{iM} + \mathbf{k} \mathbf{e}_\gamma} - 2 \delta_{\mathbf{n}_{iM}, \mathbf{n}'_{iM}} + \delta_{\mathbf{n}_{iM}, \mathbf{n}'_{iM} - \mathbf{k} \mathbf{e}_\gamma} \right) - (4/3) (\mathbf{n}_{iM})_\gamma \left( \delta_{\mathbf{n}_{iM}, \mathbf{n}'_{iM} + \mathbf{k} \mathbf{e}_\gamma} - \delta_{\mathbf{n}_{iM}, \mathbf{n}'_{iM} - \mathbf{k} \mathbf{e}_\gamma} \right) \\ &\left. - (\mathbf{n}_{iM})_\beta (\mathbf{n}_{iM})_\gamma \left( \delta_{\mathbf{n}_{iM}, \mathbf{n}'_{iM} + \mathbf{k} \mathbf{e}_\beta + \mathbf{k} \mathbf{e}_\gamma} + \delta_{\mathbf{n}_{iM}, \mathbf{n}'_{iM} - \mathbf{k} \mathbf{e}_\beta - \mathbf{k} \mathbf{e}_\gamma} - \delta_{\mathbf{n}_{iM}, \mathbf{n}'_{iM} - \mathbf{k} \mathbf{e}_\beta + \mathbf{k} \mathbf{e}_\gamma} - \delta_{\mathbf{n}_{iM}, \mathbf{n}'_{iM} + \mathbf{k} \mathbf{e}_\beta - \mathbf{k} \mathbf{e}_\gamma} \right) \right] . \end{aligned} \quad (4.29)$$

and the two-body one coincides with

$$\begin{aligned} \langle \mathbf{n}_{1M} \mathbf{n}_{2M} \dots \mathbf{n}_{CM} | \mathcal{L}_i' \cdot \mathcal{L}_j' | \mathbf{n}'_{1M} \mathbf{n}'_{2M} \dots \mathbf{n}'_{CM} \rangle_{\mathbf{p}_{CM}=0} &= -a^2 \hbar^2 \sum_{\beta, \gamma} \sum_{k=1}^K C_k^{(2M, K)} \left[ \prod_{\substack{l=1 \\ l \neq i, j}}^{M-1} \delta_{\mathbf{n}'_{lM}, \mathbf{n}_{lM}} \right] \\ &\cdot \left[ (\mathbf{n}_{iM})_\beta (\mathbf{n}_{jM})_\beta \left( \delta_{\mathbf{n}_{iM}, \mathbf{n}'_{iM} + \mathbf{k} \mathbf{e}_\gamma} \delta_{\mathbf{n}_{jM}, \mathbf{n}'_{jM} + \mathbf{k} \mathbf{e}_\gamma} + \delta_{\mathbf{n}_{iM}, \mathbf{n}'_{iM} - \mathbf{k} \mathbf{e}_\gamma} \delta_{\mathbf{n}_{jM}, \mathbf{n}'_{jM} - \mathbf{k} \mathbf{e}_\gamma} \right. \right. \\ &\quad \left. \left. - \delta_{\mathbf{n}_{iM}, \mathbf{n}'_{iM} - \mathbf{k} \mathbf{e}_\gamma} \delta_{\mathbf{n}_{jM}, \mathbf{n}'_{jM} + \mathbf{k} \mathbf{e}_\gamma} - \delta_{\mathbf{n}_{iM}, \mathbf{n}'_{iM} + \mathbf{k} \mathbf{e}_\gamma} \delta_{\mathbf{n}_{jM}, \mathbf{n}'_{jM} - \mathbf{k} \mathbf{e}_\gamma} \right) \right. \\ &\left. - (\mathbf{n}_{iM})_\beta (\mathbf{n}_{jM})_\gamma \left( \delta_{\mathbf{n}_{iM}, \mathbf{n}'_{iM} + \mathbf{k} \mathbf{e}_\gamma} \delta_{\mathbf{n}_{jM}, \mathbf{n}'_{jM} + \mathbf{k} \mathbf{e}_\beta} + \delta_{\mathbf{n}_{iM}, \mathbf{n}'_{iM} - \mathbf{k} \mathbf{e}_\gamma} \delta_{\mathbf{n}_{jM}, \mathbf{n}'_{jM} - \mathbf{k} \mathbf{e}_\beta} \right. \right. \\ &\quad \left. \left. - \delta_{\mathbf{n}_{iM}, \mathbf{n}'_{iM} - \mathbf{k} \mathbf{e}_\gamma} \delta_{\mathbf{n}_{jM}, \mathbf{n}'_{jM} + \mathbf{k} \mathbf{e}_\beta} - \delta_{\mathbf{n}_{iM}, \mathbf{n}'_{iM} + \mathbf{k} \mathbf{e}_\gamma} \delta_{\mathbf{n}_{jM}, \mathbf{n}'_{jM} - \mathbf{k} \mathbf{e}_\beta} \right) \right] . \end{aligned} \quad (4.30)$$

Like in the previous case, the application of the discretized version of this operator in absolute and relative (i.e. primed) coordinates to the relative basis, even if followed by the cancellation of the center of mass momentum, gives rise to two unequal results, namely

$$\mathcal{L}_{\mathbf{n}', \mathbf{n}}^{2(r, 0)} \neq \mathcal{L}_{\mathbf{n}', \mathbf{n}}^{(r, 0)} . \quad (4.31)$$

respectively. This is a consequence of the discretization of the one-body terms containing second mixed and pure derivatives (cf. eq. (4.23)), which transform together under linear coordinate changes. As observed, also the cancellation of diagonal terms in the Greek indices in the summations for the one-body terms of  $L_{\text{tot}}^2$  (i.e. the ones with  $\beta = \gamma$  in the second row



of eq. (4.23)), that are straightforward in the continuum, does not occur in the lattice. Nevertheless, in the large volume and small lattice spacing limit, the average values of the squared collective angular momentum operator calculated in the two approaches (cf. eq. (4.31)) coincide, as expected in the case of the kinetic energy operator.

Finally, another feature of the discretized version of  $L_{\text{tot}}^2$  is represented by the loss of hermiticity, due again to the last two terms of the one-body part in eq. (4.23), whose sum is self-adjoint only in the continuum.

## 4.4 Symmetries

Let us begin the analysis of the transformation properties of the Hamiltonian under spacetime symmetries. Since the potentials depend only on interparticle distances, eq. (4.1) is invariant under parity,  $\mathcal{P}$ ,

$$[H, \mathcal{P}] = 0, \quad (4.32)$$

a feature that is preserved by its realization on the cubic lattice. This invariance allows for the construction of projectors to the two irreducible representations,  $+$  and  $-$ , of the parity group ( $\approx \mathcal{G}_2$ ),

$$P_{\pm} = \mathbb{1} \pm \mathcal{P} \quad (4.33)$$

acting on continuum (and lattice) eigenfunctions of  $H$  (resp.  $\mathcal{H}$ ), that can thus bear the two irrep labels. Moreover, the implementation of the reducible  $3M - 3$  dimensional representation of the inversion operator on the lattice,  $\mathcal{P}$ , omitted in the last section, depends on the choice of the map between lattice points  $\mathbf{n}_{iM}$  and the physical points on  $\mathbb{R}^3$ .

Furthermore, the Hamiltonian of a system of  $M$  particles interacting with central forces is rotationally invariant,

$$[H, \mathbf{L}_{\text{tot}}] = 0 \text{ and } [H, L_i^2] = 0 \quad (4.34)$$

with  $i = 1, 2, \dots, M$ . Switching to the relative reference frame, cf. eq. (4.13), and setting the center of mass momentum to zero,  $H|_{\mathbf{p}_{CM}=0} \equiv H_r$ , this invariance is naturally preserved, but the relative squared angular momentum operator  $L_{iM}^2 \equiv (L_i')^2$  of each of the particles no longer commutes with the relative Hamiltonian, due to the non-orthogonality of the linear transformation,  $\mathbb{J}$ , to the relative reference frame, cf. eq. (4.20),

$$[H_r, (L_i')^2] \neq 0 \quad (4.35)$$

where  $i = 1, 2, \dots, M - 1$ . Therefore, continuum eigenstates of  $H_r$  can be labeled with the eigenvalues of the squared collective angular momentum, quadratic Casimir operator of  $\text{SO}(3)$ , and by the ones of its third component,  $L_{\text{tot},z}$ , Casimir of the group of rotations on the plane,

$$\begin{array}{ccc} \text{SO}(3) & \supset & \text{SO}(2) \\ \downarrow & & \downarrow \\ \ell & & m, \end{array} \quad (4.36)$$

i.e. as basis of the  $2\ell + 1$  dimensional irreducible representation of  $\text{SO}(3)$  and eigenstates of rotations about the  $z$  axis. However, the discretized Hamiltonian on the cubic lattice does not inherit this symmetry, being left invariant only by a subset of  $\text{SO}(3)$ , forming the cubic group,  $\mathcal{O}$ , of order 24 and isomorphic to the permutation group of four elements,  $S_4$ . Equivalently,

the dependence of the collective angular momentum on spatial derivatives and, therefore, the necessity of resorting to an approximation scheme, prevents its commutation with the lattice Hamiltonian.

Nevertheless, like in the previous case, the basis vectors of each irrep of  $\mathcal{O}$  can be chosen to be simultaneously diagonal with respect to a subset of its operations. Considering again the  $z$  axis, the set generated by a counterclockwise rotation of  $\pi/2$ ,  $\mathcal{R}_z^{\pi/2}$ , forms an abelian group, isomorphic to the cyclic group of order four,  $\mathcal{C}_4$ . Like  $\text{SO}(2)$  with  $\text{SO}(3)$ , also  $\mathcal{C}_4$  is not a normal subgroup of  $\mathcal{O}$ , as the conjugacy classes  $3C_4^2(\pi)$  and  $6C_4(\pi/2)$  of the latter are only partially included in the cyclic group. Since the complex 1-dimensional inequivalent irreps of  $\mathcal{C}_4$  are four and the distinct eigenvalues of  $\mathcal{R}_z^{\pi/2}$  are  $\pm 1$  and  $\pm i$ , we can label the irreducible representations of the cyclic group with the integers  $I_z$  ranging from 0 to three,

$$R_z^{\pi/2} = \exp\left(-i\frac{\pi}{2}I_z\right) . \quad (4.37)$$

Diagonalizing the lattice Hamiltonian together with  $\mathcal{R}_z^{\pi/2}$ ,

$$(\mathcal{H} + \mathcal{R}_z^{\pi/2})\Psi = (E + R_z^{\pi/2})\Psi , \quad (4.38)$$

the simultaneous eigenstates  $\Psi$  can be denoted, thus, with the irreducible representations of  $\mathcal{O}$  and  $\mathcal{C}_4$  (i.e. *quantum numbers*)

$$\begin{array}{ccc} \mathcal{O} & \supset & \mathcal{C}_4 \\ \downarrow & & \downarrow \\ \Gamma & & I_z , \end{array} \quad (4.39)$$

where  $\Gamma \in A_1, A_2, E, T_1$  and  $T_2$ . Due to this descent in symmetry, each of the original  $2\ell + 1$  degenerate eigenstates of  $H$  is split into smaller multiplets, their dimension ranging from one to three (cf. tab. 4.2).

As in the case of parity, by expressing the cubic group elements  $g$  as terns of Euler angles,  $(\alpha, \beta, \gamma)$ , it is possible to construct projectors on the irreps of  $\mathcal{O}$  for spherical tensors of rank  $2\ell + 1$  [137],

$$P_\Gamma^{2\ell+1} = \sum_{g \in \mathcal{O}} \chi_\Gamma(g) D^\ell(g) , \quad (4.40)$$

where the  $D^\ell(g)$  are Wigner D-matrices,  $D_{mk}^\ell(\alpha, \beta, \gamma)$ , and  $\chi_\Gamma(g)$  are characters of the irrep  $\Gamma$  of the cubic group. It is exactly from the columns (rows) of the projector matrix that cubic basis vectors (tensors) from spherical basis vectors (tensors) can be constructed [188]. Nevertheless, when the same irrep of  $\mathcal{O}$  appears more than once in the decomposition of  $D^\ell$  (cf. tab. 4.2) further rearrangement on the outcoming linear combinations is needed (cf. app. C.3). Moreover, only tensors or basis vectors having the same projection of the angular momentum along the  $z$  axis,  $m$ , *modulo* 4 mix among themselves when projected to any cubic group irrep.

Eventually, we conclude the subsection with particle space symmetries. Since both the relative and the full Hamiltonian commute with the permutation operators of  $M$  particles,

$$[H, \mathcal{S}_g] = [H_r, \mathcal{S}_g] = 0 , \quad (4.41)$$

where  $g \in \mathcal{S}_M$ , the permutation group of  $M$  elements represents a symmetry for the system. Since the representatives of the sequences of transpositions,  $\mathcal{S}_g$  does not affect the configura-

tion space on which  $\mathcal{O}$  and  $\mathcal{P}$  act, they naturally commute with the elements of the space-time symmetry groups. In the  ${}^8\text{Be}$  case, where two particle transposition (12) coincides with parity, the latter assertion is ensured by means of commutation between rotations and space inversion.

$\Gamma$	$D^0$	$D^1$	$D^2$	$D^3$	$D^4$	$D^5$	$D^6$	$D^7$	$D^8$
$A_1$	1	0	0	0	1	0	1	0	1
$A_2$	0	0	0	1	0	0	1	1	0
$E$	0	0	1	0	1	1	1	1	2
$T_1$	0	1	0	1	1	2	1	2	2
$T_2$	0	0	1	1	1	1	2	2	2

TABLE 4.1 – Coefficients of the decomposition of the representations of the spherical tensors of rank  $2\ell + 1$ ,  $D^\ell$  into irreps of the cubic group. These can be obtained by repeated application of the Great Orthogonality Theorem for characters to the  $2\ell + 1$ -dimensional representations of  $\text{SO}(3)$  and the irreps of  $\mathcal{O}$ .

In the general case, whenever the states do not transform according to the bosonic representations,

$$\square\square\dots\square \sim [M] , \quad (4.42)$$

or the fermionic ones,

$$\begin{array}{c} \square \\ \vdots \\ \square \end{array} \sim [1^M] , \quad (4.43)$$

they appear in the energy spectrum as repeated degenerate cubic group multiplets, their multiplicity being equal to the dimension of the irrep of  $S_M$  to which they belong. It follows that Young diagrams or partitions can be included among the labels of the simultaneous eigenstates  $\Psi$  (cf. eq. (4.38)). Due to the bosonic nature of the  $\alpha$ -particles, the construction of the projector on the completely symmetric irrep of the permutation group,

$$P_{\square\square\dots\square} = \sum_{g \in \mathcal{S}_M} \chi_{\square\square\dots\square}(g) \mathcal{S}_g = \sum_{g \in \mathcal{S}_M} \mathcal{S}_g , \quad (4.44)$$

turns out to be useful in the computation of the numerical eigenstates of the lattice Hamiltonian  $\mathcal{H}_r$ , see sec. 4.5.1, since unphysical eigenstates of parastatistic or fermionic nature are filtered out. In analogous way the projectors to all the other irreducible representations of  $S_M$  can be constructed.

## 4.5 Physical Observables

In the analysis of the low-lying eigenstates of the  ${}^8\text{Be}$ ,  ${}^{12}\text{C}$  and  ${}^{16}\text{O}$  nuclei in chaps. 5, 6 and 7, we focus mainly on the average values of the kinetic and potential energy and the total squared angular momentum, presented in operator form in sec. 4.3. However, the discretization scheme for the differential operators adopted in the latter section (cf. apps. C.1 and C.2), may apply also for a precise implementation of the electric (magnetic) multipole transition operators [135], whose matrix elements with the lattice eigenstates yield the reduced transition probabilities,  $B(E\ell)$  [ $B(M\ell)$ ], and the electric (magnetic) multipole moments [135], not covered

by the present dissertation. In the  $^{12}\text{C}$  case, the resulting selection rules can be compared with the ones from the triangular  $\alpha$ -cluster model in refs. [158, 159].

Eventually, the average value of the interparticle distance is also object of our study of finite-volume and discretization effects and the realization of the associated operator is based on the map between lattice and physical coordinates given in the next subsection.

#### 4.5.1 Space coordinates

The computation of matrix elements of lattice operators in the configuration-space representation requires the replacement of the lattice coordinates  $n_{nM,\alpha}$  introduced in sec. 4.3.1 by their physical counterpart  $(r_{nM,\alpha})_{\text{phys}}$ . This is the case of the collective squared angular momentum operator (cf. eqs. (4.27)-(4.29)) and  $V^{\text{II}}$  and  $V^{\text{III}}$  terms of the Hamiltonian which are diagonal in the  $3M - 3$  dimensional configuration space, due to the absence of velocity-dependent potentials.

Therefore, it is necessary to define a map between lattice points and the physical coordinates. If we encode the former by an unique positive integer index  $r$ , ranging from 0 to  $N^{3M-3} - 1$ , the lattice coordinates  $n_{nM,\alpha}$  are can be extracted from  $r$  via the *modulus* function,

$$n_{nM,x} = \text{mod} \left( \left\lfloor \frac{r}{N^n} \right\rfloor, N \right), \quad n_{nM,y} = \text{mod} \left( \left\lfloor \frac{r}{N^{n+1}} \right\rfloor, N \right), \quad n_{nM,z} = \text{mod} \left( \left\lfloor \frac{r}{N^{n+2}} \right\rfloor, N \right), \quad (4.45)$$

with  $n \in 1, 2, \dots, M - 1$ . An invertible map from the latter to physical coordinates is provided by

$$(r_{nM,\alpha})_{\text{phys}} = \begin{cases} a n_{nM,\alpha} & \text{if } n_{nM,\alpha} < N/2 \\ a (n_{nM,\alpha} - N) & \text{if } n_{nM,\alpha} \geq N/2 \end{cases} \quad (4.46)$$

where the lattice spacing  $a$  is treated here as a dimensional parameter, expressed in femtometres. The three-dimensional configuration space is, thus, reduced to a cubic finite set of points encompassing the origin, which coincides with the centroid of the lattice only when the number of points per dimension  $N$  is odd. However, the cubic region can be centered in the origin of the axes by considering the following definition of the physical coordinates [156]

$$(r_{nM,\alpha})_{\text{phys}} = a \left( n_{nM,\alpha} - \frac{N-1}{2} \right). \quad (4.47)$$

As a consequence, when  $N$  is even the physical points  $(r_{nM,\alpha})_{\text{phys}}$  do not include the origin any more and assume only half-integer values. This second map between lattice and physical coordinates, that had been already adopted in a study on rotational invariance restoration of lattice eigenfunctions in ref. [156], is preferable for plotting the discretized wavefunctions.

Finally, it is worth remarking that, if the lattice configuration space is restricted to the first octant of the three-dimensional space (cf. eq. (4.46) with a sign reversal in the argument of the second row) the average values of  $\mathcal{L}^2$  on states with good angular momentum converge to incorrect values in the continuum and infinite volume limit, due to the exclusion of physical points bearing negative entries.

### 4.5.2 Binding energy

Another physical quantity of interest for our analysis is the binding energy  $BE(Z, N)$  that can be obtained from the energy of the lattice Hamiltonian  $\mathcal{H}$  ground state,  $E_{0+}$ , via the relation

$$BE(2M, 2M) = 2Mm_{1H}c^2 + 2Mm_n c^2 - Mm_{4He}c^2 - E_{0+} . \quad (4.48)$$

Since the parameters of the Ali-Bodmer potential are fitted to the  $\alpha - \alpha$  scattering lengths, the experimental value of the binding energy of  ${}^8\text{Be}$  from eq. (4.48) differs from the observational one, even in the large boxes limit. On the other hand, for  ${}^{12}\text{C}$  the addition of a 3-body potential permitted to fix the ground state energy to the  $3\alpha$  decay threshold, thus yielding binding energies consistent with their experimental counterparts, provided the experimental energy gap between the Hoyle state and the former breakup threshold is added to  $E_{0+}$ .

### 4.5.3 Multiplet averaging

The multiplet averaged value of energy the is defined in ref. [3] as

$$E(\ell_A^P) = \sum_{\Gamma \in \mathcal{O}} \frac{\chi^\Gamma(E)}{2\ell + 1} E(\ell_\Gamma^P) , \quad (4.49)$$

where  $\Gamma$  is an irreducible representation of the cubic group (cf. tab. C.8),  $\chi^\Gamma(E)$  is its character with respect to the conjugacy class of the identity and  $P$  is the eigenvalue of the inversion operator,  $\mathcal{P}$ . The same operation can be performed for average values of operators representing physical observables  $\mathcal{Q}$  on lattice eigenstates,

$$\langle \mathcal{Q} \rangle(\ell_A^P) = \sum_{\Gamma \in \mathcal{O}} \frac{\chi^\Gamma(E)}{2\ell + 1} \langle \mathcal{Q} \rangle(\ell_\Gamma^P) . \quad (4.50)$$

In particular, the latter formula that has been extensively applied for the squared angular momentum operator,  $\mathcal{L}^2$ , in the analysis of finite-volume and discretization effects.

## 4.6 Boundary conditions

So far, no reference to the way in which the Cauchy problem associated to the relative Hamiltonian  $H_r$  (plus, eventually, the cubic group operation) has been made. A customary choice in lattice realizations of Schrödinger equation is the imposition of periodic boundary conditions (PBC) on the eigenfunctions,

$$\Psi^{(q)}(\mathbf{n} + \mathbf{m}N) = \Psi^{(q)}(\mathbf{n}), \quad (4.51)$$

where  $\mathbf{n}$  and  $\mathbf{m}$  are two vectors of integers. A practical realization of this constraint is provided by the application of the *modulo*  $N$  functions on the array indices corresponding to hopping terms of the lattice operators involved. This yields the appearance of more entries in the matrix realizations of quantum mechanical operators, whose explicit storage has been wisely avoided.

Another choice of boundary conditions, subject of a recent investigation on three-body systems

[89], is given by the twisted boundary conditions (TBC) [189],

$$\Psi^{(q)}(\mathbf{n} + \mathbf{m}N) = e^{i\theta \cdot \mathbf{m}} \Psi^{(q)}(\mathbf{n}) . \quad (4.52)$$

Since for twisting angles equal to zero,  $\theta_\alpha = 0$ , the two constraints coincide, eq. (4.52) can be considered as a generalization to complex phases of the usual PBC. In particular, it has been proven that in two-body systems *i-periodic* boundaries, i.e. with  $\theta_\alpha = \pi/2$ , reduce significantly the leading order exponential dependence of the finite-volume energy corrections and that analogous suppressions of finite-volume effects for three-body systems can be achieved [89]. Nevertheless, since our aim is the analysis of the breaking of rotational invariance in four  $\alpha$  particle systems, we chose the computationally cheaper PBC.

## 4.7 Deterministic approaches

As it can be inferred from sec. 4.5.1, the extent of configuration space of  $^{12}\text{C}$  and  $^{16}\text{O}$  on the cubic lattice requires the storage of vectors and matrices with a huge amount of entries. For instance, any eigenvector of the lattice Hamiltonian with  $N = 31$  for the former nucleus implies the storage of almost nine hundred millions of entries, a number that rises to circa  $32 \cdot 10^9$  double precision items if all the meaningful operators involved in the diagonalization and eigenspace analysis stored as sparse matrices are considered. Although in the previous literature on the subject (cf. refs. [3] and [68]) pre-built numerical diagonalization functions for the Hamiltonian matrix were considered, the increased dimension of the lattice operators acting on the eigenvectors led us to the choice of the memory-saving *Lanczos algorithm*, already adopted in ref. [190]. This iterative method (cf. sec. 4.7.1) reduces the overall storage cost to the one of the subset of eigenvectors of interest and makes extensive use of indexing.

### 4.7.1 The Lanczos algorithm

The algorithm chosen for the simultaneous diagonalization of  $\mathcal{H}_r$  and  $\mathcal{R}_z^{\pi/2}$  is an implementation of the *Lanczos algorithm* and is based on the repeated multiplication of the matrix of interest on a vector followed by its subsequent normalization, like the *power* or *Von Mises iteration*. Once a suitable initial state is constructed, our method produces a c-number and a vector, that reproduce the lowest signed eigenvalue of the matrix and the relevant eigenvector respectively with increasing precision after an increasing number of iterations.

Now, let us denote the trial state, to be initialized before the beginning of the iteration loop, with  $\Psi_0$ . Although also random states could be used for the purpose, the construction of trial states that reflect the symmetries of the Hamiltonian often reduces the number of necessary iterations. Besides, an initial value for the eigenenergy,  $E_0$ , is entered together with  $\Psi_0$  and the *pivot energy*,  $E_p$ , a c-number that ensures the convergence of the desired eigenvector to the one corresponding to the lowest signed eigenvalue. Once  $\Psi_0$  is passed into the loop, the updated vector in the beginning of the  $k + 1$ -th iteration,  $\Psi_{k+1}^{\text{new}}$ , is related to the resulting state from the previous iteration,  $\Psi_k$ , via the recursive expression

$$\Psi_{k+1}^{\text{new}} = (\mathcal{H}_r + \mathcal{R}_z^{\pi/2} - E_p) \Psi_k , \quad (4.53)$$



i.e. a multiplication of  $\Psi_k$  by the matrices to be simultaneously diagonalized followed by the subtraction of the same vector multiplied by  $E_p$ . Next, the updated value of the energy eigenvalue is drawn from the updated state by taking the scalar product of  $\Psi_{k+1}^{new}$  with  $\Psi_k$ ,

$$E_{k+1} = (\Psi_k, \Psi_{k+1}^{new}) + E_p . \quad (4.54)$$

Then, also the pivot energy undergoes an update. If the quantity  $E_{k+1} - E_k$  turns out to be positive (negative), in fact,  $E_p$  is incremented (decremented) by a positive integer, whose magnitude is usually different in the two cases,

$$E_p^{new} = E_p + \Delta[\text{sign}(E_{k+1} - E_k)] \quad (4.55)$$

where  $\Delta[+1] > \Delta[-1]$ , in order to make the series  $\{E_k\}$  converge to  $E_r$ . More precisely, in all the computations that follow,  $\Delta[+1]$  is tuned to be approximately ten times larger than  $\Delta[-1]$ , even if further adjustment of these two parameters depending on the  $\mathcal{O}$  irreps of the eigenstates of interest leads to faster convergence. At this point, it is worth observing that, if the pivot energy is set equal to zero and its update loop, cf. eq. (4.55), is suppressed, the body of this version of the Lanczos algorithm would exactly coincide with the one of the *power iteration*. Finally, as in the *Von Mises iteration*, the normalization of the  $k + 1$ -times improved eigenfunction,

$$\Psi_{k+1} = \frac{\Psi_{k+1}^{new}}{\|\Psi_{k+1}^{new}\|} , \quad (4.56)$$

ends the body of the iteration loop, that runs until the absolute value of the difference between the updated energy eigenvalue and  $E_k$  falls below a given value of precision,  $\delta_C$ , customarily set equal to  $10^{-9}$  or  $10^{-10}$  MeV. The convergence of the outcoming state vector to the actual eigenfunction of  $\mathcal{H}_r$  and  $\mathcal{R}_Z^{\pi/2}$  is ensured by both the non-degeneracy of the common eigenvalues of the two matrices and by the construction of a trial state with a nonzero component in the direction of the eigenvector associated to the ground state: in case one of these two conditions is not satisfied, convergence of the  $\{\Psi_k\}$  series is no longer guaranteed.

Moreover, the number of iterations required to attain the given precision,  $\delta_C$ , in the extraction of the eigenvalues grows not only with the box size,  $N$ , (i.e. with the dimension of the Hamiltonian matrix), but also with the inverse of lattice spacing. This is due to the fact that eigenenergies get closer in magnitude for small values of  $a$  and the eigenvector under processing,  $\Psi_k$ , may *oscillate* many times about the neighbouring eigenstates during the iterations before converging. Besides, a wise choice of the trial wavefunction turns out to reduce significantly the number of required iterations and can stabilize the process.

The bare Lanczos iteration just described, however, does not allow for the extraction of any other eigenvector than the ground state unless an orthogonalization scheme involving the already extracted states is introduced. In order to access a wider region of the spectrum (e.g.  $n + 1$  eigenstates), *Gram-Schmidt* orthogonalization has been introduced into the body of the iteration loop. If  $\Psi^{(0)}, \Psi^{(1)}, \dots, \Psi^{(n-1)}$  is a set of  $n$  converged states, the remaining eigenstate,  $\Psi_{k+1}^{(n)}$ , is finally orthogonalized in the end of each iteration with respect to the former eigensubspace. It is exactly this piece of the puzzle that prevents  $\Psi_{k+1}^{(n)}$  to collapse into the ground state of the system, even when the initial trial function maximizes the overlap with the target eigenstate.

Furthermore, projectors upon cubic and permutation group irreps (cf. eq. (4.44)) have been

applied to the  $\Psi_{k+1}^{(n)}$  state just before orthonormalization, thus allowing for the investigation of specific regions of the spectrum of the two compatible operators. A projector on a cubic group irrep, for instance, is constructed from eq. (4.40), with the Wigner D matrix,  $D^J(\alpha, \beta, \gamma)$ , replaced by a representative of the element  $(\alpha, \beta, \gamma) \in \mathcal{O}$  in the reducible  $N^{3M-3}$ -dimensional representation of the eigenstates of  $\mathcal{H}_r$ .

Before concluding the paragraph, special attention has to be devoted to the  $T_1$  and  $T_2$  eigenstates of  $\mathcal{H}_r + \mathcal{R}_z^{\pi/2}$ . Even if the spectrum of the matrix is complex, the power method implemented in the space of real vectors of dimension  $N^{3M-3}$ , does not allow for the extraction of complex eigenvalues with nonzero imaginary part and the relevant eigenvectors, transforming as the 1 and 3 irreps of  $\mathcal{G}_4$ . The outcoming vectors are real and orthogonal among themselves and remain associated to (almost) degenerate real energy eigenvalues. Since the remaining partner of the  $T_1$  ( $T_2$ ) multiplet, with  $I_z = 0$  (2), transforms in a separate block under the operations of  $\mathcal{G}_4$  and the exact eigenvectors are related by complex conjugation,

$$\Psi_{\Gamma, I_z=3} = [\Psi_{\Gamma, I_z=1}]^* \quad (4.57)$$

the true common eigenvectors of  $\mathcal{H}_r$  and  $\mathcal{R}_z^{\pi/2}$  can be drawn from the real degenerate ones,  $\Psi_{\Gamma}^{(p)}$  and  $\Psi_{\Gamma}^{(q)}$ , by means of a SU(2) transformation on the corresponding eigensubspace,

$$\begin{pmatrix} \Psi_{\Gamma, I_z=1} \\ \Psi_{\Gamma, I_z=3} \end{pmatrix} = \frac{1}{\sqrt{2}} \begin{pmatrix} \Psi_{\Gamma}^{(p)} + i\Psi_{\Gamma}^{(q)} \\ \Psi_{\Gamma}^{(p)} - i\Psi_{\Gamma}^{(q)} \end{pmatrix}. \quad (4.58)$$

Since  $\mathcal{G}_4$  is Abelian, made of four rotations about the same axis, any 2-dimensional representation of it can be reduced to a direct sum of 1-dimensional irreps, provided the similarity matrix is allowed to be complex.

As done with the cubic and the permutation group, projectors on the real ( $I_z = 0, 2$ ) irreducible representation of  $\mathcal{G}_4$  can be constructed and introduced in the iteration loop, thus halving (reducing to one third) the memory consumption for the storage of  $E$  ( $T_1$  and  $T_2$ ) states and extending the accessible region of the low-energy spectrum of the two nuclei considered here.

#### a) Parallel implementation

The iteration code pointed out in the previous section has been written first in MATLAB and in Fortran 90 and, finally, in CUDA C++. Although devoid of the vector indexing conventions of MATLAB, Fortran 90 permitted us to perform parallel computations on the available clusters of CPU processors (cf. *Acknowledgements*). The original MATLAB codes drafted for the first tests, in fact, have been rewritten in the latter language using the pre-built Message Passing Interface (MPI) routines. In particular, each of the converged eigenvectors has been assigned to a different processor (referred also as *rank*) on the same node whereas, in the succeeding versions of the MPI codes, the eigenvectors themselves have been split into different ranks, in order to achieve further speedup. Nevertheless, for the large-lattice ( $25 \leq N \leq 31$ ) diagonalizations concerning  $^{12}\text{C}$ , the exploitation of the graphic cards (GPUs) of the same cluster has been considered, thus leading to a significant reduction in the computational times (up to a factor of  $5 \cdot 10^{-2}$ ) for the given box size interval. Accordingly, the Fortran MPI code has been rewritten in CUDA C++ in such a way that each of the vectors, assigned to a single CPU (*host*), is copied, processed and analyzed entirely on a single GPU core (*device*)



and only finally copied back to the host, for the backup of the vector in the hard disk memory. This final rewriting of the codes for the diagonalization and the analysis of the state vectors allowed us to process vectors with  $N = 31$  of  $^{12}\text{C}$  and  $N = 10$  of  $^{16}\text{O}$  and a precision  $\delta_C = 10^{-10}$  (cf. sec. 4.7.1) within six hours of running time per each lattice eigenstate. Finally, the use of both the GPU units contained in a single node for the storage of each state vector allows for an extension of the  $^{12}\text{C}$  diagonalizations to the region  $32 \leq N \leq 35$ , whereas for  $^{16}\text{O}$  with  $N \geq 11$  more nodes are required.

### 4.7.2 The Adiabatic Projection Method

We conclude the treatment of deterministic approaches to the eigenvalue problem by illustrating a method that underlies our implementation of the Worldline Monte Carlo approach in sec. 4.8.1. The technique sinks its roots in the definition of transition amplitudes, calculated between a general  $M$ -particle trial state  $|\Psi(0)\rangle$  and its evolution at time  $t$  under the action of the Hamiltonian  $H$  (e.g. eq. (4.1)),

$$\langle 0|t\rangle \equiv \langle \Psi(0)|e^{-itH/\hbar}|\Psi(0)\rangle. \quad (4.59)$$

In the lattice framework,  $|\Psi(0)\rangle$  represents a vector of  $N^{3M}$  entries, which can be resized to  $N^{3M-3}$  elements in the relative reference frame. In the latter case,  $\mathcal{H}$  is replaced by the lattice Hamiltonian  $\mathcal{H}_r$ , which represents a  $N^{3M-3} \times N^{3N-3}$  band-diagonal matrix (cf. sec. 4.2).

In a fashion that recalls the construction of Feynman path integrals (cf. sec. 2.1 in ref. [191]), let us perform a *Wick rotation* to Euclidean time [192],  $\tau \equiv it$ , a quantity that in the Monte Carlo simulations is regarded as a real parameter [12], in analogy with the factor  $\beta = 1/k_B T$  in statistical mechanics [191]. Next, we split the imaginary time variable into  $N_t$  intervals of step  $a_t$ , treating  $\tau$  as a real variable. Since  $\mathcal{H}$  is time-independent, the time evolution operator or *transfer matrix* [12, 193, 194] for the lattice Hamiltonian can be rewritten as

$$e^{-\tau\mathcal{H}/\hbar} = \lim_{N_t \rightarrow \infty} \left( e^{-a_t\mathcal{H}/\hbar} \right)^{N_t}, \quad (4.60)$$

where  $\tau = a_t N_t$ . If  $N_t$  is large enough, the expression on the r.h.s. of eq. (4.61) can be reduced to the one of a product between elementary transfer matrices,

$$e^{-\tau\mathcal{H}/\hbar} \approx \prod_{i=1}^{N_t} e^{-a_t\mathcal{H}/\hbar} = \left( e^{-a_t\mathcal{H}/\hbar} \right)^{N_t}. \quad (4.61)$$

a rewriting referenced in literature as *Trotter-Suzuki approximation* [195, 196]. When the latter condition is verified and  $a_t$  is sufficiently small, the elementary transfer matrix can be simplified in turn by an expansion in powers of  $a_t$ ,

$$\mathcal{T} \equiv e^{-a_t\mathcal{H}/\hbar} \approx \mathbb{1} - \frac{a_t}{\hbar} \sum_i \mathcal{H}_i^I - \frac{a_t}{\hbar} \sum_{i<j} \mathcal{H}_{ij}^{II} - \frac{a_t}{\hbar} \sum_{i<j<k} \mathcal{H}_{ijk}^{III}, \quad (4.62)$$

where the ellipsis stands for terms of second or higher order in  $a_t$ , whereas  $i, j, k = 1, \dots, M$  and  $\mathcal{H}_i^I$ ,  $\mathcal{H}_{ij}^{II}$  and  $\mathcal{H}_{ijk}^{III}$  denote the one-, two- and three-body parts of the original lattice Hamiltonian for the particle(s)  $i$ ,  $(i, j)$  and  $(i, j, k)$  respectively. However, it is customary to

improve the approximation of the elementary transfer matrix in eq. (4.62) as follows,

$$\mathcal{T} \equiv e^{-a_t \mathcal{H}/\hbar} \approx \prod_s e^{-a_t \mathcal{H}_s^I/\hbar} - a_t \sum_{i < j} \mathcal{H}_{ij}^{II} \prod_{s \neq i, j} e^{-a_t \mathcal{H}_s^I/\hbar} - a_t \sum_{i < j < k} \mathcal{H}_{ijk}^{III} \prod_{s \neq i, j, k} e^{-a_t \mathcal{H}_s^I/\hbar}, \quad (4.63)$$

where certain higher order terms in  $a_t$  have been added and  $s = 1, \dots, M$ . The new terms include chains of free single-particle transfer matrices, or two- and three-body parts of the original Hamiltonian multiplied by one-body transfer matrices referring to particles not involved in the interactions.

Equipped with the approximated expression of the transfer matrix in eq. (4.61), we consider the ratio between the average values of the  $N_t$ -fold and the  $N_t - 1$ -fold product of the elementary transfer matrix respectively in the lattice trial state  $|\Psi(0)\rangle$ ,

$$\lambda_{\mathcal{T}}(N_t) \equiv \frac{\langle \Psi(0) | \mathcal{T}^{N_t} | \Psi(0) \rangle}{\langle \Psi(0) | \mathcal{T}^{N_t-1} | \Psi(0) \rangle}. \quad (4.64)$$

When  $N_t$  is odd and large, the quantity shown in the last equation represents an estimator for the average value of the operator  $e^{-a_t \mathcal{H}_r/\hbar}$  computed in the *dressed* lattice state

$$|\Psi\left(\frac{N_t-1}{2}\right)\rangle = \mathcal{T}^{\frac{N_t-1}{2}} |\Psi(0)\rangle, \quad (4.65)$$

that can be interpreted as the time evolution of the original trial lattice state towards the ground state of the Hamiltonian of the system. This fact is ensured by the condition  $N_t \gg 1$ , that permits to cancel virtually all the overlaps between the original trial state  $\Psi(0)$  and the exact eigenstates of the lattice Hamiltonian, with exception of the ground state. Evidence for this assertion is provided by quantum mechanics. With reference to the continuum and infinite volume counterpart of our  $M$ -body problem in the opening of this subsection, the application of the exact Euclidean-time evolution operator  $e^{-itH/\hbar}$  on the trial state  $|\Psi(0)\rangle$ , expanded in the basis of exact eigenstates of  $H$ , yields

$$e^{-itH/\hbar} |\Psi(0)\rangle = \sum_{n=0}^{+\infty} \langle n | \Psi(0) \rangle e^{-\tau E_n/\hbar} |n\rangle, \quad (4.66)$$

where  $|n\rangle$  denotes the exact eigenstate of  $H$  associated to the energy  $E_n$  and  $n$  encodes succinctly a set of quantum numbers. Then, a nonzero overlap between the trial state and the exact ground state, labeled with  $n = 0$ , is sufficient to guarantee the convergence of  $|\Psi(0)\rangle$  to  $|0\rangle$ ,

$$e^{-\tau H/\hbar} |\Psi(0)\rangle \approx e^{-\tau E_0/\hbar} |0\rangle. \quad (4.67)$$

In this guise, increasing the Euclidean time  $\tau$  adiabatically from 0 towards  $+\infty$ , all the overlaps implied in the expansion of the trial state over the eigenstates of  $H$  in eq. (4.66) become increasingly more suppressed by the exponential factors as compared to the one with the ground state [117], that eventually dominates for large Euclidean times. Hence, we are allowed to consider the r.h.s. of eq. (4.64) as an approximate eigenvalue of  $e^{-a_t \mathcal{H}_r/\hbar}$ , thus justifying the notation,

$$\lambda_{\mathcal{T}_{g.s.}} \equiv \lambda_{\mathcal{T}}(+\infty) = \lim_{N_t \rightarrow +\infty} \lambda_{\mathcal{T}}(N_t), \quad (4.68)$$

where  $\lambda_{\mathcal{T}_{g.s.}}$  is the exact ground state eigenvalue of the elementary transfer matrix. Eventually, from eq. (4.64), the approximate ground state eigenvalue of the Hamiltonian matrix  $\mathcal{H}_r$  can

be extracted via the exponential map,

$$\mathcal{E}_{g.s.}(N_t) = -\frac{\hbar}{a_t} \log[\lambda_{\mathcal{T}}(N_t)] . \quad (4.69)$$

The eigenvalues in eqs. (4.64) and (4.69) provide the natural benchmark for  $r_g/S$  and  $\mathcal{E}_{g.s.}$  (cf. eq. (4.88)) extracted through the Worldline Monte Carlo approach on chains of  $N_t$  transfer matrix elements, see sec. 4.8.1.

## 4.8 Stochastic approaches

In the last section, the memory-saving approach based on the Lanczos iteration for the diagonalization of the lattice Hamiltonians of the three  $\alpha$ -conjugate nuclei has been outlined, but few hints have been given regarding the  $N \geq 11$  regime of the  $\mathcal{H}_r$  matrix for  $^{16}\text{O}$ .

A direct inspection on the extent of the configuration space for  $N = 30$  indicates that each  $^{16}\text{O}$  wavefunction occupies  $1,9683 \cdot 10^{13}$  double precision entries, corresponding to about  $1.5 \cdot 10^5$  GB of memory. Considered the present limitations in the capacity of each GPU node (around 32 GB), the carrying-out itself of the eigenvalue extraction process via eigenvector-based approaches becomes prohibitive. It follows that, for  $N \sim 30$ , the storage of the  $^{16}\text{O}$  state vectors in configuration space has to be avoided in the diagonalization process of the lattice Hamiltonian. At the same time, all the information concerning eigenvalues and average values of physical quantities has to be conserved.

The natural candidates for the task are provided by the stochastic approaches, namely quantum Monte Carlo methods [12, 197–200]. Such techniques are based on the idea of extracting random numbers for the purpose of generating  $M$ -body configurations, that can be represented by the set of the positions and/or the velocities of the  $M$  particles. Other random numbers become part of the dynamics of the method, acting as a *discrimen* for the updated configurations of the system.

Among the many available Monte Carlo algorithms, the one we adopt is based on the *Metropolis-Hastings question* [201, 202], that can be summarized as follows. Let us introduce the time variable  $t$ , that grows monotonically at the same rate of the number of sampled configurations,  $S$ , and a positive-definite function  $P(c, t)$  associated to the configuration  $c$  of the system, to be interpreted as a time-dependent probability. Suppose the system at time  $t$  lies in the configuration  $c_s$  and  $c_s^{new}$  represents a new configuration, produced randomly. Then a number  $u$  is extracted from an uniform distribution,  $\mathcal{U}(0, 1)$ , with support in the interval  $(0, 1)$ . If the condition

$$u < \frac{P(c_s^{new}, t)}{P(c_s, t)} \quad (4.70)$$

is fulfilled, the configuration  $c_s^{new}$  is accepted and replaces the original one, otherwise  $c_s$  is conserved [203]. Subsequently, based on the accepted configuration, the expectation values of the physical observables to be estimated in the Monte Carlo simulation are updated. As in sec. 4.5.3, let us denote one of these by  $Q$  and the total number of sampled states at time  $t$  by  $S$ . An estimator of  $Q$  is, then, given by the average value among the results of each accepted configuration [198],

$$\langle Q \rangle_S = \frac{1}{S} \sum_{s=1}^S Q(c_s) , \quad (4.71)$$

and its associated statistical error  $\sigma_{Q_S}$  is given by the *unbiased* variance of the sample of  $S$  elements,

$$\sigma_{Q_S} = \sqrt{\frac{\sum_{s=1}^S [Q(c_s) - \langle Q \rangle_S]^2}{S-1}} . \quad (4.72)$$

The process continues with the generation of a new configuration and is repeated until statistical errors decrease below a given input threshold.

Before dwelling in the details of the implementations of the Metropolis-Hastings algorithm for our physical system (cf. sec. 4.8.1), we focus on the basic properties and the implications of the probabilistic criterion adopted for the selection of the configurations. First of all, the technique that permits to generate the random states according to the distribution  $P(c, t)$  possesses the properties of a *Markov Process* in case the probability distribution in eq. (4.70) is time-independent. This condition ensures that the probability of accessing a state  $c_s^{new}$  does not depend on the preceeding configurations of the system. Hence Markov processes are *ergodic*, since all the states of the system can be reached from any initial state. Even if this condition is reached only in the infinite time limit,

$$\lim_{t \rightarrow +\infty} P(c_s, t) = P(c_s) , \quad (4.73)$$

in practice, after a sufficiently large number of *warmup* configurations, the Monte-Carlo simulation is supposed to *thermalize* and reach ergodicity in a good approximation.

Furthermore, eq. (4.70) is the result of the *detailed balance* condition [198,203], namely

$$P(c_s^{new}, t) \Omega(c_s^{new} \rightarrow c_s) = P(c_s, t) \Omega(c_s \rightarrow c_s^{new}) , \quad (4.74)$$

where  $\Omega(c_s \rightarrow c_s^{new})$  represents the transition probability from the state  $c_s$  to  $c_s^{new}$  and satisfies the properties required for a probability mass function,

$$\Omega(c_s \rightarrow c_s^{new}) \geq 0 \quad \text{and} \quad \sum_s \Omega(c_k \rightarrow c_s) = 1 , \quad (4.75)$$

where the sum extends to all the possible configurations of the system. As hinted, in a Markov chain the transition probabilities  $\Omega(c_k \rightarrow c_s)$  are time independent and their values do not depend on any other state prior to  $c_k$ , so that ergodicity is preserved.

In conclusion, the essential advantage in the approach for the selection of new configurations for the system outlined here resides in its efficiency [203]. If the r.h.s. of eq. (4.70) is replaced by  $P(c_s^{new}, t)$  alone, in the large  $S$  limit almost all the proposed new configurations will be discarded, since the latter acceptance condition itself is prone to retain states associated to small values of the probability  $P(c_s^{new}, t)$  [198].

### 4.8.1 The Worldline Monte Carlo algorithm

While the starting-point of the Lanczos method outlined in sec. 4.7.1 was the lattice Hamiltonian, the cornerstone of our implementation of the worldline Monte Carlo algorithm is the transfer matrix [12] defined in sec. 4.7.2, a choice that is motivated by the positive-definiteness of the latter.

The same operator provides the basis for other stochastic algorithms, among these *Auxiliary Field Monte Carlo* (AFMC) [12,199,204]. Despite the success of the latter in the framework

of EFT for nucleons [205–207], the approach has been discarded, due to the appearance of the phase problem [208]. This drawback is caused by the implementation of the Hubbard-Stratonovich transform [209–212] for general local interactions [213] to the repulsive part of the Ali-Bodmer potential (cf. eq. (4.2)), which produces a nonzero imaginary part in the total action with auxiliary fields, hence the phase problem. Although the issue can be mitigated by remedies [214] such as the symmetry-sign extrapolation (SSE) [215,216], the required computational efforts plead for the adoption of the Worldline algorithm.

Although the latter can be tailored pairwise on the elementary transfer matrix of the  $M$ -body problem in eq. (4.63), we opt for a single-particle picture. In this implementation, the lattice action operator in Euclidean time  $\tau = a_t N_t$  is defined as follows,

$$\hat{S} = a_t \sum_{n_t} \hat{\mathcal{K}}_s + a_t \sum_{n_t} \hat{\mathcal{V}}^{\text{II}} + a_t \sum_{n_t} \hat{\mathcal{V}}^{\text{III}}, \quad (4.76)$$

where  $\hat{\mathcal{K}}_s$  represents the kinetic energy operator for the particle  $s$ ,

$$\hat{\mathcal{K}}_s = -\frac{\hbar^2}{2m} \sum_{\mathbf{n}_s} \sum_{k=-K}^K \sum_{\hat{\mathbf{l}}_s} C_k^{(2D,K)} a^\dagger(\mathbf{n}_s) a(\mathbf{n}_s + k\hat{\mathbf{l}}_s), \quad (4.77)$$

that in configuration space generates a  $N^3 \times N^3$  matrix, while the index  $n_t = 1, \dots, N_t$  has been dropped from the arguments of the second quantization operators, since the lattice Hamiltonian is time-independent. Similarly, in the notation of sec. 4.3,

$$\hat{\mathcal{V}}^{\text{II}} = \sum_{\mathbf{n}_s} \sum_{i \neq s} \left[ V^{\text{II}}(\mathbf{r}_s, \mathbf{r}_i) + \frac{1}{2} \sum_{j \neq s, i} V^{\text{II}}(\mathbf{r}_i, \mathbf{r}_j) \right] a^\dagger(\mathbf{n}_s) a(\mathbf{n}_s) \quad (4.78)$$

and

$$\hat{\mathcal{V}}^{\text{III}} = \frac{1}{2} \sum_{\mathbf{n}_s} \sum_{i \neq s} \sum_{j \neq s, i} \left[ V^{\text{III}}(\mathbf{r}_s, \mathbf{r}_i, \mathbf{r}_j) + \frac{1}{3} \sum_{k \neq s, i, j} V^{\text{III}}(\mathbf{r}_i, \mathbf{r}_j, \mathbf{r}_k) \right] a^\dagger(\mathbf{n}_s) a(\mathbf{n}_s) \quad (4.79)$$

denote the lattice counterpart of the two and the three-body potentials in eqs. 4.2, 4.3 and 4.4 in operator form and  $i, j, k = 1, \dots, M$ . In this picture, many-body potentials reduce to one-body ones, whose effect on the single particle depends on the distribution in space of the  $M - 1$  particles excluded from the action. Concerning the temporal direction, we again consider  $N_t$  time steps separated by the interval  $a_t$ , small enough to neglect its associated discretization effects in the simulations. If  $N_t$  is a large positive integer, the normal-ordered transfer matrix operator becomes susceptible of the Trotter-Suzuki approximation [195,196],

$$e^{-\hat{S}/\hbar} \approx \prod_{n_t=1}^{N_t} e^{-a_t \hat{\mathcal{K}}_s/\hbar} e^{-a_t \hat{\mathcal{V}}^{\text{II}}/\hbar} e^{-a_t \hat{\mathcal{V}}^{\text{III}}/\hbar}, \quad (4.80)$$

which permits to rewrite the transfer matrix operator for the full temporal interval on the l.h.s of eq. (4.80) as a chain of transfer matrices referring to the elementary lattice time interval  $[n_t, n_t + 1]$ . The latter, that we denote as

$$\hat{\mathcal{T}} \equiv e^{-a_t \hat{\mathcal{K}}_s/\hbar} e^{-a_t \hat{\mathcal{V}}^{\text{II}}/\hbar} e^{-a_t \hat{\mathcal{V}}^{\text{III}}/\hbar}, \quad (4.81)$$

can be considered as the building block of our implementation of the Worldline algorithm [12], often employed in condensed matter physics for systems of bosons [217] or in the nuclear context when the sign problem (cf. refs. [203, 208]) is not severe, as in the triton nucleus in the framework of pionless EFT [205]. Due to the numerical challenges imposed by the exponentiation of the operators  $\hat{\mathcal{T}}$  in matrix form,

$$\mathcal{T}_{\mathbf{n},\mathbf{n}'}^{(a)} \equiv \langle \mathbf{n}_s | \hat{\mathcal{T}} | \mathbf{n}'_s \rangle , \quad (4.82)$$

where the superscript  $(a)$  denotes the absolute reference frame, it is convenient to expand the exponentials in eq. (4.81) in powers of  $a_t$ ,

$$\hat{\mathcal{T}} \approx \mathbb{1} - \frac{a_t}{\hbar} \hat{\mathcal{K}}_s - \frac{a_t}{\hbar} \hat{\mathcal{V}}^{\text{II}} - \frac{a_t}{\hbar} \hat{\mathcal{V}}^{\text{III}} , \quad (4.83)$$

where  $\mathbb{1}$  denotes the identity lattice operator and the ellipsis refers to terms of higher order in  $a_t$ . The smallness of the dimensionless quantity  $\alpha_t \equiv a_t/a$  [12] in natural units  $\hbar = c = 1$  in the typical Monte Carlo simulations, in fact, justifies the linear approximation of the transfer-matrix operator. In that units, it is indeed customary to divide the dimensional constants of the Hamiltonian by suitable units of the lattice spacing [12], whose dimensions coincide with the ones of time and the inverse of energy. On the other hand, a drawback in the linear approximation of the transfer matrix operator is given by the loss of positive-definiteness. While a small value of  $a_t$  is sufficient to guarantee positive diagonal matrix elements without restrictions on the potentials, the non-diagonal terms of the kinetic matrix can assume negative values when the derivative improvement index  $K$  in eq. (4.77) is greater or equal to two. In order to preserve this property, for the Monte Carlo simulations in chap. 7 we set  $K = 1$ , corresponding to the basic approximation of the Laplacian operator.

Thanks to the positive definiteness of the transfer matrix  $\mathcal{T}_{\mathbf{n},\mathbf{n}'}^{(a)}$ , it is possible to exploit the  $N_t$ -fold matrix product implied by the r.h.s. of eq. 4.80 for the formulation of the *Metropolis-Hastings* question [198]. Differently from AFMC [12, 199, 203, 204], in the Worldline approach the product of matrices reduces to a product of matrix elements [202]. As a consequence, the chain of  $N_t$  elementary transfer matrices turns into a chain of  $N_t$  matrix entries, whose internal indices are repeated pairwise. Denoting the latter as  $\mathbf{n}^{(1)} \dots \mathbf{n}^{(N_t+1)}$ , the sequence of transfer matrix elements is defined as

$$\mathcal{T}^{[N_t]} \equiv \mathcal{T}_{\mathbf{n}^{(1)},\mathbf{n}^{(2)}}^{(a)} \mathcal{T}_{\mathbf{n}^{(2)},\mathbf{n}^{(3)}}^{(a)} \dots \mathcal{T}_{\mathbf{n}^{(N_t)},\mathbf{n}^{(N_t+1)}}^{(a)} , \quad (4.84)$$

where  $\mathcal{T}^{[N_t]}$  is now a positive scalar. Besides the latter, we introduce the  $N_t - 1$  transfer matrix chain,

$$\mathcal{T}^{[N_t-1]} \equiv \mathcal{T}_{\mathbf{n}^{(1)},\mathbf{n}^{(2)}}^{(a)} \mathcal{T}_{\mathbf{n}^{(2)},\mathbf{n}^{(3)}}^{(a)} \dots \mathcal{T}_{\mathbf{n}^{(N_t-1)},\mathbf{n}^{(N_t)}}^{(a)} , \quad (4.85)$$

whose purpose, that will be clarified later, is limited to the evaluation of the main physical observables of interest, the energy eigenvalues.

Equipped with the basis of our formalism, we can now outline our implementation of the Worldline algorithm (cf. ref. [202]). As hinted in the opening of sec. 4.8, the code begins with the definition of the initial configuration of the system. This consists in a *worldline* (cf. fig. 4.3) composed by  $N_t + 1$  matrix indices for each of the  $M$  particles of the system. At each step in the chain in eq. 4.84, the position vector of all the particles is, thus, specified. For the latter, it is convenient to chose the initial guess in such a way that the matrix elements in the chain



belong to the diagonal of the transfer matrix. At the same time, the *ratio* variable,  $r_g$ , that stores the information for the energy eigenvalue, is initialized to zero [202].

The subsequent step in the algorithm is given by the update of an element belonging to one of the  $M$  worldlines. For the purpose, four random numbers are extracted. First, a particle label is selected. Then, a random single-particle index of the chain in eq. (4.84) is chosen. Finally, the other two random numbers are generated for the definition of the updated position for the selected particle.

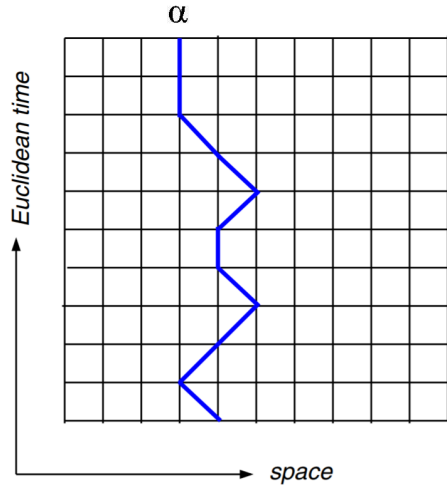


FIGURE 4.3 – Illustration of the worldline of an  $\alpha$  particle. According to the algorithm, each  ${}^4\text{He}$  nucleus moves under the action of an effective one-particle potential generated by the other  $M - 1$  particles, see eqs. (4.78) and (4.79). The path of each worldline appears rather straight, since only one-step hopping terms are allowed in the kinetic energy matrix. Edited, from ref. [218].

Once the worldline update is completed, the transfer matrix chains  $\mathcal{T}^{[N_t]}$  and  $\mathcal{T}_{new}^{[N_t]}$  are computed by making use of eq. (4.84) with the transfer matrix in the linear approximation, see eq. (4.83). In the procedure, the whole spatial arrangement of the  $\alpha$  particles at each step of the chain of transfer matrices is exploited, since the position of the other  $M - 1$   ${}^4\text{He}$  nuclei not involved in the update enter in the potential part of the action (cf. eqs. (4.78) and (4.79)). Starting from  $\mathcal{T}^{[N_t]}$ ,  $\mathcal{T}_{new}^{[N_t]}$ , a random number  $u$  is sampled from the uniform distribution  $\mathcal{U}(0, 1)$  and the Metropolis-Hastings question is formulated [202],

$$u < \frac{\mathcal{T}_{new}^{[N_t]}}{\mathcal{T}^{[N_t]}}. \quad (4.86)$$

If the criterion in eq. (4.86) is met, the update in the worldline of the selected particle is confirmed, otherwise the change is rejected. In the positive case, a control variable that accounts for the number of accepted worldline updates is incremented by one unit, thus monitoring the efficiency of the algorithm. As it can be inferred from eq. (4.86), in this implementation of the Worldline approach, the role of the probabilities  $P(t, c_s^{new})$  and  $P(t, c_s)$  in eq. (4.70) is now covered by the sequences of transfer matrix elements  $\mathcal{T}_{new}^{[N_t]}$  and  $\mathcal{T}^{[N_t]}$ , whereas the configurations  $c_s^{new}$  and  $c_s$  are identified with the updated and the original worldlines. Besides, it is evident from eq. (4.86) that a single negative entry in the matrix chains causes the breakdown of our stochastic interpretation of the transfer matrix.

The closing part of the body of the iteration loop is occupied by the measurement of the physical observables from the worldlines of the  $M$  particles. If the latter consists in the energy eigenvalue of the ground state,  $\mathcal{E}_{g,s,n}$ , it is sufficient to construct an *if* loop checking whether the  $n_{M+1}$  index of the worldline of the preselected particle coincides with the  $n_M$  index. When

the condition is satisfied, the ratio variable is updated [202],

$$r_g^{\text{new}} = r_g + \frac{\mathcal{T}^{[N_t-1]}}{\mathcal{T}^{[N_t]}} = r_g + \frac{1}{\mathcal{T}_{\mathbf{n}^{(N_t)}, \mathbf{n}^{(N_t+1)}}} , \quad (4.87)$$

where  $\mathcal{T}^{[N_t-1]}$  is obtained via eq. (4.85) by copying the first  $N_t - 1$  elements of  $\mathcal{T}^{[N_t]}$ . Exploiting the inversion of the exponential map between the transfer matrix and the Hamiltonian eigenvalues, the value of  $r_g^{\text{new}}$ , in turn, updates the estimate of the ground state energy,

$$\mathcal{E}_{g.s.} = \frac{\hbar}{a_t} \log \left( \frac{r_g}{S} \right) , \quad (4.88)$$

where  $S$  represents the number of successful updates of the variable  $r_g$  from its initial value equal to zero. After the update of the physical observable in eq. (4.88), the above process restarts by modifying another element of a particle worldline. The main loop on Monte Carlo configurations terminates as soon as the input number of worldline updates is reached.

However, our realizations of the worldline algorithm are designed for multiple processors in the same CPU node, in order to monitor the convergence process to the exact eigenvalue through the standard deviation among the ground state energies extracted from the different processors in which the simulation is running. Therefore, the application of the exponential map is preceeded by the averaging of the argument of the logarithm of eq. (4.88) among the results from the processors, where the random number generators have been initialized with a different seed.

Furthermore, the extracted energy eigenvalues  $\mathcal{E}_{g.s.}$  are expected to agree with the exact ground state estimations obtained via the adiabatic projection method (cf. sec. 4.7.2) at a given value of  $N_t$  and of the temporal lattice spacing,  $a_t$ . Additionally, in the zero temporal lattice spacing and infinite  $N_t$  limit, the ground state energy from the Worldline Monte Carlo algorithm coincides, within the statistical uncertainty, with the exact counterpart from the diagonalization of the lattice Hamiltonian matrix. In practice, in order to reproduce the exact eigenvalues from simulations with finite  $N_t$  and  $a_t$ , an *Euclidean time extrapolation* [216] is performed, by selecting a small value of the temporal lattice spacing and fitting the data with large and finite values of time steps,  $N_t$ . An illustrative example is shown in fig. 4.4, where the ground state eigenvalue of the lattice Hamiltonian with  $L = 10$  and  $a \approx 0.49$  fm is extracted from a sample of energies with  $141 \leq N_t \leq 271$  and  $a_t = 1/3500$  and the interpolating curve coincides with the law

$$E(N_t) = \frac{b}{N_t^\xi} + c , \quad (4.89)$$

where  $b$  and  $c$  are parameters of the fit and  $\xi$  is chosen to maximize the coefficient of determination  $R^2$  associated to the family of fitting functions in eq. (4.90).

Another aspect of the extraction of the eigenvalues via eq. (4.88) that is worthy to underline is represented by the correlation between the accepted worldlines. From the update process of the latter, it is indeed evident that the modification of a single unit of the original worldline produces a system configuration tightly correlated with the preceeding one. At the same time, acceptable configurations which differ sensibly from the original worldline cannot be accessed after one iteration only, thus the main requirement for a Markov process seems compromised. However, if a large number of worldline updates is allowed to occur between each increment of  $r_g$  (cf. eq. (4.87)), the property is approximately restored.



So far, in the description of the algorithm we have left aside the symmetry properties of the state whose energy is extracted. Due to the presence of negative entries in the projectors on irreducible representations of the pertinent point groups (cf. sec. 4.4), it is not possible to apply such operators to the transfer matrix elements in the  $N_t$  chain. However, the approach guarantees the belonging of the eigenstate associated to the lowest signed eigenvalue of the Hamiltonian matrix,  $\mathcal{E}_{g.s.}$ , to the completely symmetric representation of the permutation group of four particles  $S_4$ .

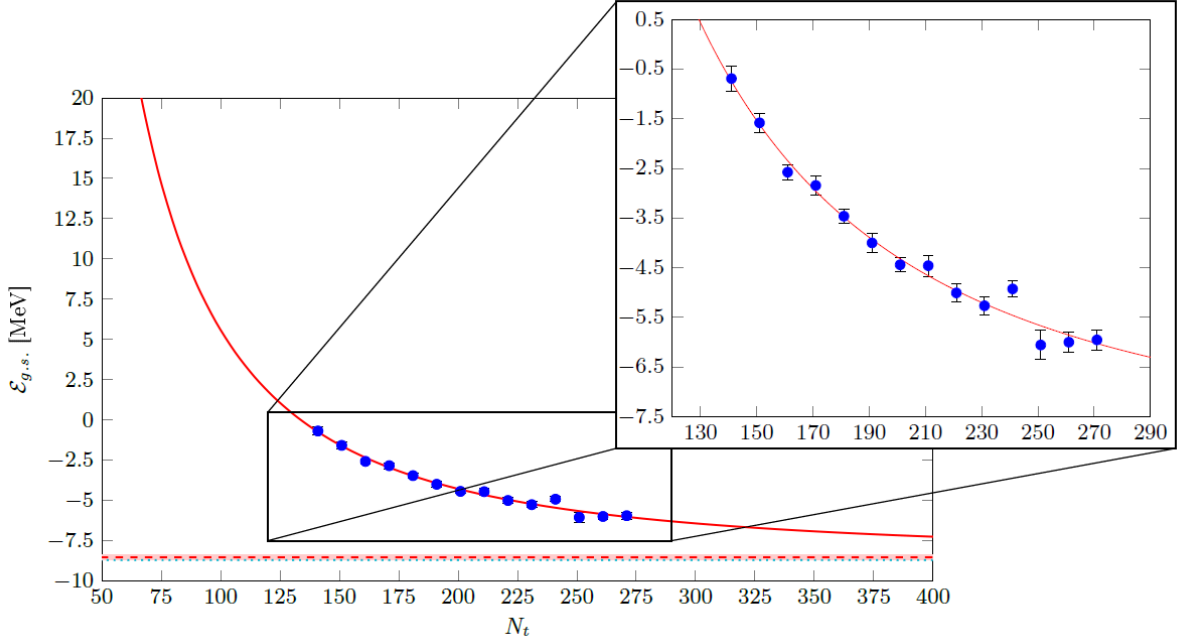


FIGURE 4.4 – Euclidean Time Extrapolation of the ground state energy of the lattice Hamiltonian with  $L = 10$  and  $a \approx 0.49$  fm from a sample of  $\mathcal{E}_{g.s.}$  at finite  $N_t$  and  $a_t = 1/3500$  extracted through the Worldline Monte Carlo approach. The dashed red line represents the asymptotic value of  $\mathcal{E}_{g.s.}$  obtained from the fit (cf. param.  $c$  in eq. (4.90)), equal to  $-8.54(18)$  MeV. The adjacent shaded area denotes the associated confidence interval, delimited by one unit of standard deviation. The turquoise dotted line corresponds to the exact energy eigenvalue,  $-8.710$  MeV, obtained from the diagonalization of  $\mathcal{H}_r$  via the Lanczos algorithm (cf. sec. 4.7.1). The two values are compatible within one standard deviation, indicating that temporal discretization errors caused by the Trotter-Suzuki approximation at the chosen value of  $a_t$  can be neglected.

The statement extends to the excited states, whose energies are extracted through the algorithm described in the next subsection. Although other physical observables have not been included in the Monte Carlo simulations, it is possible that a construction similar to the one adopted for the energy eigenvalue is suitable for the purpose, provided the operators are exponentiated. As an example, we pick the squared total angular momentum operator,  $\hat{\mathcal{L}}^2$  and initialize the associated variable  $r_{\mathcal{L}^2}$  to zero. Then after each modification of the worldline (cf. eq. (4.86)) and the ground state energy (cf. eq. (4.87)), the variable just defined can be updated,

$$r_{\mathcal{L}^2}^{\text{new}} = r_{\mathcal{L}^2} + \frac{1}{(e^{-b\mathcal{L}^2}/\hbar^2)_{\mathbf{n}^{(N_t)}, \mathbf{n}^{(N_t+1)}}}, \quad (4.90)$$

where  $b$  represents an arbitrary real non-zero constant. Any improvement in the value of  $r_{\mathcal{L}^2}$  should be respectful of the constraint  $\mathbf{n}^{(N_t)} = \mathbf{n}^{(N_t+1)}$  if  $\hat{\mathcal{L}}^2$  is the single-particle squared angular

momentum operator. In case  $\hat{\mathcal{L}}$  coincides with the  $M$ -particles operator, the constraint has to be extended to the  $M$  worldlines.

Concerning the energy eigenvalues of the excited states, the algorithm turns out to inherit the same structure of the code described above. The major modification is represented by the addition of two subsidiary matrices and by the diagonalization of a suitable combination of the two, as illustrated in the next subsection.

#### a) The extension to excited states

In the previous section, a Monte Carlo algorithm for the extraction of the lowest eigenvalue of the transfer matrix has been outlined. As hinted, the same approach serves as a basis for the computation of other lattice energy eigenvalues,  $\mathcal{E}$ , which belong to higher angular momentum,  $\ell$ , multiplets in the continuum and infinite-volume limit. A pivotal role in the code, that we now describe, is played by the definition of a suitable radius vector (cf. sec. I of ref. [193]), whose modulus grows with the radius of the nucleus. In our implementation, this vector has been chosen to coincide with the  $M - 1^{\text{th}}$  Jacobi coordinate [8],

$$\mathbf{r}_{M-1}^J = \frac{1}{M-1} \sum_{i=1}^{M-1} \mathbf{r}_i - \mathbf{r}_M, \quad (4.91)$$

where  $\mathbf{r}_i$  denotes the coordinate of the  $\alpha$  particle  $i$  in the absolute reference frame. Since states with increasing energy are associated with a broader spatial distribution,  $\mathbf{r}_{M-1}^J$  provides an indicator of the value of  $\mathcal{E}$  associated to different eigenstates of the Hamiltonian of our  $M$  particle system.

First of all, it is convenient to structure the code into two parts. For any input value of  $N_t$ , in fact, we sample separately and independently the worldlines associated to the  $N_t$  and  $N_t - 1$  sequences of transfer matrix elements,

$$\mathcal{T}^{[N_t]} = \mathcal{T}_{\mathbf{n}^{(1)}, \mathbf{n}^{(2)}}^{(a)} \mathcal{T}_{\mathbf{n}^{(2)}, \mathbf{n}^{(3)}}^{(a)} \cdots \mathcal{T}_{\mathbf{n}^{(N_t)}, \mathbf{n}^{(N_t+1)}}^{(a)}, \quad \text{and} \quad \mathcal{T}^{[N_t-1]} = \mathcal{T}_{\mathbf{n}^{(1)}, \mathbf{n}^{(2)}}^{(a)} \mathcal{T}_{\mathbf{n}^{(2)}, \mathbf{n}^{(3)}}^{(a)} \cdots \mathcal{T}_{\mathbf{n}^{(N_t-1)}, \mathbf{n}^{(N_t)}}^{(a)}, \quad (4.92)$$

respectively and we collect in parallel the energy eigenvalues associated to the two chains,  $\mathcal{E}_{g.s.}^{N_t}$  and  $\mathcal{E}_{g.s.}^{N_t-1}$  together with the statistical errors, obtained from the outcomes of different processors in the same CPU node, as in sec. 4.8.1.

In the same fashion as in sec. III of ref. [193], we introduce in the respective codes the *transfer matrix*  $\mathbb{T}$  and the *norm matrix*  $\mathbb{N}$ , whose size is equal to  $N^3 \times N^3$ . Their indices are defined by integers which encode the three components of the  $M - 1^{\text{th}}$  Jacobi coordinate in eq. (4.91), calculated on lattice points. Moreover, the row index of the two matrices is associated to  $\mathbf{r}_{M-1}^J$ , evaluated at the initial point of the worldline of each particle,  $\mathbf{r}_{M-1}^J(i) \equiv a\mathbf{r}_{M-1}^J(\mathbf{n}_1^{(1)}, \dots, \mathbf{n}_M^{(1)})$ . Similarly, the column index of the  $\mathbb{T}$  and  $\mathbb{N}$  matrices is obtained from the final point of the worldline of each particle,  $\mathbf{r}_{M-1}^J(f) \equiv a\mathbf{r}_{M-1}^J(\mathbf{n}_1^{(N_t)}, \dots, \mathbf{n}_M^{(N_t)})$  or  $a\mathbf{r}_{M-1}^J(\mathbf{n}_1^{(N_t+1)}, \dots, \mathbf{n}_M^{(N_t+1)})$  respectively. The elements of these matrices, initially set to zero, are modified by adding one unity to the relevant element,

$$\mathbb{T}_{if}^{\text{new}} = \mathbb{T}_{if} + 1, \quad \text{and} \quad \mathbb{N}_{if}^{\text{new}} = \mathbb{N}_{if} + 1, \quad (4.93)$$

where  $i \equiv \mathbf{r}_{M-1}^J(i)$  and  $f \equiv \mathbf{r}_{M-1}^J(f)$ , after each update of the ratio variable,  $r_g$ . It follows that, differently from  $\mathcal{T}_{\mathbf{n}, \mathbf{n}'}^{(a)}$ , the matrices  $\mathbb{T}$  and  $\mathbb{N}$  are not function of a lattice physical observable,

but merely count the number of sampled  $M$ -particle worldlines whose endpoints correspond to a given couple of  $M - 1^{\text{th}}$  Jacobi coordinates.

Once the fixed number of Monte Carlo configurations is sampled, the independent outcomes of the codes for the  $\mathbb{T}$  and  $\mathbb{N}$  matrices are analysed. With regards to the discussion on correlation in sec. 4.8.1, let  $S$  denote the total number of updates of the variable  $r_g$  produced from the worldlines of the chain of  $N_t$  transfer matrices,  $\mathcal{T}^{[N_t]}$ . Then, we define the *adiabatic* transfer matrix (cf. ref. [193, 194]) as

$$\mathbb{T}^{ad} \equiv \frac{S}{r_g} \mathbb{N}^{-1/2} \mathbb{T} \mathbb{N}^{-1/2} , \quad (4.94)$$

where for  $\mathbb{N}$  the notion of square root applied to matrices is understood. By exploiting again the exponential map in eq. (4.88), the eigenvalues of the latter matrix,  $\lambda_{\mathbb{T}_n^{ad}}$  are real, since both  $\mathbb{N}$  and  $\mathbb{T}$  consist of integers, and yield the lowest  $N^3$  symmetric eigenvalues  $\mathcal{E}_n$  of the lattice Hamiltonian of the  $M$ -particle system,

$$\mathcal{E}_n = -\frac{\hbar}{a_t} \log(\lambda_{\mathbb{T}_n^{ad}}) , \quad (4.95)$$

where  $n = 0, \dots, N^3$ . As it can be inferred from the last two equations, the energy eigenvalue of the ground state covers a pivotal role in the determination of the excited states, since it appears as a constant factor in eq. (4.94). Besides, the two matrices of dimensionless integers,  $\mathbb{T}$  and  $\mathbb{N}$  turn out to provide the proper weights capable of reproducing the expected sequence of energy eigenvalues. However, slight imbalance in the total number of updates,  $S$ , in the entries of the of the two matrices can produce sensible inconsistencies with respect to the expected eigenvalues. In such cases, it is recommendable to normalize the two matrices through the division by the total number of updates.

Concerning statistical and systematic errors, the convergence of the excited states can be monitored by keeping track of the random errors associated to the ground state energy eigenvalue extracted by the transfer and norm matrix worldlines. More precisely, for the derivation of the statistical errors reported in tab. 4.2, we have proceeded as follows. First, from the results of the single processors involved in the Monte Carlo simulation, an average transfer matrix,  $\langle \mathbb{T} \rangle$ , and norm matrix,  $\langle \mathbb{N} \rangle$ , are constructed, together with the associated matrices of standard deviations,  $\sigma_{\mathbb{T}}$  and  $\sigma_{\mathbb{N}}$  respectively. Then, sampling from a Normal distribution  $\mathcal{N}(0, \sigma)$  with mean equal to zero and  $\sigma$  equal to  $\sigma_{S/r_g}$ , the standard deviation of the transfer matrix ground state eigenvalue associated to the  $N_t$  chain,  $N^3$  random transfer and norm matrices are built,

$$\mathbb{T}_i = \langle \mathbb{T} \rangle + n\sigma_{\mathbb{T}} , \quad \text{and} \quad \mathbb{N}_i = \langle \mathbb{N} \rangle + n\sigma_{\mathbb{N}} , \quad (4.96)$$

where  $i = 1, \dots, N^3$  and  $n \in \mathcal{N}(0, \sigma)$  is a random real number. Subsequently, the eigenvalues of

$$\mathbb{T}_i^{ad} \equiv \left( \frac{S}{r_g} + n\sigma_{S/r_g} \right) \mathbb{N}_i^{-1/2} \mathbb{T}_i \mathbb{N}_i^{-1/2} , \quad (4.97)$$

are extracted and the energy eigenvalues are obtained from the latter via the exponential map (cf. eq. (4.95)). Finally, on the  $N^3$  copies of each energy eigenvalue, the average and the standard deviation are computed, and the  $N^3$  sorted energy eigenvalues with the related statistical uncertainties are produced. From tab. 4.2, it is evident that even when the ground state energy eigenvalue associated to the  $N_t$  chain overlaps the exact eigenvalue from the adiabatic

projection method (cf. sec. 4.7.2) within the second decimal digit, the energy eigenvalues from the diagonalization of the adiabatic transfer matrix are affected by statistical errors more than one order of magnitude larger. Moreover, it is evident that the systematic errors affecting the eigenvalues in tab. 4.2 are about  $10^1$  times larger than their associated statistical errors, indicating that further sampling in the transfer and norm matrix worldlines is recommendable. Furthermore, consistent results are also obtained from the diagonalization of the non-Hermitian version of  $\mathbb{T}^{ad}, (S/r_g)\mathbb{T} \mathbb{N}^{-1}$ , provided the imaginary part of the energy eigenvalues in eq. (4.95) is discarded. Exactly this approach has been followed for the reproduction of the low-energy spectrum of the  $^{16}\text{O}$  presented in tab. 4.2.

As it can be inferred from the latter table, the outlined technique permits to attack successfully the eigenvalue problem associated to the  $^{16}\text{O}$  lattice Hamiltonian  $\mathcal{H}_r$  with size  $N^9 \times N^9$ , by reducing the overall computational load to the numerical diagonalization of a  $N^3 \times N^3$  matrix alone. However, a drawback in the method is represented by the slowness of the update process of the transfer and norm matrix elements. Even in the  $N = 3$  case (cf. tab. 4.2), precise data can be obtained only after some days of simulations in transfer and norm matrix worldlines. Nevertheless, it is possible that a reduction in the extent of the configuration space associated to the Jacobi coordinate in eq. (4.91) yields  $\mathbb{T}$  and  $\mathbb{N}$  matrices of smaller or fixed size, so that the low-energy spectrum problem for  $\mathcal{H}_r$  with  $N \sim 30$  can be tackled within more reasonable computational times.

$\begin{array}{c c} & S \\ \hline n & \end{array}$	$0.100 \cdot 10^6$	$0.500 \cdot 10^6$	$144.00 \cdot 10^6$	$300.00 \cdot 10^6$	$600.00 \cdot 10^6$
$\mathcal{E}_{g.s.} [\text{MeV}]$	$-10.875 \pm 0.405$	$-10.402 \pm 0.197$	$-10.329 \pm 0.023$	$-10.315 \pm 0.025$	$-10.339 \pm 0.0157$
0	$-56.585 \pm 12.237$	$-26.165 \pm 1.029$	$-11.202 \pm 0.102$	$-10.835 \pm 0.073$	$-10.777 \pm 0.057$
1	$-42.319 \pm 11.457$	$-20.419 \pm 0.938$	$-0.931 \pm 0.083$	$-0.708 \pm 0.051$	$-0.906 \pm 0.079$
2	$-37.196 \pm 10.561$	$-18.593 \pm 0.934$	$-0.685 \pm 0.123$	$0.080 \pm 0.077$	$0.598 \pm 0.043$
3	$-34.416 \pm 8.618$	$-14.038 \pm 0.917$	$-0.374 \pm 0.104$	$0.908 \pm 0.074$	$0.856 \pm 0.045$
4	$-21.260 \pm 11.083$	$-11.834 \pm 0.835$	$1.959 \pm 0.094$	$1.482 \pm 0.060$	$1.842 \pm 0.052$
5	$-20.887 \pm 11.159$	$-9.053 \pm 0.816$	$2.085 \pm 0.085$	$1.840 \pm 0.045$	$2.162 \pm 0.039$
6	$-18.113 \pm 10.865$	$-4.944 \pm 0.834$	$3.093 \pm 0.071$	$2.758 \pm 0.099$	$2.387 \pm 0.051$
7	$-12.271 \pm 11.126$	$2.686 \pm 0.686$	$9.546 \pm 0.088$	$10.198 \pm 0.047$	$10.147 \pm 0.075$
8	$-6.564 \pm 11.214$	$4.673 \pm 0.962$	$10.033 \pm 0.142$	$11.244 \pm 0.086$	$11.355 \pm 0.042$
9	$-4.146 \pm 11.823$	$6.217 \pm 0.946$	$10.358 \pm 0.114$	$11.724 \pm 0.054$	$12.037 \pm 0.045$
10	$-2.538 \pm 11.952$	$7.049 \pm 0.550$	$12.383 \pm 0.107$	$12.242 \pm 0.078$	$12.633 \pm 0.073$
11	$-0.392 \pm 12.543$	$8.436 \pm 1.101$	$12.822 \pm 0.088$	$12.567 \pm 0.072$	$13.149 \pm 0.056$
12	$2.384 \pm 11.439$	$11.570 \pm 0.804$	$13.072 \pm 0.069$	$12.921 \pm 0.074$	$13.285 \pm 0.053$
13	$3.897 \pm 12.669$	$14.086 \pm 0.722$	$13.487 \pm 0.081$	$13.269 \pm 0.083$	$13.429 \pm 0.057$
14	$17.975 \pm 11.386$	$16.031 \pm 0.838$	$13.611 \pm 0.076$	$13.527 \pm 0.067$	$13.773 \pm 0.039$
15	$21.535 \pm 11.643$	$20.220 \pm 0.607$	$14.786 \pm 0.095$	$14.084 \pm 0.038$	$14.024 \pm 0.024$
16	$25.784 \pm 11.113$	$21.388 \pm 0.577$	$15.321 \pm 0.087$	$14.383 \pm 0.043$	$14.360 \pm 0.043$
17	$30.600 \pm 9.887$	$22.139 \pm 0.728$	$15.730 \pm 0.077$	$15.189 \pm 0.056$	$14.508 \pm 0.029$
18	$34.303 \pm 10.861$	$25.283 \pm 0.533$	$16.195 \pm 0.046$	$15.537 \pm 0.070$	$15.016 \pm 0.052$
19	$37.634 \pm 11.692$	$26.779 \pm 0.707$	$20.974 \pm 0.115$	$22.419 \pm 0.060$	$22.514 \pm 0.055$
20	$45.200 \pm 10.160$	$30.432 \pm 0.659$	$23.727 \pm 0.098$	$23.830 \pm 0.057$	$24.152 \pm 0.051$
21	$46.574 \pm 11.978$	$34.167 \pm 0.399$	$24.572 \pm 0.0919$	$24.389 \pm 0.091$	$24.832 \pm 0.045$
22	$51.276 \pm 11.222$	$36.524 \pm 0.055$	$25.069 \pm 0.070$	$25.026 \pm 0.063$	$24.962 \pm 0.043$
23	$61.534 \pm 11.182$	$39.836 \pm 1.075$	$25.863 \pm 0.080$	$25.585 \pm 0.062$	$25.719 \pm 0.049$
24	$74.480 \pm 11.701$	$41.730 \pm 0.571$	$26.938 \pm 0.079$	$26.060 \pm 0.022$	$25.888 \pm 0.033$
25	$77.718 \pm 10.479$	$46.392 \pm 0.966$	$27.327 \pm 0.047$	$26.833 \pm 0.061$	$26.477 \pm 0.056$
26	$87.266 \pm 11.111$	$48.376 \pm 0.779$	$28.703 \pm 0.084$	$27.369 \pm 0.066$	$26.682 \pm 0.041$

TABLE 4.2 – Sample of the spectrum of the  $^{16}\text{O}$  lattice Hamiltonian with  $N = 3$ ,  $a \approx 1.98$  fm,  $N_t = 5$  and  $a_t = 0.001$  s, from the *Worldline Monte Carlo* approach for excited states. The 27 lowest energy permutation-symmetric state multiplets are extracted from  $\mathbb{T}^{ad} = (S/r_g)\mathbb{T} \mathbb{N}^{-1}$ , where the number of updates in the transfer and norm matrices has been varied from  $0.100 \cdot 10^6$  (ca. 50 mins) to  $599.98 \cdot 10^6$  (ca. 120 hrs). In the second row of the table, the energy eigenvalue of the ground extracted from the update of the transfer matrix worldlines is reported together with the associated statistical error, for the five values of  $S$ . From comparison of  $\mathcal{E}_{g.s.}$  in the rightmost column with the predicted value at  $-10.374$  MeV in the adiabatic projection approach, it is evident that the number of updates  $S$  suffices for a good agreement between the two energies within the statistical uncertainty. Concerning the eigenvalues extracted from  $\mathbb{T}^{ad}$ , an overall discrepancy of about 0.40 MeV between the  $n = 0$  eigenvalue and  $\mathcal{E}_{g.s.}$  in the rightmost column is still detectable, signalling that a systematic error of the same magnitude may affect also the other eigenvalues in the same column. Since the latter exceeds the reported statistical uncertainties by an order of magnitude, further Monte Carlo sampling is required in order to reach compatibility with the benchmark values from the adiabatic projection approach. Nevertheless, an overview of the data in the five columns permits to conclude that the Monte Carlo spectrum is gradually assuming the pattern of a lattice spectrum, with energy eigenvalues nearly arranged in cubic-group multiplets, of size equal to 1, 2 or 3. Quasi-degenerate **doublets** and **triplets** of states are highlighted.



We begin our treatment of rotational symmetry breaking effects in  $\alpha$ -conjugate nuclei with the case of  $^8\text{Be}$ . After presenting a sample of the spectrum of the lattice Hamiltonian  $\mathcal{H}_r$  in sec. 5.1, we concentrate on the analysis of finite volume and discretization effects in the energy eigenvalues of the cubic group multiplets that correspond to the  $0_1^+$  and  $2_1^+$  states in infinite volume. Even if the latter states were first identified in ref. [3], in our analysis we add a new tool, the total angular momentum squared operator,  $\hat{\mathcal{L}}^2$  (cf. sec. 4.3.3), and we investigate more in depth the correlation between discretization effects and the spatial distribution of the squared modulus of the lattice wavefunctions.

Although the Hamiltonian in sec. 4.2 would allow for the existence of a shallow bound state alone we increase the magnitude of the strength parameter of the attractive Ali-Bodmer potential,  $V_1$ , so that a significant number of bound states belonging to different irreducible representations of the rotational group is produced.

This expedient permits us to extend the analysis in secs. III A and B of ref. [3], to higher angular momentum multiplets, such as the  $4_2^+$  and  $6_1^+$  presented in sec. 5.3. The associated wavefunctions display a number of extrema, whose correlation with discretization effects in the energy eigenvalues are explored in the concluding section.

## 5.1 The spectrum

It is firmly enstablished that the actual ground state of this nucleus lies 91.84 keV above the  $\alpha - \alpha$  decay threshold, thus making it the only unbound  $\alpha$ -conjugate nucleus with  $A \leq 40$ . However, it remains of interest to dwell shortly on the behaviour of the binding energy (cf. eq. (4.48)) of this nucleus for different values of  $N$  and lattice spacing kept fixed to 0.75 fm.

As it can be inferred from fig. 5.1, the infinite volume value ( $L \equiv Na = 40$  fm) of the binding energy ( $\approx 57.67$  MeV) is inconsistent of about 1.2 MeV with the observational value ( $\approx 56.50$  MeV [219]), due to the choice of tuning the parameters of the Ali-Bodmer potential [219] on the  $0_1^+ - 0_2^+$  gap of  $^{12}\text{C}$ .

Nevertheless, the binding energy grows with the volume of the lattice, in accordance with the sign of the leading order finite volume correction for a  $0^+ A_1$  state [71]. Besides, due to the choice of the  $\mathcal{O}(a^8)$  approximation for the dispersion term, the smallest lattice of interest is the one with  $N = K = 4$ , in which the binding energy turns out to be largely underestimated

( $\approx 12$  MeV).

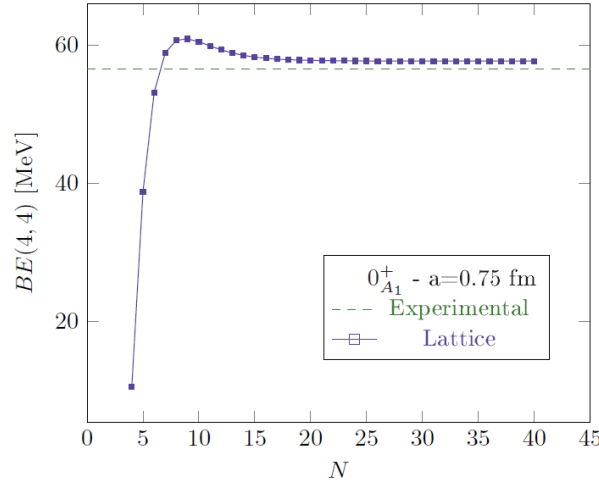


FIGURE 5.1 – Lattice binding energy of the  ${}^8\text{Be}$  as a function of the box size  $N$ . The spacing has been kept fixed to 0.75 fm, thus reducing discretization effects to about  $10^{-3}$  MeV.

As discussed in sec. 4.4, the spectrum of the  ${}^8\text{Be}$  Hamiltonian (cf. eq. (4.1) with  $M = 2$ ) on the lattice is made of simultaneous eigenstates of the cubic group, the cyclic group of order four generated by  $\mathcal{R}_z^{\pi/2}$ , spatial (and time) inversion and  $S_2$ , the permutation group of two elements. In particular, being particle exchange equivalent to the reversal of the sign of the relative coordinate  $\mathbf{r}_{12}$ , bosonic (fermionic) eigenstates possess even (odd) parity. In order to assess the capability of the model of describing the observed  $\alpha$ -cluster lines of this nucleus and receive some guidance for the subsequent choice of the multiplets of interest, we present a short excerpt of the low-energy spectrum of  $\mathcal{H}_r$  for a box with  $a = 0.5$  fm and  $N = 36$  in tab. 5.1.

$E$ [MeV]	$\Gamma$	$I_z$	$\mathcal{P}$	$S_2$	$\langle \mathcal{L}_{\text{tot}}^2 \rangle [\hbar^2]$	$E$ [MeV]	$\Gamma$	$I_z$	$\mathcal{P}$	$S_2$	$\langle \mathcal{L}_{\text{tot}}^2 \rangle [\hbar^2]$
-1.106778	$A_1$	0	+	$\square\square$	-0.056	2.834477	$E$	0	+	$\square\square$	15.332
		0						2			
0.353021	$T_1$	1	-	$\square$	2.086	3.133750	$T_2$	1	-	$\square$	12.676
		3						2			
0.948046	$A_1$	0	+	$\square\square$	2.507			3			
1.721746	$E$	0	+	$\square\square$	6.899	3.868673	$T_2$	1	+	$\square\square$	17.451
		2						2			
		0						3			
2.261133	$T_1$	1	-	$\square$	10.029	3.960128	$T_1$	0	-	$\square$	23.629
		3						1			
		1				4.289695	$A_1$	3	+	$\square\square$	30.743
2.532701	$T_2$	2	+	$\square\square$	7.090	4.302368	$A_2$	0	-	$\square$	14.698
		3						2			
2.651441	$A_1$	0	+	$\square\square$	18.908	4.308802	$E$	0	+	$\square\square$	10.620
								2			

TABLE 5.1 – Sample of the spectrum of the  ${}^8\text{Be}$  lattice Hamiltonian with  $N = 35$  and  $a = 0.5$  fm, consisting of the 14 lowest energy state multiplets. Considered the size of the lattice and its spacing, it is evident that the  $\mathcal{H}_r$  is able to generate only one bound state. Its energy displays a slight disagreement ( $\approx 1.2$  MeV) with its experimental counterpart.



Noticeable are the discrepancies between the eigenvalues of the squared angular momentum operator and the average values of the latter reported in the table. Since the volume of the box ( $Na = 17.5$  fm) is large enough to reduce finite-volume effects to the third decimal digit of the energy, these disagreements are due to discretization effects, whose magnitude increases with excitation energy and make the reconstruction of the infinite-volume angular momentum multiplet from the  $\langle \mathcal{L}_{\text{tot}}^2 \rangle \equiv \mathcal{L}^2$  hardly reliable. For instance, in the case of the first  $2^+$  multiplet, consisting of an  $E$  plus a  $T_2$  state,  $\Delta \mathcal{L}^2$  is already 15 % of the expected angular momentum eigenvalue. The behaviour of the squared angular momentum, therefore, suggests that wavefunctions corresponding to states of increasing energy are also increasingly position-dependent.

In addition the presence of an  $A_1^+$  state at 0.948 MeV, that further diagonalizations of the lattice Hamiltonian indicate as  $0^+$ , appears to be in contrast with the present observational data, that position the first excited  $0^+$  at 27.494 MeV [220].

## 5.2 The $0_1^+$ and $2_1^+$ energy levels

In order to study a larger number of bound states as well as to test the results reported in ref. [3], we increment the strength parameter of the attractive part of the Ali-Bodmer potential,  $V_0$ , by a 30 % with respect to its original value, see the dashed curve in fig. 4.1. Accordingly, the *artificial* ground state lies approximately 10.70 MeV below its observational counterpart. Besides the fundamental state, the infinite-volume spectrum of the Hamiltonian includes also a  $2^+$  multiplet, made of an  $E$  and a  $T_2$  state and another  $0^+$  state, the closest to the  $\alpha$ - $\alpha$  decay threshold. Since the latter appears only at relatively large volumes ( $Na \geq 25$  fm), in this section we focus the attention only on the  $2_1^+$  multiplet, as in ref. [3]. Fixing the lattice spacing to  $a = 0.25$  fm in order to reduce discretization effects and enlarge the samples of data, we investigate the finite-volume effects on the energy and the squared angular momentum of the three multiplets of states.

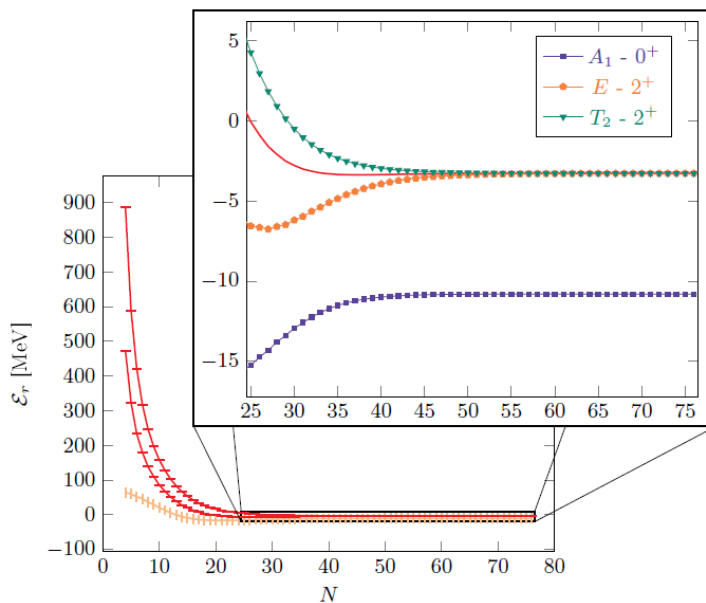


FIGURE 5.2 – Behaviour of the energies of the lowest  $0^+$  (vertical bars) and  $2^+$  (horizontal bars) eigenstates as a function of the box size  $N$  for  $a = 0.25$  fm. As expected, the eigenenergies associated to states belonging to the same irrep of  $SO(3)$  but to different irreps of  $\mathcal{O}$  become almost degenerate at the infinite-size limit. Residual discretization effects amount to about  $10^{-5}$  MeV for the ground state and  $10^{-4}$  MeV for the  $2^+$  multiplet. The multiplet-averaged energy of the latter in the magnification has been denoted by a solid line.

With this choice of the lattice spacing, the ground state energy reaches its infinite-volume value within the third decimal digit for  $Na = 13.25$  fm, while the two multiplets,  $E$  and  $T_2$  become degenerate within the same precision only for  $Na = 17$  fm. Nevertheless, convergence for the latter can be boosted by considering the multiplet averaged energy [3],  $E(2_1^+)$ , of the five states composing the  $2_1^+$  line in the continuum, third-digit accuracy is already achieved by  $E(2_A^+)$  at  $Na = 14.25$  fm. The theoretical justification underlying this procedure resides in the cancellation of the polynomial dependence on  $N$  of the lowest order finite-volume energy correction for the multiplet-averaged state. The main contribution to this energy shift is proportional to  $\exp(-\kappa N)$ , where  $\kappa = \sqrt{-2mE}$  is the binding momentum of the state, and turns out to be negative for all the values of  $N$  (cf. eq. (19) of [3]) and even angular momentum.

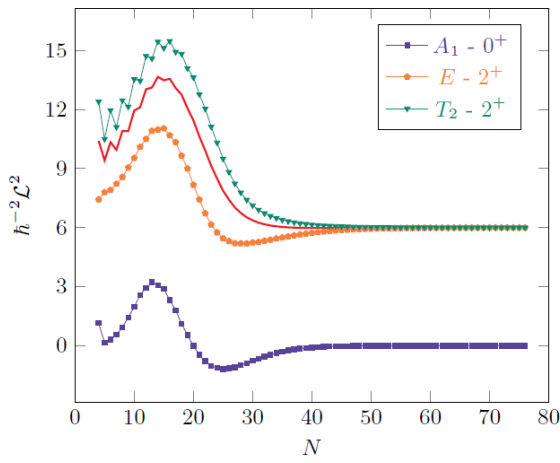


FIGURE 5.3 – Average value of the squared angular momentum for the three bound state multiplets as a function of the lattice size. As predicted, the average values of  $\mathcal{L}^2$  for the  $0_{A_1}^+$ ,  $2_E^+$  and  $2_{T_2}^+$  states smoothly converge to the eigenvalues equal to 0, 6 and 6 units of  $\hbar^2$  respectively of the same operator. Residual discretization effects amount to  $10^{-5}$  and  $10^{-4}\hbar^2$  for the  $0^+$  and  $2^+$  states respectively.

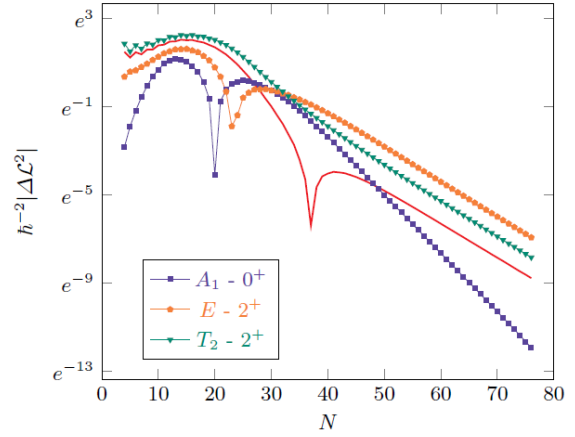


FIGURE 5.4 – Difference between the average value and the expected eigenvalue of the squared angular momentum for the three bound state multiplets as a function of the lattice size. Logscale is set on the y axis, thus unveiling a regular linear behaviour in the finite volume  $\mathcal{L}^2$  corrections for boxes large enough, analogous to the well-known one of the energies of bound states [71]. Unlike the latter, the three spikes due to sign reversal of the  $\Delta\mathcal{L}^2$  suggest that the finite volume corrections to this observable are not constant in sign.

Even though we do not have an analytical formula for the finite-volume corrections to the average values of  $\mathcal{L}^2$  at our disposal, we extend the use of the average on the dimensions of cubic group representations to the latter. As for the energies, an overall smoothing effect on the discrepancies between the average values and the eigenvalues of the squared angular momentum can be observed: a two digit accuracy in the estimates of the latter is reached at  $N = 37$  by the multiplet-averaged  $\mathcal{L}^2$  for the  $2_1^+$  multiplet, see the red dashed line in fig. 5.3, while the individual members of the multiplet reach the same precision only at  $N = 51$ . Moreover, in the large volume limit ( $N = 72$ ) the  $0_1^+$  state approaches the angular momentum eigenvalue within  $2 \times 10^{-5}$  units of  $\hbar^2$ , whereas for the  $E$  and  $T_2$  states of the  $2_1^+$  multiplet the accuracy is poorer, i.e.  $2 \times 10^{-3}\hbar^2$  and  $8 \times 10^{-4}\hbar^2$ , in order.

Plotting finally the discrepancies between the average values and the expected eigenvalues of the squared angular momentum of the three sets of degenerate energy eigenstates as function of the number of box sites per dimension, an exponential behavior of the former,

$\Delta\mathcal{L}^2 = A \exp(mN)$  with  $A$  and  $m$  real parameters, can be recognized, cf. fig. 5.4.

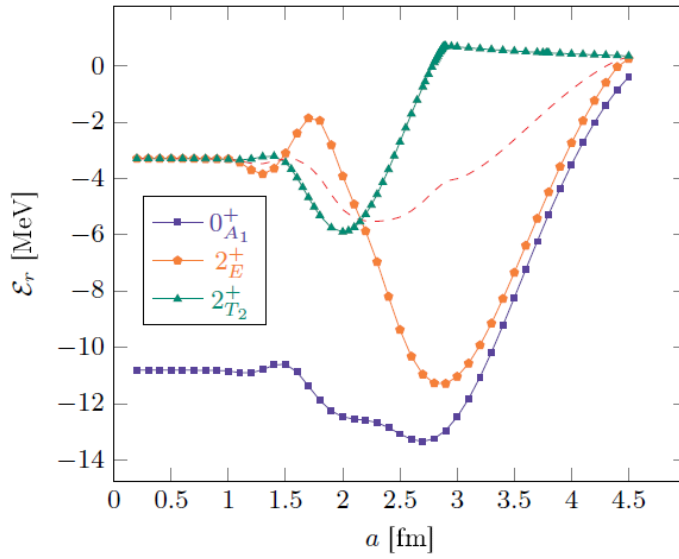


FIGURE 5.5 – Behaviour of the energies of the bound eigenstates as a function of the lattice spacing  $a$  for  $Na \geq 18$  fm ( $\ell = 0$ ) and  $Na \geq 19$  fm ( $\ell = 2$ ). As expected, the eigenenergies associated to states belonging to the same irrep of  $SO(3)$  but to different irreps of  $\mathcal{O}$  become almost degenerate in the zero-spacing limit. In the opposite direction, another level crossing is expected to occur at  $a \approx 4.5$  fm. Residual finite volume effects amount to  $10^{-5}$  MeV for the  $0^+$  state and to  $10^{-4}$  MeV for the  $2_1^+$  states. Multiplet-averaged energy of the  $2_1^+$  states has been denoted by a dashed line.

A linear regression with slope  $m$  and intercept  $\log A$  on the points with  $N \gtrsim 35$  can be performed, highlighting a distinct descending behaviour for each of the multiplets: the  $\Delta\mathcal{L}^2$  of the  $2_1^+$  states decreases, in fact, with the same angular coefficient within three-digit precision. It follows that the precision with which the squared angular momentum average values agree with their expectation values is an increasing function of the the binding momentum: the more the state is bound, the greater is the reliability of the  $\mathcal{L}^2$  estimation. Nevertheless, the derivation of an analytical formula for the finite volume corrections to the eigenvalues of the squared angular momentum operator remains a subject of interest for further investigations. Besides, once finite volume effects are reduced to the fourth decimal digit in the energies via the constraint  $Na \geq 18$  fm, the effects of discretization for different values of  $a$  can be inspected. As observed in ref. [3], the energies as function of the lattice spacing display an oscillatory behaviour, whose amplitudes for the  $A_1$  state are limited to the first decimal digit for  $0.9 \lesssim a \lesssim 1.2$  fm, then second digit precision is achieved for  $0.7 \lesssim a \lesssim 0.9$  fm.

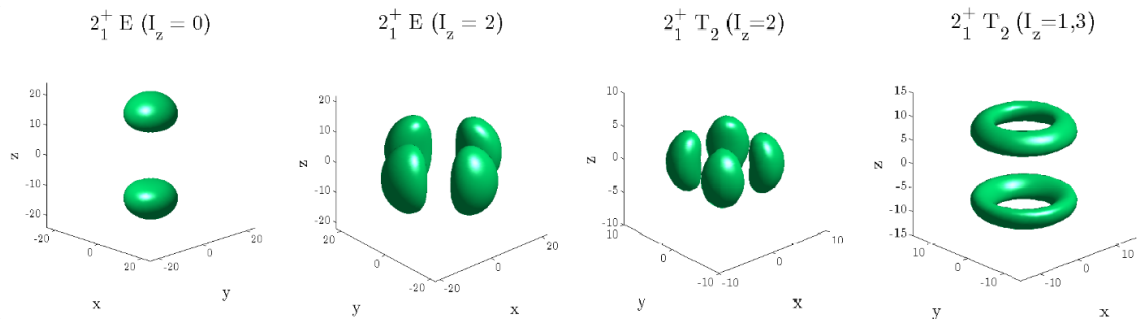


FIGURE 5.6 – The 3-d probability density distributions of the  $\alpha$ - $\alpha$  separation for the  $2_1^+$  states. As in figs. 5.8 and 5.10, the distances along the axes are measured in units of lattice spacing ( $a = 0.2$  and  $0.5$  fm for the  $E$  and  $T_2$  states respectively). In each subfigure the isohypses with 25% of the maximal probability density are shown. Due to time-reversal symmetry the PDF corresponding to the  $T_2$   $I_z = 1$  and 3 states exactly coincide.

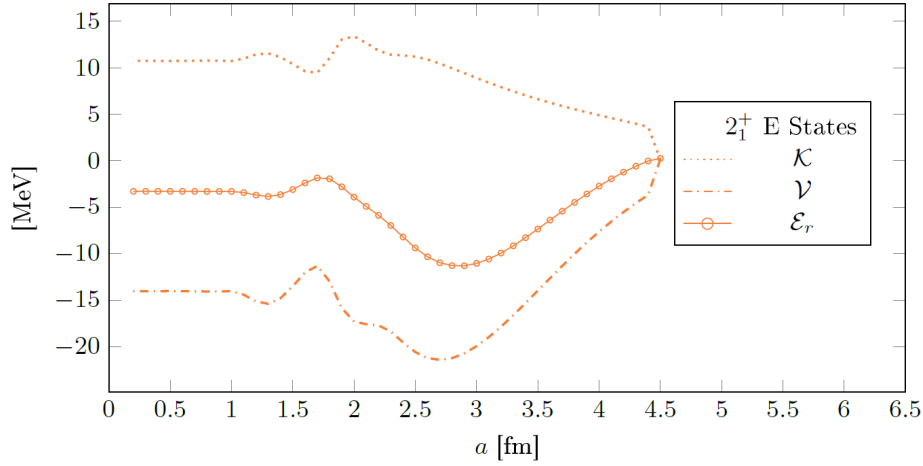


FIGURE 5.7 – Behaviour of the average values of the kinetic energy,  $\mathcal{K}$ , and the potential operator,  $\mathcal{V}$ , on the  $2_1^+$   $E$  eigenstates as a function of the lattice spacing  $a$  for  $Na \geq 19$  fm. The sum of the two average values produce the already displayed  $\mathcal{E}_r$  curve (cf. fig. 5.5), that almost intercepts the dotted one of  $\mathcal{K}$  as soon as the potential energy vanishes ( $a \approx 4.5$  fm) and the two states of the multiplet become unbound.

For the members of the  $2_1^+$  multiplet the fluctuations about the continuum value of the energies become more pronounced, being the achievement of a three digit precision confined to  $a \lesssim 0.5$  fm. Since only lattices with odd number of sites per dimension contain the origin of the axes, cf. the definition of the map between lattice sites and physical coordinates in eq. (4.47), that is supposed to give important contribution to the lattice eigenenergies when the wavefunction is concentrated about the former point, only lattices with odd values of  $N$  have been considered for the large ( $a \gtrsim 1.25$  fm) lattice spacing analysis.

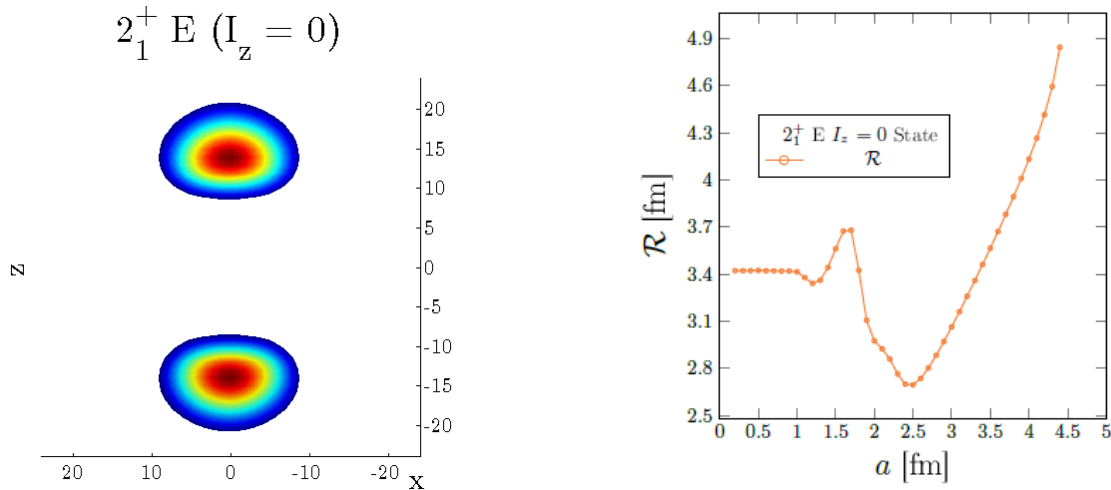


FIGURE 5.8 – Cross-sectional plot ( $xz$  plane) of the PDF of the  $2_1^+$   $E$   $I_z = 0$  state (left) and behaviour of the average value of the interparticle distance as a function of the lattice spacing for the same eigenstate (right). In particular, the outer isohypsic surfaces of the former plot correspond to a probability density equal to the 25% (dark blue) of the maximum value of the PDF (dark red). Distances along the axes are measured in lattice spacing units ( $a = 0.2$  fm). In the other graph, two minima of  $\mathcal{R}$  at  $a \approx 1.4$  and  $2.5$  fm are visible, implying that the condition on the decay of the wavefunction with increasing  $\alpha$ - $\alpha$  distance is only approximately fulfilled. In the same panel, residual finite volume effects amount to approximately  $10^{-3}$  fm.

Although a closed form for the leading order discretization corrections to the energy eigenvalues does not exist, it is still possible to associate some extrema of the latter, see fig. 5.5 and fig. 3 in ref. [3], to the maxima of the squared modulus of the associated eigenstates. This interpretation rests on the assumption that  $\mathcal{E}_r(a)$  reaches a local minimum for all the values of the spacing  $a$  such that all the maxima of the squared modulus of the corresponding eigenfunction,  $|\Psi_r(\mathbf{r})|^2$ , are included in the lattice. This condition is satisfied when all the maxima lie along the symmetry axes of the cubic lattice. In case  $|\Psi_r(\mathbf{r})|^2$  possesses only primary maxima, i.e. points lying at distance  $d^*$  from the origin such that the most probable  $\alpha$ - $\alpha$  separation,  $\mathcal{R}^*$ , coincides with  $d^*$ , the description of the behaviour of  $\mathcal{E}_r(a)$  in terms of the spatial distribution of the associated wavefunction becomes more predictive.

In particular, when all the maxima lie along the lattice axes and the decay of the probability density function (PDF) associated to  $\Psi_r(\mathbf{r})$  with radial distance is fast enough, i.e.  $|\Psi_r(\mathbf{r})|_{\text{Max}}^2 \gg |\Psi_r(\mathbf{r})|^2$  for  $|\mathbf{r}| = nd^*$  and  $n \geq 2$ , the average value of the interparticle distance coincides approximately with the most probable  $\alpha$ - $\alpha$  separation,  $\mathcal{R} \approx d^*$ , and the average value of the potential,  $\mathcal{V}$ , is minimized at the same time.

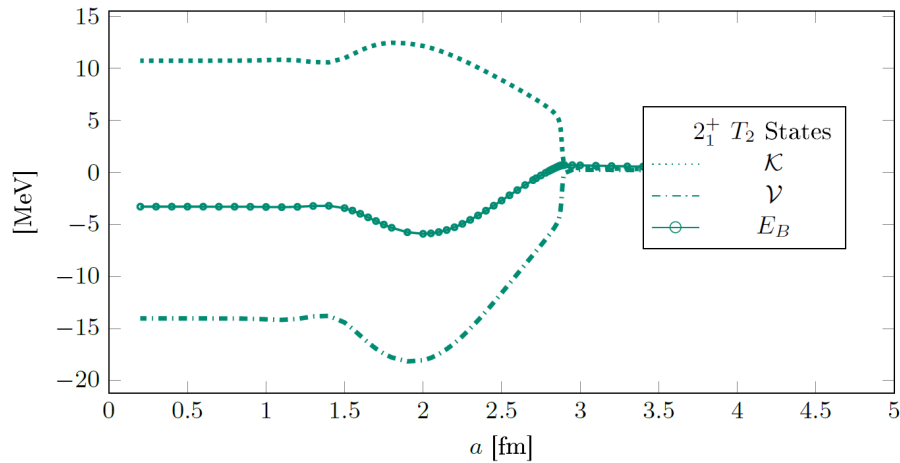


FIGURE 5.9 – Behaviour of the average values of the kinetic energy,  $\mathcal{K}$ , and the potential operator,  $\mathcal{V}$ , on the  $2_1^+ T_2$  eigenstates as a function of the lattice spacing  $a$  for  $Na \geq 19$  fm. The sum of the two average values produce the already displayed  $\mathcal{E}_r$  curve (cf. fig. 5.5), that almost overlaps the dotted one of  $\mathcal{K}$  when the potential energy is negligible ( $a \gtrsim 2.8$  fm) and the three states of the multiplet are unbound.

Since the maxima of the eigenfunctions of both the  $2_1^+ E$  states ( $I_z = 0, 2$ ) lie on the lattice axes at distance  $d^* \approx 2.83$  fm and no secondary maximum is found, cf. fig. 5.6, the energy eigenvalues of the two states are expected to display minima for  $a = d^*/n$  with  $n \in \mathbb{N}$ , i.e. for  $a \approx 2.83, 1.42, 0.94, \dots$  fm. Effectively, two energy minima at  $a \approx 2.85$  and  $1.36$  fm are detected (cf. fig. 5.7). In addition, for  $a \approx d^*$  it is found that  $\mathcal{R} \approx 2.88$  fm and  $\mathcal{V} \approx -21.21$  MeV, both the values being in appreciable agreement with the minimum values of the two respective quantities,  $2.70$  fm and  $-21.40$  MeV, see figs. 5.7 -5.8: it follows that also the requirement on the decrease of the PDF with distance is approximately fulfilled.

On the other hand, the PDF of the  $2_1^+ T_2$   $I_z = 2$  state possesses four absolute maxima in the intersections between the  $xy$  plane and the  $y = \pm x$  planes lying at the same distance  $d^* \approx 2.83$  fm from the origin of the axes, whereas for the  $I_z = 1, 3$  states there are two

circles of absolute maxima about the  $z$  axis, located at the same distance from the origin, cf. figs. 5.6 and 5.10. The two different patterns lead to the same inclusion conditions for the principal maxima,  $a = d^*/\sqrt{2}n$  with  $n \in \mathbb{N}$ , i.e.  $a \approx 2.02, 1.01, 0.67, \dots$  fm. In practice, two well-developed minima for  $a \approx 2.02$  and  $1.05$  fm are observed, still in agreement with the predictions. Moreover, two minima are detected in the potential at  $a \approx 1.96$  and  $1.05$  fm, whereas no extremum is found for around  $a = d^*$ , due to the absence of maxima along the lattice axes (cf. fig. 5.9).

Therefore, the interpretation of the behaviour of the eigenenergies of bound states based on the spatial configuration of the corresponding eigenfunctions and the average value of potential  $\mathcal{V}$  on the latter reviewed also in sect. III A of ref. [3] is further supported by our findings.

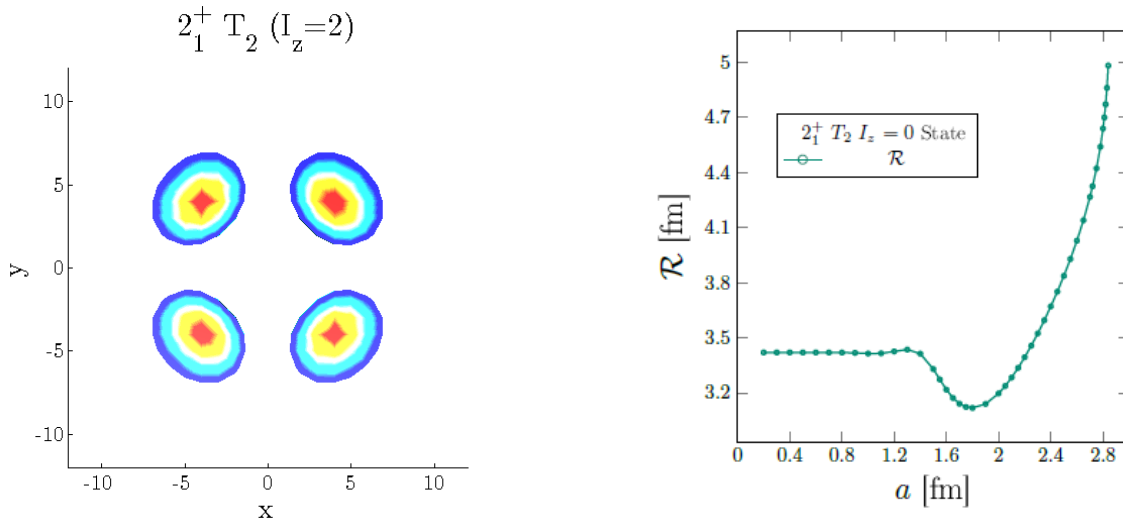


FIGURE 5.10 – Cross-sectional plot (xy plane) of the PDF of the  $2_1^+ T_2 I_z = 2$  state (left) and behaviour of the average value of the interparticle distance as a function of the lattice spacing for the same eigenstate (right). In particular, the outer isohypses of the former plot correspond to a probability density equal to the 25% (dark blue) of the maximum value of the PDF (dark red). Distances along the axes are measured in lattice spacing units ( $a = 0.5$  fm). In the other graph, two minima of  $\mathcal{R}$  at  $a \approx 1.0$  and  $1.8$  fm are visible, implying that the condition on the decay of the wavefunction with increasing  $\alpha$ - $\alpha$  distance is satisfied only to a first approximation. In the same panel, residual finite volume effects amount approximately to  $5 \cdot 10^{-4}$  fm.

However, also the behaviour of the energy eigenvalue as a function of the lattice spacing for the ground state (cf. fig. 5.5) can find an interpretation if the extrema of the two-body potentials  $V^{\text{II}}$  are considered. Since the spatial distribution of the PDF of the  $0_1^+$  state is spherical with a maximum when the two  $\alpha$  particles completely overlap ( $d^* = 0$ ), minima of  $\mathcal{E}_r$  may occur when the only minimum of  $V^{\text{II}}$  at  $2.64$  fm is mapped in the cubic lattice, i.e. for spacings equal to  $2.64, 1.32, 0.85 \dots$  fm. Effectively, two minima at about  $1.25$  and  $2.70$  fm are found together with a quasi-stationary point at  $2.35$  fm, perhaps due to the inclusion of the shallow maximum of the two-body potentials at  $6.71$  fm, see fig. 2.1.

Concerning the angular momentum, similar considerations on fluctuations can be drawn: first decimal digit oscillations are associated to the region  $0.96 \lesssim a \lesssim 1.55$  fm of the ground state, the  $1.05 \lesssim a \lesssim 1.58$  fm one of the  $2_E^+$  state and the  $0.96 \lesssim a \lesssim 1.7$  fm one of the  $2_{T_2}^+$ , while third decimal digit accuracy is achieved for  $a \lesssim 0.6$  fm by the  $0_1^+$  and only at  $a \lesssim 0.2$  fm and  $a \lesssim 0.55$  fm for the two members of the  $2_1^+$  multiplet, respectively. The overall behaviour of the angular momentum average values of the three states seems unaffected by level crossings



and turns out to be smooth, with the noticeable exception of the evolution curve for the  $2_{T_2}^+$  state. In correspondence with the local maximum of the energy eigenvalue at  $a = 2.9$  fm a rapid *step* increase of the average value of the squared angular momentum of the latter eigenstate takes place, see fig. 5.11. This phase transition-like behaviour is perhaps related to the exclusion of a sharp extremum characterizing the wavefunction from the lattice, thus preventing an unambiguous determination of the angular momentum content of the  $2_{T_2}^+$  state for  $a \gtrsim 2.9$  fm.

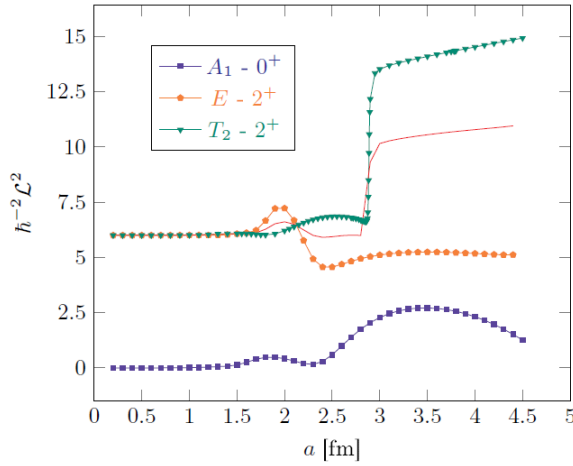


FIGURE 5.11 – Average value of the squared angular momentum for the six bound states as a function of the lattice spacing when  $Na \geq 18$  fm ( $\ell = 0$ ) and  $Na \geq 19$  fm ( $\ell = 2$ ). As previously, convergence of the average values of  $\mathcal{J}^2$  to its expected eigenvalues is attained in the zero-spacing limit. Residual finite-volume errors amount to about  $10^{-5}\hbar^2$  for the  $0_1^+$  state and  $5 \cdot 10^{-4}\hbar^2$  for the  $2_1^+$  states.

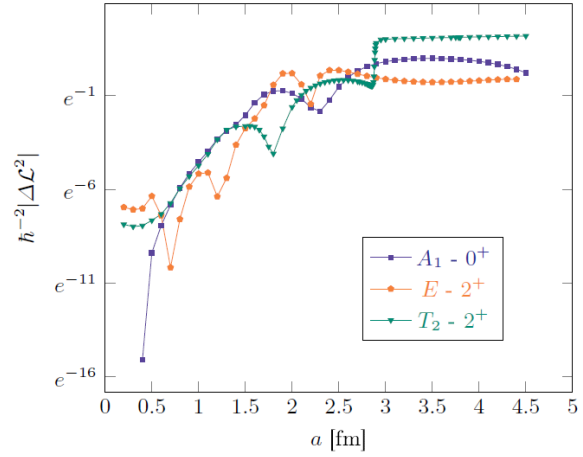


FIGURE 5.12 – Difference between the average value and the expected eigenvalue of the squared angular momentum for the six bound states as a function of the lattice spacing for  $Na \geq 18$  fm ( $\ell = 0$ ) and  $Na \geq 19$  fm ( $\ell = 2$ ). Even if a log-scale is set on the  $y$  axis, no regular behaviour in the finite volume  $\mathcal{L}^2$  corrections can be detected, apart from an overall negative concavity and piecewise linearity of the  $0_{A_1}^+$  and  $2_{T_2}^+$  curves.

Contrary to the finite-volume analysis, few conclusions can be drawn from the plot of the  $\Delta \mathcal{L}^2$  average values (cf. fig. 5.12). Even if one keeps the logscale in the ordinate axis, the behaviour remains far from linear, due both to sign oscillations of the corrections and to a certain overall negative concavity. In addition, multiplet averaging seems to have little effect in smoothing these fluctuations.

### 5.3 The $4_2^+$ and $6_1^+$ energy levels

With the aim of extending the previous analysis to higher angular momentum states and assessing the effectivity of multiplet averaging, we increase artificially the strength parameter of the attractive part of the Ali-Bodmer potential up to the 150 % of its original value, see the dotted curve in fig. 2.1. By means of this artifact, the wavefunctions of the  $^4\text{He}$  nuclei in this section become more localized about the origin, a consequence of the enhanced attraction of the  $\alpha - \alpha$  potential. Moreover, finite volume effects in lattices with size  $Na = 12$  fm are already limited to the third decimal digit for the energies of the bound states, a precision that, in the previous case, was attained by the  $2_1^+$  multiplet only at 17 fm.



Besides the latter states and the fundamental one, the bound region of the spectrum now contains four  $0^+$  and two further  $2^+$  multiplets, together with two  $4^+$  and the expected  $6^+$ , in whose decomposition into irreps of the cubic group all the representations appear at least once.

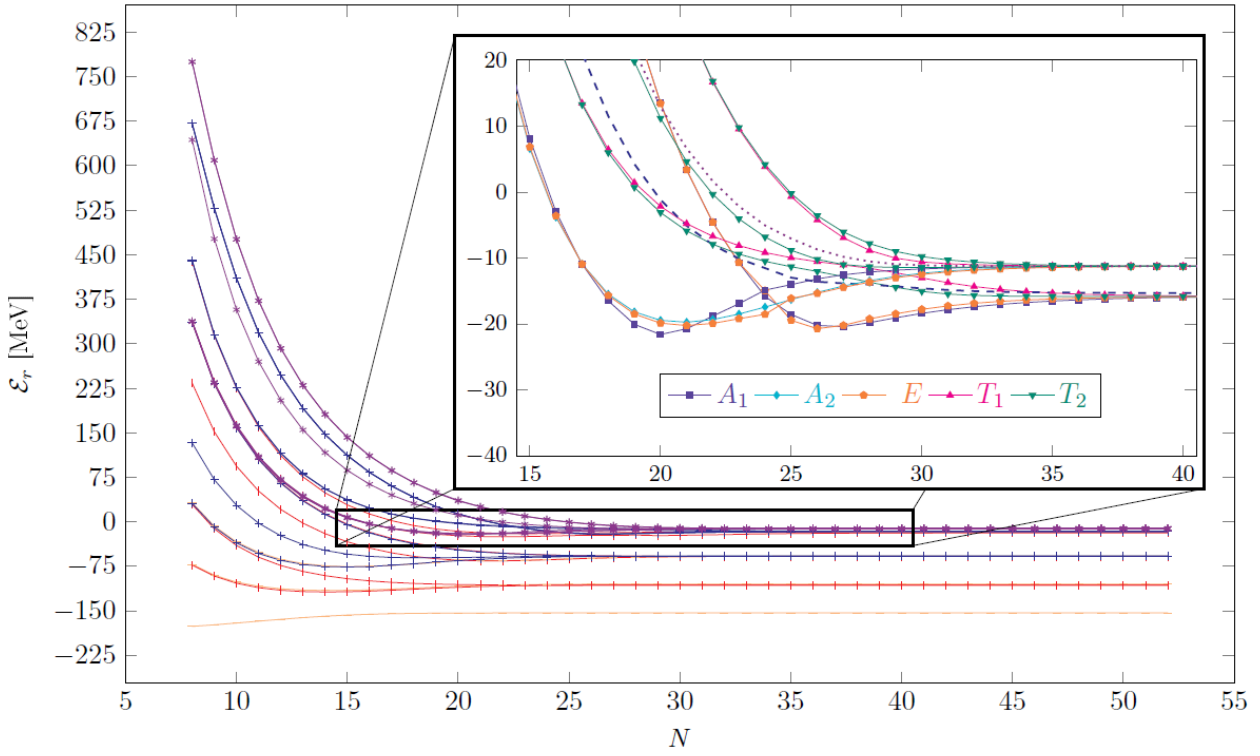


FIGURE 5.13 – Behaviour of the energies of the bound eigenstates as a function of the box size  $N$  for  $a = 0.25$  fm. In the background graph, lines marked by horizontal bars are associated to  $0^+$  states, lines marked by vertical bars with  $2^+$  states, lines marked by greek crosses with  $4^+$  and lines marked by asterisks with  $6^+$ . As expected, rotational symmetry is almost restored in the large box size limit ( $N = 52$ ). The magnification resolves the  $4_2^+$  and  $6_1^+$  states in terms of the underlying cubic group multiplets. Residual discretization errors amount to about  $10^{-3}$  and  $5 \cdot 10^{-4}$  MeV for the  $4_2^+$  and the  $6_1^+$  states respectively. Multiplet-averaged eigenenergies of the two are denoted by dashed and dotted lines, in order.

As in the previous case, multiplet averaging of the energies of the  $4^+$  and  $6^+$  multiplets finds further justification with the cancellation of the polynomial dependence on the lattice size  $N$  in the lowest order finite-volume energy corrections (FVECs). More precisely, the leading order correction for the multiplet averaged energies with angular momentum  $\ell$  and parity  $P$  assumes the universal form [3]

$$E_\infty(\ell_A^P) - E_N(\ell_A^P)|^{LO} = (-1)^{\ell+1} 3|\gamma|^2 \frac{e^{-\kappa N}}{mN}, \quad (5.1)$$

as its magnitude is independent on the particular  $\text{SO}(3)$  irrep according to which the energy eigenstate transforms. Keeping the lattice spacing invariant with respect to the previous case, we repeat the finite-volume analysis for all the bound states, but dedicating a special attention to the two uppermost  $\text{SO}(3)$  multiplets,  $4_2^+$  and  $6_1^+$ . Even if the extraction of a greater number of bound states increases the runtime of the numerical computations, the faster decay of the wavefunctions with distance allows to keep the same lattice spacings. Due to the changes in the spatial distribution, the cubic group multiplets composing the  $\text{SO}(3)$  ones become degener-

ate with a minimum precision of  $10^{-3}$  MeV already at  $N = 52$ , while the average values of the squared angular momentum reach the expectation values with a four decimal digit minimum accuracy. As it can be inferred from the magnification in fig. 5.13, at least two level crossings between states with the same transformation properties under the operations of the cubic group take place: the involved states are the  $A_1$  and the  $E$  ones of the two  $\text{SO}(3)$  multiplets.

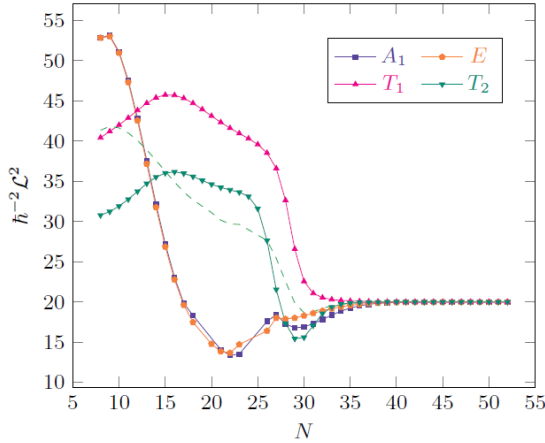


FIGURE 5.14 – Average value of the squared angular momentum for the  $4_2^+$  states as a function of the lattice size. As predicted, the average values of  $\mathcal{L}^2$  for the cubic group partners of the  $\text{SO}(3)$  multiplet converge to the eigenvalue of 20 units of  $\hbar^2$  of the same operator, even if with a well-pronounced oscillatory behaviour for relatively small lattices ( $N \lesssim 32$ ). Residual discretization effects amount to about  $10^{-4}\hbar^2$ .

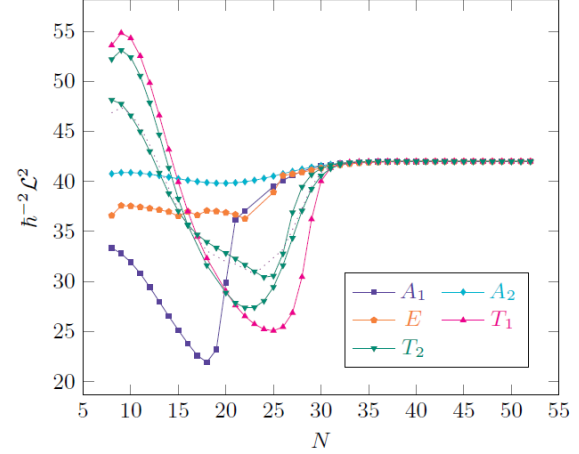


FIGURE 5.15 – Average value of the squared angular momentum for the  $6_1^+$  states as a function of the lattice size. As predicted, the average values of  $\mathcal{L}^2$  for the cubic group partners of the  $\text{SO}(3)$  multiplet converge to the eigenvalue of 42 units of  $\hbar^2$  of the same operator, even if with a very pronounced oscillatory behaviour for relatively small lattices ( $N \lesssim 32$ ). Residual discretization effects amount to about  $10^{-4}\hbar^2$ .

These intersections are at the origin of sudden *spikes* in the evolution curves of the average values of the squared angular momentum with  $N$  for the latter states. As this is presumably due to the insufficient sampling in these regions limited by the lattice spacing constraint, these points have been accurately removed from the plots in figs. 5.14 and 5.15. Therefore, better estimations of the intrinsic behaviour of these angular momentum evolution lines can be drawn from  $\mathcal{O}$  multiplets that never experience level crossings with states having the same transformation properties under the cubic group. Optimal candidates for such curves are the smooth ones associated to the  $6_{A_2}^+$ ,  $4_{T_1}^+$ ,  $4_{T_2}^+$  and  $6_{T_2}^+$  I levels. The latter represents the  $T_2$  multiplet lying always below in energy with respect to the  $J = 6$  partner bearing the same cubic irrep.

The plot of the differences between the average values and the expected values of  $\mathcal{L}^2$  with the number of lattice sites per dimension enables us to confirm the qualitative observations on the finite volume corrections for the squared angular momentum. For lattices large enough ( $N \gtrsim 26$ ), the latter decreases exponentially with  $N$ , the decay constant being approximately shared by all the members of the same  $\text{SO}(3)$  multiplet. Besides, convergence to the expected angular momentum is faster for more tightly bound states, suggesting again a dependence of the decay constants on the energies of the spectral lines. Moreover, the chosen value of the lattice spacing is responsible of the *saturation* behaviour of the lines for the  $6_{T_1}^+$  and  $6_{T_2}^+$  II for  $N \geq 37$ : as observed in fig. 5.12, discretization affects states belonging to different  $\text{SO}(3)$  and

$\mathcal{O}$  irreps in different extent.

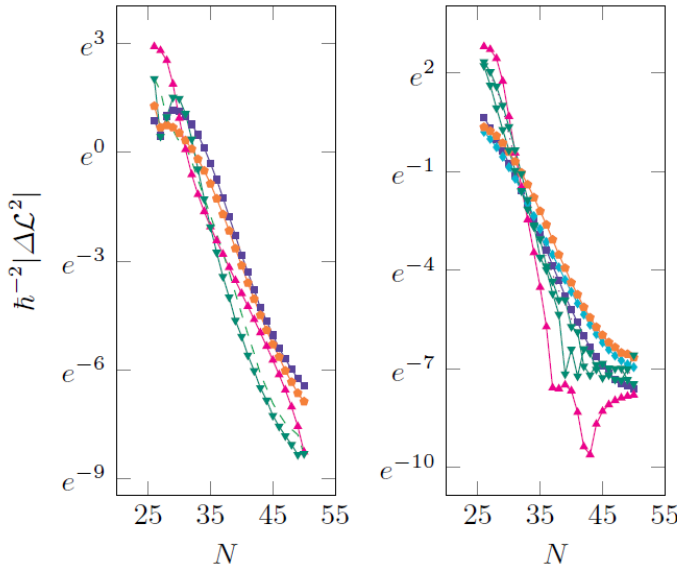


FIGURE 5.16 – Difference between the average value and the expected eigenvalue of the squared angular momentum for the  $4_2^+$  (left) and  $6_1^+$  (right) states as a function of the lattice size. A regular linear behaviour in the finite-volume  $\mathcal{L}^2$  corrections for boxes large enough neatly emerges by setting the log-scale on the y axis. The same convention on the markers for the cubic group irreps of figs. 5.10-5.8 is used.

Setting a box size equal to 12 fm, we can now concentrate on discretization effects. As expected, here the consequences of a more localized distribution of the wavefunctions about the origin become even more evident. Discretization errors for the energies remain large in a wide range of lattice spacing, dropping to the first decimal digit for most of the bound states only at  $a \approx 0.60$  fm and then reaching third digit precision only at 0.25 fm. Nevertheless, the behaviour of the  $4_2^+$  and  $6_1^+$  eigenenergies as function of the lattice spacing appears smooth in the interval of interest,  $0.24 \leq a \leq 1.8$  fm.

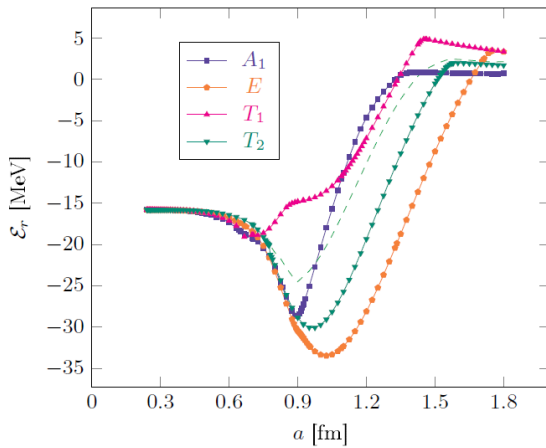


FIGURE 5.17 – Behaviour of the energies of the  $4_2^+$  eigenstates as a function of the lattice spacing for  $Na \geq 12$  fm. Residual finite-volume effects amount to about  $10^{-3}$  MeV.

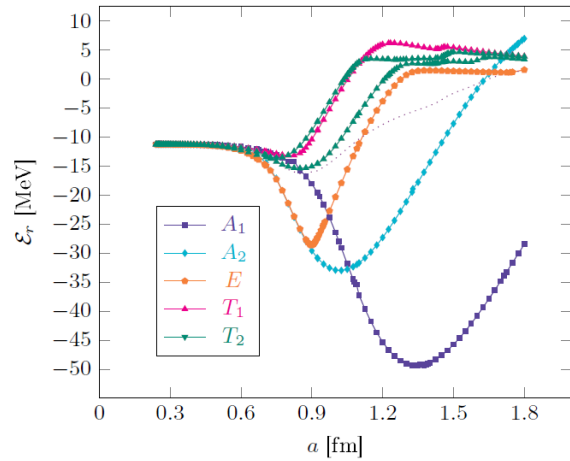


FIGURE 5.18 – Behaviour of the energies of the  $6_1^+$  eigenstates as a function of the lattice spacing for  $Na \geq 12$  fm. Residual finite-volume effects amount to about  $10^{-4}$  MeV.

In particular, the curves for the  $4_2^+$   $E$ ,  $A_1$  and  $T_2$  multiplets display a deep minimum located around 0.95 fm, cf. fig. 5.17, whereas the one of the  $T_1$  levels possesses a shallower pocket, closer to the origin ( $a \approx 0.75$  fm). Similarly, the energy curves of the  $6_{A_1}^+$ ,  $6_{A_2}^+$  and  $6_E^+$  states possess a well developed first minimum about 1.38, 1.02 and 0.91 fm, respectively, while  $T_1$  and  $T_2$  states are characterized by a first shallow minimum at about 0.9 fm followed by a second

even less-developed one around 1.5 fm.

As illustrated for  $2_1^+$  states and in ref. [3], the position of these minima can find an interpretation via the analysis of the spatial distribution of the PDFs associated to the relevant states. However, the presence of secondary maxima and of absolute maxima off the lattice symmetry axes in the  $4_2^+$  and  $6_1^+$  PDFs make these predictions less effective than in the previous case. Nevertheless, the inclusion conditions for the maxima of the  $6_{A_2}^+$   $I_z = 2$  state are satisfied in good approximation for a relatively large value of the spacing,  $a$ , leading to a successful description of the behaviour of the turquoise curve in fig. 5.18.

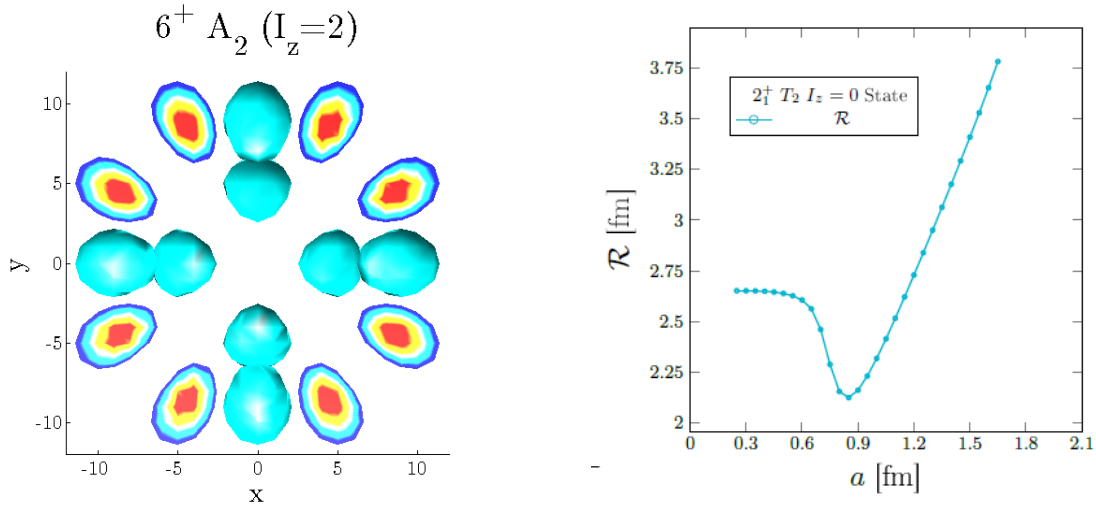


FIGURE 5.19 – Cross-sectional plot (xy plane) of the PDF of the  $6_1^+ A_2$  state (left) and behaviour of the average value of the interparticle distance as a function of the lattice spacing for the same eigenstate (right). In particular, the outer isohypses of the former plot correspond to a probability density equal to the 25% (dark blue) of the maximum value of the PDF (dark red). Distances along the axes are measured in lattice spacing units ( $a = 0.24$  fm). Despite the strong resemblance, the arrangement of the maxima in the xy, xz and yz planes is not octagonal. In the other graph, a minimum in  $\mathcal{R}$  at  $a \approx 0.88$  fm is visible, implying that the condition on the decay of the wavefunction with increasing  $\alpha$ - $\alpha$  distance is appreciably satisfied. In the same panel, residual finite-volume effects amount to approximately  $10^{-3}$  fm.

The probability density function for this  $6^+$  state is characterized by four equidistant couples of principal maxima separated by an angle  $\gamma \approx 34.2^\circ$  and located at a distance  $d^* \approx 2.31$  fm from the origin in the  $x, y$  and  $z = 0$  planes. Even if the 24 maxima cannot be simultaneously included in the cubic lattice, the inclusion conditions on the lattice spacing approximately match for  $1.02 \lesssim a \lesssim 1.08$  fm. From the inclusion conditions of a pair of maxima in the first quadrant of the xy plane, see figs. 5.19 and 5.21, in fact, it follows that

$$a_x = \frac{d^*}{n} \cos \left( \frac{\pi}{4} - \frac{\gamma}{2} \right), \quad (5.2)$$

i.e.  $a_x \approx 2.04, 1.02, 0.68 \dots$  for the x-axis and

$$a_y = \frac{d^*}{n} \sin \left( \frac{\pi}{4} - \frac{\gamma}{2} \right), \quad (5.3)$$

i.e.  $a_y \approx 1.08, 0.54, 0.36 \dots$  for the y-axis. Effectively, a sharp minimum of the total energy (cf. fig. 5.19) is detected, confirming the predictions. On the other hand, the minimum of the average value of the potential, cf. fig. 5.19, and the  $\alpha$ - $\alpha$  distance see fig. 5.20, is shifted towards smaller spacings ( $\approx 0.85$  fm), due to a slow decrease of the associated probability

density function in the vicinity the maxima.

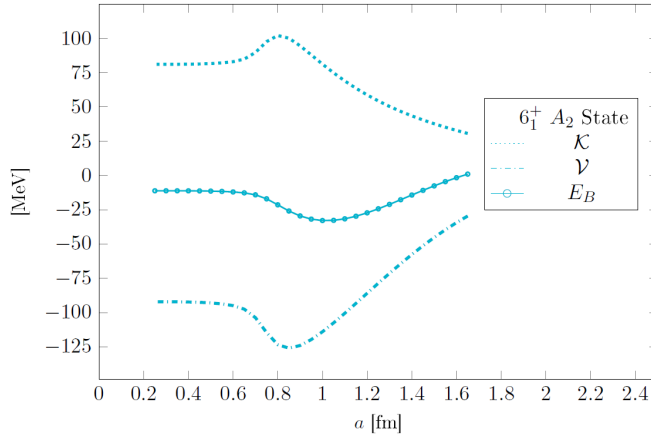


FIGURE 5.20 – Behaviour of the average values of the kinetic energy,  $\mathcal{K}$ , and the potential operator,  $\mathcal{V}$ , on the  $6_1^+ A_2$  eigenstate as a function of the lattice spacing  $a$  for  $Na \geq 12$  fm. The sum of the two average values produce the already displayed  $\mathcal{E}_r$  curve, see fig. 5.18.

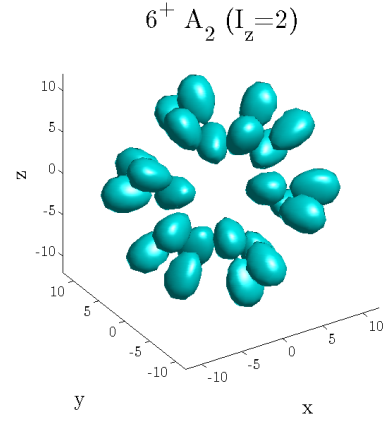


FIGURE 5.21 – Three-dimensional probability density distribution of the  $\alpha$ - $\alpha$  separation referring to the isohypses with 25% of the maximal value of the  $6_1^+ A_2$  state PDF. As in figs. 5.10, 5.7 and 5.9, the distances along the axes are measured in units of lattice spacing ( $a = 0.24$  fm).

Concerning the angular momentum, the fluctuations of the average values of  $\mathcal{L}^2$  about the corresponding expectation values for  $a \gtrsim 0.6$  fm are even larger than the ones of the energies. The effect is even amplified for the  $0_3^+$  and the  $A_1$  member of the lowest  $4_1^+$  state due to their quasi-degeneracy and the many level crossings they undergo before reaching their continuum eigenvalues (cf. fig. 5.22).

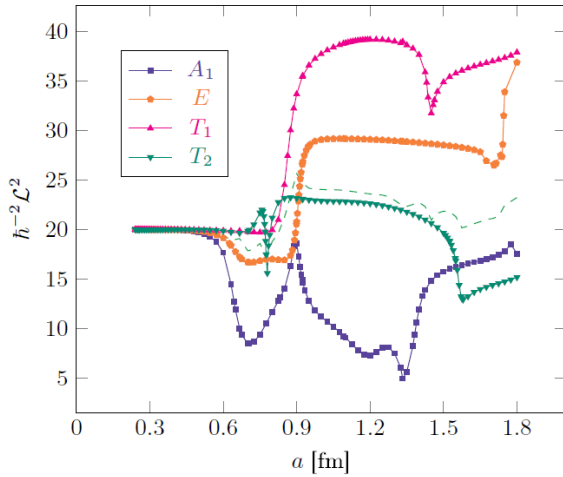


FIGURE 5.22 – Behaviour of the squared angular momentum of the  $4_2^+$  eigenstates as a function of the lattice spacing for  $Na \geq 12$  fm. As before, convergence of the average values of  $\mathcal{L}^2$  to its expected eigenvalues is achieved in the zero-spacing limit. Residual finite volume effects amount to about  $10^{-3}\hbar^2$ .

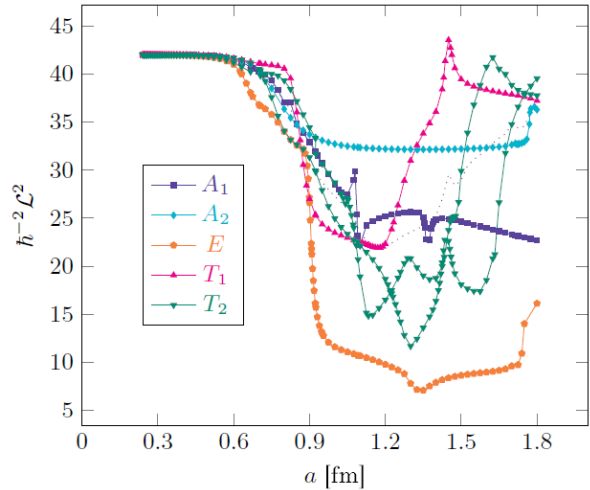


FIGURE 5.23 – Behaviour of the squared angular momentum of the  $6_1^+$  eigenstates as a function of the lattice spacing for  $Na \geq 12$  fm. Convergence of the average values of  $\mathcal{L}^2$  to its expected eigenvalues is attained in the zero-spacing limit. Residual finite volume effects amount to about  $10^{-4}\hbar^2$ .

Due both to the absence of nearby levels with the same transformation properties under  $\mathcal{O}$  and the smaller number of these crossings, the  $4_2^+$  and the  $6_1^+$  multiplets converge sensibly faster to their expected squared angular momentum eigenvalues in the zero spacing limit. Nevertheless, the appreciable continuity of the evolution curves of  $\mathcal{L}^2$  with  $a$  remains seldom interrupted by sharp spikes and wells, witnessing level crossings of the aforementioned kind, see figs. 5.22 and 5.23. Due to the presence of many low-lying  $0^+$  and  $2^+$  states,  $A_1$  and, to a smaller extent,  $T_2$  and  $E$  lines are more heavily affected by cusps than  $T_1$  and  $A_2$  states, whose behaviour exhibits the transition-like features already observed in fig. 5.12. The onset point of these step-growing and falling parts marks the upper bound of the lattice spacing interval in which the observed levels can be classified as partners of a  $SO(3)$  multiplet.

Beyond  $a \approx 0.9$  fm, the characterizing part of all the wavefunctions composing the  $4_2^+$  and  $6_1^+$  multiplets is not sampled any more by the lattice, thus making angular momentum classification of the states almost unreliable.

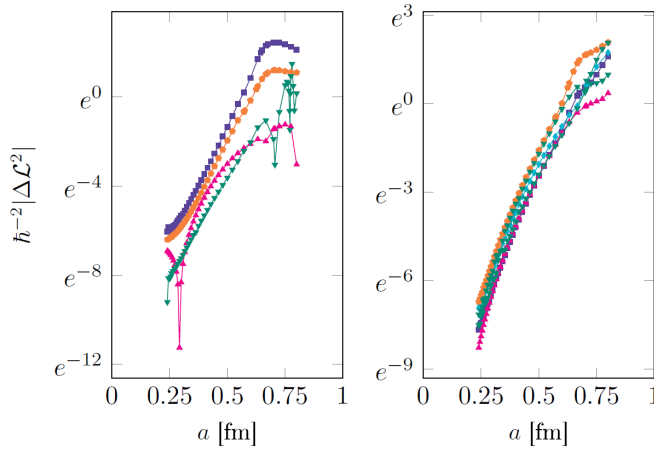


FIGURE 5.24 – Difference between the average value and the expected eigenvalue of the squared angular momentum for the  $4_2^+$  (left) and the  $6_1^+$  states (right) as a function of the lattice spacing. The same convention on the markers for the cubic group irreps of figs. 5.13-5.20 is used.

Since the  $|\Delta\mathcal{L}^2|(a)$  curve for the  $2_E^+$  state in the above is heavily affected by the sign inversions of the angular momentum correction, no particular conclusion was drawn from the graph in fig. 5.12. In this case, apart from a spike in the  $4_{T_1}^+$  curve around 0.3 fm and some disturbance in the  $4_{T_2}^+$  one around 0.75 fm, an appreciable quasi-linear behaviour of the  $\log|\Delta\mathcal{L}^2|$ 's can be inferred from 0.7 fm towards the continuum limit, see fig. 5.24. Consequently, the corrections to the squared angular momentum average values for lattice cubic group eigenstates can be reproduced by a positive exponential of  $a$ ,

$$|\Delta\mathcal{L}^2(\ell)| \underset{a \rightarrow 0}{\approx} \mathcal{A}_\ell \exp(a \cdot \kappa_\ell) . \quad (5.4)$$

in the small-spacing region. In particular, the constant in the argument of the exponential,  $\kappa_\ell$ , is approximately independent on the cubic group irrep  $\Gamma$  according to which each state of a given angular momentum multiplet  $\ell$  transforms. Moreover, the proportionality constant  $\mathcal{A}_\ell$  in eq. (5.4) vanishes exactly for infinite-volume lattices and is expected to decrease with increasing box size  $Na$ .

However, the extent of the region where this approximation can be successfully applied depends on the onset point of the step growing or falling parts of the squared angular momentum curves. Since the  $\alpha$ - $\alpha$  average distance is larger for the  $6_1^+$  than for the  $4_2^+$ , this interval is wider for the former and the positive exponential behaviour more evident.





We continue the investigation of rotational symmetry breaking effects in  $\alpha$ -conjugate nuclei with the case of  $^{12}\text{C}$ . Due to the addition of a three-body potential to the  $^8\text{Be}$  Hamiltonian, the ground state of  $\mathcal{H}_r$  is now anchored on the observed energy gap between the Hoyle state [221, 222],  $0_2^+$ , and the fundamental state,  $0_1^+$ , a fact that guarantees the presence of a certain number of bound states in the spectrum of the physical Hamiltonian. Therefore, we choose to fix the parameters of the Ali-Bodmer potential [4] to their physical values.

After showing an excerpt of the spectrum of the lattice Hamiltonian  $\mathcal{H}_r$  in sec. 6.1, we concentrate on the analysis of finite volume and discretization effects in the energy eigenvalues of the cubic group multiplets that correspond to the  $0_1^+$  and  $2_1^+$  states in infinite volume. Although the latter states were first inspected in ref. [3], in our analysis we reduce the lattice spacing and we increase the number of mesh points per dimension,  $N$ . In particular, we enrich the treatment with the average values of the total angular momentum squared,  $\mathcal{L}^2$ , (cf. sec. 4.3.3) and the  $\alpha$ - $\alpha$  separation,  $\mathcal{R}$ .

Furthermore, in sec. 6.2 we extend the above analysis to the  $3_1^-$  multiplet, and display the probability density functions associated to the  $0_{A_1}^+$ ,  $2_E^+$  and  $3_{T_1}^-$  lattice eigenfunctions. As for  $^8\text{Be}$  nucleus, the correlation between the position of their extrema and discretization effects in the energy eigenvalues is explored in the concluding part of the section.

## 6.1 The spectrum

After the study of finite-volume and discretization effects in the spectrum of  $^8\text{Be}$ , we focus on the bound states of a system three interacting  $\alpha$  particles, the  $^{12}\text{C}$  nucleus. Due to the particular choice of the parameters of  $V_{AB}$ , the addition of the attractive phenomenological three-body potential in eq. (4.4) permits us to reproduce the binding energy of this nucleus. Although the ground state is tuned on the energy of the Hoyle state rather than on the  $3\alpha$  decay threshold, in fact, the binding energy can be still recovered, provided the well-established positive gap between the latter two is added to the ground state energy,  $E_{0^+}$  in eq. (4.48).

Even if the behaviour of lattice binding energy (cf. eq. (4.48)) with the box size  $N$  is all in all analogous to the one of Beryllium, two digit accuracy with the observational counterpart ( $\approx 92.16$  MeV) of the former is finally reached at  $N = 24$  and spacing equal to 0.75 fm. Therefore, finite-volume effects can be reasonably neglected for our purpose in lattices with size

$Na \geq 18$  fm.

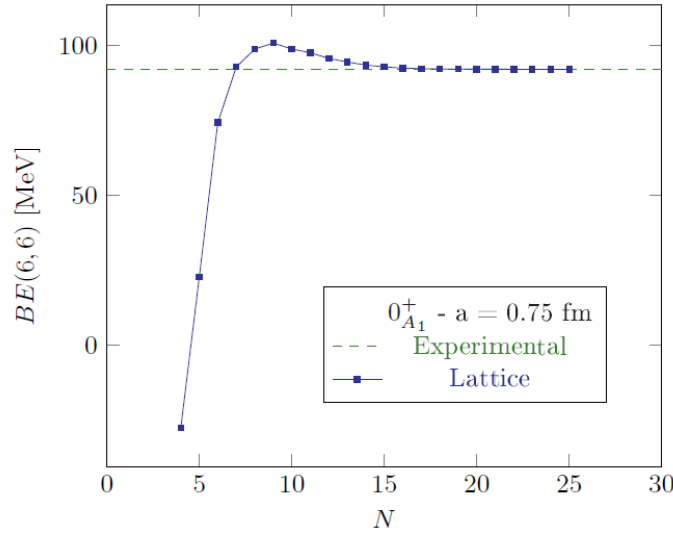


FIGURE 6.4 – Lattice binding energy of the  $^{12}\text{C}$  as a function of the box size  $N$ . The spacing has been kept fixed to 0.75 fm, with the aim of reducing the residual discretization effects to about  $5 \cdot 10^{-3}$  MeV.

Differently from the preceeding case, there is no more isomorphism between parity and particle permutation group,  $\mathcal{S}_3$ , a six element non-abelian group bearing also a 2-dimensional irreducible representation (diagrammatically  $\begin{smallmatrix} \square & \square \end{smallmatrix}$ ).

$E$ [MeV]	$\Gamma$	$I_z$	$\mathcal{P}$	$\mathcal{S}_3$	$\langle \mathcal{L}_{\text{tot}}^2 \rangle [\hbar^2]$	$E$ [MeV]	$\Gamma$	$I_z$	$\mathcal{P}$	$\mathcal{S}_3$	$\langle \mathcal{L}_{\text{tot}}^2 \rangle [\hbar^2]$
<b>-7.698420</b>	<b><math>A_1</math></b>	<b>0</b>	<b>+</b>	$\begin{smallmatrix} \square & \square & \square \end{smallmatrix}$	<b>0.373</b>	-2.686463	$A_1$	0	+	$\begin{smallmatrix} \square & \square & \square \end{smallmatrix}$	1.690
-6.306062	$T_1$	1	-	$\begin{smallmatrix} \square & \square \end{smallmatrix}$	2.429	-2.637041	$T_1$	1	-	$\begin{smallmatrix} \square & \square \end{smallmatrix}$	8.320
-5.457046	$T_1$	1	+	$\begin{smallmatrix} \square & \square \end{smallmatrix}$	2.466	-2.483865	$T_2$	2	-	$\begin{smallmatrix} \square & \square \end{smallmatrix}$	12.603
-4.550694	$T_2$	2	+	$\begin{smallmatrix} \square & \square \end{smallmatrix}$	6.612	-2.297536	$A_2$	2	-	$\begin{smallmatrix} \square & \square \end{smallmatrix}$	12.493
-4.470975	$E$	0	+	$\begin{smallmatrix} \square & \square \end{smallmatrix}$	6.175	-2.281911	$T_1$	1	-	$\begin{smallmatrix} \square & \square \end{smallmatrix}$	7.943
<b>-3.420394</b>	<b><math>E</math></b>	<b>0</b>	<b>+</b>	$\begin{smallmatrix} \square & \square & \square \end{smallmatrix}$	<b>6.729</b>	<b>-1.981923</b>	<b><math>T_2</math></b>	<b>2</b>	<b>-</b>	$\begin{smallmatrix} \square & \square & \square \end{smallmatrix}$	<b>12.536</b>
<b>-3.177991</b>	<b><math>T_2</math></b>	<b>2</b>	<b>+</b>	$\begin{smallmatrix} \square & \square & \square \end{smallmatrix}$	<b>6.824</b>	<b>-1.797457</b>	<b><math>T_1</math></b>	<b>1</b>	<b>-</b>	$\begin{smallmatrix} \square & \square & \square \end{smallmatrix}$	<b>12.360</b>
-2.873875	$T_2$	2	-	$\begin{smallmatrix} \square & \square \end{smallmatrix}$	7.086	<b>-1.779066</b>	<b><math>A_2</math></b>	<b>2</b>	<b>-</b>	$\begin{smallmatrix} \square & \square & \square \end{smallmatrix}$	<b>12.384</b>
-2.862931	$A_1$	0	+	$\begin{smallmatrix} \square & \square \end{smallmatrix}$	2.074	-1.706789	$T_1$	1	-	$\begin{smallmatrix} \square & \square \end{smallmatrix}$	4.441

TABLE 6.4 – Sample of the spectrum of the  $^{12}\text{C}$  Hamiltonian with  $N = 15$  and  $a = 1$  fm, consisting of the 17 lowest degenerate energy multiplets. The  $\text{SO}(3)$  multiplets of interest,  $0_1^+$ ,  $2_1^+$  and  $3_1^-$  are highlighted in bold. Cubic group multiplets labeled by the Young Tableau with three unaligned boxes appear twice in the spectrum, since the irrep of the permutation group according to which they transform is 2-dimensional.

As a consequence, besides bosonic and fermionic symmetry, the eigenstates of the lattice Hamiltonian  $\mathcal{H}_r$  can be now symmetric with respect to the exchange of a pair of particles and antisymmetric with respect to the transposition of another couple of them, resulting in the appearance of *unphysical* parastatistic eigenstates.

Given the duration and memory consumption of the eigenvector extraction process and being parity itself uncorrelated with particle exchange symmetry, also projectors on parity and  $\mathcal{G}_4$  irreps have been incorporated in the iteration loop, thus minimizing the number of eigenvectors involved in the Gram-Schmidt orthogonalization. On the other hand, the matrix  $\mathcal{R}_z^{\pi/2}$ , (cf. eq. (4.37)) to be simultaneously diagonalized together with the Hamiltonian, has been excluded from the iteration loop.

## 6.2 The $0_1^+$ , $2_1^+$ and $3_1^-$ energy levels

Since the actual nucleus is naturally bound, no artificial increase of the Ali-Bodmer potential attractive parameter is needed for the investigation of finite-volume and discretization effects in the lowest bound eigenstates presented in this section. By sampling the spectrum of the relative Hamiltonian with  $N = 15$  and  $a = 1.0$  fm, see tab. 6.1, and the one with  $N = 20$  and  $a = 0.9$  fm to a smaller extent, it turns out that this nucleus possesses seven SO(3) multiplets of completely-symmetric bound states, namely three  $0^+$ , a  $1^-$ , two  $2^+$  and a  $3^-$ , in the continuum and infinite-volume limit. Experimentally, only a  $2^+$  line at 4.44 MeV is found to lie below the  $3\alpha$  decay threshold [223], while the lowest  $3^-$  and  $1^-$  observed excitations result to be unbound by circa 1.9 and 2.2 MeV respectively.

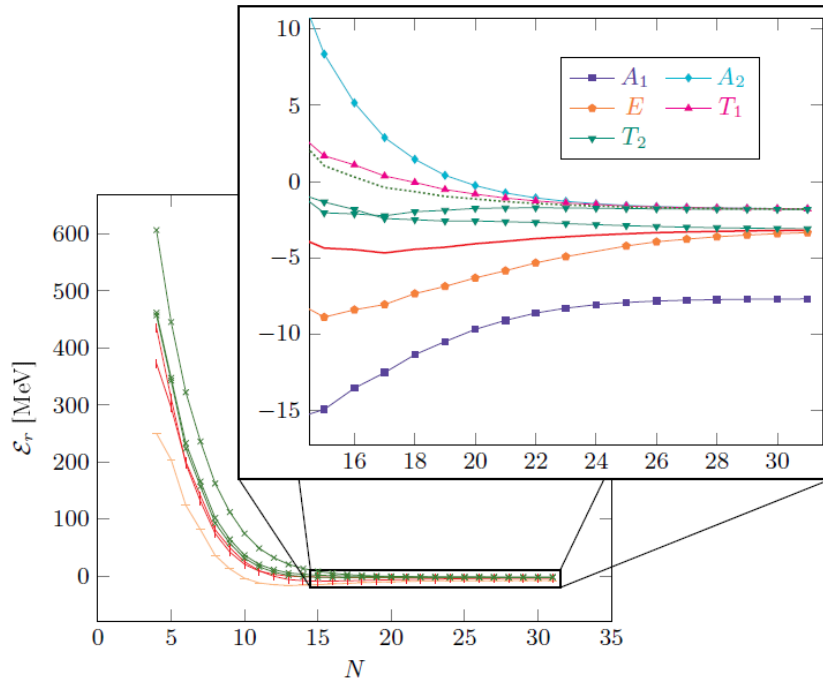


FIGURE 6.2 – Behaviour of the energies of the lowest  $0^+$  (horizontal bars),  $2^+$  (vertical bars) and  $3^-$  (diagonal crosses) bound eigenstates as a function of the box size  $N$  for  $a = 0.50$  fm. As expected, the eigenenergies associated to states belonging to the same irrep of SO(3) but to different irreps of  $\mathcal{O}$  become almost degenerate at the infinite-size limit. The same convention on the markers for the cubic group irreps adopted in the figures of chap. 5 is understood. Residual discretization effects amount to about  $10^{-2}$  MeV for the  $0^+$  and  $2^+$  states and to  $5 \cdot 10^{-3}$  MeV for the  $3^-$  states.

Starting from this set of bound eigenstates, we choose to restrict our analysis to the ground state at  $-7.65$  MeV, the  $2_1^+$  state at  $-3.31$  MeV and the  $3_1^-$  multiplet at  $-1.80$  MeV, decomposing into an  $A_2$ , a  $T_1$  and a  $T_2$  multiplet with respect to the cubic group.

Analogously to the Beryllium case, we fix the lattice spacing in such a way to reduce the discretization errors to less than two decimal digits in the infinite-volume limit ( $Na \gtrsim 19$  fm) for all the multiplets of interest and plot the behaviour of the energy as a function of the lattice size  $N$  (cf. fig. 6.2). The evolution curve for the energy of the ground state follows a similar path to the ones of the  $0^+$  states of  $^8\text{Be}$ : after a minimum at  $Na \approx 6$  fm, the continuum and infinite-volume eigenvalue is reached asymptotically from below, as prescribed by the FVEC formulas from ref. [77] for a two-body system.

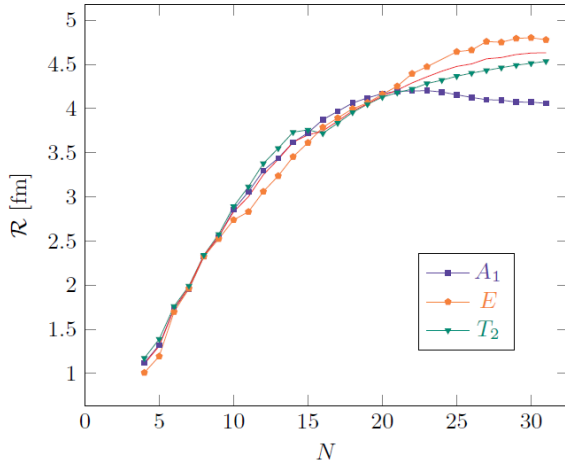


FIGURE 6.3 – Behaviour of the average interparticle distance for the  $0_1^+$  and  $2_1^+$  multiplets as a function of the lattice size. Due to the broader spatial distribution of the  $2_E^+$  and  $T_2^+$  wavefunctions, the finite-volume effects on the average values of the  $\alpha - \alpha$  separation distance remain sensitive ( $\approx 0.24$  fm at  $N = 31$ ). Residual discretization effects amount to about  $10^{-3}$  fm for the ground state and  $5 \cdot 10^{-3}$  fm for the  $2^+$  states.

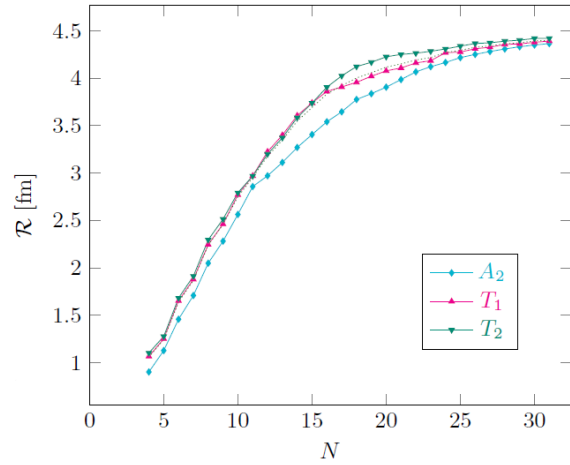


FIGURE 6.4 – Behaviour of the average interparticle distance for the  $3_1^-$  multiplet of states as a function of the lattice size. As expected, both the three members of this  $\text{SO}(3)$  multiplet converge to same average values of the  $\alpha$ - $\alpha$  separation distance, that at  $N = 31$  coincide within 0.05 fm accuracy. Residual discretization effects amount to about  $5 \cdot 10^{-3}$  fm.

In particular, an agreement within one decimal digit with the fitted value of  $-7.65$  MeV is already reached at  $Na \approx 13$  fm, whereas the overlap with all the meaningful digits is expected to be achieved at  $Na \approx 16.5$  fm.

However, the  $2^+$  doublet is expected to become degenerate within one-digit precision only at  $Na \approx 16$  fm, due to a broader spatial distribution of the  $E$  and  $T_2$  eigenfunctions. The average separation between the  $\alpha$  particles in the equilateral triangular equilibrium configuration, in fact, amounts approximately to 4.65 fm for the doublet of states and to 4.05 fm for the  $0_1^+$  state, see fig. 6.3. From the ground state value of the  $\alpha$ - $\alpha$  separation, an estimate of the nuclear radius can be obtained by computing the distance between the barycentre and the vertices of the triangle,  $R/\sqrt{3}$ . The outcoming value gives 2.34 fm, which slightly underestimates the observational charge radius of the nucleus in ref. [224], equal to 2.47 fm.

Furthermore, in the  $3^-$  energy multiplet the  $T_1$  and the  $A_2$  states approach the continuum and infinite-volume energy from above, whereas the  $T_2$  multiplet requires corrections of opposite sign, see fig. 6.2. Although analytical formulas for the leading order FVEC for three body systems are still unknown, the sign of these corrections for the  $\ell = 3$  multiplet seem coincide with the one of the FVECs for a multiplet of bound eigenstates with the same angular momentum of a two-body system.

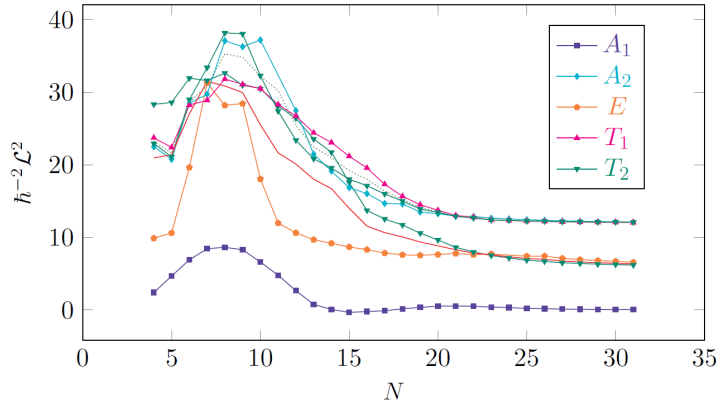


FIGURE 6.5 – Average value of the squared angular momentum for the six bound states as a function of the lattice size. After displaying a peak in the interaction region, the average values of the squared angular momentum for the  $0_1^+$ ,  $2_1^+$  and  $3_1^-$  states converge to the eigenvalues of  $\mathcal{L}^2$  equal to 0, 6 and  $12\hbar^2$  respectively in the infinite-volume limit. The multiplet averages of the  $2_1^+$  and  $3_1^-$  states are denoted by solid and dotted lines. Residual discretization effects amount to  $5 \cdot 10^{-2}\hbar^2$  for the  $0^+$  and  $3^-$  states and to  $10^{-1}\hbar^2$  for the  $2^+$  states.

Besides, rotational symmetry for this multiplet is already restored within one decimal digit accuracy for  $Na \approx 14$  fm, due to the more localized spatial distribution of the wavefunctions, see fig. 6.4. The infinite-volume value of the average  $\alpha - \alpha$  distance for the states of these multiplets is 4.40 fm, in between the one of the  $0_1^+$  and the  $3_1^-$  multiplets.

The average values of the angular momentum as function of the lattice size  $N$  for both the three  $SO(3)$  multiplets considered display a well-developed maximum at about  $N = 7$ , eventually followed by a shallow minimum lying between  $N = 15$  and  $N = 20$ .

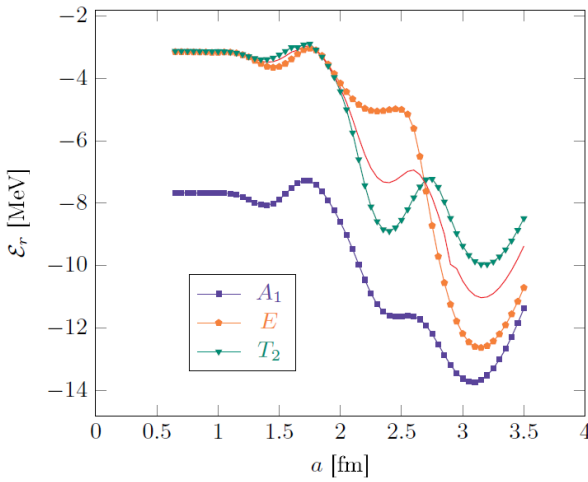


FIGURE 6.6 – Behaviour of the energies of the  $0_1^+$  and  $2_1^+$  eigenstates as a function of the lattice spacing for  $Na \geq 19$  fm. Although the multiplet-averaged  $2_1^+$  energy (solid line) improves the convergence rate to the continuum and infinite-volume counterpart, for  $a \gtrsim 2.0$  fm discretization corrections amount to more than 33% of the asymptotic energy eigenvalue. Residual finite volume effects are expected to amount to  $10^{-3}$  MeV for the ground state and to  $5 \cdot 10^{-3}$  MeV for the  $2^+$  states.

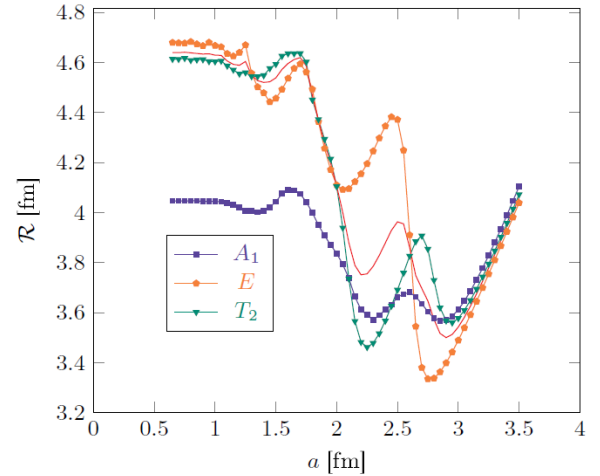


FIGURE 6.7 – Behaviour of the average  $\alpha - \alpha$  distance of the  $0_1^+$  and  $2_1^+$  eigenstates as a function of the lattice spacing for  $Na \geq 19$  fm. It is worth observing that the values of  $\mathcal{R}$  to which the  $2_E^+$  and the  $2_{T_2}^+$  states seem to converge do not coincide by an amount of 0.06 fm. It is possible that this small bias is due to residual finite-volume effects, since, as noticed in fig. 6.3, for  $a = 0.5$  fm and  $N = 31$  the two average interparticle distances differ still by 0.24 fm. Nevertheless, the other observables concerning this angular momentum multiplet, cf. figs. 6.6 and 6.13, perhaps less sensitive to finite-volume effects, do not display this behaviour in the small-spacing limit. Residual finite-volume effects for the ground state are expected to be smaller by an order of magnitude.

In particular, the angular momentum of the  $0_1^+$  state reaches the expected asymptotic value from below, as observed in the beryllium case (cf. fig. 5.3), while the  $2_E^+$  and  $2_{T_2}$  multiplets approach the continuum and infinite volume limit from below and above, respectively. This suggests the sign of the leading order finite volume corrections for the eigenvalues of the  $\mathcal{L}^2$  operator. Although the  $\mathcal{L}^2$  evolution curves for the three  $\text{SO}(3)$  multiplets resemble the ones of the  $0_1^+$  and  $2_1^+$  states of the  $^8\text{Be}$  nucleus, cf. fig. 5.3, the  $E$  and the  $A_2$  levels for  $N \lesssim 14$  seem to be heavily affected by level crossings with adjacent energy states (note that a spike marking the  $2_E^+$  evolution curve at  $N = 11$  has been omitted).

Next, we concentrate the attention to the systematic errors due to finite lattice spacing. By fixing the size of the lattice at  $Na \geq 19$  fm in order to reduce finite-volume errors to the third decimal digit, we inspect the behaviour of the energy eigenvalues of the aforementioned  $0_1^+$ ,  $2_1^+$  and  $3_1^-$  multiplets for lattice spacings  $a$  ranging from 0.65 to 3.50 fm. From the plot in fig. 6.6, the  $0_{A_1}^+$  state already equates the fitted energy eigenvalue of  $-7.65$  MeV within one and two decimal digit precision at  $a \approx 1.15$  and  $1.00$  fm, whereas the two members of the  $2_1^+$  multiplet become degenerate within the same accuracy for  $a = 1.30$  and  $0.75$  fm respectively. As outlined in sec. 5.2, some of the minima of the energy curves can be associated to the values of the lattice spacing that permit the inclusion of relative maxima of the probability distribution functions of the states into the lattice.

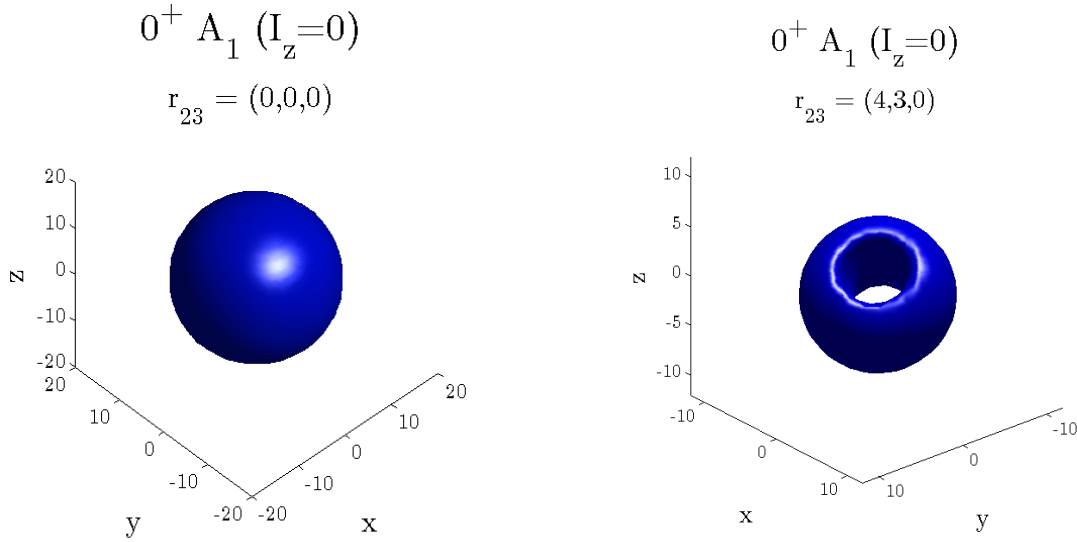


FIGURE 6.8 – Spatial distribution of the PDF of the  $0_1^+ A_1$  state with  $I_z = 0$  in the configuration space slices with  $\mathbf{r}_{23} = (0,0,0)$  (left) and  $\mathbf{r}_{23} = (4,3,0)$  (right). The outer isohypsic surfaces of the former plot correspond to a probability density equal to 50 times the local minimum value of the PDF ( $\approx 2.6 \cdot 10^{-16} \text{ fm}^{-6}$ ), whereas the one of the latter is equal to 10% the probability density of the absolute maximum ( $\approx 1.7 \cdot 10^{-9} \text{ fm}^{-6}$ ). Distances along the axes are measured in lattice spacing units ( $a = 0.65$  fm). In particular, the toroidal region in the right panel encompasses an entire circle of maxima, which correspond to principal extrema of the wavefunction. In the other plot, the probability density increases with the distance from the origin, until a saddle point consisting of a spherical shell is reached. Then the probability density decreases more slowly to zero. Finally, it is worth remarking that symmetry under particle exchange ensures that the two plots would remain unaffected if the two slices were kept from the  $\mathbf{r}_{13}$  subspace.

Differently to the two-body case, the  $^{12}\text{C}$  eigenfunctions may possess a huge amount of local extrema and display rather complex spatial distributions, thus making the analysis of the PDF maxima by far more involved than in the beryllium case, see figs. 6.8-6.12.



Since the interactions are isotropic, the most probable separation distance between any of the pairs of  $\alpha$  particles is expected to coincide exactly for all the eigenfunctions belonging to the same  $SO(3)$  multiplet in the zero-spacing limit.

Contrary to the beryllium case, the PDF of the ground state of this nucleus has a local non-zero minimum when  $\mathbf{r}_{13} = \mathbf{r}_{23} = (0, 0, 0)$ , meaning that configuration in which all the  $\alpha$  particles completely overlap has become unstable. In addition, the squared modulus of the  $0_1^+$  wavefunction possesses also maxima, the absolute ones corresponding to equilateral triangular equilibrium configurations in which  $\alpha$ -particles are separated by  $d^* \approx 3.3$  fm, see. fig. 6.8. Even if none of these maxima can be exactly included in the lattice, both the three minima of the energy eigenvalue at  $a \approx 1.40, 2.35$  and  $3.10$  fm are in good correspondence with the ones of the potential energy  $\mathcal{V}$ . In particular, for the latter two values of the spacing the average interparticle distance  $\mathcal{R}$  differs from  $d^*$  by only  $0.3$  fm, cf. fig. 6.8.

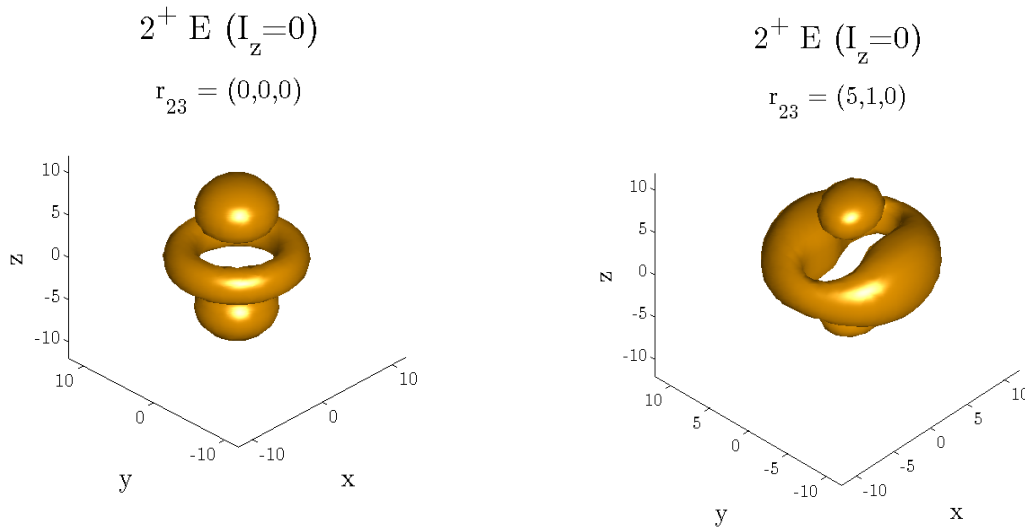


FIGURE 6.9 – Spatial distribution of the PDF of the  $2_1^+ E$  state with  $I_z = 0$  in the configuration space slices with  $\mathbf{r}_{23} = (0, 0, 0)$  (left) and  $\mathbf{r}_{23} = (5, 1, 0)$  (right). The outer isohypsic surfaces of the two plots correspond to probability densities equal to the 15% and the 10% of the largest extremal values of the squared modulus of the wavefunction enclosed by the surfaces. Distances along the axes are measured in lattice spacing units ( $a = 0.65$  fm). In particular, the bulges in the toroidal regions in the right plot encompass one single PDF extremum each, which correspond to principal maxima of the wavefunction ( $\approx 3.2 \cdot 10^9 \text{ fm}^{-6}$ ). On the other hand, all the extrema in the  $\mathbf{r}_{23} = (0, 0, 0)$  slice of the PDF are indeed saddle points. It follows that the configurations with two overlapping  $\alpha$ -particles and the third one lying in the centre of one of the spheres or in the inner circle of the regular torus are unstable.

For what concerns the  $2_E^+$  multiplet, its energy eigenvalue reaches a shallow minimum for  $a \approx 2.30$  fm and two well-developed minima for  $a \approx 1.45$  and  $3.10$  fm (cf. fig. 6.6 and fig. 7 in ref. [3]). As before, these minima are found to be in correspondence with the ones of the average values of the potential energy.

Although none of the absolute maxima of the associated PDFs lies on the lattice axes (cf. fig. 6.8), the average value of the interparticle distance at  $a \approx 3.1$  fm is in reasonable agreement with the most probable  $\alpha - \alpha$  separation distance  $d^*$ , equal to  $\approx 3.3$  fm, see fig. 6.7. Conversely, for  $a \approx 1.45$  and  $2.30$  fm  $\mathcal{R}$  appears far from  $d^*$ , due to the contributions of the tails of the wavefunction, certainly more significant than the ones of the ground state.

Analogous is the situation of the  $2_{T_2}^+$  multiplet, for which the energy minima are in optimal agreement with the minima of the average values of the potential energy, and lie at spacings



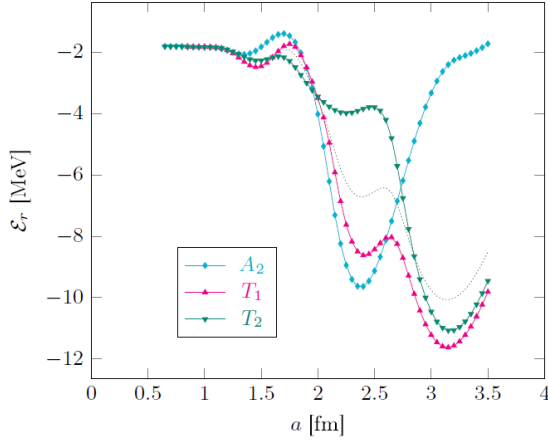


FIGURE 6.10 – Behaviour of the energies of the  $3_1^-$  eigenstates as a function of the lattice spacing for  $Na \geq 19$  fm. Even if the multiplet-averaged  $3_1^-$  energy (densely dotted line) improves the convergence rate to the continuum and infinite-volume counterpart, for  $a \gtrsim 2.0$  fm discretization corrections amount to more than 100% of the asymptotic energy eigenvalue. Residual finite volume effects are expected to amount to  $5 \cdot 10^{-3}$  MeV.

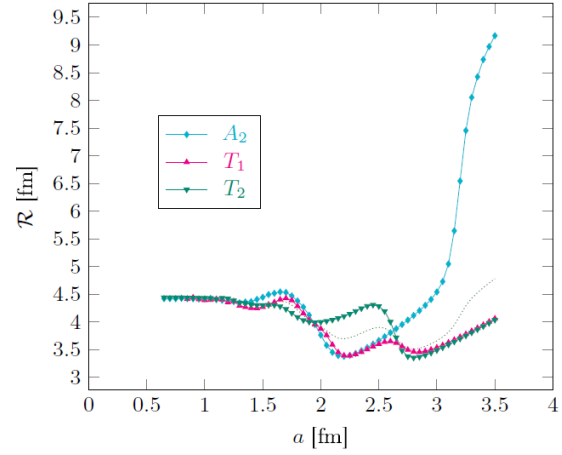


FIGURE 6.11 – Behaviour of the average  $\alpha - \alpha$  distance of the  $3_1^-$  eigenstates as a function of the lattice spacing for  $Na \geq 19$  fm. Although slower than in the  $^8\text{Be}$  case, convergence of the average values of  $\mathcal{L}^2$  to its expected eigenvalues is attained in the zero-spacing limit. Residual finite volume effects are expected to amount to  $5 \cdot 10^{-3}$  fm.

almost equal to the ones of the  $2_E^+$  multiplet ( $a \approx 1.40, 2.35$  and  $3.20$  fm). Even if they do not lie on the lattice axes, the absolute maxima of the PDF can be exactly mapped in the cubic lattice and correspond to equilateral triangular configurations with side  $d^*$  equal to  $3.3$  fm, as in the previous case.

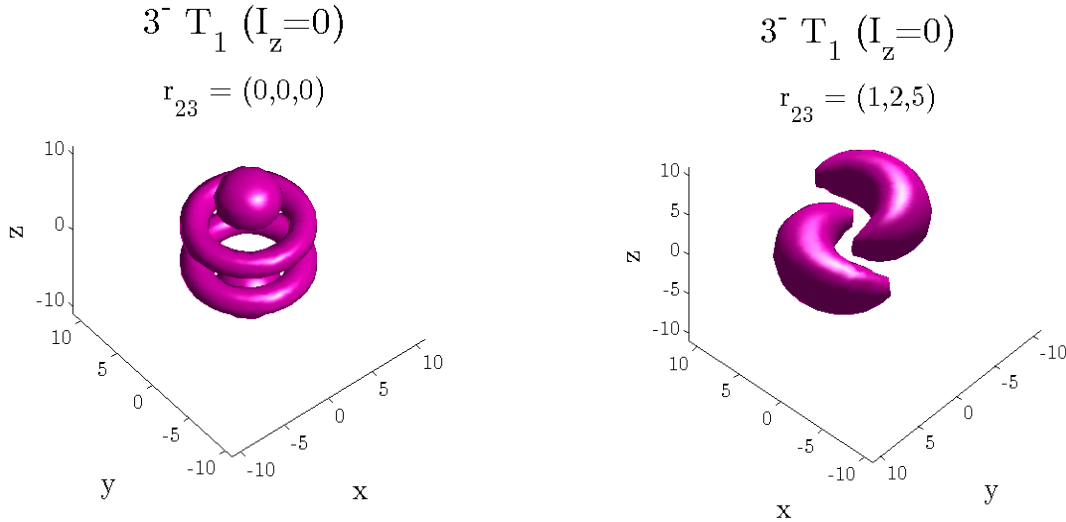


FIGURE 6.12 – Spatial distribution of the PDF of the  $3_1^- T_1$  state with  $I_z = 0$  in the configuration space slices with  $\mathbf{r}_{23} = (0,0,0)$  (left) and  $\mathbf{r}_{23} = (1,2,5)$  (right). The outer isohypsic surfaces of the two plots correspond to a probability density equal to the 10% of the maximum value of the PDF ( $\approx 4.4 \cdot 10^{-9} \text{ fm}^{-6}$ ). Distances along the axes are measured in lattice spacing units ( $a = 0.65$  fm). In particular, the crescent-shaped regions in the right plot encompass one single local PDF extremum each, which correspond to principal maxima of the wavefunction. As for the  $2_E^+$   $I_z = 0$  state, all the extrema in the  $\mathbf{r}_{23} = (0,0,0)$  slice of the PDF are indeed saddle points. Consequently, the configurations with two overlapping  $\alpha$ -particles and the third one lying in the centre of one of the spheres or in the inner circle of one of the two tori are unstable.

Besides, the average values of  $\mathcal{R}$  at  $a \approx 2.35$  and  $3.20$  fm roughly agree with the most probable  $\alpha - \alpha$  separation distance  $d^*$ , although for the latter value of the interparticle distance the discrepancy is larger, see fig. 6.7.

Concerning the  $3_1^-$  multiplet, the three bound multiplets reach the asymptotic region after some oscillations at  $a \lesssim 1.30$  fm, where they become degenerate within  $0.12$  MeV, and eventually overlap with two digit accuracy at  $a \approx 0.80$  fm, see fig. 6.7. All the PDF associated to the wavefunctions of the present multiplet are found to have well-developed principal maxima ( $\approx 10^4$  times deeper than any any other PDF extremum), corresponding to  $\alpha - \alpha$  separations  $d^*$  of about  $3.4$  fm. Moreover, both the energy eigenvalue and the average value of the potential energy of the  $3_{A_2}^-$  state is minimized for lattice spacings equal to  $\approx 1.35$  and  $2.35$  fm. In particular, for the latter value of the spacing  $\mathcal{R} \approx 3.45$  fm (cf. figs. 6.10 and 6.11), a reasonable agreement with  $d^*$ .

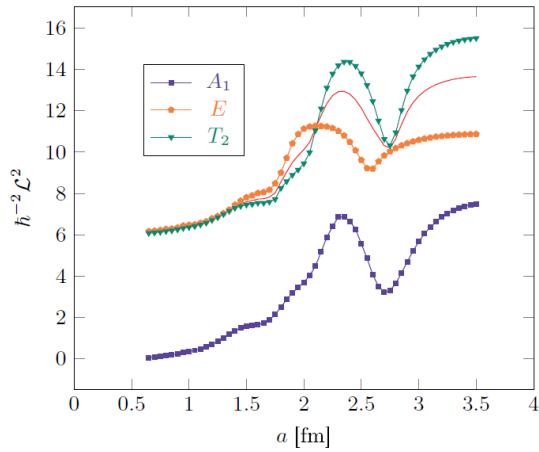


FIGURE 6.13 – Behaviour of the average values of the squared total angular momentum of the  $0_1^+$  and  $2_1^+$  eigenstates as a function of the lattice spacing for  $Na \geq 19$  fm. Residual finite-volume effects are expected to amount to about  $5 \cdot 10^{-3} \hbar^2$  for the  $0^+$  state and to  $10^{-2} \hbar^2$  for the  $2^+$  state.

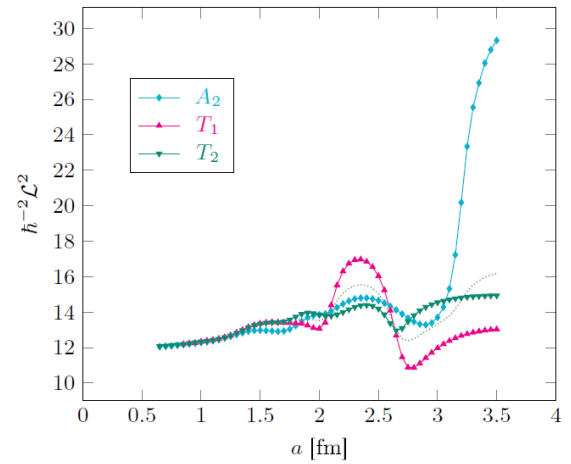


FIGURE 6.14 – Behaviour of the squared total angular momentum of the  $3_1^-$  eigenstates as a function of the lattice spacing for  $Na \geq 19$  fm. Even if slowly, convergence of the average values of  $\mathcal{L}^2$  to its expected eigenvalues is attained in the zero-spacing limit. Residual finite volume effects are expected to amount to about  $5 \cdot 10^{-3} \hbar^2$ .

On the other hand, for the former spacing the average value of the  $\alpha - \alpha$  distance is strongly influenced by the tails of the wavefunction. Both the minima can be related to the exact inclusion of the principal maxima of the PDF associated to the aforementioned state into the lattice. In the case of the  $3_{T_1}^-$  states, the energy minima at  $a \approx 1.45$ ,  $2.40$  and  $3.15$  fm are still found to be in good correspondence with the ones of  $\mathcal{V}$ .

Moreover, not all the principal maxima detected in the PDFs can be exactly (or in good approximation) included in the cubic lattice, due to the non-trivial spatial orientation of the probability density surfaces encompassing the absolute maxima, cf. fig. 6.12. Nevertheless, the two minima of  $\mathcal{E}_r$  at  $2.40$  and  $3.15$  fm correspond to values of the average interparticle distance  $\mathcal{R}$  of about  $3.45$  fm, again in good agreement with  $d^*$ .

Similarly to the previous case, not all the principal maxima of the probability density functions associated to the  $3_{T_2}^-$  states can be exactly mapped in the cubic lattice. Although the shallow minimum of the energy eigenvalue of the multiplet between  $a = 2.25$  and  $2.3$  fm is shifted by about  $0.2$  fm from the nearest minimum of  $\mathcal{V}$ , the remaining two energy minima at  $a \approx 1.45$

and 3.15 fm are in good correspondence with the ones of the average values of the potential energy. Concerning the average values of the interparticle distance, the agreement between  $\mathcal{R}$  at  $a \approx 2.3$  and 3.15 fm and  $d^*$  is worse than in the previous case (cf. fig. 6.11), due to the spatial distribution of the  $3_{T_2}^-$  wavefunctions.

Switching now to the average values of the squared total angular momentum, the convergence rate of the  $0_1^+$  and  $2_1^+$  states to the expected  $\mathcal{L}^2$  eigenvalues (cf. figs. 6.11 and 6.14) is sensibly slower than the one of the homologous states of beryllium, see fig. 5.11.

In particular, one decimal digit agreement between the  $\mathcal{L}^2$  average value on the ground state and the expected eigenvalue is reached for  $a \approx 1.0$  fm, whereas two decimal digit precision is attained only at  $a \approx 0.65$  fm. Besides, for the  $2_1^+$  multiplet one decimal digit precision in the angular momentum estimation is reached only at  $a \approx 0.70$  fm, even if, for the  $T_2$  multiplet convergence is slightly faster, as observed in the  $-3.3$  MeV multiplet of  $^8\text{Be}$  (cf. fig. 5.11).

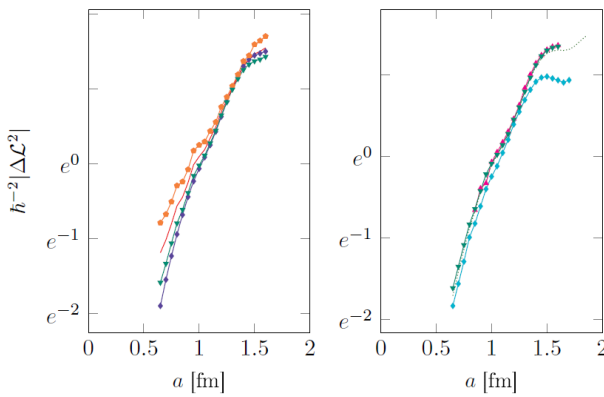


FIGURE 6.15 – Difference between the average value and the expected eigenvalue of the squared angular momentum for the  $2_1^+$  (left) and the  $3_1^-$  states (right) as a function of the lattice spacing. The same convention on the markers for the cubic group irreps of figs. 6.7-6.10 is understood. It is worth remarking that the deviations from linearity for small values of the spacing in the  $2_E^+$  curve (cf. the left panel of the figure) are sensibly larger than the ones of the other multiplets, an effect perhaps due to residual finite-volume effects.

For the  $3_1^-$  state the situation is similar, since one-digit precision in the estimation of the eigenvalue of the squared total angular momentum is reached only at  $a = 0.85, 0.80$  and  $0.75$  fm for the  $3_{A_2}^-, 3_{T_1}^-$  and  $3_{T_2}^-$  multiplets respectively. Contrary to the case of the  $0_1^+$  and  $2_1^+$  states of  $^8\text{Be}$ , it turns out that the computation of the average values of  $\mathcal{L}^2$  does not provide more precise information on the transformation properties of the group of states under  $\text{SO}(3)$  rotations, since the energies themselves become degenerate with greater accuracy at larger lattice spacings.

Nevertheless, by subtracting the expected squared angular momentum eigenvalues from the  $\mathcal{L}^2$  average values and then taking the absolute value the observations on the asymptotic corrections to the latter in chap. 5 find another confirmation. If the spacing is small enough, i.e.  $a \lesssim 1.4$  fm for the  $0_1^+$  and  $2_1^+$  states or  $a \lesssim 1.3$  fm for the  $3^-$  multiplet, the  $\log |\Delta \mathcal{L}^2|$  behave almost linearly with the lattice spacing, with a positive slope, see fig. 6.15.

We conclude our study of rotational symmetry breaking in  $\alpha$ -conjugate nuclei with the low-energy sector of the spectrum of  $^{16}\text{O}$ . Conserving the three-body Gaussian interaction adopted for the  $^{12}\text{C}$  nucleus, we predict that the binding energy of  $^{16}\text{O}$  is underestimated by about 11 MeV. However, the lattice spectrum with  $N \approx 10$  and  $a \sim 1.0$  fm unveils a number of bound states, converging to different  $\text{SO}(3)$  multiplets in the infinite volume.

Therefore, we leave the parameters of the Ali-Bodmer potential [4] fixed to their physical values and we analyse finite-volume and discretization effects in the energy eigenvalues of the  $0_1^+$ ,  $2_1^\pm$ ,  $3_1^\pm$  and  $4_1^-$  states.

With the growth of the M-body configuration space, it is apparent that the extraction of lattice eigen-energies at large values of the box size,  $N$ , becomes even more computationally demanding and, eventually, prohibitive. Consequently, in the finite-volume (discretization) plots, residual discretization (finite-volume) effects will be not suppressed to the same extent as in the  $^8\text{Be}$  and  $^{12}\text{C}$  spectra. Nevertheless, for sufficiently large (small) values of the lattice size (spacing), an approximate restoration of rotational symmetry becomes visible, both in the eigen-energies and in the average values of the squared angular momentum,  $\mathcal{L}^2$ , and  $\alpha$ - $\alpha$  separation,  $\mathcal{R}$ .

## 7.1 The spectrum

The  $\alpha$ -cluster structure in  $^{16}\text{O}$  is a subject of investigation from the earliest models [161, 162]. Motivated by the renewed interest in the topic [8, 225], we apply the M-body Hamiltonian,  $H$ , in eq. (4.1) to the nucleus  $^{16}\text{O}$  as a cluster of four  $\alpha$ -particles.

Due to the increased size of the lattice counterpart of the  $H$ , we compute of the ground-state eigenvalue via the Lanczos method for the GPU units (cf. secs. 4.7.1 and 4.7.1 a)) for  $N \leq 10$ , then we explore the large lattice size region until  $N = 40$  by resorting to the Worldline Monte Carlo algorithm (cf. sec. 4.8.1) with  $a_t$  fixed to  $1/3500$  s (cf. fig. 4.4). Differently from the  $^8\text{Be}$  and  $^{12}\text{C}$  case, we set the lattice spacing to  $\approx 0.497$  fm instead of 0.75 fm, in order to keep discretization effects suppressed. Due to the expansion of the transfer-matrix in the WMC approach (cf. eq. (4.83)), in fact, the derivative improvement index for the discretized Laplacian,  $K$ , has to be fixed to unity in order to preserve its positive-definiteness.

Collecting Monte Carlo samples with  $141 \leq N_t \leq 281$ , the ground state eigenvalue for  $N \geq 10$

is extracted through Euclidean time extrapolations. As shown in fig. 4.4, the fitting function has been chosen to coincide with  $E(N_t)$  in eq. (4.90). The data outcoming from these extrapolations are displayed in fig. 7.1, where the error bars represent three times the statistical uncertainty associated to the parameter  $c$  of each fit. Although the data at  $N = 40$  already correspond to lattices with size  $L = 20$  fm, we extract the continuum and infinite-volume energy eigenvalue by modeling the asymptotic region with the function

$$h(N) = \frac{m}{N^v} + q \quad m, q, v \in \mathbb{R}, \quad (7.1)$$

where  $q$  represents the estimate for the ground state eigenvalue,  $\mathcal{E}_{g.s.}(\infty)$  and  $v$  minimizes the coefficient of determination of the regression,  $R^2$ . Even if some data at intermediate lattice sizes in the region with  $N \geq 30$  are missing, it is evident from fig. 7.1 that the convergence towards the asymptotic value of  $\mathcal{E}_{g.s.}(N)$  is slower than in the  $^8\text{Be}$  and  $^{12}\text{C}$  case, see figs. 5.1 and 6.1. In particular, at  $L = 20$  fm the lattice eigenvalue seems still separated from the continuum and infinite-volume counterpart by about 4 MeV. Whether this behaviour is a consequence of a genuinely broader spatial distribution of the wavefunction or is a mere effect of the lack of statistics in the infinite-volume extrapolation in eq. (7.1), only further data in the region  $30 \leq N \leq 40$  can shed some light on this.

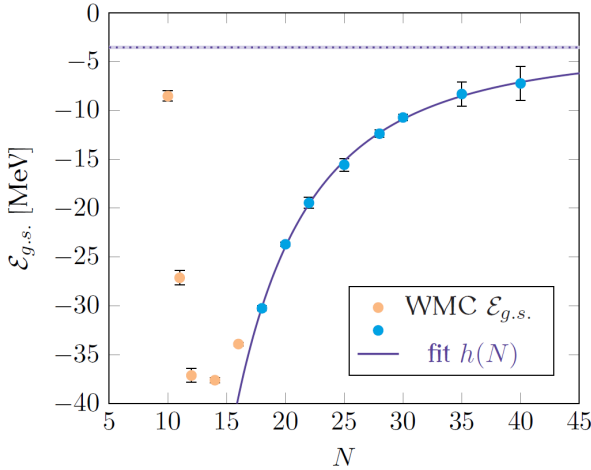


FIGURE 7.1 – Ground state eigenvalue of the  $^{16}\text{O}$  lattice Hamiltonian with  $a \approx 0.49$  fm, as a function of the box size  $N$ . The fitting function for the infinite volume extrapolation is denoted by a solid line, whereas the asymptotic energy eigenvalue is represented by a dashed line, with a shaded area generated by the statistical error. The WMC data that are (not) involved in the  $1/N^\xi$  regression are marked in light blue (orange). Their error bars are enhanced by a factor of three with respect to the statistical uncertainties resulting from the Euclidean time extrapolations (cf. sec. 4.8.1).

As shown in fig. 4.4, the regression returns a value of  $\mathcal{E}_{g.s.}(\infty)$  equal to  $-3.55(16)$  MeV, a result that appears to be concordant with literature [226]. It is established, in fact, that the addition of the  $3\alpha$  potential presented in sec. 4.2.1 to the Coulomb and angular momentum dependent Ali-Bodmer potentials [4] leads to an underestimation of the  $g.s.$  energy of the  $^{16}\text{O}$  nucleus by about 10 MeV [226]. Moreover, a re-fitting of the parameters of the Ali-Bodmer potentials to the  $\alpha$ -decay threshold and width of the  $^8\text{Be}$ , followed by the superposition of the three-body Gaussian potential in eq. (4.4) overbinds the same nucleus by more than 10 MeV [6]. Nevertheless, the results of the variational calculation for the fitting of the parameter  $V_3$  on the  $4\alpha$  decay threshold (cf. tab. 8.6) are expected to yield a substantial agreement with the experimental counterpart of  $\mathcal{E}_{g.s.}(\infty)$ .

As a consequence, applying eq. (4.48), we notice that the infinite-volume binding energy of the nucleus,  $BE(8,8)$ , is underestimated by 10.93 MeV with respect to the observational value of 127.61 MeV [227]. However, our estimation of  $BE(8,8)$  from  $\mathcal{E}_{g.s.}(\infty)$  in fig. 7.1, equal to 116.73(16) MeV, is compatible with the result of the multi-centre  $\alpha$ -particle model by

Brink [162], when the clusters are arranged at the vertices of a tetrahedron (cf. tab. III in ref. [162]).

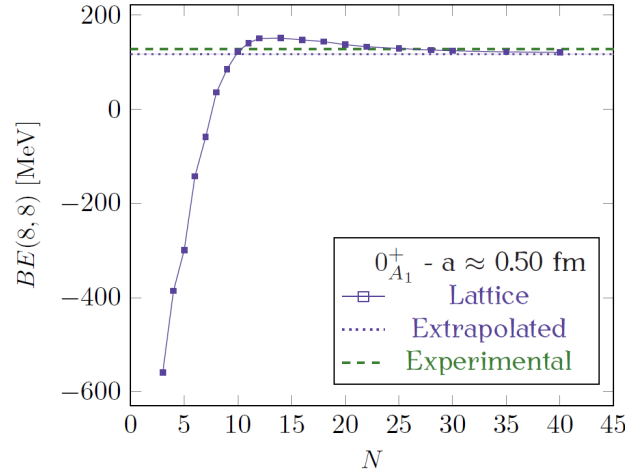


FIGURE 7.2 – Lattice binding energy of the  $^{16}\text{O}$  as a function of the box size  $N$ . The spacing has been kept fixed to  $\approx 0.49$  fm, with the aim of reducing the residual discretization effects to about  $\sim 10^{-3}$  MeV.

Exactly the tetrahedral group,  $\mathcal{T}_d$  [131], is now isomorphic to both the cubic group,  $\mathcal{O}$  and the permutation group of four particle,  $\mathcal{S}_4$ , albeit the 24 operations of two act on different spaces. As a consequence, each multiplet of states of the cubic group can now occur once, twice or thrice in the spectrum of the lattice Hamiltonian, depending on the dimension of the irreducible representation of  $\mathcal{S}_4$  according to which the given set of degenerate eigenstates transforms. In particular, if the bosonic (fermionic) irrep  $A_1$  ( $A_2$ ) of  $\mathcal{S}_4$  [131] is represented by the Young diagram with four boxes aligned in a row (column), whereas the 2-dim  $E$  irrep corresponds to the diagram with two rows of two boxes,  $\begin{smallmatrix} \square & \square \\ \square & \square \end{smallmatrix}$ . Concerning the three dimensional representations, the  $T_1$  ( $T_2$ ) irreps are denoted by a row (column) of three boxes followed below (resp. on the right) by a 1-box row (column),

$$\begin{smallmatrix} \square & \square & \square \\ \square & & \end{smallmatrix} \quad \text{and} \quad \begin{smallmatrix} \square & \\ \square & \\ \square & \end{smallmatrix},$$

respectively. Restricting ourselves to the completely symmetric eigenstates of the lattice Hamiltonian with  $N = 10$  and  $a = 1.20$  fm, the 18 cubic group multiplets with energy lower than  $\approx -11$  MeV, reported in tab. 7.1, are found. With reference to the multiplet-averaged energy eigenvalues (cf. eq. (4.49)) in the latter table, in the continuum and infinite-volume limit the cubic group multiplets give rise to a  $0_1^+$  line at -23.60 MeV, a  $0_2^+$  at -18.47 MeV, a  $2_1^+$  at -18.35 MeV, a  $3_1^-$  at -17.32 MeV, a  $3_1^+$  at -15.01 MeV, a  $3_2^-$  at -13.03 MeV, a  $2_1^-$  at -12.66 MeV and a  $4_1^-$  at -11.57 MeV. Although the asymptotic eigenvalues in the large  $N$  and small lattice spacing limit may differ from the latter also by 10 MeV, the classification of the eigenvalues in terms of  $\text{SO}(3)$  irreps leaves little space for ambiguity, as shown in the next sections of the chapter. Except for the absence of a  $0_2^+$ , a  $1_1^-$  and a  $2_2^+$  in the lattice sample of low-energy states, the extracted multiplet-averaged eigenvalues can be directly put in relation with the observed levels of  $^{16}\text{O}$  credited in literature [7, 8, 160] as candidates for  $\alpha$ -clustering. Besides the ground state,  $3_1^+$ ,  $2_1^+$  and  $2_1^-$  lines are found at 6.13, 6.92 and 8.87 MeV above the  $0_1^+$  state, in the vicinity



of the  $\alpha + ^{12}\text{C}$  decay threshold at 7.16 MeV (cf. sec. 8.5.1). Moreover,  $3_1^+$  and  $3_2^-$  levels are detected 11.08 and 11.60 MeV above the ground state, just below the  $4\alpha$  decay threshold at 14.43 MeV (cf. sec. 8.5.1), whereas a  $4_1^-$  line is predicted to appear circa 12.0 MeV above the  $0_1^+$  state [8] by the Algebraic Cluster Model [228–230], but is yet unobserved experimentally. In the next three sections, we will focus on the properties of the  $0_1^+$ ,  $2_1^+$ ,  $3_1^\pm$  and  $4_1^-$  lines, in our attempt to restore, at least approximately, the rotational symmetry of the Euclidean three-dimensional space.




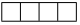
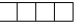


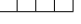



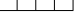

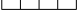




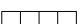


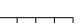



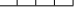
$E$ [MeV]	$\Gamma$	$I_z$	$\mathcal{P}$	$S_3$	$\langle \mathcal{L}_{\text{tot}}^2 \rangle [\hbar^2]$	$E$ [MeV]	$\Gamma$	$I_z$	$\mathcal{P}$	$S_3$	$\langle \mathcal{L}_{\text{tot}}^2 \rangle [\hbar^2]$
-23.598121	$A_1$	0	+		3.572	-13.296256	$T_1$	0	-		18.319
-19.622346	$E$	0	+		12.188			1			
-18.479851	$A_1$	0	+		8.621	-13.269656	$T_2$	2	-		20.651
-17.500590	$T_2$	1	+		11.220			3			
		2	+			-13.026827	$A_2$	2	+		22.732
-17.359338	$T_2$	3	-		15.923			0	-		13.985
		1	-			-12.773621	$E$	2	-		
-17.297202	$T_1$	3	-		15.922			1			
-17.289884	$A_2$	0	-		15.654	-12.587589	$T_2$	2	-		15.419
-15.350538	$T_2$	1	+		23.054			3			
		3	+			-12.269123	$T_1$	1	-		15.008
-15.328890	$T_1$	0	+		23.140			3	-		20.428
		3	+			-11.522579	$A_2$	2	-		27.757
						-11.489194	$T_2$	2	-		26.552
						-11.246100	$A_1$	0	-		24.829
						-10.824181	$E$	0	-		
								2	-		

TABLE 7.1 – Sample of the spectrum of the  $^{16}\text{O}$  Hamiltonian with  $N = 10$  and  $a \approx 1.20$  fm, consisting of the 18 lowest degenerate energy multiplets completely symmetric under particle permutation.

Due to the still long duration of the eigenvalue computation process via the Wordline Monte Carlo code for excited states (cf. sec. 4.8.1 a)), for the diagonalization of the lattice Hamiltonian in secs. 7.2–7.4 the GPU implementation of the Lanczos algorithm (cf. sec. 4.7.1 a)) has been adopted. As in the  $^{12}\text{C}$  case, the code makes use of the projectors on the irreducible representations of the parity group  $\mathcal{P}$ , the cubic-group  $\mathcal{O}$ , the cyclic group  $\mathcal{G}_4$ , and the permutation group  $S_4$ . Moreover, the extraction of the excited eigenstates with the same transformation properties according to the relevant point groups via Gram-Schmidt orthogonalization has been made possible by storing only two eigenvectors simultaneously in the GPU node.

## 7.2 The $0_1^+$ and $2_1^+$ energy levels

Let us initiate our analysis with the two deepest energy levels of the  $^{16}\text{O}$  spectrum, the  $0_1^+$  and  $2_1^+$  states, whose energy at  $N = 10$  and  $a = 1.20$  fm is equal to -23.60 and -18.35 MeV respectively. In order to suppress the discretization effects to at least  $\lesssim 10^{-1}$  MeV, we first fix the lattice spacing to  $a \approx 0.59$  fm. With the aim of allowing for an extension of the analysis to larger volumes by means of the Worldline algorithm for excited states (cf. sec. 4.8.1 a)),



we set the derivative improvement index for the Laplacian to one, thus constraining slightly the reduction of finite lattice spacing effects. The subsequent diagonalization of the lattice Hamiltonian  $\mathcal{H}_r$  for  $N \leq 10$ , returns the solid lines in fig. 7.3, whose behaviour closely resembles the one of the  $0_1^+$  and  $2_1^+$  curves in figs. 5.2 and 6.2 in the small  $N$  regime. In this region, the lattice eigenstates are sharply unbound, and their energy, independently on the discretization scheme adopted for the kinetic term of the Hamiltonian, reaches hundreds of MeV. The effect is merely a consequence of the repulsive part of the isotropic Ali-Bodmer potential, that moulds the behaviour of the wavefunctions at low values of the  $\alpha$ - $\alpha$  separation.

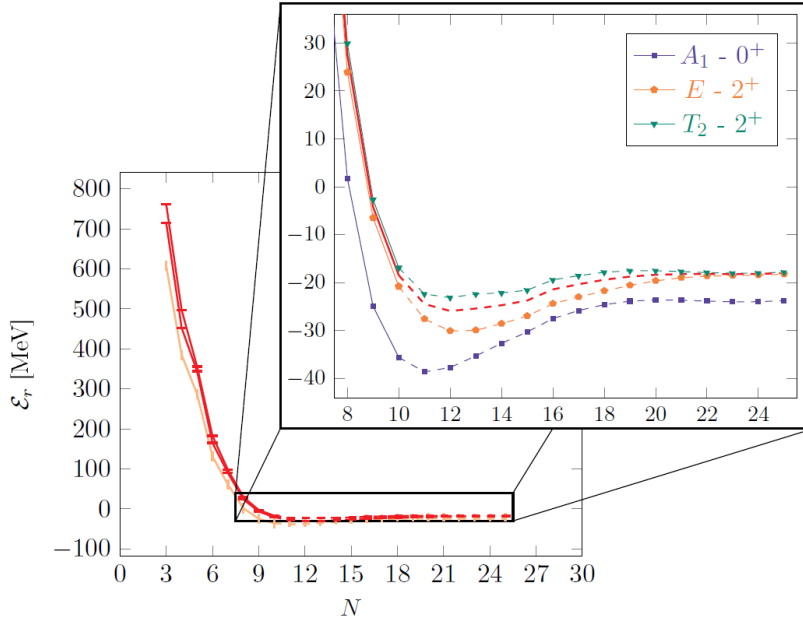


FIGURE 7.3 – Behaviour of the energies of the lowest  $0^+$  (horizontal bars) and  $2^+$  (vertical bars) eigenstates as a function of the box size  $N$  for  $a \approx 0.59$  fm. The multiplet-averaged eigenvalue of the  $2_1^+$  state is denoted in red. The same convention on the markers for the cubic group irreps adopted in the figures of chaps. 5 and 6 is understood. The dashed lines denote the expected behaviour of the solid curves in the large  $N$  regime, but their predictive power is limited by discretization errors increasing with  $N$ .

With the aim of pursuing the analysis beyond the present-day limitations of the GPU cards, we allow the lattice spacing to vary in order to predict the eigenenergy at any value of  $N$ , in the large lattice size region. More precisely, for each point with  $N \geq 11$  in fig. 7.3, we perform a Lanczos diagonalization with lattice size  $N^{\text{eff}}$  equal to 10 and lattice spacing  $a_{\text{eff}} = a \cdot N/N^{\text{eff}}$ , where  $a$  is the original value, equal to 0.59 fm. In this guise, we enable the exploration of the region of lattice volumes where the restoration of  $\text{SO}(3)$  symmetry takes place, at the price of losing information on the exact eigenvalues in the continuum and infinite-volume limit.

As a consequence, the dashed part of the curves in fig. 7.3 is a result of an interweaving of both finite volume and discretization effects. Despite the increase of the latter towards the infinite  $N$  limit, the  $E$  and  $T_2$  multiplets become degenerate within  $\approx 0.42$  MeV at  $N = 25$  and the overall behaviour of the curves in the asymptotic region recalls rather accurately the one of the  $2_E^+$  and  $2_{T_2}^+$  states in figs. 5.2 and 6.2. Besides, it is likely to expect that both the  $0_1^+$  and the  $2_E^+$  ( $2_{T_2}^+$ ) multiplets approach the asymptotic eigenvalue from below (above), as observed in the  $^8\text{Be}$  and  $^{12}\text{C}$  case.

Such a faithful reproduction of the infinite-volume behaviour of the curves was also ensured by the increase of the derivative improvement index to 4, thus quenching the growth of discretization artifacts in the reconstructed energy eigenvalues with  $N$ . However, considered the result of the infinite-volume extrapolation in fig. 7.1, it is evident that the asymptotic energy eigenvalues in fig. 7.3 may differ from the exact ones of about  $10^0$  to  $\sim 10^1$  MeV.

Next, we concentrate on the behaviour of the average values of the total squared angular

momentum operator with the lattice size  $N$ . Implementing the same strategy adopted for the energy eigenvalues, we obtain for the  $0_1^+$  and  $2_1^+$  states the solid and dashed curves in fig. 7.4. As it can be observed, both the three curves display an evident peak in the region with  $N \sim 7$ , as in the  $^{12}\text{C}$  case in fig. 6.5, followed by a rather smooth settling of  $\mathcal{L}^2$  towards the asymptotic average value. Although the squared angular momenta of the  $2_E^+$  and  $2_{T_2}^+$  multiplets overlap within 0.17 units of  $\hbar^2$  of precision at  $N = 25$ , the interplay between residual finite volume and discretization effects results into a discrepancy of about  $6 \hbar^2$  with respect to the exact eigenvalue of  $\mathcal{L}^2$ . A similar conclusion holds for the ground state, where the closest approach of the squared angular momentum to zero, equal to  $\approx 3.6 \hbar^2$ , is recorded at  $N = 20$ .

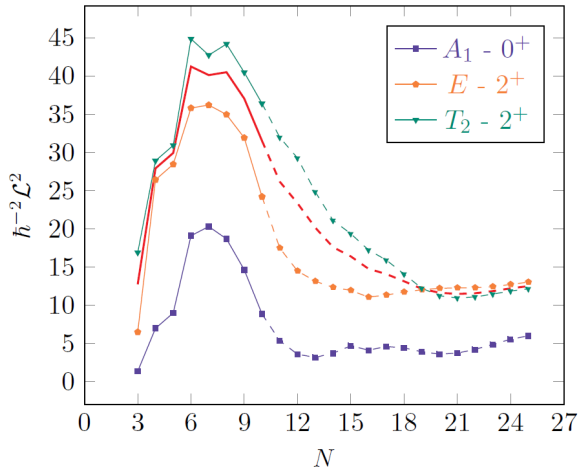


FIGURE 7.4 – Average value of the squared angular momentum for the  $0_1^+$  and  $2_1^+$  states as a function of the lattice size for  $a \approx 0.59$  fm. The multiplet average of  $\mathcal{L}^2$  for the  $2_1^+$  state is denoted by a red line. Dashed lines denote the expected behaviour of  $\mathcal{L}^2$  in the large  $N$  regime, but their predictive power is limited by discretization errors increasing with  $N$ .

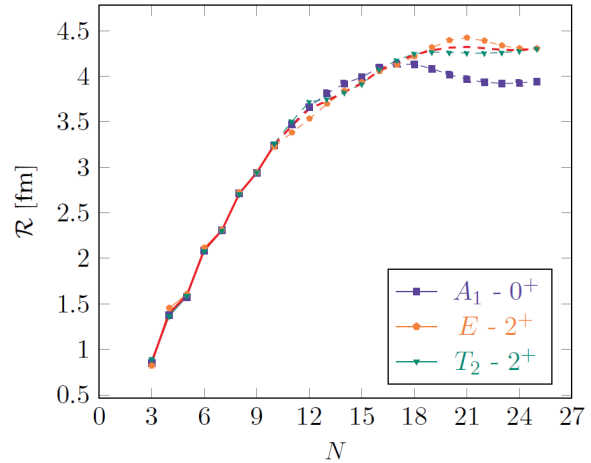


FIGURE 7.5 – Behaviour of the average  $\alpha$ - $\alpha$  distance for the  $0_1^+$  and  $2_1^+$  multiplets as a function of the lattice size for  $a \approx 0.59$  fm. The multiplet average of  $\mathcal{R}$  for the  $2_1^+$  state is denoted with a red line. The dashed lines denote the expected behaviour of  $\mathcal{R}$  in the large  $N$  regime, but their reliability is affected by discretization errors increasing with  $N$ .

As in sec. 7.2, we now consider the average values of the  $\alpha$ - $\alpha$  separation,  $\mathcal{R}$ , as a function of the lattice size. Although at  $N = 25$ , the edge of the cubic box measures only 12.50 fm, the dashed curves of the interparticle distance for the  $0_1^+$  and  $2_1^+$  states almost reach a plateau as the ones in fig. 6.3, with  $\mathcal{R}$  equal to  $\approx 3.94$  and  $4.30$  fm respectively. Since the equilibrium arrangement of the  $^4\text{He}$  clusters within the nucleus is tetrahedral, an estimate of the residual finite-volume and discretization errors introduced by  $a_{\text{eff}} > a$  at  $N = 25$  can be obtained from comparison of the ground state value of the centroid to vertex distance,  $\sqrt{3}\mathcal{R}/\sqrt{8}$ , with the experimental charge radius of  $^{16}\text{O}$  in ref. [224, 231], corresponding to  $\approx 2.69$  fm. Despite the quite large *effective* lattice spacing, our lattice estimate at  $N = 25$  of the latter is equal to  $\approx 2.41$  fm, in reasonably close to the observational radius and in good agreement with the numerical result of the unitary-model-operator approach (UMOA) in ref. [232] (2.44 fm).

It follows that  $\mathcal{R}$ , in the asymptotic region of fig. 7.5, is rather insensitive to finite-volume and discretization artifacts. Concerning the  $2_E^+$  and  $2_{T_2}^+$  states, the average values of  $\alpha$ - $\alpha$  separation at  $N = 25$  already overlap within an astonishing precision, equal to 0.004 fm.

We now proceed by analogy with secs. 6.2 and 7.2, displaying the behaviour of physical observables with the lattice spacing  $a$ . Although the extent of residual finite-volume effects for

the energy eigenvalues of the  $0_1^+$  and  $2_1^+$  states at  $Na \sim 20$  fm is not known with precision, we assume from comparison with the data in figs. 7.2 and 8.1 that for lattices with  $Na \gtrsim 20$  these artifacts lie between  $10^0$  and  $10^{-1}$  MeV. Therefore, we fix the constraint  $Na \geq 20$  fm and explore the behaviour of the energy eigenvalues in the interval  $2.0 \leq a \leq 5.0$  fm for the two angular momentum multiplets (cf. fig. 7.6), denoting the curves with solid lines. In sight of the extension of the curves towards the  $a < 2.0$  fm region, we set the derivative improvement index to unity, as done in the  $N \leq 10$  region of figs. 7.3-7.5.

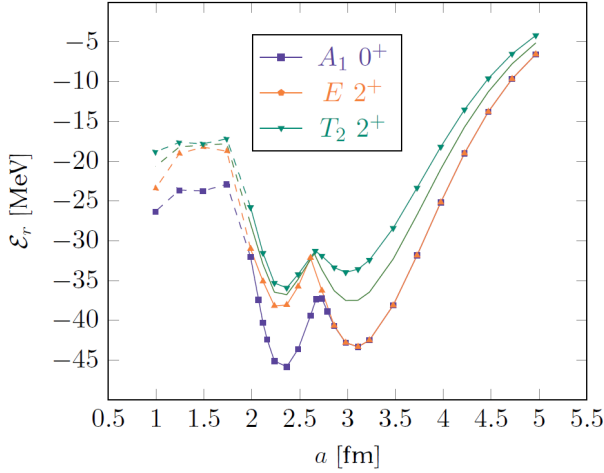


FIGURE 7.6 – Behaviour of the energies of the  $0_1^+$  and  $2_1^+$  eigenstates as a function of the lattice spacing for  $Na \geq 20$  fm. The multiplet-averaged  $2_1^+$  energy is denoted with a red line. The dashed part of the curves denote the expected behaviour of  $\mathcal{E}_r$  in the small  $a$  regime, but its predictive power is limited by finite-volume effects, inversely proportional to  $a$ .

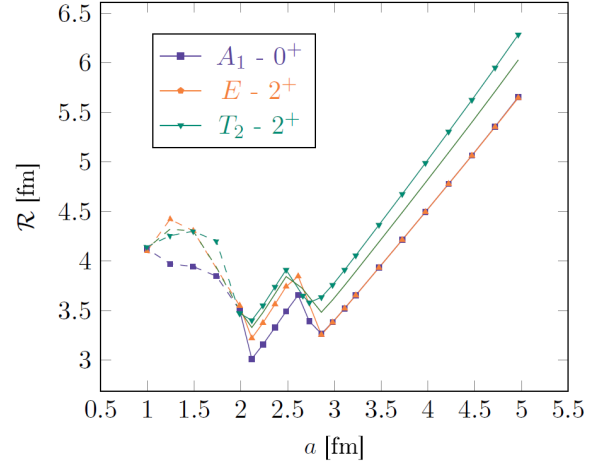


FIGURE 7.7 – Behaviour of the average  $\alpha$ - $\alpha$  distance of the  $0_1^+$  and  $2_1^+$  eigenstates as a function of the lattice spacing for  $Na \geq 20$  fm. The multiplet-averaged values of  $\mathcal{R}$  for the  $2_E^+$  and  $2_{T_2}^+$  states are connected with a red line. The dashed part of the curves denote the expected behaviour of average  $\alpha$ - $\alpha$  separation in the small  $a$  regime, but its predictive power is limited by finite-volume effects, inversely proportional to  $a$ .

As noticed in figs. 5.5 and 6.6 and in ref. [3], the evolution curves of the energy eigenvalue display an oscillatory behaviour and their extremal points are susceptible of a geometric interpretation, based on the spatial distribution of the probability density functions (PDF) associated to the lattice wavefunctions. Differently from the  $^8\text{Be}$  and  $^{12}\text{C}$  nuclei, the  $^{16}\text{O}$  PDFs in the small-spacing limit can not be faithfully represented, due to the present limitations in the number of mesh points per dimension,  $N$ . Nevertheless, at least the region  $a < 2.0$  fm of the discretization plot in fig. 7.6 (dashed lines) can be approximately reconstructed, albeit tolerating the presence of larger finite-volume errors. The points with  $a < 2.0$ , in fact, refer to lattices with only  $N = 10$  points per dimension. Additionally, in the dashed part of the curves the derivative improvement index,  $K$ , has been restored to 4, in order to reproduce asymptotic energy eigenvalues consistent with the ones in fig. 7.3.

In the solid part of the curves for the  $0_1^+$  and  $2_1^+$  states in fig. 7.6 two well-developed minima can be observed at  $a \approx 2.3$  and  $3.1$  fm. In addition, the minima of the average  $\alpha$ - $\alpha$  distance in fig. 7.7, detected at  $a \approx 2.1$  and  $2.9$  fm and the ones of the potential energy  $\mathcal{V}$ , at  $a \approx 2.25$  and  $3.05$  fm, lend weight to the hypothesis that a maximum of the related PDFs is included exactly or in good approximation in the lattice configuration space. An analogous behaviour was observed for the  $2_E^+$  and  $2_{T_2}^+$  multiplets of  $^8\text{Be}$ , whose PDF in figs. 5.8 and 5.10 exhibit deep minima located on the lattice axes.

Finally, it is noteworthy the accidental quasi-degeneracy of the energy eigenvalues of the  $0_{A_1}^+$  and  $2_E^+$  multiplets for  $a \lesssim 2.9$  fm that is accompanied by a neat overlap in the average values of  $\mathcal{R}$  (cf. fig. 7.7) and  $\mathcal{L}^2$ , a fact that may disorient in the classification of states in terms of irreps of  $\text{SO}(3)$ .

### 7.3 The $2_1^-$ and $3_1^+$ energy levels

We now switch to the analysis of the  $2_1^-$  and  $3_1^+$  states, whose energy at  $N = 10$  and  $a = 1.20$  fm is equal to -15.01 and -12.66 MeV respectively. Adopting the same convention for the solid and dashed lines outlined in sec. 7.2, we plot in fig. 7.8 the energy eigenvalues of the constituents of the two states as a function of the lattice size. The behaviour of the curves in the low  $N$  region highlights the action of the repulsive component of the Ali-Bodmer potential, encoding the effect of the Pauli exclusion principle, see eq. (4.2). As soon as the lattice volume increases the energy eigenvalues reach again a minimum, determined by the interplay of the attractive part of the Ali-Bodmer potential and the three-body force in eq. (4.3), then the infinite-volume eigenenergies are reached asymptotically. Despite the gradual increase of the lattice spacing from the initial value of  $a = 0.59$  fm, the  $2_E^-$  multiplet reaches again the  $N \rightarrow +\infty$  eigenvalue from below, whereas the  $2_{T_2}^-$  approaches the limit from above, and the two curves eventually overlap at  $N = 25$  within 0.37 MeV.

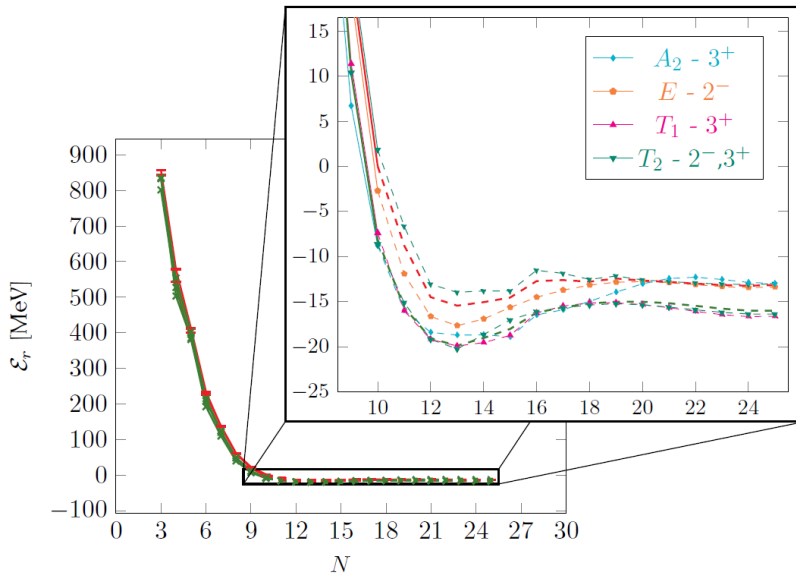


FIGURE 7.8 – Behaviour of the energies of the lowest  $2^-$  (vertical bars) and  $3^+$  (diagonal crosses) eigenstates as a function of the box size  $N$  for  $a = 0.59$  fm. The multiplet-averaged eigenvalue of the  $2_1^+$  ( $3_1^+$ ) state is denoted in red (green). The same convention on the markers for the cubic group irreps adopted in the figures of chap. 5 is understood. The dashed lines denote the expected behaviour of the solid curves in the large  $N$  regime, but are affected by discretization errors increasing with  $N$ .

On the other hand, the behaviour of the members of the  $3_1^-$  state appears less clear. While the  $3_{T_1}^+$  and  $3_{T_2}^+$  levels become degenerate within 0.25 MeV at  $N = 25$ , the  $3_{A_2}^+$  multiplet remains separated from the two by about 3.5 MeV. With reference to fig. 6.2, these effects seem solely due to discretization and do not prevent us from observing that the  $3_{A_2}^+$  state approaches the infinite-volume limit from above.

We now continue our investigation of finite-volume effects by considering the average values of the total squared angular momentum operator (cf. sec. 4.3.3). Besides the spikes in the  $N \lesssim 12$  region, the behaviour of the  $2_E^-$  and  $2_{T_2}^-$  multiplets is quite smooth and resembles the one in fig. 7.4. However, in the asymptotic region a breakup between the curves prompted by the increased lattice spacing appears and the asymptotic average value is shifted on average by 9 units of  $\hbar^2$  (cf. the red dotted line in fig. 7.9).

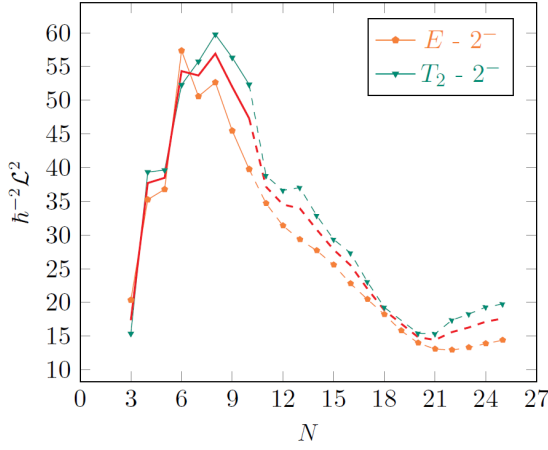


FIGURE 7.9 – Average value of the squared angular momentum for the multiplets of the  $2_1^-$  state as a function of the lattice size for  $a \approx 0.59$  fm. As in fig. F-7-04, the multiplet average of  $\mathcal{L}^2$  is denoted by a red line. The dashed curves shows the expected behaviour of  $\mathcal{L}^2$  in the large  $N$  regime, but their predictive power is limited by discretization errors increasing with  $N$ .

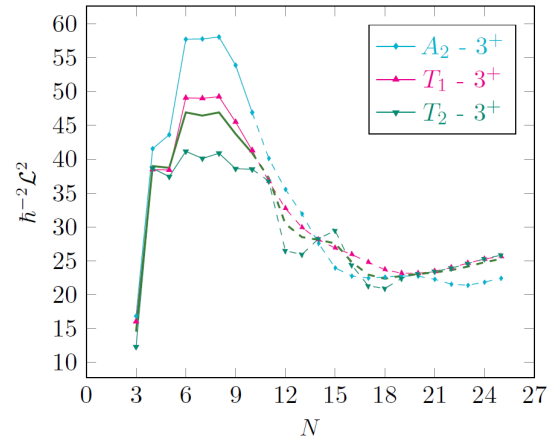


FIGURE 7.10 – Average value of the squared angular momentum for the multiplets of the  $3_1^+$  state as a function of the lattice size for  $a \approx 0.59$  fm. The multiplet average of  $\mathcal{L}^2$  is denoted by a green line, while the dashed curves displays the expected behaviour of the squared angular momentum in the large  $N$  region, but increasing discretization effects with  $N$  are present.

Concerning the  $3_1^+$  level, the scenario is not different from the one observed in fig. 7.8. While the curves of the  $3_{T_1}^+$  and  $3_{T_2}^+$  multiplet intersect each other and overlap in the asymptotic region within 0.18 units of  $\hbar^2$ , the  $3_{A_2}^+$  displays a higher peak around  $N = 7$  and is shifted downwards by  $3.4 \hbar^2$  at  $N = 25$ . Besides, the oscillatory behaviour in the  $3_{T_2}^+$  curve at  $N \sim 15$  is dictated its quasi-degeneracy with a  $T_2^+$  multiplet lying slightly above in energy, omitted from our investigation. This effect has already emerged in the discussion of finite volume effects for the  $4_2^+$  and  $6_1^+$  states of  $^8\text{Be}$  (cf. sec. 5.3).

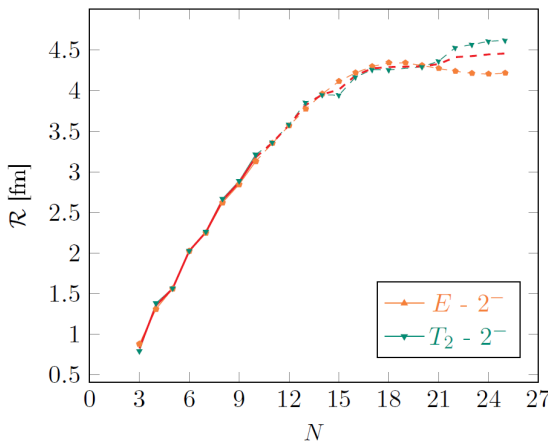


FIGURE 7.11 – Behaviour of the average inter-particle distance for the  $2_1^-$  multiplets as a function of the lattice size. The multiplet average of  $\mathcal{R}$  for the  $2_1^-$  state is traced with a red line. The dashed lines denote the behaviour of  $\mathcal{R}$  in the  $N > 10$  region and are subject to larger discretization errors.

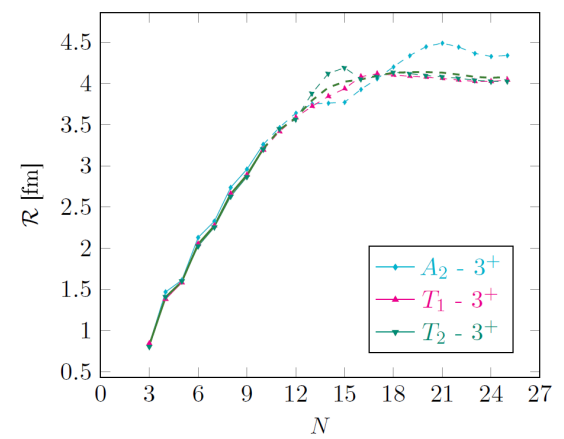


FIGURE 7.12 – Behaviour of the average inter-particle distance for the  $3_1^+$  multiplets as a function of the lattice size. The multiplet average of  $\mathcal{R}$  for the  $3_1^+$  state is denoted with a green line, while the dashed lines constitute the expected behaviour of  $\mathcal{R}$  in the large  $N$  regime, as hinted in the text.



The average values of the  $\alpha$ - $\alpha$  separation, shown in figs. 7.11 and 7.12 recall closely certain features observed in the behaviour of the squared angular momentum, see figs. 7.9 and 7.10. In particular, the multiplet average of  $\mathcal{R}$  for the  $2_E^-$  and  $2_{T_2}^-$  states reaches an asymptotic value of 4.42 fm, but the two individual values for the interparticle distance are separated by  $\approx 0.45$  fm at  $N = 25$ . Regarding the  $3_1^+$  level, the  $T_2$  component shows the same disturbance around  $N = 13$ , then follows smoothly the  $T_1$  multiplet until  $N = 25$ , where it reaches 4.06 fm. The curve of the  $3_{A_2}^+$  state, on the other hand, displays a more pronounced oscillatory behaviour and settles  $\approx 0.39$  fm above the other two members of the  $3_1^+$  line.

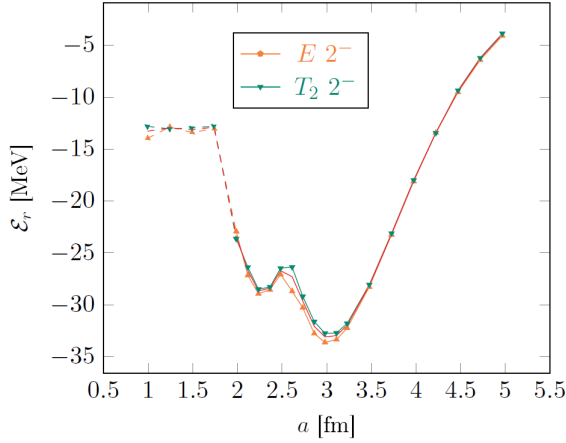


FIGURE 7.13 – Behaviour of the energy of the  $2_1^-$  multiplet eigenstates as a function of the lattice spacing for  $Na \geq 20$  fm (solid lines). Although the multiplet-averaged  $2_1^-$  energy (red line) reduces the fluctuations towards the continuum and infinite-volume counterpart, the two cubic group multiplets almost follow the same path. The dashed lines denote the behaviour of  $\mathcal{R}$  in the  $N > 10$  regime.

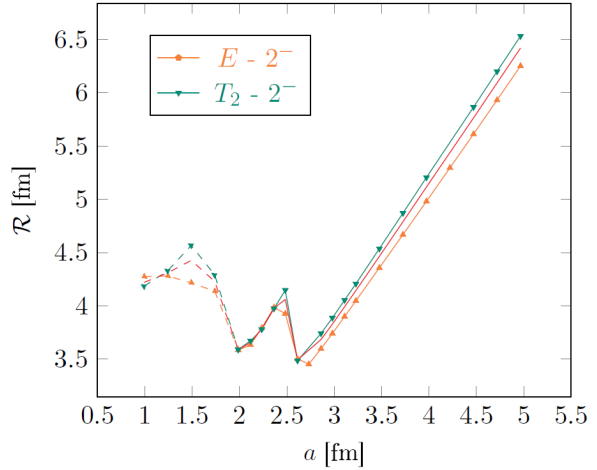


FIGURE 7.14 – Behaviour of the average  $\alpha - \alpha$  distance of the  $2_1^-$  eigenstates as a function of the lattice spacing for  $Na \geq 20$  fm. The multiplet average of  $\mathcal{R}$  for the  $2_1^-$  state is denoted with a red line, while the dashed lines represent the expected behaviour of  $\mathcal{R}$  in the large  $N$  regime, affected by larger finite-volume errors.

Let us now examine the behaviour of the energy eigenvalues of the states of interest with the lattice spacing. Fixing, again, the constraint  $Na \geq 20$  fm for the solid lines, we first concentrate on the  $2_E^-$  and  $2_{T_2}^-$  states. Differently from the  $2_1^+$  case, we observe that curves of the two multiplets overlap with surprising precision along all the path from 5.0 fm to the dashed part of the curve, except for the endpoint at  $a \approx 1.0$  fm, where a shift of  $\approx 1.15$  MeV is detected (cf. fig. 7.13). Noticeable are also the two overlapping minima at  $\approx 2.30$  and  $3.07$  fm, which are correlated to the minima at  $\approx 2.21$  and  $3.0$  fm of the potential energy,  $\mathcal{V}$ . Although the latter are found in weaker agreement with the two minima of the  $\alpha$ - $\alpha$  separation at  $\approx 2.0$  and  $2.65$  fm in fig. 7.14, it is still possible to draw a parallel between the maxima of the PDFs for the  $2_E^-$  and  $2_{T_2}^-$  multiplets and the minima of  $\mathcal{E}_r$  and  $\mathcal{R}$ .

Concerning the  $3_1^+$  multiplet, the three curves for the energy eigenvalue in fig. 7.15 follow three separate paths, except for the  $a \gtrsim 4.25$  fm region. Nevertheless, the minimum points at  $a \approx 2.3$  and  $3.0$  fm of the three lines coincide in good approximation and can be associated with higher precision to the minima of the interparticle distance at  $a \approx 2.1$  and  $2.8$  fm in fig. 7.16. Moreover, as noticed in fig. 7.8, the  $3_{A_2}^+$  multiplet is subject to large finite-volume and discretization errors and seems to converge only accidentally with the  $3_{T_1}^+$  and  $3_{T_2}^+$  states, which reach the asymptotic region with a tiny energy shift,  $\approx 0.10$  fm (cf. fig. 7.15).

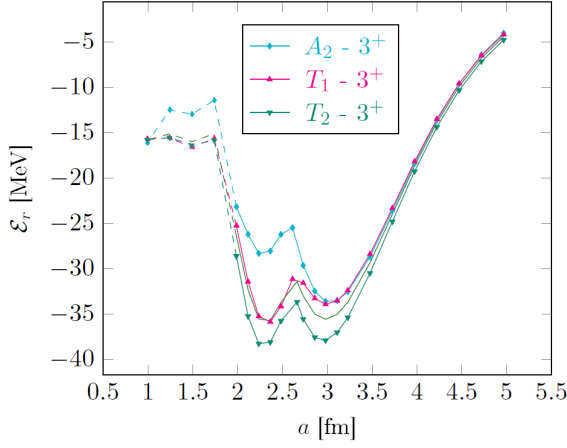


FIGURE 7.15 – Behaviour of the energy of the  $3_1^+$  multiplet eigenstates as a function of the lattice spacing for  $Na \geq 20$  fm (solid lines). The multiplet-averaged  $3_1^+$  energy (green line) quenches the deviations in the path towards the continuum and infinite-volume counterpart, while the dashed lines denote the behaviour of  $\mathcal{R}$  in the  $N > 10$  regime.

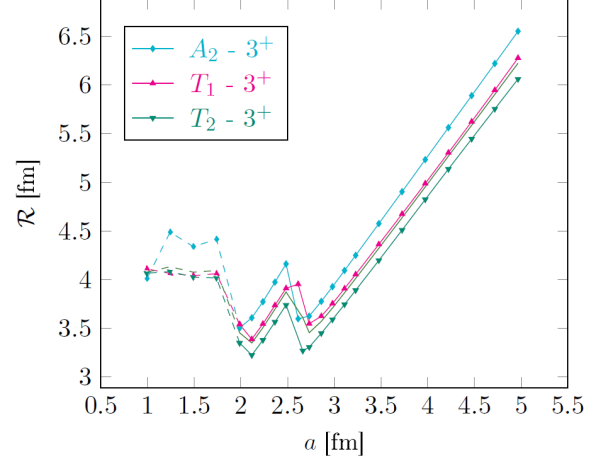


FIGURE 7.16 – Behaviour of the average  $\alpha - \alpha$  distance of the  $3_1^+$  eigenstates as a function of the lattice spacing for  $Na \geq 20$  fm. The multiplet-averaged of  $\mathcal{R}$  for the  $3_1^+$  state is denoted with a green line, while the dashed lines simulate the behaviour of  $\mathcal{R}$  in the large  $N$  regime, but are affected by finite-volume errors increasing with  $1/a$ .

## 7.4 The $3_1^-$ and $4_1^-$ energy levels

We conclude our exploration of the low-energy spectrum of the  $^{16}\text{O}$  with the  $3_1^-$  and  $4_1^-$  lines, whose energy at  $N = 10$  and  $a = 1.20$  fm corresponds to  $-17.32$  and  $-11.57$  MeV, respectively. First of all, let us consider the behaviour of the energy eigenvalues as a function of the number of points per dimension,  $N$ . As pointed out earlier in the chapter, the continuous part of the curves ( $a \approx 0.59$  fm) is characterized in both the cases by a descending behaviour with  $N$ , from energies of almost 900 MeV to a minimum, situated at  $N = 11$  to 15, with sensitive differences between the different multiplets. These features derive essentially from the Ali-Bodmer potential, with minor contributions ( $\sim 10^1$  MeV) from the Coulomb and thre-body interactions.

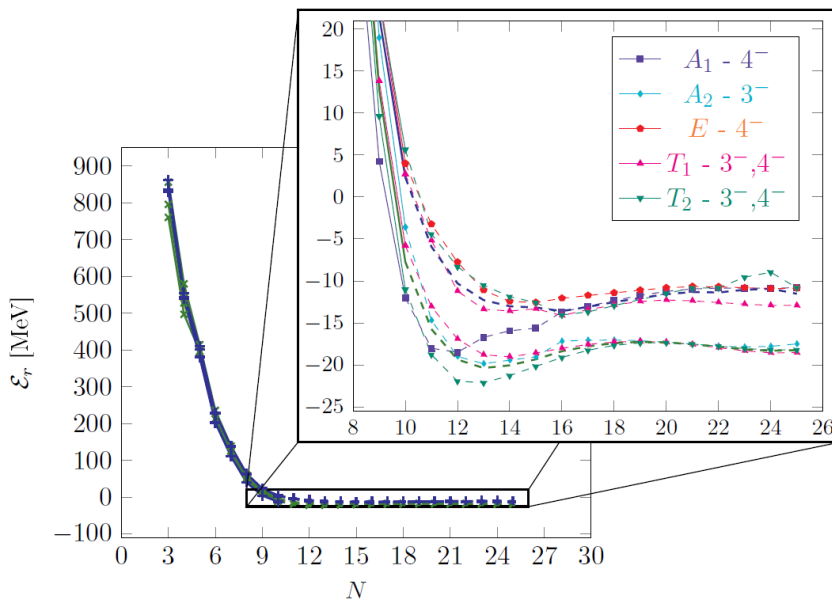


FIGURE 7.17 – Behaviour of the energies of the lowest  $3_1^-$  (diagonal crosses) and  $4_1^-$  (greek crosses) eigenstates as a function of the box size  $N$  for  $a \approx 0.59$  fm (solid lines). The multiplet-averaged eigenvalues of the  $3_1^-$  and the  $4_1^-$  states are denoted in green and blue respectively. The same convention on the markers for the cubic group irreps adopted in the figures of chap. 5 is understood. The dashed lines represents the simulated behaviour of the solid curves in the large  $N$  regime and are affected by discretization errors increasing with the box size.



Differently from the  $3_1^+$  state, the path traced by the three components of the  $3_1^-$  line is smooth and possesses almost the expected shape in the case of exact restoration of rotational symmetry. In particular, at  $N = 25$ , the energies of  $3_{A_2}^-$ ,  $3_{T_1}^-$  and  $3_{T_2}^-$  overlap within 0.96 MeV. Concerning the  $4_1^-$  level, its  $T_2$  component displays some deviations at  $N \sim 23$ , already detected in the same region in the  $2_{T_2}^-$  multiplet (cf. figs. 7.9 and 7.11). However, it is possible to infer from fig. 7.17, that the  $4_{T_1}^-$  and  $4_{T_2}^-$  at  $N = 25$  reach the multiplet-averaged eigenvalue from above, whereas the  $4_{A_1}^-$  and  $4_E^-$  approach the latter from below, as observed for the  $4_2^+$  state of  $^8\text{Be}$  in fig. 5.13.

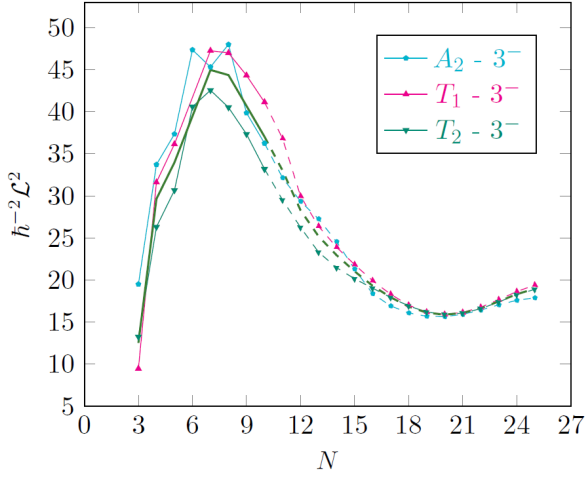


FIGURE 7.18 – Average value of the squared angular momentum for the multiplets of the  $3_1^-$  state as a function of the lattice size for  $a \approx 0.59$  fm. As in fig. F-7-04, the multiplet average of  $\mathcal{L}^2$  is denoted by a red line. The dashed curves denote the expected behaviour of  $\mathcal{L}^2$  in the large  $N$  regime, but their predictive power is limited by discretization errors increasing with  $N$ .

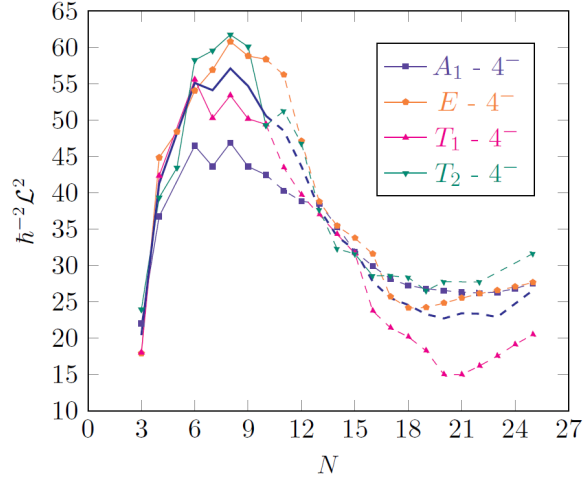


FIGURE 7.19 – Average value of the squared angular momentum for the multiplets of the  $4_1^-$  state as a function of the lattice size for  $a \approx 0.59$  fm. The blue line represents the multiplet average of  $\mathcal{L}^2$ , while the dashed curves denote the expected behaviour of the squared angular momentum in the large  $N$  region, but increasing discretization effects with  $N$  are present.

We pursue our analysis of finite-volume effects by computing the average values of the total squared angular momentum operator (cf. sec. 4.3.3). Differently from the  $3_1^+$  line of the previous section, the values of  $\mathcal{L}^2$  for the  $3_1^-$  multiplets follow a smoother path, even in the region of the maximum. Besides a shift of  $\approx 5.5 \hbar^2$  with respect to the exact eigenvalue, the curves overlap at  $N = 25$  region within  $\approx 1.5$  units of  $\hbar^2$  and seem to tolerate better the augmented discretization errors in dashed part of the curves, see fig. 7.18.

On the other hand, the average values of  $\mathcal{L}^2$  for the  $4_1^-$  multiplets follow a separate paths in almost all the considered box size interval, except for the neighbourhood of  $N \approx 13$ , where the four curves intersect and the  $N \lesssim 5$  region. It is evident that the discrepancies for  $N \lesssim 13$  are essentially genuine finite-volume effects, whereas the visible separation between the curves in the asymptotic region is prompted by discretization artifacts.

The average values of the inter- $\alpha$  distance, displayed in figs. 7.20 and 7.21 confirm some of the trends observed in the  $\mathcal{L}^2$  plots in figs. 7.18 and 7.19). The multiplet average of  $\mathcal{R}$  for the  $3_{A_2}^-$ ,  $3_{T_1}^-$  and  $3_{T_2}^-$  states, in fact, reaches smoothly a value of 3.95 fm at  $N = 25$  and the three individual values for the interparticle distance overlap within  $\approx 0.15$  fm in that limit. The components of the  $4_1^-$  level, on the other hand, reveal a more oscillatory behaviour, albeit not comparable with the one in fig. 7.19.

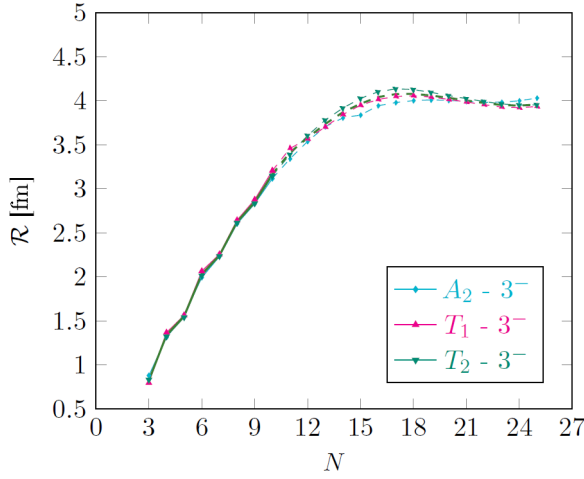


FIGURE 7.20 – Behaviour of the average inter-particle distance for the  $3_1^-$  multiplets as a function of the lattice size. The multiplet average of  $\mathcal{R}$  for the  $3_1^-$  state is denoted with a green line, while the dashed curves represent the behaviour of  $\mathcal{R}$  in the  $N > 10$  region and are subject to larger discretization errors, increasing as  $1/a$ .

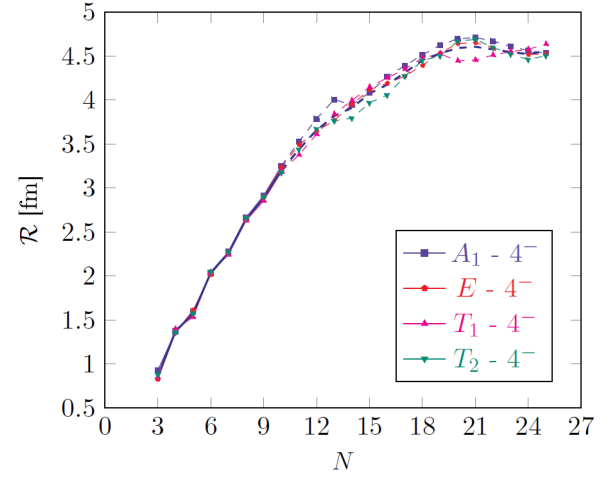


FIGURE 7.21 – Behaviour of the average inter-particle distance for the  $4_1^-$  multiplets as a function of the lattice size. The multiplet average of  $\mathcal{R}$  for the  $4_1^-$  state is denoted with a blue line, while the dashed lines represent the expected behaviour of  $\mathcal{R}$  in the large  $N$  regime and are affected by discretization errors increasing with the inverse of the lattice spacing.

In particular, the  $4_{T_2}^-$  multiplet displays some disturbance around  $N = 15$ , then follows smoothly the  $A_1$  and  $E$  multiplets until  $N = 25$ , where it reaches 4.51 fm. The curve of the  $4_{T_1}^-$  state, instead, gives rise to a shallow minimum at  $N \sim 21$ , then increases until 4.64 fm at  $N = 25$ .

Finally, we conclude the chapter with the behaviour of the energy eigenvalues of the  $3_1^-$  and  $4_1^-$  states as a function of the lattice spacing.

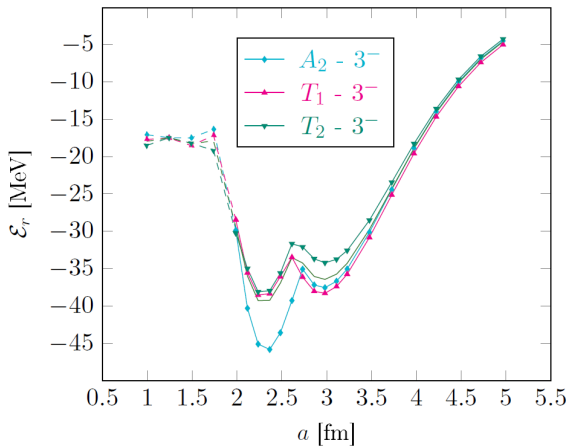


FIGURE 7.22 – Behaviour of the energy of the  $3_1^-$  multiplet eigenstates as a function of the lattice spacing for  $Na \geq 20$  fm (solid lines). The multiplet-averaged  $3_1^-$  energy (green line) quenches the deviations in the path towards the continuum and infinite-volume counterpart, while the dashed lines denote the behaviour of  $\mathcal{R}$  in the  $N > 10$  region.

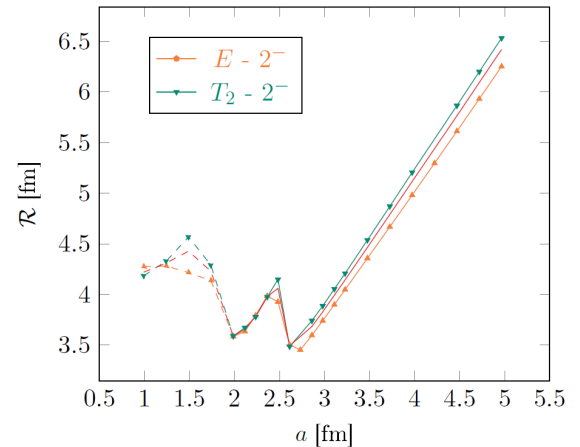


FIGURE 7.23 – Behaviour of the average  $\alpha - \alpha$  distance of the  $3_1^-$  eigenstates as a function of the lattice spacing for  $Na \geq 20$  fm. As before, the multiplet average of  $\mathcal{R}$  for the  $3_1^-$  state is denoted with a green line, while the dashed lines constitute the expected behaviour of  $\mathcal{R}$  in the large  $N$  regime.

We first concentrate on the  $3_1^-$  multiplets and adopt for solid and dashed lines the same conventions as in secs. 7.2 and 7.3. The curves of the three multiplets overlap with appreciable precision along all the path from 5.0 fm to the dashed part of the curve, except in the regions of the two minima at  $a \approx 2.2$  and 3.0 fm. At the endpoint ( $a \approx 1.0$  fm), the superposition between the three curves is reached within  $\approx 1.42$  MeV precision, see fig. 7.22. Analogously as in the  $2_1^-$  case, the two minima seem correlated with the ones at  $\approx 2.2$  and 2.9 fm of the potential energy,  $\mathcal{V}$ , which, in turn, are in quite good agreement with the two minima of the  $\alpha$ - $\alpha$  separation at  $\approx 2.15$  and 2.80 fm in fig. 7.23. Therefore, the connection between the maxima of the PDFs for the  $3_{A_2}^-$ ,  $3_{T_1}^-$  and  $3_{T_2}^-$  multiplets and the minima of  $\mathcal{E}_r$  and  $\mathcal{R}$  can be still established. Noteworthy is also the overlap between the three  $3_1^-$  curves at  $a \approx 1.0$  fm, equal to  $\approx 0.16$  fm.

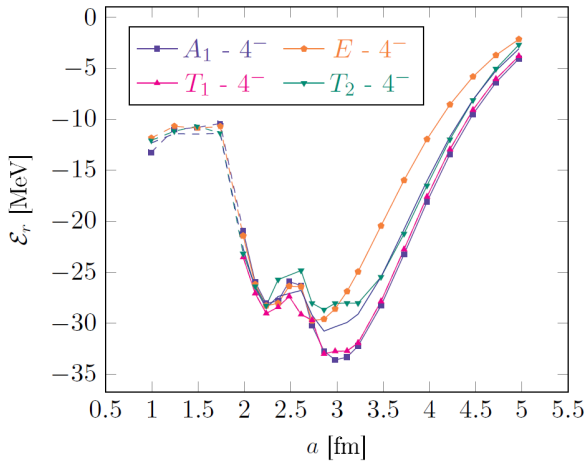


FIGURE 7.24 – Behaviour of the energy of the  $4_1^-$  multiplet eigenstates as a function of the lattice spacing for  $Na \geq 20$  fm (solid lines). Although the multiplet-averaged  $4_1^-$  energy (blue line) quenches the fluctuations towards the continuum and infinite-volume counterpart, the two cubic group multiplets almost follow the same path. The dashed lines denote the behaviour of  $\mathcal{R}$  in the  $N > 10$  regime and are affected by larger finite-volume errors.

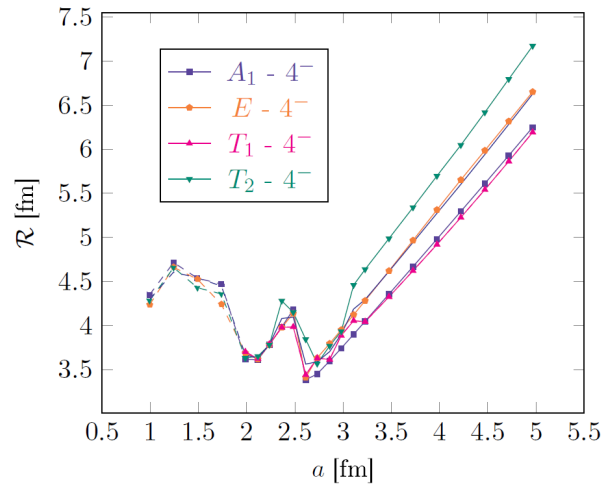


FIGURE 7.25 – Behaviour of the average  $\alpha - \alpha$  distance of the  $4_1^-$  eigenstates as a function of the lattice spacing for  $Na \geq 20$  fm. The multiplet average of  $\mathcal{R}$  for the  $4_1^-$  state is denoted with a blue line, while the dashed lines reproduce the behaviour of  $\mathcal{R}$  in the large  $N$  regime, but are affected by finite-volume errors increasing with  $1/a$ .

Regarding the the  $4_1^-$  line, the four curves for the energy eigenvalue in fig. 7.24 follow separate paths, except for the  $A_1^-$  and  $T_1^-$  multiplets. Additionally, not all the minimum points are found in the same position. While the latter two multiplets display common minima at  $a \approx 2.2$  and 3.0 fm, the  $T_2^-$  extrema appear weakly pronounced and uncertain, whereas of the minima of the  $4_E^-$  is found at a slightly shifted position ( $a \approx 2.75$  fm). The average values of the  $\alpha$ - $\alpha$  separation, instead, highlight more agreement among the four multiplets in the region of the two minimum point, located at  $a \approx 2.1$  and 2.75 fm.

Despite the sizable shifts between the paths until  $a \approx 2.25$  fm, in the asymptotic region the energy eigenvalues of the four cubic-group multiplets overlap in good approximation, overlapping within 1.3 MeV at  $a \approx 1$ . Similarly, the dotted part of the  $\mathcal{R}$  curves in fig. 7.25 display negligible discrepancies and reach a value of  $\approx 4.28$  fm with discrepancy of  $\approx 0.10$  fm, despite the finite-volume errors.

## CHAPTER 8

# VARIATIONAL CALCULATION OF THE STRENGTH PARAMETER OF THE $3\alpha$ GAUSSIAN POTENTIAL FOR $^{16}\text{O}$

As shown in fig. 8.1, the  $M\text{-}\alpha$  Hamiltonian with a superposition of the isotropic Ali-Bodmer potential (cf. eq. (4.2)) with the Coulomb (cf. eq. (4.3)) and  $3\alpha$  Gaussian potentials (cf. eq. (4.3)) with the parameters displayed in sec. 4.2.1 underbinds the  $^{16}\text{O}$  nucleus by circa 11 MeV.

Without resorting to the addition of further interacting terms in the Hamiltonian, in this section we aim at re-adjusting the parameter  $V_3$  of the  $3\alpha$  potential so that the energy eigenvalue of the ground state coincides with the opposite of the  $4\alpha$  dissociation energy gap ( $\approx 14.42$  MeV). Knowing both the three potentials, we perform a linear variational calculation based on ref. [5] in a model space made of four-body harmonic-oscillator functions. The latter are completely symmetric under particle exchange, translationally invariant and possess a well-defined orbital angular momentum. We extend the calculation by anchoring the  $V_3$  parameter to the  $\alpha + ^{12}\text{C}$  threshold at  $\approx 7.16$  MeV. Additionally, we perform the variational calculation in the case of Dirac-delta distribution of the electric charge, in which the Coulomb potential assumes its original form for pointlike  $\alpha$  particles. The results are presented in secs. 8.5.1 and 8.5.2 in the optimized and non-optimized approach with respect to the frequency  $2\pi\omega$  of the harmonic oscillator respectively.

### 8.1 Preamble

The reproduction of the  $^{16}\text{O}$  spectrum and its binding energy in terms of  $\alpha$ -cluster models is a long-standing problem [161, 164, 233] in nuclear physics. In particular, in ref. [161], the linearity of the behaviour of the binding energy  $BE(Z, N)$  as a function of the number of bonds between the  $\alpha$  particles arranged in ordered structures within the nuclides with  $4n \leq 32$  where  $N = Z \equiv 2n$  was revealed. In correspondence of such nuclei, the binding energy per nucleon reaches local maxima. At higher values of  $n$ , the macroscopic  $\alpha$ -cluster viewpoint introduced in sec. A of ref. [157] loses effectiveness, since each  $\alpha$  particle are more prone to nucleon exchanges with the nearest neighbours, thus breaking the symmetry of the configuration.

Furthermore, in ref. [157], a method alternative to the Hartree-Fock approach for the construction of the  $A$ -nucleon wavefunctions was formulated, by adopting a molecular viewpoint. The technique, referenced as the *Resonating Group Structure Method* (RGM), is intended for variational calculations of the low-energy excitations in light nuclei, including estimations

of their binding energy. According to the latter description, nuclear matter is distributed in groups of protons and neutrons whose composition is allowed to vary with time [234]. This distribution reflects into the structure of the wavefunctions of the  $A$ -body system, that are now given by the superposition of several *partial* wavefunctions, representing stable cluster configurations, properly antisymmetrized with respect to neutron and proton exchange [234]. Due to the saturation property of nuclear forces, most of the binding energy of the nucleus is stored by the partitions, while a residual fraction is responsible of the bonds between the groupings. When the latter coincide with  $\alpha$ -particles, two- and three-body interactions between the  ${}^4\text{He}$  clusters can be derived [235].

In recent times, the RGM approach, combined with the *ab initio* no-core shell model (NCSM) [236], has been employed for the estimation of the binding energy in a number of light nuclei, including  ${}^{16}\text{O}$  [237]. Adopting a similarity renormalization group (SRG) [238] evolved chiral N<sup>3</sup>LO NN potential [239], in ref. [237] a binding energy of 139.0(8) MeV has been obtained, a value that exceeds the experimental counterpart of  $BE(8,8)$  by only  $\approx 11.4$  MeV.

An equivalent [240] viewpoint for the description of the properties of light  $\alpha$ -conjugate nuclei is offered by the Generator Coordinate Method (GCM) [162]. In this approach, the construction of the  $A$ -body wavefunction exploits the Slater determinant of single-particle wavefunctions, depending on auxiliary parameters, the *coordinate generators*, that are functions of the spatial coordinates of the clusters in which the original nucleus is subdivided. Since the latter are not eigenfunctions of parity or the angular momentum, the many-nucleon wavefunctions are assumed to coincide with integrals of Slater determinants multiplied by weight functions and performed in the space of the coordinate generators [162, 165]. The proper weight functions are obtained by applying the variational principle, i.e. coincide with the solutions of the Hill-Wheeler equations [165, 168, 241].

Among the applications to  ${}^{16}\text{O}$ , noteworthy is the calculation in the framework of the GCM and Antisymmetrized Molecular Dynamics (AMD) of the binding energy of the nucleus in ref. [242], by means of a NN Volkov No. 2 potential with the Majorana parameter  $M$  fitted to the  ${}^{12}\text{C}$  binding energy. The result is a value of  $BE(8,8)$  of  $\approx 152$  MeV [242], more recently improved via the addition of a three-body Toshaki interaction, which permits to reduce the discrepancy with the experimental binding energy of  ${}^{16}\text{O}$  to  $\approx 3$  MeV [243].

Rather than reconstructing the binding energy of  ${}^{16}\text{O}$  from first principles as in refs. [225, 237] or searching for a common satisfactory description of the low energy spectrum of both  ${}^{12}\text{C}$  and  ${}^{16}\text{O}$  as in ref. [243], here we aim at finding a new value for the parameter  $V_3$  of the  $3\alpha$  Gaussian potential that fits the opposite of the  $4\alpha$  breakup threshold for  ${}^{16}\text{O}$  at  $\approx 14.42$  MeV. Since the latter permits to reconstruct the binding energy of the nucleus via eq. (4.48), we may refer to this dissociation energy as the *binding energy* in the framework of our macroscopic  $\alpha$ -cluster model (cf. sec. 4.2). Based on refs. [5, 244], we perform a variational calculation, expanding the trial wave function in the space of four-body harmonic oscillator (HO) wavefunctions (cf. sec. 8.2) *à la* Moshinsky [245–251]. By construction, the latter are translationally invariant, completely symmetric and possess a well-defined orbital angular momentum [252–254], see sec. 8.3.

The calculation, outlined in sec. 8.4, is justified by the results of the infinite-volume extrapolation of the energy of the  ${}^{16}\text{O}$  ground state in sec. 7.2. As shown in fig. 8.2, our model, whose  $3\alpha$  force is fitted to the Hoyle state gap of  ${}^{12}\text{C}$ , underestimates the binding energy of  ${}^{16}\text{O}$  by about 11 MeV. Moreover, in ref. [255] it is established that the superposition of our three-body poten-



tial with the parameters set in ref. [5], the Coulomb interaction and the angular-momentum dependent Ali-Bodmer potential in ref. [4] with the parameters  $(d'_0, d_2, d_4)$  fitted to the  $S$ ,  $D$  and  $G$  wave  $\alpha$ - $\alpha$  phase shifts overbinds the  $^{16}\text{O}$  nucleus already when the HO basis is truncated at 6 quanta.

Hence our intention to redetermine the strength parameter,  $V_3$ , of the  $3\alpha$  Gaussian potential follows, leaving the range parameter  $\lambda = 0.005 \text{ fm}^{-2}$  unchanged (cf. eq. (4.3)). Hopefully, our fit of the  $V_3$  parameter will yield an overall improvement in the capability of our model to reproduce the low-lying spectrum of  $^{16}\text{O}$  [256–258]. Encouraging, in this direction, seems the  $\alpha$ -cluster model in ref. [169], where the  $\alpha$  particles are arranged in the  $\alpha + ^{12}\text{C}$  configuration [259] and interactions are ruled by an S-wave Ali-Bodmer potential [4] plus two distinct  $3\alpha$  potentials, one within the  $^{12}\text{C}$  grouping and the other outside the latter. Taking also the Coulomb effects into account and fitting the parameters of the three-body potentials to the experimental  $^{16}\text{O}$  binding energy and the root-mean-square radius, the Faddeev and Yakubovsky equations are solved numerically via the cluster-reduction method. The result is an accurate reconstruction of the  $0_2^+$  energy level, with a discrepancy with respect to the experimental datum equal to  $\approx 0.46 \text{ MeV}$  [169]. Additionally, the minima of the charge form factor of the  $^{16}\text{O}$  nucleus are faithfully reproduced [169].

Finally, another promising example comes from the Algebraic Cluster Model (ACM) [230]. Considering a tetrahedral arrangement of the  $^4\text{He}$  groupings [7, 171, 260] and setting the parameters of the ACM Hamiltonian on the experimental energies of the  $0_1^+$ ,  $3_1^-$  and  $0_2^+$  lines, an overall satisfactory agreement with the observational  $\alpha$ -cluster levels is reached, with discrepancies ranging from 0.1 to 1.1 MeV [8]. The subsequent comparison of the reduced electric multipole transition probabilities,  $B(E\ell)$ , in tab. 5 of ref. [8] with the experimental counterparts [227] provide further support to the model.

## 8.2 The Hamiltonian

The interactions between the four  $\alpha$  particles within the  $^{16}\text{O}$  nucleus are here described by the isotropic Ali-Bodmer (cf. eq. (4.2)) potential and by a three-body Gaussian potential (cf. eq. (4.3)), as anticipated in the opening of the chapter. Besides, we account for the effects of the electrostatic repulsion between  $\alpha$  particles the Coulomb potential, either in the version in eq. (4.3) (henceforth referenced as *Erf-Coulomb*) or in its standard form for pointlike particles with charge  $+2e$ . Therefore, the Hamiltonian of the resulting system becomes

$$H = K + V = -\frac{\hbar^2}{2m_\alpha} \sum_{i=1}^4 \nabla_i^2 + \sum_{i<j=2}^4 [V_C(r_{ij}) + V_{AB}(r_{ij})] + \sum_{i<j<k=3}^4 V_T(r_{ij}, r_{ik}, r_{jk}) \quad (8.1)$$

where  $r_{ij} = |\vec{r}_i - \vec{r}_j|$  are the inter-particle distances. Switching to the Jacobi coordinates through the orthogonal transformation,

$$\mathbf{r}^i = \sum_{j=1}^4 J_{ij} \mathbf{r}^j \quad \mathbf{J} = \begin{pmatrix} \sqrt{1/2} & -\sqrt{1/2} & 0 & 0 \\ \sqrt{1/6} & \sqrt{1/6} & -\sqrt{2/3} & 0 \\ \sqrt{1/12} & \sqrt{1/12} & \sqrt{1/12} & -\sqrt{3/2} \\ 1/2 & 1/2 & 1/2 & 1/2 \end{pmatrix}, \quad (8.2)$$

the center of mass (CoM) motion can be separated from the relative motion of the  $\alpha$  particles, encoded in the Hamiltonian  $H_I$ ,

$$H \equiv -\frac{\hbar^2}{2m_\alpha} \nabla_{\vec{r}_4}^2 + H_I, \quad (8.3)$$

where  $\nabla_{\vec{r}_4}^2$  refers to the position vector  $\vec{r}_4$ . Neglecting the CoM motion as in ref. [248], we rewrite the intrinsic Hamiltonian as a superposition of a three-body harmonic oscillator,  $H_0$  and a potential term,  $U$ ,

$$H_I = H_0 + U \quad U \equiv V - \frac{m\omega^2}{2} \sum_{i=1}^3 r_i^2, \quad (8.4)$$

by adding and subtracting a quadratic potential with a strength  $m_\alpha\omega^2$ , whose variational determination is shown below. Accordingly, the evaluation of matrix elements between  $H_r$  and the basis states can be performed by means of Talmi Integrals (cf. pag. 6 and ref. [251]), except for the straightforward diagonal contribution from  $H_0$  and the Erf-Coulomb term, that requires a numerical evaluation.

### 8.3 The model space

Since the angular momentum and parity content of the ground state of the  $^{16}\text{O}$  is known, the single-particle three-dimensional harmonic oscillator eigenfunctions can be more conveniently chosen in the spherical basis, where the labels,  $\dot{n}_i$ ,  $\dot{\ell}_i$  and  $\dot{m}_i$  denote the order of the radial eigenfunction, the magnetic quantum number and the angular momentum projection along the  $z$  axis in unit of  $\hbar$ . The wavefunction, in turn, is given by a Gaussian exponential times a generalized Laguerre polynomial on the squared radius of order  $n_i$  and shift  $\ell_i$ . Exploiting spherical symmetry, the most general eigenfunction with

$$\dot{N}_i = 2\dot{n}_i + \dot{\ell}_i, \quad (8.5)$$

can be written in factorized form,

$$\langle \vec{r}_i | \dot{n}_i \dot{\ell}_i \dot{m}_i \rangle = R_{\dot{n}_i \dot{\ell}_i}(\dot{r}_i) Y_{\dot{\ell}_i \dot{m}_i}(\dot{\phi}_i, \dot{\theta}_i), \quad (8.6)$$

where the radial part is expressed as a product of the Gaussian exponential and a power series, in sight of the evaluation of the matrix elements through Talmi integrals,

$$R_{\dot{n}_i \dot{\ell}_i}(\dot{r}_i) = \dot{r}_i^{\dot{\ell}_i} \sum_{k=0}^{\dot{n}_i} a_{\dot{n}_i \dot{\ell}_i k} \dot{r}_i^{2k} e^{-\frac{\dot{r}_i^2}{2\xi^2}} \quad \text{with} \quad \xi \equiv \sqrt{\frac{\hbar}{m_\alpha \omega}} \quad (8.7)$$

where the normalized coefficients  $a_{\dot{n}_i \dot{\ell}_i k}$  are given by

$$a_{\dot{n}_i \dot{\ell}_i k} = \frac{(-1)^k}{k!} \left( \frac{1}{\xi} \right)^{\dot{\ell}_i + \frac{3}{2}} \left[ \frac{(2\dot{n}_i)!}{\Gamma(\dot{n}_i + \dot{\ell}_i + 3/2)} \right]^{\frac{1}{2}} \frac{\Gamma(\dot{n}_i + \dot{\ell}_i + 3/2)}{(\dot{n}_i - k)! \Gamma(k + \dot{\ell}_i + 3/2)}. \quad (8.8)$$



The same eigenfunctions can be derived in the second quantization formalism by repeated application on the normalized ground state

$$\langle \mathbf{r}_i | 0 \rangle = \left( \frac{\xi^{-2}}{\pi} \right)^{\frac{3}{4}} e^{-\frac{r_i^2}{2\xi^2}} \quad (8.9)$$

of the creation operators associated to the relative coordinate  $i$  [261],

$$\mathbf{a}_i^\dagger = \frac{1}{\sqrt{2\xi}} \left( \mathbf{r}_i + i\xi^2 \nabla_i \right), \quad (8.10)$$

arranged in a homogeneous polynomial of degree  $\dot{N}_i$ , eigenstate of the squared angular momentum operator and its projection along the  $z$  axis (cf. eq. (8.10) in ref. [251]). Recalling the definition of the *solid* spherical harmonic,

$$\mathcal{Y}_{\ell,m}(\mathbf{r}) = r^\ell Y_{\ell,m}(\phi, \theta). \quad (8.11)$$

the single-particle eigenfunction can be, in fact, expressed as

$$\langle \mathbf{r}_i | \dot{n}_i, \dot{\ell}_i, \dot{m}_i \rangle = \langle \mathbf{r}_i | A_{\dot{n}_i \dot{\ell}_i} (\mathbf{a}_i^\dagger \cdot \mathbf{a}_i^\dagger)^{\dot{n}_i} \mathcal{Y}_{\dot{\ell}_i \dot{m}_i}(\mathbf{a}_i^\dagger) | 0 \rangle \quad (8.12)$$

where  $A_{\dot{n}_i \dot{\ell}_i}$  is the normalization constant,

$$A_{\dot{n}_i \dot{\ell}_i} = \frac{(-1)^{\dot{n}_i}}{\xi^{\dot{\ell}_i}} \sqrt{\frac{4\pi}{(2\dot{n}_i + 2\dot{\ell}_i + 1)!! (2\dot{n}_i)!!}}, \quad (8.13)$$

see sec. 8 of ref. [251]. Once defined the single-particle harmonic oscillator eigenfunction (cf. eq. (8.9)), the three one-body eigenstates can be coupled to zero angular momentum,

$$\langle \mathbf{r}_1, \mathbf{r}_2, \mathbf{r}_3 | \dot{n}_1 \dot{\ell}_1, \dot{n}_2 \dot{\ell}_2, \dot{n}_3 \dot{\ell}_3 \rangle = \left[ \langle \mathbf{r}_1 | \dot{n}_1 \dot{\ell}_1 \rangle \otimes \langle \mathbf{r}_2 | \dot{n}_2 \dot{\ell}_2 \rangle \otimes \langle \mathbf{r}_3 | \dot{n}_3 \dot{\ell}_3 \rangle \right]_0 \quad (8.14)$$

obtaining the building blocks of the completely symmetric three-body eigenstate. Due to the bosonic nature of the  $\alpha$  particles, the states of the basis for the (truncated) expansion of the ground state of  $H_I$  have to be symmetric under the exchange of any couple of particle labels in the laboratory reference frame. Their explicit construction, shown in refs. [251] and [248], is conveniently carried out through the definition of another set of coordinates, the symmetric relative or Kramer-Moshinsky [255] coordinates (cf. eq. (21.6) in ref. [251]),  $\tilde{\mathbf{r}}^i$  with  $i = 1, 2, 3$ ,

$$\tilde{\mathbf{r}}^i = \sum_{j=1}^3 K_{ij} \mathbf{r}^j, \quad \mathbf{K} \equiv \begin{pmatrix} \sqrt{1/2} & \sqrt{1/6} & -\sqrt{1/3} \\ -\sqrt{1/2} & \sqrt{1/6} & \sqrt{1/3} \\ 0 & -\sqrt{2/3} & -\sqrt{1/3} \end{pmatrix}, \quad (8.15)$$

where  $\mathbf{K}$  is an orthogonal transformation. Denoting the three-body HO states in the latter coordinates with round brackets, the fully-symmetrized states coupled to zero angular momentum take the form

$$|n_1, \ell_1, n_2, \ell_2, n_3, \ell_3\rangle_{\mathcal{S}} = \mathcal{A} \left[ \sum_{\sigma \text{ even}} |n_{\sigma(1)}, \ell_{\sigma(1)}, n_{\sigma(2)}, \ell_{\sigma(2)}, n_{\sigma(3)}, \ell_{\sigma(3)}\rangle + (-1)^{\ell_1 + \ell_2 + \ell_3} \sum_{\sigma \text{ odd}} |n_{\sigma(1)}, \ell_{\sigma(1)}, n_{\sigma(2)}, \ell_{\sigma(2)}, n_{\sigma(3)}, \ell_{\sigma(3)}\rangle \right], \quad (8.16)$$

where  $\sigma(\cdot)$  denote the  $3!$  operations of the permutation group of three elements,  $\mathcal{S}_3$ . The connection between permutation symmetry and the many-body harmonic oscillator eigenstates, highlighted by eq. (8.16), has been first explored in ref. [248].

Following the same convention adopted in refs. [251] and [255], we use the dot for the labels of the eigenstates in the Jacobi coordinates and undotted symbols for the ones in the Kramer-Moshinsky coordinates, defined in a fashion fully analogous to eq. (8.14). Since the parity of the  $^{16}\text{O}$  ground state is positive, the sum of the individual angular momenta,  $\ell_1 + \ell_2 + \ell_3$  has to be even, implying that either all the three orbital quantum numbers are even or two of them are odd. However, as the latter choice cause the resulting state to vanish, the  $\ell_i$  need to be all even (cf. secs. 21-22. of ref. [251] and eq. (2.3) in ref. [5]). Having regards to these prescriptions, the completely symmetric states with  $\mathfrak{N}$  three-body relative HO quanta equal or lower than 10 are the ones reported in tab. 8.1.

$\mathfrak{N}$	$ n_1\ell_1, n_2\ell_2, n_3\ell_3\rangle_{\mathcal{S}}$
0	$ 00, 00, 00\rangle$
2	$ 10, 00, 00\rangle$
4	$ 20, 00, 00\rangle,  10, 01, 01\rangle,  02, 02, 00\rangle$
6	$ 30, 00, 00\rangle,  20, 10, 00\rangle,  12, 02, 00\rangle,  10, 02, 02\rangle,  02, 02, 02\rangle,  10, 10, 10\rangle$
8	$ 40, 00, 00\rangle,  30, 10, 00\rangle,  22, 02, 00\rangle,  10, 10, 20\rangle,  02, 02, 04\rangle,  02, 02, 20\rangle,  02, 10, 12\rangle,  02, 02, 12\rangle,  12, 12, 00\rangle,  20, 20, 00\rangle,  04, 04, 00\rangle$
10	$ 50, 00, 00\rangle,  40, 10, 00\rangle,  32, 02, 00\rangle,  30, 10, 10\rangle,  30, 02, 02\rangle,  30, 20, 00\rangle,  10, 20, 20\rangle,  04, 04, 02\rangle,  14, 04, 00\rangle,  22, 12, 00\rangle,  14, 02, 02\rangle,  22, 02, 10\rangle,  22, 02, 02\rangle,  12, 04, 02\rangle,  20, 12, 02\rangle,  12, 12, 02\rangle,  12, 12, 10\rangle,  10, 04, 04\rangle$

TABLE 8.1 – The fourty lowest energy three-body relative harmonic oscillator eigenstates, with zero total angular momentum and completely symmetric with respect to particle exchange. The  $\mathcal{S}$  subscript (cf. eq. (8.16)) for symmetrized states has been omitted in the lists for the sake of brevity.

## 8.4 The matrix elements

While the Kramer-Moshinsky coordinates allow for a cleaner determination of the fully-symmetrized zero angular momentum states, the Jacobi coordinates remain the preferred reference for the evaluation of the matrix elements between any two three-body harmonic oscillator states (cf. eq. (8.15)) and the intrinsic Hamiltonian operator,  $H_I$ . Accordingly, we express the round kets in terms of the angle kets,

$$|n_1\ell_1, n_2\ell_2, n_3\ell_3\rangle = \sum_{\substack{\dot{n}_1\dot{\ell}_1 \\ \dot{n}_2\dot{\ell}_2 \\ \dot{n}_3\dot{\ell}_3}} \langle \dot{n}_1\dot{\ell}_1, \dot{n}_2\dot{\ell}_2, \dot{n}_3\dot{\ell}_3 | n_1, \ell_1, n_2, \ell_2, n_3, \ell_3 \rangle | \dot{n}_1\dot{\ell}_1, \dot{n}_2\dot{\ell}_2, \dot{n}_3\dot{\ell}_3 \rangle, \quad (8.17)$$

an expansion whose coefficients can be interpreted as rotation matrix elements in the space of particles,

$$\langle \dot{n}_1\dot{\ell}_1, \dot{n}_2\dot{\ell}_2, \dot{n}_3\dot{\ell}_3 | n_1\ell_1, n_2\ell_2, n_3\ell_3 \rangle \equiv \langle \dot{n}_1\dot{\ell}_1, \dot{n}_2\dot{\ell}_2, \dot{n}_3\dot{\ell}_3 | \mathcal{R}(\mathbf{K}) | n_1\ell_1, n_2\ell_2, n_3\ell_3 \rangle, \quad (8.18)$$

where  $\mathbf{K}$  represents the orthogonal transformation and  $\mathcal{R}(\mathbf{K})$  the relevant operator. Decomposing the latter transformation into a succession of three rotations,  $\mathcal{R}(\mathbf{M}_1)\mathcal{R}(\mathbf{M}_2)\mathcal{R}(\mathbf{M}_3)$  with (cf. sec. 22 of ref. [251] for the full procedure)

$$\mathbf{M}_1 = \begin{pmatrix} \sqrt{1/2} & \sqrt{1/2} & 0 \\ -\sqrt{1/2} & \sqrt{1/2} & 0 \\ 0 & 0 & 1 \end{pmatrix}, \quad \mathbf{M}_2 = \begin{pmatrix} 1 & 0 & 0 \\ 0 & \sqrt{1/3} & \sqrt{2/3} \\ 0 & -\sqrt{2/3} & \sqrt{1/3} \end{pmatrix}, \quad \text{and} \quad \mathbf{M}_3 = \begin{pmatrix} 1 & 0 & 0 \\ 0 & 1 & 0 \\ 0 & 0 & -1 \end{pmatrix} \quad (8.19)$$

the matrix elements in eq. (8.19) can be rewritten as sums of standard Moshinsky brackets (SMB) [254] and generalized Moshinsky brackets (GMB), denoted by the ' $\pi/2$ ' and ' $\gamma = \arccos(\sqrt{1/3})$ ' subscripts respectively,

$$\begin{aligned} \langle \dot{n}_1 \dot{\ell}_1, \dot{n}_2 \dot{\ell}_2, \dot{n}_3 \dot{\ell}_3 | n_1, \ell_1, n_2, \ell_2, n_3, \ell_3 \rangle &= (-1)^{\ell_3} \sum_{\dot{n}_2' \dot{\ell}_2'} \langle \dot{n}_2' \dot{\ell}', \dot{n}_3 \dot{\ell}_3, \ell_1 | n_2 \ell_2, n_3 \ell_3, \ell_1 \rangle_{\gamma} \\ &\quad \cdot \langle \dot{n}_1 \dot{\ell}_1, \dot{n}_2 \dot{\ell}_2, \dot{\ell}_3 | n_1 \ell_1, \dot{n}_2' \dot{\ell}_2', \dot{\ell}_3 \rangle_{\pi/2}. \end{aligned} \quad (8.20)$$

In particular,  $\mathbf{M}_1$  gives rise to the standard Moshinsky brackets,  $\mathbf{M}_2$  generates the the generalized ones, while the  $\mathbf{M}_3$  rotation is responsible of the phase factor  $(-1)^{\ell_3}$ . In the derivation of eq. (8.20) the following equalities

$$|n_1 \ell_1, n_2 \ell_2, n_3 \ell_3\rangle = [|n_1 \ell_1, n_2 \ell_2, \ell_3\rangle \otimes |n_3 \ell_3\rangle]_0 = [|n_2 \ell_2, n_3 \ell_3, \ell_1\rangle \otimes |n_1 \ell_1\rangle]_0 = [|n_1 \ell_1, n_3 \ell_3, \ell_2\rangle \otimes |n_2 \ell_2\rangle]_0, \quad (8.21)$$

together with the definition of the standard Moshinsky bracket have been taken into account. These transformation brackets coincide with the matrix elements between any two two-body harmonic oscillator states in the spherical basis coupled to the same total angular momentum and a rotation in the particle space,

$$\mathbf{m}_1 = \begin{pmatrix} \sqrt{1/2} & \sqrt{1/2} \\ -\sqrt{1/2} & \sqrt{1/2} \end{pmatrix}, \quad (8.22)$$

a linear transformation coinciding with the one carrying from the absolute to the Jacobi two-body coordinates. The evaluation of these coefficients can be carried out iteratively from the matrix elements of the kind

$$\langle \dot{n}_1 \dot{\ell}_1, \dot{n}_2 \dot{\ell}_2, \Lambda | 0 \ell_1, 0 \ell_2, \Lambda \rangle_{\pi/2}, \quad (8.23)$$

by exploiting the following recurrence relations between the SMB's

$$\langle \dot{n}_1 \dot{\ell}_1, \dot{n}_2 \dot{\ell}_2, \Lambda | n_1 + 1 \ell_1, n_2 \ell_2, \Lambda \rangle_{\pi/2} = \sqrt{(n_1 + 1) \left( n_1 + \ell_1 + \frac{3}{2} \right)} C(\dot{n}_1 \dot{\ell}_1, \dot{n}_2 \dot{\ell}_2; \dot{\ell}_1' \dot{\ell}_1', \dot{n}_2' \dot{\ell}_2', \Lambda), \quad (8.24)$$

and

$$\langle \dot{n}_1 \dot{\ell}_1, \dot{n}_2 \dot{\ell}_2, \Lambda | n_1 \ell_1, n_2 + 1 \ell_2, \Lambda \rangle_{\pi/2} = \sqrt{(n_2 + 1) \left( n_2 + \ell_2 + \frac{3}{2} \right)} C(\dot{n}_1 \dot{\ell}_1, \dot{n}_2 \dot{\ell}_2; \dot{\ell}_1' \dot{\ell}_1', \dot{n}_2' \dot{\ell}_2', \Lambda), \quad (8.25)$$

with

$$C(\dot{n}_1 \dot{\ell}_1, \dot{n}_2 \dot{\ell}_2; \dot{\ell}'_1 \dot{\ell}'_1, \dot{n}'_2 \dot{\ell}'_2, \Lambda) = \sum_{\substack{\dot{n}'_1 \dot{\ell}'_1 \\ \dot{n}'_2 \dot{\ell}'_2}} c(\dot{n}_1 \dot{\ell}_1, \dot{n}_2 \dot{\ell}_2; \dot{\ell}'_1 \dot{\ell}'_1, \dot{n}'_2 \dot{\ell}'_2, \Lambda) \langle \dot{n}'_1 \dot{\ell}'_1, \dot{n}'_2 \dot{\ell}'_2, \Lambda | n_1 \ell_1, n_2 \ell_2, \Lambda \rangle_{\pi/2} \quad (8.26)$$

where the coefficients  $c(\dot{n}_1 \dot{\ell}_1, \dot{n}_2 \dot{\ell}_2; \dot{\ell}'_1 \dot{\ell}'_1, \dot{n}'_2 \dot{\ell}'_2, \Lambda)$ , derived in sec. 10 of ref. [251], are reported in the tab. 8.2. On the other hand, for the matrix elements with both the Laguerre polynomials of order zero on the ket (cf. eq. (8.23)) the formula derived in sec. 4 of ref. [245] and appearing in refs. [262], [263], [264] and [265] can be adopted,

$$\begin{aligned} \langle \dot{n}_1 \dot{\ell}_1, \dot{n}_2 \dot{\ell}_2, \Lambda | 0 \ell_1, 0 \ell_2, \Lambda \rangle_{\pi/2} &= \left[ \frac{\ell_1! \ell_2!}{(2\ell_1)!(2\ell_2)!} \frac{(2\dot{\ell}_1 + 1)(2\dot{\ell}_2 + 1)}{2^{\dot{\ell}_1 + \dot{\ell}_2}} \frac{(\dot{n}_1 + \dot{\ell}_1)!}{\dot{n}_1!(2\dot{n}_1 + 2\dot{\ell}_1 + 1)!} \frac{(\dot{n}_2 + \dot{\ell}_2)!}{\dot{n}_2!(2\dot{n}_2 + 2\dot{\ell}_2 + 1)!} \right]^{\frac{1}{2}} \\ &\cdot \left[ \frac{\ell_1! \ell_2!}{(2\ell_1)!(2\ell_2)!} \frac{(2\dot{\ell}_1 + 1)(2\dot{\ell}_2 + 1)}{2^{\dot{\ell}_1 + \dot{\ell}_2}} \right]^{\frac{1}{2}} (-1)^{\dot{n}_1 + \dot{\ell}_1 + \dot{\ell}_2 - \Lambda} \sum_x \left\{ (2x + 1) A(\ell_1 \dot{\ell}_1, \ell_2 \dot{\ell}_2, x) W(\dot{\ell}_1 \dot{\ell}_2 \ell_1 \ell_2; \Lambda x) \right\}, \end{aligned} \quad (8.27)$$

where the dummy index  $x$  assumes all the integer values allowed by the Racah  $W$  coefficient [135, 266] and

$$\begin{aligned} A(\ell_1 \dot{\ell}_1, \ell_2 \dot{\ell}_2, x) &\equiv \left[ \frac{(\ell_1 + \dot{\ell}_1 + x + 1)!(\ell_1 + \dot{\ell}_1 - x)!(\ell_1 + x - \dot{\ell}_1)!}{(\dot{\ell}_1 + x - \ell_1)!} \right]^{\frac{1}{2}} \\ &\cdot \left[ \frac{(\ell_2 + \dot{\ell}_2 + x + 1)!(\ell_2 + \dot{\ell}_2 - x)!(\ell_2 + x - \dot{\ell}_2)!}{(\dot{\ell}_2 + x - \ell_2)!} \right]^{\frac{1}{2}} \sum_q \frac{(\dot{\ell}_1 + q - \ell_1)!}{\left[ \frac{1}{2}(\dot{\ell}_1 + q - \ell_1) \right]! \left[ \frac{1}{2}(\dot{\ell}_1 + \ell_1 - q) \right]!} \\ &\frac{(-1)^{\frac{1}{2}(\dot{\ell}_1 + q - \ell_1)}}{(q - x)!(q + x + 1)!} \frac{(\dot{\ell}_2 + q - \ell_2)!}{\left[ \frac{1}{2}(\dot{\ell}_2 + q - \ell_2) \right]! \left[ \frac{1}{2}(\dot{\ell}_2 + \ell_2 - q) \right]!}, \end{aligned} \quad (8.28)$$

with  $q$  restricted to the integer values for which the arguments of the factorials implied are non-zero. The implementation of eq. (8.27) turned out to be faster than the one in eq. (10.30) in ref. [251], because of the smaller number of summations involved. For the sake of completeness, in the latter expression a phase factor  $(-1)^{\ell'_2 + \ell_2}$  coming from eqs. (10.21) and (10.22) of ref. [251] reduces to unity.

While the SMBs are matrix elements between harmonic oscillator states connected by a rotation of  $\pi/4$  (cf.  $\mathbf{m}_1$  in eq. (8.22)) in the two body coordinate space, their generalized version appearing in eq. (8.20) refers to a rotation of angle  $\gamma/2$  performed in the same space. The expression of these  $\gamma$ -dependent brackets in terms of the SMBs is derived in [251] exploiting again the factorization of the rotation  $\mathbf{m}_1$ , and coincides with

$$\begin{aligned} \langle \dot{n}_1 \dot{\ell}_1, \dot{n}_2 \dot{\ell}_2, \Lambda | n_1 \ell_1, n_2 \ell_2, \Lambda \rangle_\gamma &= i^{2\dot{n}_2 + \dot{\ell}_2 - 2n_2 - \ell_2} \sum_{\substack{n'_1 \dot{\ell}'_1 \\ n'_2 \dot{\ell}'_2}} \exp \left[ \frac{1}{2} i \gamma (2n'_2 + \dot{\ell}'_2 - 2n'_1 - \dot{\ell}'_1) \right] \\ &\cdot (-1)^{\dot{\ell}_2 + \dot{\ell}_2} \langle n'_1 \dot{\ell}'_1, n'_2 \dot{\ell}'_2, \Lambda | \dot{n}_1 \dot{\ell}_1, \dot{n}_2 \dot{\ell}_2, \Lambda \rangle_{\pi/2} \langle n'_1 \dot{\ell}'_1, n'_2 \dot{\ell}'_2, \Lambda | n_1 \ell_1, n_2 \ell_2, \Lambda \rangle_{\pi/2}. \end{aligned} \quad (8.29)$$

Even if a complex exponential and an overall complex phase factor are present, the reality of these generalized Moshinsky brackets is ensured by the conservation of the total number

of quanta in the brackets,

$$2n_1 + \ell_1 + 2n_2 + \ell_2 = 2\dot{n}_1 + \dot{\ell}_1 + 2\dot{n}_2 + \dot{\ell}_2 = 2n'_1 + \ell'_1 + 2n'_2 + \ell'_2, \quad (8.30)$$

and by the exchange property of the 1-body HO quantum numbers in the bra of the SMB [252],

$$\langle \dot{n}_1 \dot{\ell}_1, \dot{n}_2 \dot{\ell}_2, \Lambda | n_1 \ell_1, n_2 \ell_2, \Lambda \rangle_{\pi/2} = (-1)^{\ell_1 - \Lambda} \langle \dot{n}_2 \dot{\ell}_2, \dot{n}_1 \dot{\ell}_1, \Lambda | n_1 \ell_1, n_2 \ell_2, \Lambda \rangle_{\pi/2}. \quad (8.31)$$

$n'_1$	$\ell'_1$	$n'_2$	$\ell'_2$	$c(\dot{n}_1 \dot{\ell}_1, \dot{n}_2 \dot{\ell}_2; \dot{\ell}'_1 \dot{\ell}'_2, \dot{n}'_1 \dot{n}'_2, \Lambda)$
$n_1 - 1$	$\ell_1$	$n_2$	$\ell_2$	$\frac{1}{2} \sqrt{n_1(n_1 + \ell_1 + \frac{1}{2})}$
$n_1$	$\ell_1$	$n_2 - 1$	$\ell_2$	$\frac{1}{2} \sqrt{n_2(n_2 + \ell_2 + \frac{1}{2})}$
$n_1 - 1$	$\ell_1 + 1$	$n_2 - 1$	$\ell_2 + 1$	$\frac{1}{2} \sqrt{n_1 n_2 (\ell_1 + 1)(\ell_2 + 1)} (-1)^{\ell_1 + \ell_2 + \Lambda} W(\ell_1 \ell_1 + 1 \ell_2 \ell_2 + 1; 1 \Lambda)$
$n_1 - 1$	$\ell_1 + 1$	$n_2$	$\ell_2 - 1$	$\frac{1}{2} \sqrt{n_1(n_2 + \ell_2 + \frac{1}{2})(\ell_1 + 1) \ell_2} (-1)^{\ell_1 + \ell_2 + \Lambda} W(\ell_1 \ell_1 + 1 \ell_2 \ell_2 - 1; 1 \Lambda)$
$n_1$	$\ell_1 - 1$	$n_2 - 1$	$\ell_2 + 1$	$\frac{1}{2} \sqrt{(n_1 + \ell_1 + \frac{1}{2}) n_2 \ell_1 (\ell_2 + 1)} (-1)^{\ell_1 + \ell_2 + \Lambda} W(\ell_1 \ell_1 - 1 \ell_2 \ell_2 + 1; 1 \Lambda)$
$n_1$	$\ell_1 - 1$	$n_2$	$\ell_2 - 1$	$\frac{1}{2} \sqrt{(n_1 + \ell_1 + \frac{1}{2})(n_2 + \ell_2 + \frac{1}{2}) \ell_1 \ell_2} (-1)^{\ell_1 + \ell_2 + \Lambda} W(\ell_1 \ell_1 - 1 \ell_2 \ell_2 - 1; 1 \Lambda)$

TABLE 8.2 – The lowercase C coefficients implied in the recurrence relationships between standard Moshinsky brackets. The  $W$ 's denote the Racah coefficients for the coupling of three angular momenta.

After having introduced the standard Moshinsky brackets and their generalization, we can switch to the evaluation of the matrix elements of  $H_0$  and  $U$  where both the HO states (cf. eq. (8.17)) and the operators are written in Jacobi coordinates (cf. eq. (8.3)). If

$$\mathfrak{N} \equiv \sum_{i=1}^3 (2n_i + \ell_i) = \sum_{i=1}^3 (2\dot{n}_i + \dot{\ell}_i) \quad (8.32)$$

denotes the total number of quanta, the computation of the matrix elements with the three-body relative harmonic oscillator hamiltonian,  $H_0$  reduces to

$$\langle \dot{n}'_1 \dot{\ell}'_1, \dot{n}'_2 \dot{\ell}'_2, \dot{n}'_3 \dot{\ell}'_3 | H_0 | \dot{n}_1 \dot{\ell}_1, \dot{n}_2 \dot{\ell}_2, \dot{n}_3 \dot{\ell}_3 \rangle = \delta_{\dot{n}_1 \dot{n}'_1} \delta_{\dot{\ell}_1 \dot{\ell}'_1} \delta_{\dot{n}_2 \dot{n}'_2} \delta_{\dot{\ell}_2 \dot{\ell}'_2} \delta_{\dot{n}_3 \dot{n}'_3} \delta_{\dot{\ell}_3 \dot{\ell}'_3} \hbar \omega \left( \mathfrak{N} + \frac{9}{2} \right). \quad (8.33)$$

Conversely, in the matrix elements involving  $U$ , the symmetry of the three-body relative HO states under the exchange of the particle coordinates  $\mathbf{r}_i$  leads us to the following simplified expression,

$$\begin{aligned} \langle \dot{n}'_1 \dot{\ell}'_1, \dot{n}'_2 \dot{\ell}'_2, \dot{n}'_3 \dot{\ell}'_3 | U | \dot{n}_1 \dot{\ell}_1, \dot{n}_2 \dot{\ell}_2, \dot{n}_3 \dot{\ell}_3 \rangle &= 4 \delta_{\dot{\ell}'_1 \dot{\ell}_1} \delta_{\dot{\ell}'_2 \dot{\ell}_2} \delta_{\dot{n}'_3 \dot{n}_3} \delta_{\dot{\ell}'_3 \dot{\ell}_3} \langle \dot{n}'_1 \dot{\ell}_1 \dot{n}'_2 \dot{\ell}_2 || V_T(\mathbf{r}_1, \mathbf{r}_2, \mathbf{r}_3) || \dot{n}_1 \dot{\ell}_1 \dot{n}_2 \dot{\ell}_2 \rangle \\ &+ 6 \delta_{\dot{\ell}'_1 \dot{\ell}_1} \delta_{\dot{n}'_2 \dot{n}_2} \delta_{\dot{\ell}'_2 \dot{\ell}_2} \delta_{\dot{n}'_3 \dot{n}_3} \delta_{\dot{\ell}'_3 \dot{\ell}_3} \langle \dot{n}'_1 \dot{\ell}_1 || \left[ V_C(\dot{\mathbf{r}}_1) + V_{AB}(\dot{\mathbf{r}}_1) - \frac{m_\alpha \omega^2}{4} \dot{\mathbf{r}}_1^2 \right] || \dot{n}_1 \dot{\ell}_1 \rangle, \end{aligned} \quad (8.34)$$

since each of the six (four) terms in the second (third) summation in eq. (8.1) involving two (resp. three) body potentials gives the same contribution to the matrix elements. By the same token, all the three addends coming from the subtracted harmonic potential (cf. eq. (8.4)) give the same contribution to the matrix elements. The double vertical lines in eq. (8.34) denote the reduced matrix elements, independent on the third component of the angular momentum of

the states. Making use of the Talmi integrals in sec. 2 of ref. [251], the two body Erf-Coulomb, Ali-Bodmer and Harmonic contributions can be written explicitly as

$$\langle \dot{n}'_1 \dot{\ell}_1 || V_C(\dot{\mathbf{r}}_1) || \dot{n}_1 \dot{\ell}_1 \rangle = \frac{\sqrt{2}\xi^2}{\pi\epsilon_0} \sum_{p=\dot{\ell}_1}^{\dot{\ell}_1+\dot{n}_1+\dot{n}'_1} \frac{B(p; \dot{n}'_1, \dot{\ell}_1, \dot{n}_1, \dot{\ell}_1)}{\Gamma(p + \frac{3}{2})} \int_0^{+\infty} d\rho \rho^{2p+1} e^{-\rho^2} \operatorname{erf}\left(\frac{\sqrt{6}\xi}{2R_\alpha}\rho\right), \quad (8.35)$$

$$\langle \dot{n}'_1 \dot{\ell}_1 || V_{AB}(\dot{\mathbf{r}}_1) || \dot{n}_1 \dot{\ell}_1 \rangle = \xi^3 \sum_{p=\dot{\ell}_1}^{\dot{\ell}_1+\dot{n}'_1+\dot{n}_1} B(p; \dot{n}'_1, \dot{\ell}_1, \dot{n}_1, \dot{\ell}_1) \left[ \frac{V_0}{(2\eta_0\xi^2 + 1)^{\frac{3}{2}+p}} + \frac{V_1}{(2\eta_1\xi^2 + 1)^{\frac{3}{2}+p}} \right], \quad (8.36)$$

and

$$\langle \dot{n}'_1 \dot{\ell}_1 || -\frac{m_\alpha \omega^2}{4} \dot{\mathbf{r}}_1^2 || \dot{n}_1 \dot{\ell}_1 \rangle = -\xi^5 \frac{m_\alpha \omega^2}{4} \sum_{p=\dot{\ell}_1}^{\dot{\ell}_1+\dot{n}'_1+\dot{n}_1} B(\dot{n}'_1, \dot{\ell}_1, \dot{n}_1, \dot{\ell}_1; p) \frac{\Gamma(p + 1 + \frac{3}{2})}{\Gamma(p + \frac{3}{2})} \quad (8.37)$$

where

$$B(\dot{n}'_1, \dot{\ell}_1, \dot{n}_1, \dot{\ell}_1; p) = \frac{1}{2} \sum_{k=0}^{\dot{n}_1} \Gamma\left(p + \frac{3}{2}\right) a_{\dot{n}'_1 \dot{\ell}_1, p-\dot{\ell}_1-k}^* a_{\dot{n}_1 \dot{\ell}_1 k} \quad (8.38)$$

and the  $a_{n\ell k}$  are the normalized coefficients of the polynomial part of the HO wavefunctions, defined in eq. (8.13) and the dummy  $k$ 's are constrained to the values for which all the arguments of the factorials in the  $a_{n\ell k}$  are non-negative. Alternatively, the latter, henceforth collectively called B-coefficients, can be expressed via the following formula [262],

$$B(n, \ell, n', \ell'; p) = (-1)^{p-\frac{\ell+\ell'}{2}} \frac{(2p+1)!}{2^{n+n'} p!} \sqrt{\frac{n!n'!(2n+2\ell+1)!(2n'+2\ell'+1)!}{(n+\ell)!(n'+\ell')!}} \quad (8.39)$$

$$\cdot \sum_{k=\alpha}^{\beta} \frac{(\ell+k)!(p-(\ell-\ell')/2-k)!}{k!(2\ell+2k+1)!(2p-\ell+\ell'-2k+1)!(n'-p+(\ell+\ell')/2+k)!(p-(\ell+\ell')/2-k)!}$$

where  $\alpha = \max[0, p - (\ell + \ell')/2 - n']$  and  $\beta = \min[n, p - (\ell + \ell')/2]$ , a rewriting that skips the definition of the intermediate coefficients  $a_{n\ell k}$ . In the case of Dirac-delta distribution of the electric charge, the Coulomb potential  $V_C$  in eq. (4.3) assumes its standard form for pointlike particles and eq. (8.35) becomes

$$\langle \dot{n}'_1 \dot{\ell}_1 || V_C(\dot{\mathbf{r}}_1) || \dot{n}_1 \dot{\ell}_1 \rangle = \frac{\sqrt{2}\xi^2}{\pi\epsilon_0} \sum_{p=\dot{\ell}_1}^{\dot{\ell}_1+\dot{n}_1+\dot{n}'_1} \frac{p!}{\Gamma(p + \frac{3}{2})} B(p; \dot{n}'_1, \dot{\ell}_1, \dot{n}_1, \dot{\ell}_1), \quad (8.40)$$

leading to a significant reduction in the implementation time of the matrix elements. Concerning the three-body potential, since  $V_T(\mathbf{r}_1, \mathbf{r}_2, \mathbf{r}_3)$  turns out to depend only on two Jacobi coordinates,

$$V_T(\mathbf{r}_1, \mathbf{r}_2, \mathbf{r}_3) = V_3 e^{-3\lambda(\dot{\mathbf{r}}_1^2 + \dot{\mathbf{r}}_2^2)} \quad (8.41)$$

the integration on the  $\mathbf{r}_1$  and  $\mathbf{r}_2$  in the relevant matrix element gives

$$\langle \dot{n}'_1 \dot{\ell}'_1 \dot{n}'_2 \dot{\ell}'_2 || V_T(\mathbf{r}_1, \mathbf{r}_2, \mathbf{r}_3) || \dot{n}_1 \dot{\ell}_1 \dot{n}_2 \dot{\ell}_2 \rangle = V_3 \sum_{p=\dot{\ell}_1}^{\dot{\ell}_1 + \dot{n}'_1 + \dot{n}_1} \sum_{q=\dot{\ell}_2}^{\dot{\ell}_2 + \dot{n}'_2 + \dot{n}_2} \xi^3 \left(1 + 3\lambda \xi^2\right)^{-p-q-3} \cdot B(\dot{n}'_1, \dot{\ell}'_1, \dot{n}_1, \dot{\ell}_1; p) B(\dot{n}'_2, \dot{\ell}'_2, \dot{n}_2, \dot{\ell}_2; q) . \quad (8.42)$$

Nevertheless, for the implementation of this part of the matrix elements is preferable to return to the Kramer-Moshinsky basis (i.e. the round kets in eq. (8.17)) and perform a  $\pi/4$  clockwise rotation about the  $\hat{\mathbf{r}}_1$  axis,

$$\ddot{\mathbf{r}}^i = \sum_{i=1}^3 A_{ij} \ddot{\mathbf{r}}^j \quad \mathbf{A} = \begin{pmatrix} 1 & 0 & 0 \\ -0 & \sqrt{1/2} & -\sqrt{1/2} \\ 0 & \sqrt{1/2} & \sqrt{1/2} \end{pmatrix} . \quad (8.43)$$

Next, we recast the matrix element in eq. (8.43) by expanding one of the exponentials in series of spherical Bessel functions and by exploiting eq. (38) in ref. [266], in a form analogous to eq. (3.28) in ref. [255],

$$\begin{aligned} & \langle n'_1 \ell'_1, n'_2 \ell'_2, n'_3 \ell'_3 | V_T | n_1 \ell_1, n_2 \ell_2, n_3 \ell_3 \rangle \\ &= \sum_{\substack{\dot{n}_2 \dot{\ell}_2 \dot{n}'_2 \dot{\ell}'_2 \\ \dot{n}_3 \dot{\ell}_3 \dot{n}'_3 \dot{\ell}'_3}} \langle \dot{n}_2 \dot{\ell}_2, \dot{n}_3 \dot{\ell}_3, \ell_1 | n_2 \ell_2, n_3 \ell_3, \ell_1 \rangle_{\pi/2} \langle \dot{n}'_2 \dot{\ell}'_2, \dot{n}'_3 \dot{\ell}'_3, \ell'_1 | n'_2 \ell'_2, n'_3 \ell'_3, \ell'_1 \rangle_{\pi/2} \delta_{\dot{\ell}'_2 \dot{\ell}_2} \langle \dot{n}_2 \dot{\ell}_2 || V_3 e^{-3\lambda \ddot{\mathbf{r}}_2^2} || \dot{n}_2 \dot{\ell}_2 \rangle \\ & \cdot \sum_{\ell=0}^{+\infty} (-1)^{\ell'_1 + \dot{\ell}_3 - \dot{\ell}_2} (2\ell + 1) \sqrt{(2\ell_1 + 1)(\dot{\ell}_3 + 1)(\ell \ell_1 \ell'_1 | 000)(\ell \dot{\ell}_3 \dot{\ell}'_3 | 000)} W(\ell'_1 \dot{\ell}'_3 \ell_1 \dot{\ell}_3, \dot{\ell}_2 \ell) \\ & \cdot \sum_{r=\frac{\dot{\ell}_1 + \dot{\ell}'_1}{2}}^{\dot{n}'_1 + \dot{n}_1 + \frac{\dot{\ell}_1 + \dot{\ell}'_1}{2}} \sum_{s=\frac{\dot{\ell}_3 + \dot{\ell}'_3}{2}}^{\dot{n}'_3 + \dot{n}_3 + \frac{\dot{\ell}_3 + \dot{\ell}'_3}{2}} \xi^{2\ell+6} (2\lambda^2)^{\frac{\ell}{2}} \left(2\lambda \xi^2 + 1\right)^{-r - \frac{\ell}{2} - \frac{3}{2}} \left(\lambda \xi^2 + 1\right)^{-s - \frac{\ell}{2} - \frac{3}{2}} \\ & \cdot \frac{\Gamma(r + \frac{\ell}{2} + \frac{3}{2}) \Gamma(s + \frac{\ell}{2} + \frac{3}{2})}{\Gamma(r + \frac{3}{2}) \Gamma(s + \frac{3}{2})} \frac{\Gamma(\frac{3}{2})}{\Gamma(\ell + \frac{3}{2})} B(n'_1 \ell'_1, n_1 \ell_1; r) B(\dot{n}'_3 \dot{\ell}'_3, \dot{n}_3 \dot{\ell}_3; s) \\ & \cdot {}_2F_1 \left[ r + \frac{\ell}{2} + \frac{3}{2}, s + \frac{\ell}{2} + \frac{3}{2}, \ell + \frac{3}{2}; \frac{2\lambda^2 \xi^4}{(2\lambda \xi^2 + 1)(\lambda \xi^2 + 1)} \right] , \end{aligned} \quad (8.44)$$

where

$${}_2F_1(a, b, c; z) = \sum_{m=0}^{\infty} \frac{z^m}{m!} \frac{\Gamma(a+m)}{\Gamma(a)} \frac{\Gamma(b+m)}{\Gamma(b)} \frac{\Gamma(c)}{\Gamma(c+m)} , \quad (8.45)$$

is the ordinary hypergeometric function, represented as a power series expansion. The choice of this apparently more involved rewriting of the three-body part of the matrix elements is well motivated by the smaller time required for its implementation on a computing machine. In fact, by comparing eq. (8.42) with eqs. (8.17), (8.20), (8.34) and (8.41), it follows that four summations have been suppressed. Leaving the sums over the first argument of the  $B$  coefficients apart, the evaluation of this part of the matrix elements truncating the basis at  $\mathfrak{N}$  quanta in the apparently simpler first method requires  $17\mathfrak{N}/2 + 12$  terms, whereas the one involving eq. (8.42) only  $15\mathfrak{N}/2 + 8$  terms.



## 8.5 Estimation of the parameters

After introducing the states of the truncated basis together with a method for the evaluation of the matrix elements, we focus on the procedure for the estimation of the strength of the  $3\alpha$  potential,  $V_3$ , and the variational parameter  $\omega$  with an increasing number of basis states. The task has been accomplished by following two slightly different routes, of which only the second (cf. sec. 8.5.1) permitted to expand the HO model space up to the desired number quanta,  $\mathfrak{N}$ . Starting from the data in the latter section, the parameter  $V_3$  has been estimated from the results of the extrapolation towards infinite HO quanta, by exploiting the energy gap of both the  $\alpha + {}^{12}\text{C}$  and the  $4\alpha$  decay channels of  ${}^{16}\text{O}$  at 7.1571 and 14.4265 MeV [267, 268] respectively. As hinted in sec. 8.1, the expectation values of the ground state eigenenergy, denoted as  $E_{0_1^+}^{(\alpha+{}^{12}\text{C})}$  and  $E_{0_1^+}^{(4\alpha)}$ , correspond to the opposite of the latter energy gaps and can be expressed as

$$E_{0_1^+}^{(\alpha+{}^{12}\text{C})} = m_{16\text{O}} c^2 - m_{4\text{He}} c^2 - m_{12\text{C}} c^2 \quad (8.46)$$

and

$$E_{0_1^+}^{(4\alpha)} = m_{16\text{O}} c^2 - 4m_{4\text{He}} c^2, \quad (8.47)$$

respectively. We choose to denote collectively the latter henceforth as  $E_{0_1^+}^{(t)}$  where  $t = 4\alpha$  and  $\alpha + {}^{12}\text{C}$  labels the reference threshold. The two outcoming estimations have been repeated in the pointlike approximation of the charge distribution of  $\alpha$  particles (cf. eq. (8.40)).

### 8.5.1 Optimized approach

Let us begin with the description of the first approach and consider the pair formed by the frequency of the HO and strength parameter of the  $3\alpha$  potential,  $(\omega, V_3)$ , as unknown. The first estimate of the latter parameters,  $(\omega^{(0)}, V_3^{(0)})$ , corresponds to a basis of HO states truncated to  $\mathfrak{N} = 0$  quanta, i.e. a single state,  $|00, 00, 00\rangle$ . The two parameters are obtained by constraining the average value of  $H_I$  with respect to the state  $|00, 00, 00\rangle$  to the energy in eqs. (8.46) or (8.47),

$$(00, 00, 00|H_I|00, 00, 00)_{\mathcal{S}} = E_{0_1^+}^{(t)}, \quad (8.48)$$

and by extracting the minimum of the average value with respect to  $\omega$ ,

$$\left. \frac{\partial}{\partial \omega} (00, 00, 00|H_I|00, 00, 00)_{\mathcal{S}} \right|_{V_3=V_3(\omega)} = 0, \quad (8.49)$$

where  $V_3(\omega)$  is the expression of the depth parameter in terms of  $\omega$  coming from the linear constraint given by eq. (8.48). In this case, the average value turns out to have only real minimum of the average value with respect to  $\omega$ , by using both the Erf-Coulomb interaction and the one for pointlike particles.

Since the  $\omega$  dependence of the Erf-Coulomb part of the two-body matrix elements is not analytical, an input value for  $\omega$  is needed in order to carry out the integration in eq. (8.35) numerically. To this aim, the first estimate of  $(\omega, V_3)$  is extracted from the Hamiltonian with the Coulomb interaction for pointlike  $\alpha$  particles, see eq. (8.40).

The outcoming value of  $\omega$  enables the numerical evaluation the integral in eq. (8.35), implied in the matrix element in eqs. (8.48) and (8.49). Performing again the derivative in  $\omega$  analytically, the system defined by eqs. (8.48) and (8.49) can be solved and an estimate for  $(\omega^{(0)}, V_3^{(0)})$  in

presence of  $\alpha$  particles with a spherical Gaussian distribution of charge is obtained. In a self-consistent way, the latter set of parameters can be improved by plugging the new value of  $\omega$  in the numerical intergral over  $V_C$  and by solving the system defined by the variables  $(\omega, V_3)$  once more. However, after the second iteration in the process, no sizable improvements are detected, therefore we can proceed with the next step of the variational calculation.

The constrained minimization procedure just introduced for the  $\mathfrak{N} = 0$  state can be generalized to higher-dimensional bases of states as follows. When the the basis of harmonic oscillator states is truncated at  $\mathfrak{N} > 0$  quanta, the effective eigenspace is spanned by the all the states with an even number of oscillator quanta ranging from 0 to  $\mathfrak{N}$  (cf. tab. 8.1). As a consequence, the  $|00, 00, 00\rangle$  ket in eq. (8.48) has to be replaced with the lowest energy eigenstate,

$$|\omega^{(\mathfrak{N}-2)}, \mathfrak{N}, 0^+\rangle_{\mathcal{S}} = \sum_{\substack{n_1 \ell_1, n_2 \ell_2, n_3 \ell_3 \\ 2n_1 + \ell_1 + 2n_2 + \ell_2 + 2n_3 + \ell_3 \leq \mathfrak{N}}} a(n_1 \ell_1, n_2 \ell_2, n_3 \ell_3) |n_1 \ell_1, n_2 \ell_2, n_3 \ell_3\rangle_{\mathcal{S}}, \quad (8.50)$$

of the Hamiltonian matrix  $\mathbf{H}_I(\omega^{(\mathfrak{N}-2)}, V_3^{(\mathfrak{N}-2)})$  whose entries are defined as the matrix elements between  $H_I$  and any pair of states with a number of quanta  $\leq \mathfrak{N}$  (cf. tab. 8.1),

$$(n'_1 \ell'_1, n'_2 \ell'_2, n'_3 \ell'_3 | H_I | n_1 \ell_1, n_2 \ell_2, n_3 \ell_3)_{\mathcal{S}} \bigg|_{\substack{\omega = \omega^{(\mathfrak{N}-2)} \\ V_0 = V_0^{(\mathfrak{N}-2)}}}. \quad (8.51)$$

In order to solve the eigenvalue problem, the entries of  $\mathbf{H}_I(\omega, V_3)$ , thought as functions of the frequency and the strength parameter, are evaluated with the outcomes of the antecedent estimation, where the basis is truncated to  $\mathfrak{N} - 2$  quanta. However, unlike the  $\mathfrak{N} = 0$  case, for  $\mathfrak{N} \geq 2$  it is unnecessary to resort to the results of the Hamiltonian with the Coulomb potential for pointlike  $\alpha$  particles in order to the evaluate the integral in eq. (8.35) numerically. When the HO basis is truncated to  $\mathfrak{N} > 0$  quanta, in fact, an initial ansatz for the value of the frequency is naturally provided by the previous estimation (including the zero quanta one).

NUMBER OF QUANTA	NUMBER OF STATES	$\omega$ [ $10^{20} \text{ s}^{-1}$ ]		$\lambda$ [ $\text{fm}^{-2}$ ]	$V_3$ [MeV]	
		$^{12}\text{C} + \alpha$	$4\alpha$		$^{12}\text{C} + \alpha$	$4\alpha$
0	1	9.493	11.628	0.00506	-10.076	-13.441
2	2	6.567	11.628		-9.524	-13.441
4	5	6.836	13.272		-9.961	-12.898
6	11	7.699	14.266		-9.720	-12.455
8	22	8.764	15.702		-9.304	-12.133

TABLE 8.3 – Optimized estimation of  $V_3$  for the  $\alpha$  – cluster Hamiltonian with the Coulomb potential for  $\alpha$  particles with Dirac-delta distribution of charge.

Nevertheless, the estimation of the strength parameter of the latter Hamiltonian remains of interest, since it allows to weigh the effects of the modification of the Coulomb potential into the Erf-Coulomb one in eq. (4.3), proposed by ref. [4] in the same context.

The scheme just outlined has been, therefore, applied for both the Coulomb and the Erf-Coulomb Hamiltonians and both the energy thresholds up to  $\mathfrak{N} = 8$  and 6 harmonic oscillator quanta respectively, as reported in tabs. 8.3 and 8.4. The results of these computations highlight a decreasing behaviour of the frequency of the harmonic oscillators, ranging from an initial

value of  $9.5 \cdot 10^{20} \text{s}^{-1}$  to  $7.2 \cdot 10^{20} \text{s}^{-1}$  for both the Hamiltonians, with a noticeable *jump* between the zero and the two quanta approximations. In parallel, the magnitude of the strength parameter  $V_3$  experiences a step-decrease, see the  $\mathfrak{N} = 2$  and  $\mathfrak{N} = 4$  rows in tabs. 8.3 and 8.4. Moreover, as it can be inferred from the latter, the variational estimates of  $V_3$  are expected to reach the  $\mathfrak{N} \rightarrow +\infty$  counterpart monotonically from above.

NUMBER OF QUANTA	NUMBER OF STATES	$\omega [10^{20} \text{s}^{-1}]$		$\lambda [\text{fm}^{-2}]$	$V_3 [\text{MeV}]$	
		$^{12}\text{C}+\alpha$	$4\alpha$		$^{12}\text{C}+\alpha$	$4\alpha$
0	1	9.477	11.625	0.00506	-9.947	-13.313
2	2	9.238	11.391		-9.953	-13.283
4	5	10.327	12.848		-9.586	-12.827
6	11	11.157	14.830		-9.188	-12.329

TABLE 8.4 – Optimized estimation of  $V_3$  for the  $\alpha$  – *cluster* Hamiltonian with the Coulomb potential for  $\alpha$  particles with a Gaussian distribution of charge (cf. eq. (4.3)).

As proof of correctness for the procedure adopted, it is worth stressing that the overlap of the variational lowest energy eigenstate obtained by matrix diagonalization with the zero quanta eigenstate remains the largest. The relevant coefficient of the expansion,  $a(00,00,00)$  (cf. eq. (8.50)), in fact, turns out to range from 1 to circa 0.74 (0.72) throughout the  $H_I$  calculations with the  $^{12}\text{C}+\alpha$  ( $4\alpha$ ) energy threshold.

### 8.5.2 Non-optimized approach

The main drawback of the optimized version of the variational calculation of the strength parameter of the three-body potential presented in the previous paragraph resides certainly in the computational difficulty of evaluating symbolic matrix elements and performing derivatives of rather cumbersome functions of the frequency of the harmonic oscillator,  $\omega$ .

Accordingly, with the aim of both expanding the basis of the trial states and then performing a reliable estimation of the basis truncation error, we choose to adopt a numerical non-optimized approach, in which the value of  $\omega$  is kept fixed throughout the calculation to its initial value, obtained analytically in the zero quanta approximation (cf. eqs. (8.48) and (8.49)). Since the Hamiltonian is independent on the frequency of the harmonic oscillator (cf. eq. (8.1)) unlike the basis states, the results of this calculation are expected to match the ones of the optimized estimation in the completeness of the basis limit [251].

The resulting method, thus, consists merely on the evaluation of the matrix elements with respect to the  $\mathfrak{N}$ -quanta basis of states and in the subsequent diagonalization of the matrix, in which the input values of  $\omega$  and the  $V_3$  are inherited from the preceeding iteration (i.e. with  $\mathfrak{N} - 2$  quanta), with the exception of the case  $\mathfrak{N} - 2 = 0$ , in which the parameters are borrowed from the optimized approach (cf. tabs. 8.3 and 8.4). After each diagonalization, the extraction of the new value of the strength parameter is performed from the constraint in eq. (8.48), although in a non-symbolic fashion,

$$V_3^{(\mathfrak{N})} = V_3^{(\mathfrak{N}-2)} \frac{E_{0_1^+}^{(t)} - (\omega^{(0)}, \mathfrak{N}, 0^+ | H_I^{\text{I}} | \omega^{(0)}, \mathfrak{N}, 0_1^+)_{\mathcal{J}} - (\omega^{(0)}, \mathfrak{N}, 0^+ | H_I^{\text{II}} | \omega^{(0)}, \mathfrak{N}, 0_1^+)_{\mathcal{J}}}{(\omega^{(0)}, \mathfrak{N}, 0^+ | H_I^{\text{III}} | \omega^{(0)}, \mathfrak{N}, 0_1^+)_{\mathcal{J}}}, \quad (8.52)$$

where the superscripts I, II and III on  $H_I$  denote respectively the one-, the two- and the three-body contributions to the Hamiltonian matrix.

The absence of the optimization step (cf. eq. (8.49)) at each iteration allowed for a general rewriting of the code, in which all the symbolic functions are replaced by numeric ones and by sparse arrays, an operation that has been realized in *Matlab* language by means of the *Matlab Tensor Toolbox 2.6* library [269]. Moreover, important speedup of the code has been achieved by rewriting the routines for the implementation of the SMB and RMB in such a way to exploit the symmetry properties of the Moshinsky brackets discussed in refs. [252,254].

NUMBER OF QUANTA	NUMBER OF STATES	$\omega [10^{20} \text{ s}^{-1}]$		$\lambda [\text{fm}^{-2}]$	$V_3 [\text{MeV}]$	
		$^{12}\text{C}+\alpha$	$4\alpha$		$^{12}\text{C}+\alpha$	$4\alpha$
0	1				-10.076	-13.441
2	2				-10.076	-13.441
4	5				-9.707	-12.986
6	11	9.493	11.628	0.00506	-9.375	-12.604
8	22				-9.154	-12.361
10	40				-8.978	-12.168
12	72				-8.813	-11.994
$\infty$	$\infty$				-7.219(27)	-10.499(25)

TABLE 8.5 – Non-optimized estimation of  $V_3$  for the  $\alpha$ -cluster Hamiltonian in sec. 4.2.1 with the Coulomb potential for  $\alpha$  particles with Dirac-delta distribution of charge.

The results of this calculation, reported in tabs. 8.5 and 8.6, highlight a monotonic descreasing behaviour in the value of  $V_3$  with increasing dimension of the basis of harmonic oscillator states. As it can be seen from comparison, in both the approaches the transition from zero to two HO quanta brings no overall improvement in the extracted value of the strength parameter. Differently from the test-cases treated in refs. [251] and [253] with two-body potentials only, this effect is due to the almost exact cancellation between the  $2\alpha$  and the  $3\alpha$  contributions in the off-diagonal elements of the Hamiltonian matrix, causing the resulting  $H_I$  to be already nearly diagonal. Conversely, in the subsequent step in the iteration process a large drop-off in the value of  $V_3$  takes place, due to the large overlap between the exact ground state and the three  $\mathfrak{N} = 4$  states, see tabs. 8.5 and 8.6.

NUMBER OF QUANTA	NUMBER OF STATES	$\omega [10^{20} \text{ s}^{-1}]$		$\lambda [\text{fm}^{-2}]$	$V_3 [\text{MeV}]$	
		$^{12}\text{C}+\alpha$	$4\alpha$		$^{12}\text{C}+\alpha$	$4\alpha$
0	1				-9.947	-13.313
2	2				-9.946	-13.285
4	5				-9.611	-12.871
6	11	9.477	11.625	0.00506	-9.290	-12.497
8	22				-9.075	-12.262
10	40				-8.908	-12.078
12	72				-8.741	-11.903
$\infty$	$\infty$				-7.048(35)	-10.334(33)

TABLE 8.6 – Non-optimized estimation of  $V_3$  for the  $\alpha$ -cluster Hamiltonian in sec. 4.2.1 with the Coulomb potential for  $\alpha$  particles with a Gaussian distribution of charge (cf. eq. (4.3)).

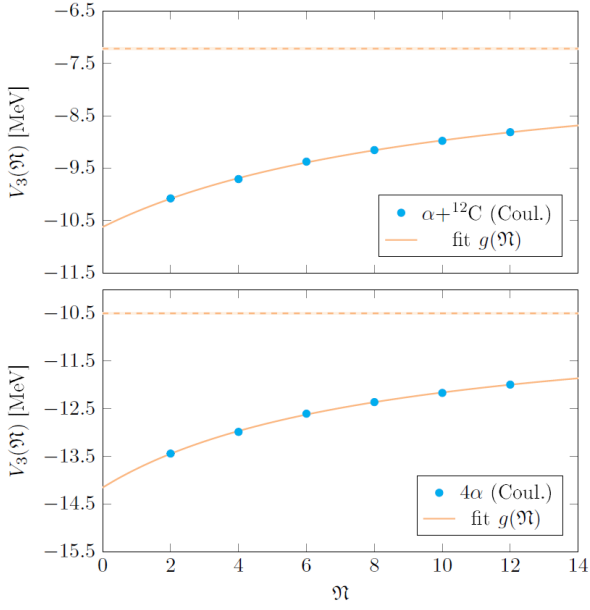


FIGURE 8.1 – Infinite- $\eta$  extrapolation of the strength parameter  $V_3$  adjusted to the  $4\alpha$  ( $\alpha+^{12}\text{C}$ ) decay threshold of  $^{16}\text{O}$ , in the pointlike approximation for the charge distribution of  $\alpha$  particles. The dashed line represent the asymptotic value of the parameter (cf.  $c$  in eq. (8.53)), reported in the last row of tab. 8.6 together with the associated statistical uncertainty. For  $(t) = 4\alpha$  ( $\alpha+^{12}\text{C}$ ), the parameter  $a$  is equal to  $-30.43(36)$  ( $-36.05(45)$ ) and  $\beta = 8.3258(10)$  ( $10.5964(13)$ ), while the coefficient of determination coincides with 0.9995 (0.9994), thus witnessing a good adhesion of the input data with the homographic function in both the cases.

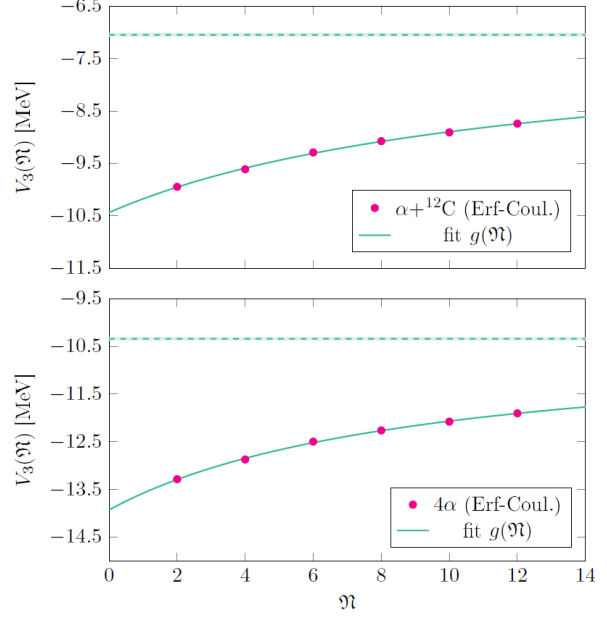


FIGURE 8.2 – Infinite- $\eta$  extrapolation of the strength parameter  $V_3$  adjusted to the  $4\alpha$  ( $\alpha+^{12}\text{C}$ ) decay threshold of  $^{16}\text{O}$ , in the spherical Gaussian approximation for the charge distribution of  $\alpha$  particles. The dashed line represent the asymptotic value of the parameter (cf.  $c$  in eq. (8.53)), reported in the last row of tab. 8.6 together with the associated statistical uncertainty. For  $(t) = 4\alpha$  ( $\alpha+^{12}\text{C}$ ), the parameter  $a$  is equal to  $-33.30(36)$  ( $-40.72(63)$ ) and  $\beta = 9.2823(11)$  ( $12.0181(13)$ ). The coefficient of determination coincides with 0.9991 (0.9990) and substantiates again the choice of the function  $g(\eta)$  for the fit.

Noteworthy is also the fact that the overall differences between the  $V_3$  estimates of the two methods are moderate, ranging from  $\approx 0.05$  to  $0.25$  MeV. However, it is possible to detect a slightly slower convergence rate of  $V_3$  towards its asymptotic value in the non-optimized approach, as expected.

We now conclude our variational calculation with the extrapolation of the infinite  $\eta$  limit of the strength parameter  $V_3$  from the results obtained at  $\eta \leq 12$  in tabs. 8.5 and 8.6. Discarding the  $\eta = 0$  data, we adopt as a fitting model the homographic function,

$$g(\eta) = c + \frac{a}{\beta + \eta} \quad a, \beta, c \in \mathbb{R}, \quad (8.53)$$

where  $c$  coincides with the asymptotic value of  $V_3$  and  $\beta$  is chosen to maximize the coefficient of determination  $R^2$  of the fit, as done for the parameter  $\xi$  in the Euclidean time extrapolations in sec. 4.8.1. The results of the extrapolations, reported in the last row of tabs. 8.5 and 8.6 put in evidence rather small statistical errors in  $c$ , thus permitting a precise assessment of the HO basis truncation errors at finite values of  $\eta$ . Such expansion errors, discussed in detail in refs. [270] and [271] in the context of variational calculations applied to elliptic differential equations as the Schrödinger time-independent one, can be inferred directly from tabs. 8.5 and 8.6. Irrespective on whether the charge distribution of the  $\alpha$  particles is a Dirac delta or a Gaussian, at  $\eta = 0$  these errors can be quantified in a  $\approx 3$  MeV shift of  $V_3$  with respect to

its expectation value. At  $\mathfrak{N} = 8$  the discrepancy reduces to  $\approx 2$  MeV, whereas at 14 harmonic oscillator quanta the systematic deviation approaches 1.6 MeV, meaning that 120 HO basis states are required in order to reach that precision. The latter is expected to fall below 1 MeV at  $\mathfrak{N} = 30$  oscillator quanta, as it can be estimated from the fitting functions (cf. eq. (8.53)) of the four treated cases in figs. 8.1 and 8.2.

Although our outcomes in the last row of tabs. 8.5 and 8.6 have not been benchmarked with the infinite-volume extrapolation of the energy eigenvalue of the ground state in the limit of small lattice spacing (i.e.  $a \lesssim 0.5$  fm) yet, a direct comparison with the result at  $V_3 = -4.41$  MeV reported in sec. 7.2 (cf. fig. 7.1) seems to corroborate the result of our fit for the Hamiltonian with the Coulomb potential for  $\alpha$ -particles with Gaussian charge distribution and  $(t) = 4\alpha$ . Indeed, it is to be expected that a slightly more attractive  $3\alpha$  potential is needed in order to lift  $\mathcal{E}_{g.s.}(\infty)$  from  $-3.55(16)$  MeV to the expected value of  $-14.42$  MeV, thus reproducing faithfully the experimental binding energy,  $BE(8,8)$ , of  $^{16}\text{O}$  (cf. fig. 7.2). Furthermore, it remains to be proven whether such  $3\alpha$  force yields, at the same time, a satisfactory reproduction of the  $0_2^+$  and  $2_1^+$  lines at 6.05 and 6.92 MeV [227], like the model in ref. [6]. In the latter reference, a four body isotropic Gaussian interaction is introduced on top of a  $3\alpha$  Gaussian and an Ali-Bodmer potential, whose parameters are fitted to the decay width of the  $^8\text{Be}$  ground state and to the energy gap of the Hoyle state of  $^{12}\text{C}$  [187].

Concerning the  $\alpha + ^{12}\text{C}$  threshold, the estimated value of  $V_3$  in tab. 8.6 may find an application in an analysis of finite-volume and discretization effects a different subset of bound eigenstates of  $^{16}\text{O}$ , or in a comparison with the predictions of a model in which the  $\alpha + ^{12}\text{C}$  configuration plays a role, as the one in ref. [169]. Finally, the  $V_3$  results in the pointlike approximation of the  $\alpha$  particles in tab. 8.5, may be employed for the benchmarking of  $\alpha$ -cluster models where the finite-size of  $^4\text{He}$  nuclei as clusters is neglected.





In this dissertation we have reported our original analytical and numerical results concerning the effects induced by the lattice environment on two-fermion systems and the three lightest  $\alpha$  conjugate nuclei. Almost all the presented data have been obtained using state-of-the-art supercomputers with an estimated computational cost of  $\approx 3.5$  millions hours of CPU time, predominantly devoted to the numerical diagonalization of the lattice Hamiltonian in the second part of the dissertation. However, a fraction of the allocated computational hours has been devoted to the evaluation of the sums of the 3D Riemann series implied in the expansions of the Lüscher functions in chap. 3. The code used for that purpose is designed for GPU architectures, and allowed for the evaluation of billions of terms of the sums simultaneously. The treatment begins with the analytical investigation of finite volume effects in the lowest energy eigenvalues. The theoretical framework of our research is provided by pionless Effective Field Theory and non-relativistic QED for spinless particles, recapitulated in chap. 1, where the strong potentials coupling the fermions to arbitrary  $\ell$  units of angular momentum have been presented. This fundamental tool allowed for the plain and comprehensive description of elastic scattering processes in the low-energy regime shown in ref. [2] for spinless protons and antiprotons coupled to zero units of angular momentum, both in presence and in absence of QED. Among the forces of electromagnetic nature, the electrostatic interaction represents the dominant contribution to T-matrix elements in the low-energy sector and the Coulomb ladders have to be resummed to all orders in the fine-structure constant.

Differently from the transverse photons, the Coulomb ones do not propagate between the fermionic bubbles in the diagrams, a crucial feature that permitted to rewrite the full two-body Green function operator in terms of the Coulomb one and operator representing the S-wave strong interaction. Exactly the same property allowed for the derivation of a closed expression for the T-matrix element of the scattering processes and the full Green's function, thus paving the way to the derivation of the quantization conditions.

After summarizing the main results of the latter work (cf. secs. 2.1.1-2.1.3), now applied to fermions and antifermions, we have extended the investigation to strong interactions carrying one unit of angular momentum (cf. secs. 3.1.1-3.1.3). In the processs, the novel P-wave expressions for the T matrix element, the scattering length and the effective range, with and without the QED contributions have been derived. Moreover, the analysis of the attractive Coulomb case offered an occasion for confirming the observations on the scattering parameters pointed out in sec. 3.4 of ref. [2] and recalled in sec. 2.1.3.

Second, the infinite-volume analysis of fermion-fermion scattering in secs. 3.1.1-3.1.3 allowed us to attain our main goal, the derivation of finite-volume energy corrections for two-body P-wave bound and scattering states, by providing an extension of the analysis on S-wave states

in ref. [1], reviewed in secs. 2.2.1-2.2.3. Motivated by the growing interest for lattice EFTs and, above all, LQCD, in fact, we have transposed our system of charged particles in a cubic box with periodic boundary conditions.

With regards to the prescriptions from the literature [99, 128], we have removed the zero momentum modes from the relevant three-dimensional sums and considered the QED corrections to the mass of the spinless particles [46, 54], in sight of the application of our results to realistic baryon-baryon systems on the lattice [64]. Furthermore, the characteristic size of our cubic box has been chosen to fulfill the constraint  $ML \ll 1/\alpha$ , which is required for the viability of the perturbative approach of QED in the cubic finite volume. Under this hypothesis, the non-relativistic relation between the finite-volume energy of two composite fermions in the  $T_1$  representation of the cubic group and its P-wave scattering parameters receives QED corrections obtainable in closed form.

Although more cumbersome than the S-wave counterpart, the expression we have presented in sec. 3.2.3 a) for the energy shift of the lowest unbound state resembles the features of the one in sec. 2.2.3 a) (cf. sec. III D 1 of ref. [1]), except for the appearance of higher-order scattering parameters. Besides, the finite-volume corrections for the P-wave bound state prove to have the opposite sign and the same magnitude of the ones for the S-wave state in sec. 2.2.3 b) (cf. sec. III D 3 of ref. [1]), up to contributions of order  $1/L^3$ . This fact confirms the long-standing observations on the  $A_1$  and  $T_1$  finite-volume energy eigenvalues in the analysis of refs. [71, 77], drawn in the context of a two-body system governed by finite-range interactions in the non-relativistic regime. In the latter work, the interplay of parity and angular momentum quantum numbers in the wavefunctions was found to be responsible of the relation between the leading-order S- and P-wave energy shifts. Only the generalization of our analysis will tell if the existing relationships between the finite-volume shifts in tab. I of ref. [71] for two-body states with higher angular momentum remain, at least approximately valid in presence of QED.

In the second part of this thesis work we have dealt numerically with the most striking consequence of finite-volume (and discretization) effects, the breaking of rotational symmetry. The laboratory for such a study has been now provided by the three lightest  $\alpha$ -conjugate nuclei, and the main theoretical tools have been inherited from refs. [3, 68].

The reduction of rotational symmetry to cubic group symmetry affects the average values of all the operators transforming as spherical tensors under the elements of  $SO(3)$  [68]. Nevertheless, the construction of the lattice counterpart of the squared total angular momentum operator allows for an unambiguous identification of the lattice Hamiltonian eigenstates in terms of  $SO(3)$  irreps, provided the spatial distribution of the eigenfunctions is localized and smooth enough to fit the size and the spacing of the lattice. This is exactly the case of the  $2_E^+$  and  $2_{T_2}^+$  multiplets of  $^8\text{Be}$ , where the average value of the squared angular momentum operator reaches its expectation value with deviations of 0.01% already at  $a \approx 1.8$  fm, see fig. 5.11, a spacing for which the energy eigenvalues of the two multiplets are still separated by more than 2 MeV, fig. 5.5.

Furthermore, the asymptotic finite volume corrections to the average values of the squared angular momentum operator approximately fit a negative exponential of the lattice size (cf. figs. 5.4 and 5.16), like the leading-order ones for the energy [71]. This inference has not been tested in the  $^{16}\text{O}$ , where the large-volume region of the curves in figs. 7.4, 7.9, 7.10, 7.18 and 7.19 is affected by increasing discretization errors. Discretization corrections for the

average values of the same operator turned out also to depend exponentially on  $a$  in the zero lattice-spacing limit, although with a positive decay constant (cf. figs. 5.16 and 6.15).

Besides exploring the role of  $\mathcal{L}^2$  in the classification of the lattice Hamiltonian eigenstates in terms of the angular momentum quantum number, the model offered us also the possibility to test the interpretation of the local minima of energy eigenvalues in terms of the spatial distribution of the relevant eigenfunctions (cf. the  $4_2^+$  and the  $6_1^+$  multiplets of  $^8\text{Be}$  and the  $0_1^+$ ,  $2_1^+$  and  $3_1^-$  multiplets of  $^{12}\text{C}$ ) as well as the results presented in ref. [3] (cf. the  $0_1^+$  and  $2_1^+$  states of  $^8\text{Be}$ ). In case a local maximum of the squared modulus of a lattice eigenfunction is included within the mesh points, in fact, the corresponding energy eigenvalue as a function of the lattice spacing displays a minimum. An approximate correspondence between the minima of the energy eigenvalues and the ones of the  $\alpha$ - $\alpha$  separation has been observed also in the  $0_1^+$ ,  $2_1^\pm$ ,  $3_1^\pm$  and  $4_1^-$  states of  $^{16}\text{O}$ , even if the lattice wavefunctions have not been inspected.

Moreover, we have shown that the use of multiplet-averaging (cf. sec. 5.3) for the energies and the average values of the squared angular momentum for states with  $\ell = 0, 2, 3, 4$  and 6 (cf. chaps. 5-7) reduces both discretization and finite-volume effects by evening the fluctuations about the continuum and infinite-volume counterparts, as predicted in ref. [3].

Likewise interesting are the computational implications of this work. In the attempt of suppressing both discretization and finite-volume effects for the three-body system, considerable efforts have been devoted in developing memory-saving and fast codes for the diagonalization of the lattice Hamiltonian. The final choice of the *Lanczos algorithm* and of the GPU as a support for the state vectors processing permitted us to monitor the evolution of the eigen-energies and the average values of other physical observables concerning the six cubic-group multiplets of  $^{12}\text{C}$  for a significant range of box-sizes and spacings. The same algorithm has been exploited in the  $^{16}\text{O}$  case, although the  $N \geq 11$  and  $a > 2.0$  regimes of the physical observables have been explored by introducing discretization and finite-volume effects of increasing extent, due to the present-day limitations in the capacity of the single GPU units. However, by renouncing the storage of the lattice eigenfunction, an exact reconstruction of the large-volume behaviour of the  $0_1^+$  state of  $^{16}\text{O}$  at  $a \approx 0.50$  fm has been made possible (cf. fig. 7.1). At present only stochastic approaches as the *Worldline Monte Carlo* method in sec. 4.8.1 seem to capable to access the energy eigenvalues and, perhaps, the average values of other physical observables in the  $N \geq 11$  region for  $^{16}\text{O}$ . Hopefully, the Monte Carlo algorithm in sec. 4.8.1 a) may contribute in shedding light on the energy eigenvalues of the excited states of the latter nucleus in the near future.

In addition, the extensive usage of projectors in the iterative diagonalization process allowed us to extend the analysis of ref. [3] to higher angular momentum multiplets, both for the  $^8\text{Be}$  and the  $^{12}\text{C}$ , discarding all the possible intermediate states devoid of the desired transformation properties under the elements of the permutation group and the cubic group.

Finally, the treatment reached its conclusion with the variational calculation for the fitting of the strength parameter of the three-body interaction to the  $\alpha + ^{12}\text{C}$  and  $4\alpha$  decay thresholds of  $^{16}\text{O}$ . In chap. 7, in fact, we have shown that the parameters of the  $3\alpha$  Gaussian potential in the model in ref. [3] underbind the  $^{16}\text{O}$  nucleus by  $\approx 11$  MeV. Although the extrapolated values for  $V_3$  in tabs. 8.5 and 8.6 have not been exploited for the analysis in chap. 7, their capability in reproducing the features of the low-energy spectrum of  $^{16}\text{O}$  may be soon assessed and compared with other  $\alpha$ -cluster models such as the ones in refs. [6] and [7,8].



# Appendices



This appendix serves as a supplemental material mainly for the first part of chap. 3, in which the system is embedded in the continuum and infinite volume configuration space. While app. A.1 is referenced in the whole part I of the present dissertation, app. A.2 and A.3 are devoted to the calculation of integrals apperaring in secs. 3.1.1 and 3.1.2 respectively. Finally, sec. A.4 represents a deepening on a functional identity implied in the development of the calculations in app. A.3.

## A.1 Feynman rules

For the computation of the amplitude associated to each Feynman diagram in the framework of the non-relativistic effective field theory for spinless fermions with NRQED outlined in secs. 1.2-1.2.1, the rules in fig. A.3 are understood. The imaginary part in the denominator of the retarded fermion propagators  $\epsilon$  and the photon mass  $\lambda$  are arbitrarily small quantities.

## A.2 Integrals in Dimensional Regularization

We begin this appendix with the derivation of the second term on the r.h.s. of eq. (3.20) for  $T_{\text{SC}}^{\text{tree}}(\mathbf{p}, \mathbf{p}')$ , that is the new contribution to eq. (2.6). In  $d$  dimensions, the last integral in eq. (3.20) becomes

$$\mathfrak{I} \equiv D(E^*)M \int_{\mathbb{R}^3} \frac{d^d l}{(2\pi)^d} \frac{e^2}{\mathbf{l}^2 + \lambda^2} \frac{\mathbf{p}' \cdot \mathbf{l}}{\mathbf{l}^2 - 2\mathbf{p} \cdot \mathbf{l} + i\epsilon} . \quad (\text{A.54})$$

Since the loop integral is not going to be performed in the complex plane, the parameter  $\epsilon$  can be set to zero. Applying the Feynman parametrization for the denominators, we obtain

$$\mathfrak{I} = D(E^*)Me^2 \frac{\Gamma(2)}{\Gamma(1)\Gamma(1)} \int_0^1 d\omega \int_{\mathbb{R}^d} \frac{d^d l}{(2\pi)^d} \frac{\mathbf{p}' \cdot \mathbf{l}}{[\omega(\mathbf{l}^2 + \lambda^2) + (\mathbf{l}^2 - 2\mathbf{p} \cdot \mathbf{l})(1 - \omega)]^2} . \quad (\text{A.55})$$

We rewrite the polynomial in the denominator as  $\mathbf{l}^2 - 2\mathbf{p} \cdot \mathbf{l}(1 - \omega) + \omega\lambda^2$  and consider the application of the dimensional regularization formula in eq. (B.17) in ref. [132] for the carrying-out of the momentum integral,

$$\mathfrak{I} = Me^2 \frac{\Gamma(2 - \frac{d}{2})}{(4\pi)^{d/2}\Gamma(2)} \int_0^1 d\omega \frac{(1 - \omega) \mathbf{p} \cdot \mathbf{p}' D(E^*)}{[\omega\lambda^2 - \mathbf{p}^2(1 - \omega)^2]^{2-d/2}} . \quad (\text{A.56})$$



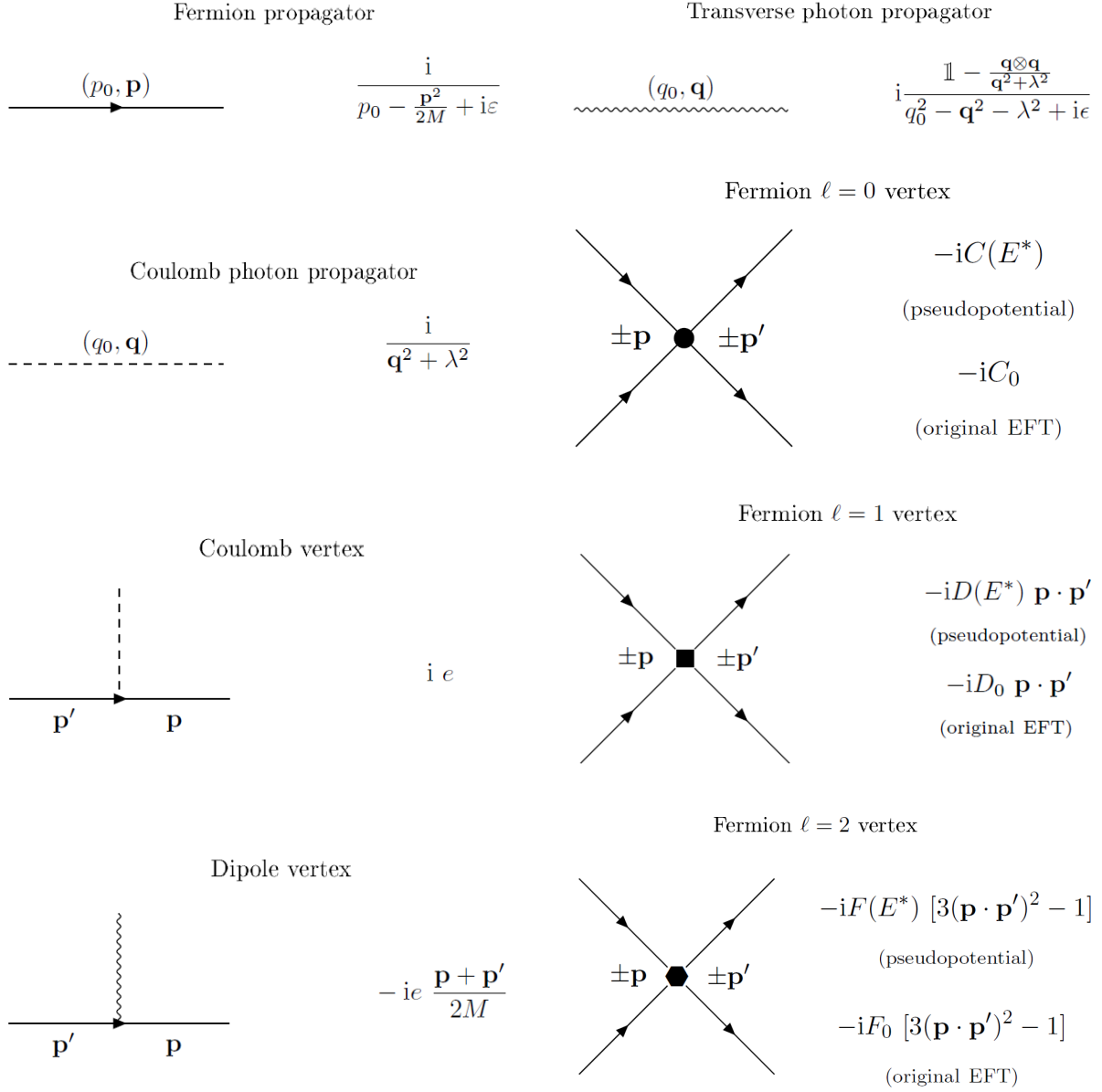


FIGURE A.3 – Feynman rules for spinless fermions and scalar and vector photons in our non-relativistic EFT with non-relativistic QED.

As the r.h.s. of the last equation is non-singular in three dimensions, the limit  $d \rightarrow 3$  can be safely taken. Furthermore, we define the auxiliary quantities

$$\beta = 1 + \frac{\lambda^2}{2\mathbf{p}^2} \quad \text{and} \quad \gamma = \frac{\lambda}{\sqrt{2}|\mathbf{p}|} \sqrt{2 + \frac{\lambda^2}{2\mathbf{p}^2}}. \quad (\text{A.57})$$

Performing the change of variables  $\omega \mapsto \omega' \equiv (\omega - \beta)/\gamma$  in the integrand of eq. (A.56), we obtain

$$\mathfrak{K} \equiv \int_0^1 d\omega \frac{(1 - \omega)}{[\omega\lambda^2 - \mathbf{p}^2(1 - \omega)^2]^{1/2}} = \int_{-\frac{\beta}{\gamma}}^{\frac{1-\beta}{\gamma}} d\omega' \frac{1 - \gamma\omega' - \beta}{|\mathbf{p}| \sqrt{1 - (\omega')^2}}. \quad (\text{A.58})$$

The last expression can be rapidly integrated,

$$-\int_{-\frac{\beta}{\gamma}}^{\frac{1-\beta}{\gamma}} \frac{d\omega' \omega' \gamma}{|\mathbf{p}| \sqrt{1-(\omega')^2}} + \int_{-\frac{\beta}{\gamma}}^{\frac{1-\beta}{\gamma}} \frac{(1-\beta)d\omega'}{|\mathbf{p}| \sqrt{1-(\omega')^2}} = \frac{\gamma}{|\mathbf{p}|} \sqrt{1-(\omega')^2} \Big|_{-\frac{\beta}{\gamma}}^{\frac{1-\beta}{\gamma}} + \frac{1-\beta}{|\mathbf{p}|} \arcsin(\omega') \Big|_{-\frac{\beta}{\gamma}}^{\frac{1-\beta}{\gamma}}. \quad (\text{A.59})$$

After evaluating the results of the integration over  $\omega'$  in terms of the original variables,  $\mathbf{p}$  and  $\lambda$ , a closed form for  $\mathfrak{K}$  is found,

$$\mathfrak{K} = \frac{i}{|\mathbf{p}|} + \frac{\lambda}{\mathbf{p}^2} - \frac{\pi\lambda^2}{4|\mathbf{p}|^3} + \frac{i\lambda^2}{2|\mathbf{p}|^3} \log \frac{2|\mathbf{p}|}{\lambda} + \frac{i\lambda^2}{2|\mathbf{p}|^3} \log \left( 1 + \frac{\lambda i}{2|\mathbf{p}|} \right). \quad (\text{A.60})$$

where the conventions  $\log(-i) = -i\pi/2$  and  $\sqrt{-1} = -i$  are understood. Plugging eq. (A.60) into eq. (A.56), the desired result is obtained,

$$\mathfrak{J} = \mathbf{p} \cdot \mathbf{p}' D(E^*) \frac{e^2 M}{4\pi} \frac{1}{2} \left\{ \frac{i}{|\mathbf{p}|} + \frac{\lambda}{\mathbf{p}^2} + i \frac{\lambda^2}{2|\mathbf{p}|^3} \left[ -i \frac{\pi}{2} + \log \frac{2|\mathbf{p}|}{\lambda} + \log \left( 1 + \frac{\lambda i}{2|\mathbf{p}|} \right) \right] \right\}. \quad (\text{A.61})$$

In the second part of this appendix, we evaluate the momentum integrals appearing in the 1-loop diagram with one Coulomb photon exchange inside the loop, i.e. the right part of fig. 3.2 and eq. (3.23). To this aim, we first introduce the notation  $\gamma^2 \equiv -\mathbf{p}^2$  for the physical momenta, we set  $\varepsilon$  to zero and rewrite eq. (3.23) in arbitrary dimensions  $d$  as

$$\mathfrak{L} \equiv T_{\text{SC}}^{1\text{-loop}}(\mathbf{p}, \mathbf{p}'; d) = -[D(E^*)]^2 M^2 \cdot \int_{\mathbb{R}^d} \frac{d^d \mathbf{k}}{(2\pi)^d} \int_{\mathbb{R}^d} \frac{d^d \mathbf{q}}{(2\pi)^d} \frac{i\mathbf{p}' \cdot \mathbf{k}}{(\mathbf{q} + \mathbf{k})^2 + \gamma^2} \frac{e^2 i(\mathbf{q} + \mathbf{k}) \cdot \mathbf{p}}{\mathbf{k}^2 + \gamma^2}. \quad (\text{A.62})$$

where the fictitious photon mass has been set to zero, since no infrared divergences occur in the integration (cf. Appendix A of ref. [2]). Second, we decide to carry out the integration over  $\mathbf{k}$  first and merge the relevant denominators again by means of Feynman's trick, obtaining

$$\mathfrak{L} = p_i p'_j M^2 [D(E^*)]^2 \frac{\Gamma(2)}{\Gamma(1)\Gamma(1)} \int_0^1 d\omega \int_{\mathbb{R}^d} \frac{d^d \mathbf{q}}{(2\pi)^d} \frac{e^2}{\mathbf{q}^2} \int_{\mathbb{R}^d} \frac{d^d \mathbf{k}}{(2\pi)^d} \frac{q_i k_j + k_i k_j}{[\mathbf{k}^2 + 2(1-\omega)\mathbf{q} \cdot \mathbf{k} + \Delta^2]^2}, \quad (\text{A.63})$$

where  $\Delta^2 \equiv \gamma^2 + \mathbf{q}^2(1-\omega)$  and Einstein's convention for repeated indices is understood. Now, we can proceed by evaluating the two integrals over  $\mathbf{k}$  generated by  $q_i k_j$  and  $k_i k_j$  separately. The former integral turns out to be an application of eq. (B.18) in ref. [132] and gives

$$\int_{\mathbb{R}^d} \frac{d^d \mathbf{k}}{(2\pi)^d} \frac{q_i k_j}{[\mathbf{k}^2 + 2(1-\omega)\mathbf{q} \cdot \mathbf{k} + \Delta^2]^2} = -\frac{q_i q_j (1-\omega)}{[\Delta^2 - (1-\omega)^2 \mathbf{q}^2]^{2-d/2}} \frac{\Gamma(2 - \frac{d}{2})}{(4\pi)^{d/2} \Gamma(2)}. \quad (\text{A.64})$$

The second term of eq. (A.63), instead, yields two contributions, one of the two being proportional to the r.h.s. of eq. (A.64). The application of eq. (B.18) in ref. [132] indeed leads to

$$\begin{aligned} \int_{\mathbb{R}^d} \frac{d^d \mathbf{k}}{(2\pi)^d} \frac{k_i k_j}{[\mathbf{k}^2 + 2(1-\omega)\mathbf{q} \cdot \mathbf{k} + \Delta^2]^2} &= \frac{1}{(4\pi)^{d/2}} \frac{1}{\Gamma(2)} \\ &\cdot \left[ \frac{q_i q_j (1-\omega)^2 \Gamma(2 - \frac{d}{2})}{[\Delta^2 - (1-\omega)^2 \mathbf{q}^2]^{2-d/2}} + \frac{1}{2} \frac{\delta_{ij} \Gamma(1 - \frac{d}{2})}{[\Delta^2 - (1-\omega)^2 \mathbf{q}^2]^{1-d/2}} \right]. \end{aligned} \quad (\text{A.65})$$

By comparison of the last equation with eq. (A.63), we observe that the  $\mathbf{q}$  integrals involving  $q_i q_j$  can be performed together. Therefore, we merge the two terms and, after few manipulations,

we define

$$\mathcal{L}_1 \equiv -p_i p'_j [D(E^*)]^2 M^2 \frac{\Gamma(2 - \frac{d}{2})}{(4\pi)^{d/2}} \int_0^1 d\omega \int_{\mathbb{R}^d} \frac{d^d q}{(2\pi)^d} \frac{q_i q_j (1 - \omega) \omega}{[\gamma^2 + \mathbf{q}^2 (1 - \omega) \omega]^{2-d/2}} \frac{e^2}{\mathbf{q}^2} . \quad (\text{A.66})$$

With the help of the auxiliary parameter  $\Xi_4^2 \equiv \gamma^2 / [\omega(1 - \omega)]$  we apply again the Feynman parametrization for the two denominators and rewrite the last equation as

$$\mathcal{L}_1 = -p_i p'_j e^2 D_0^2 M^2 \frac{\Gamma(3 - \frac{d}{2})}{(4\pi)^{d/2}} \int_0^1 d\omega [(1 - \omega) \omega]^{d/2-1} \int_0^1 d\phi \phi^{1-d/2} \int_{\mathbb{R}^d} \frac{d^d q}{(2\pi)^d} \frac{q_i q_j}{[\mathbf{q}^2 + \phi \Xi_4^2]^{3-d/2}} . \quad (\text{A.67})$$

In this form, the application of eq. (B.18) in ref. [132] with  $\mathbf{q} = 0$  suffices for the carrying out of the momentum integral in  $\mathcal{L}_1$ ,

$$\int_{\mathbb{R}^d} \frac{d^d q}{(2\pi)^d} \frac{q_i q_j}{[\mathbf{q}^2 + \phi \Xi_4^2]^{3-d/2}} = \frac{\delta_{ij}}{2} \frac{\Gamma(2 - d)}{\Gamma(3 - \frac{d}{2})} \frac{\phi^{d-2} \gamma^{2d-4}}{(4\pi)^{d/2}} [\omega(1 - \omega)]^{2-d} , \quad (\text{A.68})$$

and eq. (A.67) becomes

$$\mathcal{L}_1 = -\mathbf{p} \cdot \mathbf{p}' e^2 [D(E^*)]^2 \frac{M^2}{2} \frac{\gamma^{2d-4}}{(4\pi)^d} \frac{\Gamma(3 - d)}{(2 - d)} \int_0^1 d\omega [\omega(1 - \omega)]^{1-d/2} \int_0^1 d\phi \phi^{d/2-1} , \quad (\text{A.69})$$

where the Gamma functions have been simplified. While the integration over  $\phi$  is straightforward and gives  $2/d$ , the remaining one can be performed in an analogous fashion as eq. (A.6) of ref. [2]. By considering  $\epsilon \equiv 3 - d$ , in fact, the integrand can be expanded in power series in  $\epsilon$ , giving

$$\int_0^1 d\omega [\omega(1 - \omega)]^{1-d/2} = \int_0^1 d\omega e^{\epsilon \log \sqrt{\omega - \omega^2}} \cdot [\omega(1 - \omega)]^{-1/2} = \pi - 2\pi\epsilon \log 2 + \mathcal{O}(\epsilon^2) . \quad (\text{A.70})$$

Introducing also the renormalization scale  $\mu$ , the part of the scattering amplitude of interest can be recast as

$$\mathcal{L}_1 = -\cos \theta [D(E^*)]^2 M^2 e^2 \frac{\mathbf{p}^2}{d} \left(\frac{\mu}{2}\right)^{3-d} \cdot \frac{\gamma^{2d-4} \Gamma(\epsilon)}{(4\pi)^d (2 - d)} \left[ \pi - 2\pi\epsilon \log 2 + \mathcal{O}(\epsilon^2) \right] . \quad (\text{A.71})$$

It displays a pole singularity in the limit  $d \rightarrow 3$  and a simple PDS pole at  $d = 2$ . By exploiting the Laurent series expansion of the Gamma function for small arguments and truncating it at NLO,  $\mathcal{L}_1$  finally becomes

$$\mathcal{L}_1 = -\cos \theta [D(E^*)]^2 \frac{\alpha M^2}{16\pi} \frac{\mathbf{p}^4}{3} \left[ \frac{1}{3 - d} - \gamma_E + \frac{4}{3} + i\pi + \log \left( \frac{\pi \mu}{2\mathbf{p}^2} \right) \right] , \quad (\text{A.72})$$

where the regular parts of the amplitude have been evaluated in the three-dimensional limit. Now, due to the presence of a  $d = 2$  singularity, the PDS correction to  $\mathcal{L}_1$  is non-zero. Introducing again the renormalization scale  $\mu$  of the  $\overline{\text{MS}}$  scheme and noticing that the integrand in eq. (A.71) in the  $d \rightarrow 2$  limit coincides with 1, the correction turns out to be

$$\delta \mathcal{L}_1 = \cos \theta [D(E^*)]^2 \frac{\alpha M^2}{4\pi} \frac{\mu \mathbf{p}^2}{4} . \quad (\text{A.73})$$

Subtracting the latter equation to eq. (A.72), the PDS corrected part of the amplitude can be

obtained,

$$\mathfrak{L}_1^{\text{PDS}} = \mathfrak{L}_1 - \delta\mathfrak{L}_1 = -\cos\theta[D(E^*)]^2 \frac{\alpha M^2}{4\pi} \frac{\mathbf{p}^2}{4} \left[ \frac{1}{3-d} - \gamma_E + \frac{4}{3} - \log \frac{2\mathbf{p}^2}{\pi\mu} + i\pi \right] + \mu \quad (\text{A.74})$$

Next, we concentrate on the evaluation of the second term on the second row of eq. (A.63). Considering the original constant factors and the integral over the  $\mathbf{q}$ , we define

$$\mathfrak{L}_2 \equiv \mathbf{p} \cdot \mathbf{p}' [D(E^*)]^2 \frac{M^2}{2} \frac{\Gamma(1 - \frac{d}{2})}{(4\pi)^{d/2}} \int_0^1 d\omega \int_{\mathbb{R}^d} \frac{d^d \mathbf{q}}{(2\pi)^d} \frac{e^2}{\mathbf{q}^2} \frac{1}{[\gamma^2 + \omega(1-\omega)\mathbf{q}^2]^{1-d/2}} \quad (\text{A.75})$$

and the constant  $\Xi_5^2 \equiv \gamma^2/[\omega(1-\omega)]$ , so that we can exploit again the Feynman parametrization for the denominators, obtaining

$$\mathfrak{L}_2 = \mathbf{p} \cdot \mathbf{p}' e^2 [D(E^*)]^2 \frac{M^2}{2} \frac{\Gamma(2 - \frac{d}{2})}{(4\pi)^{d/2}} \int_0^1 d\omega [\omega(1-\omega)]^{d/2-1} \int_0^1 d\phi \int_{\mathbb{R}^d} \frac{d^d \mathbf{q}}{(2\pi)^d} \frac{\phi^{-d/2}}{[\phi\Xi_5^2 + \mathbf{q}^2]^{2-d/2}} \quad (\text{A.76})$$

The integral over the  $\mathbf{q}$  can be now carried out as a straightforward application of eq. (B.16) in ref. [132], yielding

$$\mathfrak{L}_2 = \mathbf{p} \cdot \mathbf{p}' e^2 [D(E^*)]^2 \frac{M^2}{2} \frac{\Gamma(2 - \frac{d}{2})}{(4\pi)^{d/2}} \int_0^1 d\omega [\omega(1-\omega)]^{d/2-1} \int_0^1 d\phi \frac{\phi^{-d/2} (\phi\Xi_5^2)^{d-2}}{(4\pi)^{d/2}} \frac{\Gamma(2-d)}{\Gamma(2 - \frac{d}{2})} \quad (\text{A.77})$$

In the last rewriting, the integral over the  $\phi$  can be immediately performed, while the Gammas can again be simplified and reduced, so that eq. (A.77) transforms into

$$\mathfrak{L}_2 = -\mathbf{p} \cdot \mathbf{p}' e^2 [D(E^*)]^2 \gamma^{2d-4} \frac{M^2}{4} \left(\frac{\mu}{2}\right)^{3-d} \frac{\Gamma(3-d)}{(4\pi)^d (1 - \frac{d}{2})^2} \int_0^1 d\omega [\omega(1-\omega)]^{1-d/2}, \quad (\text{A.78})$$

where the conventional renormalization scale factor  $(\mu/2)^{3-d}$  has been introduced as in eq. (A.71). The remaining integral has been already met in eq. (A.73) and it can be evaluated exactly in  $d = 2$  or expanded in powers of  $3-d$  in the three-dimensional case. Plugging eq. (A.70) into eq. (A.77), it turns out that the integral is again divergent in the limit  $d \rightarrow 3$  and includes also a threefold PDS pole in  $d \rightarrow 2$ . Taking the former limit, the Gamma function can be expanded in Laurent series as before and the amplitude can be re-expressed as

$$\mathfrak{L}_2 = \cos\theta[D(E^*)]^2 \frac{\alpha M^2}{4\pi} \frac{\mathbf{p}^4}{4} \left[ \frac{1}{3-d} - \gamma_E + 2 + i\pi - \log \frac{\mathbf{p}^2}{8\pi\mu} \right], \quad (\text{A.79})$$

where the ultraviolet divergence of the original integral is made explicit. Then, the application of the PDS scheme to the  $d \rightarrow 2$  pole yields the following correction,

$$\delta\mathfrak{L}_2^{\text{PDS}} = -\alpha \cos\theta D_0^2 M^2 \frac{\mu \mathbf{p}^2}{8\pi}. \quad (\text{A.80})$$

Finally, we subtract the PDS contribution just determined to eq. (A.79), obtaining

$$\mathfrak{L}_2^{\text{PDS}} = \cos\theta[D(E^*)]^2 \frac{\alpha M^2}{4\pi} \frac{\mathbf{p}^2}{2} \left\{ \frac{1}{2} \left[ \frac{1}{3-d} - \gamma_E + 2 + i\pi - \log \left( \frac{2\mathbf{p}^2}{\pi\mu} \right) \right] + \mu \right\}. \quad (\text{A.81})$$

Now we collect the two results in eqs. (A.74) and (A.81) and write the one-loop scattering

amplitude with one photon exchange in the power divergence subtraction scheme,

$$T_{\text{SC}}^{1\text{-loop}}(\mathbf{p}, \mathbf{p}') \Big|_{\text{PDS}} = \cos \theta [D(E^*)]^2 \frac{\alpha M^2}{4\pi} \left\{ \frac{\mu \mathbf{p}^2}{4} + \frac{\mathbf{p}^4}{6} \left[ \frac{1}{3-d} - \gamma_E + \frac{7}{3} - \log \left( \frac{2\mathbf{p}^2}{\pi\mu} \right) + i\pi \right] \right\}. \quad (\text{A.82})$$

### A.3 Three dimensional integrations

Here, we focus our attention on the computation of the leading order matrix element of the Coulomb-corrected strong fermion-fermion scattering amplitude in eq. (3.28). The process can be reduced to the evaluation of only one of the two integrals presented in the first row of the latter equation, by virtue of the complex-conjugation property satisfied by the repulsive Coulomb wavefunctions,  $\psi_{\mathbf{p}'}^{(-)*} = \psi_{-\mathbf{p}'}^{(+)}$ . In particular, we choose to concentrate on the first term on the l.h.s. of eq. (3.29),

$$\mathfrak{F} \equiv i \nabla \psi_{\mathbf{p}}^{(-)*}(\mathbf{r}) \Big|_{\mathbf{r}=\mathbf{0}} = i \int_{\mathbb{R}^3} d^3 r' \delta(\mathbf{r}') \nabla' \psi_{\mathbf{p}'}^{(-)*}(\mathbf{r}'). \quad (\text{A.83})$$

Recalling the parity rule of the spherical harmonics (cf. sec.  $A_{VI}$  in ref. [272]), the repulsive Coulomb eigenstate turns out to be given by

$$\psi_{\mathbf{p}'}^{(-)*}(\mathbf{r}') = \frac{4\pi}{|\mathbf{p}'| r'} \sum_{\ell=0}^{+\infty} \sum_{m=-\ell}^{\ell} (-i)^\ell e^{i\sigma_\ell} Y_\ell^{m*}(\hat{\mathbf{p}}') Y_\ell^m(\hat{\mathbf{r}}') F_\ell(\eta, |\mathbf{p}'| r'). \quad (\text{A.84})$$

Now, we start by observing that the three-dimensional Dirac delta function peaked at the origin can be rewritten in spherical coordinates as

$$\delta(\mathbf{r}) \equiv \delta(x)\delta(y)\delta(z) = \frac{\delta(r)}{4\pi r^2}, \quad (\text{A.85})$$

due to rotational invariance (cf. app. A.4). The rewriting in eq. (A.85) paves the way for the integration of the angular variables and on the radial distance on which the Dirac delta effectively acts separately. Equipped with the last equation, we can split the expression in eq. (A.83) into two parts,

$$\mathfrak{F} = \mathfrak{F}_1 + \mathfrak{F}_2, \quad (\text{A.86})$$

where

$$\mathfrak{F}_1 \equiv i \int_0^{2\pi} d\varphi' \int_0^\pi d\theta' \int_0^{+\infty} dr' \delta(r') \sum_{\ell=0}^{+\infty} \sum_{m=-\ell}^{\ell} (-i)^\ell e^{i\sigma_\ell} Y_\ell^{m*}(\hat{\mathbf{p}}') Y_\ell^m(\hat{\mathbf{r}}') \nabla' \frac{F_\ell(\eta, |\mathbf{p}'| r')}{|\mathbf{p}'| r'}. \quad (\text{A.87})$$

and

$$\mathfrak{F}_2 \equiv i \int_0^{2\pi} d\varphi' \int_0^\pi d\theta' \int_0^{+\infty} dr' \delta(r') \sum_{\ell=0}^{+\infty} \sum_{m=-\ell}^{\ell} (-i)^\ell e^{i\sigma_\ell} Y_\ell^{m*}(\hat{\mathbf{p}}') \frac{F_\ell(\eta, |\mathbf{p}'| r')}{|\mathbf{p}'| r'} \nabla' Y_\ell^m(\hat{\mathbf{r}}'). \quad (\text{A.88})$$

Considering the explicit expression for the regular repulsive Coulomb eigenfunctions in eq. (1.18), we first concentrate on the application of the gradient to  $F_\ell(\eta, |\mathbf{p}'| r')/|\mathbf{p}'| r'$ . Recalling the transformation property of the Kummer functions, i.e. the confluent Hypergeometric

functions  ${}_1F_1$ , under differentiation with respect to their third argument

$$\frac{\partial}{\partial z} M(a, b, z) = \frac{a}{b} M(a + 1, b + 1, z) \quad a, b, z \in \mathbb{C}, \quad (\text{A.89})$$

we can rewrite the term of interest as

$$\begin{aligned} \nabla' \left( \frac{F_\ell(\eta, |\mathbf{p}'|r')}{|\mathbf{p}'|r'} \right) &= |\mathbf{p}'| \hat{\mathbf{r}}' \frac{2^\ell e^{-\pi\eta/2} |e^{i|\mathbf{p}'|r'}| \Gamma(\ell + 1 + i\eta)}{(2\ell + 1)!} (|\mathbf{p}'|r')^{\ell-1} \\ &\cdot \left[ (i\mathbf{r}'|\mathbf{p}'| + \ell) M(\ell + 1 + i\eta, 2\ell + 2, -2i|\mathbf{p}'|r') - i|\mathbf{p}'|r' \frac{\ell + 1 + i\eta}{\ell + 1} M(\ell + 2 + i\eta, 2\ell + 3, -2i|\mathbf{p}'|r') \right]. \end{aligned} \quad (\text{A.90})$$

In the last equation, we note that the application of the gradient effectively reduces to the application of the derivative with respect to the radial variable  $r'$ , therefore the resulting vector is parallel to  $\mathbf{r}'$ . It is then convenient to exploit the expression of the latter vector in terms of the spherical harmonics given in eq. (5.24) and sec. 5.1 of ref. [135], in order to perform the integration on the radial and the angular variables  $\varphi'$  and  $\theta'$  associated to  $\mathbf{r}'$  in eq. (A.87) separately. Making use of the complex conjugation (cf. eq. (4.31) in ref. [273]) and the orthonormality (cf. chap. VI of ref. [274]) properties of spherical harmonics, the integral over  $\Omega' \equiv (\varphi', \theta')$  can be carried out rapidly, obtaining

$$\begin{aligned} \mathfrak{F}_1 &= \sum_{\ell=0}^{+\infty} \sum_{m=-\ell}^{\ell} (-i)^\ell 2i \sqrt{\frac{\pi}{3}} \int_0^{+\infty} dr' \delta(r') e^{i\sigma_\ell} Y_\ell^{m*}(\hat{\mathbf{p}}') \frac{\partial}{\partial r'} \left[ \frac{F_\ell(\eta, |\mathbf{p}'|r')}{|\mathbf{p}'|r'} \right] \\ &\cdot (\delta_{m1} \delta_{\ell 1} \mathbf{e}_1 + \delta_{m0} \delta_{\ell 1} \mathbf{e}_0 + \delta_{m-1} \delta_{\ell 1} \mathbf{e}_{-1}). \end{aligned} \quad (\text{A.91})$$

Recalling eq. (5.24) and sec. 5.1 in ref. [135], the remaining spherical harmonic on the last row of eq. (A.91) together with the round bracket with the Kronecker deltas can be identified as the unit-vector parallel to  $\mathbf{p}'$ , up to a multiplication factor that cancels out with  $2\sqrt{\pi/3}$  on the left of the last integration sign. Then, exploiting eq. (A.90) for  $\ell = 1$ , eq. (A.91) can be rewritten as

$$\begin{aligned} \mathfrak{F}_1 &= \int_0^{+\infty} dr' \delta(r') e^{i\sigma_1} \frac{\partial}{\partial r'} \left[ \frac{F_1(\eta, |\mathbf{p}'|r')}{r'} \right] \mathbf{p}' \\ &= \frac{|\Gamma(2 + i\eta)|}{3 e^{-i\sigma_1} e^{\pi\eta/2}} \lim_{r' \rightarrow 0} \left[ (1 + i|\mathbf{p}'|r') M(2 + i\eta, 4, -2i|\mathbf{p}'|r') - i|\mathbf{p}'|r' \frac{2 + i\eta}{2} M(3 + i\eta, 5, -2i|\mathbf{p}'|r') \right] \mathbf{p}'. \end{aligned} \quad (\text{A.92})$$

The explicit evaluation of the limit leads immediately to the disappearance of the terms depending linearly on the radial coordinate  $r'$ , since the Kummer functions are equal to unity for zero values of the third argument,

$$\lim_{z \rightarrow 0} M(a, b, z) = \lim_{z \rightarrow 0} {}_1F_1(a, b, z) = 1 \quad a, b, z \in \mathbb{C}. \quad (\text{A.93})$$

Besides, by exploiting the fundamental property  $\Gamma(z + 1) = z\Gamma(z)$  of the Gamma functions, the constants outside the limit in eq. (A.92) can be rewritten in terms of the Sommerfeld factor (cf. eq. (1.20)),

$$\frac{|\Gamma(2 + i\eta)|}{e^{\pi\eta/2}} = \frac{\sqrt{1 + \eta^2}}{e^{\pi\eta/2}} |\Gamma(1 + i\eta)| = \sqrt{1 + \eta^2} C_\eta, \quad (\text{A.94})$$

thus recovering the polynomial on the r.h.s of the generalized effective range expansion (cf. eq. (1.29) with  $\ell = 1$ ). Equipped with the two last results we can, finally, obtain the desired

expression for the r.h.s. of eq. (A.91),

$$\mathfrak{F}_1 = e^{i\sigma_1} C_\eta \sqrt{1 + \eta^2} \frac{\mathbf{p}'}{3}. \quad (\text{A.95})$$

Now, we can proceed with the application of the gradient to the spherical harmonics (cf. eq. (A.88)). From ref. [135], the result of the latter derivative can be rewritten as a linear combination of spherical harmonics as in eqs. (5.24) and (5.27) in ref. [135]. In particular, by the introduction of  $1 = \sqrt{4\pi} Y_0^{0*}(\theta, \varphi)$  in the relevant integral of eq. (A.88), we can observe that the surface integrals over the  $Y_{\ell+1}^\mu(\theta, \varphi)$  yield no contribution, since  $\ell$  cannot assume negative values. It follows that our term of interest becomes

$$\mathfrak{F}_2 = - \sum_{\ell, m} (-i)^{\ell+1} \sqrt{\frac{4\pi\ell}{2\ell+1}} \frac{(\ell+1)}{|\mathbf{p}'|} e^{i\sigma_\ell} Y_\ell^{m*}(\hat{\mathbf{p}}') \int_0^{+\infty} dr' \delta(r') \frac{F_\ell(\eta, |\mathbf{p}'|r')}{r'^2} \sum_{\mu, \mu'} \delta_{\ell 1} \delta_{\mu 0} (\ell-1) \ell |\mu \mu' m| \mathbf{e}_{\mu'}, \quad (\text{A.96})$$

where the Clebsch-Gordan coefficients  $\langle j_1 j_2 J | m_1 m_2 M \rangle \equiv \langle JM, j_1 j_2 | j_1 m_1, j_2 m_2 \rangle$  vanish whenever  $m \neq \mu + \mu'$ . The evaluation of the latter in the last row of eq. (A.96) leads to

$$\begin{aligned} \mathfrak{F}_2 &= \sqrt{\frac{4\pi}{3}} e^{i\sigma_1} \int_0^{+\infty} dr' \delta(r') \frac{2}{r'} \frac{F_1(\eta, |\mathbf{p}'|r')}{|\mathbf{p}'|r'} \left( Y_1^{-1*}(\hat{\mathbf{p}}') \mathbf{e}_1 + Y_1^{0*}(\hat{\mathbf{p}}') \mathbf{e}_0 + Y_1^{1*}(\hat{\mathbf{p}}') \mathbf{e}_{-1} \right) \\ &= 2\mathbf{p}' \frac{|\Gamma(2+i\eta)|}{3 e^{\pi\eta/2} e^{-i\sigma_1}} \lim_{r \rightarrow 0} \left[ e^{i|\mathbf{p}'|r'} M(2+i\eta, 4, -2i|\mathbf{p}'|r') \right]. \end{aligned} \quad (\text{A.97})$$

Then, exploiting again the results in eqs. (A.93) and (A.94), the limit in the equation can be evaluated and the expression simplified as eq. (A.95), giving

$$\mathfrak{F}_2 = e^{i\sigma_1} C_\eta \sqrt{1 + \eta^2} \frac{2\mathbf{p}'}{3}. \quad (\text{A.98})$$

Combining the last result together with the one in eq. (A.95), we obtain the expression of the complete integral in eq. (A.83),

$$i \int_{\mathbb{R}^3} d^3 r' \delta(r') \nabla' \psi_{\mathbf{p}'}^{(-)*}(\mathbf{r}') = e^{i\sigma_1} C_\eta \sqrt{1 + \eta^2} \mathbf{p}'. \quad (\text{A.99})$$

By exploiting the complex-conjugation property of the regular Coulomb repulsive wavefunction  $\psi_{\mathbf{p}}^{(-)}(\mathbf{r}) = \psi_{-\mathbf{p}}^{(+)*}(\mathbf{r})$ , also the remaining part of eq. (3.29) can be evaluated, by noticing that the latter property implies only the disappearance of a  $(-1)^\ell$  factor in eq. (A.84), that for  $\ell = 1$  is compensated by the overall minus sign in front of the integral,

$$-i \int_{\mathbb{R}^3} d^3 r \delta(r) \nabla \psi_{\mathbf{p}}^{(+)}(\mathbf{r}) = e^{i\sigma_1} C_\eta \sqrt{1 + \eta^2} \mathbf{p}. \quad (\text{A.100})$$

Therefore, the full leading order  $T_{\text{SC}}$  matrix element in eq. (3.28) reads

$$\langle \psi_{\mathbf{p}'}^{(-)} | \hat{\mathcal{V}}^{(1)} | \psi_{\mathbf{p}}^{(+)} \rangle = e^{2i\sigma_1} C_\eta^2 D(E^*) (1 + \eta^2) \mathbf{p}' \cdot \mathbf{p} = \cos \theta D(E^*) C_\eta^2 e^{2i\sigma_1} (1 + \eta^2) \mathbf{p}^2, \quad (\text{A.101})$$

where  $\theta$  is the scattering angle.



## A.4 Dirac Delta function

In this section we aim at rewriting the three-dimensional Dirac delta function peaked at the origin,

$$\delta(\mathbf{r}) \equiv \delta(x)\delta(y)\delta(z) , \quad (\text{A.102})$$

in spherical coordinates, in order to facilitate the integrations in which such a Dirac delta appears within the integrand. With this aim, it is convenient to rewrite the delta in momentum space [274],

$$\delta(\mathbf{r}) = \int_{\mathbb{R}^3} \frac{d^3q}{(2\pi)^3} e^{i\mathbf{q}\cdot\mathbf{r}} , \quad (\text{A.103})$$

and replace the exponential with its expansion into spherical Bessel functions and spherical harmonics, obtaining

$$\begin{aligned} \delta(\mathbf{r}) &= 4\pi \sum_{\ell=0}^{+\infty} \sum_{m=-\ell}^{\ell} i^{\ell} Y_{\ell}^{m*}(\hat{\mathbf{r}}) \int_0^{+\infty} \frac{dq}{(2\pi)^3} q^2 j_{\ell}(qr) \int_0^{2\pi} d\varphi \int_0^{\pi} d\theta \sin\theta Y_{\ell}^m(\theta, \varphi) \\ &= (4\pi)^{3/2} \sum_{\ell=0}^{+\infty} \sum_{m=-\ell}^{\ell} i^{\ell} Y_{\ell}^{m*}(\hat{\mathbf{r}}) \int_0^{+\infty} \frac{dq}{(2\pi)^3} q^2 j_{\ell}(qr) \int_0^{2\pi} d\varphi \int_0^{\pi} d\theta \sin\theta Y_{\ell}^m(\theta, \varphi) Y_0^{0*}(\theta, \varphi) \quad (\text{A.104}) \\ &= (4\pi)^{3/2} \sum_{\ell=0}^{+\infty} \sum_{m=-\ell}^{\ell} i^{\ell} Y_{\ell}^{m*}(\hat{\mathbf{r}}) \int_0^{+\infty} \frac{dq}{(2\pi)^3} q^2 j_{\ell}(qr) \delta_{\ell 0} \delta_{m 0} = 2 \int_0^{+\infty} \frac{dq}{(2\pi)^2} q^2 j_0(qr) , \end{aligned}$$

where the integration property in eq. (A.104) of spherical harmonics *filters out* all the contributions coming from the spherical tensors transforming according to the  $\ell \geq 1$  irreps of  $\text{SO}(3)$ . The remaining integration can be carried out by referencing to the identity in sec. 11.2 of ref. [275]

$$\int_0^{+\infty} dq q^2 j_{\alpha}(uq) j_{\alpha}(vq) = \frac{\pi}{2u^2} \delta(u - v) \quad (\text{A.105})$$

in the particular case in which  $\alpha = 0$  and  $v = 0$ . The desired expression for the three-dimensional Dirac delta is, then, recovered

$$\delta(\mathbf{r}) = \frac{\delta(r)}{4\pi r^2} , \quad (\text{A.106})$$

from which we observe that the sequence of three deltas in eq. (A.102) has been reduced into a single delta over the radial coordinate. It is, finally, interesting to note that the denominator  $4\pi r^2$  in the last equation coincides with the absolute value of the Jacobian of the transformation from Cartesian to spherical coordinates, in which the integration over the domain of the angular variables has been performed. This integration is only allowed when the delta is spherically symmetric, which is not the case for the translated Dirac delta,  $\delta(\mathbf{r} - \mathbf{r}_0)$ , by a non-null vector  $\mathbf{r}_0$ .



This appendix provides complementary material to the second part of chap. 2 and 3, in which the system is immersed in a cubic finite volume. In particular, app. B.1 with its subunits B.1.1 and B.1.2 discusses the Riemann sums appearing in the derivation of the finite-volume corrections to the lowest S- and P-wave scattering states in secs. 2.2.3 a) and 3.2.3 a). Indeed apps. B.2, B.2.1 and B.2.2 the large binding momentum limit of the Riemann sums  $S_2(i\tilde{\kappa})$  and  $S_3(i\tilde{\kappa})$  implied in the derivation of the finite-volume shifts to the deepest unbound  $\ell = 0$  and 1 states in secs. 2.2.3 b) and 3.2.3 b) are illustrated.

## B.1 Three-dimensional Riemann sums

The derivation of the energy corrections from the finite volume ERE for the lowest-energy  $A_1$  and  $T_1$  scattering states implies the computation of the sum of the single and double three-dimensional Riemann series treated in this appendix.

### B.1.1 Single sums

Let us begin with the derivation of the sum of  $S_0(\tilde{p}) \equiv Y$ ,

$$Y = \sum_{\mathbf{n}}^{\Lambda_n} 1 - \frac{4\pi}{3} \Lambda_n^3 = 0 \quad (\text{B.107})$$

which can be carried out analytically. After rewriting the series over three-vectors of integers in integral form,

$$\sum_{\mathbf{n}}^{\Lambda_n} 1 = \int_{\mathbb{R}^3} d^3\mathbf{k} \sum_{\mathbf{n}}^{\Lambda_n} \delta(\mathbf{k} - \mathbf{n}) = \int_{\Lambda_n} d^3\mathbf{k} \sum_{\mathbf{n}}^{\infty} \delta(\mathbf{k} - \mathbf{n}) , \quad (\text{B.108})$$

the *Poisson summation formula* for a three-dimensional Dirac delta function,

$$\sum_{\mathbf{n}}^{\infty} \delta(\mathbf{k} - \mathbf{n}) = \sum_{\mathbf{n}}^{\infty} e^{-2\pi i \mathbf{n} \cdot \mathbf{k}} , \quad (\text{B.109})$$

can be directly applied, obtaining

$$\Upsilon = \sum_{\mathbf{n}}^{\Lambda_n} 1 - \frac{4\pi}{3} \Lambda_n^3 = \int_{\Lambda_n} d^3k \sum_{\mathbf{n}}^{\infty} e^{-2\pi i \mathbf{k} \cdot \mathbf{n}} - \frac{4\pi}{3} \Lambda_n^3. \quad (\text{B.110})$$

Then, the remaining integral can be computed by singling out the zero mode,

$$\int_{\Lambda_n} d^3k \sum_{\mathbf{n}}^{\infty} e^{-2\pi i \mathbf{k} \cdot \mathbf{n}} = \int_{\Lambda_n} d^3k + \sum_{\mathbf{n} \neq 0}^{\infty} \int_{\Lambda_n} d^3k e^{-2\pi i \mathbf{k} \cdot \mathbf{n}} = \frac{4\pi}{3} \Lambda_n^2 + \sum_{\mathbf{n} \neq 0}^{\infty} \delta(2\pi \mathbf{n}) = \frac{4\pi}{3} \Lambda_n^2, \quad (\text{B.111})$$

where the second integral vanishes, since the sum excludes the null vector. Equipped with the last result, it immediately follows that

$$\Upsilon = \sum_{\mathbf{n}}^{\Lambda_n} 1 - \frac{4\pi}{3} \Lambda_n^3 = \frac{4\pi}{3} \Lambda_n^2 - \frac{4\pi}{3} \Lambda_n^3 = 0. \quad (\text{B.112})$$

Second, we report the sum of the series whose general term is given by the inverse of the norm of the three vector of integers  $\mathbf{n}$  [46],

$$\mathcal{G}^{(0)} = \sum_{\mathbf{n} \neq 0}^{\Lambda_n} \frac{1}{|\mathbf{n}|} - 2\pi \Lambda_n^2 = -2.8372. \quad (\text{B.113})$$

Although it does not play any role in the expression of the finite volume energy corrections, the sum of the series shares its asymptotic behaviour with the one of  $\mathcal{Q}_1$ . A precise determination of the sum of  $\mathcal{G}^{(0)}$ , thus, provides a benchmark test, which has to be passed successfully before addressing the  $\mathcal{Q}_1$  calculation. Due to the rapid oscillation of the sum of the series for similar values of the cutoff constant  $\Lambda_n$ , the original series in eq. (B.114) has been recast as

$$\mathcal{G}^{(0)} = \lim_{\epsilon \rightarrow 0^+} \left[ \sum_{\mathbf{n}}^{\Lambda_n} \frac{e^{-\epsilon |\mathbf{n}|}}{|\mathbf{n}|} - 4\pi \int_0^{\Lambda_n} dn n e^{-\epsilon n} \right], \quad (\text{B.114})$$

where  $\epsilon$  is a small real constant and the exponential factor proves to quench the oscillations of  $\mathcal{G}^{(0)}$  for neighbouring values of  $\Lambda_n$ . Considering the interval  $0.1 \leq \epsilon \leq 1$ , the sum of the series proves to decrease monotonically towards  $\epsilon = 0$  in the  $\Lambda_n \rightarrow +\infty$  limit and the behaviour is linear with  $\epsilon$ , with small quadratic corrections. The subsequent quadratic interpolation, in fact, returns a value of  $\mathcal{G}^{(0)}$  compatible with the exact one in literature (cf. eq. (B.114) and ref. [46]),

$$\mathcal{G}^{(0)} \approx -2.83739(11). \quad (\text{B.115})$$

It follows that the chosen approach (cf. eq. (B.114)) is successful in the evaluation of the sum of the series and can be promoted to more involved cases. Moreover, exploring a larger interval of  $\epsilon$  towards larger values, further deviations from linearity are likely to appear in the fit. In particular, the following class of fitting functions,

$$f(\epsilon) = \frac{a}{\epsilon + b} + c \quad a, b, c \in \mathbb{R}, \quad (\text{B.116})$$

is expected to provide a satisfactory description of the behaviour of  $\mathcal{G}^{(0)}$  with  $\epsilon$  both in the vicinity of zero and in the infinite  $\epsilon$  limit. The approach adopted for  $\mathcal{G}^{(0)}$  can be immediately

exploited for the computation of another three-dimensional sum regulated by a spherical cutoff,

$$\mathcal{H}^{(0)} = \sum_{\mathbf{n} \neq 0}^{\Lambda_n} \frac{1}{|\mathbf{n}|^3} - 4\pi \log \Lambda_n = \lim_{\varepsilon \rightarrow 0^+} \left[ \sum_{\mathbf{n}}^{\Lambda_n} \frac{e^{-\varepsilon|\mathbf{n}|}}{|\mathbf{n}|^3} - 4\pi \int_1^{\Lambda_n} dn \frac{1}{n} e^{-\varepsilon n} \right]. \quad (\text{B.117})$$

Even if the latter does not occur in any of the calculations presented in part I of the thesis, its numerical evaluation, that gives

$$\mathcal{H}^{(0)} = 3.8219, \quad (\text{B.118})$$

serves as a bootstrap to the computation of the double sum  $\mathcal{R}^{(0)}$  in the tail-singularity separation approach (cf. ref. [276]) performed in ref. [1], subject of the next subunit of the appendix.

Correlated to  $\mathcal{G}^{(0)}$  is the  $\mathcal{F}^{(0)}$  series, whose importance is witnessed by the numerous occasions in which it appears throughout part I of the present dissertation. Its implications include the finite-volume corrections to the mass of the fermions, the primed scattering parameters (cf. eqs. (1.40)-(1.44)), the finite-volume eigenvalues of the lowest  $A_1$  unbound state and the large binding momentum limit of the Lüscher functions  $\mathcal{S}_2(i\tilde{\kappa})$  and  $\mathcal{S}_3(i\tilde{\kappa})$ , see eqs. (B.182) and (B.208). The sum of this series is already known in literature [1, 46, 75] and is given by

$$2\pi\mathcal{G}^{(0)} = \mathcal{F}^{(0)} = \sum_{\mathbf{n} \neq 0}^{\Lambda_n} \frac{1}{|\mathbf{n}|^2} - 4\pi\Lambda_n = -8.9136, \quad (\text{B.119})$$

where the first equality is shown in tab. 1 and eq. (2.61) of ref. [75]. A precise evaluation of  $\mathcal{F}^{(0)}$  can be attained by isolating the cutoff-dependent part of the series via the Poisson summation formula. In particular, the addition and subtraction of a  $1/(|\mathbf{n}|^2 + 1)$  term in the original series yields

$$\mathcal{F}^{(0)} = \sum_{\mathbf{n} \neq 0}^{\Lambda_n} \frac{1}{|\mathbf{n}|^2(|\mathbf{n}|^2 + 1)} + \sum_{\mathbf{n} \neq 0}^{\Lambda_n} \frac{1}{|\mathbf{n}|^2 + 1} - 4\pi\Lambda_n, \quad (\text{B.120})$$

where the first term on the r.h.s proves to converge in the  $\Lambda \rightarrow +\infty$  limit as fast as the  $\mathcal{F} \equiv \mathcal{F}^{(0)}$  series in ref. [1] and the linear divergence is confined into the second summation. Exploiting the Poisson formula in eq. (B.109), the non-regularized series can be evaluated as follows,

$$\sum_{\mathbf{n} \neq 0}^{\Lambda_n} \frac{1}{|\mathbf{n}|^2 + 1} = -1 + \sum_{\mathbf{n}}^{\infty} \int_{S^2(\Lambda_n)} \frac{d^3k}{\mathbf{k}^2 + 1} \delta(\mathbf{n} - \mathbf{k}) = -1 + \sum_{\mathbf{n}}^{\infty} \int_{S^2(\Lambda_n)} \frac{d^3k}{\mathbf{k}^2 + 1} e^{-2\pi i \mathbf{k} \cdot \mathbf{n}}, \quad (\text{B.121})$$

where the zero  $\mathbf{n}$  term has been added to the sum and, then, the spherical cutoff has been moved from the sum to the integral over the finite-volume momenta. Separating the zero modes from the others in the result of eq. (B.120), we obtain

$$-1 + \int_{S^2(\Lambda_n)} \frac{d^3k}{\mathbf{k}^2 + 1} + \sum_{\mathbf{n} \neq 0}^{\infty} \int_{S^2(\Lambda_n)} \frac{d^3k}{\mathbf{k}^2 + 1} e^{-2\pi i \mathbf{k} \cdot \mathbf{n}} = -1 + 4\pi\Lambda_n + 4\pi \sum_{\mathbf{n} \neq 0}^{\infty} \int_0^{\Lambda_n} dk \frac{k}{i|\mathbf{n}|} \frac{e^{2\pi i k |\mathbf{n}|} - e^{-2\pi i k |\mathbf{n}|}}{|\mathbf{k}|^2 + 1}, \quad (\text{B.122})$$

where the third and the fourth term on the r.h.s. turn out to be finite in the infinite cutoff limit and the last integral can be performed in the complex plane, by collecting the residues according to Jordan's Lemma. Performing the remaining integration, in fact, the last expression

becomes

$$-1 + 4\pi\Lambda_n - 2\pi^2 + \pi \sum_{\mathbf{n} \neq 0}^{\infty} \frac{e^{-2\pi|\mathbf{n}|}}{|\mathbf{n}|} , \quad (\text{B.123})$$

that can be directly plugged into eq. (B.120), obtaining the desired result,

$$\mathcal{G}^{(0)} = -1 - 2\pi^2 + \sum_{\mathbf{n} \neq 0}^{\infty} \frac{1}{|\mathbf{n}|^2(|\mathbf{n}|^2 + 1)} + \pi \sum_{\mathbf{n} \neq 0}^{\infty} \frac{e^{-2\pi|\mathbf{n}|}}{|\mathbf{n}|} \equiv -1 - 2\pi^2 + \gamma_1 + \pi\lambda_0 , \quad (\text{B.124})$$

As it can be observed, the cutoff dependent term in the original series has been removed and, at the same time, two rapidly convergent sums,  $\lambda_0 = 0.0125$  and  $\gamma_1$  (cf. eq. (B.126)) replaced the divergent one, thus reducing significantly the computational efforts. The procedure is completely analogous to the one adopted in Appendix B 1 of ref. [72] and can be applied to other cutoff-regulated single sums.

Concerning the other single sums that arise in the expansion in powers of  $\delta\tilde{p}^2$  of the Lüscher functions  $S_1(\tilde{p})$  and  $S_2(\tilde{p})$  around  $\tilde{p}^2 = 0$ , their numerical evaluation does not require manipulations in the argument. Adopting a notation similar to the one used for eq. (B.114) and (B.117), the sums of relevant three-dimensional Riemann series yield

$$\begin{aligned} \mathcal{G}^{(0)} &= \sum_{\mathbf{n} \neq 0} \frac{1}{|\mathbf{n}|^4} = 16.5323 , & \mathcal{K}^{(0)} &= \sum_{\mathbf{n} \neq 0} \frac{1}{|\mathbf{n}|^6} = 8.4019 , \\ \mathcal{L}^{(0)} &= \sum_{\mathbf{n} \neq 0} \frac{1}{|\mathbf{n}|^8} = 6.9458 , & \mathcal{O}^{(0)} &= \sum_{\mathbf{n} \neq 0} \frac{1}{|\mathbf{n}|^{10}} = 6.4261 . \end{aligned} \quad (\text{B.125})$$

In particular, the results for  $\mathcal{G}^{(0)}$ ,  $\mathcal{K}^{(0)}$  and  $\mathcal{L}^{(0)}$  in eq. (B.125) coincide with the one of  $\mathcal{G}$ ,  $\mathcal{K}$  and  $\mathcal{L}$  reported in the appendix of ref. [1]. Indeed, the sums appearing as coefficients in the  $\delta\tilde{p}^2$  expansion of the Lüscher functions  $S_1(\tilde{p})$ ,  $S_2(\tilde{p})$  and  $S_3(\tilde{p})$  around  $\tilde{p}^2 = 1$  give

$$\begin{aligned} \mathcal{G}^{(1)} &= \sum_{\mathbf{n} \neq 0}^{\Lambda_n} \frac{1}{|\mathbf{n}|^2 - 1} - 4\pi\Lambda_n = -1.2113 , & \mathcal{G}^{(1)} &= \sum_{\mathbf{n} \neq 0} \frac{1}{(|\mathbf{n}|^2 - 1)^2} = 23.2432 , \\ \mathcal{K}^{(1)} &= \sum_{\mathbf{n} \neq 0} \frac{1}{(|\mathbf{n}|^2 - 1)^3} = 13.0594 , & \mathcal{L}^{(1)} &= \sum_{\mathbf{n} \neq 0} \frac{1}{(|\mathbf{n}|^2 - 1)^4} = 13.7312 , \\ \mathcal{O}^{(1)} &= \sum_{\mathbf{n} \neq 0} \frac{1}{(|\mathbf{n}|^2 - 1)^5} = 11.3085 , \end{aligned} \quad (\text{B.126})$$

where the first three coincide respectively with  $\mathcal{G}_1$ ,  $\mathcal{G}_1$  and  $\mathcal{K}_1$  in Appendix C of ref. [72]. Similarly, all the series not regulated by a cutoff can be computed directly, without the need to resort to the techniques outlined above. Conversely, the sum of  $\mathcal{G}^{(1)}$  can be obtained rapidly from the existing result for  $\mathcal{G}^{(0)}$ . In fact, the addition and subtraction of a  $1/|\mathbf{n}|^2$  term gives

$$\mathcal{G}^{(1)} = \sum_{|\mathbf{n}| \neq 0,1}^{+\infty} \frac{1}{|\mathbf{n}|^2(|\mathbf{n}|^2 - 1)} + \mathcal{G}^{(0)} + 5 \equiv \mathcal{F}_1 + \mathcal{G}^{(0)} + 5 , \quad (\text{B.127})$$

where in the first term on the r.h.s. the limit  $\Lambda_n \rightarrow +\infty$  has been taken. Moreover, replacing  $\mathcal{G}^{(0)}$  with its expression given in eq. (B.117), the last formula can be rewritten in a compact

fashion as

$$\mathcal{G}^{(1)} = 9 - 2\pi^2 + 2 \sum_{|\mathbf{n}| \neq 1}^{+\infty} \frac{1}{|\mathbf{n}|^2 + 1} \frac{1}{|\mathbf{n}|^2 - 1} + \pi \sum_{\mathbf{n} \neq 0}^{\infty} \frac{e^{-2\pi|\mathbf{n}|}}{|\mathbf{n}|} \equiv 9 - 2\pi^2 + 2\gamma_2 + \pi\lambda_0, \quad (\text{B.128})$$

so that  $\mathcal{G}^{(1)}$  can be evaluated independently from  $\mathcal{G}^{(0)}$ . Finally, we conclude the paragraph by enumerating the single series which do not appear directly in the  $\delta\tilde{p}^2 \sim 0$  expansions of the Lüscher functions but that play an ancillary role in the evaluation of the single sums listed in eqs. (B.124) and (B.128) (cf.  $\gamma_1$ ,  $\gamma_2$  and  $\mathcal{F}_1$ ) or in the double sums in eqs. (B.134) and (B.135) (cf.  $\mathcal{F}_1 - \mathcal{F}_4$ ),

$$\gamma_1 = \sum_{\mathbf{n} \neq 0}^{\infty} \frac{1}{|\mathbf{n}|^2(|\mathbf{n}|^2 + 1)} = 11.7861, \quad \gamma_2 = \sum_{|\mathbf{n}| \neq 1}^{+\infty} \frac{1}{|\mathbf{n}|^2 + 1} \frac{1}{|\mathbf{n}|^2 - 1} = 10.7442, \quad (\text{B.129})$$

and

$$\begin{aligned} \mathcal{F}_1 &= \sum_{|\mathbf{n}| > 1}^{\infty} \frac{1}{|\mathbf{n}|^2} \frac{1}{|\mathbf{n}|^2 - 1} = 14.7022, \quad \mathcal{F}_2 = \sum_{|\mathbf{n}| > 1}^{\infty} \frac{1}{|\mathbf{n}|^2} \frac{1}{(\mathbf{n}^2 - 1)^2} = 7.5410, \\ \mathcal{F}_3 &= \sum_{|\mathbf{n}| > 1}^{\infty} \frac{1}{|\mathbf{n}|^2} \frac{1}{(|\mathbf{n}|^2 - 1)^3} = 6.5185, \quad \mathcal{F}_4 = \sum_{|\mathbf{n}| > 1}^{\infty} \frac{1}{|\mathbf{n}|^2} \frac{1}{(\mathbf{n}^2 - 1)^4} = 6.2128. \end{aligned} \quad (\text{B.130})$$

Both the classes of series in eqs. (B.129) and (B.130) do not display convergence issues and can be directly evaluated. Note that  $\mathcal{F}_1$  coincides with the sum listed as  $\chi_3$  in eq. (A1) of ref. [1].

### B.1.2 Double Sums

Differently from their single counterparts, double sums appear only in the purely Coulombic contributions in the  $\ell = 0$  and 1 ERE and arise from the  $\tilde{p}^2 \rightarrow 0$  and 1 limits of the Lüscher functions  $\mathcal{S}_2(\tilde{p})$  and  $\mathcal{S}_3(\tilde{p})$ . Furthermore, the  $\tilde{p}^2 \approx 1$  expansion of the functions  $\mathcal{S}_2(\tilde{p})$  and  $\mathcal{S}_3(\tilde{p})$  in secs. 3.2.3 a) generates two categories of double sums. The simplest of them consists in one three-dimensional Riemann sum performed on  $\mathbb{Z}^3$ , followed by a sum over the six possible unit-vectors parallel to the axes normal to the faces of a cube. Adopting the notation introduced for the derivation of the of the  $\tilde{p}^2 \approx 1$  limit of  $\mathcal{S}_2(\tilde{p})$  in sec. III D 2 of ref. [1], we write

$$\begin{aligned} \chi_0 &= \sum_{|\mathbf{n}|=1} \sum_{\substack{|\mathbf{m}|=1 \\ \mathbf{n} \neq \mathbf{m}}} \frac{1}{|\mathbf{m} - \mathbf{n}|^2} = \frac{27}{2}, \quad \chi_1 = \sum_{|\mathbf{n}|=1} \sum_{\substack{\mathbf{m} \neq \mathbf{n} \\ |\mathbf{m}| \neq 1}}^{\infty} \frac{1}{|\mathbf{m}|^2 - 1} \frac{1}{|\mathbf{n} - \mathbf{m}|^2} = 86.1806, \\ \chi_2 &= \sum_{|\mathbf{n}|=1} \sum_{\substack{|\mathbf{m}| \neq 1 \\ \mathbf{m} \neq \mathbf{n}}}^{\infty} \frac{1}{(|\mathbf{m}|^2 - 1)^2} \frac{1}{|\mathbf{n} - \mathbf{m}|^2} = 52.5687, \quad \chi_3 = \sum_{|\mathbf{n}|=1} \sum_{\substack{|\mathbf{m}| \neq 1 \\ \mathbf{m} \neq \mathbf{n}}}^{\infty} \frac{1}{(|\mathbf{m}|^2 - 1)^3} \frac{1}{|\mathbf{n} - \mathbf{m}|^2} = 34.0562, \\ \chi_4 &= \sum_{|\mathbf{n}|=1} \sum_{\substack{|\mathbf{m}| \neq 1 \\ \mathbf{m} \neq \mathbf{n}}}^{\infty} \frac{1}{(|\mathbf{m}|^2 - 1)^4} \frac{1}{|\mathbf{n} - \mathbf{m}|^2} = 44.1196. \end{aligned} \quad (\text{B.131})$$

The presence of the factor  $1/|\mathbf{m} - \mathbf{n}|^2$  in the sums  $\chi_1 - \chi_4$  of eq. (B.131) ensures convergence without the need for the introduction of spherical cutoffs and regulators. Besides, the sum  $\chi_0$



is analytical and denoted as  $\chi_1$  in ref. [1], whereas the series  $\chi_2$  and  $\chi_3$  coincide with the  $\chi_2$  and  $\chi_5$ , respectively, in the latter work, except for the inclusion of the zero mode in the sum over  $\mathbf{m}$ .

Another group of series belonging to the same category is provided by the sums which are not present in the expansions of the  $\mathcal{S}_2(\tilde{p})$  and  $\mathcal{S}_3(\tilde{p})$  Lüscher functions, but occur in the rewriting of certain double sums in terms of the existing S-wave results in literature [1]. Due to the fast convergence, the evaluation such sums does not display difficulties and gives

$$\begin{aligned}\lambda_1 &= \sum_{|\mathbf{n}|=1}^{\infty} \sum_{|\mathbf{m}|>1}^{\infty} \frac{1}{|\mathbf{m}|^2} \frac{1}{|\mathbf{m}-\mathbf{n}|^2} = 65.3498, & \lambda_2 &= \sum_{|\mathbf{n}|=1}^{\infty} \sum_{|\mathbf{m}|>1}^{\infty} \frac{1}{|\mathbf{m}|^4} \frac{1}{|\mathbf{m}-\mathbf{n}|^2} = 14.9350, \\ \lambda_3 &= \sum_{|\mathbf{n}|=1}^{\infty} \sum_{|\mathbf{m}|>1}^{\infty} \frac{1}{|\mathbf{m}|^6} \frac{1}{|\mathbf{m}-\mathbf{n}|^2} = 5.8426, & \lambda_4 &= \sum_{|\mathbf{n}|=1}^{\infty} \sum_{|\mathbf{m}|>1}^{\infty} \frac{1}{|\mathbf{m}|^8} \frac{1}{|\mathbf{m}-\mathbf{n}|^2} = 2.6217, \end{aligned} \quad (\text{B.132})$$

thus permitting to express  $\mathcal{R}^{(1)}$  and  $\mathcal{R}_{2i\ 2j}^{(1)}$  in terms of  $\mathcal{R}^{(0)}$  and  $\mathcal{R}_{2i\ 2j}^{(0)}$ . Finally, of the same kind of the sums in eqs. (B.131) and (B.132) is the series  $\varrho_0$  in eq. (3.167), which appears as a proportionality constant in the  $\mathcal{O}(1/\delta\tilde{p}^2)$  contributions to  $\mathcal{S}_3$  (cf. eq. (3.173)) and allows for a pairwise elementary numerical evaluation,

$$\varrho_0 = \sum_{|\mathbf{n}|=1}^{\infty} \sum_{|\mathbf{m}|\neq 1}^{\infty} \frac{\mathbf{m} \cdot \mathbf{n} - 1}{(|\mathbf{m}|^2 - 1)|\mathbf{m} - \mathbf{n}|^2} = -29.85670(03). \quad (\text{B.133})$$

Now we switch to the second category of double sums, the one consisting of two three-dimensional sums performed on  $\mathbb{Z}^3$ . First, we consider the series stemming from the  $\tilde{p} \sim 0$  approximations of  $\mathcal{S}_2(\tilde{p})$ , see eq. (2.106). These sums, in fact, are the counterpart of divergent double integrals contributing to the amplitudes of the relevant two-particle scattering processes. Due to the large increase of the configuration space, for the numerical calculation of the sum of such series it is advisable to parallelize the operations via the development of GPU codes (e.g. in Cuda C++). The computational efforts can be significantly reduced by subdividing the original double sum into an arbitrarily large finite number of single sums, characterized by a three dimensional vector of integers. Then, assigning each of the outgoing single sums to a different subunit of a graphic card, the sum of the original double series is derived by gathering the results obtained simultaneously by each operating unit.

First, we start by reporting the calculation procedure for  $\mathcal{R}^{(0)}$  via the tail-singularity separation (TSS) [276] approach carried out in the appendix of ref. [1]. In this method, a three-dimensional Riemann sum is subdivided into an infrared part, dominated by the singularities of the summand and an UV part, expressed in the form of a three-dimensional integral and describing the behaviour of the argument of the original sum towards the infinity. As shown in app. A of ref. [276] for the sums  $\theta_{As}$  and  $\theta_{Bs}$ , the TSS approach holds also for double sums regulated asymmetrically, like

$$\mathcal{R}^{(0)} = \sum_{\mathbf{n} \neq \mathbf{0}}^{\Lambda_n} \sum_{\mathbf{m} \neq \mathbf{0}, \mathbf{n}}^{\infty} \frac{1}{|\mathbf{n}|^2 |\mathbf{m}|^2} \frac{1}{|\mathbf{n} - \mathbf{m}|^2} - 4\pi^4 \log \Lambda_n \equiv \sum_{\mathbf{n} \neq \mathbf{0}}^{\Lambda_n} \mathcal{R}_{\text{sub}}(\mathbf{n}) - 4\pi^4 \log \Lambda_n \quad (\text{B.134})$$

where  $\mathcal{R}_{\text{sub}}$  represents the inner sum indexed by  $\mathbf{m}$ . The latter exhibits singularities for  $\mathbf{m} = \mathbf{0}$  and  $\mathbf{n}$  that can be isolated from the rest of the sum via the introduction of negative

exponential factors depending on a small auxiliary parameter  $\varepsilon$ . Promoting the sum deprived of the singularities to a three dimensional integral, as prescribed by ref. [276], we find

$$\begin{aligned} \mathcal{R}_{\text{sub}}^{(0)}(\mathbf{n}) &= \sum_{\mathbf{m} \neq \mathbf{0}, \mathbf{n}}^{\infty} \frac{1}{|\mathbf{n}|^2 |\mathbf{m}|^2} \frac{1}{|\mathbf{n} - \mathbf{m}|^2} = -2\varepsilon(1 - e^{-\varepsilon|\mathbf{n}|^2}) \frac{1}{|\mathbf{n}|^2} \\ &+ \sum_{\mathbf{m} \neq \mathbf{0}, \mathbf{n}}^{\infty} \frac{1}{|\mathbf{m}|^2 D_{\mathbf{n}\mathbf{m}}} \left[ e^{-\varepsilon D_{\mathbf{n}\mathbf{m}}} + e^{-\varepsilon|\mathbf{m}|^2} - e^{-\varepsilon(D_{\mathbf{n}\mathbf{m}} + |\mathbf{m}|^2)} \right] + \int_{\mathbb{R}^3} d^3\mathbf{m} \frac{1 - e^{-\varepsilon D_{\mathbf{n}\mathbf{m}}}}{D_{\mathbf{n}\mathbf{m}}} \frac{1 - e^{-\varepsilon|\mathbf{m}|^2}}{|\mathbf{m}|^2}, \end{aligned} \quad (\text{B.135})$$

where  $D_{\mathbf{n}\mathbf{m}}$  denotes  $|\mathbf{m} - \mathbf{n}|$ . The latter formula can be further simplified by evaluating the  $\varepsilon$ -independent part of the integral over  $\mathbf{m}$ ,

$$\begin{aligned} \mathcal{R}_{\text{sub}}^{(0)}(\mathbf{n}) &= \frac{\pi^3}{|\mathbf{n}|} - 2\varepsilon(1 - e^{-\varepsilon|\mathbf{n}|^2}) \frac{1}{|\mathbf{n}|^2} + \sum_{\mathbf{m} \neq \mathbf{0}, \mathbf{n}}^{\infty} \frac{1}{|\mathbf{m}|^2 D_{\mathbf{n}\mathbf{m}}} \left[ e^{-\varepsilon D_{\mathbf{n}\mathbf{m}}} + e^{-\varepsilon|\mathbf{m}|^2} - e^{-\varepsilon(D_{\mathbf{n}\mathbf{m}} + |\mathbf{m}|^2)} \right] \\ &- 2\pi \int_0^{+\infty} dm \int_{-1}^1 d\cos\theta \left( e^{-\varepsilon D_{\mathbf{n}\mathbf{m}} \cos\theta} + e^{-\varepsilon|\mathbf{m}|^2} - e^{-\varepsilon(|\mathbf{m}|^2 + D_{\mathbf{n}\mathbf{m}} \cos\theta)} \right) \frac{1}{|\mathbf{m}|^2 D_{\mathbf{n}\mathbf{m}}}, \end{aligned} \quad (\text{B.136})$$

where  $D_{\mathbf{n}\mathbf{m}} \cos\theta = |\mathbf{n}|^2 - 2|\mathbf{n}||\mathbf{m}| \cos\theta + |\mathbf{m}|^2$ . Recalling the outer sum in eq. (B.134), the sum of the series  $\mathcal{R}^{(0)}$  can be finally computed by exploiting the known value of  $\mathcal{H}^{(0)}$  in eq. (B.118) and by choosing a range of values of  $\varepsilon$  that stabilizes the integral and the double sums. The subsequent extrapolation to the limit  $\varepsilon \rightarrow 0$  of the sum of the original cutoff-regulated double series yields

$$\mathcal{R}^{(0)} = \pi^3 \mathcal{H}^{(0)} - 2\varepsilon \mathcal{J}^{(0)} + 2\varepsilon \mathcal{J}_{\varepsilon}^{(0)} + \mathcal{T}_1^{(0)} - 2\pi \mathcal{T}_2^{(0)} = -178.42(01), \quad (\text{B.137})$$

where the  $\varepsilon$ -dependent sums are given by

$$\mathcal{J}_{\varepsilon}^{(0)} \equiv \sum_{\mathbf{n} \neq \mathbf{0}}^{\infty} \frac{e^{-\varepsilon|\mathbf{n}|^2}}{|\mathbf{n}|^4}, \quad (\text{B.138})$$

$$\mathcal{T}_1^{(0)} = \sum_{\mathbf{n} \neq \mathbf{0}}^{\infty} \sum_{\mathbf{m} \neq \mathbf{0}, \mathbf{n}}^{\infty} \frac{1}{|\mathbf{m}|^2 D_{\mathbf{n}\mathbf{m}}} \left[ e^{-\varepsilon D_{\mathbf{n}\mathbf{m}}} + e^{-\varepsilon|\mathbf{m}|^2} - e^{-\varepsilon(D_{\mathbf{n}\mathbf{m}} + |\mathbf{m}|^2)} \right], \quad (\text{B.139})$$

and

$$\mathcal{T}_2^{(0)} = \sum_{\mathbf{n} \neq \mathbf{0}} \frac{1}{|\mathbf{n}|^2} \int_0^{+\infty} dm \int_{-1}^1 d\cos\theta \left[ e^{-\varepsilon D_{\mathbf{n}\mathbf{m}} \cos\theta} + e^{-\varepsilon|\mathbf{m}|^2} - e^{-\varepsilon(|\mathbf{m}|^2 + D_{\mathbf{n}\mathbf{m}} \cos\theta)} \right] \frac{1}{|\mathbf{m}|^2 D_{\mathbf{n}\mathbf{m}} \cos\theta}. \quad (\text{B.140})$$

Differently from  $\mathcal{R}^{(0)}$ , the evaluation of the double sums

$$\mathcal{R}_{2i\ 2j}^{(0)} = \sum_{\mathbf{n} \neq \mathbf{0}}^{\infty} \sum_{\mathbf{m} \neq \mathbf{0}, \mathbf{n}}^{\infty} \frac{1}{|\mathbf{n}|^i |\mathbf{m}|^j} \frac{1}{|\mathbf{n} - \mathbf{m}|^2}, \quad (\text{B.141})$$

with  $i, j \geq 1$  and  $i + j > 2$  appearing in the higher order perturbative expansion of  $\mathcal{S}_2(\tilde{p})$  around  $\tilde{p} = 0$  does not require the adoption of stabilization techniques, due to their faster convergence. In particular, the only  $\mathcal{R}_{2i\ 2j}^{(0)}$  sum referenced in eqs. (2.114) and (2.115) for the lowest unbound S-wave energy eigenvalue is  $\mathcal{R}_{24}^{(0)}$ , that gives 170.97(01) [1].

Second, we consider the series stemming from the  $\tilde{p} \sim 1$  approximations of  $\mathcal{S}_2(\tilde{p})$ , see eq. (3.157). The series  $\mathcal{R}^{(1)}$  in eq. (3.155) indeed can be expressed in terms of the already known  $\mathcal{R}^{(0)}$  in eq. (2.103). By adding and subtracting  $\mathcal{R}^{(0)}$  from  $\mathcal{R}^{(1)}$  and performing few manipulations, the latter series can be conveniently recast as

$$\mathcal{R}^{(1)} = \sum_{|\mathbf{n}|>1} \sum_{\substack{|\mathbf{m}|>1 \\ \mathbf{m} \neq \mathbf{n}}} \frac{|\mathbf{n}|^2 + |\mathbf{m}|^2 - 1}{|\mathbf{n}|^2(|\mathbf{n}|^2 - 1)|\mathbf{m}|^2(|\mathbf{m}|^2 - 1)|\mathbf{m} - \mathbf{n}|^2} + \mathcal{R}^{(0)} - 2\chi_0 - 2\lambda_1 - 2F_1 = -101.016(11) . \quad (\text{B.142})$$

Once in this form, the sum of  $\mathcal{R}^{(1)}$  can be obtained by exploiting the existing result for the cutoff-regularized sum  $\mathcal{R}^{(0)}$  in eq. (B.137), together with the single sums in eqs. (B.130), (B.131) and (B.132). The only additional computational effort is given by the double sum explicitly shown on the r.h.s of eq. (B.142), which proves to converge rapidly, unlike  $\mathcal{R}^{(0)}$ .

Subsequently, we switch to the series of the kind  $\mathcal{R}_{2i\ 2j}^{(1)}$  in eq. (3.156). Even if the evaluation of such sums does not require stabilization techniques, we present for completeness the expression of  $\mathcal{R}_{2i\ 2j}^{(1)}$  in terms of  $\mathcal{R}_{2i\ 2j}^{(0)}$  and ancillary single and double sums:

$$\begin{aligned} \mathcal{R}_{2i\ 2j}^{(1)} = \sum_{|\mathbf{n}|>1} \sum_{\substack{|\mathbf{m}|>1 \\ \mathbf{m} \neq \mathbf{n}}} \left[ \frac{1}{(|\mathbf{n}|^2 - 1)^i} \frac{1}{(|\mathbf{m}|^2 - 1)^j} - \frac{1}{|\mathbf{n}|^{2i} |\mathbf{m}|^{2j}} \right] \\ \cdot \frac{1}{|\mathbf{m} - \mathbf{n}|^2} + \mathcal{R}_{2i\ 2j}^{(0)} - 2\chi_0 - \lambda_i - \lambda_j + (-1)^j F_i + (-1)^i F_j . \end{aligned} \quad (\text{B.143})$$

Analogously to the S-wave case, the only contribution of such sums in the expression of the finite volume energy corrections for the lowest energy  $T_1$  eigenstate (cf. eq. (3.182) and (3.183)) is provided by  $\mathcal{R}_{24}^{(1)} = \mathcal{R}_{42}^{(1)}$ , whose explicit evaluation gives  $-93.692(10)$ .

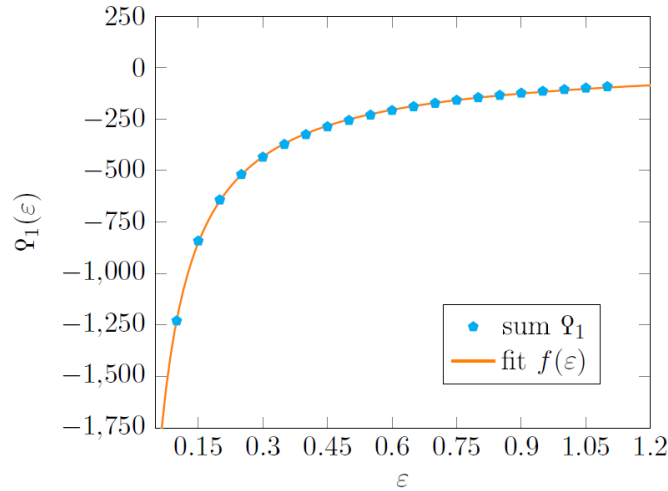


FIGURE B.4 – Sum of the stabilized  $\Omega_1$  series as a function of the parameter  $\epsilon$ . The fitting model, marked by the continuous orange line, corresponds to  $f(\epsilon)$  in eq. (B.116) with  $a = -149.59(47)$ ,  $b = 0.0185484(64)$  and  $c = 36.5(1.4)$ . The value of the parameter  $b$  plays a crucial role in determining the sum of the series and maximizes the value of the coefficient of determination ( $R^2$ ) of the fit for the considered fitting function. In particular, the R squared is equal to 0.999815, thus ensuring the reliability of the interpolation.

Finally, we present the double sums arising from the  $\tilde{p} \sim 1$  approximation of  $\mathcal{S}_3(\tilde{p})$  in eq. (3.173), starting with the cutoff-regularized double sum  $\Omega_1$  in eq. (3.168). Since the argument

of the sum is quadratically divergent with the spherical cutoff, it is convenient to adopt a stabilization technique for the evaluation of the sum. To this purpose, we chose to apply the approach in eq. (B.114) to the cutoff-regularized sum over  $\mathbf{n}$ ,

$$\Omega_1 = \lim_{\varepsilon \rightarrow 0^+} \left[ \sum_{|\mathbf{n}| \neq 1}^{\Lambda_n} \sum_{\substack{\mathbf{m} \neq \mathbf{n} \\ |\mathbf{m}| \neq 1}}^{\infty} \frac{e^{-\varepsilon|\mathbf{n}|}}{|\mathbf{n}|^2 - 1} \frac{1}{|\mathbf{m}|^2 - 1} \frac{\mathbf{n} \cdot \mathbf{m} - 1}{|\mathbf{n} - \mathbf{m}|^2} - 2\pi^4 \int_0^{\Lambda_n} dn \, n e^{-\varepsilon n} \right]. \quad (\text{B.144})$$

Since the  $\varepsilon$ -dependent  $\Omega_1$  sums display a non-linear behaviour in the interval  $0 \leq \varepsilon \leq 1.1$ , we choose to interpolate the data with the fitting function in eq. (B.116). As shown in fig. B.4,  $f(\varepsilon)$  describes the behaviour of the sum of the stabilized series as a function of  $\varepsilon$  satisfactorily, therefore the sum of the series becomes

$$\Omega_1 = \sum_{|\mathbf{n}| \neq 1}^{\Lambda_n} \sum_{\substack{\mathbf{m} \neq \mathbf{n} \\ |\mathbf{m}| \neq 1}}^{\infty} \frac{1}{|\mathbf{n}|^2 - 1} \frac{1}{|\mathbf{m}|^2 - 1} \frac{\mathbf{n} \cdot \mathbf{m} - 1}{|\mathbf{n} - \mathbf{m}|^2} - \pi^4 \Lambda_n^2 = -8028.1(24.2). \quad (\text{B.145})$$

Conversely, the double sum  $\Omega_2$  (cf. eq. (3.169)) appearing at order  $\delta \tilde{p}^2$  in the power series expansion of  $\mathcal{S}_3(\tilde{p})$  can be calculated efficiently even without stabilization approaches, despite its sign-changing numerator. Its numerical evaluation yields

$$\Omega_2 = \sum_{|\mathbf{n}| \neq 1}^{\infty} \sum_{\substack{\mathbf{m} \neq \mathbf{n} \\ |\mathbf{m}| \neq 1}}^{\infty} \frac{1 - |\mathbf{m}|^2 |\mathbf{n}|^2 + \mathbf{n} \cdot \mathbf{m} (|\mathbf{n}|^2 + |\mathbf{m}|^2 - 2)}{(|\mathbf{m}|^2 - 1)^2 (|\mathbf{n}|^2 - 1)^2 |\mathbf{m} - \mathbf{n}|^2} = -315.981(74). \quad (\text{B.146})$$

Analogous considerations hold for the  $\Omega_3$  series (cf. eq. (3.170)) emerging from the  $\delta \tilde{p}^4$  contributions to  $\mathcal{S}_3(\tilde{p})$ . For large values of  $|\mathbf{n}|$  the series proves to converge even more rapidly than  $\Omega_2$ , therefore the statistical errors associated to the sum are smaller,

$$\Omega_3 = \sum_{|\mathbf{n}| \neq 1}^{\infty} \sum_{\substack{\mathbf{m} \neq \mathbf{n} \\ |\mathbf{m}| \neq 1}}^{\infty} \frac{q_S(\mathbf{n}, \mathbf{m}) + \mathbf{m} \cdot \mathbf{n} q_X(\mathbf{n}, \mathbf{m})}{(|\mathbf{m}|^2 - 1)^3 (|\mathbf{n}|^2 - 1)^3 |\mathbf{m} - \mathbf{n}|^2} = -384.169(03). \quad (\text{B.147})$$

where the polynomials  $q_S(\mathbf{n}, \mathbf{m})$  and  $q_X(\mathbf{n}, \mathbf{m})$  (cf. eqs. (3.171) and (3.172)) in the numerator are given by

$$q_S(\mathbf{n}, \mathbf{m}) = -1 + 3|\mathbf{n}|^2 |\mathbf{m}|^2 - |\mathbf{m}|^2 |\mathbf{n}|^2 (|\mathbf{n}|^2 + |\mathbf{m}|^2) \quad (\text{B.148})$$

and

$$q_X(\mathbf{n}, \mathbf{m}) = 3 - 3(|\mathbf{n}|^2 + |\mathbf{m}|^2) + |\mathbf{m}|^2 |\mathbf{n}|^2 + |\mathbf{m}|^4 + |\mathbf{n}|^4. \quad (\text{B.149})$$

## B.2 Lüscher functions

We concentrate on the derivation of the large imaginary momentum  $\tilde{p} = i\tilde{k}$  limit of the double sums  $\mathcal{S}_2(\tilde{p})$  in eq. (2.98) and  $\mathcal{S}_3(\tilde{p})$  in eq. (3.148), encountered in the derivation of the finite volume energy corrections for the lowest bound  $A_1$  and  $T_1$  states in secs. 2.2.3 b) and 3.2.3 b) respectively.

### B.2.1 The $S_2$ sum

The large imaginary momentum limit of the double sum  $S_2(i\tilde{\kappa})$ , is recalled in the derivation of both the  $\ell = 0$  and in the  $\ell = 1$  finite volume energy corrections for the deepest bound states,  $\tilde{\kappa} \gg 1$ . Considering its expression in eq. (2.98),

$$S_2(i\tilde{\kappa}) = \sum_{\mathbf{n}} \sum_{\mathbf{m} \neq \mathbf{n}}^{\Lambda_n} \frac{1}{|\mathbf{m}|^2 + \tilde{\kappa}^2} \frac{1}{|\mathbf{n}|^2 + \tilde{\kappa}^2} \frac{1}{|\mathbf{m} - \mathbf{n}|^2} - 4\pi^4 \log \Lambda_n , \quad (\text{B.150})$$

we observe that the singularity  $\mathbf{m} = \mathbf{n}$  can be moved to  $\mathbf{m} = \mathbf{0}$  by operating a translation  $\mathbf{m} \mapsto \mathbf{n} + \mathbf{p}$  in the index of the unbound sum,

$$S_2(i\tilde{\kappa}) = \sum_{\mathbf{n}} \sum_{\mathbf{p} \neq \mathbf{0}}^{\Lambda_n} \frac{1}{|\mathbf{n} + \mathbf{p}|^2 + \tilde{\kappa}^2} \frac{1}{|\mathbf{n}|^2 + \tilde{\kappa}^2} \frac{1}{|\mathbf{p}|^2} - 4\pi^4 \log \Lambda_n . \quad (\text{B.151})$$

Now, we concentrate on the cutoff-regulated sum over  $\mathbf{n}$  and rewrite the argument of the latter in integral form,

$$S_2(i\tilde{\kappa}) = \sum_{\mathbf{p} \neq \mathbf{0}} \frac{1}{|\mathbf{p}|^2} \sum_{\mathbf{n}}^{\Lambda_n} \int_{\mathbb{R}^3} d^3q \frac{\delta(\mathbf{q} - \mathbf{n})}{|\mathbf{q} + \mathbf{p}|^2 + \tilde{\kappa}^2} \frac{\theta(\mathbf{q}^2 - \Lambda_n^2)}{|\mathbf{q}|^2 + \tilde{\kappa}^2} - 4\pi^4 \log \Lambda_n . \quad (\text{B.152})$$

where the integration variable represents dimensionless momentum in the continuum. Exploiting the Poisson summation formula for the infinite sum over  $\delta(\mathbf{q} - \mathbf{n})$ , eq. (B.152) becomes

$$S_2(i\tilde{\kappa}) = \sum_{\mathbf{p} \neq \mathbf{0}} \frac{1}{|\mathbf{p}|^2} \sum_{\mathbf{n}}^{\Lambda_n} \int_{\mathbb{R}^3} d^3q \frac{e^{-2\pi i \mathbf{q} \cdot \mathbf{n}}}{|\mathbf{q} + \mathbf{p}|^2 + \tilde{\kappa}^2} \frac{\theta(\mathbf{q}^2 - \Lambda_n^2)}{|\mathbf{q}|^2 + \tilde{\kappa}^2} - 4\pi^4 \log \Lambda_n . \quad (\text{B.153})$$

The argument of the integral can be simplified through the application of Feynman parametrization for the denominators, obtaining

$$S_2(i\tilde{\kappa}) = \sum_{\mathbf{p} \neq \mathbf{0}} \frac{1}{|\mathbf{p}|^2} \sum_{\mathbf{n}}^{\Lambda_n} \int_0^1 d\omega \int_{S_{\Lambda_n}^2} d^3q \frac{e^{-2\pi i \mathbf{q} \cdot \mathbf{n}}}{\{[\mathbf{q} + (1 - \omega)\mathbf{p}]^2 + \omega(1 - \omega)\mathbf{p}^2 + \tilde{\kappa}^2\}^2} - 4\pi^4 \log \Lambda_n . \quad (\text{B.154})$$

We operate in the integrand of the last equation the translation  $\mathbf{q} \mapsto \mathbf{q} - (1 - \omega)\mathbf{p}$ , which results into a spherical integration region of radius  $\Lambda_n$  displaced by  $-(1 - \omega)\mathbf{p}$  from the origin, that we denote with  $S_{\Lambda_n}^{\prime 2}$ . Therefore, eq. (B.154) becomes

$$S_2(i\tilde{\kappa}) = \sum_{\mathbf{p} \neq \mathbf{0}} \frac{1}{|\mathbf{p}|^2} \sum_{\mathbf{n}}^{\Lambda_n} \int_0^1 d\omega \int_{S_{\Lambda_n}^{\prime 2}} d^3q \frac{e^{-2\pi i \mathbf{q} \cdot \mathbf{n}} e^{+2\pi i (1 - \omega)\mathbf{p} \cdot \mathbf{n}}}{[\mathbf{q}^2 + \omega(1 - \omega)\mathbf{p}^2 + \tilde{\kappa}^2]^2} - 4\pi^4 \log \Lambda_n . \quad (\text{B.155})$$

The effect of the last operation consists in the shift of the anisotropy of the denominator into the integration region. In order to proceed further and unlock the evaluation of the integral, approximations in the original denominator or, equivalently, in the integration region have to be considered. With this purpose, we observe that the argument of the inner sum can be rewritten in a spherically symmetric fashion,

$$S_2(i\tilde{\kappa}) = \sum_{\mathbf{p} \neq \mathbf{0}} \frac{1}{|\mathbf{p}|^2} \sum_{\mathbf{n}}^{\Lambda_n} \int_0^1 d\omega \int_{S_{\Lambda_n}^{\prime 2}} d^3q \frac{e^{-2\pi i \mathbf{q} \cdot \mathbf{n}} e^{+2\pi i (1 - \omega)\mathbf{p} \cdot \mathbf{n}}}{[\mathbf{q}^2 + \omega(1 - \omega)\mathbf{p}^2 + \tilde{\kappa}^2]^2} + \mathcal{O}(\tilde{\kappa}^0) - 4\pi^4 \log \Lambda_n . \quad (\text{B.156})$$

at the expense of terms involving negative powers in  $\tilde{\kappa}$  smaller or equal than  $-2$ . Since we are only interested in tightly bound states, i.e.  $\tilde{\kappa} \gg 1$ , the approximation is justified, thus  $\mathcal{O}\left(\frac{1}{\tilde{\kappa}^2}\right)$  terms can be safely discarded henceforth. The crucial result in eq. (B.156) can be proven from the Taylor expansion of the denominator in the expression on the second row of eq. (B.154). After recalling that the sum over  $\mathbf{n}$  is real and smaller than the one with the modulus in the integrand,

$$\begin{aligned} & \sum_{\mathbf{n}} \int_{S_{\Lambda_n}^2} d^3q \frac{e^{-2\pi i \mathbf{q} \cdot \mathbf{n}}}{\{\mathbf{q}^2 + \tilde{\kappa}^2 + \omega(1-\omega)\mathbf{p}^2 + [(1-\omega)^2\mathbf{p}^2 + 2\mathbf{q} \cdot \mathbf{p}(1-\omega)]\}^2} \\ & \leq \sum_{\mathbf{n}} \int_{S_{\Lambda_n}^2} d^3q \frac{1}{\{\mathbf{q}^2 + \tilde{\kappa}^2 + \omega(1-\omega)\mathbf{p}^2 + [(1-\omega)^2\mathbf{p}^2 + 2\mathbf{q} \cdot \mathbf{p}(1-\omega)]\}^2}, \end{aligned} \quad (\text{B.157})$$

the anisotropic part of the denominator can be singled out and rewritten in power series of  $\mathbf{s} \equiv (1-\omega)\mathbf{p}$  with  $\mathcal{Q}^2 \equiv \tilde{\kappa}^2 + \omega(1-\omega)\mathbf{p}^2$ ,

$$\begin{aligned} \int_{S_{\Lambda_n}^2} d^3q \frac{1}{[\mathbf{q}^2 + \mathcal{Q}^2 + (\mathbf{s}^2 + 2\mathbf{q} \cdot \mathbf{s})]^2} &= \int_{S_{\Lambda_n}^2} d^3q \frac{1}{[\mathbf{q}^2 + \mathcal{Q}^2]^2} \left\{ 1 - 2 \frac{\mathbf{s}^2 + 2\mathbf{q} \cdot \mathbf{s}}{\mathbf{q}^2 + \mathcal{Q}^2} \right. \\ &\quad \left. + 3 \left[ \frac{\mathbf{s}^2 + 2\mathbf{q} \cdot \mathbf{s}}{\mathbf{q}^2 + \mathcal{Q}^2} \right]^2 - 4 \left[ \frac{\mathbf{s}^2 + 2\mathbf{q} \cdot \mathbf{s}}{\mathbf{q}^2 + \mathcal{Q}^2} \right]^3 + 5 \left[ \frac{\mathbf{s}^2 + 2\mathbf{q} \cdot \mathbf{s}}{\mathbf{q}^2 + \mathcal{Q}^2} \right]^4 + \dots \right\}. \end{aligned} \quad (\text{B.158})$$

Once in this form, the integral can be performed piecewise by grouping the terms containing the same powers of  $\mathbf{s}$ . Apart from the zero order term of the expansion, which gives rise to the approximation in eq. (B.156), the linear term in  $\mathbf{p}$  vanishes,

$$-4 \int_{S_{\Lambda_n}^2} d^3q \frac{\mathbf{q} \cdot \mathbf{s}}{[\mathbf{q}^2 + \mathcal{Q}^2]^3} = 0, \quad (\text{B.159})$$

due to the spherical symmetry of the cutoff. Concerning the quadratic term, the integration over momenta gives

$$\begin{aligned} -2 \int_{S_{\Lambda_n}^2} d^3q \frac{1}{[\mathbf{q}^2 + \mathcal{Q}^2]^3} \left[ \mathbf{s}^2 - 6 \frac{(\mathbf{s} \cdot \mathbf{q})^2}{\mathbf{q}^2 + \mathcal{Q}^2} \right] &= -8\pi \mathbf{s}^2 \left[ -\frac{\Lambda_n}{8\mathcal{Q}^2} \frac{\Lambda_n^2 - \mathcal{Q}^2}{(\Lambda_n^2 + \mathcal{Q}^2)^2} \right. \\ &\quad \left. - \frac{\Lambda_n}{24\mathcal{Q}^2} \frac{(\mathcal{Q}^2 - 3\Lambda_n^2)(3\mathcal{Q}^2 + \Lambda_n^2)}{(\mathcal{Q}^2 + \Lambda_n^2)^3} \right] = -\frac{\Lambda_n^3}{3} \frac{8\pi \mathbf{s}^2}{(\mathcal{Q}^2 + \Lambda_n^2)^3} = \mathcal{O}\left(\frac{\mathbf{p}^2}{\Lambda_n^3}\right) + \mathcal{O}\left(\frac{\mathbf{p}^2 \tilde{\kappa}^2}{\Lambda_n^5}\right) + \mathcal{O}\left(\frac{\mathbf{p}^4}{\Lambda_n^5}\right) + \dots \end{aligned} \quad (\text{B.160})$$

where the ellipsis denotes further powers of  $\mathbf{p}^2$ ,  $\tilde{\kappa}^2$  and  $\Lambda^{-1}$ , that can be concisely summarized as  $\mathcal{O}(\mathbf{p}^{2n} \tilde{\kappa}^{2(m-n)} \Lambda_n^{-2m-1})$  where  $m$  and  $n$  are positive nonzero integers. With reference to the external sum over  $\mathbf{p}$  and to the factor  $\mathbf{p}^{-2}$  in eq. (B.156), we infer that only the  $\tilde{\kappa}^2$ -dependent terms vanish in the  $\Lambda_n \rightarrow +\infty$  limit. The other terms, in fact, yield zero contribution only if the latter limit is taken before evaluating the outer sum. In the opposite case, the sum over  $\mathbf{p}$  produces an additive constant independent on  $\tilde{\kappa}$ , therefore it is possible to ignore it in the next developments of the calculation. On the other hand, the cubic terms in  $\mathbf{s}$  yield again zero, as all the other terms containing odd powers of  $(1-\omega)\mathbf{p}$ ,

$$-4 \int_{S_{\Lambda_n}^2} d^3q \frac{1}{[\mathbf{q}^2 + \mathcal{Q}^2]^4} \left[ 3\mathbf{s}^2 \mathbf{q} \cdot \mathbf{s} + \frac{8(\mathbf{s} \cdot \mathbf{q})^3}{\mathbf{q}^2 + \mathcal{Q}^2} \right] = 0. \quad (\text{B.161})$$

The next non-vanishing contributions are, then, given by the fourth order terms in  $\mathbf{s}$ , which turn out to be of the same order of the ones found in eq. (B.160),

$$\begin{aligned} \int_{S_{\Lambda_n}^2} d^3q \frac{1}{[\mathbf{q}^2 + \mathcal{Q}^2]^4} \left[ 3\mathbf{q}^4 - 48\mathbf{s}^2 \frac{(\mathbf{q} \cdot \mathbf{s})^2}{\mathbf{q}^2 + \mathcal{Q}^2} + 80 \frac{(\mathbf{q} \cdot \mathbf{s})^4}{(\mathbf{q}^2 + \mathcal{Q}^2)^2} \right] &= 4\pi\mathbf{s}^4 \left[ -\frac{\Lambda_n}{16\mathcal{Q}^4} \frac{(\mathcal{Q}^2 - 3\Lambda_n^2)(3\mathcal{Q}^2 + \Lambda_n^2)}{(\mathcal{Q}^2 + \Lambda_n^2)^3} \right. \\ &+ \frac{\Lambda_n}{8\mathcal{Q}^4} \frac{(\mathcal{Q}^2 - \Lambda_n^2)(3\mathcal{Q}^4 + 14\mathcal{Q}^2\Lambda_n^2 + 3\Lambda_n^4)}{(\mathcal{Q}^2 + \Lambda_n^2)^4} - \frac{\Lambda_n}{80\mathcal{Q}^4} \frac{15\mathcal{Q}^8 + 70\mathcal{Q}^6\Lambda_n^2 + 128\mathcal{Q}^4\Lambda_n^4 - 70\mathcal{Q}^2\Lambda_n^6 - 15\Lambda_n^8}{(\mathcal{Q}^2 + \Lambda_n^2)^5} \Big] \\ &= 2\pi\mathbf{s}^4 \frac{35\Lambda_n^7 - 6\mathcal{Q}^2\Lambda_n^5 + 10\Lambda_n^3\mathcal{Q}^4}{5\mathcal{Q}^2(\mathcal{Q}^2 + \Lambda_n^2)^5} = \mathcal{O}\left(\frac{\mathbf{p}^2}{\Lambda_n^3}\right) + \mathcal{O}\left(\frac{\mathbf{p}^2\tilde{\kappa}^2}{\Lambda_n^5}\right) + \mathcal{O}\left(\frac{\mathbf{p}^4}{\Lambda_n^5}\right) + \mathcal{O}\left(\frac{\mathbf{p}^4\tilde{\kappa}^2}{\Lambda_n^7}\right) + \mathcal{O}\left(\frac{\mathbf{p}^6}{\Lambda_n^7}\right) + \dots \end{aligned} \quad (\text{B.162})$$

The only menaingful contributions are provided by the  $\mathbf{p}^{2m}/\Lambda_n^{2m+1}$  terms, which sum up to another constant when the limit  $\Lambda_n \rightarrow +\infty$  is taken after the evaluation of the sum over  $\mathbf{p}$  or, otherwise, to zero. Analogous contributions are produced by the other powers of  $\mathbf{s}$ , whose results are omitted for brevity. Thus, we can concluede that the anisotropic effects in the integration region  $\delta S_{\Lambda_n}^2 = S'_{\Lambda_n} - S_{\Lambda_n}^2$  produced by the above translation in momentum space  $\mathbf{q} \mapsto \mathbf{q} - (1 - \omega)\mathbf{p}$  do not depend on the finite-volume binding momentum  $\tilde{\kappa}$ .

At this stage, we resume the spherically symmetric version of  $\mathcal{S}(i\tilde{\kappa})$  in eq. (B.156) and we isolate the zero modes from the others in the sum over  $\mathbf{n}$ ,

$$\begin{aligned} S_2(i\tilde{\kappa}) &= \sum_{\mathbf{p} \neq 0} \frac{1}{|\mathbf{p}|^2} \int_0^1 d\omega \int_{S_{\Lambda_n}^2} d^3q \frac{1}{[\mathbf{q}^2 + \omega(1 - \omega)\mathbf{p}^2 + \tilde{\kappa}^2]^2} - 4\pi^4 \log \Lambda_n \\ &+ \sum_{\mathbf{p} \neq 0} \frac{1}{|\mathbf{p}|^2} \sum_{\mathbf{n} \neq 0} \int_0^1 d\omega \int_{S_{\Lambda_n}^2} d^3q \frac{e^{-2\pi i \mathbf{q} \cdot \mathbf{n}} e^{+2\pi i (1 - \omega)\mathbf{p} \cdot \mathbf{n}}}{[\mathbf{q}^2 + \omega(1 - \omega)\mathbf{p}^2 + \tilde{\kappa}^2]^2} + \mathcal{O}(\tilde{\kappa}^0), \end{aligned} \quad (\text{B.163})$$

and we analyze separately the contributions stemming from the two terms. Let us start with the discussion of the contribution in the first row of eq. (B.163),

$$\begin{aligned} &\sum_{\mathbf{p} \neq 0} \frac{1}{|\mathbf{p}|^2} \int_0^1 d\omega \int_{S_{\Lambda_n}^2} d^3q \frac{1}{[\mathbf{q}^2 + \omega(1 - \omega)\mathbf{p}^2 + \tilde{\kappa}^2]^2} - 4\pi^4 \log \Lambda_n \\ &= - \sum_{\mathbf{p} \neq 0} \frac{4\pi}{|\mathbf{p}|^2} \int_0^1 d\omega \frac{\Lambda_n}{2} \frac{1}{\Lambda_n^2 + \mathcal{Q}^2} + \sum_{\mathbf{p} \neq 0} \frac{4\pi}{|\mathbf{p}|^2} \int_0^1 d\omega \frac{1}{2\mathcal{Q}} \arctan\left(\frac{\Lambda_n}{\mathcal{Q}}\right) - 4\pi^4 \log \Lambda_n, \end{aligned} \quad (\text{B.164})$$

where, in the intermediate step, the quantity  $\mathcal{Q}^2 \equiv \omega(1 - \omega)\mathbf{p}^2 + \tilde{\kappa}^2$  has been defined and the integration over the angular variables associated to  $\mathbf{q}$  has been performed. In particular, the first term in the third row of the last equation proves to converge to a constant in the large cutoff  $\Lambda_n$  limit, as it can be shown by splitting the summation over  $\mathbf{p}$  into two parts,

$$- \sum_{\mathbf{p} \neq 0} \frac{4\pi}{|\mathbf{p}|^2} \int_0^1 d\omega \frac{\Lambda_n}{2} \frac{1}{\Lambda_n^2 + \mathcal{Q}^2} = - \sum_{\mathbf{p} \neq 0} \frac{2\pi}{|\mathbf{p}|^2} \int_0^1 d\omega \frac{\Lambda_n}{\Lambda_n^2 + \mathcal{Q}^2} - \sum_{|\mathbf{p}| > 2\tilde{\kappa}} \frac{2\pi}{|\mathbf{p}|^2} \int_0^1 d\omega \frac{\Lambda_n}{\Lambda_n^2 + \mathcal{Q}^2}, \quad (\text{B.165})$$

where the absolute value of the first term on the r.h.s. gives

$$\sum_{\mathbf{p} \neq 0} \frac{2\pi}{|\mathbf{p}|^2} \int_0^1 d\omega \frac{\Lambda_n}{\Lambda_n^2 + \mathcal{Q}^2} < \sum_{\mathbf{p} \neq 0} \frac{2\pi}{|\mathbf{p}|^2} \frac{\Lambda_n}{\Lambda_n^2 + \kappa^2} < \frac{2\pi}{\Lambda_n} \sum_{\mathbf{p} \neq 0} \frac{1}{|\mathbf{p}|^2} = \frac{2\pi}{\Lambda_n} \mathcal{G}^{(0)} + \frac{16\pi^2}{\Lambda_n} \tilde{\kappa}, \quad (\text{B.166})$$



which vanishes in the  $\Lambda_n \rightarrow +\infty$  limit. On the other hand, the second term is finite,

$$\begin{aligned} \sum_{|\mathbf{p}| > 2\tilde{\kappa}}^{\infty} \frac{2\pi}{|\mathbf{p}|^2} \int_0^1 d\omega \frac{\Lambda_n}{\Lambda_n^2 + \mathbf{q}^2} &= \sum_{|\mathbf{p}| > 2\tilde{\kappa}}^{\infty} \frac{2\pi}{|\mathbf{p}|^3} \frac{\Lambda_n}{\sqrt{4\tilde{\kappa}^2 + 4\Lambda_n^2 + \mathbf{p}^2}} \\ &\cdot \left( \log(|\mathbf{p}| + \sqrt{4\tilde{\kappa}^2 + 4\Lambda_n^2 + \mathbf{p}^2}) - \log(|\mathbf{p}| - \sqrt{4\tilde{\kappa}^2 + 4\Lambda_n^2 + \mathbf{p}^2}) \right) < +\infty, \end{aligned} \quad (\text{B.167})$$

as it can be proven numerically by promoting the remaining sum into an integral. The subsequent evaluation of the integral for a wide range of  $\tilde{\kappa} \geq 1$  and  $\Lambda_n \gg \tilde{\kappa}$ , in fact, yields  $2\pi\lambda_1$  where  $\lambda_1 = 4.9348(1)$ . From the numerical result, it follows that the original sum is bound and independent on the binding momentum. Since real constants do not deliver any contribution to the finite volume energy corrections, also the  $\tilde{\kappa}$ -independent nonzero term from eq. (B.167) can be neglected, as done in eq. (B.156).

Now we resume the evaluation of the second term in the second row of eq. (B.164), which contains the logarithmic divergence. As in eq. (B.165), we split the summation over  $\mathbf{p}$  into two pieces and perform the integration on  $\omega$  separately,

$$\begin{aligned} \sum_{\mathbf{p} \neq 0}^{\infty} \frac{4\pi}{|\mathbf{p}|^2} \int_0^1 d\omega \frac{1}{2\Omega} \arctan\left(\frac{\Lambda_n}{\Omega}\right) - 2\pi^4 \log \Lambda_n &= \sum_{\mathbf{p} \neq 0}^{2\tilde{\kappa}} \frac{2\pi}{|\mathbf{p}|^2} \int_0^1 d\omega \frac{1}{\Omega} \arctan\left(\frac{\Lambda_n}{\Omega}\right) \\ &+ \sum_{|\mathbf{p}| > 2\tilde{\kappa}}^{\infty} \frac{2\pi}{|\mathbf{p}|^2} \int_0^1 d\omega \frac{1}{\Omega} \arctan\left(\frac{\Lambda_n}{\Omega}\right) - 4\pi^4 \log \Lambda_n. \end{aligned} \quad (\text{B.168})$$

Focusing on the first term on the r.h.s. of the last equation, we replace the arctangent function by its maximum value assumed for real arguments,

$$\begin{aligned} \sum_{\mathbf{p} \neq 0}^{2\tilde{\kappa}} \frac{2\pi}{|\mathbf{p}|^2} \int_0^1 d\omega \frac{1}{\Omega} \arctan\left(\frac{\Lambda_n}{\Omega}\right) &< \sum_{\mathbf{p} \neq 0}^{2\tilde{\kappa}} \frac{2\pi}{|\mathbf{p}|^2} \int_0^1 d\omega \frac{1}{\Omega} \frac{\pi}{2} \\ &= \pi^2 \sum_{\mathbf{p} \neq 0}^{2\tilde{\kappa}} \frac{1}{\mathbf{p}^2} \int_0^1 d\omega \frac{1}{\sqrt{\omega(1-\omega)\mathbf{p}^2 + \tilde{\kappa}^2}} = 2\pi^2 \sum_{\mathbf{p} \neq 0}^{2\tilde{\kappa}} \frac{1}{|\mathbf{p}|^3} \arctan\left(\frac{|\mathbf{p}|}{2\tilde{\kappa}}\right), \end{aligned} \quad (\text{B.169})$$

thus binding the series from above and allowing for a straightforward evaluation of the integral over the  $\omega$ . Then, we observe that the arctangent is always evaluated for arguments smaller or equal to one in the considered interval of  $\mathbf{p}$ , so that the series can be constrained again from above, replacing  $\arctan\left(\frac{|\mathbf{p}|}{2\tilde{\kappa}}\right)$  by  $|\mathbf{p}|/2\tilde{\kappa}$ ,

$$2\pi^2 \sum_{\mathbf{p} \neq 0}^{2\tilde{\kappa}} \frac{1}{|\mathbf{p}|^3} \arctan\left(\frac{|\mathbf{p}|}{2\tilde{\kappa}}\right) < \sum_{\mathbf{p} \neq 0}^{2\tilde{\kappa}} \frac{1}{|\mathbf{p}|^2} \frac{\pi^2}{\tilde{\kappa}} = \frac{\pi^2}{\tilde{\kappa}} \sum_{\mathbf{p} \neq 0}^{2\tilde{\kappa}} \frac{1}{\mathbf{p}^2} = \frac{\pi^2}{\tilde{\kappa}} \mathcal{G}^{(0)} + 8\pi^3. \quad (\text{B.170})$$

Differently from the previous cases, the result is a function of  $\tilde{\kappa}$  which provides a contribution to the finite volume energy corrections, therefore has to be conserved. Finally, we concentrate on the second term on the r.h.s. of eq. (B.168), which is responsible of the ultraviolet logarithmic divergence. As in eq. (B.169), we proceed by binding the series from above, exploiting

the properties of the arctangent function,

$$2\pi \sum_{|\mathbf{p}| > \tilde{\kappa}} \int_0^1 d\omega \frac{\arctan\left(\frac{\Lambda_n}{\sqrt{\tilde{\kappa}^2 + \omega(1-\omega)\mathbf{p}^2}}\right)}{|\mathbf{p}|^2 \sqrt{\tilde{\kappa}^2 + \omega(1-\omega)\mathbf{p}^2}} - 4\pi^4 \log \Lambda_n < \sum_{|\mathbf{p}| > \tilde{\kappa}} \frac{\pi^2}{\mathbf{p}^2} \int_0^1 \frac{d\omega}{\sqrt{\tilde{\kappa}^2 + \omega(1-\omega)\mathbf{p}^2}} - 4\pi^4 \log \Lambda_n . \quad (\text{B.171})$$

Performing the integral over  $\omega$  and capturing the asymptotic behaviour of the remaining summation over  $\mathbf{p}$ , eq. (B.171) can be rewritten as

$$\sum_{|\mathbf{p}| > \tilde{\kappa}} \frac{2\pi^2}{\mathbf{p}^3} \arctan\left(\frac{|\mathbf{p}|}{2\tilde{\kappa}}\right) - 4\pi^4 \log \Lambda_n = \sum_{|\mathbf{p}| > \tilde{\kappa}} \frac{\pi^3}{|\mathbf{p}|^3} \approx \lim_{\Lambda_p \rightarrow +\infty} 4\pi^4 \log \Lambda_p \quad (\text{B.172})$$

$$-4\pi^4 \log 2\tilde{\kappa} - 4\pi^4 \log \Lambda_n = -4\pi^4 \log 2\tilde{\kappa} ,$$

where the find another meaningful contribution to the original double sum  $S_2(i\tilde{\kappa})$ , which is expected to dominate in the large binding momentum regime. Now, we switch to the evaluation of the second term on the r.h.s. of eq. (B.163), involving the non-zero modes of the original Poisson formula. Performing the integration over the angular variables, we obtain

$$\begin{aligned} \sum_{\mathbf{p} \neq 0} \frac{1}{|\mathbf{p}|^2} \sum_{\mathbf{n} \neq 0} \int_0^1 d\omega e^{-i2\pi(1-\omega)\mathbf{p} \cdot \mathbf{n}} \int_{S_{\Lambda_n}^2} d^3q \frac{e^{i2\pi\mathbf{q} \cdot \mathbf{n}}}{[\mathbf{q}^2 + \omega(1-\omega)\mathbf{p}^2 + \tilde{\kappa}^2]^2} \\ = \sum_{\mathbf{p} \neq 0} \frac{1}{|\mathbf{p}|^2} \sum_{\mathbf{n} \neq 0} \int_0^1 d\omega e^{-i2\pi(1-\omega)\mathbf{p} \cdot \mathbf{n}} \int_0^{\Lambda_n} dq \frac{|\mathbf{q}|}{i|\mathbf{n}|} \frac{e^{i2\pi|\mathbf{q}||\mathbf{n}|} - e^{-i2\pi|\mathbf{q}||\mathbf{n}|}}{[\mathbf{q}^2 + \omega(1-\omega)\mathbf{p}^2 + \tilde{\kappa}^2]^2} . \end{aligned} \quad (\text{B.173})$$

In this form, it becomes evident that the argument of the radial integral over the momenta  $\mathbf{q}$  is even and tends uniformly to zero in the limit  $|\mathbf{q}| \rightarrow +\infty$  and is analytical all over the complex plane  $q \in \mathbb{C}$ , except for two double poles at  $q_{\pm} = \pm i\sqrt{\tilde{\kappa}^2 + \omega(1-\omega)\mathbf{p}^2}$ , located along the imaginary axis. Since the spherical cutoff is large, the integration region can be extended to an arbitrary large circular region about the origin of the complex plane encompassing the two singularities. Moreover, the integrand can be split into two functions of complex variable  $q = |\mathbf{q}|$ ,

$$f_{\pm}(q) = \frac{q}{i|\mathbf{n}|} \frac{e^{\pm i2\pi q|\mathbf{n}|}}{(q - q_+)^2(q - q_-)^2} , \quad (\text{B.174})$$

so that  $f_+(q)$  (resp.  $f_-(q)$ ) can be integrated in a semicircle with radius  $\Lambda_n$  about the origin in the upper (resp. lower) part of the complex plane picking up the  $q_+$  (resp.  $q_-$ ) singularity, according to Jordan's Lemma. The residues about the two double poles turn out to coincide and eq. (B.173) becomes

$$\sum_{\mathbf{p} \neq 0} \frac{1}{|\mathbf{p}|^2} \int_0^1 d\omega \sum_{\mathbf{n} \neq 0} \frac{\pi}{|\mathbf{n}|} \frac{1 + 2\pi|\mathbf{n}|\sqrt{\omega(1-\omega)\mathbf{p}^2 + \tilde{\kappa}^2}}{\omega(1-\omega)\mathbf{p}^2 + \tilde{\kappa}^2} e^{-2\pi|\mathbf{n}|\sqrt{\omega(1-\omega)\mathbf{p}^2 + \tilde{\kappa}^2}} e^{-i2\pi(1-\omega)\mathbf{p} \cdot \mathbf{n}} . \quad (\text{B.175})$$

Even if the two series in eq. (B.175) can not be evaluated analytically, their sum is expected to converge, since the logarithmic divergence with the three-dimensional cutoff has been already absorbed by the summation in eq. (B.172). Nevertheless, the convergence of eq. (B.175) can be

demonstrated independently, by finding suitable upper bounds to eq. (B.175) and performing the final sums numerically. With this aim, we split the last equation into two parts according to the numerator of the inner sum and constrain eq. (B.175) from above by taking the modulus of the argument of the inner sum,

$$\sum_{\mathbf{p} \neq 0} \frac{1}{|\mathbf{p}|^2} \int_0^1 d\omega \sum_{\mathbf{n} \neq 0} \frac{\pi}{|\mathbf{n}|} \frac{e^{-2\pi|\mathbf{n}|\sqrt{\omega(1-\omega)\mathbf{p}^2 + \tilde{\kappa}^2}}}{\omega(1-\omega)\mathbf{p}^2 + \tilde{\kappa}^2} + \sum_{\mathbf{p} \neq 0} \frac{2\pi^2}{|\mathbf{p}|^2} \int_0^1 d\omega \sum_{\mathbf{n} \neq 0} \frac{e^{-2\pi|\mathbf{n}|\sqrt{\omega(1-\omega)\mathbf{p}^2 + \tilde{\kappa}^2}}}{\sqrt{\omega(1-\omega)\mathbf{p}^2 + \tilde{\kappa}^2}}. \quad (\text{B.176})$$

In this guise, the oscillating complex exponential has been ruled out. Next, we factorize the exponential term as follows,

$$e^{-2\pi|\mathbf{n}|\sqrt{\tilde{\kappa}^2 + \omega(1-\omega)\mathbf{p}^2}} = e^{-\frac{2\pi}{3}|\mathbf{n}|\sqrt{\tilde{\kappa}^2 + \omega(1-\omega)\mathbf{p}^2}} e^{-\frac{2\pi}{3}|\mathbf{n}|\sqrt{\tilde{\kappa}^2 + \omega(1-\omega)\mathbf{p}^2}} \cdot e^{-\frac{2\pi}{3}|\mathbf{n}|\sqrt{\tilde{\kappa}^2 + \omega(1-\omega)\mathbf{p}^2}} \leq e^{-\frac{2\pi}{3}\tilde{\kappa}} e^{-\frac{2\pi}{3}\tilde{\kappa}|\mathbf{n}|} e^{-\frac{\pi}{3}\sqrt{\omega(1-\omega)}|\mathbf{p}|}, \quad (\text{B.177})$$

where the constraint  $|\mathbf{n}|, |\mathbf{p}| \geq 1$  have been exploited, in order to isolate the dependence on  $\mathbf{p}$ ,  $\mathbf{n}$  and  $\tilde{\kappa}$  and to enable a separate evaluation of the sums over the finite-volume momenta. Plugging the result of eq. (B.177) into the first term of eq. (B.176), we find

$$\sum_{\mathbf{p} \neq 0} \frac{1}{|\mathbf{p}|^2} \int_0^1 d\omega \sum_{\mathbf{n} \neq 0} \frac{\pi}{|\mathbf{n}|} \frac{e^{-2\pi|\mathbf{n}|\sqrt{\omega(1-\omega)\mathbf{p}^2 + \tilde{\kappa}^2}}}{\omega(1-\omega)\mathbf{p}^2 + \tilde{\kappa}^2} < \sum_{\mathbf{p} \neq 0} \int_0^1 d\omega \frac{e^{-\frac{\pi}{3}\sqrt{\omega(1-\omega)}|\mathbf{p}|}}{|\mathbf{p}|^2} \sum_{\mathbf{n} \neq 0} \frac{\pi}{|\mathbf{n}|} \frac{e^{-\frac{2\pi}{3}\tilde{\kappa}} e^{-\frac{2\pi}{3}\tilde{\kappa}|\mathbf{n}|}}{\omega(1-\omega)\mathbf{p}^2 + \tilde{\kappa}^2}. \quad (\text{B.178})$$

Considering the limit  $\tilde{\kappa} \gg 1$ , a complete factorization between the summations over  $\mathbf{p}$  and  $\mathbf{n}$  can be achieved,

$$\begin{aligned} \sum_{\mathbf{p} \neq 0} \int_0^1 d\omega \frac{e^{-\frac{\pi}{3}\sqrt{\omega(1-\omega)}|\mathbf{p}|}}{|\mathbf{p}|^2} \sum_{\mathbf{n} \neq 0} \frac{\pi}{|\mathbf{n}|} \frac{e^{-\frac{2\pi}{3}\tilde{\kappa}} e^{-\frac{2\pi}{3}\tilde{\kappa}|\mathbf{n}|}}{\omega(1-\omega)\mathbf{p}^2 + \tilde{\kappa}^2} \\ < e^{-\frac{2\pi}{3}\tilde{\kappa}} \left[ \sum_{\mathbf{p} \neq 0} \frac{\pi}{\mathbf{p}^2} \int_0^1 d\omega \frac{e^{-\frac{\pi}{3}\sqrt{\omega(1-\omega)}|\mathbf{p}|}}{\omega(1-\omega)\mathbf{p}^2 + 1} \right] \sum_{\mathbf{n} \neq 0} \frac{e^{-\frac{2\pi}{3}|\mathbf{n}|}}{|\mathbf{n}|} = \lambda_2 \lambda_3 e^{-\frac{2\pi}{3}\tilde{\kappa}}, \end{aligned} \quad (\text{B.179})$$

where in the argument of the sums over  $\mathbf{p}$  and  $\mathbf{n}$ ,  $\tilde{\kappa}$  has been replaced by its lowest allowed value and  $\lambda_2, \lambda_3$  are numerical constants, equal to 1.65744(1) and 641.79(20) respectively. Moreover, the factor in front of the two summations ensures that the first term in eq. (B.176) gives rise to finite volume corrections which are exponentially suppressed with respect to the ones in eqs. (B.170) and (B.172), thus can be neglected. Similarly, thanks to eq. (B.177), the second term in eq. (B.176) can be recast as

$$\sum_{\mathbf{p} \neq 0} \frac{2\pi^2}{|\mathbf{p}|^2} \int_0^1 d\omega \sum_{\mathbf{n} \neq 0} \frac{e^{-2\pi|\mathbf{n}|\sqrt{\omega(1-\omega)\mathbf{p}^2 + \tilde{\kappa}^2}}}{\sqrt{\omega(1-\omega)\mathbf{p}^2 + \tilde{\kappa}^2}} < \sum_{\mathbf{p} \neq 0} \frac{2\pi^2}{|\mathbf{p}|^2} \int_0^1 d\omega e^{-\frac{\pi}{3}\sqrt{\omega(1-\omega)}|\mathbf{p}|} \sum_{\mathbf{n} \neq 0} \frac{e^{-\frac{2\pi}{3}\tilde{\kappa}} e^{-\frac{2\pi}{3}\tilde{\kappa}|\mathbf{n}|}}{\sqrt{\omega(1-\omega)\mathbf{p}^2 + \tilde{\kappa}^2}}, \quad (\text{B.180})$$

which factorizes into

$$\begin{aligned} \sum_{\mathbf{p} \neq 0} \frac{2\pi^2}{|\mathbf{p}|^2} \int_0^1 d\omega e^{-\frac{\pi}{3}\sqrt{\omega(1-\omega)}|\mathbf{p}|} \sum_{\mathbf{n} \neq 0} \frac{e^{-\frac{2\pi}{3}\tilde{\kappa}} e^{-\frac{2\pi}{3}\tilde{\kappa}|\mathbf{n}|}}{\sqrt{\omega(1-\omega)\mathbf{p}^2 + \tilde{\kappa}^2}} \\ < e^{-\frac{2\pi}{3}\tilde{\kappa}} \left[ \sum_{\mathbf{p} \neq 0} \frac{2\pi^2}{|\mathbf{p}|^2} \int_0^1 d\omega \frac{e^{-\frac{\pi}{3}\sqrt{\omega(1-\omega)}|\mathbf{p}|}}{\sqrt{\omega(1-\omega)\mathbf{p}^2 + 1}} \right] \sum_{\mathbf{n} \neq 0} e^{-\frac{2\pi}{3}|\mathbf{n}|} = \lambda_4 \lambda_5 e^{-\frac{2\pi}{3}\tilde{\kappa}}. \end{aligned} \quad (\text{B.181})$$

The numerical evaluation of the two sums in the brackets of eq. (B.181) yields finite results  $\lambda_4 = 2.23861(1)$  and  $\lambda_5 = 1080.48(57)$ . At this point, the proof can be concluded by collecting the results from eqs. (B.166), (B.167), (B.170) and (B.172), which reconstruct the behaviour of the double sum  $S_2(i\tilde{\kappa})$  in the tight binding limit,

$$S_2(i\tilde{\kappa}) = \sum_{\mathbf{n}}^{\Lambda_n} \sum_{\mathbf{m} \neq \mathbf{n}}^{\infty} \frac{1}{|\mathbf{m}|^2 + \tilde{\kappa}^2} \frac{1}{|\mathbf{n}|^2 + \tilde{\kappa}^2} \frac{1}{|\mathbf{m} - \mathbf{n}|^2} - 2\pi^4 \log \Lambda_n = \frac{\pi^2}{\tilde{\kappa}} \mathcal{G}^{(0)} - 4\pi^4 \log 2\tilde{\kappa} + \dots, \quad (\text{B.182})$$

where the ellipsis stands for real constants or exponentially suppressed contributions with  $\tilde{\kappa}$  analogous to the ones in eqs. (B.179) and (B.181).

### B.2.2 The $S_3$ sum

We now embark on the derivation of the large imaginary momentum limit of the double sum  $S_3(i\tilde{\kappa})$  in eq. (3.148), implied in the calculation of the finite volume shifts for the lowest bound  $T_1$  state. With this aim, we start by splitting the original Lüscher function  $S_3(i\tilde{\kappa})$  into three parts,

$$S_3(i\tilde{\kappa}) = \sum_{\mathbf{n}}^{\Lambda_n} \sum_{\mathbf{m} \neq \mathbf{n}}^{+\infty} \frac{1}{|\mathbf{n}|^2 + \tilde{\kappa}^2} \frac{1}{|\mathbf{m}|^2 + \tilde{\kappa}^2} \frac{\mathbf{n} \cdot \mathbf{m} + \tilde{\kappa}^2}{|\mathbf{n} - \mathbf{m}|^2} - \pi^4 \Lambda_n^2 = \lim_{\Lambda_m \rightarrow \infty} \left\{ \mathfrak{S}_1^{\Lambda_m} + \mathfrak{S}_2^{\Lambda_m} + \mathfrak{S}_3^{\Lambda_m} \right\} - \pi^4 \Lambda_n^2, \quad (\text{B.183})$$

where  $\Lambda_m$  is a spherical cutoff accounting for the divergence of the following sums over  $\mathbf{m}$ ,

$$\mathfrak{S}_1^{\Lambda_m} = \frac{1}{2} \sum_{\mathbf{n}}^{\Lambda_n} \sum_{\mathbf{m} \neq \mathbf{n}}^{\Lambda_m} \frac{1}{|\mathbf{m}|^2 + \tilde{\kappa}^2} \frac{1}{|\mathbf{m} - \mathbf{n}|^2}, \quad (\text{B.184})$$

$$\mathfrak{S}_2^{\Lambda_m} = \frac{1}{2} \sum_{\mathbf{n}}^{\Lambda_n} \sum_{\mathbf{m} \neq \mathbf{n}}^{\Lambda_m} \frac{1}{|\mathbf{n}|^2 + \tilde{\kappa}^2} \frac{1}{|\mathbf{m} - \mathbf{n}|^2}, \quad (\text{B.185})$$

$$\mathfrak{S}_3^{\Lambda_m} = -\frac{1}{2} \sum_{\mathbf{n}}^{\Lambda_n} \sum_{\mathbf{m} \neq \mathbf{n}}^{\Lambda_m} \frac{1}{|\mathbf{n}|^2 + \tilde{\kappa}^2} \frac{1}{|\mathbf{m}|^2 + \tilde{\kappa}^2}. \quad (\text{B.186})$$

Due to the presence of a cutoff in the inner sum, the translation in momentum space operated in the  $S_2(i\tilde{\kappa})$  case (cf. Appendix A3 in ref. [1] and app. B.2.1) is no longer allowed in the individual sums (cf. eqs. (B.184)-(B.186)). Nevertheless, since the purpose is the extraction of the finite and  $\tilde{\kappa}$ -dependent contributions from each of the three double sums in eq. (B.183), terms depending on nonzero powers of  $\Lambda_m$  and  $\Lambda_n$  can be neglected without loss of information

for the FVECs. Therefore, we assume henceforth the limits  $\Lambda_n, \Lambda_m \rightarrow +\infty$  and extract the finite parts from the sums depending on the binding momentum. Now, we consider the first of the three double sums in the last row of eq. (B.183). After the translation in the momenta  $\mathbf{m} \mapsto \mathbf{m} - \mathbf{n} \equiv \mathbf{p}$ , we rewrite the argument of the inner sum in integral form,

$$\mathfrak{S}_1^\infty = \frac{1}{2} \sum_{\mathbf{p} \neq 0} \frac{1}{|\mathbf{p}|^2} \int_{\mathbb{R}^3} d^3\mathbf{q} \sum_{\mathbf{n}} \frac{\delta^3(\mathbf{q} - \mathbf{n})}{|\mathbf{q} + \mathbf{p}|^2 + \tilde{\kappa}^2}. \quad (\text{B.187})$$

We apply the Poisson summation formula to the unconstrained sum over  $\mathbf{n}$  and isolate the zero modes from the nonzero ones,

$$\mathfrak{S}_1^\infty = \frac{1}{2} \sum_{\mathbf{p} \neq 0} \frac{1}{|\mathbf{p}|^2} \int_{\mathbb{R}^3} d^3\mathbf{q} \frac{1}{|\mathbf{q} + \mathbf{p}|^2 + \tilde{\kappa}^2} + \frac{1}{2} \sum_{\mathbf{p} \neq 0} \frac{1}{|\mathbf{p}|^2} \sum_{\mathbf{n} \neq 0} \int_{\mathbb{R}^3} d^3\mathbf{q} \frac{e^{-i2\pi\mathbf{q} \cdot \mathbf{n}}}{|\mathbf{q} + \mathbf{p}|^2 + \tilde{\kappa}^2}. \quad (\text{B.188})$$

Concentrating on the first term of eq. (B.188), we perform the translation in momentum space  $\mathbf{q} \mapsto \mathbf{q} - \mathbf{p} \equiv \mathbf{l}$  and integrate over the angular variables associated to  $\mathbf{l}$ ,

$$\frac{1}{2} \sum_{\mathbf{p} \neq 0} \frac{1}{|\mathbf{p}|^2} \int_{\mathbb{R}^3} d^3\mathbf{q} \frac{1}{|\mathbf{q} + \mathbf{p}|^2 + \tilde{\kappa}^2} = 2\pi \sum_{\mathbf{p} \neq 0} \frac{1}{|\mathbf{p}|^2} \int_0^{+\infty} dl - 2\pi \sum_{\mathbf{p} \neq 0} \frac{1}{|\mathbf{p}|^2} \int_0^{+\infty} dl \frac{\tilde{\kappa}^2}{l^2 + \tilde{\kappa}^2}. \quad (\text{B.189})$$

As it can be inferred, the first term on the r.h.s. of the last equation is independent on  $\tilde{\kappa}$  and unbound, thus it can be neglected. On the other hand, the integral in the second term is finite and generates linear contributions in the binding momentum,

$$-2\pi \sum_{\mathbf{p} \neq 0} \frac{1}{|\mathbf{p}|^2} \int_0^{+\infty} dl \frac{\tilde{\kappa}^2}{l^2 + \tilde{\kappa}^2} = -2\pi\tilde{\kappa} \sum_{\mathbf{p} \neq 0} \frac{1}{|\mathbf{p}|^2} \arctan(x) \Big|_0^{+\infty} = -\pi^2\tilde{\kappa} \sum_{\mathbf{p} \neq 0} \frac{1}{|\mathbf{p}|^2}. \quad (\text{B.190})$$

Moreover, the remaining sum in eq. (B.189) can be evaluated by splitting it into two parts,

$$-\pi^2\tilde{\kappa} \sum_{\mathbf{p} \neq 0} \frac{1}{|\mathbf{p}|^2} = -\pi^2\tilde{\kappa} \sum_{\mathbf{p} \neq 0} \frac{1}{\mathbf{p}^2} - \pi^2\tilde{\kappa} \sum_{|\mathbf{p}| > 2\tilde{\kappa}} \frac{1}{\mathbf{p}^2} \approx -\pi^2\tilde{\kappa}(\mathcal{G}^{(0)} + 8\pi\tilde{\kappa}) - 4\pi^3\tilde{\kappa} \int_{2\tilde{\kappa}}^{+\infty} dp \rightarrow -\pi^2\mathcal{G}^{(0)}\tilde{\kappa}, \quad (\text{B.191})$$

where, in the last step, the sum has been approximated by an integral, since the binding momentum is expected to be large,  $\tilde{\kappa} \gg 1$ . Additionally, the linearly divergent part of the radial integral has been consistently discarded. At this stage, we focus on the nonzero modes, i.e. the second term in eq. (B.188). After performing the translation  $\mathbf{q} \mapsto \mathbf{q} - \mathbf{p} \equiv \mathbf{l}$ , we integrate over the angular variables associated to  $\mathbf{l}$  and simplify the expression as

$$\frac{1}{2} \sum_{\mathbf{p} \neq 0} \frac{1}{|\mathbf{p}|^2} \sum_{\mathbf{n} \neq 0} \int_{\mathbb{R}^3} d^3\mathbf{q} \frac{e^{-i2\pi\mathbf{q} \cdot \mathbf{n}}}{|\mathbf{q} + \mathbf{p}|^2 + \tilde{\kappa}^2} = \frac{1}{2} \sum_{\mathbf{p} \neq 0} \frac{1}{\mathbf{p}^2} \sum_{\mathbf{n} \neq 0} \int_0^{+\infty} dl \frac{l}{i|\mathbf{n}|} \frac{e^{2\pi il|\mathbf{n}|} - e^{-2\pi il|\mathbf{n}|}}{l^2 + \tilde{\kappa}^2}, \quad (\text{B.192})$$

where  $l \equiv |\mathbf{l}|$  and the additional exponential factor  $e^{2\pi i\mathbf{p} \cdot \mathbf{n}}$  has been dropped, since for integer momenta it is equal to one. Furthermore, the argument of the radial integral over the momenta  $|\mathbf{l}|$  is even, thus the integration region can be extended to the whole real axis. Additionally, the integrand tends uniformly to zero in the limit  $l \rightarrow \pm\infty$  and it is analytical all over the complex plane  $l \in \mathbb{C}$ , except for two simple poles at  $l_{\pm} = \pm i\tilde{\kappa}$ , located along the imaginary axis. It follows that the integration region can be extended to an arbitrary large circular re-

gion about the origin of the complex plane encompassing the two singularities. Besides, the integrand can be split into two functions of complex variable  $l$

$$g_{\pm}(l) = \frac{l}{i|\mathbf{n}|} \frac{e^{\pm i2\pi l|\mathbf{n}|}}{(l - l_+)(l - l_-)} , \quad (\text{B.193})$$

so that  $g_+(l)$  ( $g_-(l)$ ) can be integrated in a semicircle with arbitrarily large radius about the origin in the upper (lower) part of the complex plane picking up the  $l_+$  ( $l_-$ ) singularity, according to Jordan's Lemma. The residues associated to the two poles turn out to coincide and to depend on  $|\mathbf{n}|$  through negative exponentials. Observing again that  $e^{-2\pi|\mathbf{n}|\tilde{\kappa}} \leq e^{-\pi\tilde{\kappa}} e^{-\pi|\mathbf{n}|}$ , eq. (B.192) becomes

$$\frac{1}{2} \sum_{\mathbf{p} \neq 0} \frac{1}{|\mathbf{p}|^2} \sum_{\mathbf{n} \neq 0} \frac{\pi}{|\mathbf{n}|} e^{-2\pi|\mathbf{n}|\tilde{\kappa}} \leq \frac{1}{2} \sum_{\mathbf{p} \neq 0} \frac{1}{|\mathbf{p}|^2} e^{-\pi\tilde{\kappa}} \sum_{\mathbf{n} \neq 0} \frac{\pi}{|\mathbf{n}|} e^{-\pi|\mathbf{n}|} = \lambda_6 \frac{\pi}{2} e^{-\pi\tilde{\kappa}} \sum_{\mathbf{p} \neq 0} \frac{1}{|\mathbf{p}|^2} , \quad (\text{B.194})$$

where  $\lambda_6$  is a small constant equal to 0.400982(1). Finally, we evaluate the sum over  $\mathbf{p}$  in the same fashion as eq. (B.191) and we single out the non-divergent part, finding

$$\begin{aligned} & \frac{1}{2} \sum_{\mathbf{p} \neq 0} \frac{1}{|\mathbf{p}|^2} \sum_{\mathbf{n} \neq 0} \int_{\mathbb{R}^3} d^3\mathbf{q} \frac{e^{-i2\pi\mathbf{q}\cdot\mathbf{n}}}{|\mathbf{q} + \mathbf{p}|^2 + \tilde{\kappa}^2} \leq \lambda_6 \frac{\pi}{2} \sum_{\mathbf{p} \neq 0} \frac{e^{-\pi\tilde{\kappa}}}{|\mathbf{p}|^2} \\ & = \lambda_6 \frac{\pi}{2} e^{-\pi\tilde{\kappa}} \sum_{\mathbf{p} \neq 0} \frac{1}{|\mathbf{p}|^2} + \lambda_6 \frac{\pi}{2} e^{-\pi\tilde{\kappa}} \sum_{|\mathbf{p}| > \tilde{\kappa}} \frac{1}{|\mathbf{p}|^2} \\ & \approx \lambda_6 \frac{\pi}{2} e^{-\pi\tilde{\kappa}} (\mathcal{G}^{(0)} + 8\pi\tilde{\kappa}) + \lambda_6 2\pi^2 e^{-\pi\tilde{\kappa}} \int_{2\tilde{\kappa}}^{+\infty} dp \rightarrow \frac{\pi}{2} \lambda_6 \mathcal{G}^{(0)} e^{-\pi\tilde{\kappa}} . \end{aligned} \quad (\text{B.195})$$

The finite contribution arising from the non-zero modes in eq. (B.195) decays exponentially with  $\tilde{\kappa}$ , thus it is negligible in the large binding momentum regime in comparison with the one in eq. (B.191). Therefore, we retain only the latter and write

$$\mathfrak{S}_1^{\infty} \rightarrow -\pi^2 \mathcal{G}^{(0)} \tilde{\kappa} . \quad (\text{B.196})$$

At this stage, we switch to the second term on the r.h.s. of eq. (B.183) and we observe that, in the  $\Lambda_n, \Lambda_m \rightarrow +\infty$  limits, translational symmetry is restored and  $\mathfrak{S}_2^{\infty}$  coincides with  $\mathfrak{S}_1^{\infty}$ . As a consequence, we are allowed to write

$$\mathfrak{S}_2^{\infty} = \frac{1}{2} \sum_{\mathbf{n}} \sum_{\mathbf{m} \neq \mathbf{n}} \frac{1}{|\mathbf{n}|^2 + \tilde{\kappa}^2} \frac{1}{|\mathbf{m} - \mathbf{n}|^2} \rightarrow -\pi^2 \mathcal{G}^{(0)} \tilde{\kappa} . \quad (\text{B.197})$$

It follows that we can concentrate directly on the last term in the second row of eq. (B.183), which can be conveniently split as follows,

$$\mathfrak{S}_3^{\infty} = \frac{1}{2} \sum_{\mathbf{n}} \frac{1}{(|\mathbf{n}|^2 + \tilde{\kappa}^2)^2} - \frac{1}{2} \sum_{\mathbf{n}} \sum_{\mathbf{m}} \frac{1}{|\mathbf{n}|^2 + \tilde{\kappa}^2} \frac{1}{|\mathbf{m}|^2 + \tilde{\kappa}^2} , \quad (\text{B.198})$$

so that the second term on the r.h.s. of the last equation is factorized. Since the two disentangled sums in the product are identical, it is sufficient to evaluate only one of them and, then, to take the square of the retained finite parts. We first rewrite the argument of the sum

in integral form and then exploit the Poisson summation formula,

$$\sum_{\mathbf{n}} \frac{1}{\mathbf{n}^2 + \tilde{\kappa}^2} = \sum_{\mathbf{n}} \int_{\mathbb{R}^3} d^3\mathbf{q} \frac{\delta^3(\mathbf{q} - \mathbf{n})}{\mathbf{q}^2 + \tilde{\kappa}^2} = \int_{\mathbb{R}^3} d^3\mathbf{q} \frac{1}{\mathbf{q}^2 + \tilde{\kappa}^2} + \sum_{\mathbf{n} \neq 0} \int_{\mathbb{R}^3} d^3\mathbf{q} \frac{e^{-2\pi i \mathbf{n} \cdot \mathbf{q}}}{\mathbf{q}^2 + \tilde{\kappa}^2}, \quad (\text{B.199})$$

where the zero modes have been isolated. The expression on the r.h.s. of eq. (B.199) is identical to the one in eq. (B.188) after the translation  $\mathbf{q} \mapsto \mathbf{q} - \mathbf{p} \equiv \mathbf{l}$  in momentum space, except for the outer sum over  $\mathbf{p}$  and the factor 1/2. Therefore, we are allowed to exploit the results in eq. (B.190) and (B.194) for zero and non-zero modes respectively, obtaining

$$\int_{\mathbb{R}^3} d^3\mathbf{q} \frac{1}{\mathbf{q}^2 + \tilde{\kappa}^2} + \sum_{\mathbf{n} \neq 0} \int_{\mathbb{R}^3} d^3\mathbf{q} \frac{e^{-2\pi i \mathbf{n} \cdot \mathbf{q}}}{\mathbf{q}^2 + \tilde{\kappa}^2} \rightarrow -2\pi^2 \tilde{\kappa} + \lambda_6 \pi e^{-\pi \tilde{\kappa}}. \quad (\text{B.200})$$

As a consequence, the second term on the r.h.s. of eq. (B.198) can be finally rewritten as

$$-\frac{1}{2} \sum_{\mathbf{n}} \sum_{\mathbf{m}} \frac{1}{|\mathbf{n}|^2 + \tilde{\kappa}^2} \frac{1}{|\mathbf{m}|^2 + \tilde{\kappa}^2} \rightarrow -2\pi^4 \tilde{\kappa}^2 - \lambda_6^2 \frac{\pi^2}{2} e^{-2\pi \tilde{\kappa}} + 2\pi^3 \lambda_6 \tilde{\kappa} e^{-\pi \tilde{\kappa}}, \quad (\text{B.201})$$

where the last two terms on the r.h.s. are exponentially suppressed and they have to be neglected for consistency. Second, we switch to the single sum on the r.h.s. of eq. (B.198). Introducing the integral sign and exploiting again the Poisson summation formula, the last contribution to  $\mathcal{S}_3(i\tilde{\kappa})$  becomes

$$\frac{1}{2} \sum_{\mathbf{n}} \frac{1}{(|\mathbf{n}|^2 + \tilde{\kappa}^2)^2} = \frac{1}{2} \int_{\mathbb{R}^3} \frac{1}{(\mathbf{q}^2 + \tilde{\kappa}^2)^2} + \frac{1}{2} \sum_{\mathbf{n} \neq 0} \int_{\mathbb{R}^3} d^3\mathbf{q} \frac{e^{-2\pi i \mathbf{n} \cdot \mathbf{q}}}{(\mathbf{q}^2 + \tilde{\kappa}^2)^2}, \quad (\text{B.202})$$

where the zero modes have been again isolated from the non-zero ones. The first integral in eq. (B.202) can be carried out after few manipulations,

$$\frac{1}{2} \int_{\mathbb{R}^3} d^3\mathbf{q} \frac{1}{(\mathbf{q}^2 + \tilde{\kappa}^2)^2} = \frac{2\pi}{\tilde{\kappa}} \arctan(x) \Big|_0^{+\infty} - \frac{\pi x}{x^2 + \tilde{\kappa}^2} \Big|_0^{+\infty} - \frac{\pi}{\tilde{\kappa}} \arctan\left(\frac{x}{\tilde{\kappa}}\right) \Big|_0^{+\infty} = \frac{\pi^2}{2\tilde{\kappa}}. \quad (\text{B.203})$$

Then, the integration over the angular variables associated to  $\mathbf{q}$  in eq. (B.203) gives

$$\frac{1}{2} \sum_{\mathbf{n} \neq 0} \int_{\mathbb{R}^3} d^3\mathbf{q} \frac{e^{-2\pi i \mathbf{n} \cdot \mathbf{q}}}{(\mathbf{q}^2 + \tilde{\kappa}^2)^2} = \sum_{\mathbf{n} \neq 0} \int_0^{+\infty} dq \frac{q}{i|\mathbf{n}|} \frac{e^{2\pi i q |\mathbf{n}|} - e^{-2\pi i q |\mathbf{n}|}}{(q^2 + \tilde{\kappa}^2)^2}. \quad (\text{B.204})$$

where  $q \equiv |\mathbf{q}|$ . The r.h.s. of eq. (B.204) is an even function of  $q$ , thus the integration region can be extended to the whole real axis. Besides, the integrand tends uniformly to zero in the limit  $l \rightarrow \pm\infty$  and is analytical all over the complex plane  $l \in \mathbb{C}$ , except for two double poles at  $q_{\pm} = \pm i\tilde{\kappa}$ , located along the imaginary axis. It follows that the integration region can be extended to an arbitrary large circular region about the origin of the complex plane encompassing the two singularities. Moreover, the argument of the integral can be split into two functions of complex variable  $q$

$$h_{\pm}(q) = \frac{q}{i|\mathbf{n}|} \frac{e^{\pm i 2\pi q |\mathbf{n}|}}{(q - q_+)^2 (q - q_-)^2}, \quad (\text{B.205})$$



so that  $h_+(q)$  ( $h_-(q)$ ) can be integrated in a semicircle with arbitrarily large radius about the origin in the upper (lower) part of the complex plane picking up the  $q_+$  ( $q_-$ ) singularity, according to Jordan's Lemma. Again, the residues about the two double poles turn out to coincide and to depend on  $|\mathbf{n}|$  through negative exponentials,

$$\sum_{\mathbf{n} \neq 0}^{\infty} \int_0^{+\infty} dq \frac{q}{i|\mathbf{n}|} \frac{e^{2\pi i q |\mathbf{n}|} - e^{-2\pi i q |\mathbf{n}|}}{q^2 + \tilde{\kappa}^2} = \frac{\pi^2}{2\tilde{\kappa}} \sum_{\mathbf{n} \neq 0}^{\infty} e^{-2\pi \tilde{\kappa} |\mathbf{n}|}. \quad (\text{B.206})$$

Now, observing again that  $e^{-2\pi |\mathbf{n}| \tilde{\kappa}} \leq e^{-\pi \tilde{\kappa}} e^{-\pi |\mathbf{n}|}$ , the sum in eq. (B.206) can be bound from above

$$\frac{\pi^2}{2\tilde{\kappa}} \sum_{\mathbf{n} \neq 0}^{\infty} e^{-2\pi \tilde{\kappa} |\mathbf{n}|} \leq \frac{\pi^2}{2\tilde{\kappa}} e^{-\pi \tilde{\kappa}} \sum_{\mathbf{n} \neq 0}^{\infty} e^{-\pi |\mathbf{n}|} = \lambda_7 \frac{\pi^2}{2\tilde{\kappa}} e^{-\pi \tilde{\kappa}}, \quad (\text{B.207})$$

where  $\lambda_7$  is a small constant equal to 0.485647(1). It follows that the contribution of the nonzero modes associated to the single sum in the second row of eq. (B.198) is exponentially suppressed and can be neglected in the large binding momentum limit. Collecting all the results in eqs. (B.196), (B.197), (B.201) and (B.203), the large binding momentum limit of the double sum  $\mathcal{S}_3(i\tilde{\kappa})$  is found,

$$\mathcal{S}_3(i\tilde{\kappa}) = \sum_{\mathbf{n}}^{\Lambda_n} \sum_{\mathbf{m} \neq \mathbf{n}}^{+\infty} \frac{1}{|\mathbf{n}|^2 + \tilde{\kappa}^2} \frac{1}{|\mathbf{m}|^2 + \tilde{\kappa}^2} \frac{\mathbf{n} \cdot \mathbf{m} + \tilde{\kappa}^2}{|\mathbf{n} - \mathbf{m}|^2} - \pi^4 \Lambda_n^2 \rightarrow \frac{\pi^2}{2\tilde{\kappa}} - 2\pi^2 g^{(0)} \tilde{\kappa} - 2\pi^4 \tilde{\kappa}^2, \quad (\text{B.208})$$

where the ellipses include the cutoff-dependent divergent terms and functions of  $\tilde{\kappa}$  which are suppressed by negative exponentials.

This appendix is primarily devoted on technicalities related to the representation of the physical system outlined in chap. 4 on a cubic lattice. In particular, app. C.1 and C.2 offer a detailed description on the implementation of differential operators. Conversely, app. C.3 focuses on the cubic group,  $\mathcal{O}$ , its irreducible representations and their link to the ones of the rotation group in the continuum,  $\text{SO}(3)$ . The transformation tables reported in the closing of the appendix may provide a useful tool for the extension of the analysis in ref. [68] to spherical tensors transforming as higher-dimensional irreps of  $\text{SO}(3)$  as well as for the derivation of the finite-volume mass shifts for bound states with  $\ell \geq 4$  of a two-body system ruled by short range interactions alone (cf. eq. (66) and tab. I in ref. [77]).

## C.1 Discretization of derivatives

In the lattice environment, spatial derivatives have to be expressed in terms of finite differences. As a consequence, all the differential operators are represented by non-commuting matrices, whose non diagonal elements are collectively referred as hopping terms. For the discretization of all the differential operators of interest in chap. 4 the improvement scheme presented in sec. 9.1.1 of ref. [146] is implemented.

First, let us consider a  $\mathcal{O}^{2K}$  function  $f(x \pm ka)$  on the lattice with  $k \in \mathbb{K}$ . About any point  $x$  of its domain, the function admits a Taylor expansion,

$$f(x \pm ka) = f(x) \pm ka f^{(1)}(x) + \frac{k^2 a^2}{2!} f^{(2)}(x) \pm \frac{k^3 a^3}{3!} f^{(3)}(x) + \dots \pm \frac{(ka)^{2K-1}}{2K-1!} f^{(2K-1)}(x) + \mathcal{O}(a^{2K}). \quad (\text{C.209})$$

From the subtraction of  $f(x - ka)$  from  $f(x + ka)$ , it is possible to construct an approximation scheme for the first derivative,

$$\begin{aligned} f_{ka}^- \equiv f(x + ka) - f(x - ka) &= 2ka f^{(1)}(x) + 2 \frac{k^3 a^3}{3!} f^{(3)}(x) + 2 \frac{k^5 a^5}{5!} f^{(5)}(x) \\ &+ \dots + 2 \frac{(ka)^{2K-1}}{2K-1!} f^{(2K-1)}(x) + \mathcal{O}(a^{2K+1}), \end{aligned} \quad (\text{C.210})$$

whose truncation error is given by  $\mathcal{O}(a^{2K+1})$ . Summing up a linear combination of  $f_{ka}^-$  with  $k$  ranging from 1 to  $K$ , in fact, all the contributions from the odd derivatives up to order  $2K-1$

in the discretized expression of the first derivative can be ruled out,

$$\begin{aligned} \sum_{k=1}^K C_k^{(1,K)} f_{ka}^- &= 2a f^{(1)}(x) \sum_{k=1}^K C_k^{(1,K)} k + 2 \frac{a^3}{3!} f^{(3)}(x) \sum_{k=1}^K C_k^{(1,K)} k^3 \\ &+ \dots + 2 \frac{a^{2K-1}}{2K-1!} f^{(2K-1)}(x) \sum_{k=1}^K C_k^{(1,K)} k^{2K-1} + \mathcal{O}(a^{2K+1}) . \end{aligned} \quad (\text{C.211})$$

At this stage, it is sufficient to impose to the unknown coefficients  $C_k^{(1,K)}$  the following constraints,

$$\sum_{k=1}^K C_k^{(1,K)} k^{2l-1} = \begin{cases} 1/2a & \text{if } l = 1 \\ 0 & \text{if } 2 \leq l \leq K \end{cases} , \quad (\text{C.212})$$

in order to recover the desired approximated expression for  $f^{(1)}(x)$ ,

$$f^{(1)}(x) \approx \sum_{k=1}^K C_k^{(1,K)} f_{ka}^- . \quad (\text{C.213})$$

Analytically, the coefficients take the form

$$C_k^{(1,K)} = (-1)^{k+1} \frac{1}{2a} \frac{2}{k} \frac{(K!)^2}{K + k!K - k!} , \quad (\text{C.214})$$

as it can be proven by solving the associated linear system in eq. (C.212),

$$\mathbf{M}^{(1,K)} \begin{pmatrix} C_1^{(1,K)} \\ C_2^{(1,K)} \\ C_3^{(1,K)} \\ \vdots \\ C_N^{(1,K)} \end{pmatrix} = \begin{pmatrix} \frac{1}{2a} \\ 0 \\ 0 \\ \vdots \\ 0 \end{pmatrix} \quad (\text{C.215})$$

where  $M_{ij}^{(1,K)} = j^{2i-1}$ , with the Cramer's rule and recalling the determinant formulas for Vandermonde matrices (cf. app. C.2). Second, the sum between  $f(x - ka)$  and  $f(x + ka)$ , permits to derive the approximation scheme for the second pure derivative,

$$\begin{aligned} f_{ka}^+ \equiv f(x + ka) + f(x - ka) &= 2f(x) + k^2 a^2 f^{(2)}(x) + 2 \frac{k^4 a^4}{3!} f^{(4)}(x) \\ &+ 2 \frac{k^6 a^6}{6!} f^{(6)}(x) + \dots + 2 \frac{(ka)^{2K}}{2K!} f^{(2K)}(x) + \mathcal{O}(a^{2K+2}) , \end{aligned} \quad (\text{C.216})$$

whose truncation error is given by  $\mathcal{O}(a^{2K+2})$ . Again, summing a linear combination of  $f_{ka}^+$  with  $k$  ranging from 1 to  $K$ , in fact, all the contributions from the even derivatives up to order  $2K$

to the discretized expression of the second derivative can be cancelled in the same fashion,

$$\begin{aligned} \sum_{k=1}^K C_k^{(2P,K)} f_{ka}^+ &= 2f(x) \sum_{k=1}^K C_k^{(2P,K)} + a^2 f^{(2)}(x) \sum_{k=1}^K C_k^{(2P,K)} k^2 + 2 \frac{a^4}{4!} f^{(4)}(x) \sum_{k=1}^K C_k^{(2P,K)} k^4 \\ &+ \dots + 2 \frac{a^{2K}}{2K!} f^{(2K)}(x) \sum_{k=1}^K C_k^{(2P,K)} k^{2K} + \mathcal{O}(a^{2K+2}) . \end{aligned} \quad (\text{C.217})$$

The constraints on the  $C_k^{(2P,K)}$  are, now, given by

$$\sum_{k=1}^K C_k^{(2P,K)} k^{2l} = \begin{cases} 1/a^2 & \text{if } l = 1 \\ 0 & \text{if } 2 \leq l \leq K, \end{cases} \quad (\text{C.218})$$

and enable us rewriting the second pure derivative on the lattice as

$$f^{(2)}(x) \approx C_0^{(2P,K)} f(x) + \sum_{k=1}^K C_k^{(2P,K)} f_{ka}^+ , \quad (\text{C.219})$$

where a coefficient for the diagonal term of the discretized operator has been introduced as in [3],

$$C_0^{(2P,K)} = -2 \sum_{k=1}^K C_k^{(2P,K)} . \quad (\text{C.220})$$

Solving the linear system associated to the coefficients with nonzero subscript in eq. (C.218),

$$\mathbf{M}^{(2P,K)} \begin{pmatrix} C_1^{(2P,K)} \\ C_2^{(2P,K)} \\ C_3^{(2P,K)} \\ \vdots \\ C_N^{(2P,K)} \end{pmatrix} = \begin{pmatrix} \frac{1}{a^2} \\ 0 \\ 0 \\ \vdots \\ 0 \end{pmatrix} \quad (\text{C.221})$$

where  $M_{ij}^{(2P,K)} = j^{2i}$ , an analytic expression for the coefficients  $C_k^{(2P,K)}$  is obtained,

$$C_k^{(2P,K)} = (-1)^{k+1} \frac{1}{a^2} \frac{2}{k^2} \frac{(K!)^2}{K + k!K - k!} . \quad (\text{C.222})$$

Equipped with the approximation schemes for both the first and the second derivatives of a function of one variable, we conclude the section with the treatment of second mixed derivatives. Denoting henceforth the mixed derivatives of an analytic function in two variables  $(x, y)$  as

$$\frac{\partial^{m+n}}{\partial^m x \partial^n y} f(x, y) = f^{(m,n)}(x, y) , \quad (\text{C.223})$$

the Taylor expansion of the two-variables functions  $f(x \pm ka, y \pm ka)$  and  $f(x \pm ka, y \mp ka)$  about  $(x, y)$  can be written as

$$\begin{aligned} f(x \pm ka, y \pm ka) &= f(x, y) \pm ak[f^{(1,0)}(x, y) + f^{(0,1)}(x, y)] \\ &+ \frac{a^2 k^2}{2}[f^{(2,0)}(x, y) + 2f^{(1,1)}(x, y) + f^{(0,2)}(x, y)] \pm \frac{a^3 k^3}{2}[f^{(3,0)}(x, y) + 3f^{(2,1)}(x, y) \\ &+ 3f^{(1,2)}(x, y) + f^{(0,3)}(x, y)] \cdots + \frac{a^{2K} k^{2K}}{2K!} \sum_{i=0}^{2K} \binom{2K}{i} f^{(2K-i,i)}(x, y) + \mathcal{O}(a^{2K+1}), \end{aligned} \quad (\text{C.224})$$

and

$$\begin{aligned} f(x \pm ka, y \mp ka) &= f(x, y) \pm ak[f^{(1,0)}(x, y) - f^{(0,1)}(x, y)] \\ &+ \frac{a^2 k^2}{2}[f^{(2,0)}(x, y) - 2f^{(1,1)}(x, y) + f^{(0,2)}(x, y)] \pm \frac{a^3 k^3}{2}[f^{(3,0)}(x, y) - 3f^{(2,1)}(x, y) \\ &+ 3f^{(1,2)}(x, y) - f^{(0,3)}(x, y)] + \cdots + \frac{a^{2K} k^{2K}}{2K!} \sum_{i=0}^{2K} \binom{2K}{i} (-1)^i f^{(2K-i,i)}(x, y) + \mathcal{O}(a^{2K+1}), \end{aligned} \quad (\text{C.225})$$

respectively. Now, by defining the following fourfold combination of displaced functions,

$$f_{ka}^M \equiv f(x + ka, y + ka) - f(x - ka, y + ka) - f(x + ka, y - ka) + f(x - ka, y - ka), \quad (\text{C.226})$$

an expression for the second mixed derivative  $f^{(1,1)}(x, y)$  in terms of mixed derivatives of higher order can be recovered,

$$\begin{aligned} \sum_{k=1}^K C_k^{(2M,K)} f_{ka}^M &= 4a^2 f^{(1,1)}(x) \sum_{k=1}^K C_k^{(2M,K)} k^2 + 4 \frac{a^4}{3!} [f^{(1,3)}(x) + f^{(3,1)}(x)] \sum_{k=1}^K C_k^{(2M,K)} k^4 \\ &+ \cdots + 4 \frac{a^{2K}}{2K!} \sum_{i=1}^K \binom{2K}{2i-1} f^{(2K-2i+1, 2i-1)}(x) \sum_{k=1}^K C_k^{(2M,K)} k^{2K} + \mathcal{O}(a^{2K+2}). \end{aligned} \quad (\text{C.227})$$

Thus, aiming at rewriting the latter as a superposition of  $f_{ka}^{M'}$ 's truncated to order  $2K$ ,

$$f^{(1,1)}(x) \approx \sum_{k=1}^K C_k^{(2M,K)} f_{ka}^M, \quad (\text{C.228})$$

we get the following constraints on the coefficients of the expansion

$$\sum_{k=1}^K C_k^{(2M,K)} k^{2l} = \begin{cases} 1/4a^2 & \text{if } l = 1 \\ 0 & \text{if } 2 \leq l \leq K. \end{cases} \quad (\text{C.229})$$

The solution of the linear system associated to the latter equation,

$$\mathbf{M}^{(2M,K)} \begin{pmatrix} C_1^{(2M,K)} \\ C_2^{(2M,K)} \\ C_3^{(2M,K)} \\ \vdots \\ C_K^{(2M,K)} \end{pmatrix} = \begin{pmatrix} \frac{1}{4a^2} \\ 0 \\ 0 \\ \vdots \\ 0 \end{pmatrix} \quad (\text{C.230})$$

where  $M_{ij}^{(2M,K)} = M_{ij}^{(2P,K)} = j^{2i}$ , coincides with the one of the preceeding case except for a factor  $1/4$ ,

$$C_k^{(2M,K)} = (-1)^{k+1} \frac{1}{4a^2} \frac{2}{k^2} \frac{(K!)^2}{K+k!K-k!} . \quad (\text{C.231})$$

From a direct comparison between the expansion coefficients of the three differential operators, the following relationship,

$$C_k^{(1,K)} = \frac{ak}{2} C_k^{(2P,K)} = 2ak C_k^{(2M,K)} , \quad (\text{C.232})$$

can be inferred, thus allowing for a quicker evaluation of the former (cf. tab. C.7).

Moreover, the discretization scheme for the first derivatives can be likewise exploited for the definition of second mixed derivatives on the lattice, thus expressing  $f^{(1,1)}(x, y)$  in terms of  $K(K-1)$  hopping terms of the kind  $f(x+ma, y+na)$ . Although straightforward, this alternative implementation is slower than the one presented here, due to repeated loops over non-diagonal terms.

K	1	2	3	4	5
$C_1^{(1,K)}$	$\frac{1}{2}$	$\frac{2}{3}$	$\frac{3}{4}$	$\frac{4}{5}$	$\frac{5}{6}$
$C_2^{(1,K)}$		$-\frac{1}{12}$	$-\frac{3}{20}$	$-\frac{1}{5}$	$-\frac{5}{21}$
$C_3^{(1,K)}$			$\frac{1}{60}$	$\frac{4}{105}$	$\frac{5}{84}$
$C_4^{(1,K)}$				$-\frac{1}{280}$	$-\frac{5}{504}$
$C_5^{(1,K)}$					$\frac{1}{1260}$

TABLE C.7 – Coefficients for the discretization of first derivatives with  $K \leq 5$  and unitary lattice spacing.

Even if in most of the calculations the derivative improvement index  $K$  has been kept equal to 4, a source of concern can be the convergence of the Taylor expansions of the functions (cf. eqs. (C.209), (C.224) and (C.225)). However the second derivative improvement scheme in the limit  $K \rightarrow \infty$  converges uniformly to the exactly quadratic operator in the momentum space over the Briullouin zone [3]. Furthermore, both the exact kinetic energy in momentum space and the respective discretized operator in the configuration space in the latter limit gave no evidence of convergence or stability issues.

## C.2 Vandermonde Matrices

In this appendix, the calculation of the determinant of the Vandermonde matrices [277] implied in the discretization of first and second derivatives of a function in ref. [146] (cf. app. C.2) is reviewed. Since the determinant of a matrix and the one of its transpose coincide, both  $\mathbf{M}^{(1P,K)}$  and  $\mathbf{M}^{(2,K)} \equiv \mathbf{M}^{(2P,K)} = \mathbf{M}^{(2M,K)}$  can be traced back to the form

$$\begin{pmatrix} x_1^m & x_1^{m+2} & x_1^{m+4} & \dots & x_1^{2K+m-2} \\ x_2^m & x_2^{m+2} & x_2^{m+4} & \dots & x_2^{2K+m-2} \\ x_3^m & x_3^{m+2} & x_3^{m+4} & \dots & x_3^{2K+m-2} \\ \vdots & \vdots & \vdots & \ddots & \vdots \\ x_N^m & x_N^{m+2} & x_N^{m+4} & \dots & x_N^{2K+m-2} \end{pmatrix} \quad (\text{C.233})$$

with  $m = 1, 2$  respectively and  $x_j = j$ . Denoting its determinant with  $V_K^{(m)}$ , and then relabeling  $x_K$  with  $x$ , we can rewrite  $|\mathbf{M}^{(m,K)}|$  as a polynomial of order  $2K + m - 2$ ,  $P^{(m)}(x)$ . The roots of the polynomial are the values of  $x$  according to which the last row can be expressed as a linear combination of the remaining  $K - 1$ . But these coincide exactly with 0 with multiplicity  $m$  and  $\pm x_1, \pm x_2, \dots, \pm x_{K-1}$  due to the fact that the function defining the entries,  $M_{ij}^{(m,K)} = j^{2i+m-2}$  preserves parity.  $P^{(1)}(x)$  can be, thus, factorized as

$$P^{(m)}(x) = C^{(m)} x^m \prod_{i=1}^{K-1} (x - x_i)(x + x_i), \quad (\text{C.234})$$

where the leading coefficient,  $C^{(m)}$  coincides with the determinant of a matrix of the same kind and rank  $K - 1$ ,  $V_{K-1}^{(m)}$ , as follows from the row expansion of  $|\mathbf{M}^{(m,K)}|$  by the last row,

$$\begin{aligned} P^{(m)}(x) = x^m & \begin{vmatrix} x_1^{m+2} & x_1^{m+4} & x_1^{m+6} & \dots & x_1^{2K+m-2} \\ x_2^{m+2} & x_2^{m+4} & x_2^{m+6} & \dots & x_2^{2K+m-2} \\ x_3^{m+2} & x_3^{m+4} & x_3^{m+6} & \dots & x_3^{2K+m-2} \\ \vdots & \vdots & \vdots & \ddots & \vdots \\ x_{K-1}^{m+2} & x_{K-1}^{m+4} & x_{K-1}^{m+6} & \dots & x_{K-1}^{2K+m-2} \end{vmatrix} + x^{m+2} \begin{vmatrix} x_1^m & x_1^{m+4} & x_1^{m+6} & \dots & x_1^{2K+m-2} \\ x_2^m & x_2^{m+4} & x_2^{m+6} & \dots & x_2^{2K+m-2} \\ x_3^m & x_3^{m+4} & x_3^{m+6} & \dots & x_3^{2K+m-2} \\ \vdots & \vdots & \vdots & \ddots & \vdots \\ x_{K-1}^m & x_{K-1}^{m+4} & x_{K-1}^{m+6} & \dots & x_{K-1}^{2K+m-2} \end{vmatrix} \\ & + \dots + x^{2K+m-2} \begin{vmatrix} x_1^m & x_1^{m+2} & x_1^{m+4} & \dots & x_1^{2K+m-2} \\ x_2^m & x_2^{m+2} & x_2^{m+4} & \dots & x_2^{2K+m-2} \\ x_3^m & x_3^{m+2} & x_3^{m+4} & \dots & x_3^{2K+m-2} \\ \vdots & \vdots & \vdots & \ddots & \vdots \\ x_{K-1}^m & x_{K-1}^{m+2} & x_{K-1}^{m+4} & \dots & x_{K-1}^{2K+m-2} \end{vmatrix}. \end{aligned} \quad (\text{C.235})$$

Replacing  $x$  back with  $x_K$ , the analytic expression of  $V_K^{(m)}$  is obtained by recursion,

$$\begin{aligned} V_K^{(m)} &= V_{K-1}^{(m)} x_K^m \prod_{i=1}^{K-1} (x_K - x_i)(x_K + x_i) = V_{K-2}^{(m)} x_K^m x_{K-1}^m \prod_{i=1}^2 \prod_{j=1}^{K-i} (x_{K-i} - x_j)(x_{K-i} + x_j) \\ &= \dots = \prod_{k=1}^{K-2} x_k^m \cdot \prod_{j=3}^K \prod_{\substack{i=1 \\ i < j}}^{K-1} (x_j - x_i)(x_j + x_i) \cdot \begin{vmatrix} x_1^m & x_1^{m+2} \\ x_2^m & x_2^{m+2} \end{vmatrix} = \prod_{k=1}^K x_k^m \cdot \prod_{1 \leq i < j \leq K} (x_j - x_i)(x_j + x_i). \end{aligned} \quad (\text{C.236})$$

Still of interest for the evaluation of the  $C_k^{(\mu,K)}$ 's <sup>1</sup> via Cramer's Rule is the determinant of the matrix obtained by replacing the row  $l$  with the covector of the right hand sides of the

<sup>1</sup>the greek indices  $\mu$  standing for 1,  $2P$  and  $2M$  have been introduced



equations (C.215), (C.221) and (C.230), i.e.

$$\begin{vmatrix} x_1^m & x_1^{m+2} & x_1^{m+4} & \dots & x_1^{2K+m-2} \\ x_2^m & x_2^{m+2} & x_2^{m+4} & \dots & x_2^{2K+m-2} \\ \vdots & \vdots & \vdots & \ddots & \vdots \\ x_{l-1}^m & x_{l-1}^{m+2} & x_{l-1}^{m+4} & \dots & x_{l-1}^{2K+m-2} \\ b^{(\mu)} & 0 & 0 & \dots & 0 \\ x_{l+1}^m & x_{l+1}^{m+2} & x_{l+1}^{m+4} & \dots & x_{l+1}^{2K+m-2} \\ \vdots & \vdots & \vdots & \ddots & \vdots \\ x_K^m & x_K^{m+2} & x_K^{m+4} & \dots & x_K^{2K+m-2} \end{vmatrix}. \quad (\text{C.237})$$

Ruling out the first column and the  $l^{\text{th}}$  row first and then iterating the procedure, the latter turns out to be

$$(-1)^{l+1} b^{(\mu)} \cdot \begin{vmatrix} x_1^m & x_1^{m+2} & x_1^{m+4} & \dots & x_1^{2K+m-2} \\ x_2^m & x_2^{m+2} & x_2^{m+4} & \dots & x_2^{2K+m-2} \\ \vdots & \vdots & \vdots & \ddots & \vdots \\ x_{l-1}^m & x_{l-1}^{m+2} & x_{l-1}^{m+4} & \dots & x_{l-1}^{2K+m-2} \\ x_{l+1}^m & x_{l+1}^{m+2} & x_{l+1}^{m+4} & \dots & x_{l+1}^{2K+m-2} \\ \vdots & \vdots & \vdots & \ddots & \vdots \\ x_K^m & x_K^{m+2} & x_K^{m+4} & \dots & x_K^{2K+m-2} \end{vmatrix} = (-1)^{l+1} b^{(\mu)} \prod_{\substack{k=1 \\ k \neq l}}^K x_k^3 \prod_{\substack{1 \leq i < j \leq K \\ i, j \neq l}} (x_j - x_i)(x_j + x_i), \quad (\text{C.238})$$

thus yielding the sought expression of the  $C_l^{(\mu, K)}$  coefficients,

$$C_l^{(\mu, K)} = b^{(\mu)} (-1)^{l+1} \frac{\prod_{\substack{j=1 \\ j \neq l}}^K x_j^2}{x_l^m \prod_{\substack{j=1 \\ j \neq l}}^K (-1)^{[l/j]} (x_j - x_l)(x_j + x_l)}, \quad (\text{C.239})$$

with  $b^{(\mu)}$  equal to  $1/2a$  ( $a^{-2}$  and  $a^{-2}/4$ ) for  $\mu$  equal to 1 ( $2P$  and  $2M$ ) and  $[\cdot]$  denoting the ceiling function.

### C.3 The cubic group

We here provide a concise review on the cubic group, together with the transformation tables for basis states of  $\text{SO}(3)$  irreps with  $\ell \leq 8$  into the  $\mathcal{O}$  ones (cf. tabs. C.10-C.19).

The group in object consists of 24 rotations about the symmetry axes of the cube (or the octahedron), subdivided into five equivalence classes. Adopting Schönflies notation [131],  $E$  represents the identity,  $3C_4^2(\pi)$  the rotations of  $180^\circ$  about the three fourfold axes orthogonal to the faces of the cube (i.e. the lattice axes),  $6C_4(\pi/4)$  the  $45^\circ$  and  $135^\circ$  rotations about the latter axes (6 elements),  $6C_4''$  the  $180^\circ$  rotations about the six diagonal axes parallel to two faces of the cube and  $8C_3'(2\pi/3)$  are rotations of  $120^\circ$  and  $240^\circ$  about the four diagonal axes passing to opposite vertexes of the lattice (8 elements).

Moreover, the characters of the five irreducible representations of  $\mathcal{O}$  are presented in tab. C.8. In the same table are also presented the characters of  $2\ell + 1$ -dimensional irreps of  $\text{SO}(3)$ , that, as known, induce reducible representations of the cubic group.

E	$6C_2''$	$3C_4^2(\pi)$	$8C_3'$	$6C_4(\frac{\pi}{2})$
$(0, 0, 0)$	$(0, \pi, \frac{\pi}{2})$	$(\pi, \pi, 0)$	$(\frac{\pi}{2}, \frac{\pi}{2}, \pi)$	$(\frac{\pi}{2}, \frac{\pi}{2}, \frac{3\pi}{2})$
	$(0, \pi, \frac{\pi}{2})$	$(0, \pi, 0)$	$(\pi, \frac{3\pi}{2}, \frac{3\pi}{2})$	$(\frac{3\pi}{2}, \frac{\pi}{2}, \frac{\pi}{2})$
	$(0, \pi, \frac{3\pi}{2})$	$(\pi, 0, 0)$	$(\pi, \frac{3\pi}{2}, \frac{\pi}{2})$	$(\pi, \frac{\pi}{2}, \pi)$
	$(\frac{3\pi}{2}, \frac{\pi}{2}, \frac{3\pi}{2})$		$(\frac{3\pi}{2}, \frac{\pi}{2}, \pi)$	$(\pi, \frac{3\pi}{2}, \pi)$
	$(0, \frac{\pi}{2}, \pi)$		$(\pi, \frac{\pi}{2}, \frac{3\pi}{2})$	$(\frac{\pi}{2}, 0, 0)$
	$(\pi, \frac{\pi}{2}, 0)$		$(\frac{\pi}{2}, \frac{3\pi}{2}, \pi)$	$(\frac{3\pi}{2}, 0, 0)$
			$(\pi, \frac{\pi}{2}, \frac{\pi}{2})$	
			$(\frac{3\pi}{2}, \frac{3\pi}{2}, \pi)$	

TABLE C.8 – Representation of the group. The elements belonging to each conjugacy class are listed as terms of Euler angles. The symmetry operation  $(\alpha, \beta, \gamma)$  consists of a rotation of angle  $\gamma$  about the  $z$  lattice axis, followed by one of angle  $\beta$  about the  $y$  axis and by another of angle  $\alpha$  about the  $z$  axis.

The full decomposition of the  $2\ell + 1$ -dimensional irreps of the rotation group, whose result for  $\ell \leq 8$  are presented in tab. C.9, can be carried out by means of the *Great orthogonality theorem* for characters. If

$$D^\ell = \sum_{\oplus} q_v D^v \quad (\text{C.240})$$

is the decomposition of the irrep  $\ell$  of  $\text{SO}(3)$  into the  $\#\mathcal{G}l$  cubic group irreps, the multiplicity of the latter is given by

$$q_v = \frac{1}{|\mathcal{O}|} \sum_{i=1}^{\#\mathcal{G}l} |\mathcal{G}l_i| [\chi_i^v]^* \chi_i^\ell \quad (\text{C.241})$$

where the order of  $\mathcal{O}$  is at the denominator, while  $\chi_i^v$  and  $\chi_i^\ell$  are respectively the characters of the irreps of the cubic and the rotation group related to the conjugacy class  $\mathcal{G}l_i$  with  $|\mathcal{G}l_i|$  elements. In particular, the map between the basis states of the latter and the  $\text{SO}(3)$  ones can be reconstructed via the projectors in eq. (4.40) (cf. tabs. C.10-C.19). Denoting with  $T_q^{(k)}$  the  $q$  component of a spherical tensor of rank  $2k + 1$ , the general component of the irreducible cubic tensor obtained from it is

$$T_q^{(\Gamma, k)} = \sum_{q'=-k}^k \sum_{g \in \mathcal{O}} \chi_\Gamma(g) D_{qq'}^k(g) T_{q'}^{(k)} \quad (\text{C.242})$$

where the index  $q$  ranges from  $-k$  to  $k$ .

$\Gamma$	E	$6C_2''$	$3C_4^2(\pi)$	$8C_3'$	$6C_4(\frac{\pi}{2})$
$A_1$	1	1	1	1	1
$A_2$	1	-1	1	1	-1
$E$	2	0	2	-1	0
$T_1$	3	-1	-1	0	1
$T_2$	3	1	-1	0	-1
$D^\ell$	$2\ell + 1$	$(-1)^\ell$	$(-1)^\ell$	$1 - \text{mod}(\ell, 3)$	$(-1)^{[\frac{\ell}{2}]}$

TABLE C.9 – Character table of the cubic group. The characters of the  $2\ell + 1$ -dimensional irrep of  $\text{SO}(3)$  with respect to cubic group operations are listed. With the exception of the  $\ell = 0, 1$  cases, this representation is fully reducible with respect to the  $\mathcal{O}$  operations.

Conversely, the *transpose* transformation rule holds for the basis states of the two groups,

$$|\ell, \Gamma, m\rangle = \sum_{m'=-\ell}^{\ell} \sum_{g \in \mathcal{O}} \chi_{\Gamma}(g) D_{m'm}^{\ell}(g) |\ell, m'\rangle. \quad (\text{C.243})$$

Due to rank deficiency of the projector, the label  $k$  in the cubic tensor does not represent any more its effective rank, but only the original irrep of  $\text{SO}(3)$  from which it has been obtained. The descent in symmetry, in fact, constrains the maximum rank of any irreducible tensor operator to run from one to three. As noticed in sec. 4.4 for the energy eigenstates, the non-null components  $q$  of  $T^{(\Gamma,k)}$  and  $|\Gamma\ell\rangle$ , admixture of the  $q \bmod 4$  components of their  $\text{SO}(3)$  counterparts, can be univocally labeled with the  $I_z$  quantum number. The ensuing distribution of  $m$  components of a spin- $l$  irrep into the  $(\ell, \Gamma)$  irreps of the cubic group is known under the name of *subduction* [155]. Furthermore, when the occurrence coefficient  $q_{\Gamma}$  the irrep  $\Gamma$  of  $\mathcal{O}$  is greater than one, further linear combinations on the outcoming states (cf. eq. (C.242)) or cubic tensor components (cf. eq. (C.243)) have to be considered, in order to block-diagonalize the relevant projector and disentangle the repeated multiplets of states.

$\begin{array}{c c c} & \ell & \\ \hline \Gamma & I_z & m \\ \hline A_1 & 0 & 1 \end{array}$		$\begin{array}{c ccccc} & \ell & & & 2 & \\ \hline \Gamma & I_z & m & & -2 & -1 & 0 & 1 & 2 \\ \hline E & 0 & & & & & 1 & & \\ & 2 & & & \sqrt{1/2} & & & & \sqrt{1/2} \\ \hline T_2 & 1 & & & & & & 1 & \\ & 2 & & & \sqrt{1/2} & & & & -\sqrt{1/2} \\ & 3 & & & & 1 & & & \end{array}$
$\begin{array}{c c ccc} & \ell & & & 1 \\ \hline \Gamma & I_z & m & & -1 & 0 & 1 \\ \hline T_1 & 0 & & & 1 & & \\ & 1 & & & & 1 & \\ & 3 & & & & & 1 \end{array}$		

TABLE C.10 – Decomposition tables for basis states of  $\text{SO}(3)$  with  $\ell \leq 2$  into irreps of  $\mathcal{O}$ .

$\begin{array}{c c cccccc} & \ell & & & & 3 & \\ \hline \Gamma & I_z & m & & -3 & -2 & -1 & 0 & 1 & 2 & 3 \\ \hline A_2 & 2 & & & \sqrt{\frac{1}{2}} & & & & & -\sqrt{\frac{1}{2}} & \\ \hline T_1 & 0 & & & & & 1 & & & & \\ & 1 & & & \sqrt{\frac{5}{8}} & & & & \sqrt{\frac{3}{8}} & & \\ & 3 & & & & \sqrt{\frac{3}{8}} & & & & & \sqrt{\frac{3}{8}} \\ \hline T_2 & 1 & & & \sqrt{\frac{3}{8}} & & & & -\sqrt{\frac{3}{8}} & & \\ & 2 & & & & \sqrt{\frac{1}{2}} & & & & \sqrt{\frac{1}{2}} & \\ & 3 & & & & & -\sqrt{\frac{5}{8}} & & & & \sqrt{\frac{3}{8}} \end{array}$		
---	--	--

TABLE C.11 – Decomposition table for basis states of  $\text{SO}(3)$  with  $\ell = 3$  into irreps of  $\mathcal{O}$ .

$\Gamma$	$\ell$ $I_z$	$m$	$4$								
			$-4$	$-3$	$-2$	$-1$	$0$	$1$	$2$	$3$	$4$
$A_1$	$0$		$\frac{1}{2}\sqrt{\frac{5}{6}}$				$\frac{1}{2}\sqrt{\frac{7}{3}}$				$\frac{1}{2}\sqrt{\frac{5}{6}}$
$E$	$0$		$\frac{1}{2}\sqrt{\frac{7}{6}}$				$-\frac{1}{2}\sqrt{\frac{5}{6}}$				$\frac{1}{2}\sqrt{\frac{7}{6}}$
	$2$				$\sqrt{\frac{1}{2}}$				$\sqrt{\frac{1}{2}}$		
$T_1$	$0$		$\sqrt{\frac{1}{2}}$								$-\sqrt{\frac{1}{2}}$
	$1$			$\frac{1}{2}\sqrt{\frac{1}{2}}$				$\frac{1}{2}\sqrt{\frac{7}{2}}$			
	$3$					$\frac{1}{2}\sqrt{\frac{7}{2}}$				$\frac{1}{2}\sqrt{\frac{1}{2}}$	
$T_2$	$1$			$-\frac{1}{2}\sqrt{\frac{7}{2}}$				$\frac{1}{2}\sqrt{\frac{1}{2}}$			
	$2$				$\sqrt{\frac{1}{2}}$				$-\sqrt{\frac{1}{2}}$		
	$3$					$\frac{1}{2}\sqrt{\frac{1}{2}}$				$-\frac{1}{2}\sqrt{\frac{7}{2}}$	

TABLE C.12 – Decomposition table for basis states of SO(3) with  $\ell = 4$  into irreps of  $\mathcal{O}$ .

$\ell \backslash m$		5											
$\Gamma$	$I_z$	-5	-4	-3	-2	-1	0	1	2	3	4	5	
$E$	0		$\sqrt{\frac{1}{2}}$									$-\sqrt{\frac{1}{2}}$	
	2				$\sqrt{\frac{1}{2}}$				$-\sqrt{\frac{1}{2}}$				
$T_1$	0		$\frac{1}{4}\sqrt{\frac{7}{3}}$				$\frac{1}{2}\sqrt{\frac{5}{6}}$				$\frac{1}{4}\sqrt{\frac{7}{3}}$		
	1			$-\frac{1}{4}\sqrt{\frac{7}{6}}$				$\frac{3}{4}$				$\frac{1}{4}\sqrt{\frac{35}{6}}$	
	3	$\frac{1}{4}\sqrt{\frac{35}{6}}$				$\frac{3}{4}$				$-\frac{1}{4}\sqrt{\frac{7}{6}}$			
	0		$\frac{1}{4}\sqrt{\frac{7}{3}}$				$-\frac{1}{2}\sqrt{\frac{5}{6}}$				$\frac{1}{4}\sqrt{\frac{7}{3}}$		
	1			$\frac{7}{8}\sqrt{\frac{7}{6}}$				$-\frac{1}{8}$				$\frac{1}{8}\sqrt{\frac{35}{6}}$	
	3	$\frac{1}{8}\sqrt{\frac{35}{6}}$				$-\frac{1}{8}$				$\frac{7}{8}\sqrt{\frac{7}{6}}$			
$T_2$	1			$\frac{1}{4}\sqrt{\frac{3}{2}}$				$\frac{\sqrt{7}}{4}$				$-\frac{1}{4}\sqrt{\frac{15}{2}}$	
	2				$\sqrt{\frac{1}{2}}$				$\sqrt{\frac{1}{2}}$				
	3	$\frac{1}{4}\sqrt{\frac{15}{2}}$				$-\frac{\sqrt{7}}{4}$				$-\frac{1}{4}\sqrt{\frac{3}{2}}$			

TABLE C.13 – Decomposition table for basis states of SO(3) with  $\ell = 5$  into irreps of  $\mathcal{O}$ .

$\Gamma$	$I_z$	$\ell \backslash m$	6						
			-6	-5	-4	-3	-2	-1	0
$A_1$	0				$\sqrt{\frac{7}{16}}$				$-\sqrt{\frac{1}{8}}$
$A_2$	2		$\frac{1}{4}\sqrt{\frac{5}{2}}$				$-\frac{11}{4}\sqrt{\frac{5}{2}}$		
$E$	0				$\frac{1}{4}$				$\frac{1}{2}\sqrt{\frac{7}{2}}$
	2		$\frac{1}{4}\sqrt{\frac{11}{2}}$				$\frac{1}{4}\sqrt{\frac{5}{2}}$		
$T_1$	0				$\sqrt{\frac{1}{2}}$				
	1					$\frac{1}{4}\sqrt{\frac{15}{2}}$			
	3		$\frac{1}{4}\sqrt{\frac{11}{2}}$					$-\frac{\sqrt{3}}{4}$	
$T_2$	1					$-\frac{1}{4}\sqrt{\frac{55}{14}}$			
	2		$\frac{1}{4\sqrt{14}}$				$\frac{1}{4}\sqrt{\frac{55}{14}}$		
	3			$\sqrt{\frac{21}{32}}$				$\frac{1}{4}\sqrt{\frac{11}{7}}$	
	1					$-\frac{5}{16}\sqrt{\frac{55}{14}}$			
	2		$-\frac{1}{4\sqrt{14}}$				$\frac{1}{4}\sqrt{\frac{55}{14}}$		
	3			$\frac{27}{16}\sqrt{\frac{3}{14}}$				$\frac{1}{16}\sqrt{\frac{11}{7}}$	

TABLE C.14 – Decomposition table for basis states of  $SO(3)$  with  $\ell = 6$  and  $m \leq 0$  into irreps of  $\mathcal{O}$ .

$\Gamma$	$I_z$	$\ell \backslash m$	6					
			1	2	3	4	5	6
$A_1$	0					$\sqrt{\frac{7}{16}}$		
$A_2$	2			$-\frac{11}{4}\sqrt{\frac{5}{2}}$				$\frac{1}{4}\sqrt{\frac{5}{2}}$
$E$	0					$\frac{1}{4}$		
	2			$\frac{1}{4}\sqrt{\frac{5}{2}}$				$\frac{1}{4}\sqrt{\frac{11}{2}}$
$T_1$	0					$-\sqrt{\frac{1}{2}}$		
	1		$-\frac{\sqrt{3}}{4}$				$\frac{1}{4}\sqrt{\frac{11}{2}}$	
	3				$\frac{1}{4}\sqrt{\frac{15}{2}}$			
$T_2$	1		$\frac{1}{4}\sqrt{\frac{11}{7}}$				$\frac{1}{4}\sqrt{\frac{21}{2}}$	
	2			$-\frac{1}{4}\sqrt{\frac{55}{14}}$				$-\frac{1}{4\sqrt{14}}$
	3				$-\frac{1}{4}\sqrt{\frac{55}{14}}$			
	1		$\frac{1}{16}\sqrt{\frac{11}{7}}$				$\frac{27}{16}\sqrt{\frac{3}{14}}$	
	2			$-\frac{1}{4}\sqrt{\frac{55}{14}}$				$\frac{1}{4\sqrt{14}}$
	3				$-\frac{5}{16}\sqrt{\frac{55}{14}}$			

TABLE C.15 – Decomposition table for basis states of  $SO(3)$  with  $\ell = 6$  and  $m > 0$  into irreps of  $\mathcal{O}$ .

$\Gamma$	$\ell$ $I_z$	$m$	$7$							
			$-7$	$-6$	$-5$	$-4$	$-3$	$-2$	$-1$	$0$
$A_2$	2			$\frac{1}{4}\sqrt{\frac{11}{3}}$				$\frac{1}{4}\sqrt{\frac{13}{3}}$		
$E$	0					$\sqrt{\frac{1}{2}}$				
	2			$\frac{1}{4}\sqrt{\frac{13}{3}}$				$-\frac{1}{4}\sqrt{\frac{11}{3}}$		
$T_1$	0					$\frac{1}{4}\sqrt{\frac{7}{10}}$				$\frac{1}{4}\sqrt{\frac{33}{5}}$
	1		$\frac{1}{8}\sqrt{\frac{65}{2}}$				$\frac{1}{8}\sqrt{\frac{77}{10}}$			
	3				$\frac{1}{8}\sqrt{\frac{7}{10}}$				$\frac{1}{8}\sqrt{\frac{231}{10}}$	
	0					$\frac{1}{4}\sqrt{\frac{7}{10}}$				$-\frac{1}{4}\sqrt{\frac{33}{5}}$
	1		$\frac{13}{32}\sqrt{\frac{13}{10}}$				$\frac{1}{32}\sqrt{\frac{385}{2}}$			
	3				$\frac{29}{32}\sqrt{\frac{7}{10}}$				$\frac{1}{32}\sqrt{\frac{231}{10}}$	
$T_2$	1		$-\frac{3}{8}\sqrt{\frac{7}{2}}$				$\frac{1}{24}\sqrt{\frac{143}{2}}$			
	2			$\frac{1}{24}$				$\frac{\sqrt{143}}{24}$		
	3				$\frac{1}{24}\sqrt{\frac{13}{2}}$				$\frac{1}{8}\sqrt{\frac{143}{6}}$	
	1		$-\frac{71}{192}\sqrt{\frac{7}{2}}$				$\frac{11}{192}\sqrt{\frac{143}{2}}$			
	2			$-\frac{1}{24}$				$\frac{\sqrt{143}}{24}$		
	3				$\frac{1}{64}\sqrt{\frac{13}{2}}$				$\frac{7}{64}\sqrt{\frac{143}{6}}$	

TABLE C.16 – Decomposition table for basis states of SO(3) with  $\ell = 7$  and  $m \leq 0$  into irreps of  $\mathcal{O}$ .

$\Gamma$	$\ell$ $I_z$	$m$	$7$						
			1	2	3	4	5	6	7
$A_2$	2			$-\frac{1}{4}\sqrt{\frac{13}{3}}$				$-\frac{1}{4}\sqrt{\frac{11}{3}}$	
$E$	0					$-\sqrt{\frac{1}{2}}$			
	2			$\frac{1}{4}\sqrt{\frac{11}{3}}$				$-\frac{1}{4}\sqrt{\frac{13}{3}}$	
$T_1$	0	$\frac{1}{4}\sqrt{\frac{33}{5}}$				$\frac{1}{4}\sqrt{\frac{7}{10}}$			
	1		$\frac{1}{8}\sqrt{\frac{231}{10}}$				$\frac{1}{8}\sqrt{\frac{7}{10}}$		
	3				$\frac{1}{8}\sqrt{\frac{77}{10}}$				$\frac{1}{8}\sqrt{\frac{65}{2}}$
	0	$-\frac{1}{4}\sqrt{\frac{33}{5}}$				$\frac{1}{4}\sqrt{\frac{7}{10}}$			
	1		$\frac{1}{32}\sqrt{\frac{231}{10}}$				$\frac{29}{32}\sqrt{\frac{7}{10}}$		
	3				$\frac{1}{32}\sqrt{\frac{385}{2}}$				$\frac{13}{32}\sqrt{\frac{13}{10}}$
$T_2$	1		$\frac{1}{8}\sqrt{\frac{143}{6}}$				$\frac{1}{24}\sqrt{\frac{13}{2}}$		
	2			$\frac{\sqrt{143}}{24}$				$\frac{1}{24}$	
	3				$\frac{1}{24}\sqrt{\frac{143}{2}}$				$-\frac{3}{8}\sqrt{\frac{7}{2}}$
	1		$\frac{7}{64}\sqrt{\frac{143}{6}}$				$\frac{1}{64}\sqrt{\frac{13}{2}}$		
	2			$\frac{\sqrt{143}}{24}$				$-\frac{1}{24}$	
	3				$\frac{11}{192}\sqrt{\frac{143}{2}}$				$-\frac{71}{192}\sqrt{\frac{7}{2}}$

TABLE C.17 – Decomposition table for basis states of SO(3) with  $\ell = 7$  and  $m > 0$  into irreps of  $\mathcal{O}$ .

$\Gamma$	$\ell$		$m$								
	$I_z$		-8	-7	-6	-5	-4	-3	-2	-1	0
$A_1$	0		$\frac{\sqrt{390}}{48}$				$\frac{\sqrt{42}}{24}$				$\frac{\sqrt{33}}{8}$
$E$	0		$-\frac{1}{8}\sqrt{\frac{455}{246}}$				$\frac{1}{4}\sqrt{\frac{41}{6}}$				$-\frac{1}{8}\sqrt{\frac{231}{41}}$
	2				$\frac{1}{4}\sqrt{\frac{273}{41}}$				$-\frac{1}{4}\sqrt{\frac{55}{41}}$		
	0		$\frac{7}{32}\sqrt{\frac{455}{246}}$				$\frac{109}{16}\sqrt{\frac{1}{246}}$				$-\frac{9}{32}\sqrt{\frac{231}{41}}$
	2				$\frac{1}{4}\sqrt{\frac{273}{41}}$				$\frac{1}{4}\sqrt{\frac{55}{41}}$		
$T_1$	0		$\frac{1}{4\sqrt{57}}$				$\frac{1}{4}\sqrt{\frac{445}{57}}$				
	1			$\frac{1}{8}\sqrt{\frac{57}{2}}$				$-\frac{3}{8}\sqrt{\frac{91}{38}}$			
	3				$\frac{5}{8}\sqrt{\frac{35}{114}}$					$\frac{1}{8}\sqrt{\frac{715}{114}}$	
	0		$-\frac{1}{4\sqrt{57}}$				$\frac{1}{4}\sqrt{\frac{455}{57}}$				
	1			$\frac{227}{32\sqrt{114}}$				$-\frac{13}{32}\sqrt{\frac{91}{38}}$			
	3				$\frac{1}{32}\sqrt{\frac{665}{6}}$					$\frac{1}{32}\sqrt{\frac{2145}{38}}$	
$T_2$	1			$\frac{1}{8}\sqrt{\frac{71}{2}}$				$\frac{3}{8}\sqrt{\frac{273}{142}}$			
	2				$\frac{3}{4}\sqrt{\frac{15}{142}}$				$\frac{1}{4}\sqrt{\frac{1001}{142}}$		
	1					$-\frac{5}{8}\sqrt{\frac{35}{142}}$				$-\frac{1}{8}\sqrt{\frac{715}{142}}$	
	1			$\frac{433}{64\sqrt{142}}$				$\frac{9}{64}\sqrt{\frac{273}{142}}$			
	2				$\frac{3}{4}\sqrt{\frac{15}{142}}$				$-\frac{1}{4}\sqrt{\frac{1001}{142}}$		
	3					$\frac{3}{4}\sqrt{\frac{15}{142}}$				$-\frac{1}{4}\sqrt{\frac{1001}{142}}$	

TABLE C.18 – Decomposition table for basis states of  $\text{SO}(3)$  with  $\ell = 8$  and  $m \leq 0$  into irreps of  $\mathcal{O}$ .



$\Gamma$	$\ell$		8							
	$I_z$	$m$	1	2	3	4	5	6	7	8
$A_1$	0	0				$\frac{\sqrt{42}}{24}$				$\frac{\sqrt{390}}{48}$
$E$	0	0				$\frac{1}{4}\sqrt{\frac{41}{6}}$				$-\frac{1}{8}\sqrt{\frac{455}{246}}$
	2	2		$-\frac{1}{4}\sqrt{\frac{55}{41}}$				$\frac{1}{4}\sqrt{\frac{273}{41}}$		
	0	0				$\frac{109}{16}\sqrt{\frac{1}{246}}$				$\frac{7}{32}\sqrt{\frac{455}{246}}$
	2	2		$\frac{1}{4}\sqrt{\frac{55}{41}}$				$\frac{1}{4}\sqrt{\frac{273}{41}}$		
$T_1$	0	0				$-\frac{1}{4\sqrt{57}}$				
	1	1	$\frac{1}{8}\sqrt{\frac{715}{114}}$				$\frac{5}{8}\sqrt{\frac{35}{114}}$			
	3	3			$-\frac{3}{8}\sqrt{\frac{91}{38}}$				$\frac{1}{8}\sqrt{\frac{57}{2}}$	
	0	0				$-\frac{1}{4}\sqrt{\frac{455}{57}}$				$\frac{1}{4\sqrt{57}}$
	1	1	$\frac{1}{32}\sqrt{\frac{2145}{38}}$				$\frac{1}{32}\sqrt{\frac{665}{6}}$			
	3	3			$-\frac{13}{32}\sqrt{\frac{91}{38}}$				$\frac{227}{32\sqrt{114}}$	
$T_2$	1	1	$-\frac{1}{8}\sqrt{\frac{715}{142}}$				$-\frac{5}{8}\sqrt{\frac{35}{142}}$			
	2	2		$-\frac{1}{4}\sqrt{\frac{1001}{142}}$				$-\frac{3}{4}\sqrt{\frac{15}{142}}$		
	3	3			$\frac{3}{8}\sqrt{\frac{273}{142}}$				$\frac{1}{8}\sqrt{\frac{71}{2}}$	
	1	1	$\frac{1}{64}\sqrt{\frac{715}{142}}$				$-\frac{103}{64}\sqrt{\frac{35}{142}}$			
	2	2		$\frac{1}{4}\sqrt{\frac{1001}{142}}$				$-\frac{3}{4}\sqrt{\frac{15}{142}}$		
	3	3			$\frac{1}{4}\sqrt{\frac{1001}{142}}$				$-\frac{3}{4}\sqrt{\frac{15}{142}}$	

TABLE C.19 – Decomposition table for basis states of  $SO(3)$  with  $\ell = 8$  and  $m > 0$  into irreps of  $\mathcal{O}$ .

## Peer-reviewed articles

1. **Electromagnetic selection rules in the triangular  $\alpha$ -cluster model of  $^{12}\text{C}$**   
G. Stellin, L. Fortunato and A. Vitturi  
*J. Phys. G: Nucl. and Part. Phys.* **43**, 8, 085104 (2016).  
e-Print: 1512.05123
2. **Breaking and restoration of rotational symmetry in the low-energy spectrum of light alpha-conjugate nuclei on the lattice I:  $^8\text{Be}$  and  $^{12}\text{C}$**   
G. Stellin, S. Elhatisari and U.-G. Meißner  
*Eur. Phys. J. A* **54**, 12, 232 (2018).  
e-Print: 1809.06109
3. **P-Wave Two-Particle Bound and Scattering States in a Finite Volume including QED**  
G. Stellin and U.-G. Meißner  
*Eur. Phys. J. A* **57**, 1, 26 (2021).  
e-Print: 2008.06553

## Conference papers

1. **Electromagnetic Selection Rules for  $^{12}\text{C}$  in a  $3\alpha$  Cluster Model**  
L. Fortunato, G. Stellin and A. Vitturi  
*Few. Body Syst.*, **58**, 1, 19 (2017). Contribution to: EFB23, 19

## Articles in preparation

1. **Breaking and restoration of rotational symmetry in the low-energy spectrum of light alpha-conjugate nuclei on the lattice II:  $^{16}\text{O}$**   
G. Stellin, S. Elhatisari and U.-G. Meißner  
to be submitted to the *Eur. Phys. J. A*.

## Poster presentations

### 1. 57th International Winter Meeting on Nuclear Physics, Bormio (Italy)

J.-Gutenberg-Universität Mainz, Technische Universität München, J.-Liebig-Universität Gießen

*Breaking and restoration of rotational symmetry in the low-energy spectrum of light alpha-conjugate nuclei on the lattice I:  $^8\text{Be}$  and  $^{12}\text{C}$*

January 2019

---

- [1] S. R. BEANE & M. J. SAVAGE; “Two-particle elastic scattering in a finite volume including QED”; *Phys. Rev. D* **90**, p. 074511 (2014).
- [2] X. KONG & F. RAVNDAL; “Coulomb effects in low energy proton–proton scattering”; *Nucl. Phys. A* **665**, pp. 137–163 (2000).
- [3] B.-N. LU, T. A. LÄHDE, D. LEE & U.-G. MEIßNER; “Breaking and restoration of rotational symmetry on the lattice for bound state multiplets”; *Phys. Rev. D* **90**, p. 034507 (2014).
- [4] S. ALI & A. R. BODMER; “Phenomenological  $\alpha$ - $\alpha$  potentials”; *Nucl. Phys.* **80**, pp. 99–112 (1966).
- [5] O. PORTILHO & S. A. COON; “Three-alpha force and the 3- $\alpha$  model of  $^{12}\text{C}$ ”; *Zeitschr. Physik A* **290**, pp. 93–105 (1979).
- [6] Y. RONEN, N. BARNEA & W. LEIDEMANN; “An  $\alpha$ -Particle Model for  $^{16}\text{O}$ : Is There a New Four-Body Scale?” *Few-Body Systems* **38**, pp. 97–101 (2006). ISSN 1432-5411.
- [7] R. BIJKER & F. IACHELLO; “Evidence for Tetrahedral Symmetry in  $^{16}\text{O}$ ”; *Phys. Rev. Lett.* **112**, p. 152501 (2014).
- [8] R. BIJKER & F. F. IACHELLO; “The algebraic cluster model: Structure of  $^{16}\text{O}$ ”; *Nuc. Phys. A* **957**, pp. 154 – 176 (2017). ISSN 0375-9474.
- [9] J. BIJNENS & U.-G. MEIßNER; “Workshop on the standard model at low-energies: Mini-proceedings”; (1996); trento ECT-96-010, TK-96-18, NORDITA-96-35-N-P; [arXiv:~hep-ph/9606301](#).
- [10] U. VAN KOLCK; “Effective field theory of short-range forces”; *Nucl. Phys. A* **645**, pp. 273–302 (1999).
- [11] E. EPELBAUM; “Few-nucleon forces and systems in chiral effective field theory”; *Prog. in Part. and Nucl. Phys.* **57**, pp. 654–741 (2006).
- [12] D. LEE; “Lattice simulations for few- and many-body systems”; *Progr. in Part. and Nucl. Phys.* **63**, pp. 117 – 154 (2009). ISSN 0146-6410.

- 
- [13] E. EPELBAUM, H.-W. HAMMER & U.-G. MEIßNER; “Modern theory of nuclear forces”; *Rev. Mod. Phys.* **81**, pp. 1773–1825 (2009).
  - [14] R. MACHLEIDT & D. ENTEM; “Chiral effective field theory and nuclear forces”; *Phys. Rep.* **503**, pp. 1 – 75 (2011). ISSN 0370-1573.
  - [15] T. LÄHDE & U.-G. MEIßNER; “Nuclear Lattice Effective Field Theory: An Introduction”; *Lect. Notes in Phys.* **957** (2019).
  - [16] H.-W. HAMMER, S. KÖNIG & U. VAN KOLCK; “Nuclear effective field theory: Status and perspectives”; *Rev. Mod. Phys.* **92**, p. 025004 (2020).
  - [17] D. B. KAPLAN, M. J. SAVAGE & M. B. WISE; “Nucleon-nucleon scattering from effective field theory”; *Nucl. Phys. B* **478**, pp. 629 – 659 (1996). ISSN 0550-3213.
  - [18] D. B. KAPLAN, M. J. SAVAGE & M. B. WISE; “A new expansion for nucleon-nucleon interactions”; *Phys. Lett. B* **424**, pp. 390 – 396 (1998). ISSN 0370-2693.
  - [19] P. F. BEDAQUE & U. VAN KOLCK; “Nucleon-deuteron scattering from an effective field theory”; *Phys. Lett. B* **428**, pp. 221 – 226 (1998). ISSN 0370-2693.
  - [20] P. F. BEDAQUE, H.-W. HAMMER & U. VAN KOLCK; “Renormalization of the Three-Body System with Short-Range Interactions”; *Phys. Rev. Lett.* **82**, pp. 463–467 (1999).
  - [21] J. GEGELIA; “EFT and NN scattering”; *Phys. Lett. B* **429**, pp. 227 – 231 (1998). ISSN 0370-2693.
  - [22] D. B. KAPLAN, M. J. SAVAGE & M. B. WISE; “Two-nucleon systems from effective field theory”; *Nucl. Phys. B* **534**, pp. 329 – 355 (1998). ISSN 0550-3213.
  - [23] D. KAPLAN; “More effective field theory for non-relativistic scattering”; *Nucl. Phys. B* **494**, pp. 471 – 483 (1997). ISSN 0550-3213.
  - [24] J.-W. CHEN, G. RUPAK & M. J. SAVAGE; “Nucleon-nucleon effective field theory without pions”; *Nucl. Phys. A* **653**, pp. 386 – 412 (1999). ISSN 0375-9474.
  - [25] P. F. BEDAQUE, H.-W. HAMMER & U. U. VAN KOLCK; “The three-boson system with short-range interactions”; *Nucl. Phys. A* **646**, pp. 444 – 466 (1999). ISSN 0375-9474.
  - [26] P. F. BEDAQUE, H.-W. HAMMER & U. VAN KOLCK; “Effective theory of the triton”; *Nucl. Phys. A* **676**, pp. 357 – 370 (2000). ISSN 0375-9474.
  - [27] I. R. AFNAN & D. R. PHILLIPS; “Three-body problem with short-range forces: Renormalized equations and regulator-independent results”; *Phys. Rev. C* **69**, p. 034010 (2004).
  - [28] H. W. GRIEßHAMMER; “Improved convergence in the three-nucleon system at very low energies”; *Nucl. Phys. A* **744**, pp. 192 – 226 (2004). ISSN 0375-9474.
  - [29] F. GABBIANI, P. F. BEDAQUE & H. W. GRIEßHAMMER; “Higher partial waves in an effective field theory approach to nd scattering”; *Nucl. Phys. A* **675**, pp. 601 – 620 (2000). ISSN 0375-9474.
-

- 
- [30] B. BLANKKREIDER & J. GEGELIA; “Doublet channel neutron-deuteron scattering in leading order effective field theory”; *AIP Conf. Proc.* **603**, p. 233 (2001).
- [31] P. F. BEDAQUE, G. RUPAK, H. W. GRIEßHAMMER & H.-W. HAMMER; “Low energy expansion in the three body system to all orders and the triton channel”; *Nucl. Phys. A* **714**, pp. 589 – 610 (2003). ISSN 0375-9474.
- [32] D. B. KAPLAN, M. J. SAVAGE & M. B. WISE; “Perturbative calculation of the electromagnetic form factors of the deuteron”; *Phys. Rev. C* **59**, pp. 617–629 (1999).
- [33] J.-W. CHEN, H. GRIEßHAMMER, M. SAVAGE & R. P. SPRINGER; “The polarizability of the deuteron”; *Nucl. Phys. A* **644**, pp. 221 – 234 (1998). ISSN 0375-9474.
- [34] M. J. SAVAGE, K. SCALDEFERRI & M. WISE; “ $n + p \rightarrow d + \gamma$  in effective field theory”; *Nucl. Phys. A* **652**, pp. 273 – 286 (1999).
- [35] X. KONG & F. RAVNDAL; “Effective-range corrections to the proton-proton fusion rate”; *Phys. Lett. B* **470**, pp. 1–5 (1999).
- [36] X. KONG & F. RAVNDAL; “Proton-proton fusion in effective field theory”; *Phys. Rev. C* **64**, p. 044002 (2001).
- [37] C. BERTULANI, H.-W. HAMMER & U. VAN KOLCK; “Effective field theory for halo nuclei: shallow p-wave states”; *Nucl. Phys. A* **712**, pp. 37–58 (2002).
- [38] J. GASSER, LYUBOVITSKIY & A. RUSETSKI; “Hadronic atoms in QCD+QED”; *Phys. Rep.* **456**, pp. 167–251 (2008).
- [39] R. J. FURNSTAHL; “Nuclear Forces 2”; Lecture notes of the course of *Nuclear Few- and Many-Body Physics*, Ohio State University (2014). <https://www.asc.ohio-state.edu/physics/ntg/8805/>.
- [40] M. BARKER, P. COLBY, W. HAEBERLI & P. SIGNELL; “Proton-Proton Scattering at Low Energies”; *Phys. Rev. Lett.* **48**, p. 918 (1982).
- [41] L. LANDAU & J. SMORODINSKI; “On the Theory of Scattering of Protons by Protons”; *J. Phys. Acad. Sci. USSR* **8**, p. 154 (1944).
- [42] H. A. BETHE; “Theory of the Effective Range in Nuclear Scattering”; *Phys. Rev.* **76**, pp. 38–50 (1949).
- [43] d. M. J. B. H. KOK, L.P. & H. VAN HAERINGEN; “Formulas for the  $\delta$ -shell-plus-Coulomb potential for all partial wavesg”; *Phys. Rev. C* **26**, pp. 2381–2396 (1982).
- [44] E. KLEMP, F. BRADAMANTE, A. MARTIN & J.-M. RICHARD; “Antinucleon–nucleon interaction at low energy: scattering and protonium”; *Phys. Rep.* **368**, pp. 119 – 316 (2002). ISSN 0370-1573.
- [45] J. CARBONELL, O. DALKAROV, K. PROTASOV & I. SHAPIRO; “The origin of P-wave enhancement in the optical model for low-energy proton-antiproton scattering”; *Nucl. Phys. A* **535**, pp. 651 – 668 (1991). ISSN 0375-9474.
-

- [46] Z. DAVOUDI & M. J. SAVAGE; “Finite-volume electromagnetic corrections to the masses of mesons, baryons, and nuclei”; *Phys. Rev. D* **90**, p. 054503 (2014).
- [47] Z. DAVOUDI, J. HARRISON, A. JÜTTNER, A. PORTELLI & M. J. SAVAGE; “Theoretical aspects of quantum electrodynamics in a finite volume with periodic boundary conditions”; *Phys. Rev. D* **99**, p. 034510 (2019).
- [48] S. DÜRR, Z. FODOR, J. FRISON, C. HOELBLING, R. HOFFMANN, S. D. KATZ, S. KRIEG, T. KURTH, L. LELLOUCH, T. LIPPERT, K. K. SZABO & G. VULVERT; “Ab Initio Determination of Light Hadron Masses”; *Science* **322**, pp. 1224–1227 (2008). ISSN 0036-8075. <https://science.sciencemag.org/content/322/5905/1224.full.pdf>.
- [49] S. AOKI, K.-I. ISHIKAWA, N. ISHIZUKA, K. KANAYA, Y. KURAMASHI, Y. NAKAMURA, Y. NAMEKAWA, M. OKAWA, Y. TANIGUCHI, A. UKAWA, N. UKITA & T. YOSHIÉ; “1+1+1 flavor QCD+QED simulation at the physical point”; *Phys. Rev. D* **86**, p. 034507 (2012).
- [50] S. DÜRR, Z. FODOR, C. HOELBLING, S. KRIEG, T. KURTH, L. LELLOUCH, T. LIPPERT, R. MALAK, T. MÉTIVET, A. PORTELLI, A. SASTRE & K. SZABÓ; “Lattice QCD at the physical point meets  $SU(2)$  chiral perturbation theory”; *Phys. Rev. D* **90**, p. 114504 (2014).
- [51] S. AOKI, Y. AOKI, D. BECIREVIĆ, C. BERNARD, T. BLUM, G. COLANGELO, M. DELLA MORTE, P. DIMOPOULOS, S. DÜRR, H. FUKAYA, M. GOLTERMAN, S. GOTTLIEB, S. HASHIMOTO, U. M. HELLER, R. HORSLEY, A. JÜTTNER, T. KANEKO, L. LELLOUCH, H. LEUTWYLER, C.-J. D. LIN, V. LUBICZ, E. LUNGLI, R. MAWHINNEY, T. ONOGI, C. PENA, C. T. SACHRAJDA, S. R. SHARPE, S. SIMULA, R. SOMMER, A. VLADIKAS, U. WENGER & H. WITTIG; “Review of lattice results concerning low-energy particle physics - Flavour Lattice Averaging Group (FLAG)”; *Eur. Phys. J. C* **77**, p. 112 (2017).
- [52] B. C. TOTH; “QED corrections to hadronic observables”; XXXVII International Symposium on Lattice Field Theory, Wuhan, China (2019). <https://pos.sissa.it/363/066>.
- [53] S. AOKI, Y. AOKI, D. BECIREVIC, T. BLUM, G. COLANGELO, S. COLLINS, M. D. MORTE, P. DIMOPOULOS, S. DÜRR, H. FUKAYA, M. GOLTERMAN, S. GOTTLIEB, R. GUPTA, S. HASHIMOTO, U. M. HELLER, G. HERDOIZA, R. HORSLEY, A. JÜTTNER, T. KANEKO, C.-J. D. LIN, E. LUNGLI, R. MAWHINNEY, T. O. A. NICHOLSON, C. PENA, A. PORTELLI, A. RAMOS, S. R. SHARPE, J. N. SIMONE, S. SIMULA, R. SOMMER, R. V. D. WATER, A. VLADIKAS, U. WENGER & H. WITTIG; “Flavour Lattice Averaging Group Review 2019”; *Eur. Phys. J. C* **80**, p. 113 (2020).
- [54] S. UNO & M. HAYAKAWA; “QED in Finite Volume and Finite Size Scaling Effect on Electromagnetic Properties of Hadrons”; *Prog. of Theor. Phys.* **120**, pp. 413–441 (2008). ISSN 0033-068X.
- [55] A. PORTELLI, S. DÜRR, Z. FODOR, J. FRISON, C. HOELBLING, S. D. KATZ, S. KRIEG, T. KURTH, L. LELLOUCH, T. LIPPERT, A. RAMOS & K. K. SZABÓ; “Systematic errors in partially-quenched QCD plus QED lattice simulations”; XIX International Symposium on Lattice Field Theory, Squaw Valley, Lake Tahoe, California (2011). <https://pos.sissa.it/139/136>.
- [56] G. M. DE DIVITIIS, R. FREZZOTTI, V. LUBICZ, G. MARTINELLI, R. PETRONZIO, G. C. ROSSI, F. SANFILIPPO, S. SIMULA & N. TANTALO; “Leading isospin breaking effects on the lattice”; *Phys. Rev. D* **87**, p. 114505 (2013).



- 
- [57] S. BORSANYI, S. DÜRR, Z. FODOR, J. FRISON, C. HOELBLING, S. D. KATZ, S. KRIEG, T. KURTH, L. LELLOUCH, T. LIPPERT, A. PORTELLI, A. RAMOS, A. SASTRE & K. SZABÓ; “Isospin Splittings in the Light-Baryon Octet from Lattice QCD and QED”; *Phys. Rev. Lett.* **111**, p. 252001 (2013).
- [58] S. DRURY, T. BLUM, M. HAYAKAWA, T. IZUBUCHI, C. SACHRAJDA & R. ZHOU; “Determination of the non-degenerate light quark masses from electromagnetic mass splittings in 2+1 flavour lattice QCD+QED”; XXXI International Symposium on Lattice Field Theory, Mainz, Germany (2013). <https://pos.sissa.it/187/268>.
- [59] S. BORSANYI, S. DURR, Z. FODOR, C. HOELBLING, S. D. KATZ, S. KRIEG, L. LELLOUCH, T. LIPPERT, A. PORTELLI, K. K. SZABO & B. C. TOTH; “Ab initio calculation of the neutron-proton mass difference”; *Science* **347**, pp. 1452–1455 (2015). ISSN 0036-8075.
- [60] R. HORSLEY, Y. NAKAMURA, H. PERLT, D. PLEITER, P. E. L. RAKOW, G. SCHIERHOLZ, A. SCHILLER, R. STOKES, H. STÜBEN, R. D. YOUNG & J. M. ZANOTTI; “QED effects in the pseudoscalar meson sector”; *J. of High Energy Phys.* **2016**, p. 93 (2016).
- [61] R. HORSLEY, Y. NAKAMURA, H. PERLT, D. PLEITER, P. E. L. RAKOW, G. SCHIERHOLZ, A. SCHILLER, R. STOKES, H. STÜBEN, R. D. YOUNG & J. M. ZANOTTI; “Isospin splittings of meson and baryon masses from three-flavor lattice QCD + QED”; *J. of Phys. G* **43**, p. 10LT02 (2016).
- [62] R. HORSLEY, Z. KOUMI, Y. NAKAMURA, H. PERLT, D. PLEITER, P. E. L. RAKOW, G. SCHIERHOLZ, A. SCHILLER, H. STÜBEN, R. D. YOUNG & J. M. ZANOTTI; “Isospin splittings in the decuplet baryon spectrum from dynamical QCD + QED”; *J. of Phys. G* **46**, p. 115004 (2019).
- [63] Z. R. KORDOV, R. HORSLEY, Y. NAKAMURA, H. PERLT, P. E. L. RAKOW, G. SCHIERHOLZ, H. STÜBEN, R. D. YOUNG & J. M. ZANOTTI; “Electromagnetic contribution to  $\Sigma$ - $\Lambda$  mixing using lattice QCD + QED”; *Phys. Rev. D* **101**, p. 034517 (2020).
- [64] S. R. BEANE, W. DETMOLD, R. HORSLEY, M. ILLA, M. JAFRY, D. J. MURPHY, Y. NAKAMURA, H. PERLT, P. E. L. RAKOW, G. SCHIERHOLZ, P. E. SHANAHAN, H. STÜBEN, M. L. WAGMAN, F. WINTER, R. D. YOUNG & J. M. ZANOTTI; “Charged multi-hadron systems in lattice QCD+QED”; (2020); [arXiv:~hep-lat/2003.12130v2](https://arxiv.org/abs/2003.12130v2).
- [65] T. MÉTIVET; *Lattice QCD at the physical point : pion-pion scattering and structure of the nucleon*; Ph.D. thesis; CEA Saclay; Saint-Aubin (Essonne) (2015). <https://tel.archives-ouvertes.fr/tel-01249608/document>.
- [66] N. RIPUNJAY ACHARYA, F.-K. GUO, U.-G. MEIßNER & C.-Y. SENG; “Connected and disconnected contractions in pion-pion scattering”; *Nucl. Phys. B* **922**, pp. 480 – 498 (2017). ISSN 0550-3213.
- [67] R. C. JOHNSON; “Angular momentum on a lattice”; *Phys. Lett. B* **114**, pp. 147 – 151 (1982). ISSN 0370-2693.
- [68] B.-N. LU, T. A. LÄHDE, D. LEE & U.-G. MEIßNER; “Breaking and restoration of rotational symmetry for irreducible tensor operators on the lattice”; *Phys. Rev. D* **92**, p. 014506 (2015).
-

- 
- [69] G. STELLIN, S. ELHATISARI & U.-G. MEIßNER; “Breaking and restoration of rotational symmetry in the low energy spectrum of light  $\alpha$ -conjugate nuclei on the lattice I:  $^8\text{Be}$  and  $^{12}\text{C}$ ”; *Eur. Phys. J. A* **54**, pp. 1–31 (2018). ISSN 1434-601X.
- [70] D. LEE & R. THOMSON; “Temperature-dependent errors in nuclear lattice simulations”; *Phys. Rev. C* **75**, p. 064003 (2007).
- [71] S. KÖNIG, D. LEE & H.-W. HAMMER; “Non-relativistic bound states in a finite volume”; *Ann. Phys.* **327**, pp. 1450 – 1471 (2012). ISSN 0003-4916.
- [72] J.-Y. PANG, J.-J. WU, H.-W. HAMMER, U.-G. MEIßNER & A. RUSETSKY; “Energy shift of the three-particle system in a finite volume”; *Phys. Rev. D* **99**, p. 074513 (2019).
- [73] K. HUANG & C. N. YANG; “Quantum-Mechanical Many-Body Problem with Hard-Sphere Interaction”; *Phys. Rev.* **105**, pp. 767–775 (1957).
- [74] M. LÜSCHER; “Volume dependence of the energy spectrum in massive quantum field theories. I. Stable particle states”; *Comm. Math. Phys.* **104**, pp. 177–206 (1986)<https://projecteuclid.org/euclid.cmp/1104114998>.
- [75] M. LÜSCHER; “Volume dependence of the energy spectrum in massive quantum field theories. II. Scattering states”; *Comm. Math. Phys.* **105**, pp. 153–188 (1986)<https://projecteuclid.org/euclid.cmp/1104115329>.
- [76] M. LÜSCHER; “Two-particle states on a torus and their relation to the scattering matrix”; *Nucl. Phys. B* **354**, pp. 531 – 578 (1991). ISSN 0550-3213.
- [77] S. KÖNIG, D. LEE & H.-W. HAMMER; “Volume Dependence of Bound States with Angular Momentum”; *Phys. Rev. Lett.* **107**, p. 112001 (2011).
- [78] T. C. LUU & M. J. SAVAGE; “Extracting scattering phase shifts in higher partial waves from lattice QCD calculations”; *Phys. Rev. D* **83**, p. 114508 (2011).
- [79] M. DÖRING, U. G. MEIßNER & A. OSET, E.and Rusetsky; “Volume dependence of the energy spectrum in massive quantum field theories. I. Stable particle states”; *Eur. Phys. J. A* **48**, p. 114 (2012). ISSN 1434-601X.
- [80] C. H. KIM, C. T. SACHRAJDA & S. R. SHARPE; “Finite-volume effects for two-hadron states in moving frames”; *Nucl. Phys. B* **727**, pp. 218 – 243 (2005). ISSN 0550-3213.
- [81] K. RUMMUKAINEN & S. GOTTLIEB; “Resonance scattering phase shifts on a non-rest-frame lattice”; *Nucl. Phys. B* **450**, pp. 397 – 436 (1995). ISSN 0550-3213.
- [82] Z. DAVOUDI & M. J. SAVAGE; “Improving the volume dependence of two-body binding energies calculated with lattice QCD”; *Phys. Rev. D* **84**, p. 114502 (2011).
- [83] S. BOUR, S. KÖNIG, D. LEE, H.-W. HAMMER & U.-G. MEIßNER; “Topological phases for bound states moving in a finite volume”; *Phys. Rev. D* **84**, p. 091503 (2011).
- [84] M. GÖCKELER, R. HORSLEY, M. LAGE, U.-G. MEIßNER, P. E. L. RAKOW, A. RUSETSKY, G. SCHIERHOLZ & J. M. ZANOTTI; “Scattering phases for meson and baryon resonances on general moving-frame lattices”; *Phys. Rev. D* **86**, p. 094513 (2012).
-

- 
- [85] A. ROKASH, E. EPELBAUM, H. KREBS, D. LEE & U.-G. MEIßNER; “Finite volume effects in low-energy neutron–deuteron scattering”; *J. of Phys. G* **41**, p. 015105 (2013).
- [86] C. T. SACHRAJDA & G. VILLADORO; “Twisted boundary conditions in lattice simulations”; *Phys. Lett. B* **609**, pp. 73 – 85 (2005). ISSN 0370-2693.
- [87] M. DÖRING, U. G. MEIßNER, E. OSET & A. RUSETSKY; “Unitarized Chiral Perturbation Theory in a finite volume: Scalar meson sector”; *Eur. Phys. J. A* **47**, p. 139 (2011). ISSN 1434-601X.
- [88] R. A. BRICEÑO, Z. DAVOUDI, T. C. LUU & M. J. SAVAGE; “Two-baryon systems with twisted boundary conditions”; *Phys. Rev. D* **89**, p. 074509 (2014).
- [89] C. KÖRBER & T. C. LUU; “Applying twisted boundary conditions for few-body nuclear systems”; *Phys. Rev. C* **93**, p. 054002 (2016).
- [90] B. SCHUETRUMPE, W. NAZAREWICZ & P.-G. REINHARD; “Time-dependent density functional theory with twist-averaged boundary conditions”; *Phys. Rev. C* **93**, p. 054304 (2016).
- [91] A. CHERMAN, S. SEN, M. L. WAGMAN & L. G. YAFFE; “Exponential reduction of finite volume effects with twisted boundary conditions”; *Phys. Rev. D* **95**, p. 074512 (2017).
- [92] V. BERNARD, M. LAGE, U.-G. MEIßNER & A. RUSETSKY; “Resonance properties from the finite-volume energy spectrum”; *J. High Energy Phys.* **2008**, pp. 024–024 (2008).
- [93] R. A. BRICEÑO & M. T. HANSEN; “Multichannel  $0 \rightarrow 2$  and  $1 \rightarrow 2$  transition amplitudes for arbitrary spin particles in a finite volume”; *Phys. Rev. D* **92**, p. 074509 (2015).
- [94] K. POLEJAEVA & A. RUSETSKY; “Three particles in a finite volume”; *Eur. Phys. J. A* **48**, p. 67 (2012). ISSN 1434-601X.
- [95] U.-G. MEIßNER, G. RÍOS & A. RUSETSKY; “Spectrum of Three-Body Bound States in a Finite Volume”; *Phys. Rev. Lett.* **114**, p. 091602 (2015).
- [96] S. KÖNIG & D. LEE; “Volume dependence of N-body bound states”; *Phys. Lett. B* **779**, pp. 9 – 15 (2018). ISSN 0370-2693.
- [97] F. ROMERO-LÓPEZ, A. RUSETSKY, N. SCHLAGE & C. URBACH; “Relativistic  $N$ -particle energy shift in finite volume”; (2020); [arXiv:~hep-lat/2010.11715](https://arxiv.org/abs/2010.11715).
- [98] R. A. BRICEÑO, J. J. DUDEK & R. D. YOUNG; “Scattering processes and resonances from lattice QCD”; *Rev. Mod. Phys.* **90**, p. 025001 (2018).
- [99] A. DUNCAN, E. EICHEN & H. THACKER; “Electromagnetic Splittings and Light Quark Masses in Lattice QCD”; *Phys. Rev. Lett.* **76**, pp. 3894–3897 (1996).
- [100] S. R. BEANE, E. CHANG, W. DETMOLD, H. W. LIN, T. C. LUU, K. ORGINOS, A. PARREÑO, M. J. SAVAGE, A. TOROK & A. WALKER-LOUD; “Deuteron and exotic two-body bound states from lattice QCD”; *Phys. Rev. D* **85**, p. 054511 (2012).
- [101] T. YAMAZAKI, K. ISHIKAWA, Y. KURAMASHI & A. UKAWA; “Helium nuclei, deuteron, and dineutron in 2+1 flavor lattice QCD”; *Phys. Rev. D* **86**, p. 074514 (2012).
-

- [102] S. R. BEANE, E. CHANG, S. D. COHEN, W. DETMOLD, H. W. LIN, T. C. LUU, K. ORGINOS, A. PARREÑO, M. J. SAVAGE & A. WALKER-LOUD; “Light nuclei and hypernuclei from quantum chromodynamics in the limit of SU(3) flavor symmetry”; *Phys. Rev. D* **87**, p. 034506 (2013).
- [103] S. R. BEANE, E. CHANG, S. D. COHEN, W. DETMOLD, P. JUNNARKAR, H. W. LIN, T. C. LUU, K. ORGINOS, A. PARREÑO, M. J. SAVAGE & A. WALKER-LOUD; “Nucleon-nucleon scattering parameters in the limit of SU(3) flavor symmetry”; *Phys. Rev. C* **88**, p. 024003 (2013).
- [104] C. DENG, H. CHEN & J. PING; “Can the state  $Y(4626)$  be a  $P$ -wave tetraquark state  $[cs][\bar{c}\bar{s}]$ ?” *Phys. Rev. D* **101**, p. 054039 (2020).
- [105] V. KOMAROV, D. TSIRKOV, T. AZARYAN, Z. BAGDASARIAN, S. DYMОВ, R. GEBEL, B. GOU, A. KACHARAVA, A. KHOUKAZ, A. KULIKOV, V. KURBATOV, B. LORENTZ, G. MACHARASHVILI, D. MCHEDLISHVILI, S. MERZLIAKOV, S. MIKIRTYTCHIANTS, H. OHM, M. PAPENBROCK, F. RATHMANN, V. SERDYUK, V. SHMAKOVA, H. STRÖHER, S. TRUSOV, Y. UZIKOV & Y. VALDAU; “Evidence for excitation of two resonance states in the isovector two-baryon system with a mass of 2.2 GeV/  $c^2$ ”; *Phys. Rev. C* **93**, p. 065206 (2016).
- [106] Y.-x. LIU, J.-s. LI & C.-g. BAO; “Low-lying S-wave and P-wave dibaryons in a nodal structure analysis”; *Phys. Rev. C* **67**, p. 055207 (2003).
- [107] H. CLEMENT; “On the history of dibaryons and their final observation”; *Prog. in Part. and Nucl. Phys.* **93**, pp. 195 – 242 (2017). ISSN 0146-6410.
- [108] F.-K. GUO, C. HANHART, U.-G. MEIßNER, Q. WANG, Q. ZHAO & B.-S. ZOU; “Hadronic molecules”; *Rev. Mod. Phys.* **90**, p. 015004 (2018).
- [109] U.-G. MEIßNER & J. A. OLLER; “Testing the  $\chi c 1 p$  composite nature of the  $P_c(4450)$ ”; *Phys. Lett. B* **751**, pp. 59 – 62 (2015). ISSN 0370-2693.
- [110] Y. YAMAGUCHI & E. SANTOPINTO; “Hidden-charm pentaquarks as a meson-baryon molecule with coupled channels for  $\bar{D}^{(*)}\Lambda_c$  and  $\bar{D}^{(*)}\Sigma_c^{(*)}$ ”; *Phys. Rev. D* **96**, p. 014018 (2017).
- [111] J. HE; “Understanding spin and parity of  $P_c(4450)$  and  $Y(4274)$  in a hadronic molecular state picture”; *Phys. Rev. D* **95**, p. 074004 (2017).
- [112] Y. SHIMIZU, Y. YAMAGUCHI & M. HARADA; “Heavy quark spin multiplet structure of Pc-like pentaquarks as a P-wave hadronic molecular state”; *Progress of Theoretical and Experimental Physics* **2019** (2019). ISSN 2050-3911; 123D01.
- [113] P. F. BEDAQUE & U. VAN KOLCK; “Effective field theory for few-nucleon systems”; *Ann. Rev. of Nucl. and Part. Sc.* **52**, pp. 339–396 (2002).
- [114] H.-W. HAMMER & L. PLATTER; “Efimov States in Nuclear and Particle Physics”; *Ann. Rev. of Nucl. and Part. Sc.* **60**, pp. 207–236 (2010).
- [115] H. W. GRIEßHAMMER, J. A. MCGOVERN, D. R. PHILLIPS & G. FELDMAN; “Using Effective Field Theory to analyse low-energy Compton scattering data from protons and light nuclei”; *Prog. in Part. and Nucl. Phys.* **67**, pp. 841 – 897 (2012). ISSN 0146-6410.

- 
- [116] S. KÖNIG, H. W. GRIEßHAMMER, H.-W. HAMMER & U. VAN KOLCK; “Effective theory of  $^3\text{H}$  and  $^3\text{He}$ ”; *J. of Phys. G.* **43**, p. 055106 (2016).
- [117] A. AGADJANOV; *Hadronic Electroweak Processes in a Finite Volume*; Ph.D. thesis; Univ. Bonn (2017). <http://hss.ulb.uni-bonn.de/2017/4907/4907.htm>.
- [118] G. STELLIN & U.-G. MEIßNER; “P-Wave Two-Particle Bound and Scattering States in a Finite Volume including QED”; *Eur. Phys. J. A* **57**, pp. 1–47 (2021).
- [119] P. F. BEDAQUE, H.-W. HAMMER & U. VAN KOLCK; “Narrow resonances in effective field theory”; *Phys. Lett. B* **569**, pp. 159 – 167 (2003). ISSN 0370-2693.
- [120] R. OMNÈS; *Introduction to Particle Physics* (Wiley Interscience, John Wiley & Sons, New York) (1970).
- [121] T. KINOSHITA & M. NIO; “Radiative corrections to the muonium hyperfine structure: The  $\alpha^2(Z\alpha)$  correction”; *Phys. Rev. D* **53**, pp. 4909–4929 (1996).
- [122] W. E. CASWELL & G. P. LEPAGE; “Effective lagrangians for bound state problems in QED, QCD, and other field theories”; *Phys. Lett. B* **167**, pp. 437 – 442 (1986). ISSN 0370-2693.
- [123] A. L. FETTER & J. D. WALECKA; *Quantum Theory of Many-Particle Systems* (1970). <http://store.doverpublications.com/0486428273.html>; pag. 21-31.
- [124] H. A. BETHE & E. E. SALPETER; “Quantum Mechanics of One- and Two-Electron Systems”; in “Encyclopedia of Physics,” , *Atome I*, volume XXXV, edited by S. FLÜGGE; pp. 88–436 (Springer-Verlag, Berlin Göttingen Heidelberg) (1957).
- [125] M. H. HULL & G. BREIT; “Coulomb Wave Functions”; in “Encyclopedia of Physics,” , *Nuclear Reactions II: Theory*, volume XLI/1, edited by S. FLÜGGE; pp. 408–465 (Springer-Verlag, Berlin Göttingen Heidelberg) (1959). [https://link.springer.com/chapter/10.1007/978-3-642-45923-8\\_2](https://link.springer.com/chapter/10.1007/978-3-642-45923-8_2).
- [126] D. R. HARRINGTON; “Separable Potentials and Coulomb Interactions”; *Phys. Rev.* **139**, pp. B691–B695 (1965).
- [127] M. L. GOLDBERGER & K. M. WATSON; *Collision Theory*, Dover, Mineola (New York), USA (1964). <https://store.doverpublications.com/0486435075.html>.
- [128] E. HILF & L. POLLEY; “Note on the continuum thermal Wilson loop with space-periodic boundary conditions”; *Phys. Lett. B* **131**, pp. 412 – 414 (1983). ISSN 0370-2693.
- [129] H. A. BETHE & P. MORRISON; *Elementary Nuclear Theory* (1956).
- [130] J. C. COLLINS; *Renormalization*, Cambridge Monographs on Mathematical Physics, Cambridge University Press, Cambridge, UK (1984).
- [131] L. R. CARTER; *Molecular Symmetry and Group Theory*, John Wiley & Sons, New York (1997). <https://www.wiley.com/en-us/Molecular+Symmetry+and+Group+Theory-p-9780471149552>.
- [132] P. RAMOND; *Field Theory: A Modern Primer*, 2nd edition, Westview Press, Boulder (Colorado), USA (1997).
-



- 
- [133] F. L. YOST, J. A. WHEELER & G. BREIT; “Coulomb Wave Functions in Repulsive Fields”; *Phys. Rev.* **49**, pp. 174–189 (1936).
  - [134] E. E. EPELBAUM & U.-G. MEIßNER; “Charge independence breaking and charge symmetry breaking in the nucleon–nucleon interaction from effective field theory”; *Phys. Lett. B* **461**, pp. 287 – 294 (1999). ISSN 0370-2693.
  - [135] W. GREINER & J. A. MARUHN; *Nuclear Models*, Springer-Verlag, Berlin (1996). <https://link.springer.com/book/10.1007/978-3-642-60970-1>.
  - [136] T. MEHEN & I. W. STEWART; “Radiation pions in two-nucleon effective field theory”; *Nucl. Phys. A* **665**, pp. 164 – 182 (2000). ISSN 0375-9474.
  - [137] S. L. ALTMANN; “On the symmetries of spherical harmonics”; *Math. Proc. of the Cambridge Phil. Soc.* **53**, p. 343–367 (1957).
  - [138] R. BROCKMANN & J. FRANK; “Lattice quantum hadrodynamics”; *Phys. Rev. Lett.* **68**, pp. 1830–1833 (1992).
  - [139] J. D. WALECKA; “A theory of highly condensed matter”; *Ann. of Phys.* **83**, pp. 491 – 529 (1974). ISSN 0003-4916.
  - [140] H.-M. MÜLLER, S. E. KOONIN, R. SEKI & U. VAN KOLCK; “Nuclear matter on a lattice”; *Phys. Rev. C* **61**, p. 044320 (2000).
  - [141] D. LEE, B. BORASOY & T. SCHAEFER; “Nuclear lattice simulations with chiral effective field theory”; *Phys. Rev. C* **70**, p. 014007 (2004).
  - [142] K. SYMANZIK; “Cutoff dependence in lattice  $\phi_4^4$  theory”; in “Recent developments in gauge theories,” , *NATO Advanced Study Institutes Series*, volume 59, edited by G. t’HOOFT; chapter 59, p. 313 (Springer, Boston, MA (USA)) (1980).
  - [143] P. WEISZ; “Continuum limit improved lattice action for pure Yang-Mills theory (I)”; *Nucl. Phys. B* **212**, pp. 1 – 17 (1983). ISSN 0550-3213.
  - [144] K. SYMANZIK; “Continuum limit and improved action in lattice theories: (I). Principles and  $\phi^4$  theory”; *Nucl. Phys. B* **226**, pp. 187 – 204 (1983). ISSN 0550-3213.
  - [145] G. PARISI; “Symanzik’s improvement program”; *Nucl. Phys. B* **254**, pp. 58 – 70 (1985). ISSN 0550-3213.
  - [146] C. GATtringER & C. B. LANG; *Quantum Chromodynamics on the Lattice*; Lecture Notes in Physics (Springer-Verlag, Berlin Heidelberg) (2010); ISBN 978-3-642-01849-7; an optional note.
  - [147] K. G. WILSON; “Confinement of quarks”; *Phys. Rev. D* **10**, pp. 2445–2459 (1974).
  - [148] K. OSTERWALDER & E. SEILER; “Gauge field theories on a lattice”; *Ann. of Phys.* **110**, pp. 440 – 471 (1978). ISSN 0003-4916.
  - [149] J.-M. DROUFFE & J.-B. ZUBER; “Strong coupling and mean field methods in lattice gauge theories”; *Phys. Rep.* **102**, pp. 1 – 119 (1983). ISSN 0370-1573.
-

- 
- [150] J. E. MANDULA, G. ZWEIG & J. GOVAERTS; "Covariant lattice glueball fields"; *Nucl. Phys. B* **228**, pp. 109 – 121 (1983). ISSN 0550-3213.
- [151] C. B. LANG; "A study of rotational symmetry of the lattice  $\phi^4$  model"; *Nucl. Phys. B - Proc. Suppl.* **17**, pp. 665 – 668 (1990). ISSN 0920-5632.
- [152] C. B. LANG & C. REBBI; "Potential and restoration of rotational symmetry in SU(2) lattice gauge theory"; *Phys. Lett. B* **115**, pp. 137 – 142 (1982). ISSN 0370-2693.
- [153] B. BERG & A. BILLOIRE; "Glueball spectroscopy in 4d SU(3) lattice gauge theory (I)"; *Nucl. Phys. B* **221**, pp. 109 – 140 (1983). ISSN 0550-3213.
- [154] Z. DAVOUDI & M. J. SAVAGE; "Restoration of rotational symmetry in the continuum limit of lattice field theories"; *Phys. Rev. D* **86**, p. 054505 (2012).
- [155] J. J. DUDEK, R. G. EDWARDS, M. J. PEARDON, D. G. RICHARDS & C. E. THOMAS; "Highly Excited and Exotic Meson Spectrum from Dynamical Lattice QCD"; *Phys. Rev. Lett.* **103**, p. 262001 (2009).
- [156] D. BAYE & P.-H. HEENEN; "Angular momentum projection on a mesh of cranked Hartree-Fock wave functions"; *Phys. Rev. C* **29**, pp. 1056–1068 (1984).
- [157] J. A. WHEELER; "Molecular Viewpoints in Nuclear Structure"; *Phys. Rev.* **52**, pp. 1083–1106 (1937).
- [158] G. STELLIN, L. FORTUNATO & A. VITTURI; "Electromagnetic selection rules in the triangular  $\alpha$ -cluster model of  $^{12}\text{C}$ "; *J. of Phys. G* **43**, p. 085104 (2016).
- [159] L. FORTUNATO, G. STELLIN & A. VITTURI; "Electromagnetic Selection Rules for  $^{12}\text{C}$  in a 3  $\alpha$  Cluster Model"; *Few-Body Systems* **58**, p. 19 (2017). ISSN 1432-5411.
- [160] C. J. HALCROW & J. I. RAWLINSON; "Electromagnetic transition rates of  $^{12}\text{C}$  and  $^{16}\text{O}$  in rotational-vibrational models"; *Phys. Rev. C* **102**, p. 014314 (2020).
- [161] L. R. HAFSTAD & E. TELLER; "The Alpha-Particle Model of the Nucleus"; *Phys. Rev.* **54**, pp. 681–692 (1938).
- [162] D. BRINK; "The Alpha Particle Model of Light Nuclei"; *Proceedings of the International School E. Fermi - Varenna* **36**, pp. 247–277 (1966).
- [163] S. SAITO; "Interaction between Clusters and Pauli Principle"; *Progr. of Theor. Phys.* **41**, pp. 705–722 (1969). ISSN 0033-068X.
- [164] S. L. KAMENY; " $\alpha$ -Particle Model of  $\text{O}^{16}$ "; *Phys. Rev.* **103**, pp. 358–364 (1956).
- [165] E. UEGAKI, Y. ABE, S. OKABE & H. TANAKA; "Structure of the excited states in  $^{12}\text{C}$ . II"; *Prog. of Theor. Phys.* **62**, pp. 1621–1640 (1979).
- [166] A. E. GLASSGOLD & A. GALONSKY; "Alpha-Particle Model of  $^{12}\text{C}$ "; *Phys. Rev.* **103**, pp. 701–703 (1956).
- [167] H. HORIUCHI; "Three-Alpha Model of  $^{12}\text{C}$ , Orthogonality Condition Model as an approximation of Resonating Group Treatment"; *Prog. of Theor. Phys.* **51**, pp. 1266–1268 (1974).
-



- 
- [168] E. UEGAKI, S. OKABE, Y. ABE & H. TANAKA; "Structure of the excited states in  $^{12}\text{C}$ . I"; *Prog. of Theor. Phys.* **57**, pp. 1262–1276 (1977).
- [169] I. N. FILIKHIN & S. L. YAKOVLEV; " $^{16}\text{O}$  nucleus in the  $4\alpha$  cluster model"; *Phys. of Atom. Nucl.* **63**, pp. 343–352 (2000).
- [170] D. J. MARÍN-LÁMBARRI, R. BIJKEER, M. FREER, M. GAL, T. KOKALOVA, D. J. PARKER & C. WHELDON; "Evidence for Triangular  $\mathcal{D}_{3h}$  Symmetry in  $^{12}\text{C}$ "; *Phys. Rev. Lett.* **113**, pp. 012502–1 (2014).
- [171] R. BIJKEER; "Discrete and continuous symmetries in  $\alpha$ -cluster nuclei"; *J. of Physics: Conf. Series* **512**, pp. 1–7 (2014).
- [172] K. IKEDA, N. TAKIGAWA & H. HORIUCHI; "The Systematic Structure-Change into the Molecule-like Structures in the Self-Conjugate  $4n$  Nuclei"; *Progr. of Theor. Phys. Suppl.* **E68**, pp. 464–475 (1968). ISSN 0375-9687.
- [173] K. IKEDA, H. HORIUCHI & S. SAITO; "Chapter I. Introduction to Comprehensive Nuclear Structure Study Based on Cluster Correlations and Molecular Viewpoint"; *Progr. of Theor. Phys. Suppl.* **68**, pp. 1–28 (1980). ISSN 0375-9687.
- [174] D. LEE, R. MINEHART, S. SOBOTTKA & K. ZIOCK; "Correlated neutron-deuteron and neutron-triton emission after pion capture on  $^{12}\text{C}$ "; *Nucl. Phys. A* **197**, pp. 106 – 110 (1972). ISSN 0375-9474.
- [175] J. HÜFNER, L. TAUSCHER & C. WILKIN; "An analysis of pion-nucleus scattering lengths within an  $\alpha$ -cluster model"; *Nucl. Phys. A* **231**, pp. 455 – 461 (1974). ISSN 0375-9474.
- [176] G. FÄLDT & L. GISLÉN; "Fragmentation of relativistic nuclei in the  $\alpha$ -particle model"; *Nucl. Phys. A* **254**, pp. 341 – 348 (1975). ISSN 0375-9474.
- [177] J.-F. GERMOND & C. WILKIN; "Pion-calcium scattering in the  $\alpha$ -particle model"; *Nucl. Phys. A* **249**, pp. 457 – 465 (1975). ISSN 0375-9474.
- [178] Z. KHAN & I. AHMAD; "Elastic and the  $2^+$  inelastic scattering of high energy protons on  $^{12}\text{C}$  and the  $\alpha$ -particle model"; *Pramana* **8**, pp. 149–158 (1977). ISSN 0973-7111.
- [179] M. FREER, H. HORIUCHI, Y. KANADA-EN'YO, D. LEE & U.-G. MEIßNER; "Microscopic clustering in light nuclei"; *Rev. Mod. Phys.* **90**, p. 035004 (2018).
- [180] J. J. GRIFFIN & J. A. WHEELER; "Collective Motions in Nuclei by the Method of Generator Coordinates"; *Phys. Rev.* **108**, pp. 311–327 (1957).
- [181] Y. C. TANG (Editor); *Proc. Int. Conf. on Clustering Phenomena in Nuclei* (IAEA, Vienna) (1969).
- [182] B. BUCK, H. FRIEDRICH & C. WHEATLEY; "Local potential models for the scattering of complex nuclei"; *Nucl. Phys. A* **275**, pp. 246 – 268 (1977). ISSN 0375-9474.
- [183] H. HORIUCHI; "A Semi-Classical Treatment of Non-Local Potentials"; *Progr. of Theor. Phys.* **64**, pp. 184–203 (1980). ISSN 0033-068X.
-

- 
- [184] S. A. SOFIANOS, K. C. PANDA & P. E. HODGSON; “The microscopic alpha-alpha potential”; *J. of Phys. G* **19**, pp. 1929–1936 (1993).
- [185] V. G. NEUDATCHIN, V. I. KUKULIN, V. L. KOROTKIKH & V. P. KORENNOY; “A microscopically substantiated local optical potential for  $\alpha$ - $\alpha$  scattering”; *Phys. Lett. B* **34**, pp. 581 – 583 (1971). ISSN 0370-2693.
- [186] V. I. KUKULIN, V. G. NEUDATCHIN & Y. F. SMIRNOV; “Microscopically substantiated local optical potentials for scattering of light nuclei”; *Nucl. Phys. A* **245**, pp. 429 – 443 (1975). ISSN 0375-9474.
- [187] S. I. FEDOTOV, O. I. KARTAVTSEV, V. I. KOCHKIN & A. V. MALYKH; “ $3\alpha$ -cluster structure of the  $0^+$  states in  $^{12}\text{C}$  and the effective  $\alpha$ - $\alpha$  interactions”; *Phys. Rev. C* **70**, p. 014006 (2004).
- [188] E. P. WIGNER; *Gruppentheorie und ihre Anwendung auf die Quantenmechanik der Atomspektren* (Vieweg & Teubner Verlag, Wiesbaden) (1931).
- [189] D. AGADJANOV; *Exploring exotic states with twisted boundary conditions*; Ph.D. thesis; Univ. Bonn (2017). <https://bonndoc.ulb.uni-bonn.de/xmlui/handle/20.500.11811/7287>.
- [190] S. ELHATISARI, K. KATTERJOHN, D. LEE, U.-G. MEIßNER & G. RUPAK; “Universal dimer–dimer scattering in lattice effective field theory”; *Phys. Lett. B* **768**, pp. 337 – 344 (2017). ISSN 0370-2693.
- [191] N. CABIBBO, L. MAIANI & O. BENHAR; *Introduzione alle Teorie di Gauge*, Editori Riuniti University Press, Roma (2016).
- [192] G. C. WICK; “Properties of Bethe-Salpeter Wave Functions”; *Phys. Rev.* **96**, pp. 1124–1134 (1954).
- [193] M. PINE, D. LEE & G. RUPAK; “Adiabatic projection method for scattering and reactions on the lattice”; *Eur. Phys. J. A* **49**, p. 151 (2013). ISSN 1434-601X.
- [194] S. ELHATISARI; “Adiabatic projection method with Euclidean time subspace projection”; *Eur. Phys. J. A* **55**, p. 144 (2019). ISSN 1434-601X.
- [195] H. F. TROTTER; “On the product of semi-groups of operators”; *Proc. Am. Math. Soc.* **10**, pp. 545–551 (1959).
- [196] M. SUZUKI; “Generalized Trotter’s formula and systematic approximants of exponential operators and inner derivations with applications to many-body problems”; *Commun. Math. Phys.* **51**, pp. 183–190 (1976).
- [197] A. BLAER & J. HAN; “Monte Carlo simulation of lattice bosons in three dimensions”; *Phys. Rev. A* **46**, pp. 3225–3233 (1992).
- [198] M. E. J. NEWMAN & G. T. BARKEMA; *Monte Carlo Methods in Statistical Physics*, Oxford University Press, Oxford (1999).
- [199] W. PURWANTO & S. ZHANG; “Quantum Monte Carlo method for the ground state of many-boson systems”; *Phys. Rev. E* **70**, p. 056702 (2004).
-

- 
- [200] B. YDRI; “Computational Physics: An Introduction to Monte Carlo Simulations of Matrix Field Theory”; (2015); [arXiv:~hep-lat/1506.02567](#).
- [201] N. METROPOLIS, A. W. ROSENBLUTH, M. N. ROSENBLUTH & A. H. TELLER; “Equation of State Calculations by Fast Computing Machines”; *J. Chem. Phys.* **21**, pp. 1087–1092 (1953).
- [202] D. LEE; “Lect. 5: *Monte Carlo methods* and Lect. 6: *Auxiliary fields*, Lecture notes on *Lattice Effective Field Theory*, Ruhr-Universität Bochum”; (2011).
- [203] S. ELHATISARI; *Low Energy Continuum and Lattice Effective Field Theories*, Ph. D. dissertation, North Carolina State University, Raleigh (2014); [arXiv:~nucl-th/1409.4048](#).
- [204] G. SUGIYAMA & S. E. KOONIN; “Auxiliary Field Monte-Carlo for Quantum Many-Body Ground States”; *Ann. Phys.* **168**, pp. 1–26 (1986). ISSN 0003-4916.
- [205] B. BORASOY, H. KREBS, D. LEE & U.-G. MEIßNER; “The triton and three-nucleon force in nuclear lattice simulations”; *Nucl. Phys. A* **768**, pp. 179 – 193 (2006). ISSN 0375-9474.
- [206] B. BORASOY, E. EPELBAUM, H. KREBS, D. LEE & U.-G. MEIßNER; “Chiral effective field theory on the lattice at next-to-leading order”; *Eur. Phys. J. A* **35**, pp. 343–355 (2008). ISSN 1434-601X.
- [207] H. KREBS, B. BORASOY, E. EPELBAUM & U.-G. MEIßNER; “Nuclear effective field theory on the lattice”; XXVI International Symposium on Lattice Field Theory, Williamsburg, USA (2008). <https://pos.sissa.it/066/023/pdf>.
- [208] J. H. SAMSON; “Auxiliary fields and the sign problem”; *Int. J. of Mod. Phys. C* **06**, pp. 427–465 (1995).
- [209] S. ZHANG; “Quantum Monte-Carlo Methods for Strongly Correlated Electron Systems”; in “Theoretical Methods for Strongly Correlated Electrons,” , edited by D. SÉNÉCHAL, A.-M. TREMBLAY & C. BOURBONNAIS; CRM Series in Mathematical Physics; pp. 39–74 (Springer, New York) (2004); ISBN 978-0-387-00895-0.
- [210] D. LEE; “Large- $N$  droplets in two dimensions”; *Phys. Rev. A* **73**, p. 063204 (2006).
- [211] D. LEE; “Lattice methods and the nuclear few- and many-body problem, LNP”; *An Advanced Course in Computational Nuclear Physics* **936**, pp. 237–261 (2017). ISSN 1432-5411.
- [212] C. KÖRBER, E. BERKOWITZ & T. C. LUU; “Hubbard-Stratonovich-like Transformations for Few-Body Interactions”; *EPJ Web Conf.* **175**, p. 11012 (2018).
- [213] D. LEE; “Spectral Convexity for Attractive  $SU(2N)$  Fermions”; *Phys. Rev. Lett.* **98**, p. 182501 (2007).
- [214] D. FRAME, R. HE, I. IPSEN, D. LEE, D. LEE & E. RRAPAJ; “Eigenvector Continuation with Subspace Learning”; *Phys. Rev. Lett.* **121**, p. 032501 (2018).
- [215] T. A. LÄHDE, T. LUU, D. LEE, U.-G. MEIßNER, E. EPELBAUM, H. KREBS & G. RUPAK; “Nuclear lattice simulations using symmetry-sign extrapolation”; *Eur. Phys. J. A* **51**, p. 92 (2015). ISSN 1434-601X.
-

- 
- [216] T. A. LÄHDE, E. EPELBAUM, H. KREBS, D. LEE, U.-G. MEIßNER & G. RUPAK; “Uncertainties of Euclidean time extrapolation in lattice effective field theory”; *J. of Phys. G* **42**, p. 034012 (2015).
- [217] G. G. BATROUNI & R. T. SCALETTAR; “World-line quantum Monte Carlo algorithm for a one-dimensional Bose model”; *Phys. Rev. B* **46**, pp. 9051–9062 (1992).
- [218] D. FRAME, T. A. LÄHDE, D. LEE & U.-G. MEIßNER; “Impurity lattice Monte Carlo for hypernuclei”; *Eur. Phys. J. A* **56**, p. 248 (2020). ISSN 1434-601X.
- [219] G. AUDI, O. BERSILLON, J. BLACHOT & A. H. WAPSTRA; “The NUBASE evaluation of nuclear and decay properties”; *Nucl. Phys. A* **624**, pp. 1–124 (1997).
- [220] J. H. KELLEY, J. E. PURCELL & C. G. SHEU; “Energy levels of light nuclei A=12”; *Nucl. Phys. A* **968**, pp. 71 – 253 (2017). ISSN 0375-9474.
- [221] D. N. F. DUNBAR, R. E. PIXLEY, W. A. WENZEL & W. WHALING; “The 7.68-Mev State in  $C^{12}$ ”; *Phys. Rev.* **92**, pp. 649–650 (1953).
- [222] T. KOKALOVA; “Who plays in the Hoyle band?” *EPJ Web of Conf.* **66**, pp. 1–7 (2014).
- [223] F. AJZENBERG-SELOVE; “Energy levels of light nuclei A = 11-12”; *Nucl. Phys. A* **506**, pp. 1 – 158 (1990). ISSN 0375-9474.
- [224] I. ANGELI & K. MARINOVA; “Table of experimental nuclear ground state charge radii: An update”; *Atomic Data and Nuclear Data Tables* **99**, pp. 69–95 (2013).
- [225] E. EPELBAUM, H. KREBS, T. A. LÄHDE, D. LEE, U.-G. MEIßNER & G. RUPAK; “Ab Initio Calculation of the Spectrum and Structure of  $^{16}\text{O}$ ”; *Phys. Rev. Lett.* **112**, p. 102501 (2014).
- [226] R. M. MENDEZ-MORENO, M. MORENO & T. H. SELIGMAN; “Alpha particle model calculations for  $^{12}\text{C}$  and  $^{16}\text{O}$ ”; *Nucl. Phys. A* **221**, pp. 381 – 391 (1974). ISSN 0375-9474.
- [227] D. TILLEY, H. WELLER & C. CHEVES; “Energy levels of light nuclei A = 16–17”; *Nucl. Phys. A* **564**, pp. 1 – 183 (1993). ISSN 0375-9474.
- [228] R. BIJKER, F. IACHELLO & A. LEVIATAN; “Algebraic Models of Hadron Structure. I. Non-strange Baryons”; *Ann. of Phys.* **236**, pp. 69 – 116 (1994). ISSN 0003-4916.
- [229] F. IACHELLO & R. LEVINE; *Algebraic Theory of Molecules*, Oxford University Press (1995).
- [230] R. BIJKER & F. IACHELLO; “Cluster states in nuclei as representations of a  $U(v+1)$  group”; *Phys. Rev. C* **61**, p. 067305 (2000).
- [231] I. ANGELI, Y. P. GANGRSKY, K. P. MARINOVA, I. N. BOBOSHIN, S. Y. KOMAROV, B. S. ISHKHANOV & V. V. VARLAMOV; “N and Z dependence of nuclear charge radii”; *J. of Phys. G* **36**, p. 085102 (2009).
- [232] T. MIYAGI, T. ABE, R. OKAMOTO & T. OTSUKA; “Ground-state energies and charge radii of  $^4\text{He}$ ,  $^{16}\text{O}$ ,  $^{40}\text{Ca}$ , and  $^{56}\text{Ni}$  in the unitary-model-operator approach”; *Prog. of Theor. and Exp. Phys.* **2015** (2015). ISSN 2050-3911; 041D01.
- [233] D. M. DENNISON; “Excited States of the  $^{16}\text{O}$  Nucleus”; *Phys. Rev.* **57**, pp. 454–456 (1940).
-

- 
- [234] G. STELLIN; "Simmetrie e Rotovibrazioni di Nuclei  $\alpha$ -Coniugati"; (2015). <http://tesi.cab.unipd.it/50308/>.
- [235] H. HACKENBROICH, T. SELIGMAN & W. ZAHN; " $\alpha^*$  clusters in  $^{12}\text{C}$ "; *Nucl. Phys. A* **259**, pp. 445 – 451 (1976). ISSN 0375-9474.
- [236] P. NAVRÁTIL, J. P. VARY & B. R. BARRETT; "Properties of  $^{12}\text{C}$  in the Ab Initio Nuclear Shell Model"; *Phys. Rev. Lett.* **84**, pp. 5728–5731 (2000).
- [237] P. NAVRÁTIL, R. ROTH & S. QUAGLIONI; "Ab initio many-body calculations of nucleon scattering on  $^4\text{He}$ ,  $^7\text{Li}$ ,  $^7\text{Be}$ ,  $^{12}\text{C}$ , and  $^{16}\text{O}$ "; *Phys. Rev. C* **82**, p. 034609 (2010).
- [238] S. K. BOGNER, R. J. FURNSTAHL & R. J. PERRY; "Similarity renormalization group for nucleon-nucleon interactions"; *Phys. Rev. C* **75**, p. 061001 (2007).
- [239] D. R. ENTEM & R. MACHLEIDT; "Accurate charge-dependent nucleon-nucleon potential at fourth order of chiral perturbation theory"; *Phys. Rev. C* **68**, p. 041001 (2003).
- [240] H. HORIUCHI; "Generator Coordinate Treatment of Composite Particle Reaction and Molecule-like Structures"; *Prog. of Theor. Phys.* **43**, pp. 375–389 (1970).
- [241] D. L. HILL & J. A. WHEELER; "Nuclear Constitution and the Interpretation of Fission Phenomena"; *Phys. Rev.* **89**, pp. 1102 – 1145 (1953).
- [242] N. ITAGAKI, A. OHNISHI & K. KATO; "Microscopic  $\alpha$ -Cluster Model for  $^{12}\text{C}$  and  $^{16}\text{O}$  Based on Antisymmetrized Molecular Dynamics: Consistent Understanding of the Binding Energies of  $^{12}\text{C}$  and  $^{16}\text{O}$ "; *Prog. of Theor. Phys.* **94**, pp. 1019–1038 (1995). ISSN 0033-068X.
- [243] N. ITAGAKI; "Consistent description of  $^{12}\text{C}$  and  $^{16}\text{O}$  using a finite-range three-body interaction"; *Phys. Rev. C* **94**, p. 064324 (2016).
- [244] V. C. AGUILERA NAVARRO, M. MOSHINSKY & W. W. YEH; "Harmonic-oscillator states for three-particle systems. Application to the form factor of the proton as a system of three quarks"; *Rev. Mex. Fis.* **17**(4), pp. 241–262 (1968)[https://rmf.smf.mx/pdf/rmf/17/4/17\\_4\\_241.pdf](https://rmf.smf.mx/pdf/rmf/17/4/17_4_241.pdf).
- [245] M. MOSHINSKY; "Transformation brackets for harmonic oscillator functions"; *Nucl. Phys.* **13**, pp. 104–116 (1959).
- [246] V. BARGMANN & M. MOSHINSKY; "Group theory of harmonic oscillators: (I). The Collective Modes"; *Nucl. Phys.* **18**, pp. 697 – 712 (1960). ISSN 0029-5582.
- [247] V. BARGMANN & M. MOSHINSKY; "Group theory of harmonic oscillators (II). The integrals of Motion for the quadrupole-quadrupole interaction"; *Nucl. Phys.* **23**, pp. 177 – 199 (1961). ISSN 0029-5582.
- [248] P. KRAMER & M. MOSHINSKY; "Group theory of harmonic oscillators (III). States with permutational symmetry"; *Nucl. Phys.* **82**, pp. 241 – 274 (1966). ISSN 0029-5582.
- [249] P. KRAMER & M. MOSHINSKY; "Group theory of harmonic oscillators: (IV). Dynamics of the two-, three- and four-particle systems"; *Nucl. Phys. A* **107**, pp. 481 – 522 (1968). ISSN 0375-9474.
-



- 
- [250] P. KRAMER & M. MOSHINSKY; "Group theory of harmonic oscillators: (V). The harmonic oscillator shell model"; *Nucl. Phys. A* **125**, pp. 321 – 338 (1969). ISSN 0375-9474.
- [251] M. MOSHINSKY; *The Harmonic Oscillator in modern Physics: from atoms to Quarks*, Gordon and Breach, New York (1969).
- [252] M. MOSHINSKY & T. BRODY; "Simetrias y reglas de suma de los parentesis de transformacion"; *Rev. Mex. Fís.* **9**(4), pp. 181–212 (1960)[https://rmf.smf.mx/pdf/rmf/09/4/09\\_4\\_181.pdf](https://rmf.smf.mx/pdf/rmf/09/4/09_4_181.pdf).
- [253] M. DUBOVOY & J. FLORES; "Some variational properties of harmonic oscillator wave functions"; *Rev. Mex. Fís.* **17**(4), pp. 289–299 (1968)[https://rmf.smf.mx/pdf/rmf/17/4/17\\_4\\_289.pdf](https://rmf.smf.mx/pdf/rmf/17/4/17_4_289.pdf).
- [254] V. AGUILERA NAVARRO & T. A. BRODY; "Sum rules for the Moshinsky brackets"; *Rev. Mex. Fís.* **19**, pp. 303–309 (1970)[https://rmf.smf.mx/pdf/rmf/19/3/19\\_3\\_303.pdf](https://rmf.smf.mx/pdf/rmf/19/3/19_3_303.pdf).
- [255] D. A. AGRELLO, V. C. AGUILERA-NAVARRO & J. N. MAKI; "Three-Alpha Forces in the  $^{16}\text{O}$  Nucleus"; *Rev. Bras. Fis.* **11**, pp. 163–181 (1981)<http://sbfisica.org.br/bjp/download/v11/v11a07.pdf>.
- [256] M. FREER; "The structure of  $^{12}\text{C}$  and  $^{16}\text{O}$ "; *J. of Physics: Conf. Series* **590**, pp. 1–6 (2015).
- [257] DIAS RODRIGUES, M. R., BORELLO-LEWIN, T., MIYAKE, H., CAPPUZZELLO, F., CAVALLARO, M., MIRANDA DUARTE, J. L., LIMA RODRIGUES, C., DE SOUZA, M. A., HORODYNSKI-MATSUSHIGUE, B., CUNSOLO, A., FOTI, A., UKITA, G. M., NETO DE FARIA, P., AGODI, C., DE NAPOLI, M., NICOLOSI, D., BONDÍ, D., CARBONE, D. & TROPEA, S.; "Alpha Cluster Structure in  $^{16}\text{O}$ "; *Eur. Phys. J.- Web of Conf.* **66**, p. 02093 (2014).
- [258] C. WHELDON, N. I. ASHWOOD, M. BARR, N. CURTIS, M. FREER, T. KOKALOVA, J. D. MALCOLM, S. J. SPENCER, V. A. ZIMAN, T. FAESTERMANN, R. KRÜCKEN, H.-F. WIRTH, R. HERTENBERGER, R. LUTTER & A. BERGMAIER; "High-resolution measurement of absolute  $\alpha$ -decay widths in  $^{16}\text{O}$ "; *Phys. Rev. C* **83**, p. 064324 (2011).
- [259] Y. SUZUKI; "Structure Study of  $T = 0$  States in  $^{16}\text{O}$  by  $^{12}\text{C} + \alpha$  Cluster-Coupling Model. I"; *Progress of Theoretical Physics* **55**, pp. 1751–1768 (1976). ISSN 0033-068X.
- [260] R. BIJKER; "Algebraic cluster model with tetrahedral symmetry"; *AIP Conf. Proc.* **1323**, pp. 28–39 (2010).
- [261] R. D. MOTA, V. GRANADOS, A. QUEIJEIRO, J. GARCIA & L. GUZMAN; "Creation and annihilation operators, symmetry and supersymmetry of the 3D isotropic harmonic oscillator"; *J. of Phys. A* **36**, pp. 4849–4856 (2003).
- [262] T. BRODY & M. MOSHINSKY; *Tables of Transformation Brackets for Nuclear Shell-model Calculations*, Gordon and Breach, New York (1967).
- [263] A. LEJEUNE & J. P. JEUKENNE; "Computation of Brody-Moshinsky brackets"; *Comp. Phys. Comm.* **2**, pp. 231 – 237 (1971). ISSN 0010-4655.
- [264] M. SOTONA & M. GMITRO; "Generalized transformation brackets for the harmonic oscillator functions"; *Comp. Phys. Comm.* **3**, pp. 53 – 60 (1972). ISSN 0010-4655.
-

- 
- [265] D. URSESCU, M. TOMASELLI, T. KÜHL & S. FRITZSCHE; “Symbolic algorithms for the computation of Moshinsky brackets and nuclear matrix elements”; *Comp. Phys. Comm.* **173**, pp. 140 – 161 (2005). ISSN 0010-4655.
- [266] G. RACAH; “Theory of Complex Spectra. II”; *Phys. Rev.* **62**, pp. 438–462 (1942).
- [267] G. AUDI, A. WAPSTRA & C. THIBAULT; “The Ame2003 atomic mass evaluation: (II). Tables, graphs and references”; *Nucl. Phys. A* **729**, pp. 337 – 676 (2003). ISSN 0375-9474; the 2003 NUBASE and Atomic Mass Evaluations.
- [268] A. H. WAPSTRA, G. AUDI & C. THIBAULT; “The Ame2003 atomic mass evaluation: (I). Evaluation of input data, adjustment procedures”; *Nucl. Phys. A* **729**, pp. 129 – 336 (2003). ISSN 0375-9474; the 2003 NUBASE and Atomic Mass Evaluations.
- [269] B. W. BADER & T. G. KOLDA ET AL.; *MATLAB Tensor Toolbox Version 2.6*, Sandia National Laboratories, Available Online (2015). <http://www.sandia.gov/~tgkolda/TensorToolbox/>.
- [270] L. M. DELVES & K. O. MEAD; “On the convergence rates of variational methods. I. Asymptotically diagonal systems”; *Math. of Comp.* **25**, pp. 699–716 (1971).
- [271] L. DELVES; *Variational Techniques in the Nuclear Three-Body Problem* (in *Advances in Nuclear Physics*, Vol. 5, ed. by M. Baranger and E. Vogt, Plenum Press, New York) (1972).
- [272] C. COHEN-TANNOUDJI, B. DIU & F. LALOË; *Quantum Mechanics*, Vol. II, 1st edition, John Wiley and Sons (1977).
- [273] M. E. ROSE; *Elementary Theory of Angular Momentum*, Struct. of Matter Series, John Wiley and Sons (1957). <https://store.doverpublications.com/0486684806.htm>; 2nd edition, Dover (1995).
- [274] C. COHEN-TANNOUDJI, B. DIU & F. LALOË; *Quantum Mechanics*, Vol. I, 1st edition, John Wiley and Sons (1977).
- [275] G. B. ARFKEN, H. J. WEBER & F. E. HARRIS; *Mathematical Methods for Physicists*, 7th edition, Academic Press, USA (2012). <https://www.sciencedirect.com/book/9780123846549/mathematical-methods-for-physicists#book-info>.
- [276] S. TAN; “Three-boson problem at low energy and implications for dilute Bose-Einstein condensates”; *Phys. Rev. A* **78**, p. 013636 (2008).
- [277] M. CANDILERA & A. BERTAPELLE; *Algebra lineare e primi elementi di geometria*, McGraw-Hill, New York (2011).
-